Pro-Ligand Approach for Constructing Molecular Architectures Based on 3d / 4f Ions: Evaluation of Optical and Biological Properties

A Thesis Submitted for the degree of DOCTOR OF PHILOSOPHY

By

Tokala Navaneetha



School of Chemistry
University of Hyderabad
Hyderabad 500046
Telangana
India

June, 2023

Dedication

This work is dedicated to my parents and my teachers

"Never stop fighting until you arrive at your destined place - that is, the unique you. Have an aim in life, continuously acquire knowledge, work hard, and have the perseverance to realize the great life"

Dr. A. P. J. Abdul Kalam

DECLARATION

I hereby declare that the matter embodied in the thesis entitled "Pro-Ligand Approach for Constructing Molecular Architectures Based on 3d / 4f Ions: Evaluation of Optical and Biological Properties" is the result of investigations carried out by me in the School of Chemistry, University of Hyderabad, Hyderabad, India, under the supervision of Prof. Viswanathan Baskar.

In keeping with the general practice of reporting scientific observations, due acknowledgments have been made on the basis of the findings of other investigators. Any omission, which might have occurred by oversight or error, is regretted. This research work is free from Plagiarism. I hereby agree that my thesis can be deposited in Shodhganga/INFLIBNET. A report on plagiarism statistics from the University Librarian is enclosed.

Prof. Viswanathan Baskar

Professor School of Chemistry University of Hyderabad Hyderabad - 500 046. T. Navaneetha
Tokala Navaneetha
(17CHPH06)

University of Hyderabad June, 2023



This is to certify that the thesis entitled "Pro-Ligand Approach for Constructing Molecular Architectures Based On 3d / 4f Ions: Evaluation of Optical and Biological Properties" submitted by Ms. Tokala Navaneetha holding registration number 17CHPH06 in partial fulfilment of the requirements for award of Doctor of Philosophy in the School of Chemistry is a bonafide work carried out by him under my supervision and guidance.

This thesis is free from plagiarism and has not been submitted previously in part or in full to this or any other University or Institution for award of any degree or diploma.

Parts of the thesis have been:

A. Published in the following publications:

- 1. **T. Navaneetha**, U. Ugandhar, J. Ali, S. Mondal, G. Vaitheeswaran, and Viswanathan Baskar. *Inorg. Chem.* **2020**, *59*, 6689–6696.
- 2. T. Navaneetha, A. Ali, Ch. V. Ramana, and V. Baskar. *Inorg. Chem.* **2023**, 62, 5237–5247.
- 3. **T. Navaneetha**, U. Ugandhar, C. Samuel, T. Guizouarn, F. Pointillart, R. Raghunathan, and Viswanathan Baskar. *Dalton Trans.* **2023**, DOI: 10.1039/D3DT01000G.

B. Presented in the following conferences:

1. IFSCMM-2018, 2. SIMS-2019, 3. MTIC- XVIII (2019), 4. Chemfest-2019, 5. Chemfest-2020, 6. Chemfest-2022.

Further the student has passed the following courses towards fulfilment of course work requirement for Ph.D.

	Course. No	Title	Credits	Pass/Fail
1.	CY-801	Research Proposal	4	Pass
2.	CY-805	Instrumental Methods A	4	Pass
3.	CY-806	Instrumental Methods B	4	Pass

Prof. Viswanathan Baskar

11 Bales

(Thesis Supervisor)

V. BASKAR
Professor
School of Chemistry
University of Hyderabad
Hyderabad - 500 046.

School of Chemistry

Achi Vengre

University of Hyderabad

Dean
SCHOOL OF CHEMISTRY
University of Hyderabae
Hyderabae-500 046

ACKNOWLEDGMENTS

This thesis embodies the results of the last few years' work whereby I have been accompanied and supported by many people. It is an honor and a very pleasant opportunity to be able to express my gratitude to all of them.

I invariably fall short of words to express my heartfelt gratitude to my supervisor Prof. Viswanathan Baskar. His unerring support, coherence of scientific thoughts, insightful guidance along with great enthusiasm for research navigated me during the finest moments and the darkest hours of scholarly tenure.

I would like to express my sincere thanks to my doctoral committee members, Prof. K. Muralidharan and Prof. Pradeepta K. Panda for their timely support.

Words are inadequate to express my heartiest obligation to Dr. Fabrice Pointillart for his help in Magnetic studies, Dr. Rajamani Raghunathan and Prof. Ganapathy Vaitheeswaran for their help in computational studies and Prof. Ch. Venkata Ramana and Dr. Ashif Ali for their help in biological studies.

I wish to express my deep sense of indebtedness to Prof. Ashwini Nangia, Dean School of Chemistry, and Prof. K. C. Kumara Swamy, former Dean School of Chemistry.

I wish to express my deep sense of appreciation to the technical staff working in NMR, Single crystal X-ray Diffraction, PXRD, and FESEM facilities of the school, especially SC-XRD operators Ramana Kumar Sir and Mahesh for their help whenever the time is required to collect the data.

With utmost sincerity, I thank my seniors Dr. Amaleswari Rasamsetty, Dr. Junaid Ali, Dr. Uppara Ugandhar, Dr. Suman Mondal, Mr. Gujju Narsimulu and my batchmate Smruti Pragya Behera and my juniors Mr. Calvin Samuel, Mrs. K. Gangajala for their generous help, critical suggestions and able guidance and creating a cordial environment during my stay in Lab. Their assistance during the tenure of my work is gratefully acknowledged.

My special thanks to friends, seniors, and juniors Vinod, Ishfaq, Hemanth, Ravindar, Radha, Sudhakar, Karthik, Vinay, Jayaprakash, Dr. Sowkat, Dr. Bilal, Dr. Manzoor, Basha, Dr. Chandrahas, Dr. Nagamaiah, Dr. Anil, Dr. Surya, Dr. Srinivas, Isha, Nurool, Mujahid, Sasikanth, Dr. Rutuparna, Ranadeep, Santhosh, Ramanaidu, Sandeep, Vinay Kumar, Surya, Hema, Irfan, Latha, Ramakrishna, Prachuritha, Kumari, Dr. Harilal, Dr.

Ankit, Vamshi, Rina, Intzar Ali, Keerthi, Bhavana, Lavanya, for their camaraderie,

constant support and helping me whenever necessary.

I will not be sincere in my acknowledgements if I will not extend it to my relatives

Lakshmaiah (grandfather), Lakshmamma (grandmother), my uncles Narsimulu,

Venkatesh, Rajendar, Sekhar, Venkataiah, my aunts Aruna, Swarna, Jyothi, Ramadevi

Pavani, Lakshmi, Roja (sister), Manicharan, Manipradeep, Neha, Pranush, Sai Sudansh,

Abhiram, Daksha, Sai Dhanvika for their love.

I would like to thank my respected teachers without them I cannot reach this position.

Kafiruddin sir, Kiran Sir, Srinivas Sir, Aruna Madam, Krishna sir, Edukondalu Sir,

Padmasri Madam, Anjaneyulu Sir, Ramana Reddy sir, Venkateswara Setty Sir,

Narsimulu Sir, Vijaya Lakshmi Madam, Vasanta Madam, Annapurna Madam.

I have no words to express my heartfelt gratitude and respect towards my mother

Padmamma and father Malkaiah Goud for their blessings, and endless love for teaching

me the essence of education and integrity.

I heartily thank my beloved sisters Mounika and Pallavi whose unconditional love and

affection have always been my strength.

I gratefully acknowledge to DST-INSPIRE for providing me with financial support and

the School of Chemistry, University of Hyderabad for providing instrumental facilities

and a peaceful environment to accomplish my Ph. D. degree.

University of Hyderabad June. 2023.

Tokala Navaneetha

vi

Name of the Student	Tokala Navaneetha			
Roll Number	17CHPH06			
School	School of Chemistry			
Name of Thesis Supervisor	Prof. V. Baskar			
Thesis Title	Pro-Ligand Approach for Constructing			
	Molecular Architectures Based on 3 <i>d</i> / 4 <i>f</i> Ions:			
	Evaluation of Optical and Biological Properties			

SYNOPSIS

The thesis entitled "Pro-Ligand Approach for Constructing Molecular Architectures Based on 3d / 4f Ions: Evaluation of Optical and Biological Properties". It is divided into five chapters and details of each chapter are given below.

Chapter 1

Introduction

The introduction to organostibonates and their reactivity/structure has been discussed in detail. The structural forms obtained like adamantane, cubane, triangle, butterfly, polyoxostibonates and their solution stability by ESI-MS have been dealt with exclusively. The biological applications of organostibonic acids and their derivatives known in literature have been discussed in detail. Since some of their systems have been used as ligands for forms of lanthanide clusters, a general overview of magnetism, a detailed explanation of single molecular magnetism (SMM), its operating principle, the relaxation mechanism involved, and many magnetism-related charts are also given.

Tunable Bandgap in Self-Assembled Transition Metal-Incorporated Heterometallic Ti₄Sb₂ and V₂Sb₄ Oxo Clusters

This chapter deals with the synthesis, characterization, and optical properties of transition metal-incorporated Sb₆ metal oxo clusters. These clusters are synthesized by a reaction of the organoantimonate-phosphonate cluster with transition metal salts in the presence of a base under solvothermal conditions. Single crystal X-ray diffraction revealed the formation of hexanuclear organoantimony (V) based oxo clusters $[(RSb)_2Ti_4(\mu_3-O)_2(\mu_2-O)_2(t-BuPO_3)_4(\mu_2-OCH_3)_4(OCH_3)_4]$, where $R = p-i-PrC_6H_4$ (2.1), $p-ClC_6H_4$ (2.2) and $[(p-ClC_6H_4Sb)_4V_2(O)_2(\mu_3-O)_2(\mu_2-O)_2(t-BuPO_3)_4(\mu_2-OCH_3)_4]$ (2.3). Optical absorption studies show that bandgap reduction can be achieved by incorporating appropriate transition metal into the homometallic Sb₆ oxo cluster. DFT calculations were performed to compare with the experimentally observed band gaps, which show a good correlation. The details of the synthesis, structural characterization, magnetic, and optical properties are given in this chapter.

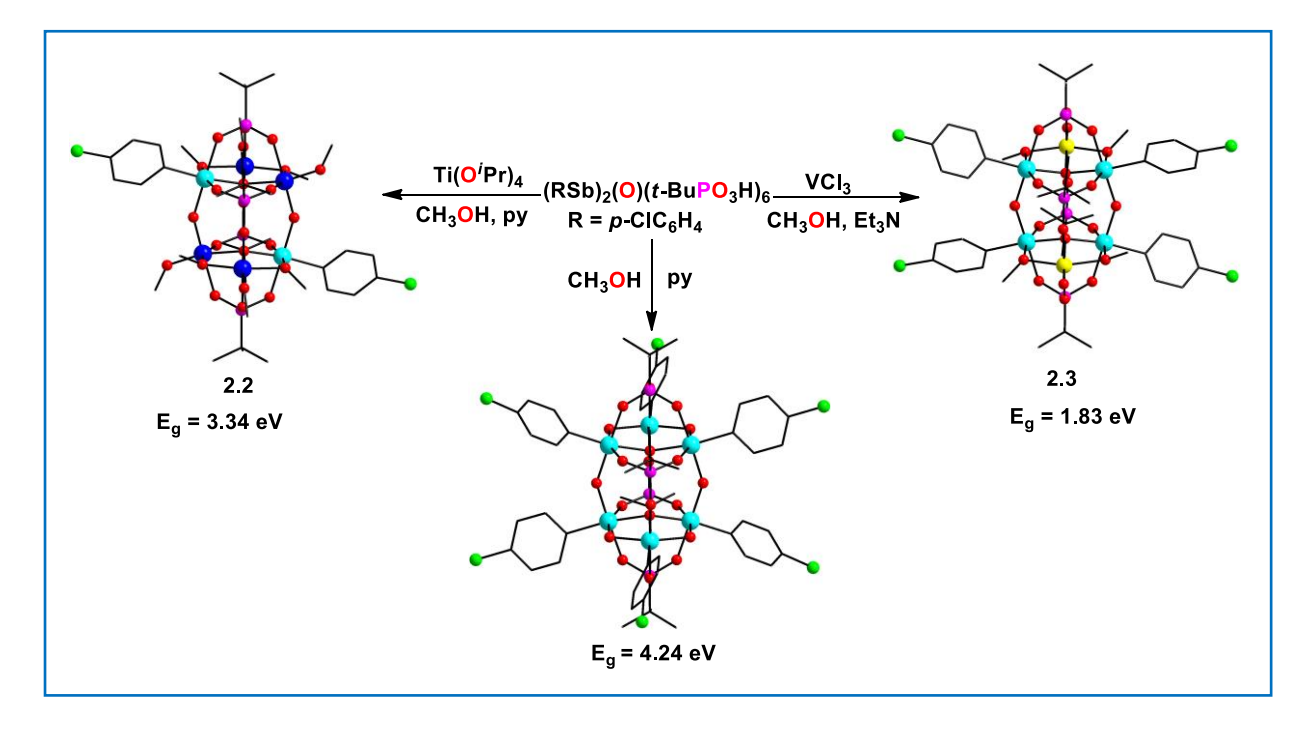


Figure 1: Synthetic scheme and molecular structures of 2.2-2.3

Discrete Metal Oxo Clusters Based on Zn^{II} and Sb^{III/V} Ions Exhibiting Interesting Antibacterial and Antioxidant Properties

This chapter deals with the synthesis, characterization, and biological properties of four different metal oxo clusters. The reactions of [Zn₃Cl₂(3,5-Me₂PzH)₄(t-BuPO₃)₂] with organostibonic acid in varying reaction conditions have been investigated. Single crystal X-ray diffraction studies reveal the formation of [Zn₂(p-ClC₆H₄Sb)₂(µ₃-O)(µ₂- $[Zn_2(p-ClC_6H_4Sb^V)_4(Sb^{III})_2(\mu_2-O)_6(\mu_3-O)_2(t-D)_5(t-D)_5($ $O(\mu_2 - OCH_3)_2(t - BuPO_3)_3(py)_2$ (3.1),(3.2),and $BuPO_3H)_4(t-BuPO_3)_2(py)_2Cl_2$ $[Zn_2(RSb)_4(\mu_3-O)_2(\mu_2-O)_2(\mu_2-OCH_3)_4(t-$ BuPO₃)₄(py)₂], where $R = p - ClC_6H_4$ (3.3) and $R = p - iPrC_6H_4$ (3.4) respectively. Interestingly, in the synthesis of 2, complete dearylation of organoantimony moieties followed by C-F bond formation, a reduction from Sb (V) to Sb (III), and Sb---Cl weak intermolecular interactions have been observed. ESI-MS studies suggested that clusters **3.1-3.4** maintained their structural integrity in the solution state also. Solution NMR studies (¹H, ³¹P, and ¹³C) support well with observed solid-state structures. **3.1-3.4** were tested for antibacterial activity using a microdilution assay. 3.1 and 3.4 showed the best activity with lower MIC values (0.78 - 6.25 µg/mL) against all the tested pathogens. activity of 3.1-3.4 The antioxidant was evaluated phosphomolybdenum assay, which showed a total antioxidant activity ranging from 28.96 to 86.46 mg AAE/g compound with the ascorbic acid standard.

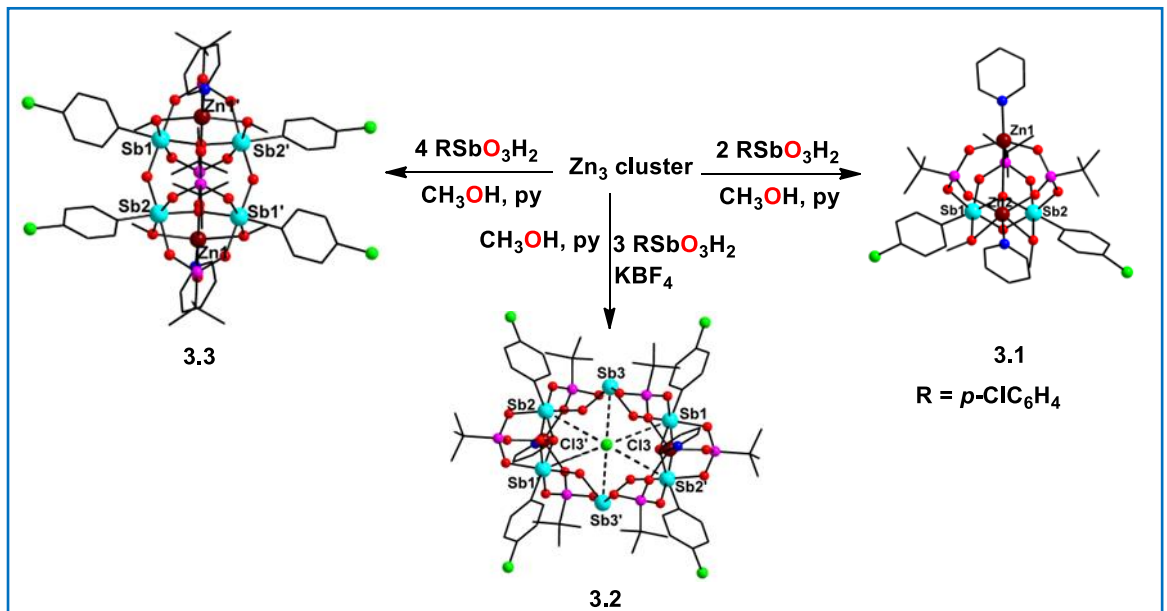


Figure 2: Synthetic scheme and molecular structures of 3.1-3.3

Octanuclear Lanthanide Oxo Clusters Stabilized by a Pro-Ligand Approach

This chapter deals with the synthesis and structural characterization of a series of mixed 4*f*-main group metal-based oxo clusters. The clusters [(*p*-ClC₆H₄Sb)₄Ln₈(μ_4 -O)₄(μ_2 -O)₂(*t*-BuPO₃)₈(μ_2 -OCH₃)₈{O₂PC(CH₃)₂C(CH₃)₂PO₂}₂(H₂O)₄], where Ln= Sm (**4.1**), Tb (**4.2**), and Dy (**4.3**) have been obtained from a reaction of the organoantimonate-phosphonate cluster with lanthanide nitrate salts in the presence of a base under solvothermal conditions. Compounds **4.1-4.3** have been characterized by single-crystal X-ray diffraction, elemental analysis, and TGA analysis. An octanuclear Ln₈ cluster, which is built of two Ln₄ distorted cubane has been stabilized by organostibonate as a ligand. Interestingly, in compounds **4.1-4.3** ethane elimination followed by C-C bond formation has been observed. The details of the synthesis and characterization are given in this chapter.

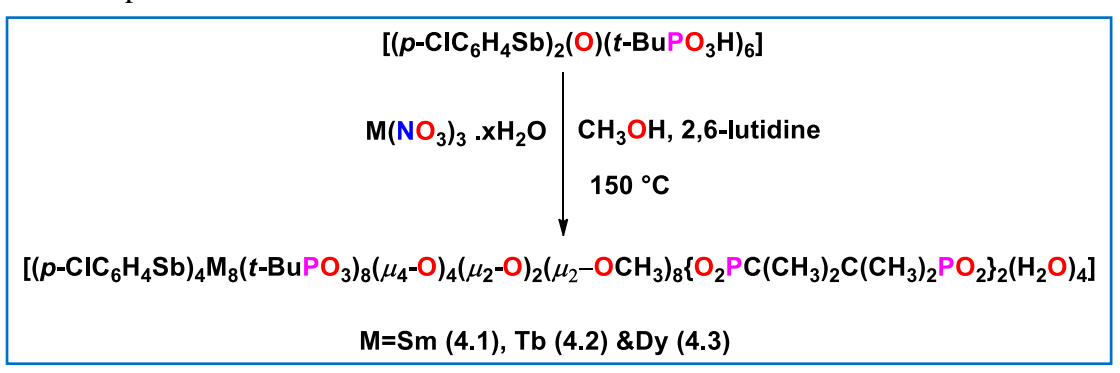


Figure 3: Synthetic scheme of 4.1-4.3

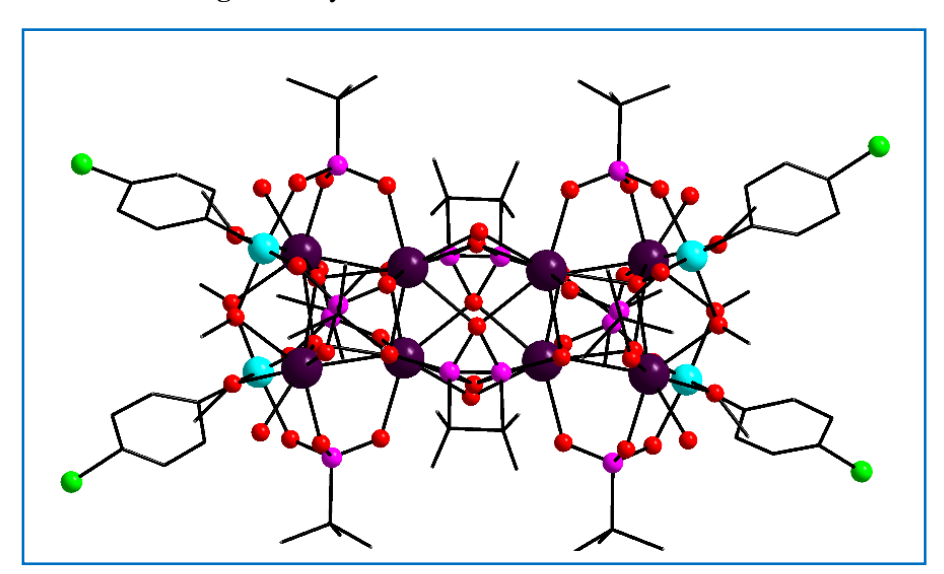


Figure 4: Molecular structure of 4.1

Ce^{IV}/Sb^V Metal Oxo Clusters Resemble Structure of Platonic Solids

This chapter deals with the synthesis and structural characterization of novel two cerium-based metal oxo clusters. These clusters are synthesized by a reaction of two different organoantimony (V) clusters with hydrated cerium nitrate in the presence of a base under solvothermal conditions. Single crystal X-ray diffraction analysis reveals the formation of clusters $[Ce^{IV}_6(p-ClC_6H_4Sb^V)_4(\mu_4-O)_4(\mu_3-O)_4(t-BuPO_3)_8(\mu_2-OCH_3)_8]$ (5.1) and $[Ce^{IV}_6(PhSb^V)_8(\mu_4-O)_8(\mu_2-O)_8(t-BuPO_3)_8(\mu_3-OCH_3)_8]$ (5.2). These two clusters were further characterized by elemental analysis, TGA analysis, and ESI-MS studies. Hexanuclear Ce₆ metal oxo clusters stabilized by *in-situ* generated pro-ligand systems. The details of the synthesis and characterization are given in this chapter.

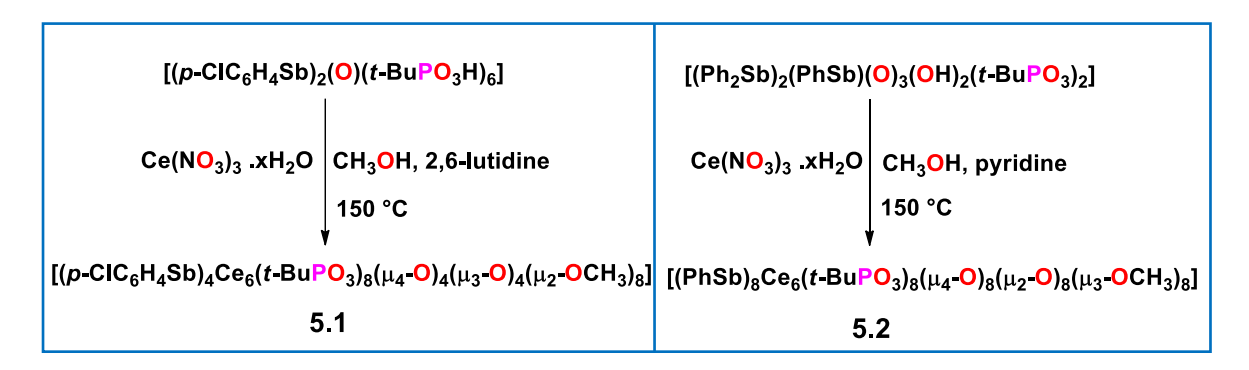


Figure 5: Synthetic scheme of 5.1-5.2

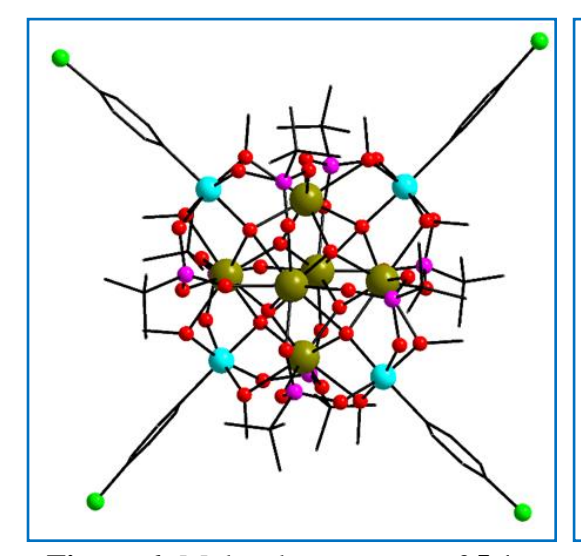


Figure 6: Molecular structure of 5.1

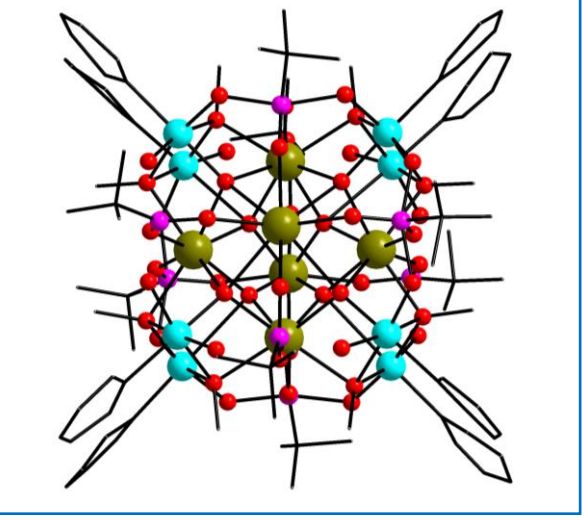


Figure 7: Molecular structure of 5.2

ABBREVIATIONS

MOF Metal-Organic Framework

POM Polyoxometalate

DMSO Dimethyl Sulfoxide

iOPr Isopropoxide

3,5-DMPz 3,5-Dimethyl Pyrazole

DCM Dichloromethane

DMF Dimethylformamide

EtOH Ethanol

MeOH Methanol

Py Pyridine

Ln Lanthanides

TM Transition Metal

MIC Minimum Inhibitory Concentration

hTopo Human Topoisomerases

Ape Apurinic/apyrimidinic Endonuclease

PTPs Protein tyrosine phosphatases

DNA Deoxyribonucleic acid

B-ZIP Basic Leucine Zipper

MTCC Microbial Type Culture Collection

MHB Mueller Hinton Broth

SMM Single-Molecule Magnet

SIM Single Ion Magnet

QTM Quantum Tunneling of Magnetization

ZFS Zero Field Splitting

Pc Phthalocyanine

Cp Cyclopentadienyl

Ac Alternating Current

Dc Direct Current

HOMO Highest Occupied Molecular Orbital

LUMO Lowest Unoccupied Molecular Orbital

DFT Density Functional Theory

PAW Projector Augmented Wave

GGA Generalized Gradient Approximation

TGA Thermogravimetric Analysis

SCXRD Single Crystal X-ray Diffraction

PXRD Powder X-Ray Diffraction

EADX Energy Dispersive X-Ray Analysis

ICP-OES Inductively Coupled Plasma Optical Emission Spectroscopy

IR Infra-red Spectroscopy

UV Ultra-Violet Spectroscopy

NMR Nuclear Magnetic Resonance Spectroscopy

ESI-MS Electrospray Ionisation Mass Spectrometry

ORTEP Oak Ridge Thermal Ellipsoid Plot

CONTENTS

Declara	tion	i
Certific	ate	iii
Acknow	vledgments	v-vi
Synopsi	is	vii-xi
Abbrev	iations	xiii-xiv
Cl 4 -	1	1 (5
Chapte Introdu		1-65
1.1	General Introduction to Antimony	1
1.2	Organostibonic Acids	3
1.2.1	Synthesis of Organostibonic Acids	3
1.2.2	Molecular Structure of Organostibonic Acids	4
1.2.3	Preparation of well-defined Organostibonic Acids	5
1.2.4	Reactivity of Arylstibonic Acids with H ₂ SO ₄ and NaOH	6
1.2.5	Preparation of Reverse-Keggin Type Clusters	7
1.2.6	Preparation of Organoantimony(V) Oxido Cubane Cluster	6
1.2.7	Reactions of Organostibonic Acids with Phenolic	
	Pyrazolyl Ligands	9
1.2.8	Preparation of Tetranuclear Adamantane Type Clusters	10
1.2.9	Preparation of Polyoxometalates	11
1.2.10	Preparation of Mixed Valent Sb(III/V) Molecular Cluster	14
1.2.11	Synthesis of μ_3 -Oxo Centered Sb ₃ Triangles	15
1.3	Preparation of Organoantimony(V) Oxides	16
1.4	Introduction to Phosphonates	16
1.5	Reactions of Organoantimonate-Phosphonate Clusters	18
1.5.1	Synthesis of Organoantimonate-Phosphoseleninate	
	Clusters	21
1.5.2	Synthesis of Sb ₆ and M ₂ Sb ₄ (M=Mn, Co, Ni and Cu) Oxo	
	Clusters	22
1.6	Reactions of Arylstibonic Acid with Phosphinic Acids	23
1.7	Reactions of Polymeric Organoantimony(V) Oxide	24
1.7.1	Reactivity of Polymeric Organoantimony(V) Oxide	

	Towards Protic Ligands	24
1.7.2	Reaction of Polymeric Triphenylantimony(V) oxide with	
	Ph ₂ TeO	25
1.8	Synthesis of Trinuclear Zinc Phosphonate Cluster	26
1.9	Cleavage of an Sb-C Bond	27
1.9.1	Monodearylation of Triphenylantimony Compound	27
1.9.2	Sb-C Bond Cleavage on a Triruthenium Cluster at Room	
	Temperature	27
1.9.3	Sb-C Bond Cleavage in (CH ₃) ₃ SbCl ₂	28
1.9.4	Sb-C Bond Cleavage in Organostiboxane Cage	28
1.9.5	<i>In Situ</i> Dearylation of [Ph ₃ Sb(t-BuPO ₃ H) ₂]	29
1.9.6	Complete Dearylation of Organostibonic Acid	29
1.9.7	Monoarylation of Organoantimony Oxo Clusters	30
1.10	Biological Applications of Organostibonic Acids	31
1.11	SMM- A Family of Lanthanide Clusters	32
1.11.1	General Introduction	32
1.11.2	Single Molecule Magnets	34
1.11.3	Relaxation Processes	34
1.11.4	Characterization of SMMs Behaviour	37
1.12	Transition Metal-Based First SMM	39
1.13	Why are Lanthanides Preferred Over Transition Metals?	42
1.14	Lanthanide-Based First SMM	45
1.15	Few Breakthrough Results of Lanthanide SMM	46
1.16	Thesis Overview	56
1.17	References	57
Chapte	er 2	67-102
	le Bandgap in Self-Assembled Transition Metal-	
_	orated Heterometallic Ti ₄ Sb ₂ and V ₂ Sb ₄ Oxo Clusters	
2.1	Introduction	68
2.2	Experimental Section	69
2.2.1	General Information	69
2.2.2	Instrumentation	69
2.2.3	General Synthetic Procedures	70

2.3	Results and Discussion	71
2.3.1	Optical studies	74
2.3.2	Magnetic Measurements	76
2.3.3	Computational Studies	77
2.4	Conclusion	81
2.5	Analytical and Spectroscopic Data	82
2.6	References	99
Chapte		103-162
	e Molecular Oxo Clusters Based on Zn ^{II} and Sb ^{III/V} Ions	
	ting Interesting Antibacterial and Antioxidant Properties	
3.1	Introduction	104
3.2	Experimental Section	105
3.2.1	General Information	105
3.2.2	Instrumentation.	105
3.2.3	General Synthetic Procedures.	106
3.3	Biological Assay	108
3.3.1	Antibacterial Assay	108
3.3.2	In Silico Computational Docking of Compounds	109
3.3.3	Antioxidant Assay	109
3.3.3.1	Phosphomolybdenum Assay	109
3.4	Results and Discussion.	110
3.4.1	Antibacterial Activity	116
3.4.2	Molecular Docking of the Compounds	118
3.4.3	Antioxidant Activity	120
3.5	Conclusion.	121
3.6	Analytical and Spectroscopic Data	122
3.7	References	159
Chapte		163-190
	clear Lanthanide Oxo Clusters Stabilized by a Pro- Approach	
4.1	Introduction	164
4.2	Experimental Section	165
121	General Information	165

4.2.2	Instrumentation	165
4.2.3	General Synthetic Procedures	166
4.3	Results and Discussion.	167
4.4	Conclusion.	170
4.5	Analytical and Spectroscopic Data	171
4.6	References	187
Chapte	er 5	191-215
	ov Metal Oxo Clusters Resemble Structure of Platonic	
Solids 5.1	Introduction	192
5.2	Experimental Section.	193
5.2.1	General Information	193
5.2.2	Instrumentation	193
5.2.3	General Synthetic Procedures	194
5.3	Results and Discussion.	195
5.4	Conclusion.	199
5.5	Analytical and Spectroscopic Data	200
5.6	References	213
	Future Scope of the Thesis	216
	List of Publications	217
	Poster and Oral Presentations / Workshops	218

CHAPTER 1

1.1 General Introduction to Antimony:

Antimony (Sb) belongs to group 15 (pnictogens) in the periodic table, present between the As and Bi elements with an atomic number of 51 and atomic weight of 121.75 amu. Antimony is a metalloid, an intermediate between metals and non-metals. Two isotopes ¹²¹Sb and ¹²³Sb, occur in nature with an abundance of 57.36% and 42.64%. Antimony often exhibits the oxidation states -III, 0, III, and V; however, environmental samples often contain III and V. Selected physicochemical properties of Sb are density at 25 °C is 6692 kg/m³, hardness (Mohs scale) is 3.0, melting and boiling points are 631 °C, 1587 °C and electronegativity (Pauling scale) is 2.05. Antimony is 0.2 ppm less abundant than As and Tl in the Earth's crust. The name of antimony is derived from the Greek words' anti plus monos, which means "a metal not obtained alone." Sb is a chalcophile associated with sulfur and precious metals Cu, Ag, and Pb. More than 264 antimony mineral phases have so far been discovered in nature. Metallic Sb is generally obtained from the mineral stibnite (Sb₂S₃), which contains 71.7% of Sb in the form of black acicular crystals. Antimony is a crystalline metalloid that is silvery-white, hard and brittle, and has low electrical and thermal conductivity. In the world, China has more antimony resources, approximately 114 antimony mines. In ancient times, sulfide of antimony was used as a copper coating and eyebrow paint. In the 19th century, antimony was used in pharmacology, dyeing, ceramics, antifriction alloy metal, agriculture, pigments, printing type, vulcanizing rubber, artillery, color glass painting, cloth and paper and also in the synthesis of safety matches and thermoelectric apparatus. Antimony is used in flame retardants for textiles. In World War II, antimony-contained lead acid batteries were used in military vehicles. Sb₂S₃ was used in bomb fuses, producing white clouds on detonation and in artillery projectiles. A bearing metal made of antimony and lead alloy was utilized and a Britannia metal made of antimony and tin alloy. Antimony trioxide was utilized in polyethylene terephthalate and flame retardants. Generally, when Sb₂O₃ is present alone, its flame-retardant properties are minimal, but they become significant when it is coupled with halogens and the system is used for making plastics, adhesives, textiles, sealants, rubber, and paints. The other uses of antimony trioxide are heating stabilizer in PVC, catalyst in the preparation of PET, degassing agent in ceramic

and glass areas and opacifier pottery glazes. Antimony compounds with halogen derivatives are used as dehydrating agents, inhibiting pyrolysis in three states of matter. Sodium antimonite [NaSb(OH)₆], used in cathode ray tube glass and in the manufacture of high-quality glass, decolourant for glass sodium antimonite act as a degassing agent. Due to its antisolarant properties, sodium antimonite shields glass from being coloured by sunlight or fluorescent lighting. Sodium antimonate can also be used in smoke-suppressant and fire-retardant compounds and also in the production of metal and trioxide. Non-metallurgical uses of antimony include pharmaceuticals, fluorescent lamps, lubricants, fireworks, ammunition primers, pesticides and zinc electrowinning. Antimony with high purity is used in semiconductors which are used in diodes, Hall-effect devices and infrared detectors.¹ Antimony and antimony-based compounds have great importance in medicinal chemistry. Ancient Egyptians used antimony compounds as a medicine for fevers and skin irritation.² Brahmachari discovered Urea stibamine drug to treat the kala-azar disease in 1922.³ Antimonials in the form of meglumine antimonate (Glucantime) and sodium stibogluconate (Pentostam) are the primary drugs prescribed against leishmaniasis in the 20th century.4 Organoantimony(III) derivatives exhibit antimicrobial and antitumor properties along with cytostatic activity and their anticancer activities reveal that they are less toxic than Pt and Pd derivatives.⁵ Takahashi *et al.* reported that antimony compounds such as antimony trichloride and potassium antimony tartrate can inhibit the DNA-double strand break repair. ⁶ R. Kant and co-workers reported that the [(C₆F₅)₂SbPh] compound exhibited the potential antifungal, insecticidal and antibacterial properties and also organoantimony(III) amide derivatives have been screened to human breast adenocarcinoma and mammary cancer cell line; showed an efficient in-vitro antitumor activity and screened with different bacterial pathogens P. aeruginosa, S. aureus and K. pneumoniae; showed significant antibacterial activity and these compounds also exhibited antifungal activity. T. Kaji and co-workers reported cytotoxicity of tris(N, N-dimethylaminomethyl)phenylbismuthane (DAPBi) can be reduced by replacing Bi Sb atom, 2-(N, N-dimethylaminomethyl)phenylbis(4-methylphenyl)stibane (DAPSb). Vascular endothelial cells prevent the disorder called atherosclerosis and Metallothionein (MT) protects cells from toxic metals. The gene expression of MT-1A and MT-2A (sub isoforms of MT) induced by organoantimony derivative tris(pentafluorophenyl)stibine.⁸ Fahami et al. reported the antimicrobial activity of organoantimony(III) compounds synthesized from Schiff base ligands and these compounds also showed a pesticidal activity.9 U. Kortz et al. reported the synthesis and bioactivity of a

series of organoantimony(III) based polyoxometalates. They observed a tuning in biological

activity based on the structure-property relationship, such as changing organic groups attached to antimony and increasing the number of organoantimony(III) groups in the parent cluster.¹⁰ The metal complexes designed from an organoantimony compound have been used in the field of catalysis.¹¹

1.2 Organostibonic Acids:

In the nitrogen family, the structure of organoarsonic acid and organophosphonic acids is known, whereas the structure of organostibonic acid is not known due to poor solubility in water and organic solvents. Schmidt proposed a trimeric structure and soon after, Doak proposed a polymeric structure based on molecular weight determination. Bart reported the preparation of aromatic arsonic acids for the first time in the year 1910, aromatic arsonic acids can be prepared by a reaction of aromatic diazonium compounds with sodium arsenites in the presence of catalysts such as cupric salts or copper powder or silver powder under alkaline conditions. In the Scheller reaction (modified Bart reaction), arsonic acids are produced when aromatic diazonium salts combine with AsCl₃ in the presence of CuCl as a catalyst. The same procedure was used for the synthesis of arylstibonic acids. The Scheller reaction was used for aniline and its *m*- and *p*- substituted compounds, not for *o*-substituted compounds.

1.2.1 Synthesis of Organostibonic Acids:

Doak research group reported the preparation of organostibonic acid by Scheller reaction.¹² Yagasaki et al. reported the preparation of p-chlorophenylstibonic acid with a slight modification. ¹³ In a 500 mL conical flask, a solution of *para*-substituted aniline (0.05 mol) in EtOH (125 mL) was taken and cooled in an ice bath. To this, conc. H₂SO₄ was added with vigorous stirring. Afterward, SbCl₃ (0.05 mol) was added to the reaction mixture. Once the reaction mixture was completely dissolved, to begin diazotization, a solution of NaNO₂ was added slowly over 10 minutes. The resultant thick mixture was stirred for around 0.5 h. CuBr (1g) was added as a catalyst and the ice bath was removed. Nitrogen gas continued to evolve as the reaction mixture warmed. The latter is stirred for another 24 h at ambient temperature to remove nitrogen from the reaction mixture. A steam distillation technique was used to remove ethanol, or water (125 mL) can be added to the latter and then heated to reflux for 3 h. The precipitate was separated by filtration with a Buchner funnel, washed with water and air-dried (as dry as possible). The obtained stibonic acid having Sb₂O₃ has an impurity and they are having poor solubility in common organic solvents, so crystallization is not possible. To purify the crude stibonic acids, the obtained product is dissolved in conc. HCl or a mixture of solvents based on the solubility of crude stibonic acid and filtered again. A solution of pyridine reagent

is prepared by adding 20 mL conc. HCl to 5 mL pyridine and slowly added to the reaction mixture obtained a pyridinium salt, [pyH][ClC₆H₄SbCl₅], which is separated by filtration and washed with conc. HCl and kept for air-dried. Further, the pyridinium salt was dissolved in aq.1% Na₂CO₃ solution and added activated charcoal, then stirred for 2 to 4 h. The resultant solution is filtered and acidified with the addition of dil. HCl while vigorously stirring (**Scheme 1.1**). The free acid is separated by filtration and washed with water, then air-dried, giving a pure stibonic acid product. This preparation method is for aniline and its *para* and *meta*-substituted compounds, not for *ortho*-substituted derivatives.

Scheme 1.1: Preparation of arylstibonic acids

1.2.2 Molecular Structure of Organostibonic Acids:

After the preparation of arylstibonic acids, the precise form of arylstibonic acids was unknown. They exist as amorphous powders that are poorly soluble in organic solvents, with the exception of alkaline solutions. Schmidt proposed that arylstibonic acids exist as a trimer (I) in the solid state and dissociated as a monomer (II) in an alkaline solution (**Figure 1.1**) based on the three factors such as analytical results, pseudo acid behavior and weight loss differences on vacuum and thermal drying. In the trimeric form (I), the number of water molecules varied for different compounds and the same compound with different synthetic procedures. ¹⁴ Later, Macallum proposed a monomeric structure of arylstibonic acid based on molecular weight determination in the solution state. ¹⁵ The experimental evidence favors the Schmidt conception. Further, Doak *et al.* used new synthesis and purification methods for arylstibonic acids. Arylstibonic acid's molecular weights in various solvents were determined, and the results

showed that they exist in solid form as high molecular weight polymers with hydrogen bond formation containing the empirical formula $(ArSbO_3H_2)_x$ and $(ArSbO_3H_2.H_2O)_x$. This concept is incompatible with previous theories. Doak *et al.* also explained the pseudo-acidic behaviour of stibonic acids in the alkaline solution by observing the change from $[ArSbO_3H]^-$ to $[ArSb(OH)_5]^{.16}$ Bowen *et al.* performed the Móssbauer Study of amorphous stibonic acids. They concluded that the Sb site attained a trigonal-bipyramidal geometry and at apical positions, bridged oxygen atoms are present.¹⁷

Figure 1.1: Proposed structures of arylstibonic acids

1.2.3 Preparation of well-defined Organostibonic Acids:

In 2008, Beckmann *et al.* reported the first well-defined organostibonic acid.¹⁸ This stibonic acid can be synthesized by a kinetically controlled hydrolysis in a two-layer system of 0.1M aq. NaOH and toluene of 2, 6- Mes₂C₆H₃SbCl₄ under basic conditions (**Scheme 1.2**). SC-XRD revealed the formation of [2,6-Mes₂C₆H₃Sb(O)(OH)Cl]₂ and [2,6- Mes₂C₆H₃Sb(O)(OH)₂]₂. The crystal structure of stibonic acid consists of a Sb₂O₂ ring with two OH groups and antimony

Scheme 1.2: Synthesis of well-defined organostibonic acid

presented in the distorted trigonal-bipyramidal geometry (**Figure 1.2**). In this case, the presence of sterically hindered *m*-terphenyl moieties prevents further aggregations; hence it exists in dimeric form. The same group reported the mixed-valent Sb(III/V) oxo clusters [(2,6-Mes₂C₆H₃Sb^V)₂(ClSb^{III})₄O₈] and [(2,6-Mes₂C₆H₃Sb^V)₄(ClSb^{III})₄(HOSb^{III})₂O₁₄] under aerobic

conditions in a two-layer system of aq. NaOH and ether by a kinetically controlled basic hydrolysis of 2,6-Mes₂C₆H₃SbCl₂. Though the same reaction conditions in both cases revealed that the Sb^{III}-C linkages are more favoured towards hydrolysis compared to the Sb^V-C linkages of *m*-terphenyl groups.¹⁹

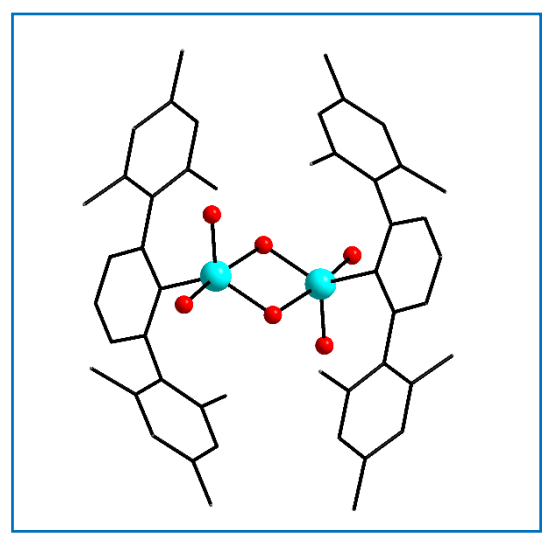
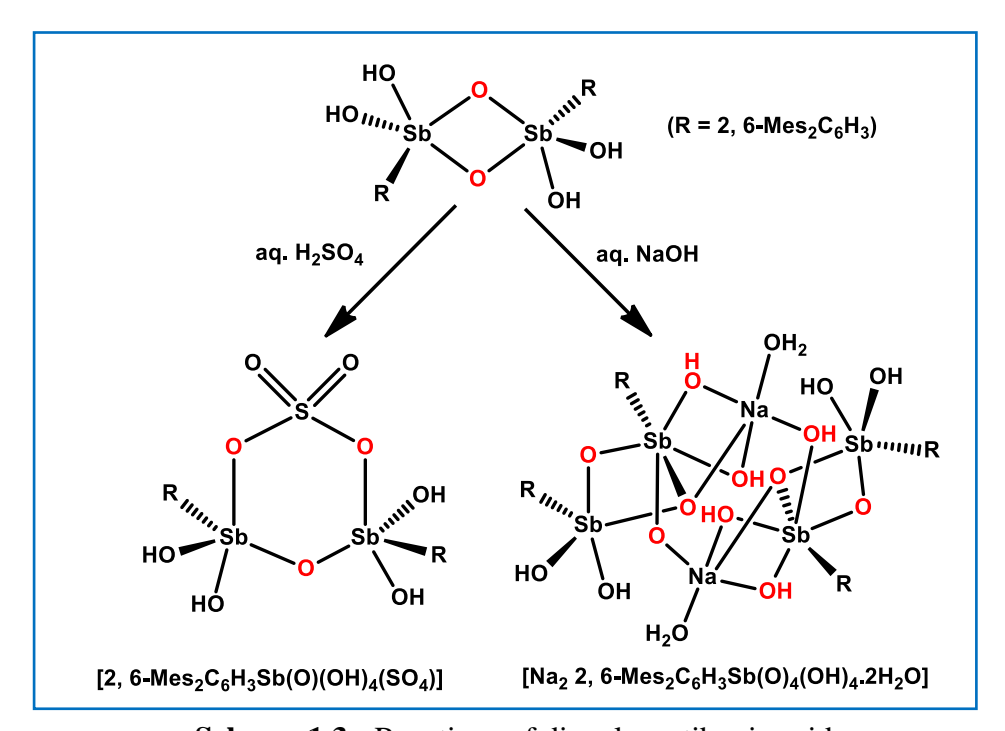


Figure 1.2: Molecular structure of [2,6-Mes₂C₆H₃Sb(O)(OH)₂]₂

1.2.4 Reactivity of Arylstibonic Acids with H₂SO₄ and NaOH:

Beckmann and co-workers reported the reactivity of stibonic acid with aq. H₂SO₄ and NaOH (**Scheme 1.3**).²⁰ The reaction between dinuclear organostibonic acid [2,6-Mes₂C₆H₃Sb(O)(OH)]₂ and sulphuric acid in a water and toluene solvent system revealed the six-membered ring [(2,6-Mes₂C₆H₃Sb)₂(O)(OH)₄SO₄]. In this case, after a reaction with the



Scheme 1.3: Reactions of dinuclear stibonic acid.

H₂SO₄, the Sb₂O₂ four-membered ring opens, followed by the generation of a six-membered heterocycle. Similarly, the reaction with 1M NaOH in a toluene and water system gave rise to tetranuclear organoantimony oxo compound [Na₂ 2,6-Mes₂C₆H₃Sb(O)₄(OH)₄.2H₂O] (**Figure 1.3**).

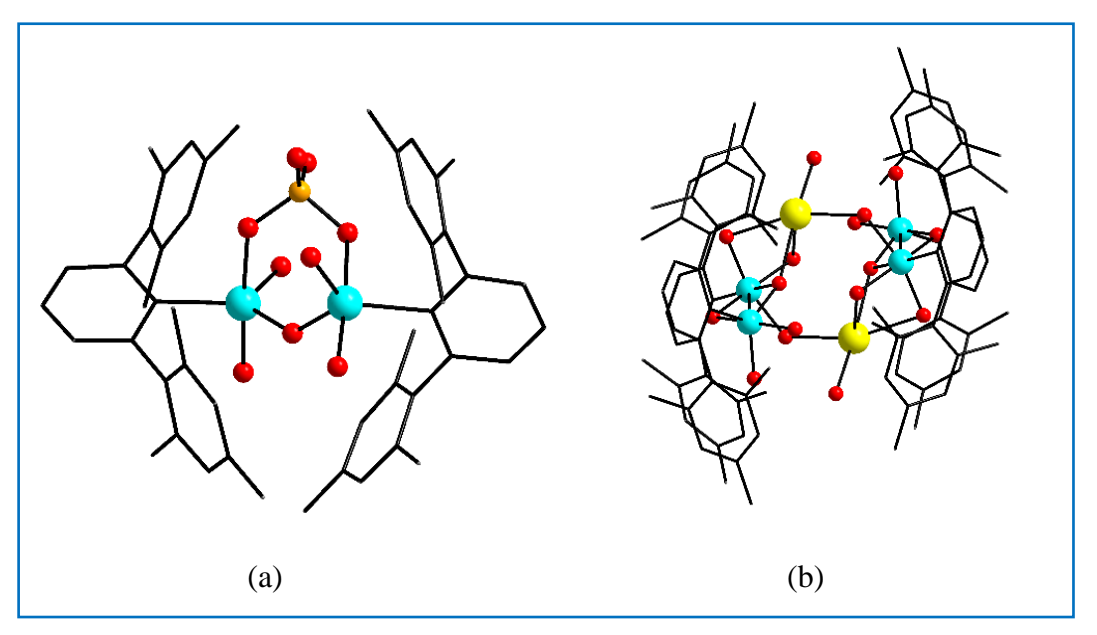


Figure 1.3: Molecular structure of (a) $[(2,6-Mes_2C_6H_3Sb)_2(O)(OH)_4SO_4]$ and (b) $[Na_2 2,6-Mes_2C_6H_3Sb(O)_4(OH)_4.2H_2O]$.

1.2.5 Preparation of Reverse-Keggin Type Clusters:

The Keggin ion with the formula $[EM_{12}O_{40}]^{x}$, where E=P, As, Sb, Bi, Co, Cu, Fe and $M=M_0$, W, V, Ti are basically well-known polyoxometalates. In Keggin ions, E (p block elements) is surrounded by tetrahedrally coordinated-oxygen atoms present at the center, with the twelve metal atoms belonging to d-block elements and metal atoms present at the corners of truncated tetrahedron arrangement. In 2007, Winpenny et al. reported the first reverse Keggin ions²¹ by a reaction of organostibonic acid with transition metal salts [Mn(OAc)₂ and Zn(OAc)₂] in the presence of a base under solvothermal conditions afforded different dodecanuclear organoantimony(V) oxo clusters $[Mn(PhSb)_{12}O_{28}\{Mn(H_2O)_3\}_2\{Mn(H_2O)_2(AcOH)\}_2]$ (Figure 1.4a), $[Mn(PhSb)_{12}O_{28}\{Mn_4(H_2O)_6(C_5H_5N)_{1.5}(MeCN)_{1.5}\}],$ [Zn(4-Cl- $C_6H_4Sb)1_2O_{28}\{Zn(H_2O)\}_4$ based on the type of base used. The solid-state structure is similar to the Keggin ions, but the p and d-block atom positions are reversed and the crystal structure description indicates that at the center of the cluster, d-block metal ions present with a tetrahedral cavity and antimony ions present at the corners of a truncated tetrahedron. This work indicates that d^5 or d^{10} metal ions are suitable for the preparation of reverse-Keggin ions and also polycondensation happens in the presence of a base. Interestingly, these POMs can

act as inorganic cryptands. Similarly, the same reaction with nickel (II) salt with NaOMe revealed the formation of polymeric nickel antimonate [Na₆(PhSb)₁₆O₃₈.10H₂O.2CH₃CN]_n, which has a one repeat unit of {Na₄(PhSb)₁₆O₃₆} cage (**Figure 1.4b**).

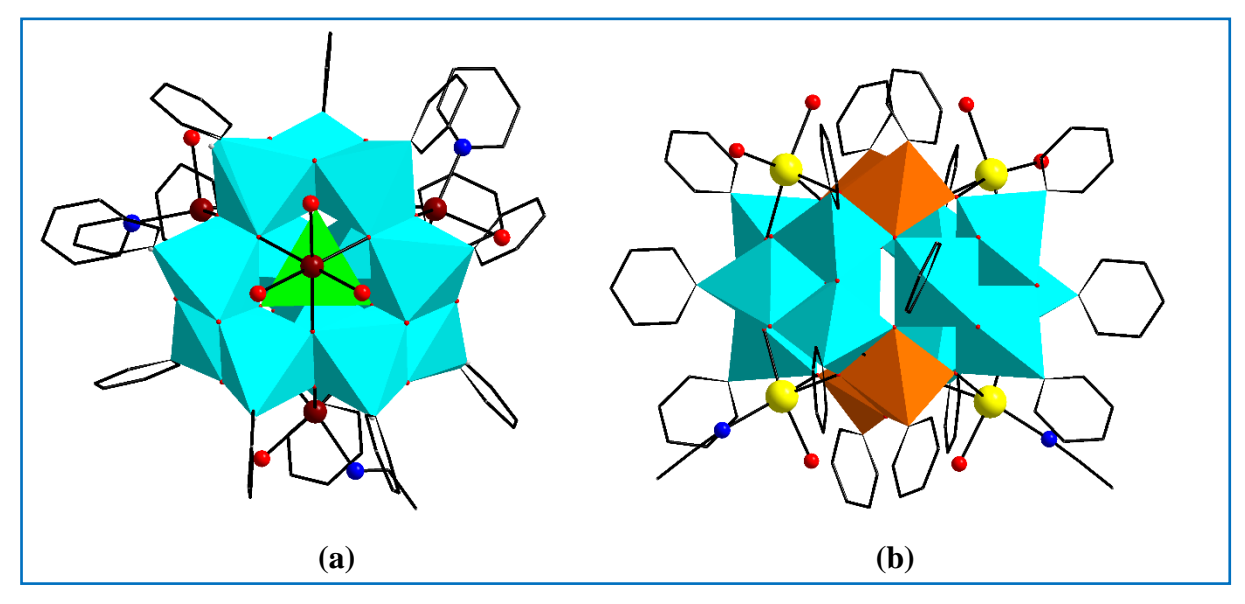
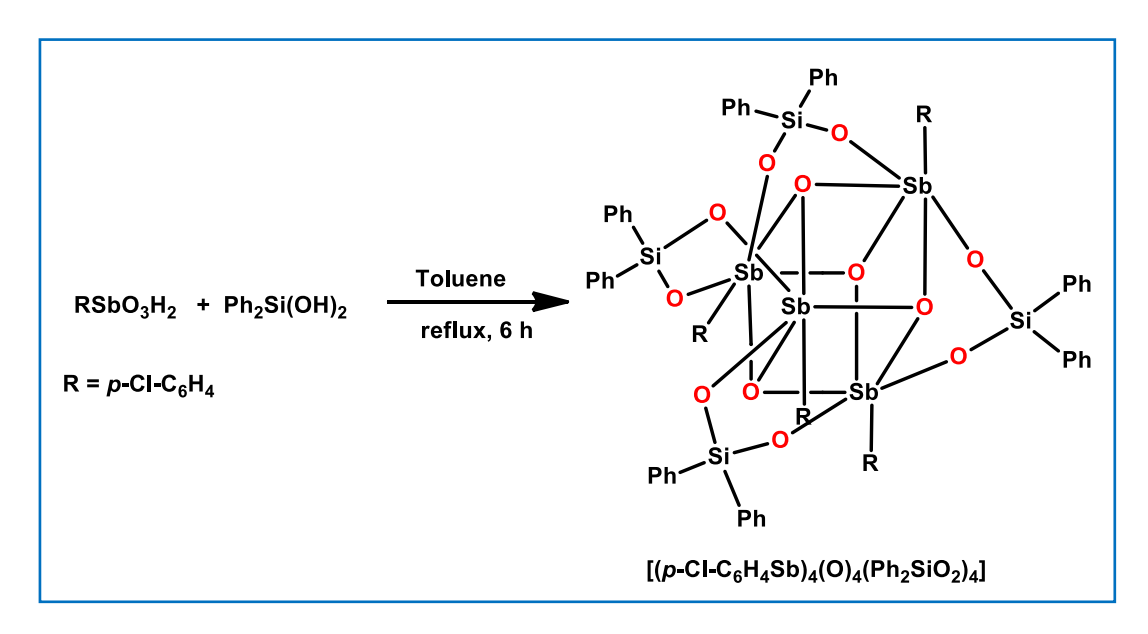


Figure 1.4: Molecular structure of (a) $[Mn(PhSb)_{12}O_{28}\{Mn(H_2O)_3\}_2\{Mn(H_2O)_2(AcOH)\}_2]$, cyan octahedra indicate SbO_5C unit and green tetrahedra indicate MnO_4 unit and (b) polymeric nickel antimonate repeat unit, $Na_4(PhSb)_{16}O_{36}\}$ cage; cyan octahedra indicate SbO_5C unit and orange octahedra indicate Sb_2O_2 units.

1.2.6 Preparation of Organoantimony(V) Oxido Cubane Cluster:

Our group successfully synthesized and characterized the first organoantimony(V) oxido cubane with an Sb^V -O-Si IV framework. The cubane cluster was synthesized by a reaction of



Scheme 1.4: Synthesis of cubane cluster.

 $RSbO_3H_2$ with diphenylsilanediol in a 1:1 ratio in reflux conditions revealing a $[(RSb)_4(O)_4(Ph_2SiO_2)_4]$ with cubane architecture (**Scheme 1.4**). The molecular core structure consists of a distorted Sb_4O_4 framework with bridging siloxide ligands across Sb atoms present at alternate corners of the Sb_4O_4 framework (**Figure 1.4**).²²

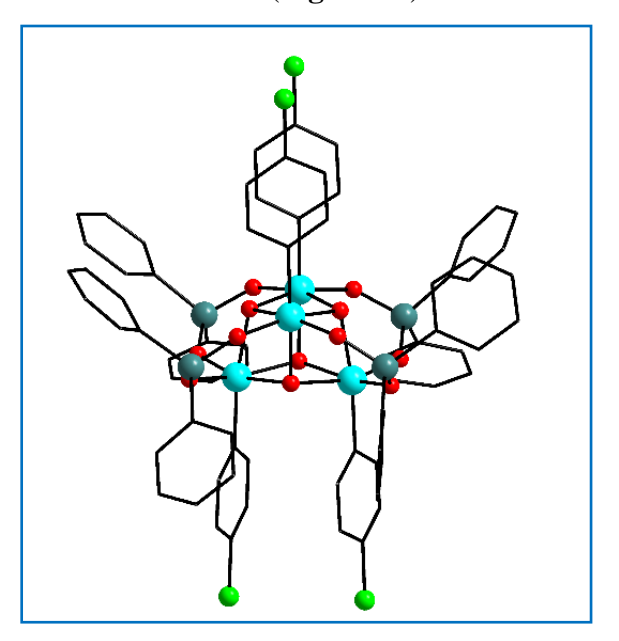


Figure 1.5: Molecular structure of [(RSb)₄(O)₄(Ph₂SiO₂)₄]

1.2.7 Reactions of Organostibonic Acids with Phenolic Pyrazolyl Ligands:

Further investigating the reactivity of organostibonic acids with phenolic pyrazolyl ligands such as H₂PhPzPh, H₂PhPzt-Bu, H₂PhPzH and 3,5-DMPz have been carried out.²³ The depolymerization reaction of RSbO₃H₂ with substituted phenolic pyrazolyl compounds in a 1:1

$$p\text{-X-C}_{6}\mathsf{H}_{4}\mathsf{SbO}_{3}\mathsf{H}_{2} + \underbrace{\mathsf{OH}\;\mathsf{HN-N}}^{\mathsf{Toluene}} \underbrace{\mathsf{I}(p\text{-X-C}_{6}\mathsf{H}_{4}\mathsf{Sb})_{4}(\mathsf{O})_{5}(\mathsf{OH})_{2}(\mathsf{HPhPzR})_{4}]}_{\mathsf{R}=\;\mathsf{Ph},\;t\text{-Bu}}$$

$$p\text{-X-C}_{6}\mathsf{H}_{4}\mathsf{SbO}_{3}\mathsf{H}_{2} + \underbrace{\mathsf{OH}\;\mathsf{HN-N}}^{\mathsf{Toluene}} \underbrace{\mathsf{I}(p\text{-X-C}_{6}\mathsf{H}_{4}\mathsf{Sb})_{4}(\mathsf{O})_{4}(\mathsf{PhPz})_{4}]}_{\mathsf{I}(p\text{-X-C}_{6}\mathsf{H}_{4}\mathsf{Sb})_{16}(\mathsf{O})_{28}(\mathsf{OH})_{8}](3,5\text{-DMPz})_{6}}$$

$$\mathsf{Toluene} \underbrace{\mathsf{Toluene}}_{\mathsf{reflux},\;6\;\mathsf{h}} \underbrace{\mathsf{I}(p\text{-X-C}_{6}\mathsf{H}_{4}\mathsf{Sb})_{16}(\mathsf{O})_{28}(\mathsf{OH})_{8}](3,5\text{-DMPz})_{6}}_{\mathsf{X}=\mathsf{Cl},\;\mathsf{Br}}$$

Scheme 1.5: Reactions of organostibonic acids.

ratio in toluene refluxed for 6 h afforded the two different tetranuclear metal oxo clusters [(p-X-C₆H₄Sb)₄O₅(OH)₂(HPhPzR)₄] and [(p-X-C₆H₄Sb)₄O₄(PhPz)₄] (**Scheme 1.5**). Here, the coordinating ability of ligands to the metal centers depends on the sterically hindered groups present on the pyrazole ligand. Interestingly, the reaction of arylstibonic acid with 3,5-dimethyl pyrazole revealed the hexadecanuclear polyoxostibonate cluster [(p-X-C₆H₄Sb)₁₆O₂₈(OH)₈](3,5-DMPz)₆], in this case, 3,5-dimethyl pyrazole act as a mild base (**Figure 1.6**).

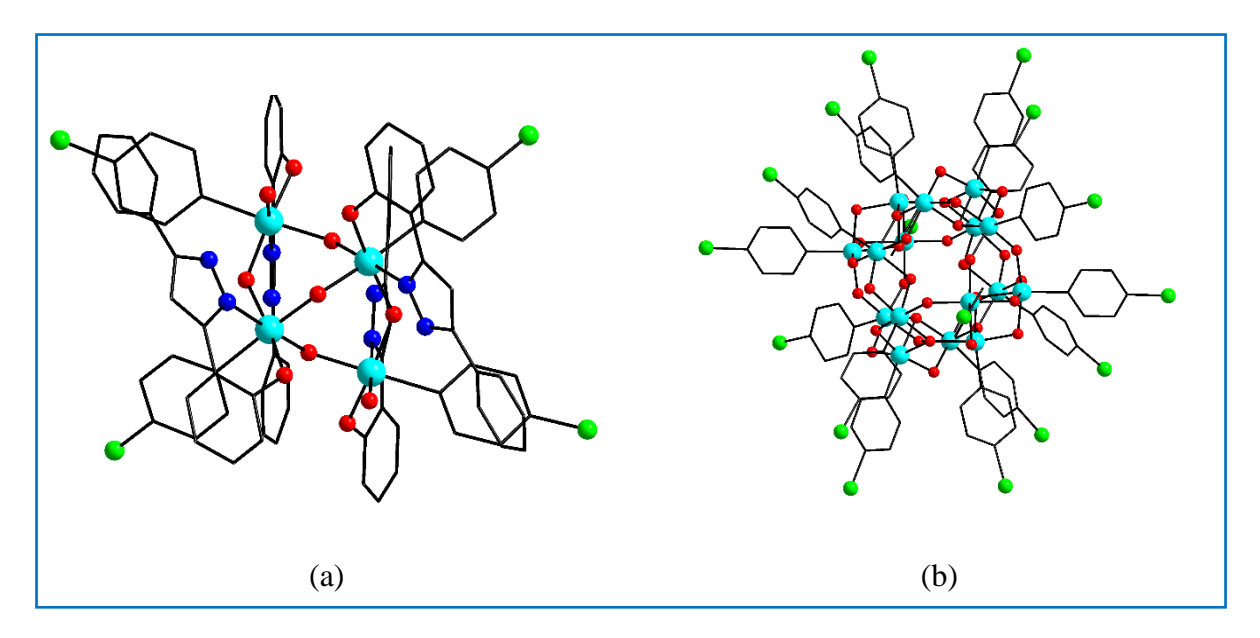
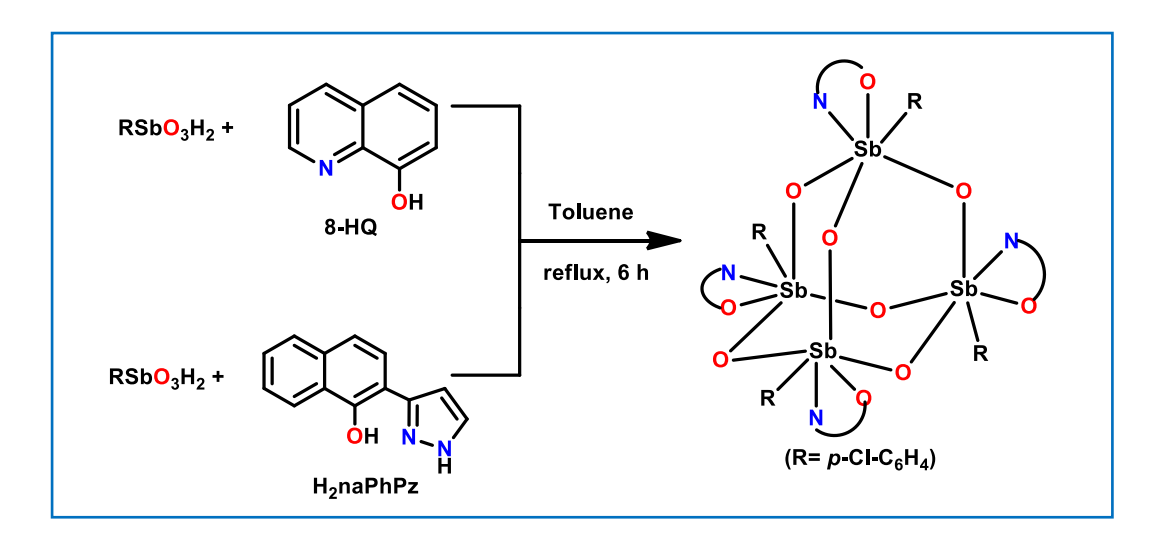


Figure 1.6: Molecular structure of (a) $[(p-X-C_6H_4Sb)_4O_5(OH)_2(HPhPzPh)_4]$ and (b) $Sb_{16}POM$.

1.2.8 Preparation of Tetranuclear Adamantane Type Clusters:

Tetranuclear stiboxanes with adamantane-type architecture were prepared by a condensation reaction of arylstibonic acid with two different ligands, 8-hydroxy quinolone and naphthyl



Scheme 1.6: Synthesis of adamantane-type cluster

phenolic pyrazole (H_2 naPhPz) in 1:2 molar ratio at reflux conditions (**Scheme 1.6**). ²⁴ SC-XRD analysis indicate the formation of [$(p-ClC_6H_4Sb)_4(O)_6(L)_4$], where L=8-HQ, H_2 naPhPz (**Figure 1.7**). These structures with Sb₄O₆ frameworks are similar to the dimer of Sb₂O₃ and Sb₂O₃ senarmontite.

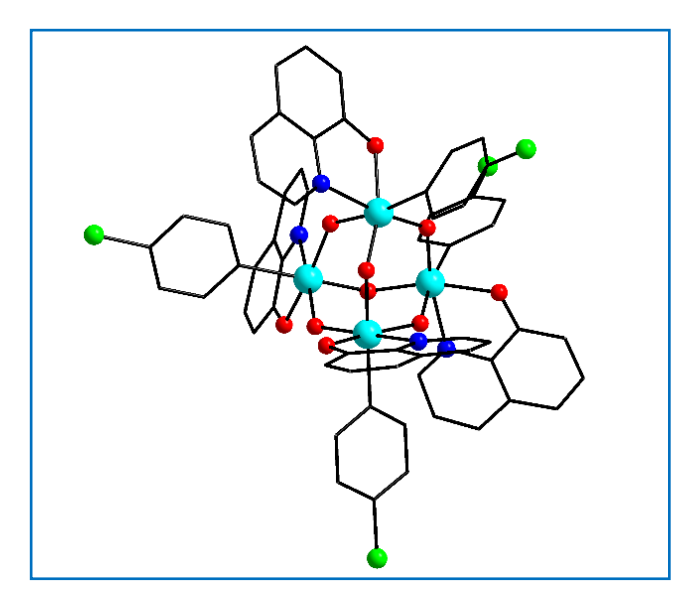


Figure 1.7: Molecular structure of $[(p-ClC_6H_4Sb)_4(O)_6(8-HQ)_4]$.

In literature, adamantane-type architectures like As₄O₆ and Bi₄O₆ are reported and so are with other main group atoms such as Sn, Al, In and Ga. Tetranuclear stiboxanes close resemble Arsenicin A, natural poly-arsenal. Arsenicin A was isolated from a poecilosclerid sponge, *Echinochalina bargibanti*, ²⁵ taken from New Caledonia. The molecular structure of Arsenicin A similar to As₄O₆, in which three CH₂ groups are replaced by oxygen atoms to generate stereocenters of As with the same configuration in every enantiomer of a racemic mixture. Wild *et al.* reported the chemical synthesis and biological activity of Arsenicin A.²⁶

Later, Beckmann *et al.* reported the second well-defined tetranuclear arystibonic acid with adamantane-type architecture.²⁷ This can be synthesized in two steps: 1) chlorination of ArSbCl₂ and 2) base hydrolysis of ArSbCl₄ affords (ArSb)₄O₆(OH)₄, where Ar= 6-diphenylphospinoacenaphth-5-yl, exhibited adamantane-type morphology. Organic substituent attached to Sb containing P-donor ligand with intramolecular nature moderates the Lewis acidity of antimony atoms avoiding the extensive aggregation and formation of polymeric structures.

1.2.9 Preparation of Polyoxometalates:

Nicholson *et al.* reported a new group of well-defined polyoxostibonates. Arylstibonic acids exist in polymeric or oligomeric form, insoluble in water and common organic solvents. A

sample of organostibonic acid is further purified by keeping the crystallization in aq.NH₃/CH₃COOH diffusion method. The obtained product is a white powder soluble in acetonitrile. The resultant solution is analyzed by using the ESI-MS technique. The ESI-MS spectrum indicates the major peak assigned as [H₇(RSb)₁₂O₂₈] and another peak assigned as a [H₆(RSb)₁₂O₂₈]². The corresponding satellite peak representing the same formula as Na⁺ is replaced by H⁺. There are a few reasons for the presence of sodium ions; stibonic acid was not completely purified, a trace amount of sodium hydroxide was added, or from the leaching of glassware. For these reasons Na⁺ is completely replaced by H⁺ in the parent stibonic acid peak forms sodium adducts $[Na_3H_3(RSb)_{12}O_{28}]^{2-}$, $[Na_2H_4(RSb)_{12}O_{28}]^{2-}$, $[NaH_5(RSb)_{12}O_{28}]^{2-}$, [Na₄H₃(RSb)₁₂O₂₈]⁻, [Na₃H₄(RSb)₁₂O₂₈]⁻.²⁸ The above POMs indicate organostibonic acids have a strong affinity with Na ions and act as an inorganic crown ligand. To avoid sodium contamination in the end product, Teflon containers were used to keep the crystallization in aq.NH₃/CH₃COOH diffusion method. Further, the reaction of the dodecanuclear organoantimony(V) cluster [H₈(RSb)₁₂O₂₈] with KOH or NaOH revealed a POMs $[M_2H_8(RSb)_{12}O_{30}]^{2-}$ (M= K or Na) (**Figure 1.8a**).²⁹ The molecular structure is present in an irregular hexagonal antiprism and contains 12 antimony atoms. The overall structure is divided into two Sb₆ arrays: the lower part of the structure attains a planar arrangement and the upper part attains a puckered chair arrangement. The encapsulated M⁺ is present in a 10-coordinate

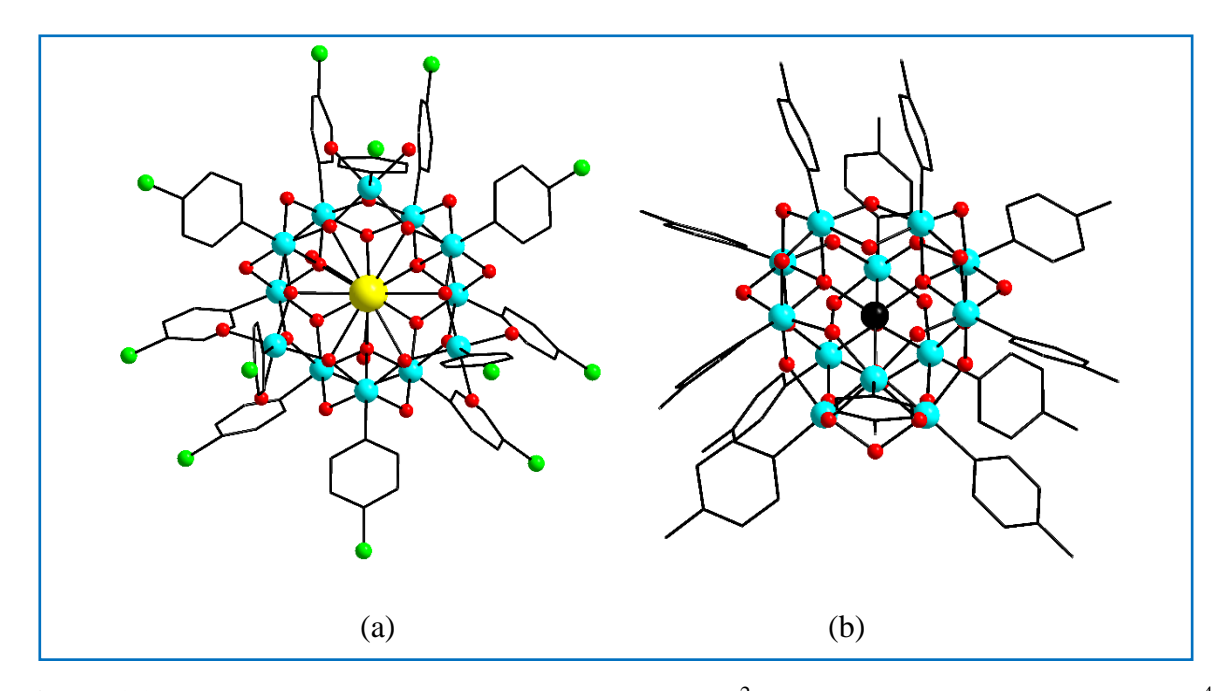


Figure 1.8: Molecular structure of (a) $[K_2H_8(RSb)_{12}O_{30}]^{2-}$ and (b) $[LiH_3(p-MeC_6H_4Sb)_{12}O_{28}]^{4-}$

mode within inorganic 12-crown-6M⁺ in the puckered hexameric face and one M⁺ six-coordinate mode. Nicholson *et al.* extended the work to know the size effect of cations to form polyoxostibonates. They choose cations that are smaller (Li) and larger (Ba) in size than Na⁺ ions. The reaction of a stibonic acid with LiOH revealed the formation of polyoxostibonate [LiH₃(*p*-MeC₆H₄Sb)₁₂O₂₈]⁴⁻. In solid-state structure, Li cation is encapsulated in {Sb₁₂O₂₈} core, which indicates the γ-Keggin ion geometry (**Figure 1.8b**). Later, the reaction of a stibonic acid with barium salts revealed the formation of POM [BaH₁₀(*p*-MeC₆H₄Sb)₁₄O₃₄].4H₂O (**Figure 1.9a**).³⁰ Incorporation of larger size Ba²⁺ ions will help to form open higher frameworks. The molecular core structure {Sb₁₄O₃₄} represents the bowl-shaped morphology. Similarly, the reaction of stibonic acid with Rb⁺ cation revealed the formation of polyoxostibonate [RbH₁₁(*p*-MeC₆H₄Sb)₁₄O₃₄] with bowl-shaped architecture.³¹ Nicholson *et al.* reported the reverse Keggins ion-based clusters under mild conditions previously winpenny *et al.* reported from solvothermal conditions. The polyoxostibonates formed under alkaline conditions, though Mo and W-based polyoxometalates formed in acidic conditions.

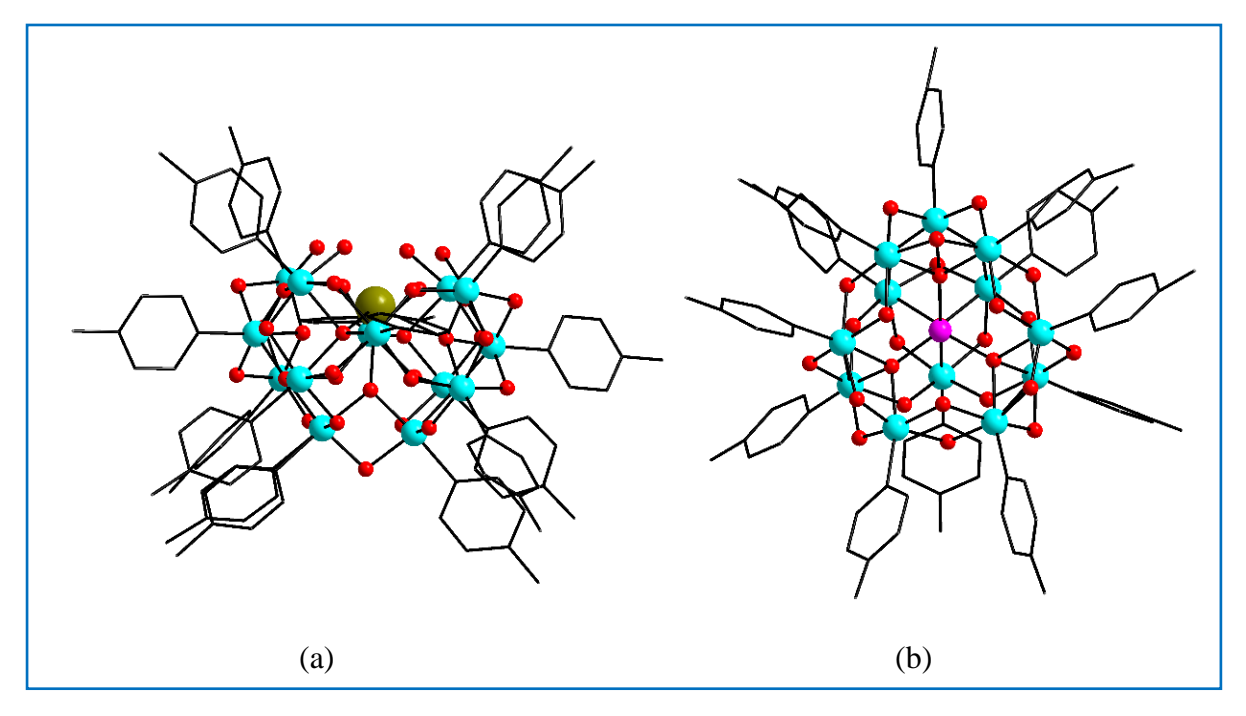


Figure 1.9: Molecular structure of (a) $[BaH_{10}(p-MeC_6H_4Sb)_{14}O_{34}].4H_2O$ and (b) $[Co(p-MeC_6H_4Sb)_{12}O_{28}\{Co(H_2O)_3\}_4]Cl_2 \cdot 6H_2O$.

The reaction between organostibonic acids and 3d metal ions Co(II) and Zn(II) in aqueous NH₃ at ambient conditions reveals the formation of four new types of polyoxometalates [Co(p-MeC₆H₄Sb)₁₂O₂₈{Co(H₂O)₃}₄]Cl₂·6H₂O, [Co(p-ClC₆H₄Sb)₁₂O₂₈{Co(H₂O)₃}₄]Cl₂·22H₂O, (PhCH₂NMe₃)₂[Zn(p-ClC₆H₄Sb)₁₂O₂₈Zn₄Cl_{2.54}Br_{1.46}]·8MeCN·H₂O and [BaCoH₄(p-MeC₆H₄Sb)O₂₈]·5H₂O.³² SC-XRD analysis indicates the presence of twelve organoantimony

groups linked with twenty-eight bridged oxygen atoms and with one 3d metal ion at the center of the tetrahedral framework (**Figure 1.9b**). Out of four structures, three clusters have ε -Keggin ion geometry and the other has a δ -Keggin ion geometry. Keggin ion isomers order was $\alpha > \beta > \gamma > \delta > \varepsilon$, it was reversed for the reverse-Keggin ion isomers. To date, antimony based ε , δ and γ isomers are known, but there are no reports on α or β isomers. ESI-MS studies confirmed the structural integrity in the solution state.

1.2.10 Preparation of Mixed Valent Sb(III/V) Molecular Cluster:

The reaction of *p*-bromophenyl stibonic acid with Ph₂TeO in a 1:1 molar ratio in toluene refluxed for 12 h reveals the formation of rare mixed valent Sb(III/V) polyoxostibonate (Ph₃Te)₂[Na₂(H₂O)₂(*p*-Br-C₆H₅Sb^V)₁₀(Sb^{III})₄(Ph₂Te)₄(O)₃₀(OH)₄] (**Scheme 1.7**).³³ The tetraphenylditelluroxane groups in this POM chelate a dianionic organoantimony oxo cluster. The total charge of the cluster is balanced by two triphenyl tellurium cations which are also present alongside the core structure. The molecular structure contains 14 antimony atoms and out of fourteen, ten antimony metal ions are in a 5+ oxidation state with an octahedral shape

RSbO₃H₂ + Ph₂TeO
$$\xrightarrow{\text{Toluene}}$$
 (Ph₃Te)₂[Na₂(H₂O)₂(RSb^V)₁₀(Sb^{III})₄(Ph₂Te)₄(O)₃₀(OH)₄]
 R= ρ -Br-C₆H₄

Scheme 1.7: Synthesis of mixed valent Sb(III/V) molecular cluster

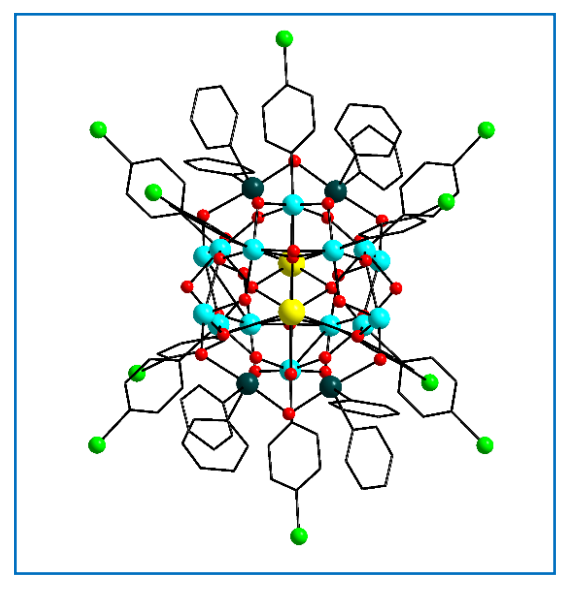
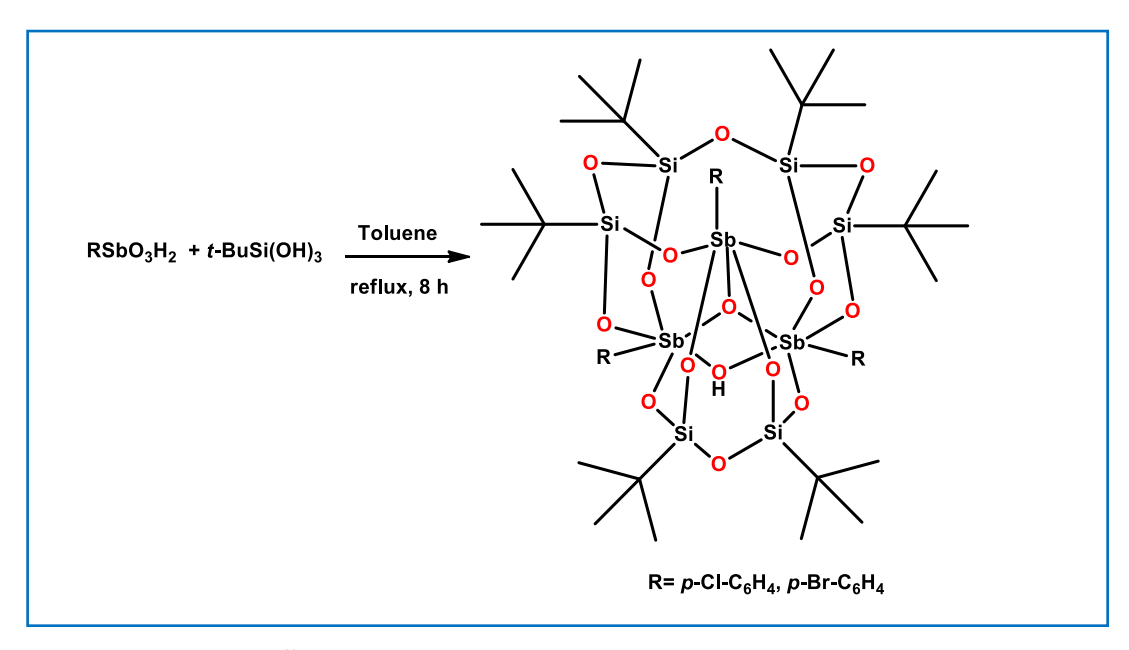


Figure 1.10: Molecular structure of $(Ph_3Te)_2[Na_2(H_2O)_2(p-Br-C_6H_5Sb^V)_{10}(Sb^{III})_4(Ph_2Te)_4(O)_{30}(OH)_4].$

and 4 antimony metal ions are in a 3+ oxidation with pseudo trigonal bipyramidal shape containing lone pair on Sb atom at the equatorial positions (**Figure 1.10**). Remarkably, complete dearylation of organostibonic acid followed by reduction of Sb(V) to Sb(III) was observed in the respective cluster. Triphenyltellurium cations present in the cluster with weak interactions stabilize the polyoxostibonates and also provide a charge balance of the overall structure.

1.2.11 Synthesis of µ3-Oxo Centered Sb3 Triangles:

Oxo-centered transition metal triangles are common and main group-based oxo centered metal triangles are scanty. Our group successfully reported the first oxo bridged oraganoantimony (V) triangle assembly by a depolymerization reaction of RSbO₃H₂ with *t*-butylsilanetriol in



Scheme 1.8: Synthesis of Sb₃ triangle

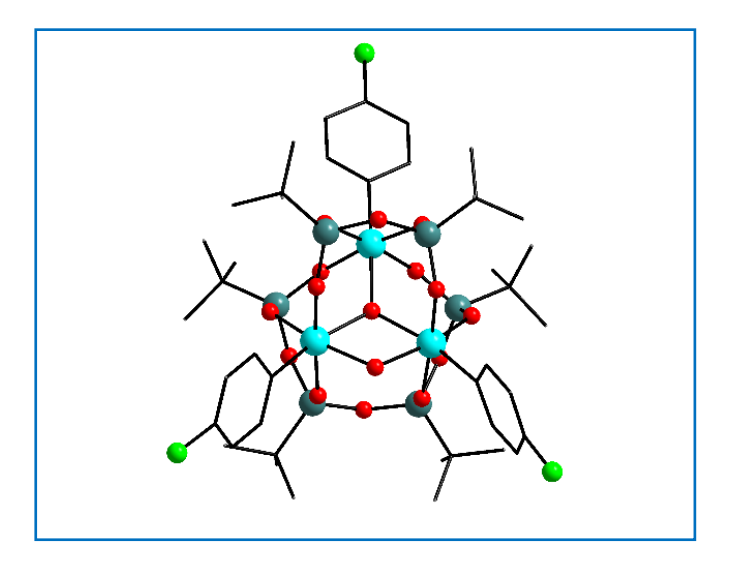


Figure 1.11: Molecular structure of $[(RSb)_3\{(t-Bu)_4Si_4O_9\}\{(t-Bu)_2Si_2O_5(\mu_3-O)(\mu-OH)].$

toluene under reflux conditions (**Scheme 1.8**). SC-XRD study elucidate the formation of $\{[C_5H_5NH][(RSb)_3\{(t-Bu)_4Si_4O_9\}\{(t-Bu)_2Si_2O_5(\mu_3-O)(\mu-OH)]\}$ (**Figure 1.11**). In this cluster, *in situ* generated a disiloxane or tetrasiloxane, or trisiloxane frameworks stabilized an Sb₃ triangle.³⁴

1.3 Preparation of Organoantimony(V) Oxides:

Polymeric triphenylantimony(V) oxides are prepared by reacting Ph_3Sb and 35% H_2O_2 in a 1:1 ratio in ice-cold acetone. ³⁵ The final reaction mixture forms a white-colored product. Similarly, the reaction of tris(2-methoxyphenyl) antimony dichloride with KO-t-Bu in 1:2.2 equivalents in the presence of H_2O in dichloromethane at 0 °C gives the tris(2-methoxyphenyl) antimony oxide (**Scheme 1.9**). ³⁶

$$Ph_{3}Sb + H_{2}O_{2} \xrightarrow{acetone} (Ph_{3}SbO)_{n}$$

$$R \xrightarrow{CI} R \xrightarrow{KO-t-Bu, H_{2}O} R \xrightarrow{R} Sb \xrightarrow{R} R$$

$$(R = 2-MeOC_{6}H_{4})$$

Scheme 1.9: Synthesis of triaryl antimony (V) oxides.

1.4 Introduction to Phosphonates:

Phosphonates have the general formula [RPO₃]²⁻, which can be obtained from the respective organophosphonic acids [RP(O)(OH)₂]. In phosphoric acid, one OH group is replaced by an alkyl/aryl group called phosphonic acids. In this case, the phosphorus atom is present in the 5+ oxidation state and contains tetra-coordination modes. Phosphonic acids belong to the group

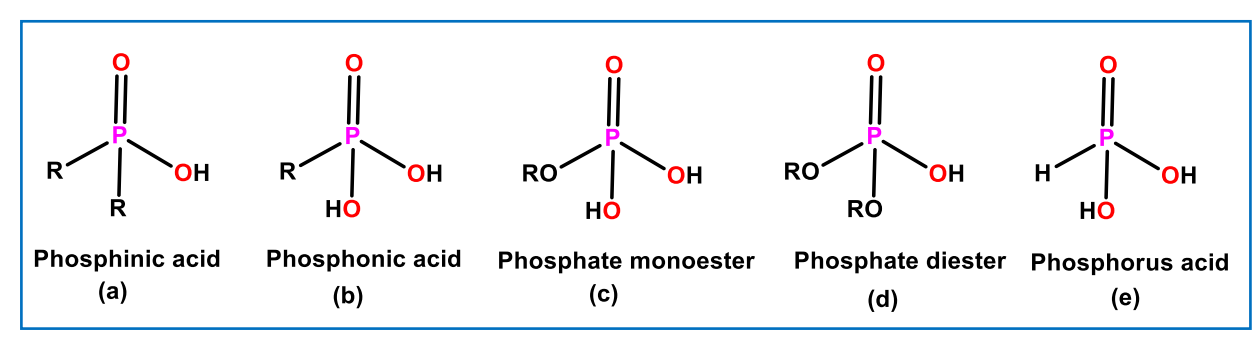


Chart 1: Representation of a group of phosphorus-based acids.

of phosphorus-based acids, which showed in Chart 1.

The organophosphonic acids are analogues to carboxylic acids and have lower pKa values. In the case of phosphonic acids, the pKa values can be reduced by replacing the organic groups on the phosphorus atom. Phosphonic acids form monoanionic or dianionic phosphonic acids when deprotonated in the presence of a base. Phosphonate ligands provide anchoring sites for building a large variety of main group, 37 3d, 38 4f and 3d-4f-based molecular clusters 39 with three tetrahedral oxygen atoms. Phosphonate ligands can coordinate to a maximum of nine metal centers with three oxygen atoms. The coordinating ability of phosphonates with metal centers afforded the formation of extended structures like 1-D, 2-D and 3-D structures. 40 The possible coordination environments of phosphonates are shown below in **Chart 2**.

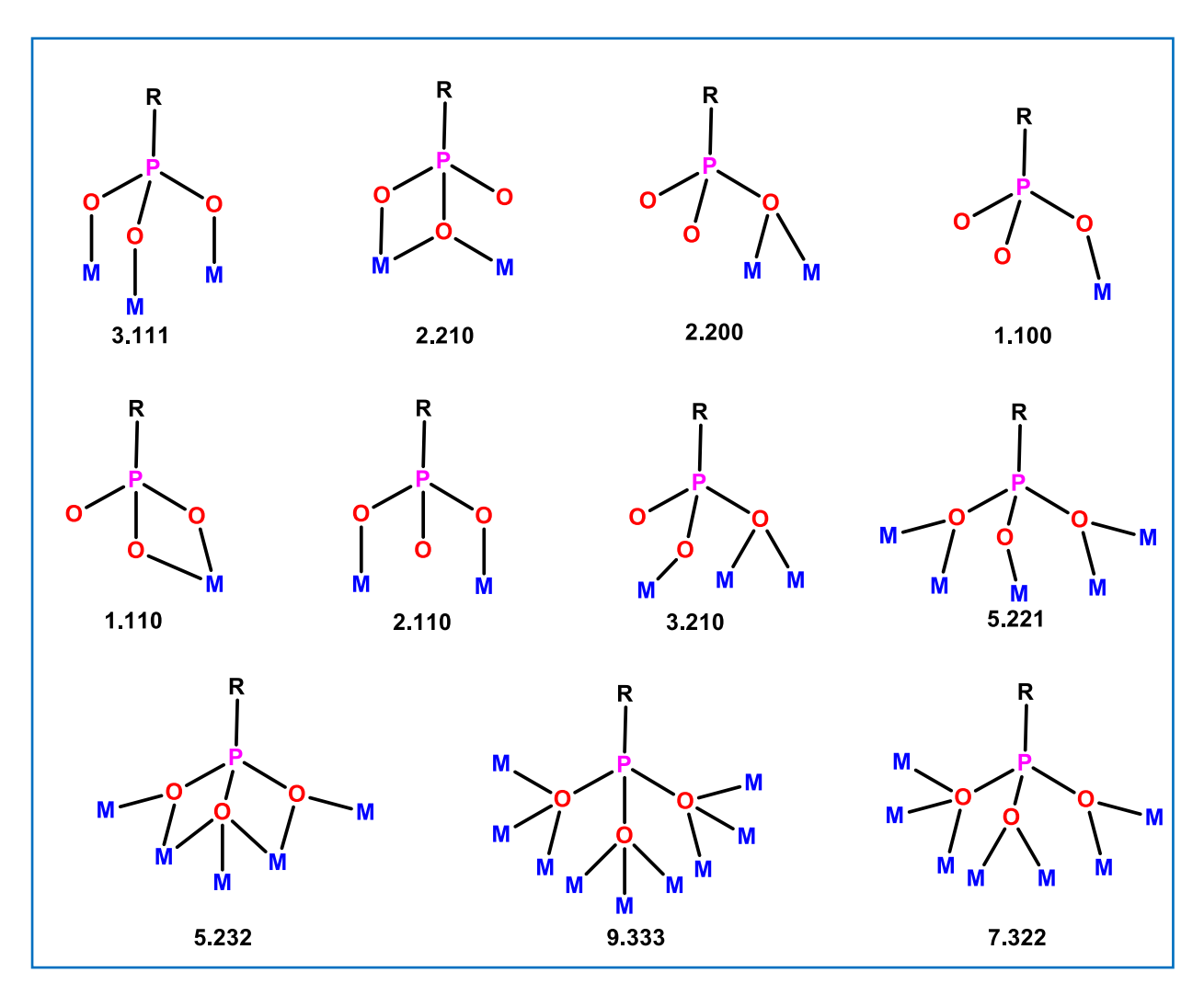


Chart 2: Different coordination modes of phosphonates.

Organophosphonic acids can be synthesized by adapting any one of the methods like the Arbuzov reaction, metal-halogen exchange, Michaelis-Becker reaction, nucleophilic addition to carbonyl groups, Clay reaction and Metal-catalyzed reactions.⁴¹ In the following chapters,

we used t-butylphosphonic acid in the reactions that can synthesize by using the Clay reaction method. The reaction of t-butyl chloride with phosphorus trichloride in the presence of aluminum chloride, followed by hydrolysis, affords the formation of t-butylphosphonic acid (**Scheme 1.10**).⁴²

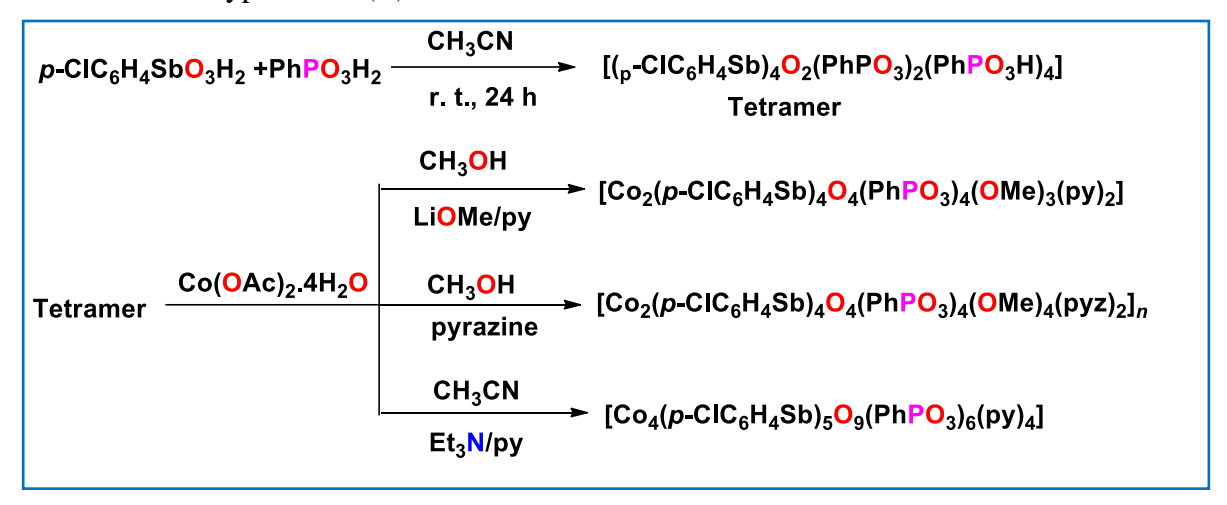
$$\begin{array}{c|c} & & & \\ \hline \end{array}$$

$$\begin{array}{c} CI & + PCI_3 & \\ \hline \\ H_2O & \\ \end{array}$$

Scheme 1.10: Synthesis of *t*-Butyl phosphonic acid.

1.5 Reactions of Organoantimonate-Phosphonate Clusters:

Organostibonic acids can act as inorganic cryptands when depolymerized in the presence of metal ions. Generally, for organostibonic acids, polycondensation is possible and for phosphonic acid ligands, polycondensation does not happen. Winpenny *et al.* reasoned that the reaction of antimonates and phosphonates could show partial condensation and revealed the formation of an organoantimonate-phosphonate cluster. Winpenny *et al.* reported that the series of organoantimonate-phosphonate-based pro-ligands. The reaction of organostibonic acid with protic ligands like *t*-BuPO₃H₂ and PhPO₃H₂ showed the formation of novel di and tetranuclear organoantimony(V) oxo clusters. Further, these pro-ligands reacted with the transition metal salts in the presence of a base under solvothermal reaction conditions (**Scheme 1.11**).⁴³ The reaction of tetranuclear organoantimony(V) cluster [(*p*-ClC₆H₄Sb)₄O₂(O₃PPh)₄(HO₃PPh)₄], cobalt acetate tetrahydrate with different bases under solvothermal conditions revealed the three different types of Co(II) clusters such as dinuclear cobalt cluster



Scheme 1.11: Reactions of organoantimonate-phosphonate clusters

 $[Co_2(p-ClC_6H_4Sb)_4O_4(PhPO_3)_4(OCH_3)_4(py)_2], \qquad 1 \qquad D-polymer \qquad [Co_2(p-ClC_6H_4Sb)_4O_4(PhPO_3)_4(OCH_3)_4(pyz)]_n, \qquad tetranuclear \qquad cobalt \qquad cluster \qquad [Co_4(p-ClC_6H_4Sb)_5O_9(PhPO_3)_6(py)_4] \ (\textbf{Figure 1.12}).$

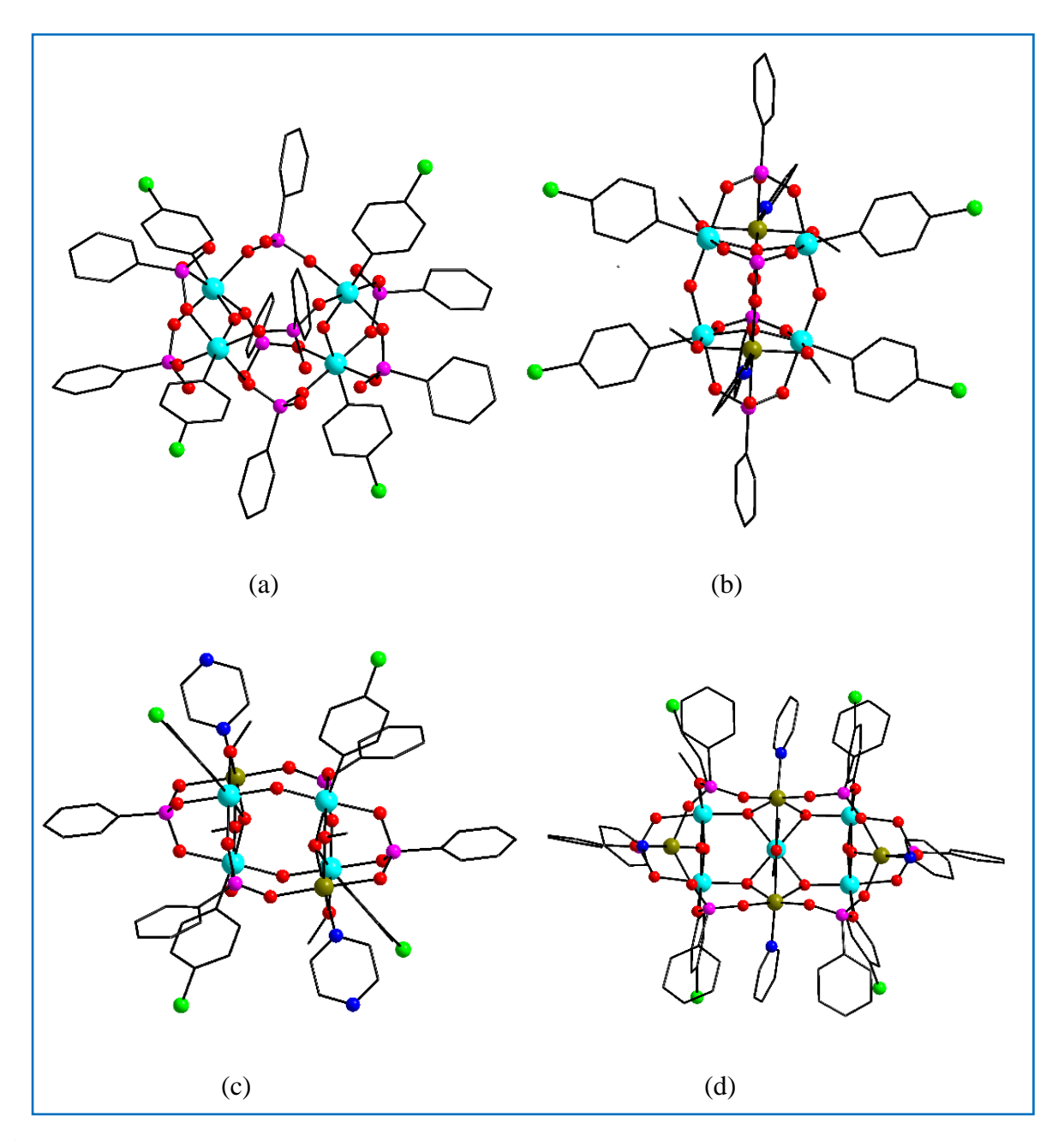


Figure 1.12: Molecular structure of (a) $[(p-ClC_6H_4Sb)_4O_2(O_3PPh)_4(HO_3PPh)_4]$, (b) $[Co_2(p-ClC_6H_4Sb)_4O_4(PhPO_3)_4(OCH_3)_4(py)_2]$, (c) $[Co_2(p-ClC_6H_4Sb)_4O_4(PhPO_3)_4(OCH_3)_4(pyz)]_n$, and (d) $[Co_4(p-ClC_6H_4Sb)_5O_9(PhPO_3)_6(py)_4]$.

Similarly, the reaction of dinuclear organoantimony(V) cluster $[(p-ClC_6H_4Sb)_2O(t-BuPO_3H)_6]$, copper acetate monohydrate with different bases under solvothermal reaction conditions (Scheme **1.12**). revealed the formation of four different Cu(II) clusters, tetranuclear cluster

Scheme 1.12: Reactions of organoantimony(V) phosphonate with 3*d* metal ion.

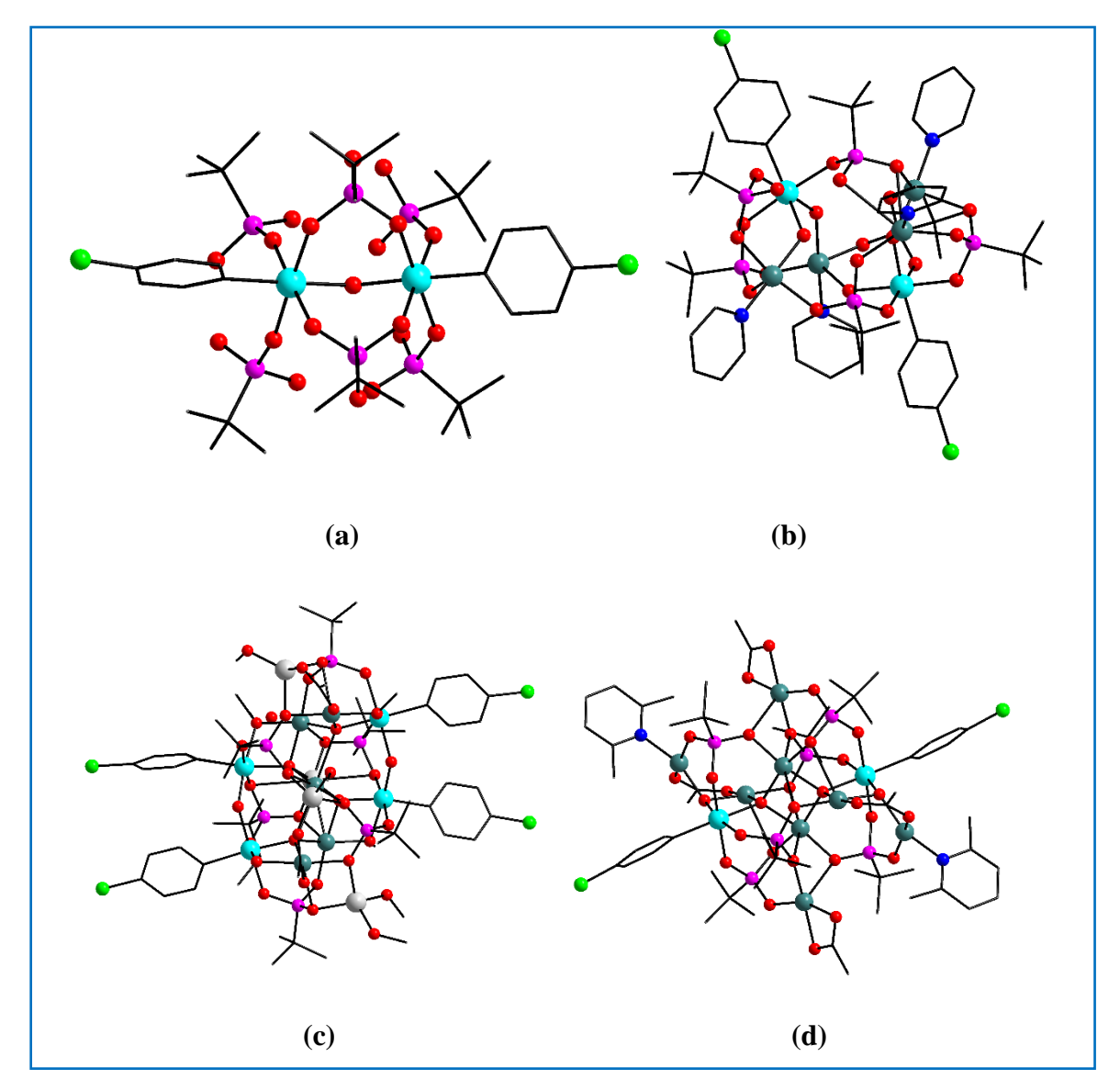


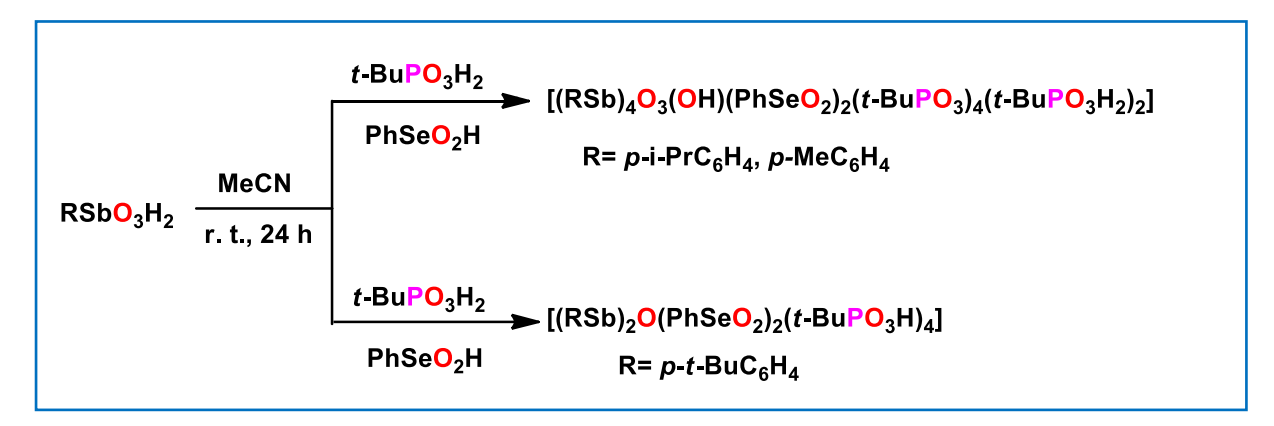
Figure 1.13: Molecular structure of (a) Sb₂ dimer, (b) Cu₄Sb₂, (c) Cu₅Li₄Sb₄ and (d) Cu₈Sb₂ oxo clusters.

 $[Cu_4O_2(p\text{-}ClC_6H_4Sb)_2(t\text{-}BuPO_3)_2(CH_3CO_2)_2(OCH_3)_6], \text{ heterometallic cluster } [Cu_5Li_4O_6(p\text{-}ClC_6H_4Sb)_4(t\text{-}BuPO_3)_6(CH_3CO_2)_2(OCH_3)_4(CH_3OH)_4] \text{ and octanuclear copper cluster } [Cu_8O_4(p\text{-}ClC_6H_4Sb)_2(t\text{-}BuPO_3)_6(CH_3CO_2)_4(lutidine)_2] \text{ (Figure 1.13)}.$

Our group investigated the reactivity of soluble arylstibonic acid (*p*-isopropylphenylstibonic acid/*p*-tertiarybutylphenylstibonic acid) with *t*-butylphosphonic acid/phenylphosphonic acid and SC-XRD revealed the formation of tetranuclear organoantimony(V) clusters [(*p*-i-PrC₆H₄Sb)₄(OH)₄(*t*-BuPO₃)₆], [(*p*-*t*-BuC₆H₄Sb)₄(O)₂(PhPO₃)₄(PhPO₃H)₄].⁴⁵

1.5.1 Synthesis of Organoantimonate-Phosphoseleninate Clusters:

Our group successfully designed and synthesized the organoantimonate-phosphoseleninate clusters by a reaction of soluble arylstibonic acid and *t*-butylphosphonic acid with benzeneseleninic acid in a 1:1:1 ratio (**Scheme 1.13**). SC-XRD revealed the formation of tetra



Scheme 1.13: Synthesis of Organoantimonate-Phosphoseleninate clusters.

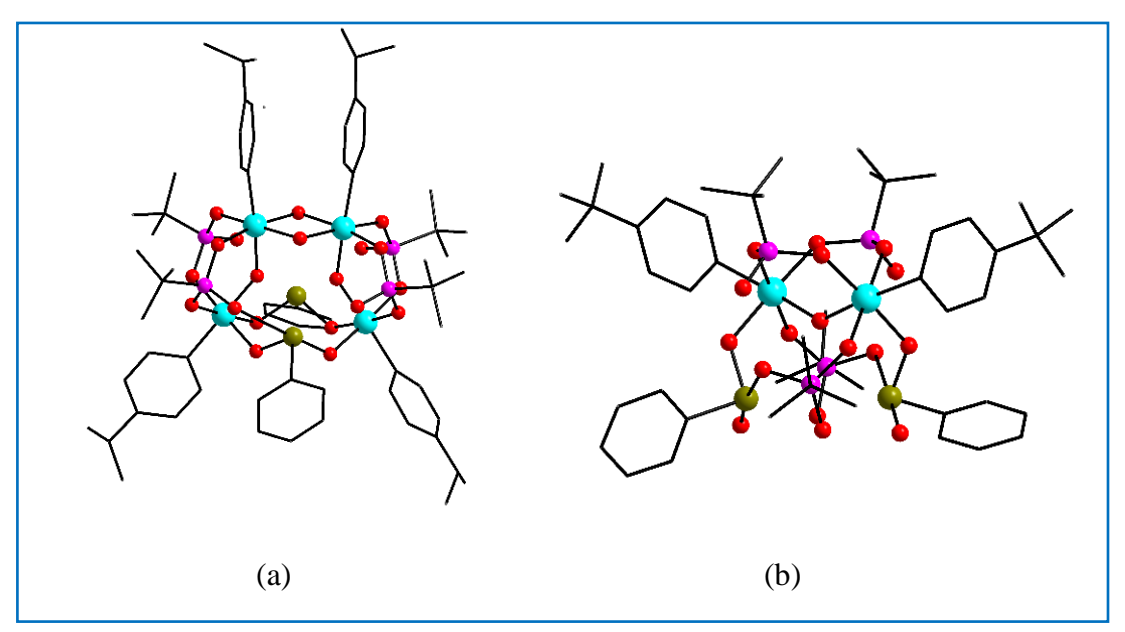
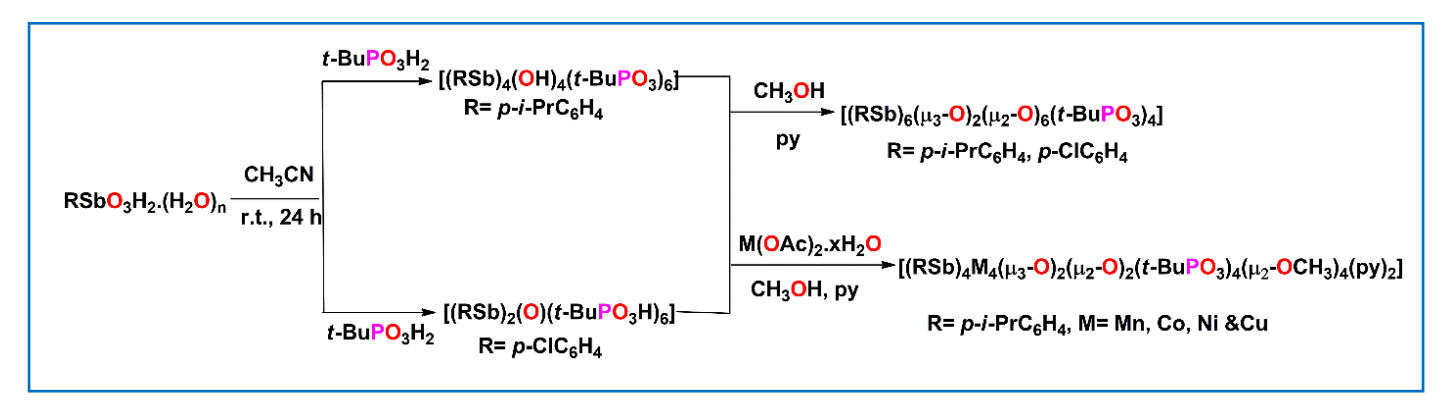


Figure 1.14: Molecular structure of (a) $[(p-i-PrC_6H_4Sb)_4(O)_3(OH)(PhSeO_2)_2(t-BuPO_3)_4(t-BuPO_3H_2)_2]$ and (b) $[(p-t-BuC_6H_4Sb)_4(O)(PhSeO_2)_2(t-BuPO_3H)_4]$.

and dinuclear organoantimony(V) clusters $[(p-i-PrC_6H_4Sb)_4(O)_3(OH)(PhSeO_2)_2(t-BuPO_3)_4(t-BuPO_3H_2)_2]$, $[(p-t-BuC_6H_4Sb)_4(O)(PhSeO_2)_2(t-BuPO_3H)_4]$ (**Figure 1.14**).⁴⁵

1.5.2 Synthesis of Sb₆ and M₂Sb₄ (M=Mn, Co, Ni and Cu) Oxo Clusters:

The reaction of both the pro-ligands $[(p-ClC_6H_4Sb)_2O(t-BuPO_3H)_6]$ and $[(p-i-PrC_6H_4Sb)_4(OH)_4(t-BuPO_3)_6]$ independently with pyridine at 100 °C formed a hexanuclear organoantimony(V) cluster $[(ArSb)_6(\mu_3-O)_2(\mu_2-O)_6(t-BuPO_3)_4]$ (Scheme 1.14). ⁴⁶ Even though different antimonate-to-phosphonate ratios (2:6/4:6) were present, it does not change the structure of the final product. Similarly, M_2Sb_4 oxo clusters synthesized by a solvothermal reaction of antimonate-phosphonate pro-ligand $[(p-iPrC_6H_4Sb)_4(OH)_4(t-BuPO_3)_6]$ with $M(CH_3COO)_2$. xH_2O [M= Mn, Co, Ni and Cu] in MeOH under solvothermal conditions, using pyridine as a base afforded heterometallic hexanuclear organoantimony(V) cluster $[M_2(p-iPr-C_6H_4Sb)_4(\mu_3-O)_2(\mu_2-O)_2(\mu_2-OCH_3)_4(t-BuPO_3)_4(py)_2]$. CH_3OH , where M=Mn, Co, Ni and Cu



Scheme 1.14: Synthesis of Sb₆ and M₂Sb₄ oxo clusters.

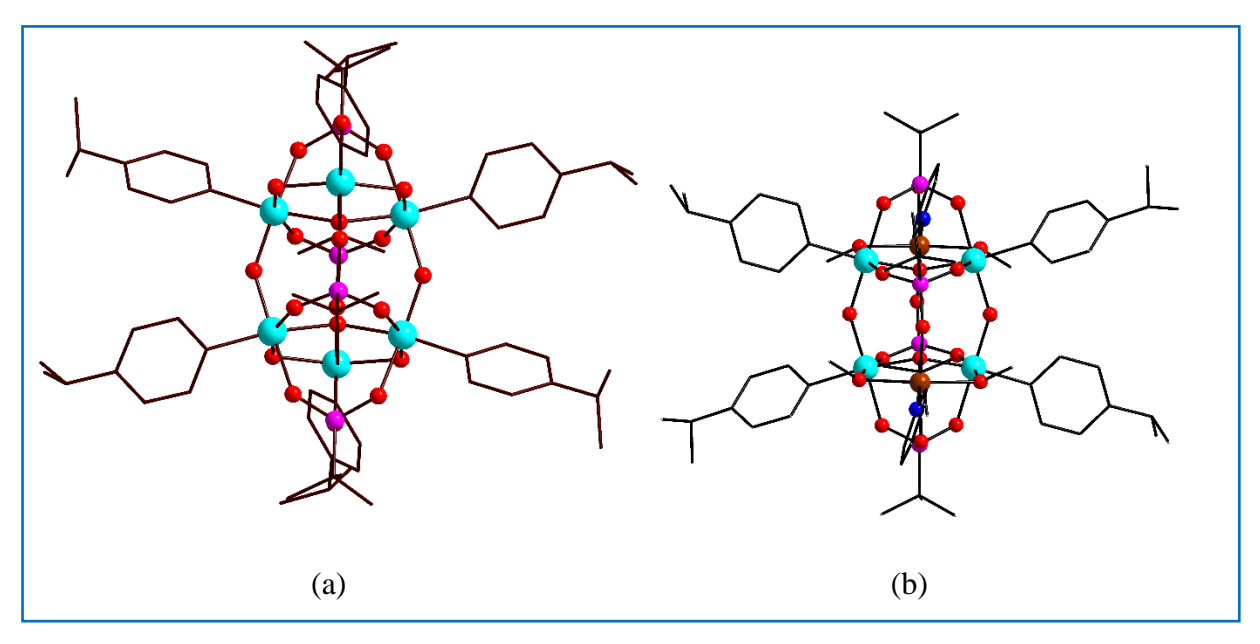


Figure 1.15: Molecular structure of (a) Sb₆ and (b) Mn₂Sb₄ oxo clusters.

(**Scheme 1.14**). These clusters are built up of two metal triangles connected through bridged phosphonate ligands and oxide ions (**Figure 1.15**). Two ³¹P NMR resonance peaks indicate the two different phosphorus environments in the cluster.

1.6 Reactions of Arylstibonic Acid with Phosphinic Acids:

The reaction of arylstibonic acid, dicyclohexylphosphinic acid/ diphenylphosphinic acid and tetraethylammonium hydroxide in a 1:2:4 ratio in acetonitrile at room temperature stirred for 24 h (**Scheme 1.15**) reveals the formation of polyoxostibonates [Na₅(*p*-MeC₆H₄Sb)₁₁(O)₂₈{(C₆H₁₁)₂PO₂}] and [Na₂(*p*-iPr-C₆H₄Sb)₁₄(O)₂₈(Ph₂PO₂)₈] (**Figure 1.16**).

Scheme 1.15: Synthesis of polyoxostibonates

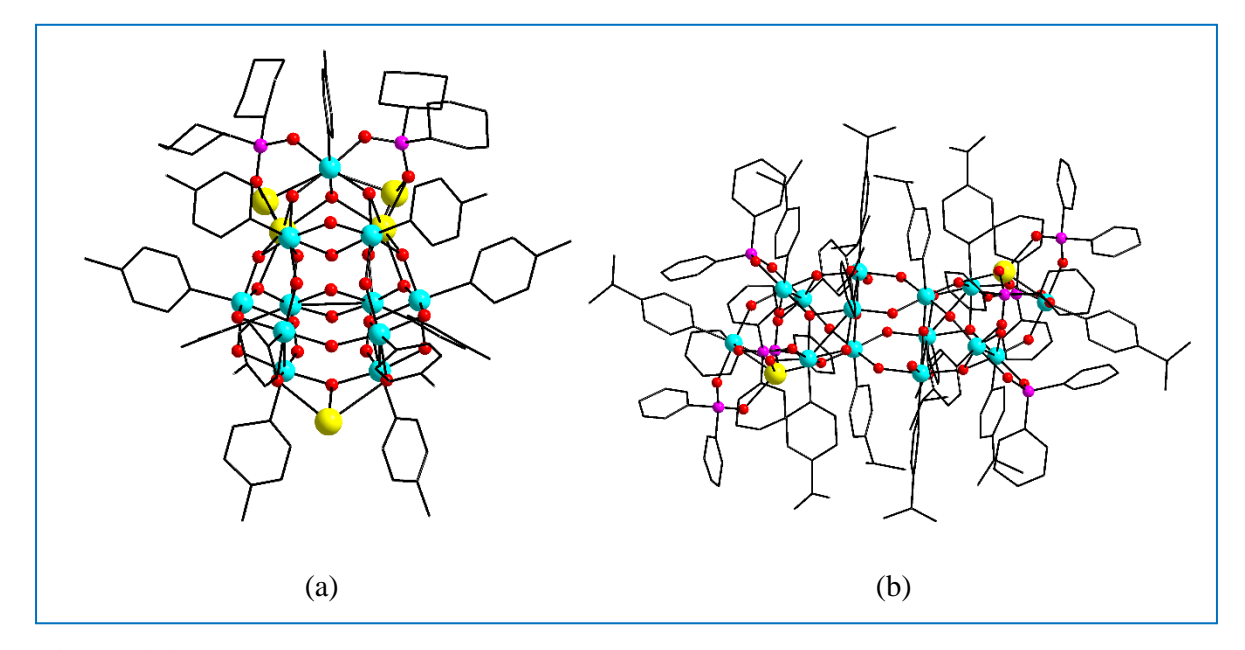


Figure 1.16: Molecular structure of (a) $[Na_5(p-MeC_6H_4Sb)_{11}(O)_{28}\{(C_6H_{11})_2PO_2\}]$ and (b) $[Na_2(p-iPr-C_6H_4Sb)_{14}(O)_{28}(Ph_2PO_2)_8]$.

The sodium ions presented in the cluster probably came from the glassware leaching in the process of crystallization. In these clusters, organostibonic acids show a strong affinity toward Na ions and also help in charge neutrality and the crystallization process.

1.7 Reactions of Polymeric Organoantimony(V) Oxide:

1.7.1 Reactivity of Polymeric Organoantimony(V) Oxide Towards Protic Ligands:

Scheme 1.16: Reactions of $(Ph_3SbO)_n$ with protic acids

The reactions of polymeric triphenylantomony oxide with different protic ligands, such as organophosphinic acids and organophosphonic acid, at room temperature revealed the formation of novel organoantimony(V) clusters. When polymeric triphenylantomony oxide reacts with phenylphosphinic acid forms the dinuclear organoantimony(V) cage $[Ph_3Sb(HPhPO_2)_2]_2$ and indicates the P-H three-bond coupling in solution state for the first in organophosphorus chemistry. Reaction of $(Ph_3SbO)_n$ with Ph_2PO_2H and t-BuPO_3H2 shows the formation of $[Ph_3Sb(Ph_2PO_2)_2]$ and $[Ph_3Sb(t$ -BuPO_3H)_2]. With another protic ligand, benzeneseleninic acid forms two different clusters, $[Ph_3Sb(PhSeO_2)_2]_2$ crystallized in dichloromethane and $[(Ph_3Sb)_2(\mu$ -O)(μ -PhSeO_2)_2] crystallized in acetonitrile solvent. Further, $[Ph_3Sb(t$ -BuPO_3H)_2] was reacted with tetraethyl ammonium hydroxide in toluene heated to reflux afforded the trinuclear organoantimony(V) cluster $\{(Ph_2Sb)_2(PhSb)(\mu_3$ -O)(μ -O)₂(OH)₂(τ -BuPO_3)₂[(C₂H₅)₄N]₂} on SC-XRD studies, which undergoes in situ dearylation and also presented an *in situ* generated PhSbO₃H₂, Ph₂Sb(O)(OH) components (**Scheme 1.16**). 47

1.7.2 Reaction of Polymeric Triphenylantimony(V) oxide with Ph₂TeO:

The reaction of (Ph₃SbO)_n with Ph₂TeO in a 1:2 ratio in toluene under reflux conditions octanuclear Sb(III/V)-based revealed molecular $\{(C_6H_5)_3T_6\}_4\{[(C_6H_5)_2S_b^V]_4(S_b^{III})_4(O)_{12}(OH)_4\}$ (Scheme 1.17).³³ The molecular structure is a tetra anionic metal oxo cluster stabilized by four triphenyltellurium cations crystalized along with the core (Figure 1.17). The overall charge neutrality is maintained by the presence of triphenyltellurium cations and also by stabilizing the octanuclear cluster with weak interactions. The molecular structure indicates the presence of a dimeric form of Sb tetramers connected via two bridged oxygens. The antimony tetramer unit has two Sb(V) and two Sb(III) in alternate arrangements and is linked by four bridging oxygens resulting in an eightmembered ring with a chair-like structure. The two Sb(III) atoms in the cluster are tri and tetra coordinated with connected oxygen atoms. The shape of tri-coordinated Sb(III) is trigonal pyramidal with a lone-pair on antimony atoms at axial positions, and tetra-coordinated Sb(III) has pseudo-trigonal bipyramidal geometry containing a lone-pair on the Sb atoms at equatorial positions. In the dimeric form of antimony tetramer contains two phenyl groups on antimony, indicating the mono diarylation of starting material, polymeric triphenylantimony oxide.

$$(Ph_3SbO)_n + Ph_2TeO$$

$$Toluene$$

$$Ph_3Te)_4[(Ph_2Sb^V)_4(Sb^{III})_4(O)_{12}(OH)_4]$$

$$reflux, 12 h$$

Scheme 1.17: Reaction of (Ph₃SbO)_n with Ph₂TeO

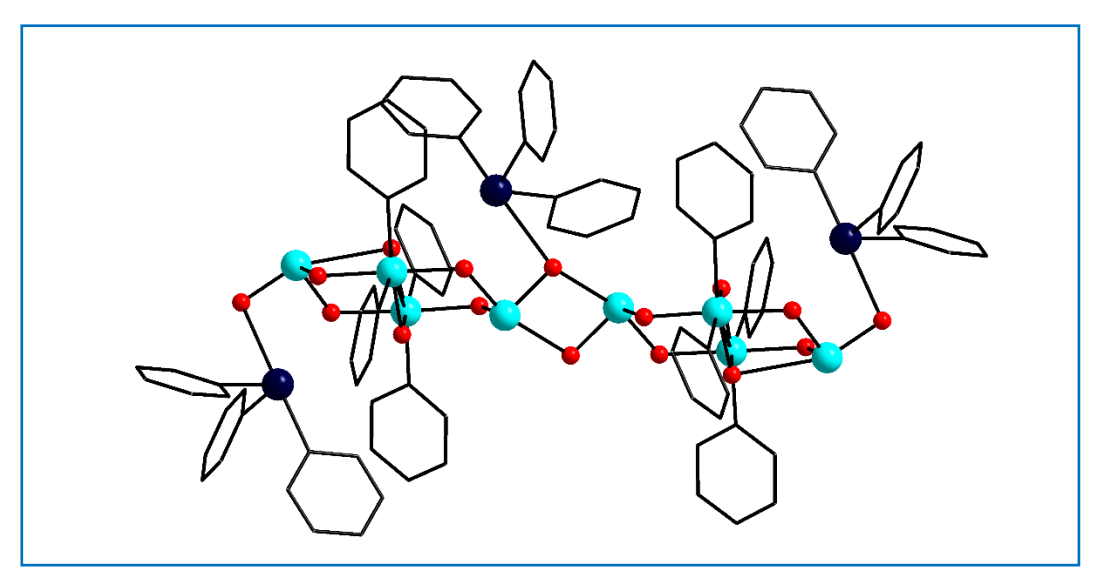


Figure 1.17: Molecular structure of $\{(C_6H_5)_3T_6\}_4\{[(C_6H_5)_2S_6V]_4(S_6U)_4(O)_{12}(OH)_4\}.$

1.8 Synthesis of Trinuclear Zinc Phosphonate Cluster:

Chandrasekhar *et al.* reported the molecular zinc phosphonates by a reaction of ZnCl₂, *t*-butylphosphonic acid and 3,5-dimethyl pyrazole in the presence of Et₃N as a base at room temperature (**Scheme 1.18**). ⁴⁸ SC-XRD analysis shows the formation of a Zn₃ oxo triangle (**Figure 1.18**). In this synthesis 3,5-dimethyl pyrazole act as coligand. Zinc phosphonate clusters with lesser nuclearity are rare in literature. We used this metal triangle as a starting precursor in Chapter 3 and investigated the reactivity with arylstibonic acids.

Scheme 1.18: Synthesis of Zn₃-oxo cluster.

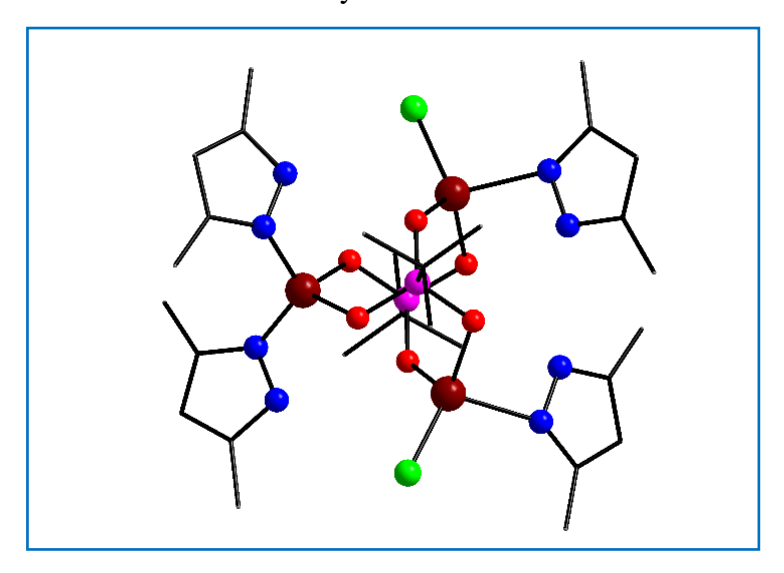


Figure 1.18: Molecular structure of $[Zn_3Cl_2(3,5-Me_2PzH)_4(t-BuPO_3)_2]$.

1.9 Cleavage of an Sb-C Bond:

1.9.1 Monodearylation of Triphenylantimony Compound:

Wittenberg *et al.* reported the cleavage of the Sb-C bond in 1958.⁴⁹ They observed Sb-C bond cleavage initially from the synthesis of diphenylstibyllithium by a reaction of triphenylantimony with Li in THF. Lithium in THF was most effective for the cleavage of heterocycles. Monodearylation was observed in nitrogen family derivatives like triphenylamine, triphenylphosphine and triphenyl arsine in the presence of Li in THF. All reactions are exothermic and yield a dark red-brown colour. The colour test was effective and observed within a few minutes after the reaction started. Further, they carried out the reaction of diphenylstibyllithium with chlorotrimethylsilane revealing the formation of trimethyl phenyl silane and diphenylstibinic acid (**Scheme 1.19**). Similar products were observed in the case of triphenyl arsine. The cleavage of the Sb-C bond of triphenylantimony was slow in Li in THF, but Hewertson *et al.* observed that the same reaction proceeds rapidly by using Na in Liq. NH₃.⁵⁰

$$Ph_3Sb + 2 Li$$
 \longrightarrow $PhLi + Ph_2SbLi$ Me_3SiCl \longrightarrow $Me_3SiPh + Ph_2Sb(O)(OH)$ $H_2O, [O]$

Scheme 1.19: Synthesis of Ph₂Sb(O)(OH)

1.9.2 Sb-C Bond Cleavage on a Triruthenium Cluster at Room Temperature:

In 2004, Shawkataly *et al.* reported the first observation of the Sb-C bond cleaving at room temperature. They performed the reaction between $[Ru_3(CO)_{12}]$ and $Sb(C_6H_5)_3$ in tetrahydrofuran under an inert atmosphere and the benzophenone ketyl radical anion acted as an initiator.⁵¹ SC-XRD studies show the formation of $[(C_6H_5)_2SbRu_3(COC_6H_5)(CO)_{10}]$. Interestingly, they observed three factors; i) the Ru-Ru bond braking followed by the formation of an open tri ruthenium cluster $[(C_6H_5)_2SbRu_3(COC_6H_5)(CO)_{10}]$ (**Figure 1.19**) instead of a simple substitution product $Ru_3(CO)_{10}[(C_6H_5)_2PCH_2P(C_6H_5)_2]$, ii) Sb-C bond cleavage at room temperature and iii) insertion of phenyl group at the carbonyl.

Figure 1.19: Structure of $[(C_6H_5)_2SbRu_3(COC_6H_5)(CO)_{10}]$.

1.9.3 Sb-C Bond Cleavage in (CH₃)₃SbCl₂:

Meinema *et al.* reported the preparation of dialkylstibylsodium compounds by a reaction of trialkylstibines with Na in Liq. NH₃ and observed an Sb-C bond cleavage (**Scheme 1.20**).⁵² They synthesized different dialkylstibylsodium compounds by changing alkyl groups like methyl, ethyl, propyl and butyl groups. For each case, cleavage of the Sb-C bond depends on reaction time and they conclude that the rate of cleavage of antimony-alkyl group decreases with the stability of the formation of anionic species.

Scheme 1.20: Preparation of dialkylstibylsodium compound.

1.9.4 Sb-C Bond Cleavage in Organostiboxane Cage:

Chandrasekhar *et al.* reported the Sb-C bond cleavage in the nonanuclear organostiboxane cluster. The reaction of triphenylantimony dichloride monohydrate with 1,1,2,3,3-pentamethyltrimethylenephosphinic acid $(cycPO_2H)$ in the presence of a base at room temperature reveals the formation of the dinuclear cluster $[(Ph_3Sb)_2(\mu-O)(\mu-cycPO_2)_2]$. Further, mild hydrolysis of the obtained product in CH₃CN/H₂O at 45 °C resulted a nonanuclear organoantimony cluster $[(Ph_2Sb)_2(PhSb)_7(\mu-O)_{11}(\mu_3-O)_3(\mu-OH)_2(\mu-cycPO_2)_2(cycPO_2)_2(H_2O)_2]\cdot 2CH_3CN.H_2O$ (Scheme 1.21). In this case, all Sb metal ions are present in a 5+ oxidation state and solid-state structure containing a Sb₉O₁₆ core.⁵³

Scheme 1.21: Synthesis of nonanuclear organostiboxane cage

1.9.5 *In Situ* Dearylation of [Ph₃Sb(t-BuPO₃H)₂]:

The reaction of polymeric triphenylantimony oxide with protic ligand t-butylphosphonic acid in a 1:2 mole ratio leads to a monomeric compound [Ph₃Sb(t-BuPO₃H)₂]. Further, a monomeric compound subjected to base-induced hydrolysis and dearylation leads to the formation of [(Ph₂Sb)₂(PhSb)(μ ₃-O)(μ ₂-O)₂(OH)₂(μ -tBuPO₃)₂{(C₂H₅)₄N}₂] (**Scheme 1.22**). The novel dianionic trinuclear cluster contains *in situ*-generated phenylstibonic and phenylstibinic acid moieties.⁴⁷

Scheme 1.22: Synthesis of $[(Ph_2Sb)_2(PhSb)(\mu_3-O)(\mu_2-O)_2(OH)_2(\mu-tBuPO_3)_2\{(C_2H_5)_4N\}_2]$.

1.9.6 Complete Dearylation of Organostibonic Acid:

Our group reported the complete dearylation of the organoantimony compound. Mixed valent Sb(III/V) POM was synthesized by a reaction of *p*-BrC₆H₄SbO₃H₂ with Ph₂TeO under reflux condition afforded (Ph₃Te)₂[Na₂(H₂O)₂(*p*-Br-C₆H₅Sb^V)₁₀(Sb^{III})₄(Ph₂Te)₄(O)₃₀(OH)₄] (**Scheme**

1.23). In this case, complete dearylation and a partial reduction were observed from Sb(V) to Sb(III).³³

RSbO₃H₂ + Ph₂TeO
$$\xrightarrow{\text{Toluene}}$$
 (Ph₃Te)₂[Na₂(H₂O)₂(RSb^V)₁₀(Sb^{III})₄(Ph₂Te)₄(O)₃₀(OH)₄]
reflux, 12 h R= p -Br-C₆H₄

Scheme 1.23: Synthesis of mixed valent Sb(III/V) cluster.

1.9.7 Monoarylation of Organoantimony Oxo Clusters:

Our group reported the series of mixed valent organoantimony oxo clusters prepared by a reaction of Ph₂SbCl₃ with protic ligands like *t*-BuSi(OH)₃, *cyclo*-C₆H₁₁Si(OH)₃ and Ph₂Si(OH)₂ in 1:1 molar ratio in the presence of base at room temperature afforded the series of organoantimony oxo clusters containing mixed valent Sb(III/V) centers (**Scheme 1.24**), which was characterized by using SC-XRD studies. In all the compounds, monoarylation has been observed.⁵⁴

$$Ph_{2}SbCl_{3} + RSi(OH)_{3} \xrightarrow{Toluene} Et_{3}N$$

$$Ph \downarrow Sb \downarrow Sb \downarrow Sb \downarrow Ph$$

$$R = t-Bu, cyclo-C_{6}H_{11}$$

$$Ph \downarrow Sb \downarrow Ph$$

$$R = t-Bu, cyclo-C_{6}H_{11}$$

$$Ph \downarrow Sb \downarrow Ph$$

$$Ph \downarrow Ph$$

Scheme 1.24: Reactions of Ph₂SbCl₃ with protic ligands

Till now, we have discussed the preparation, structure and reactivity of arylstibonic acids. Further, we are interested in exploring the biological properties of newly synthesized organoantimony(V) derivatives. The biological applications of organostibonic acids and their derivatives are known in the literature. In the introduction part, a detailed explanation of the biological applications of organostibonic acids and their derivatives are described.

Similarly, some organoantimony(V) oxo clusters have been used as pro-ligands for synthesizing lanthanide clusters. The lanthanide-based clusters have applications in the field of magnetism. In the introduction, a general overview of magnetism, a detailed explanation of single molecular magnetism (SMM), its operating principle, the relaxation mechanism involved and a few breakthrough examples in magnetism are given.

1.10 Biological Applications of Organostibonic Acids:

Arylstibonic acids have attained interest in the field of biology due to their interesting structural chemistry and reactivity. Sei et al. reported the effective anti-HIV activity of organostibonic acids; these compounds inhibit HIV-1 infection by disrupting gp120-CD4 contacts.⁵⁵ Ernst et al. reported the notable prophylactic effect in trypanosomiasis exerted by the first organoantimony compound, Sodium p-Melaminylphenylstibonate.⁵⁶ For dimerizing and binding to DNA, the B-ZIP domain modulates the gene transcription factors. In the human genome, 55 genes are present, which have B-ZIP domain dimerization properties and these transcription factors are implicated in cancer and other pathogens. Vinson et al. reported that organostibonic acids are promising candidates for anticancer agents. Organostibonic acid derivatives can bind to the leucine zipper (B-ZIP) domain, stabilizes the B-ZIP domain dimer and inhibits the B-ZIP DNA binding. They carried out an experiment on many organostibonic acids to test their capacity to prevent B-ZIP DNA binding, and they found that altering the chemical substituent on stibonic acid resulted in a range of inhibitory abilities.⁵⁷ Apurinic/Apyrimidinic Endonuclease 1 is an important protein in the human body, which can utilize in the base excision repair pathway and it will help for the total apurinic/apyrimidinic (AP) endonuclease activity in the human body. Chemotherapeutic agents can be induced by APE-1 expression. Stivers et al. and others screened APE-1 against a series of organostibonic acids and concluded that negatively charged organostiobonic acid compounds act as DNA phosphate mimics. These arylstibonic acids provide a platform for cancer drugs against APE-1.58 In the process of DNA replication and DNA transcription, Human topoisomerase IB (hTopo) controls genomic DNA morphology and hTopo has acted as an important anticancer drug target. They screened a set of arylsiobnic acids on plasmid supercoil relaxation, which can be catalyzed by hTopo. Few organostibonic acids act as potent inhibitors against hTopo and poxvirus (vTopo) cellular functions.⁵⁹ Protein tyrosine phosphatases (PTPs) have been

implicated in cellar signaling and play an important role in cancer development. Woscholski *et al.* screened different arylstibonic as an inhibitor and few were concluded as an inhibitor of Cdc25 phosphatases.⁶⁰ Oyston *et al.* reported that organostibonic acids act as novel antimicrobial agents, which can act as an inhibitor of *Yersinia pestis* DNA adenine methyltransferase.⁶¹ Recently, our group reported that organostibonic acids and their clusters good candidates for anticancer and antimicrobial agents.⁶²

1.11 SMM- A Family of Lanthanide Clusters:

1.11.1 General Introduction:

The name "lanthanides" comes from the element lanthanum. Lanthanides are categorized as rare-earth elements along with Y and Sc since these elements are frequently obtained in ore deposits from which lanthanide metals are extracted. The separation and purification of lanthanides, despite their relative abundance, is a very difficult task. Owing to the identical physical and chemical characteristics shared by numerous lanthanides, lanthanide purification is expensive and hazardous. The remarkable optical and magnetic characteristics of lanthanides, which are commonly used in modern technology, are caused by valence electrons present in 4*f* orbitals. From a magnetism point of view, for more than 50 years, ⁶³ lanthanides have been the primary magnetic component of hard magnets. The coercive field, which is influenced by magnetic anisotropy used to distinguish between soft magnets (low coercive fields) and hard (high coercive fields). Lanthanides with large anisotropy and magnetic moment attracted interest in the early stages of molecular magnetism.⁶⁴ Here is a quick overview of magnetism presented.

Diamagnetism:

In diamagnetic materials, the outermost shell is completely filled with electrons and these are spin paired, representing a lack of permanent magnetic moment. This can be demonstrated by taking two electrons with the same magnetic moment and orbiting in reverse directions, resulting in a cancel of the magnetic moment. When an external magnetic field is applied to a diamagnetic material, the result is a weak magnetic moment that goes opposite direction of the external magnetic field. As a result, diamagnetic materials show a negative susceptibility (χ < 0). This indicates that diamagnetic materials, which lose their magnetic characteristics when the external field is removed.

Paramagnetism:

In paramagnetic materials, the outermost shell is partially-filled with unpaired electrons: representing a permanent magnetic moment. When no external magnetic field is applied, these

magnetic moments have random directions and there is no magnetic moment. All unpaired electrons are affected by the applied external magnetic field and have a tendency to align themselves in that direction. Paramagnetic materials show a small positive susceptibility (χ > 0). Moreover, when the temperature rises, the magnetic behaviour of paramagnetic material decreases.

Ferromagnetism:

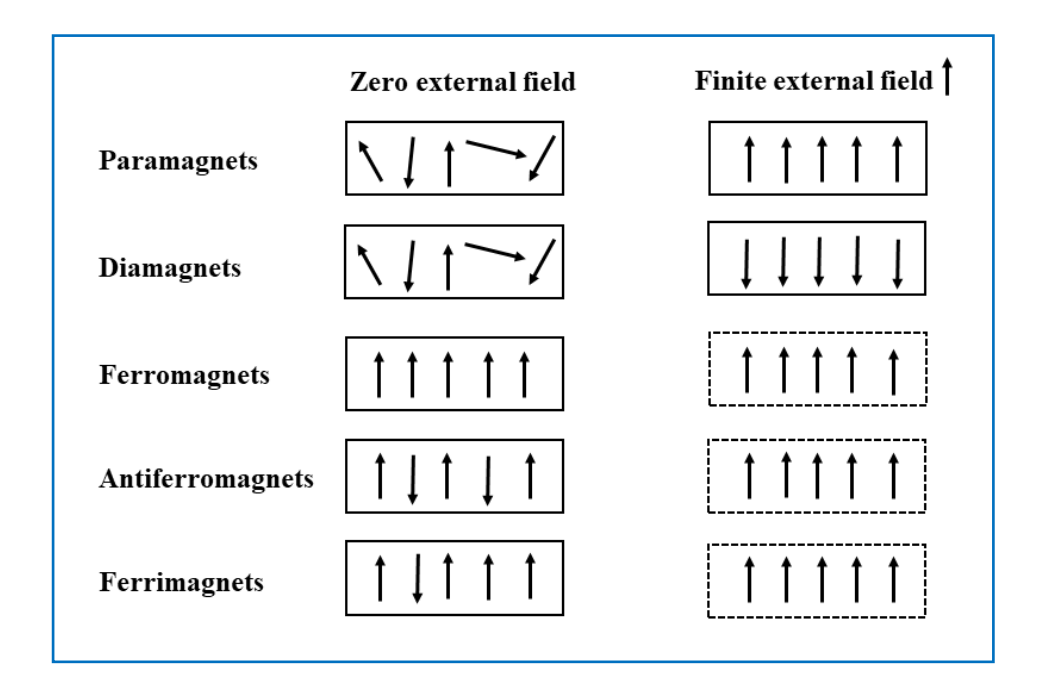
Ferromagnetism is caused by the presence of interactions between nearby magnetic moments. Due to the cooperative arrangement of magnetic moments produced by these interactions, an internal "molecular field" is produced. Due to this, magnetization persists even in the zero magnetic field. The ferromagnetic materials magnetic moments are no longer aligned above the Curie temperature and the material begins to act like a paramagnet. At high-temperature ferromagnetic materials show a positive susceptibility.

Antiferromagnetism:

Half of the magnetic moments in an antiferromagnetic material are aligned in one direction, and the other half are oriented in the opposite direction. Hence net magnetization is zero. Above a certain temperature, with disordered magnetic moments, antiferromagnetic material behaves as paramagnetic called Neel temperature. At all temperatures, antiferromagnetic material shows small and positive magnetic susceptibility.

Ferrimagnetism:

In ferrimagnetic materials, the magnetic moment alignments present like antiferromagnetic materials, but antiparallel moments do not cancel. In a zero magnetic field, net magnetization is obtained because a magnetic moment of one direction is higher than the other direction below a Neel temperature. In a zero-magnetic field, ferrimagnetic materials show spontaneous magnetization and a large susceptibility.



, **Figure 1.20:** Different types of Magnets

1.11.2 Single Molecule Magnets:

Single-Molecule Magnets (SMMs) are defined as discrete polynuclear clusters which show magnetic bistability below a certain blocking temperature, $T_{\rm B}$, due to simultaneously large uniaxial magnetic anisotropy and large ground spin state resulting from zero-field splitting, metallic core geometry and symmetry of the molecule. Generally, the magnetization and relaxation process can be explained using the double-well potential energy diagram. SMMs have drawn a great deal of research interest due to potential uses in information storage devices, ⁶⁵ molecular spintronics ⁶⁶ and quantum computing. ⁶⁷ Generally, in SMMs, the metallic core is surrounded by organic ligands, which provide exchange pathways between adjacent spins and reduce the intermolecular interactions to preserve magnetic features.

1.11.3 Relaxation Processes:

If the energy barrier has to be crossed through all excited states in order for the magnetization to be reoriented or relaxed, then any substance with a $U_{\rm eff} \sim 298~{\rm K}~(207~{\rm cm}^{-1})$ would be suitable for the information storage device. The aforementioned device's magnetization would not be lost if the temperature was kept below 298 K, resulting in a memory effect. Despite this, the relaxation mechanisms in these materials are varied, complex and highly sensitive to a wide range of variables, including intermolecular interactions, temperature, hyperfine (the electronic-nuclear spin interactions) and magnetic field. The relaxation mechanisms that take place in SMMs are spin-phonon coupling (Orbach, Raman, and direct processes) or occur by

the quantization of the materials (Quantum Tunneling of the Magnetization, QTM and Thermally Assisted QTM, TA-QTM).

Spin-phonon coupling relaxation mechanism:

This mechanism involves three processes. 1) Orbach relaxation process

- 2) Raman relaxation process
- 3) Direct relaxation process

1) Orbach relaxation process: two phonons are involved in the relaxation process. In the Orbach process, to cross the entire barrier large amount of phonon energy is needed. Initially, the SMM system absorbs phonons exact energy $((h/2\pi)\cdot\omega_1)$ to overcome from ground energy sublevels $(M_S = \pm S)$ to the highest excited energy sublevel $(M_S = 0)$. The SMM system, after relaxing to one of the ground $M_S = \pm S$ states, emits additional phonons $((h/2\pi)\cdot\omega_2)$ (Figure 1.21a) from this excited state. Interestingly, the initial and final energy states are not the same and are splitted by dipolar or electronic-nuclear spin interactions. As a result, the difference between the initial and final energy states represents the difference in energy between the ground state $\pm M_S$ sublevels. Generally, the Orbach process happens through the first or second excited state, not the highest excited state. The Orbach process occurs at the highest temperatures.

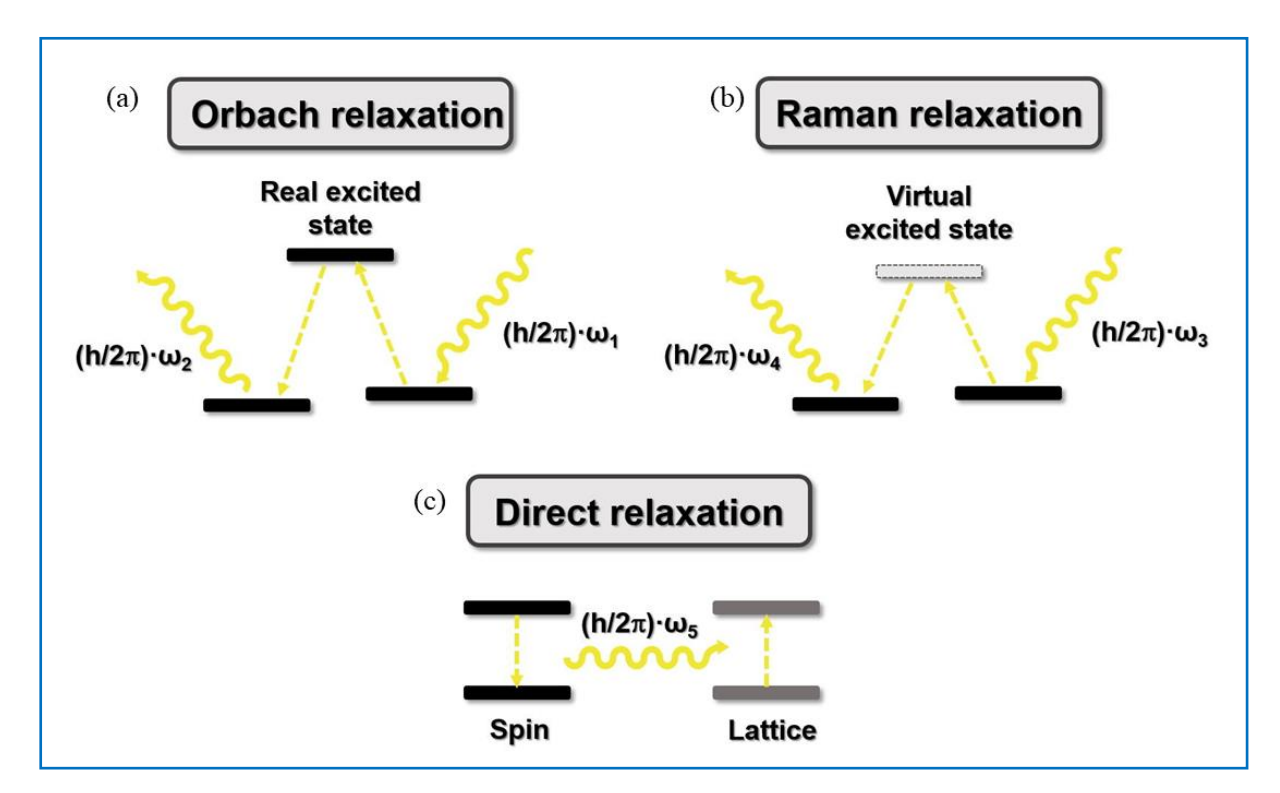


Figure 1.21: Schematic representation of relaxation processes

- 2) Raman relaxation process: two phonons phenomena. Raman mechanism does not have the energy restrictions associated with the Orbach process. In this, phonons are operated with inelastic dispersion. A phonon $(h/2 \pi) \cdot \omega_3$ is absorbed by the system, which then enters a virtual excited state and emits an additional phonon $(h/2 \pi) \cdot \omega_4$ (**Figure 1.21b**). Like the Orbach process, two phonon energy difference represents the difference in energy between the ground state $\pm M_S$ sublevels. This mechanism occurs at the whole temperature range.
- 3) Direct relaxation process: single phonon-assisted relaxation process. In which system shows a phonon $((h/2 \pi)\cdot\omega_5)$ representing the difference in energy between the ground state $\pm M_S$ sublevels (**Figure 1.21c**). This process occurs at low-temperature conditions.

Quantum Tunneling of magnetization (QTM):

The excited states may be populated with absorbing phonons and after that QTM may take place between M_S states with the same energy and opposite signs, followed by relaxing to the ground state sublevel, which might be the relaxation mechanism. This combined relaxation process is called TA-QTM (**Figure 1.22**). QTM occurs at low temperature and TA-QTM occurs at intermediate temperature. Among all relaxation processes, TA-QTM and QTM are considered barrier shortcuts because the system relaxes without overcoming the barrier. As a result, the barrier U value is reduced, resulting in the effective energy barrier, U_{eff} . This simultaneously affects the blocking temperature and the relaxing time.

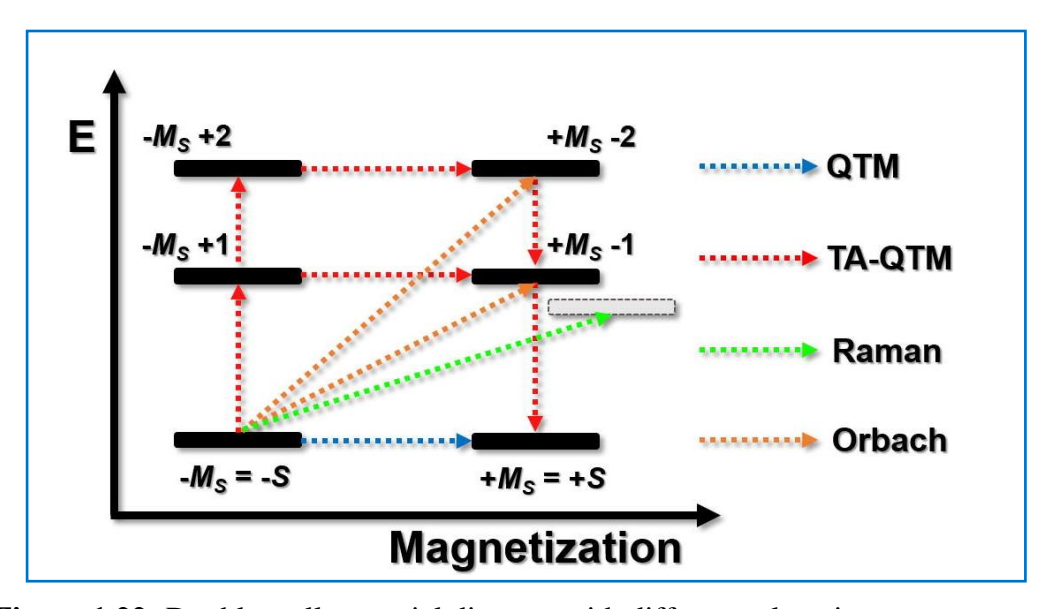


Figure 1.22: Double well potential diagram with different relaxation processes

1.11.4 Characterization of SMMs Behaviour:

Superconducting Quantum Interface Device (SQUID) magnetometer, which is incredibly sensitive and accurate and used to measure extremely tiny magnetic fields as low as 5 x 10⁻⁸ T. has been utilized to conduct magnetic measurements. The coils of a typical magnetometer are inductively connected to a superconducting loop (SQUID), which can detect very little magnetic flux rather than measuring a sample directly. The SQUID magnetometers come in two varieties that use direct and alternating currents to operate, respectively. Two methods, ac magnetic susceptivity and dc magnetic susceptibility, are frequently employed to assess whether a material exhibits slow relaxation of the magnetization. The most commonly used technique is out-in-phase (χ_M') and out-of-phase (χ_M'') ac magnetic susceptibility measurements. Generally, these measurements are performed with a temperature range from 2 K and 300 K, varying the alternating current frequency; involve two types of plots are χ''_M vs. T (**Figure 1.23a**) and χ''_M vs. v (**Figure 1.23b**). When frequency-dependent peaks are found in the χ''_M vs. T plots, the respective system exhibits an SMM property. Notably, the non-zero signals below the maximum peaks are a signal of QTM and also this can be observed in the χ''_M vs. v plots when the maxima's position, which is correlated with relaxation time, does not change as the temperature rises. When the relaxation time and the alternating current's period line up, maximum peaks can be seen in the $\chi_M''(T)$ and $\chi_M''(v)$ graphs. Using the Debye model χ''_M vs. v graphs can be fitted. In the case of the Orbach process, relaxation times adhere to Arrhenius law and fitting gives the value of energy barrier U_{eff} .

$$\tau^{-1} = \tau^{-1}_0 \exp(-U_{\text{eff}}/k_B T)$$

For other processes,

$$au^{-1} = au^{-1}_{QTM} + AT + BT^{n} + au^{-1}_{0} \exp(-U_{eff}/k_{B}T)$$

where $\tau^{-1}_{QTM} = QTM$, $BT^n = Raman$ and AT = direct relaxation processes.

Figure 1.23c represents Arrhenius fitting, where the Orbach, Raman and QTM processes are present. This can be explained by Cole-Cole plots. The semicircles in the χ_{M} " vs. χ_{M} ' at different temperatures represent the Cole-Cole plot (**Figure 1.23d**) and can be drawn by the Debye model. This curve gives α values from 0 to 1; $\alpha = 0$ represents a single relaxation process and values approximately 1 represent more relaxation mechanisms occurring simultaneously.

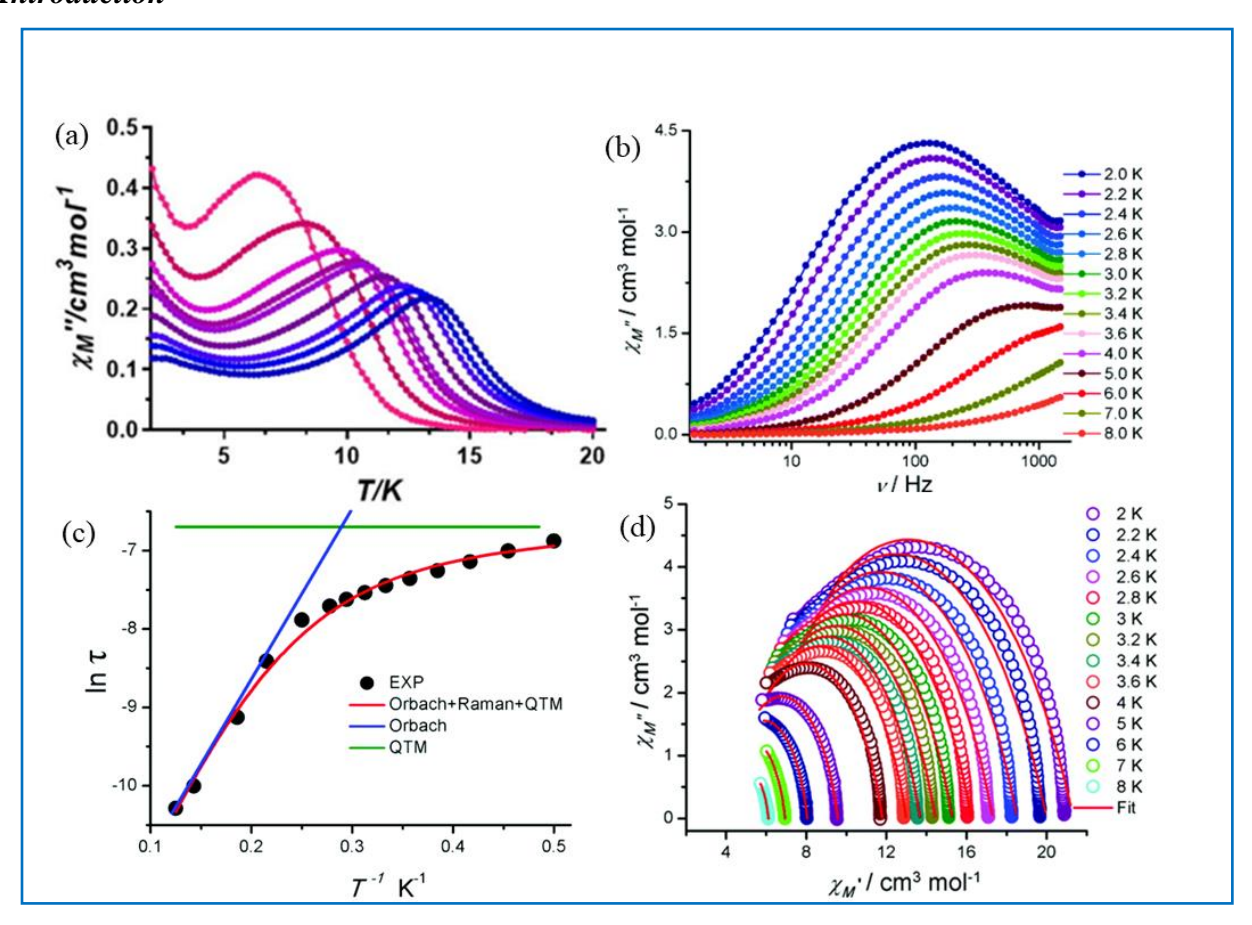


Figure 1.23: (a) temperature dependent, (b) frequency-dependent out-of-phase magnetic susceptibility (χ_M'') plots, (c) Arrhenius plot and (d) Cole–Cole plot.

The second method used to detect SMM behaviour is the field dependence of the magnetization at various temperature conditions. The open hysteresis cycles (**Figure 1.24**) display the SMM property. Even though SMMs with large $U_{\rm eff}$ (>500 K) values have been reported in the literature, but they are not observed at low temperatures (2 K), nor do they show obvious open

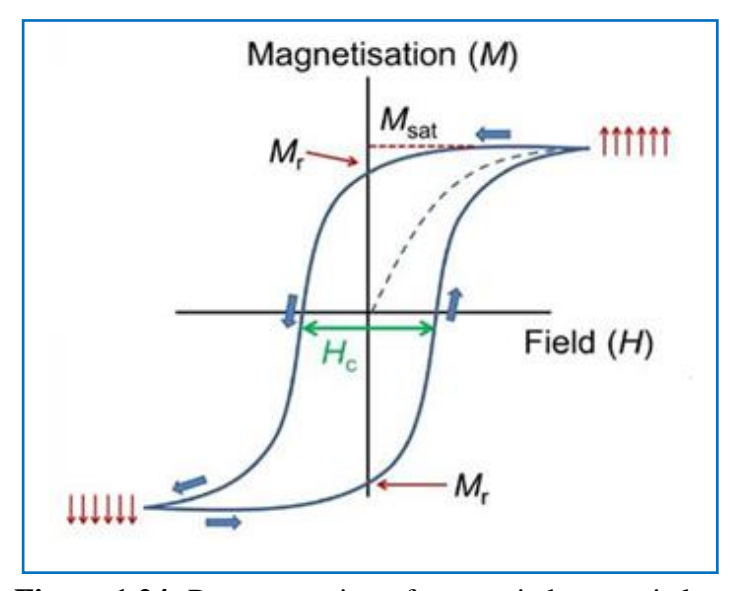


Figure 1.24: Representation of magnetic hysteresis loop

hysteresis loops. Open hysteresis loops have recently been observed at temperatures up to 80 K, which is higher than the boiling point of liquid nitrogen. This has been hailed as a significant advancement in the field. One important parameter called blocking temperature defines from this technique to characterize the SMM behaviour. The blocking temperature is mainly depending on the sweeping rate. For comparison of SMMs with $T_{\rm B}$, to make sure that hysteresis loops are studied with the same reaction conditions.

1.12 Transition Metal-Based First SMM:

In 1980, the first SMM based on transition metal, Mn₁₂-OAc was synthesized by Lis⁶⁸ and its magnetic properties were not studied until 1990. Sessoli and co-workers reported the interesting magnetic property of the Mn₁₂-OAc cluster in the year 1993, which shows that after the removal of an external magnetic field, it retained its magnetic moment. ⁶⁹ The explanation of the slow relaxation of magnetization opens the platform for the concept of SMM. The cluster $[Mn_{12}O_{12}(CH_3COO)_{16}(H_2)_4] \cdot 2CHO_3COOH \cdot 4H_2O$ (**Figure 1.25a**) contains twelve Mn ions; four Mn ions are present in 4+ oxidation state with spin S=3/2 and 8 Mn ions are present in 3+ oxidation state with spin S=2(Figure 1.25b). In the dodecanuclear cluster, four Mn(IV) ions represent an internal tetrahedron with a Mn₄O₄ cubane core. Eight Mn(III) ions represent an external octagon bridged with oxygen donor atoms forming a crown-like geometry. All the four Mn(IV) ions and eight Mn(III) ions coupled ferromagnetically among themselves and at low temperatures all 12 Mn ions coupled antiferromagnetically, giving an S=10 ground spin state. The evidence for the S=10 ground state of the Mn₁₂-OAc cluster was reported by Gatteschi et al. based on magnetic measurements and EPR studies. ⁷⁰ Sessoli et al. showed the imaginary part of AC magnetic susceptibility ($(\gamma_M")$) studies of the Mn₁₂-OAc cluster and its measurements performed in zero applied field between 4-25 K temperature range and 55-500 Hz frequency range. They observed that the Mn_{12} -OAc complex exhibited the non-zero γ_M " in the paramagnetic region and also observed relaxation effects combined with spontaneous magnetization. Parallelly, the same group reported the magnetic bistability in an Mn₁₂-OAc complex.⁷¹ They observed highly anisotropic behavior and slow relaxation of magnetization at a temperature below 4 K, giving prominent hysteresis (Figure 1.25d). This behaviour resembles that of a bulk ferromagnet, in which the motion of the domain wall provides hysteresis. This behavior of the Mn₁₂-OAc cluster indicates advancement at the molecular level. Bistable magnetic materials have applications in data storage devices. J. R. Friedman et al. 72 reported the impacts of quantum mechanics on oriented magnets to exhibit macroscopic

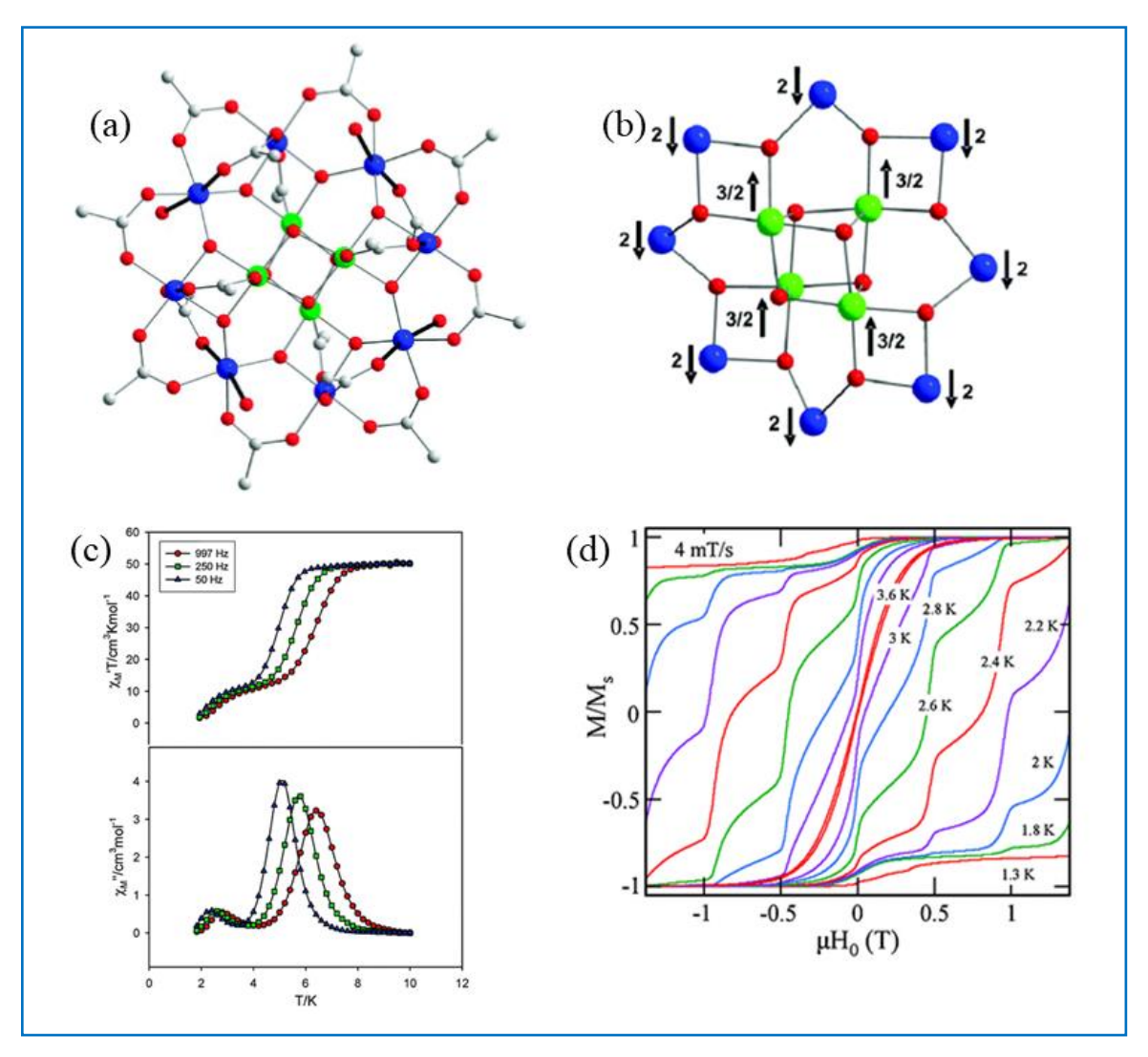


Figure 1.25: (a) Molecular, (b) core structure with the spin spin alignment of Mn_{12} cluster, (c) In-phase and out-phase ac magnetic susceptibility plots of Mn_{12} cluster and (d) Hysteresis loop.

scales in the magnetization crystals of Mn_{12} -OAc and confirmed by Thomas *et al.*⁷³ They explained this as resonant tunneling of magnetization between various quantum spin states that are thermally assisted and field-tuned and proposed that its observation in a sample that is macroscopically huge results from the tunneling of a significant number (Avogadro's) of similar high-spin clusters. This unique property linked the quantum domain to the macroscopic domain, which is why researchers are so intrigued by the Mn_{12} -OAc cluster phenomena.

The alignment of all the Mn(III) ion (high spin d⁴) Jahn-Teller axes in the same direction cause the significant, negative axial anisotropy that is the source of the Mn₁₂-OAc complex magnetic anisotropy. The Mn₁₂-OAc cluster with spin state S=10 is split into 21 (m_s =2S+1) levels by an axial zero-field splitting, which was characterized by m_s (spin quantum number), where -S $\leq m_s \leq$ S. These 21 microstates are separated by the energy equation $E(m_s)=m_s^2D$ (D is axial

anisotropy parameter). When D < 0, the low energy states with the largest m_s value, $m_s = \pm 10$ and these sublevels associated magnetism has a distinct direction along with the magnetic axial anisotropy axis. In this case, $m_s=+10$ indicates spin-up and $m_s=-10$ indicates spin-down. D > 0, on the other hand, results in the opposite and undesirable condition. The energy sublevels would be orientated in the other direction so that $m_s = 0$ would represent the ground state. Because a bistable ground state in this particular case is not possible, the system is invalid for storing data. As it happens for superparamagnetic materials, the Mn₁₂-OAc must exceed an energy barrier, U, to have reversal a of the magnetization from $m_s=+10$ to $m_s=-10$ (or vice versa). The difference between the excited state and ground state is represented by the energy barrier value and defined as $U = S^2|D|$ and $S^2 - 1/4|D|$ (for integer spin and non-integer spin values). The Mn₁₂-OAc has the value D=-50 cm⁻¹ (-70 K). The m_s = -10 sublevels are equally populated with the same energy without an external magnetic field; therefore, the system sends no magnetization. When the field is applied, Ms sublevels are stabilized and the total spin of Mn12-OAc present in the same direction attained a magnetization. When the field is off, bringing the ground state back to a doubly degenerate state. If E_T>U, the cluster will achieve equilibrium between positive and negative orientations, losing its magnetism. The magnetization will be blocked if $E_T < U$, which is the case when $T < T_B$ (T_B is the blocking temperature) (Figure 1.26) and this is how SMMs can store data. The final conclusion was that magnetization could be maintained at which system has a larger temperature and energy

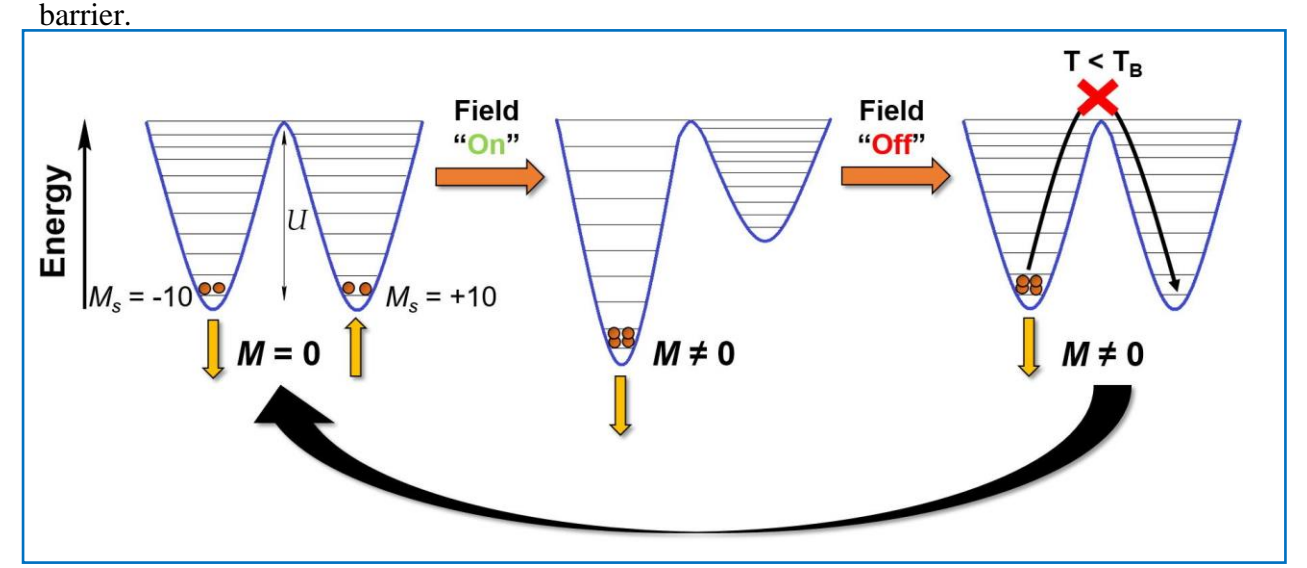


Figure 1.26: Double well potential diagram of Mn₁₂ cluster

1.13 Why are Lanthanides Preferred Over Transition Metals?

After the initial discovery of the Mn₁₂-OAc SMM, other examples of transition metal-based SMMs have been found; nevertheless, in comparison to the initial Ln-based SMM [LnPc₂] described by Ishikawa et al. 74 their blocking temperature and energy barrier for spin reversal are relatively low. Following this discovery, various lanthanide-based SMMs have reported with a wide spectrum of nuclearities, from mononuclear to Ln₂₋₆₀. Compared to SMMs based on TM, these SMMs have higher energy barriers and magnetization-blocking temperatures. Why lanthanides are preferable to transition metals due to these characteristics are large uniaxial magnetic anisotropy (D) and large ground spin state (S). Bringing together several paramagnetic metal centers that exhibit ferro or ferri magnetic spin arrangements is required in the context of transition metal ions in order to obtain a significant ground state spin term. The energy barrier for the reversal of spin magnetization is provided by the splitting of the ground state (S) into each of its separate m_s levels. Its energy is also influenced by the direction of the anisotropy axis on the discrete metal centers and the anisotropy of the discrete spin centers found in the complex or cluster. Despite the presence of strong magnetic interactions among the transition metal ions via ligand orbitals, these interactions did not produce significant anisotropies because there was insufficient spin-orbit coupling (prominent exception of Co(II)). Hence, the maximum energy barrier in SMMs based on transition metal has S=10and D varies between 0.5 and 0.9 cm⁻¹.

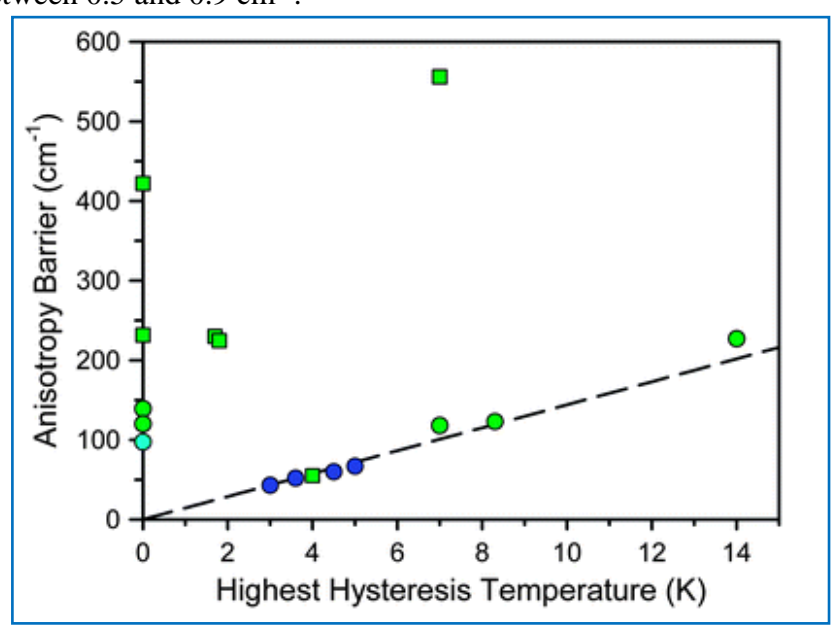


Figure 1.27: Plot of the highest recorded hysteresis temperature vs. the anisotropy barrier for the selected single-molecule magnets. Colo codes: Blue, T. M.; green, Lanthanides and cyan, actinide-based SMMs.

The advantage of lanthanides over transition metals is that lanthanides have their 4f orbitals spatially "buried" within the atom and shielded from the ligand field by the $5s^2$ and $5p^6$ orbitals. The lanthanide ion and ligands interact almost exclusively electrostatically as a result, the spinorbit coupling (the primary source of the magnetic anisotropy) cannot be quenched as readily as it can for transition metals. This indicates that the anisotropy value will often be larger for lanthanides than for transition metal complexes; hence one could anticipate the development of SMMs with superior properties. Ground-state bistability is caused by the total spin S and the consequent [2S + 1] m_S substates for transition metal-SMMs. In contrast, the spin-orbit-coupled ground term, ${}^{2S+1}L_J$, in Ln-SMMs gives rise to ground-state bistability through the [2J + 1] m_J microstates. while designing SMMs, the ground state with the largest possible MJ absolute values (provides a substantial magnetic moment) should be used; this is possible when the ground state's anisotropy is axial. Furthermore, in order to achieve large $U_{\rm eff}$ values, the difference in energy between the m_J and $m_J \pm 1$ states must be as great as possible. The ligand field symmetry can increase lanthanide ion anisotropy. The ligand field and spin-orbit coupling both play a role in the relaxation of Ln-metal ions. These inherent qualities make lanthanide ions the ideal candidates for building SMMs with improved characteristics.

Long *et al.* reported⁷⁵ a qualitative approach to forecasting the ligand designs for various f-element ions that will produce strong magnetic anisotropy. In the lanthanide series, the majority of lanthanide ions exhibit significant spin-orbit coupling, but Gd(III) is totally isotropic. Lanthanides with more unpaired electron spins has a zero potential for the creation of SMMs. Two basic categories of ions with anisotropic electron density can be identified: oblate and prolate-type ions (**Figure 1.28**).

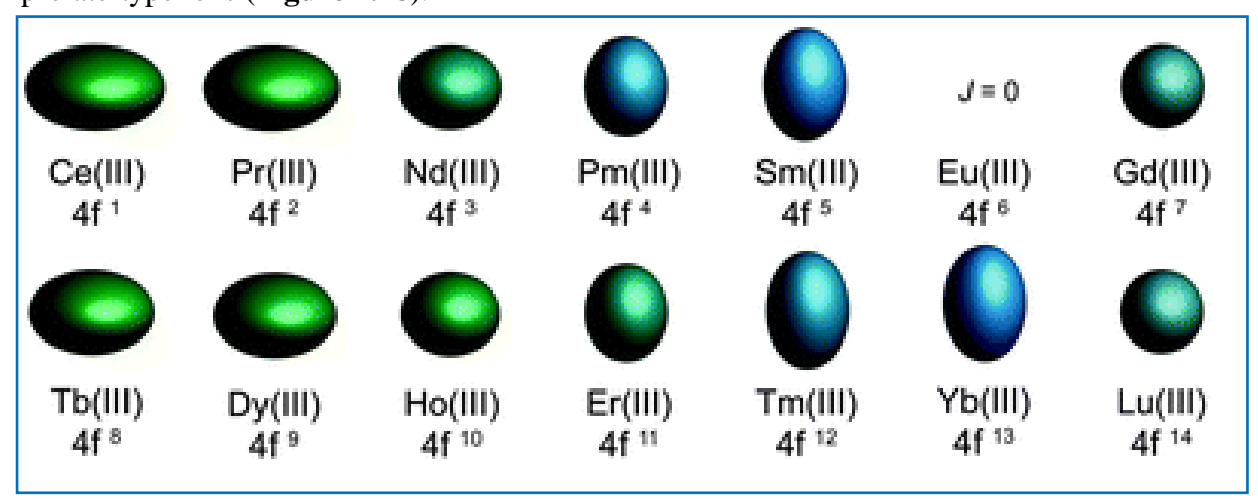


Figure 1.28: 4*f* orbital electron distribution topologies for Ln(III) ions.

For the oblate type of Ln(III) ions, the specific ligand donors with the highest electron density should coordinate at axial positions and it will cause less repulsions between the oblate ions

and ligand atoms. These repulsions are the reason for stabilizing the ground state (higher M_J values). Herein, the anisotropy axis is perpendicular to the electron density of oblate shaped, points to the higher electron density of donor atoms and reduces Ln–X (X= donor atom) distances. If donor atoms are not coordinated to equatorial positions, the plane electron density expands and plane axial anisotropy will increase. In contrast, if the ligand atoms coordinated to equatorial positions and behaviour will be isotropic and it won't be useful for SMMs. For the prolate type of Ln(III) ions, the donor atoms with the highest electron density should coordinate at equatorial positions to get axial anisotropy and it will cause less repulsions between the prolate ion and the donor atoms. In this case, the anisotropic axis parallel to the electron density of prolate lies perpendicular to the higher electron density of donor atoms present in the plane. If no ligand donors are in axial positions, prolate ion electron density will expand through the axial direction, resulting in greater axial anisotropy. On the other hand, if the ligand atoms coordinated to axial positions produce a more isotropic resulting in a reduction in anisotropy (**Figure 1.29**).

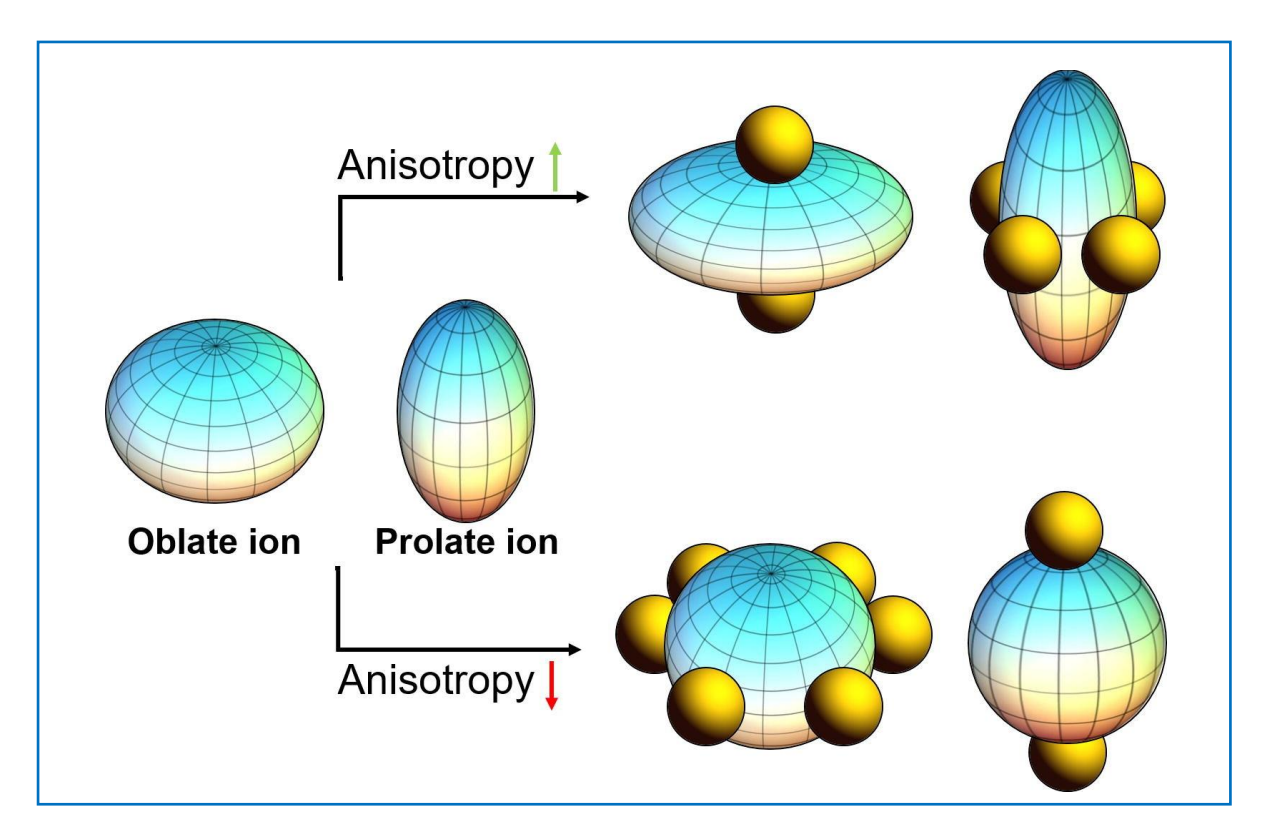


Figure 1.29: Representation of anisotropy effect for prolate and oblate type of Ln (III) ions

1.14 Lanthanide-Based First SMM:

In 2003, Ishikawa and co-workers reported the first SMMs based on lanthanide ions, [Pc₂Ln] .TBA $^+$ (Ln=Tb and Dy; TBA $^+$ =N(C₄H₉)₄ and Pc 2 =phthalocyaninato). These complexes have double-decker geometry (Figure 1.30a), in which the lanthanide ion is surrounded by phthalocyanine ligands. In contrast to transition metal-based SMMs, they described a new family of SMMs with a unique mechanism. Koike et al. reported76 the crystal structure of [Pc₂Ln]⁻.TBA⁺ complexes; the two Pc groups sandwich the core Ln(III) ions, which contain eight coordinated nitrogen atoms (Niso) of two Pc ligands that form a saucer shape and two Pc moieties are present in a staggered conformation with respect to one another. They synthesized samples by literature reports⁷⁷ and performed AC magnetic susceptibility measurements on a group of compounds [Pc₂Ln]⁻.TBA⁺ (Ln=Tb, Dy, Ho, Er, Tm, or Yb), Dy and Tb complexes displayed SMM behaviour among the others. Figure 1.30b represents the AC magnetic susceptibility measurements of [Bu₄N][TbPc₂], where χ_M ', χ_M ' and χ_M are in-phase-AC, outof-phase-AC, and DC molar magnetic susceptibilities. Slow relaxation of magnetization is intrinsic property; to confirm this property, the experiment was performed for a [Bu₄N][TbPc₂] complex doped with [Bu₄N][YPc₂] in a 1:4 molar ratio. In the diluted compound, they observed a χ_M ''/ χ_M and χ_M 'T peak shifting to a higher temperature. This experiment clearly indicates that a doped diamagnetic compound can remove the intermolecular interaction from the adjacent [Bu₄N][TbPc₂] complex and can slow down the magnetic dipole's ability to flip. With the help of this evidence, they conclude that [Bu₄N][TbPc₂] has an SMM behavior. A similar

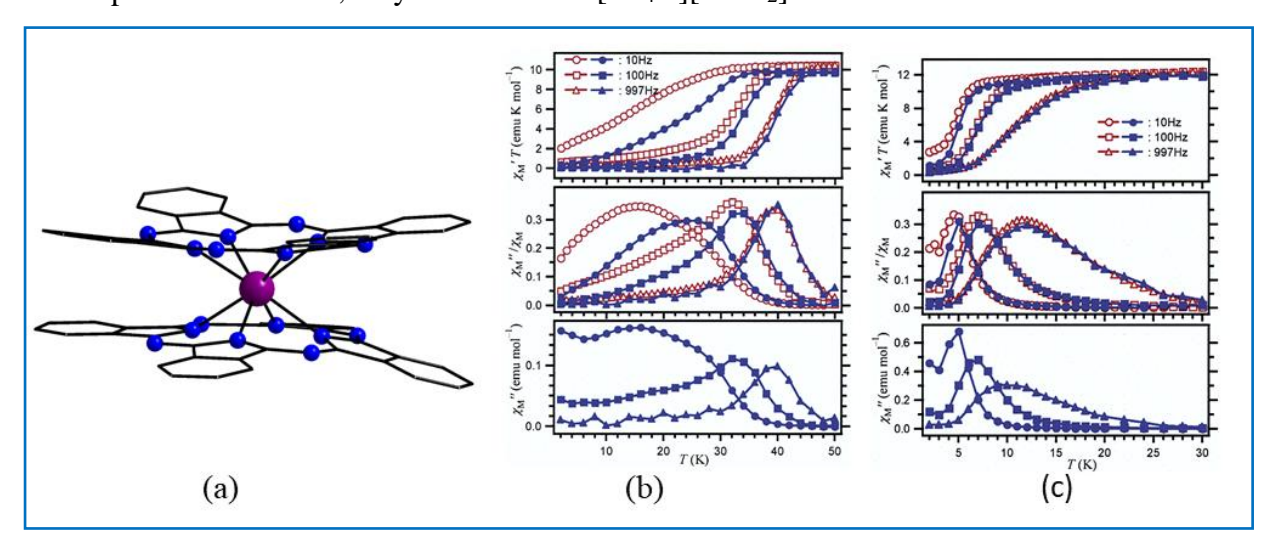


Figure 1.30: (a) Molecular structure of [LnPc₂]⁻, (b)) χ'_T (T) (top), χ'' / χ_M (T) (middle), and χ'' (T) plots for [TbPc₂]⁻ (open points) and that diluted in [Bu₄N][Pc₂Y] (filled points) and (c) χ'_T (T) (top), χ'' / χ_M (T) (middle),and χ'' (T) plots for [DyPc₂]⁻ (open points) and that diluted in [Bu₄N][Pc₂Y] (filled points).

experiment was performed for [Bu₄N][DyPc₂] and concluded that [Bu₄N][DyPc₂] has an SMM behavior(**Figure 1.30c**). The remarkable increase in temperature is associated with the sublevel structures of [Bu₄N][TbPc₂]. The sublevel structures of complexes can be determined by using ¹H NMR data and DC susceptibility measurements. For diluted complexes [Bu₄N][TbPc₂] and [Bu₄N][DyPc₂] Arrhenius plot give the $U_{\rm eff}$ =230 and 28 cm⁻¹. M. Ruben *et al.* reported⁷⁸ the group of Tb(III) complexes by using diamagnetic [TBA]^{+[}Br]⁻ material to dilute magnetically active [TbPc₂]⁻ moiety, which shows the higher energy barrier 584 cm⁻¹ -641 cm⁻¹ as compared to energy barrier of [TBA][TbPc₂] (230 cm⁻¹).

Lanthanide-based SMMs have drawn more attention after the discovery of the first lanthanide-based SMM. Researchers adopted various methodologies to synthesize the series of Ln-SMMs. Low nuclearity compounds with interesting magneto-structural relationships show a greater effective energy barrier and remarkable blocking temperatures. A large number of polynuclear lanthanide clusters were synthesized by using a serendipitous approach. In this approach, based on solvents, varying reaction conditions and the ratio of metal to ligand revealed various products with intriguing magnetic properties. In the serendipitous approach, various ligand systems phosphonates, 79 carboxylates, 80 amino acids, 81 Schiff bases, 82 β -diketones 83 and polyoxomelates 84 have been used.

1.15 Few Breakthrough Results of Lanthanide SMM:

Trinuclear clusters are uncommon among lanthanide cluster series and the majority of trinuclear SMMs containing dysprosium have been documented. Trinuclear Ln-SMMs are triangular and linear based on their structural arrangement. Dysprosium triangles have drawn a lot of attention because, while exhibiting a non-magnetic ground state, they show a slow relaxation of magnetization. Powell *et al.* reported⁸⁵ the synthesis and structural characterization and magnetic studies of two trinuclear Dy(III) clusters [Dy₃(μ₃-OH)₂L₃Cl(H₂O)₅]Cl₅ and [Dy₃(μ₃-OH)₂L₃Cl(H₂O)₅]Cl₃, where HL=*o*-vanillin (**Figure 1.31a**). These complexes exhibited complex magnetic behaviour. The trinuclear Dy(III) motifs are analogues to the gadolinium (III) motifs. The solid-state crystal structure of both the complexes reveals that all Dy(III) centers are eight-coordinated and attained a distorted geometry and the deprotonated o-vanillin group is connected to each side of the triangle by its phenoxo group. Furthermore, methoxy and aldehyde groups coordinate with the Dy(III) center. An unprecedented magnetic property, at low temperature, vanishing susceptibility displayed by two dysprosium triangles. The Dy(III) complexes contain an odd number of unpaired electrons with a non-magnetic state explained by intercluster interactions. In both dysprosium triangles,

hydrogen-bonded frameworks are present; these may lead to very weak antiferromagnetic interactions. Chibotaru *et al.* provided evidence for the toroidal alignment of magnetic moments on Dy(III) sites in Dy₃ molecular architectures. ⁸⁶ In molecular magnetism, these are the first example of the toroidal magnetic moment. Parallelly, Sessoli and co-workers explained that a non-collinear (120°) Ising model was used to interpret magnetic measurements on the dysprosium triangles, which similarly led to a non-magnetic ground state. ⁸⁷ These findings led to the astonishing phenomena known as the "toroidal magnetic moment" / "vortex spin chirality" in the molecular magnetism family. AC magnetic susceptibility measurements suggest that information data storage is possible in a non-magnetic ground state. A lot of work has been put into preparing Dy₃ triangles⁸⁸ in sight of these complexes peculiar magnetic behaviour. The temperature at which the magnetization slows down is found to dramatically increase from 8 to 25 K when two Dy₃ clusters are joined to form a Dy₆ cluster. ⁸⁹ Contrary to what was earlier reported for a similar arrangement of Dy₃ triangles, where a ferromagnetic interaction was indicated, this occurs despite the connecting promoting an antiferromagnetic contact.

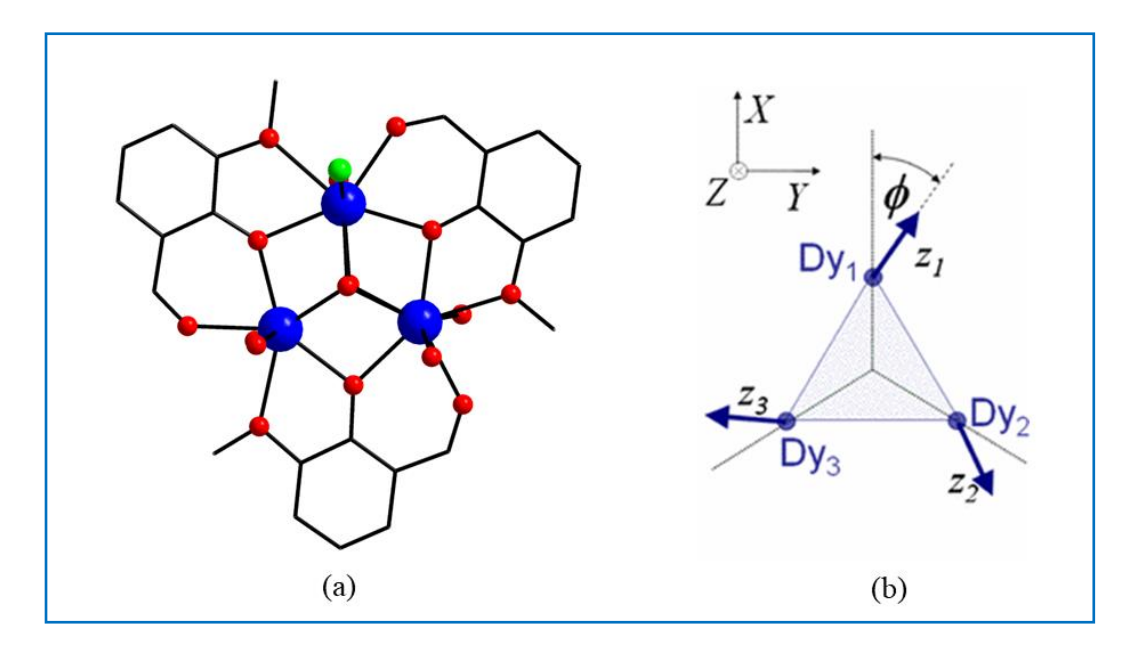


Figure 1.31: (a) Solid-state structure of $[Dy_3(\mu_3-OH)_2L_3Cl(H_2O)_5]Cl_5$ and (b) Schematic representation of the spin form of the Dy_3 cluster and of the local easy axes alignment in respect of the laboratory XYZ reference frame.

Murugesu *et al.* reported a tetranuclear dysprosium (III) complex $[Dy_4(\mu_3-OH)_2(bmh)_2(msh)_4Cl_2]$ (where $H_2bmh=1,2$ -bis [2-hydroxy-3-methoxybenzylidene]hydrazone and Hmsh=3-methoxysalicylaldehyde hydrazone) with record anisotropic energy barrier. ⁹⁰

According to SC-XRD studies, the tetranuclear cluster has a defect-dicubane central core. All coplanar Dy(III) ions are connected through two μ_3 -OH groups that are present above and below the plane of the tetranuclear cluster. All Dy(III) ions presented in an eight-coordination mode attain a square-antiprismatic geometry (**Figure 1.32**). The frequency-dependent out-of-phase ac susceptibility displayed slow relaxation of magnetization at 30 and 9 K, which represents

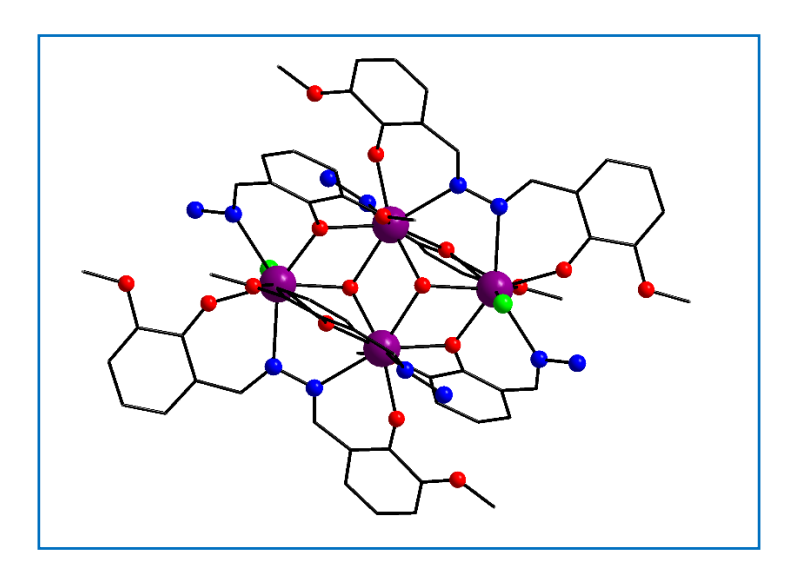


Figure 1.32: Molecular structure of $[Dy_4(\mu_3-OH)_2(bmh)_2(msh)_4Cl_2]$

the two relaxation modes. These two maxima peaks correspond to the two types of dysprosium ions in the Dy4 cluster and reveal the SMM behavior. Arrhenius plots were drawn from ac and dc magnetic susceptibility data vs. time gave energy barriers of $U_{\rm eff} = 170 \, {\rm K} \, (\tau_0 = 4 \times 10^{-7} \, {\rm s})$ and $U_{\rm eff} = 9.7 \, {\rm K} \, (\tau_0 = 3.2 \times 10^{-5} \, {\rm s})$ for high and low-temperature relaxation dynamics. At high temperature, the process of slow relaxation of the magnetization is unique, as compared to a similar type of Dy₄ complex⁹¹ and other polynuclear clusters show SMM behaviour below 10 K.

Winpenny *et al.* reported⁹² the preparation and magnetic properties of Dy(III) square-based pyramid cluster [Dy₅O(OⁱPr)₁₃]. The adopted synthetic methodology is as follows; a reaction of anhydrous DyCl₃ with freshly prepared KOⁱPr in OⁱPrH/toluene with a small amount of H₂O. In the Dy₅ cluster, all Dy(III) are connected through an oxide/alkoxide and all Dy(III) ions are hexa-coordinated with octahedral geometry. Interestingly, Dy(III) ions are presented far from the central μ_5 -oxide and moved towards terminal alkoxides, indicating all Dy(III) ions have non-crystallographic, C_{4v} symmetry (**Figure 1.33a**). The highest out-of-phase ac susceptibility peak is noticed at 40 K, indicating the SMM behaviour with an effective energy barrier of U_{eff} =528 K. Later, the same group reported the tetranuclear Ln(III) alkoxide clusters

[Ln₄K₂O(O⁶Bu)₁₂].xC₆H₁₄ (where Ln = Gd, Tb, Dy, Ho & Er) (**Figure 1.33b**) and their magnetically diluted yttrium analogues.⁹³ They explained thermal relaxation process through a higher excited state can be generated by a substantially axial crystal field and result in higher U_{eff} values. Ac susceptibility measurements show two different frequency-dependent out-of-phase peaks and from the Arrhenius graph, observed anisotropic energy barrier of $U_{\text{eff}} = 692$ K (τ_0 =6.6 ×10⁻¹¹ s) and 316 K (τ_0 =2.6×10⁻⁹ s) respectively and the magnetically diluted Y-complexes attain more high anisotropic energy barriers (U_{eff} >800 K).

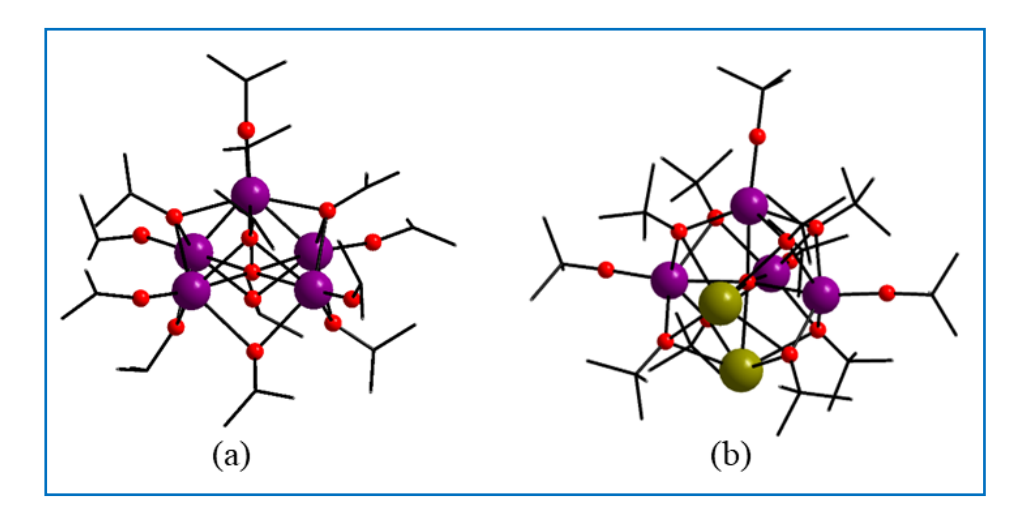


Figure 1.33: Molecular structure of (a) $[Dy_5O(O^iPr)_{13}]$ and (b) $[Ln_4K_2O(O^tBu)_{12}]$

In 2013, Chadrasekkar and co-workers reported⁹⁴ the two planar rhombus shaped homotetranuclear lanthanide complexes $[\{(LH)_2Dy_4\}(\mu_2-O)_4](H_2O)_8 \cdot 2CH_3OH \cdot 8H_2O$ and $[\{(LH)_2Ho_4\}(\mu_2-O)_4](H_2O)_8\cdot 6CH_3OH\cdot 4H_2O$ wherein, Schiff-base hydrazide ligand (6-Hydroxymethyl)-N'-((8-hydroxyquinolin-2-yl)- methylene) Picolinohydrazide (LH₃) was used. In the homometallic Ln-SMM family, these neutral complexes are the first examples where all the metal and ligand atoms are present in a single plane. SC-XRD analysis shows two clusters present in an asymmetric unit in which two different Ln(III) ions are present. One group of Ln(III) ion is 8-coordinated and contains a distorted dodecahedron geometry, and another group of Ln(III) ion is hepta-coordinated and seems to be very different from any known reference geometry. Each double-deprotonated Schiff base ligand contains two Ln³⁺ ions retained in one of the two chelating coordination pockets to form the [LH(Ln)₂]⁴⁺ units. Two $[LH(Ln)_2]^{4+}$ units are bridged with four $[\mu_2-O]^{2-}$ moieties to reveal the formation of a planar homotetranuclear assembly (Figure 1.34a). The detailed ac susceptibility studies are indicative of Dy(III) cluster SMM behaviour below 20 K. From γ_M vs T graph, observed two peaks representing the two relaxation dynamics lead to effective energy barriers of $U_{\rm eff}$ =54.2

K (τ_0 = 7.2×10⁻⁷ s) and 16.8 K (τ_0 = 1.4×10⁻⁶ s) for high and low temperatures, respectively. This SMM phenomenon is explained by two Dy(III) sites with various coordination modes and topologies. Later, same group reported the series of cubane-shaped Ln₄ clusters [Ln₄(L)₄(μ ₂- η $^1\eta$ ^1Piv)₄]·xH₂O·yCH₃OH (Ln= Gd, Tb & Dy) by using the chelating and flexible Schiffbase ligand (E)-2-((6-(hydroxymethyl) pyridin-2-yl) methylene amino) phenol (LH₂) and pivalic acid (PivH) (**Figure 1.34b**). The magnetic studies of the Dy(III) cluster show the highest effective energy barrier till 74 K (τ_0 = 4.4 × 10⁻⁸ s).

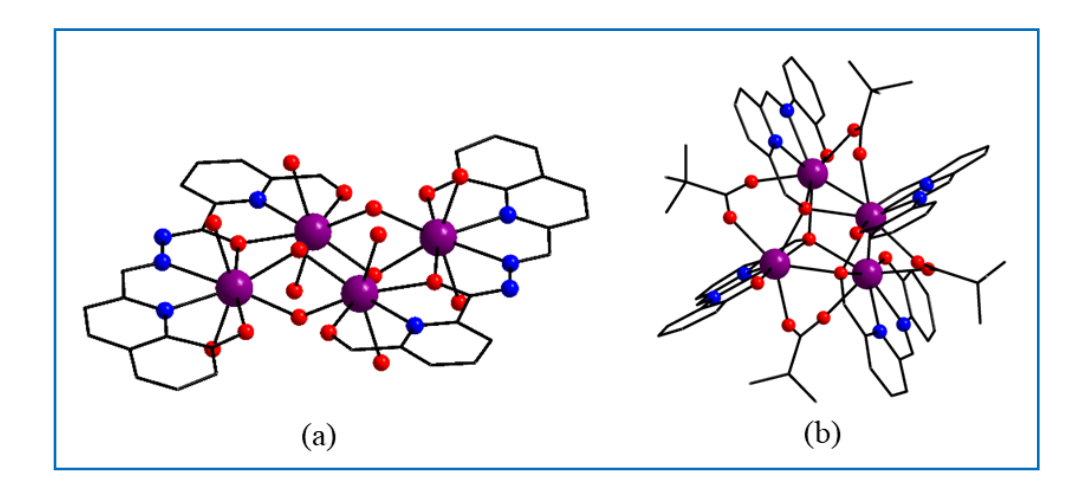


Figure 1.34: Molecular structure of (a) rhombus-shaped Dy₄ cluster and (b) cubane-shaped Dy₄ cluster

Single-ion magnets have applications in the field of spin-based systems. Lanthanide ions are considered the most alluring option for raising $T_{\rm B}$, a persistent problem that still has to be tackled. To prepare the system with large $T_{\rm B}$ and $U_{\rm eff}$, low-coordinate lanthanide compounds are desirable. The synthesis of low-coordinate 3d and 4f-based complexes is quite difficult since it not only necessitates inert environments but also produces complexes that are typically unstable in ambient aerobic environments. Murugavel and co-workers reported⁹⁶ the air-stable Dy (III) and Er (III) clusters, $[L_2Ln(H_2O)_5][I]_3.L_2.(H_2O)$ [where Ln=Dy, Er and $L=(^BuPO(NH'Pr)_2)]$. SC-XRD studies show the Dy(III) ion present in a pseudo- D_{5h} symmetry with five equatorial and two axial coordination positions occupied by an H_2O molecule and phosphonic diamide groups and coordinated Ln (III) ion through a P=O (Figure 1.35). From magnetic measurements, Dy (III) SIM displays a blocking temperature up to 12 K with the highest energy barrier of 735.4 K. It exhibits a magnetic hysteresis loop up to 12 K (30 K) with a high coercivity ~ 0.9 T (~ 1.5 T) at a field-sweep rate of ~ 0.0018 Ts⁻¹ (~ 0.02 Ts⁻¹). These values indicate the ambient stability of the cluster and represent a better SIM.

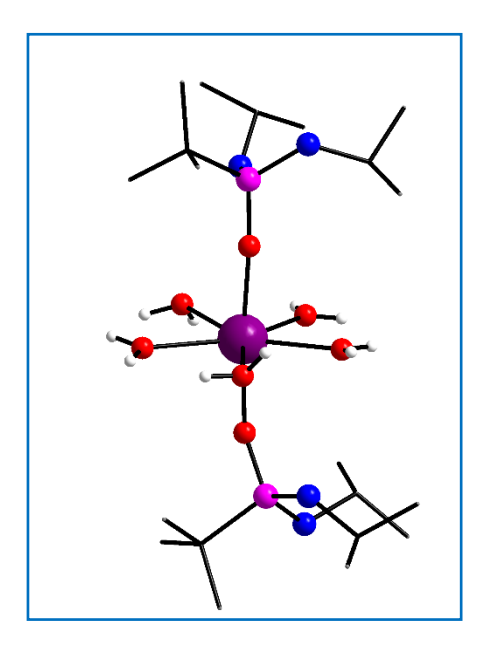


Figure 1.35: Molecular structure of $[L_2Dy(H_2O)_5]^{3+}$ [where $L=(^tBuPO(NH^tPr)_2)$]

Winpenny *et al.* reported another SIM, $[Dy(O^tBu)_2(py)_5][BPh_4]$ synthesized by a reaction of DyCl₃ with Na(O^tBu) and Na(BPh₄) in THF at room temperature.⁹⁷ The solid-state crystal structure reveals the formation of a pentagonal bipyramidal shape cluster and the Dy(III) ion is seven-coordinated (**Figure 1.36**). This Dy(III) cluster exhibits the highest effective energy barrier of $U_{eff} = 1815$ K with magnetization blocking (T_B) 14 K.

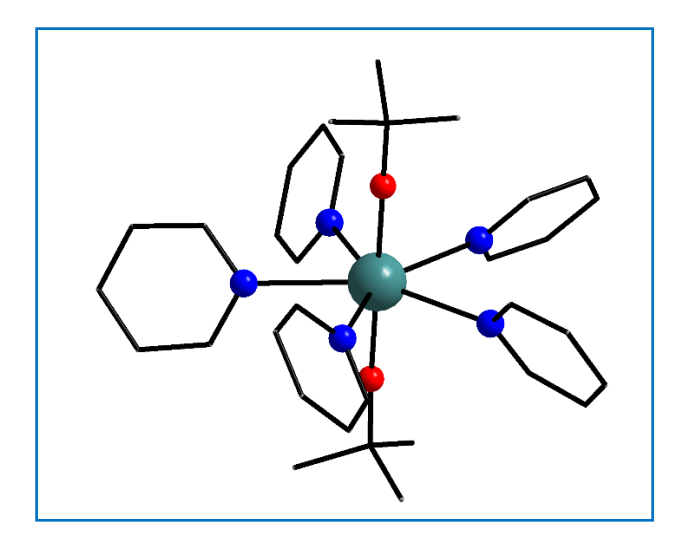


Figure 1.36: Molecular structure of $[Dy(O^tBu)_2(py)_5]^+$

Gao group reported⁹⁸ the preparation, characterization and magnetic behaviour of Dy(III) dimer. The reaction of Dy[N(SiMe₃)₂]₃ with 2,6-di-tert-butylphenolate in a small amount of water in THF reveals the formation of dimer [Dy(μ -OH)(DBP)₂(THF)]₂ (DBP =2,6-di-tert-butylphenolate), in which two Dy(III) ions are five coordinated(**Figure 1.37**). They created Ln-only dimer SMMs using the hydration approach, which included the introduction of two

bridged hydroxides between low-coordination containing two Dy(III) ions. The Arrhenius fitting obtained from the ac magnetic measurements gave an energy barrier of $U_{\rm eff}$ = 721 K (τ_0 = 6.6×10^{-12} s) at Zero static field and dual process Arrhenius fitting gave an energy barrier of $U_{\rm eff}$ = 754 K (τ_0 = 3.5×10^{-12} s), herein Orbach process is predominating. The relaxation process of SMMs with intramolecular Dy-Dy magnetic interactions can be studied using a suitable model where the quantum tunnelling region and thermal relaxation phases are separated.

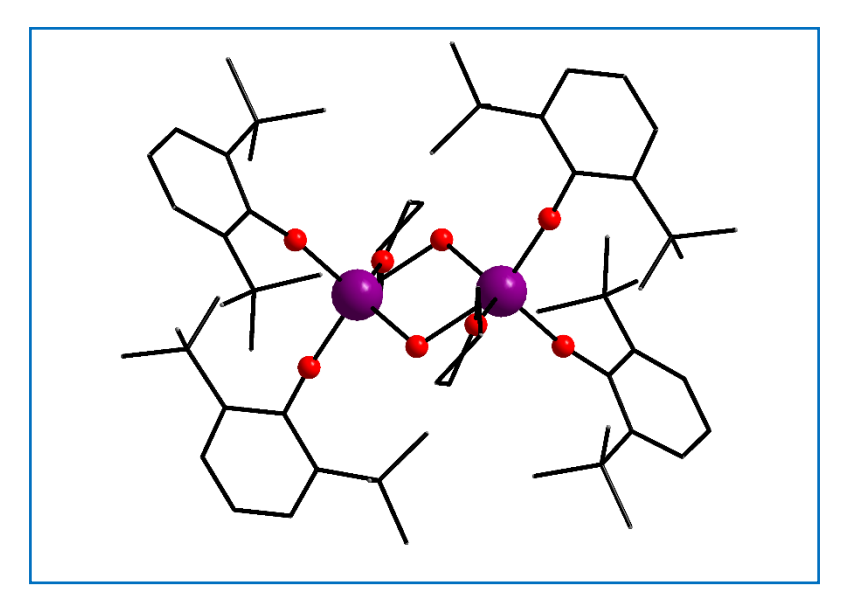


Figure 1.37: Molecular structure of $[Dy(\mu\text{-OH})(DBP)_2(THF)]_2$

Layfield and co-workers reported the first example of dysprosium-based metallocenium cation $[(Cp^{ttt})_2Dy]^+$ (**Figure 1.38b**) with non-coordinating $[B(C_6F_5)_4]^-$ anionic part was obtained by the chloride abstraction from Dy(III) metallocene $[(Cp^{ttt})_2DyCl]$ ($Cp^{ttt}=1,2,4$ -tri(tertbutyl) cyclopentadienide) (**Figure 1.38a**) by using triethylsilylium cation. The crystallographic studies of both complexes show a bent metallocene geometry with symmetric two Cp^{ttt} ligands. The complex $[(Cp^{ttt})_2Dy][B(C_6F_5)_4]$ exhibits a SMM behaviour with a record energy

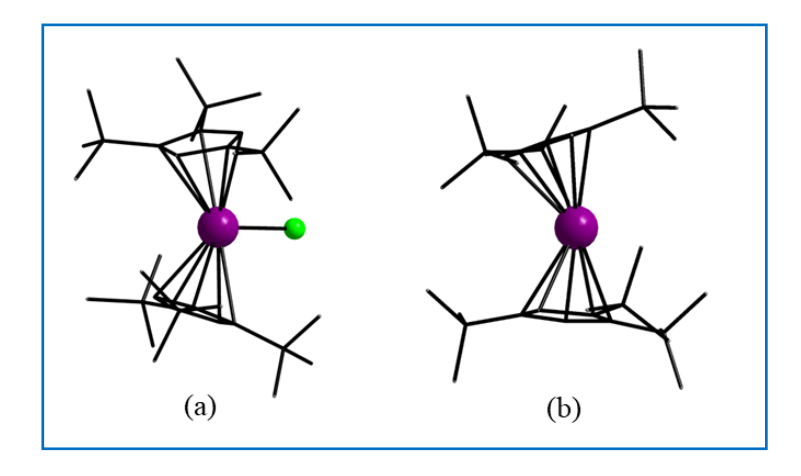


Figure 1.38: Molecular structure of (a) [(Cp^{ttt})₂DyCl] and (b) [(Cp^{ttt})₂Dy]⁺

barrier up to 1277 cm⁻¹ (1837 K) and magnetization blocking (T_B) of 60 K, along with notable coercivity. The unprecedented magnetic behaviour of Dy(III) metallocene cation is due to the magnetic axiality of Dy(III) ion in the Cp^{ttt} ligand environment.⁹⁹

Using paramagnetic bridging groups to create strong magnetic coupling between 4*f* metal ion centers has proven effective. Importantly, the anionic radical ligands' diffuse spin orbitals have a better chance of penetrating the deeply buried metal ion 4*f* orbitals core electron density. Demir *et al.* aimed to isolate the SMMs with radical ligands that allow direct exchange contact with 4*f* metal atoms reduced in coordination environments that increase strong magnetic axial anisotropy.

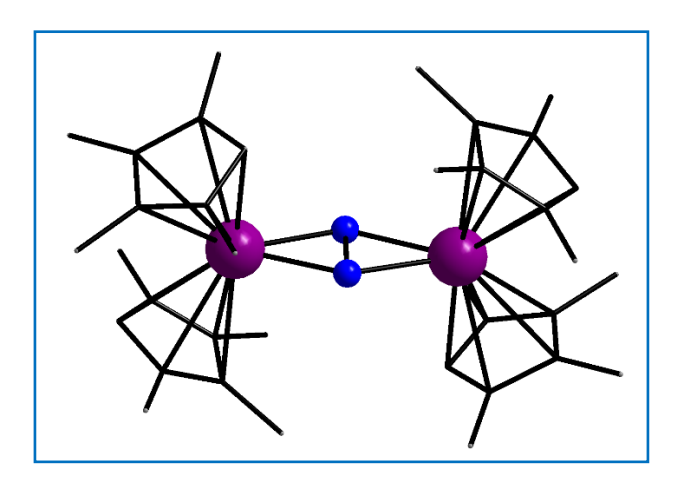


Figure 1.39: Molecular structure of $[(Cp^{Me4H_2}Tb)_2(\mu-N_2)]$

To achieve this, they synthesized the novel series of dilanthanide clusters bridged with N_2^{3-} radical is $[K(crypt-222)(THF)][(Cp^{Me4H}{}_2Ln(THF))_2(\mu-N_2)]$ (Ln= Gd, Tb and Dy) and $[K(crypt-222)][(Cp^{Me4H}{}_2Ln)_2(\mu-N_2)]$ (Ln = Tb and Dy) where Cp^{Me4H} = tetramethyl cyclopentadienyl. Interestingly, $[K(crypt-222)][(Cp^{Me4H}{}_2Tb)_2(\mu-N_2)]$ complex (**Figure 1.39**) shows an energy barrier of U_{eff} = 276 cm⁻¹ and a 100-s magnetic blocking temperature of 20 K and a coercive field of H_c = 7.9 T at 10 K.¹⁰⁰

Layfield *et al.* reported¹⁰¹ air and moisture-sensitive Dy(III) metallocene cation $[(Cp^{iPr5})Dy(Cp^*)]^+$ $(Cp^{iPr5},$ penta-iso-propylcyclopentadienyl; $Cp^*,$ pentamethylcyclopentadienyl) (**Figure 1.40**). This complex exhibits a magnetic hysteresis above a liquid nitrogen temperature boiling point ($T_B = 80 \text{ K}$) and an effective energy barrier of $U_{\text{eff}} = 1541 \text{ cm}^{-1}$. This result represents a breakthrough in the SMM family.

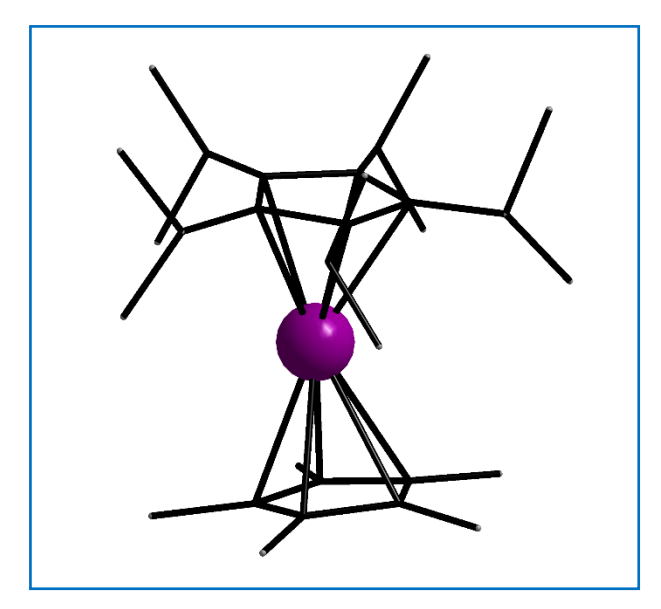


Figure 1.40: Molecular structure of [(Cp^{iPr5})Dy(Cp*)]⁺

The isolation of air-stable SMMs is crucial for their incorporation into magneto-electronic systems. Tang and co-workers reported¹⁰² the two chiral dysprosium-based macrocyclic clusters, RRRR-Dy-D_{6h}F₁₂ (a) and SSSS-Dy-D_{6h}F₁₂ (b) (**Figure 1.41**). These complexes represent the skeleton of $[Dy(L^{N6})(Ph_3SiO)_2][BPh_4]$, where ethylenediamine is used as a flexible ligand. Here, to increase the rigidity of the ligand, they introduced electron-withdrawing groups such as (1R, 2R)-1,2-bis(2,4,6-trifluorophenyl) ethane-1,2-diamine or (1S, 2S)-1,2-bis(2,4,6-trifluorophenyl) ethane-1,2-diamine on the equatorial ligand. The incorporation of fluorine atoms into equatorial ligands will likely increase their thermal stability as well as reduce the equatorial ligand field because of their electron-withdrawing features. These clusters have magnetic properties that show an U_{eff} over 1800 K and a relaxation time of up to 2500 s at 2 K. These

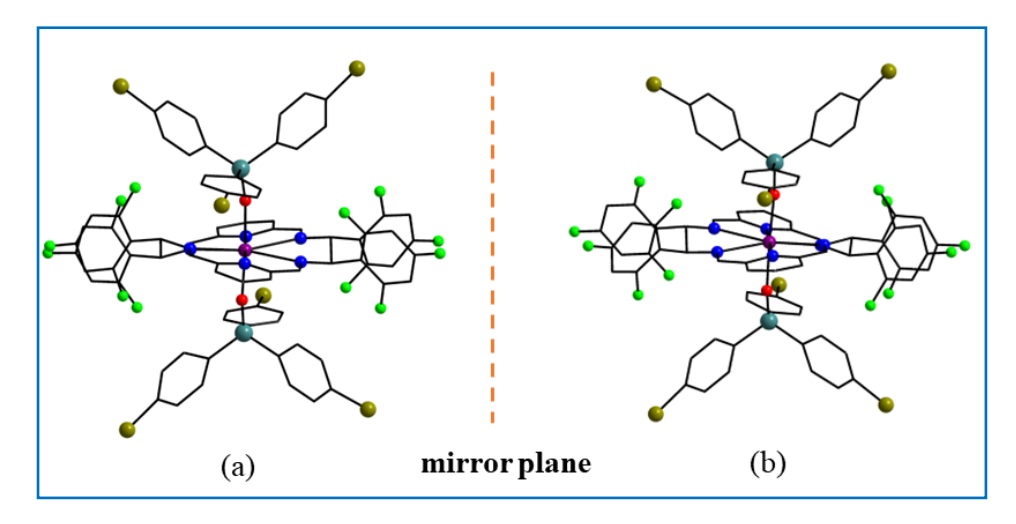


Figure 1.41: Molecular structure of (a) RRRR-Dy-D_{6h}F₁₂ and (b) SSSS-Dy-D_{6h}F₁₂

magnetic properties are because of string axial CF and equatorial ligand fluorination. This discovery opens up new possibilities for depositing SMMs on surfaces and enhances the magnetic characteristics of air-stable SMMs.

There are numerous transition metal examples that demonstrate how M-M bonding interactions can create extraordinary magnetic properties in molecules and materials. Adding the lanthanides to this paradigm, Gould et al. reported¹⁰³ the first example of mixed-valence $(Cp^{iPr5})_2Ln_2I_3$ Cp^{iPr5} , dilanthanide clusters (Ln =Gd, Tb and Dy; pentaisopropylcyclopentadienyl) (Figure 1.42b), which contain metal-metal bonding. These clusters were synthesized from a reduction of Ln (III) cluster (Cp^{iPr5})₂Ln₂I₄ (**Figure 1.42a**) in the presence of hexane containing potassium graphite. According to crystallographic investigations, the Ln(III) metal ions are all capped with a (Cp^{iPr5}) group and formation of Ln₂I₃ core by a three anionic iodide bridge with the Ln(III) metal ion centers. This structure has a trigonal symmetry. It is noteworthy that the lanthanide ions in these clusters are equivalent from a crystallographic perspective along the C₂ axis, further indicating the possibility of M-M bonding. Analytical, spectroscopic, and computational investigations reveal the generation of a single, $5d_{z2}$ -parentage Ln-Ln sigma-bonding molecular orbital in which the two Ln centers equally share the d electron. According to Hund's principles, valence delocalization results in strong parallel orientation of the 4f electrons and sigma-bonding on both Ln metals, creating high-spin ground states which are thermally well separated even at ambient temperature. The Dy (III) complex $[(Cp^{iPr5})_2Dy_2I_3]$ displays the anisotropic energy barrier of $U_{eff} = 1631(25)$ cm⁻ ¹ with blocking temperature 72 K. It gives a record coercivity with a lower range of 14 T at liquid nitrogen temperatures that are higher than even the conventional magnets.

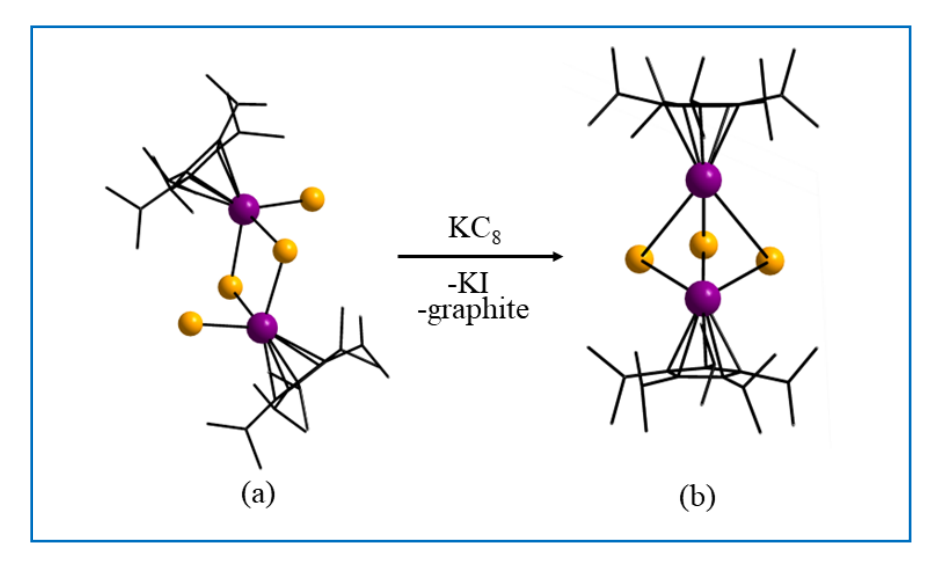


Figure 1.42: Schematic representation of the synthesis of $(Cp^{iPr5})_2Dy_2I_3$

1.16 Thesis Overview:

The thesis work mainly focuses on the design, synthesis and characterization of mixed 3*d*-main group and 4*f*-main group-based clusters.

Chapter 2 deals with the reactivity and optical properties of transition metal-incorporated organoantimony(V) clusters. We used an organoantimonate-phosphonate cluster as a proligand and a 3d-main group-based cluster synthesized by a solvothermal method. Herein, we discussed the optical properties of synthesized clusters and explained how bandgap reduction happens from homometallic clusters to heterometallic clusters by incorporating transition metal ions. The experimental bandgap values are supported by DFT calculations. The results obtained are explained in detail.

But all these mixed 3d-main group-based metal oxo clusters are insoluble in common organic solvents. To overcome the solubility issue, we focused on the synthesis and characterization of soluble mixed 3d-main group-based metal oxo clusters. In Chapter 1, metal oxo clusters were synthesized from a reaction of free acid to pro-ligand with 3d metal ions. Herein metal oxo clusters were synthesized from a reaction of 3d metal clusters with free acids. We successfully synthesized the soluble clusters with interesting molecular architectures by varied reaction conditions. The clusters were tested for antibacterial and antioxidant activity; they revealed interesting biological properties. Details are reported in Chapter 3.

In Chapter 4, we investigated the reactivity of pro-ligand toward the lanthanides. We are planning to study the magnetic behaviour of these metal clusters. In 3d-4f clusters, if the 3d metal ion chosen is diamagnetic, it exerts a significant role in directing the magnetic anisotropy of the paramagnetic ions. Based on this concept, 5p-4f-based clusters are prepared by a reaction of pro-ligand with prolate and oblate type 4f metal ions. SC-XRD reveals fascinating structures. The carried work is presented in Chapter 4.

Cerium acts as a catalyst in organic transformations because of its unique chemical properties. Chapter 5 deals with the reactivity of preformed clusters with cerium metal ion. In this work, we used two different pro-ligands; SC-XRD shows two different molecular architectures.

1.17 References:

- (a) Filella, M.; Williams, P. A.; Belzile, N. Environ. Chem. 2009, 6, 95–105. (b) Sundar, S.; Chakravarty, J. Antimony Toxicity. Int. J. Environ. Res. Public Health 2010, 7, 4267–4277. (c) Schampera, U. S. Critical Metals Handbook, First edition; John Wiley & Sons: West Sussex, 2014; pp 70-98. (d) Grund, S. C.; Hanusch, K.; Breunig, H. J.; Wolf, H. U. In Ullmann's Encyclopedia of Industrial Chemistry; Wiley, 2006. (e) Corby G. Anderson, C. G. Geochemistry 2012, 72, 3–8.
- (2) McCallum, R. I. Proc. roy. Soc. Med. 1977, 70, 756-763.
- (3) (a) Brahmachari, U. *Nature* **1940**, *145*, 1021–1022. (b) Horgan, E. S.; Kirk, R. *Nature* **1940**, *145*, 228. (c) Singh, R.; Roy, S. *Indian J. Hist. Sci.* **2019**, *54*, 35-49.
- (4) (a) Roberts, W. L.; Rainey, P. M. Antimicrob. Agents Chemother. 1993, 37, 1842–1846.
 (b) Roberts, W. L.; Mcmurray, W. J.; Rainey, P. M. Antimicrob. Agents Chemother.
 1998, 42, 1076–1082. (c) Sucre, A. P.; Gamarro, F.; Dujardin, J. C.; Barrett, M. P.; Vélez, R. L.; Hernández, R. G.; Pountain, A. W.; Mwenechanya, R.; Papadopoulou, B. PLoS Neglect. Trop. Dis. 2017, 11, e0006052.
- (5) (a) Silvestru, C.; Dumitrescu, L. S.; Haiduc, L.; Michael J. Begley, M. J.; Nunn, M.; Sowerby,
 D. B.
 J. Chem. Soc., Dalton Trans. 1986, 1031-1034. (b) Silvestru, C.; Curtui, M.; Haiduc, I.; Begley, M. J.; Sowerby, D. B. J. Organomet. Chem. 1992, 426, 49-58.
- (6) Takahashi, S.; Okayasu, R.; Sato, H.; Kubota, Y.; Bedford, J. S. *Int. Congr. Ser.* **2002**, *1236*, 327–330.
- (7) (a) Kant, R.; Chandrashekar, A. K.; Kumar, A. K. S. *Phosphorus, Sulfur Silicon Relat. Elem.* 2008, 183, 1410–1419. (b) Kant, R.; Singhal, K.; Shukla, S. K.; Chandrashekar, K.; Saxena, A. K.; Ranjan, A.; Raj, P. *Phosphorus, Sulfur Silicon Relat. Elem.* 2008, 183, 2029–2039.
- (8) (a) Fujie, T.; Murakami, M.; Yoshida, E.; Yasuike, S.; Kimura, T.; Fujiwara, Y.; Yamamoto, C.; Kaji, T. *Int. J. Mol. Sci.* **2016**, *17*, 1381. (b) Kohri, K.; Yoshida, E.; Yasuike, S.; Fujie, T.; Yamamoto, C.; Kaji, T. *J. Toxicol. Sci.* **2015**, *40*, 321–327.
- (9) Fahmi, N.; Kumari, A.; Singh, R. V. Int. J. Pharm. Sci. Res. 2014, 5, 5260–5266.
- (10) (a) Yang, P.; Lin, Z.; Alfaro-Espinoza, G.; Ullrich, M. S.; Raţ, C. I.; Silvestru, C.; Kortz, U. *Inorg. Chem.* 2016, 55, 251–258. (b) Ma, T.; Yang, P.; Dammann, I.; Lin, Z.; Mougharbel, A. S.; Adašcal'itei, F.; Mitea, R.; Silvestru, C.; Thorstenson, C.; Ullrich, M. S.; Cseh, K.; Jakupec, M. A.; Keppler, B. K.; Donalisio, M.; Cavalli, R.; Lembo, D.; Kortz, U. *Inorg. Chem.* 2020, 59, 2978–2987. (c) Yang, P.; Lin, Z.; Bassil, B. S.;

- Alfaro-Espinoza, G.; Ullrich, M. S.; Li, M. X.; Silvestru, C.; Kortz, U. *Inorg. Chem.* **2016**, *55*, 3718–3720.
- (11) (a) Chen, Y.; Qiu, R.; Xu, X.; Au, C. T.; Yin, S. F. RSC Adv. 2014, 4, 11907–11918.
 (b) Zhou, C.; Lei, J.; Liu, Y.; Au, C. T.; Chen, Y.; Yin, S. F. Appl. Organomet. Chem.
 2020, 34, 1–8. (c) Raj, P.; Rastogi, R.; Singhal, K.; Saxena, A. K. Polyhedron 1986, 5, 1581-1585. (d) Tan, N.; Nie, T.; Au, C. T.; Lan, D.; Wu, S.; Yi, B. Tetrahedron Lett.
 2017, 58, 2592–2595. (e) Tang, N.; Song, X.; Yang, T.; Qiu, R.; Yin, S. F. J. Organomet. Chem. 2021, 942, 121820. (f) Xia, J.; Qiu, R.; Yin, S.; Zhang, X.; Luo, S.; Au, C. T.; Xia, K.; Wong, W. Y. J. Organomet. Chem. 2010, 695, 1487–1492. (g) Huang, Y. Z. Acc. Chem. Res. 1992, 25, 182–187. (h) Ninagawa, A.; Matsuda, H.; Nomura, R. J. Org. Chem. 1980, 45, 3735–3738.
- (12) Doak, G. O.; Steinman, H. G. J. Am. Chem. Soc. 1946, 68, 1987–1989.
- (13) Liu, Z.; Ozawa, Y.; Yagasaki, A. Oligomeric Arylstibonates, *Bull. Chem. Soc. Jpn.* **2014**, 87, 1245–1251.
- (14) Schmidt, H. Justus Liebigs Ann. Chem. 1920, 421, 174–246.
- (15) Macallum, A. D. *Ortho-substituted Aromatic Antimony Compounds*. McGill University: Canada, 1922.
- (16) Doak, G. O. J. Am. Chem. Soc. 1946, 68, 1991–1995.
- (17) Bowen, L. H.; Long, G. G. Inorg. Chem. 1978, 17, 551–554.
- (18) Beckmann, J.; Finke, P.; Hesse, M.; Wettig, B. *Angew. Chem. Int. Ed.* **2008**, *47*, 9982–9984.
- (19) Beckmann, J. Heek, T.; Takahashi, M. Organometallics 2007, 26, 3633-3635.
- (20) Beckmann, J.; Hesse, M. Organometallics 2009, 28, 2345–2348.
- (21) Baskar, V.; Shanmugam, M.; Helliwell, M.; Teat, S. J.; Winpenny, R. E. P. *J. Am. Chem. Soc.* **2007**, *129*, 3042–3043.
- (22) Prabhu, M. S. R.; Jami, A. K.; Baskar, V. Organometallics 2009, 28, 3953–3956.
- (23) Jami, A. K.; Prabhu, M. S. R.; Baskar, V. Organometallics 2010, 29, 1137–1143.
- (24) Jami, A. K.; Baskar, V. *Dalton Trans.* **2012**, *41*, 12524–12529.
- (25) (a) Mancini, I.; Guella, G.; Frostin, M.; Hnawia, E.; Laurent, D.; Debitus, C.; Pietra, F. *Chem. A Eur. J.* 2006, 12, 8989–8994. (b) Tähtinen, P.; Saielli, G.; Guella, G.;
 Mancini, I.; Bagno, A. *Chem. A Eur. J.* 2008, 14, 10445–10452.
- (26) (a) Lu, D.; David Rae, A.; Salem, G.; Weir, M. L.; Willis, A. C.; Bruce Wild, S. *Organometallics* **2010**, 29, 32–33. (b) Lu, D.; Coote, M. L.; Ho, J.; Kilah, N. L.; Lin,

- C. Y.; Salem, G.; Weir, M. L.; Willis, A. C.; Wild, S. B.; Dilda, P. J. *Organometallics* **2012**, *31*, 1808–1816.
- (27) Brünig, J.; Hupf, E.; Lork, E.; Mebs, S.; Beckmann, J. *Dalton Trans.* **2015**, *44*, 7105–7108.
- (28) Clark, C. J.; Nicholson, K.; Wright, C. E. Chem. Commun. 2009, 8, 923–925.
- (29) Nicholson, B. K.; Clark, C. J.; Wright, C. E.; Groutso, T. *Organometallics* **2010**, 29, 6518–6526.
- (30) Nicholson, B. K.; Clark, C. J.; Wright, C. E.; Telfer, S. G.; Groutso, T. *Organometallics* **2011**, *3*, 10–14.
- (31) Nicholson, B. K.; Clark, C. J.; Jameson, G. B.; Telfer, S. G. *Inorg. Chim. Acta* **2013**, 406, 53–58.
- (32) Nicholson, B. K.; Clark, C. J.; Telferc, S. G.; Groutso, T. Dalton Trans. 2012, 41, 9964.
- (33) Srungavruksham, N. K.; Baskar, V. Dalton Trans. 2015, 44, 6358–6362.
- (34) Prabhu, M. S. R.; Ugandhar, U.; Baskar, V. Dalton Trans. 2016, 45, 6963–6967.
- (35) (a) Venezky, D. L.; Sink, C. w.; Nevett, B. A.; Fortescue. W. F. J. Organomet. Chem. 1972, 35, 131-142. (b) Bordner, J.; Doak, G. O.; Everett, T. S. J. Am. Chem. Soc. 1986, 108, 4206–4213.
- (36) Matano, Y.; Nomura, H.; Hisanaga, T.; Nakano, H.; Shiro, M.; Imahori, H. *Organometallics* **2004**, *23*, 5471–5480.
- (37) (a) Kumara Swamy, K. C.; Schmid, C. G.; Day, R. O.; Holmes, R. R. J. Am. Chem. Soc. 1988, 110, 7067–7076. (b) Murugavel, R. Kuppuswamy, S. Angew. Chem. Int. Ed. 2006, 45, 7022–7026. (c) Walawalkar, M. G.; Murugavel, R.; Roesky, H. W.; Schmidt, H. G. Organometallics 1997, 16, 516–518. (d) Chandrasekhar, V.; Baskar, V.; Steiner, A.; Zacchini, S. Organometallics 2002, 21, 4528–4532. (e) Mason, M. R.; Perkins, A. M.; Matthews, R. M.; Fisher, J. D.; Mashuta, M. S.; Vij, A. Inorg. Chem. 1998, 37, 3734–3746. (f) Yang, Y.; Walawalkar, M. G.; Pinkas, J.; Roesky, H. W.; Schmidt, H. G. Angew. Chem. Int. Ed. 1998, 37, 96–98. (g) Mehring, M.; Schürmann, M. Chem. Commun. 2001, 1, 2354–2355. (h) Gómez-Alcántara, M. M.; Cabeza, A.; Aranda, M. A. G.; Guagliardi, A.; Mao, J. G.; Clearfield, A. Solid State Sci. 2004, 6, 479–487. (i) Chandrasekhar, V.; Metre, R. K.; Suriya Narayanan, R. Dalton Trans. 2013, 42, 8709–8716. (j) Walawalkar, M. G.; Murugavel, R.; Voigt, A.; Roesky, H. W.; Schmidt, H. G. J. Am. Chem. Soc. 1997, 119, 4656–4661.
- (38) (a) Breeze, B. A.; Shanmugam, M.; Tuna, F.; Winpenny, R. E. P. *Chem. Commun.* **2007**, *48*, 5185–5187. (b) Khanra, S.; Kloth, M.; Mansaray, H.; Muryn, C. A.; Tuna,

- F.; Sañudo, E. C.; Helliwell, M.; McInnes, E. J. L.; Winpenny, R. E. P. *Angew. Chem. Int. Ed.* **2007**, *119*, 5664–5667. (c) Langley, S.; Helliwell, M.; Sessoli, R.; Teat, S. J.; Winpenny, R. E. P. *Inorg. Chem.* **2008**, *47*, 497–507. (d) Yi, X. Y.; Zheng, L. M.; Xu, W.; Feng, S. *Inorg. Chem.* **2003**, *42*, 2827–2829. (e) Du, Z. Y.; Prosvirin, A. V.; Mao, J. G. *Inorg. Chem.* **2007**, *46*, 9884–9894. (f) Ma, Y. S.; Li, Y. Z.; Song, Y.; Zheng, L. M. *Inorg. Chem.* **2008**, *47*, 4536–4544. (g) Poojary, D. M.; Zhang, B.; Clearfield, A. *Angew. Chem. Int. Ed.* **1994**, *33*, 2324–2326. (h) Walawalkar, M. G.; Horchler, S.; Dietrich, S.; Chakraborty, D.; Roesky, H. W.; Schäfer, M.; Schmidt, H. G.; Sheldrick, G. M.; Murugavel, R. *Organometallics* **1998**, *17*, 2865–2868. (i) Guzyr, O. I.; Siefken, R.; Chakraborty, D.; Roesky, H. W.; Teichert, M. *Inorg. Chem.* **2000**, *39*, 1680–1683. (j) Chandrasekhar, V.; Sasikumar, P.; Boomishankar, R. *Dalton Trans.* **2008**, *4*, 5189–5196. (j) Chandrasekhar, V.; Kingsley, S. *Angew. Chem. Int. Ed.* **2000**, *39*, 2320 —2322.
- (39) (a) Tang, X.; Hua, J.; Ma, Y.; Hori, A.; Yuan, R.; Matsuda, R. *Inorg. Chim. Acta.* 2018, 482, 900–904. (b) Zangana, K. H. *Magnetochemistry* 2018, 4, 29. (c) Hill, S.; Datta, S.; Liu, J.; Inglis, R.; Milios, C. J.; Feng, P. L.; Henderson, J. J.; Del Barco, E.; Brechin, E. K.; Hendrickson, D. N. *Dalton Trans.* 2010, 39, 4693–4707. (d) Comby, S.; Scopelliti, R.; Imbert, D.; Charbonnière, L.; Ziessel, R.; Bünzli, J. C. G *Inorg. Chem.* 2006, 45, 3158–3160. (e) Zheng, Y. Z.; Pineda, E. M.; Helliwell, M.; Winpenny, R. E. P. *Chem. A Eur. J.* 2012, 18, 4161–4165. (f) Zheng, Y. Z.; Evangelisti, M.; Tuna, F.; Winpenny, R. E. P. *J. Am. Chem. Soc.* 2012, 134, 1057–1065. (g) Pineda, E. M.; Tuna, F.; Zheng, Y. Z.; Teat, S. J.; Winpenny, R. E. P.; Schnack, J.; McInnes, E. J. L. *Inorg. Chem.* 2014, 53, 3032–3038. (h) Moreno Pineda, E.; Heesing, C.; Tuna, F.; Zheng, Y. Z.; McInnes, E. J. L.; Schnack, J.; Winpenny, R. E. P. *Inorg. Chem.* 2015, 54, 6331–6337. (i) Zangana, K. H.; Pineda, E. M.; Winpenny, R. E. P. *Dalton Trans.* 2014, 43, 17101–17107. (j) Zangana, K. H.; Pineda, E. M.; Schnack, J.; Winpenny, R. E. P. *Dalton Trans.* 2013, 42, 14045–14048. (k) Zhang, Z. M.; Zangana, K. H.; Kostopoulos, A. K.; Tong, M. L.; Winpenny, R. E. P. *Dalton Trans.* 2016, 45, 9041–9044.
- (40) Cabeza, A.; Aranda, M. A. G. *In Metal Phosphonate Chemistry: From Synthesis to Applications*; Clearfield, A., Demadis, K., Eds.; RSC Publishing: Cambridge, UK, 2012; pp 107–132.
- (41) Demmer, C. S.; Krogsgaard-Larsen, N.; Bunch, L. Chem. Rev. 2011, 111, 7981–8006.
- (42) Crofts, P. C.; Kosolapoff, G. M. J. Am. Chem. Soc. 1953, 75, 3379–3383.

- (43) (a) Ali, S.; Muryn, C. A.; Tuna, F.; Winpenny, R. E. P. *Dalton Trans.* 2010, *39*, 9588–9597.
 (b) Ali, S.; Baskar, V.; Muryn, C. A.; Winpenny, R. E. P. *Chem. Commun.* 2008, *4*, 6375–6377.
- (44) Ali, S.; Muryn, C. A.; Tuna, F.; Winpenny, R. E. P. *Dalton Trans.* **2010**, *39*, 124–131.
- (45) Ugandhar, U.; Baskar, V. Dalton Trans. 2016, 45, 6269–6274.
- (46) Ugandhar, U.; Navaneetha, T.; Ali, J.; Mondal, S.; Vaitheeswaran, G.; Baskar, V. *Inorg. Chem.* **2020**, *59*, 6689–6696.
- (47) Srungavruksham, N. K.; Baskar, V. Eur. J. Inorg. Chem. 2013, 24, 4345–4352.
- (48) Chandrasekhar, V.; Kingsley, S.; Rhatigan, B.; Lam, M. K.; Rheingold, A. L. *Inorg. Chem.* **2002**, *41*, 1030–1032.
- (49) Wittenberg, D.; Gilman, H. J. Org. Chem. 1958, 23, 1063–1065.
- (50) Hewertson, W.; Watson, H. R. J. Chem. Soc. 1962, 283, 1490–1494.
- (51) Shawkataly, O. B.; Ramalingam, K.; Fun, H. K.; Rahman, A. A.; Razak, I. A. *J. Clust. Sci.* **2004**, *15*, 387–394.
- (52) Meinema, H.A.; Martens, H.F.; Noltes, J. G. J. Organomet. Chem. 1973, 51, 223-230.
- (53) Chandrasekhar, V.; Thirumoorthi, R. Organometallics 2009, 28, 2637–2639.
- (54) Kishore, P. V. V. N.; Baskar, V. Inorg. Chem. 2014, 53, 6737–6742.
- (55) Yang, Q.; Stephen, A. G.; Adelsberger, J. W.; Roberts, P. E.; Zhu, W.; Currens, M. J.; Feng, Y.; Crise, B. J.; Gorelick, R. J.; Rein, A. R.; Fisher, R. J.; Shoemaker, R. H.; Sei, S. J. Virol. 2005, 79, 6122–6133.
- (56) Friedheim, E. A. H.; Vogel, H. J.; Berman, R. L. J. Am. Chem. Soc. **1947**, 69, 560–562.
- (57) (a) Zhao, J.; Stagno, J. R.; Varticovski, L.; Nimako, E.; Rishi, V.; McKinnon, K.; Akee, R.; Shoemaker, R. H.; Ji, X.; Vinson, C. *Mol. Pharmacol.* 2012, 82, 814–823. (b) Heyerdahl, S. L.; Rozenberg, J.; Jamtgaard, L.; Rishi, V.; Varticovski, L.; Akah, K.; Scudiero, D.; Shoemaker, R. H.; Karpova, T. S.; Day, R. N.; McNally, J. G.; Vinson, C. *Eur. J. Cell Biol.* 2010, 89, 564–573. (c) Rishi, V.; Oh, W. J.; Heyerdahl, S. L.; Zhao, J.; Scudiero, D.; Shoemaker, R. H.; Vinson, C. *J. Struct. Biol.* 2010, 170, 216–225.
- (58) (a) Seiple, L. A.; Cardellina, J. H.; Akee, R.; Stivers, J. T *Mol. Pharmacol.* 2008, 73, 669–677. (b) Srinivasan, A.; Wang, L.; Cline, C. J.; Xie, Z.; Sobol, R. W.; Xie, X.; Gold, B. *Biochemistry* 2012, 51, 6246–6259. (c) Kaur, G.; Cholia, R. P.; Mantha, A. K.; Kumar, R. *J. Med. Chem.* 2014, 57, 10241–10256. (d) Rai, G.; Vyjayanti, V. N.; Dorjsuren, D.; Simeonov, A.; Jadhav, A.; Wilson, D. M.; Maloney, D. J. *J. Med. Chem.* 2012, 55, 3101–3112.

- (59) Kim, H.; Cardellina, J. H.; Akee, R.; Champoux, J. J.; Stivers, J. T. *Bioorg. Chem.* **2008**, *36*, 190–197.
- (60) Mak, L. H.; Knott, J.; Scott, K. A.; Scott, C.; Whyte, G. F.; Ye, Y.; Mann, D. J.; Ces,
 O.; Stivers, J.; Woscholski, R. *Bioorg. Med. Chem.* 2012, 20, 4371–4376.
- (61) McKelvie, J. C.; Richards, M. I.; Harmer, J. E.; Milne, T. S.; Roach, P. L.; Oyston, P. C. F. Br. J. Pharmacol. 2013, 168, 172–188.
- (62) Ali, J.; Mubarak, M. M.; Samuel, C.; Kantroo, H. A.; Malik, A.; Ahmad, Z.; Baskar, V. *J. Inorg. Biochem.* **2022**, *235*, 111909.
- (63) Strnat, K.; Hoffer, G.; Olson, J.; Ostertag, W.; Becker, J. J. *J. Appl. Phys.* **1967**, *38*, 1001–1002.
- (64) (a) Benelli, C. Caneschi, A. Gatteschi, D. Sessoli, R. Adv. Mater. 1992, 4, 504–505.
 (b) Guillou, O.; Bergerat, P.; Kahn, O.; Bakalbassis, E.; Boubekeur, K.; Batail, P.; Guillotle, M. Inorg. Chem. 1992, 31, 110–114. (c) Beneini, A.; Benelli, C.; Caneschi, A.; Carlin, R. L.; Dei, A.; Gatteschi, D. J. Am. Chem. Soc. 1985, 107, 8128–8136.
- (65) Mannini, M.; Pineider, F.; Sainctavit, P.; Danieli, C.; Otero, E.; Sciancalepore, C.; Talarico, A. M.; Arrio, M. A.; Cornia, A.; Gatteschi, D.; Sessoli, R. *Nat. Mater.* 2009, 8, 194–197.
- (66) Frost, J. M.; Harriman, K. L. M.; Murugesu, M. Chem. Sci. 2016, 7, 2470–2491.
- (67) (a) Timco, G. A.; Carretta, S.; Troiani, F.; Tuna, F.; Pritchard, R. J.; Muryn, C. A.; McInnes, E. J. L.; Ghirri, A.; Candini, A.; Santini, P.; Amoretti, G.; Affronte, M.; Winpenny, R. E. P. Nat. Nanotechnol. 2009, 4, 173–178. (b) Wernsdorfer, W. nature materials 2007, 6, 174–176. (c) Bogani, L.; Wernsdorfer W. Nature materials 2008, 7, 179-86. (d) Thiele, S.; Balestro, F.; Ballou, R.; Klyatskaya, S.; Ruben, M.; Wernsdorfer, W. Science, 2014, 344, 1135-1138. (e) Affronte, M.; Troiani, F.; Ghirri, A.; Candini, A.; Evangelisti, M.; Corradini, V.; Carretta, S.; Santini, P.; Amoretti, G.; Tuna, F.; Timco, G.; Winpenny, R. E. P. J. Phys. D. Appl. Phys. 2007, 40, 2999–3004.
- (68) Lis, T. Acta Crystallogr. Sect. B Struct. Crystallogr. Cryst. Chem. 1980, 36, 2042–2046.
- (69) Sessoli, R.; Tsai, H. L.; Schake, A. R.; Wang, S.; Vincent, J. B.; Foiling, K.; Gatteschi,D.; Christou, G.; Hendrickson, D. N. J. Am. Chem. Soc. 1993, 115, 1804–1816.
- (70) Caneschi, A.; Gatteschi, D; Sessoli, R.; Barra, A. L.; Brunel, L. C.; Guillot, M. *J. Am. Chem. Soc.* **1991**, *113*, 5873–5874.
- (71) Sessoli, R.; Gatteschi, D.; Caneschi, A.; Novak, M.A. Magnetic bistability in a metalion cluster. *Nature* **1993**, *365*, 141-143.

- (72) Friedman, J. R.; Sarachik, M. P.; Tejada, J.; Ziolo, R. *Phys. Rev. Lett.* **1996**, *76*, 3830–3833.
- (73) Thomas, L.; Lionti, F.; Ballou, R.; Gatteschi, D.; Sessoli, R.; Barbara, B. *Nature* **1996**, 383, 145-147.
- (74) Ishikawa, N.; Sugita, M.; Ishikawa, T.; Koshihara, S. Y.; Kaizu, Y. *J. Am. Chem. Soc.*2003, 125, 8694–8695.
- (75) Rinehart, J. D.; Long, J. R. Chem. Sci. 2011, 2, 2078–2085.
- (76) Koike, N.; Uekusa, H.; Ohashi, Y.; Harnoode, C.; Kitamura, F.; Ohsaka, T.; Tokuda, K. *Inorg. Chem.* 1996, *35*, 5798-5804.
- (77) (a) Konami, H.; Hatano, M.; Tajiri, A. Chem. Phys. Lett. 1989, 160, 163-167. (b) Cian,
 A. D.; Moussavi, M.; Fischer, J.; Weiss, R. Inorg. Chem. 1985, 24, 3162–3167.
- (78) Branzoli, F.; Carretta, P.; Filibian, M.; Zoppellaro, G.; Graf, M. J.; Galan-Mascaros, J. R.; Fuhr, O.; Brink, S.; Ruben, M. J. Am. Chem. Soc. 2009, 131, 4387–4396.
- (79) Li, X.; Liu, Q.; Lin, J.; Li, Y.; Cao, R. *Inorg. Chem. Commun.* **2009**, *12*, 502-505.
- (80) (a) Palenik, G. J.; Brzyska, W.; Klimek, B.; Kula, A.; Stepniak, K. J. Coord. Chem.
 1990, 21, 183–191. (b) Zheng, X. J.; Jin, L. P.; Lu, S. Z. Eur. J. Inorg. Chem. 2002, 12, 3356–3363. (c) Song, Y. S.; Yan, B.; Chen, Z. X. Inorg. Chim. acta, 2017, 360, 3431-3435. (d) Burns, J. H.; Baldwin, W. H. Inorg. Chem. 1977, 16, 289–294.
- (81) (a) Wang, R.; Liu, H.; Carducci, M. D.; Jin, T.; Zheng, C.; Zheng, Z. *Inorg. Chem.* 2001, 40, 2743–2750. (b) Wang, R.; Carducci, M. D.; Zheng, Z. *Inorg. Chem.* 2000, 39, 1836–1837. (c) Wang, R.; Zheng, Z.; Jin, T.; Staples, R. J. *Angew. Chem. Int. Ed.* 1999, 38, 1813–1815. (d) Weiss, C. J.; Marks, T. J. *Dalton Trans.* 2010, 39, 6576–6588. (e) Kong, X. J.; Wu, Y.; Long, L. S.; Zheng, L. S.; Zheng, Z. *J. Am. Chem. Soc.* 2009, 131, 6918–6919. (f) Wang, R.; Selby, H. D.; Liu, H.; Carducci, M. D.; Jin, T.; Zheng, Z.; Anthis, J. W.; Staples, R. J. *Inorg. Chem.* 2002, 41, 278–286.
- (82) (a) Lin, P. H.; Burchell, T. J. Clérac, R.; Murugesu, M. Angew. Chem. Int. Ed. 2008, 120, 8980-8983. (b) Zou, L.; Zhao, L.; Chen, P.; Guo, Y. N.; Guo, Y.; Li, Y. H.; Tang, J. Dalton Trans. 2012, 41, 2966–2971. (c) Hewitt, I. J.; Lan, Y.; Anson, C. E.; Luzon, J.; Sessoli, R.; Powell, A. K. Chem. Commun. 2009, 3, 6765–6767. (d) Habib, F.; Lin, P. J. Am. Chem. Soc. 2011, 133, 8830–8833. (e) Yang, P. P.; Gao, X. F.; Song, H. Bin; Zhang, S.; Mei, X. L.; Li, L. C.; Liao, D. Z. Inorg. Chem. 2011, 50, 720–722. (f) Guo, Y. N.; Xu, G. F.; Guo, Y.; Tang, J. Dalton Trans. 2011, 40, 9953–9963. (g) Guo, Y. N.; Xu, G. F.; Gamez, P.; Zhao, L.; Lin, S. Y.; Deng, R.; Tang, J.; Zhang, H. J. J. Am. Chem. Soc. 2010, 132, 8538–8539.

- (83) (a) Wang, R.; Song, D.; Wang, S. Chem. Commun. 2002, 2, 368–369. (b) Andrews, P. C.; Brown, D. H.; Fraser, B. H.; Gorham, N. T.; Junk, P. C.; Massi, M.; St Pierre, T. G.; Skelton, B. W.; Woodward, R. C. Dalton Trans. 2010, 39, 11227–11234. (c) Petit, S.; Baril-Robert, F.; Pilet, G.; Reber, C.; Luneau, D. Dalton Trans. 2009, 34, 6809–6815. (d) Baskar, V.; Roesky, P. W. J. Chem. Soc. Dalton Trans. 2006, 60, 676676–679679. (e) Gamer, M. T.; Lan, Y.; Roesky, P. W.; Powell, A. K.; Clérac, R. Inorg. Chem. 2008, 47, 6581–6583. (f) Bürgstein, M. R.; Gamer, M. T.; Roesky, P. W. J. Am. Chem. Soc. 2004, 126, 5213–5218. (g) Aguilà, D.; Barrios, L. A.; Velasco, V.; Arnedo, L.; Aliaga-Alcalde, N.; Menelaou, M.; Teat, S. J.; Roubeau, O.; Luis, F.; Aromí, G. Chem. A Eur. J. 2013, 19, 5881–5891.
- (84) (a) Li, H.; Wu, H.; Wan, R.; Wang, Y.; Ma, P.; Li, S.; Wang, J.; Niu, J. *Dalton Trans*.
 2019, 48, 2813–2821. (b) AlDamen, M. A.; Cardona-Serra, S.; Clemente-Juan, J. M.;
 Coronado, E.; Gaita-Ariño, A.; Martí-Gastaldo, C.; Luis, F.; Montero, O. *Inorg. Chem*.
 2009, 48, 3467–3479. (c) AlDamen, M. A.; Clemente-Juan, J. M.; Coronado, E.; Martí-Gastaldo, C.; Gaita-Ariño, A. *J. Am. Chem. Soc.* 2008, 130, 8874–8875.
- (85) Tang, J.; Hewitt, I.; Madhu, N. T.; Chastanet, G.; Wernsdorfer, W.; Anson, C. E.; Benelli, C.; Sessoli, R.; Powell, A. K. *Angew. Chem. Int. Ed.* **2006**, *118*, 1761–1765.
- (86) Chibotaru, L. F.; Ungur, L.; Soncini, A. Angew. Chem. Int. Ed. 2008, 120, 4194–4197.
- (87) Luzon, J.; Bernot, K.; Hewitt, I. J.; Anson, C. E.; Powell, A. K.; Sessoli, R. *Phys. Rev. Lett.* **2008**, *100*, 1–4.
- (88) (a) Xue, S.; Chen, X. H.; Zhao, L.; Guo, Y. N.; Tang, J. *Inorg. Chem.* 2012, *51*, 13264–13270. (b) Novitchi, G.; Pilet, G.; Ungur, L.; Moshchalkov, V. V.; Wernsdorfer, W.; Chibotaru, L. F.; Luneau, D.; Powell, A. K. *Chem. Sci.* 2012, *3*, 1169–1176. (c) Tian, H.; Guo, Y. N.; Zhao, L.; Tang, J.; Liu, Z. *Inorg. Chem.* 2011, *50*, 8688–8690.
- (89) Hewitt, I. J.; Tang, J.; Madhu, N. T.; Anson, C. E.; Lan, Y.; Luzon, J.; Etienne, M.; Sessoli, R.; Powell, A. K. *Angew. Chem. Int. Ed.* **2010**, *122*, 6496–6500.
- (90) Lin, P.-H.; Burchell, T. J.; Ungur, L.; Chibotaru, L. F.; Wernsdorfer, W.; Murugesu,
 M. Angew. Chem. Int. Ed. 2009, 121, 9653–9656.
- (91) Zheng, Y. Z.; Lan, Y.; Anson, C. E.; Powell, A. K. *Inorg. Chem.* **2008**, *47*, 10813–10815.
- (92) Blagg, R. J.; Muryn, C. A.; McInnes, E. J. L.; Tuna, F.; Winpenny, R. E. P. *Angew. Chem. Int. Ed.* **2011**, *50*, 6530–6533.
- (93) Blagg, R. J.; Ungur, L.; Tuna, F.; Speak, J.; Comar, P.; Collison, D.; Wernsdorfer, W.; McInnes, E. J. L.; Chibotaru, L. F.; Winpenny, R. E. P. *Nat. Chem.* **2013**, *5*, 673–678.

- (94) Chandrasekhar, V.; Hossain, S.; Das, S.; Biswas, S.; Sutter, J. *Inorg. Chem.* **2013**, *52*, 6346–6353.
- (95) Das, S.; Dey, A.; Biswas, S.; Colacio, E.; Chandrasekhar, V*Inorg. Chem.* **2014**, *53*, 3417–3426.
- (96) Gupta, S. K.; Rajeshkumar, T.; Rajaraman, G.; Murugavel, R. *Chem. Sci.* **2016**, 7, 5181–5191.
- (97) Ding, Y. S.; Chilton, N. F.; Winpenny, R. E. P.; Zheng, Y. Z. Angew. Chem. Int. Ed. 2016, 55, 16071–16074.
- (98) Xiong, J.; Ding, H. Y.; Meng, Y. S.; Gao, C.; Zhang, X. J.; Meng, Z. S.; Zhang, Y. Q.; Shi, W.; Wang, B. W.; Gao, S. *Chem. Sci.* **2017**, *8*, 1288–1294.
- (99) (a) Guo, F. S.; Day, B. M.; Chen, Y. C.; Tong, M. L.; Mansikkamäki, A.; Layfield, R. A. Angew. Chem. Int. Ed. 2017, 56, 11445–11449. (b) Goodwin, C. A. P.; Ortu, F.; Reta, D.; Chilton, N. F.; Mills, D. P. Nature 2017, 548, 439–442.
- (100) Demir, S.; Gonzalez, M. I.; Darago, L. E.; Evans, W. J.; Long, J. R. *Nat. Commun.* **2017**, *8*, 1–9.
- (101) Guo, F. S.; Day, B. M.; Chen, Y. C.; Tong, M. L.; Mansikkamäki, A.; Layfield, R. A. *Science* **2018**, *362*, 1400–1403.
- (102) Zhu, Z.; Zhao, C.; Feng, T.; Liu, X.; Ying, X.; Li, X. L.; Zhang, Y. Q.; Tang, J. J. Am. Chem. Soc. **2021**, 143, 10077–10082.
- (103) Gould, C. A.; McClain, K. R.; Reta, D.; Kragskow, J. G. C.; Marchiori, D. A.; Lachman, E.; Choi, E. S.; Analytis, J. G.; Britt, R. D.; Chilton, N. F.; Harvey, B. G.; Long, J. R. *Science* **2022**, *375*, 198–202.

Tunable Bandgap in Self-Assembled Transition Metal-Incorporated Heterometallic Ti_4Sb_2 and V_2Sb_4 Oxo Clusters

CHAPTER

2

Abstract: This work investigates the reactivity and optical properties of transition metal-incorporated organoantimony(V) clusters prepared by a solvothermal route. Herein, reported the detailed structural characterizations of novel heterometallic Ti₄Sb₂ and V₂Sb₄ oxo clusters. Single crystal X-ray diffraction revealed the formation of hexanuclear organoantimony(V) based oxo clusters $[(RSb)_2Ti_4(\mu_3-O)_2(\mu_2-O)_2(t-BuPO_3)_4(\mu_2-OCH_3)_4(OCH_3)_4]$, where $R = p-i-PrC_6H_4$ (2.1), $p-ClC_6H_4$ (2.2) and $[(p-ClC_6H_4Sb)_4V_2(O)_2(\mu_3-O)_2(\mu_2-O)_2(t-BuPO_3)_4(\mu_2-OCH_3)_4]$ (2.3) Optical absorption studies show that bandgap reduction can be achieved by incorporating appropriate transition metal into the homometallic Sb₆ oxo cluster.

2.1 Introduction:

Tuning optical bandgap plays an important role in designing various optoelectronic applications. In this regard, researchers have employed varying strategies for materials and discrete molecular clusters. Zhang et al. showed that in the lead-free inorganic halide perovskites, the bandgap could be modulated by around 0.5 eV under high-pressure conditions. In inorganic halide perovskites, the bandgap was tuned via anion exchange methodology.² In the case of discrete molecular clusters, the bandgap has been narrowed by changing the size of the secondary building units or varying the conjugation of organic groups.³ It is pertinent to mention here that titanium oxo clusters have received considerable attention in recent years owing to applications in varying fields.⁴ Very recently, titanium-containing MOFs have been used in the study of sodium-assisted electron transfer reactions.⁵ In addition, polyoxotitanate-based hybrid films have been shown to display interesting electrochemical properties.⁶ By enforcing modification in the solid-state structures of titanium-based oxo clusters, one can engineer band gap modification in Ti-O frameworks. Yet another way of having control over band gaps in titanium frameworks is by doping them with a metal or a nonmetal. Zhang et al. have exploited the labile coordination sites of phosphonate-based hexanuclear titanium oxo clusters by introducing various oxo donor ligands, which help introduce the second transition-metal atom. As a result, it has been shown that the band gap can be tuned to varying extents by changing the coordination environments of incorporated metal ions. Moreover, the absorption studies reveal that the electron-withdrawing effect of organic ligands plays a significant role in switching the band gap in Ti-O clusters. Transition metal-based oxo clusters are well known to display a range of applications, like for instance, vanadium oxo clusters have been found to be employed in the field of catalysis, and optoelectronics.⁸ Mn-doped nanomaterials have been shown to display enhanced photocatalytic activity. Moreover, tuning of bandgap and structural properties of various thin films and nanomaterials have been achieved via cobalt doping. ¹⁰ Interestingly, there seems to be a correlation between the reduction of bandgap and the dopant concentration. For example, with increased Ni dopant concentration on nickel-doped zinc oxide thin films, a reduction in bandgap has been observed. 11 Transition metal ion (Cu) doped double perovskite is considered one of the low bandgap-based materials synthesized to date. Doping into perovskites seems to influence the photovoltaic behavior and optical properties of materials.¹²

Parallelly, we have been interested in investigating the reactivity of organostibonic acid as a ligand for building metal oxo clusters and exploring the organostibonate-phosphonate cluster's ability to act as a pro-ligand towards transition metal ions.¹³ Influenced by the work, a

systematic methodology was designed to synthesize 3d transition metal incorporated organoantimony-based oxo clusters. The band filling achieved by incorporating different 3d transition metal ions can lead to an increase in the on-site electron correlation as the atomic radius shrinks as we move along the period in the periodic table, which can enable us to engineer the band gap. The presumption for the work presented herein is that the incorporation/doping of a homometallic cluster (Sb₆ oxo cluster) with 3d transition metal ions would eventually improve the optoelectronic property, namely the bandgap of the assembled heterometallic cluster. Transition metal ions employed in this study are potential candidates for incorporation into the Sb₆ oxo clusters because of their abundant electron states and close ionic radius to that of Sb⁵⁺ (0.062 nm). From our research group, heterometallic hexanuclear organoantimony (V) based oxo clusters $M_2(p-iPr-C_6H_4Sb)_4(\mu_3-O)_2(\mu_2-O)_2(\mu_2-OCH_3)_4(t-BuPO_3)_4(py)_2]$. $2CH_3OH$, where M=Mn, Co, Ni and Cu have been reported. Herein, we report the synthesis, characterization of 1-3, and optical properties of heterometallic Ti₄Sb₂ and M₂Sb₄ (M= V, Mn, Co, Ni and Cu) oxo clusters. Transition metal ion-incorporated Sb₆ oxo clusters have been found to exhibit bandgap tunability.

2.2 Experimental Section:

2.2.1 General Information:

Arylstibonic acids¹⁴ (aryl =p-isopropylphenyl, p-chlorophenyl) and t-butylphosphonic acid¹⁵ were synthesized according to literature reports. Solvents and common reagents were purchased from Sigma-Aldrich. The mixed antimonate-phosphonate precursors $[(p-i-PrC_6H_4Sb)_4(OH)_4(t-BuPO_3)_6]^{16}$ and $[(p-ClC_6H_4Sb)_2(O)(t-BuPO_3H)_6]^{13a}$ were synthesized by condensation reactions of organostibonic acid with t-butylphosphonic acid. The arylstibonic acids (aryl = p-isopropylphenyl, p-chlorophenyl) and t-butylphosphonic acid were mixed in a 1:2 ratio and stirred in acetonitrile (15 mL) for 24 h at room temperature. The solutions were filtered, and crystals were isolated on slow evaporation of acetonitrile. The Sb₆ oxo clusters were synthesized by reacting (RSb)₄(OH)₄(t-BuPO₃)₆ and (RSb)₂(O)(t-BuPO₃H)₆ independently in the presence of pyridine under solvothermal conditions revealing the formation of hexanuclear organoantimonate clusters $[(RSb)_6(\mu_3-O)_2(\mu_2-O)_6(t$ -BuPO₃)₄], where R = p-i-PrC₆H₄ and p-ClC₆H₄.

2.2.2 Instrumentation:

Infrared spectra were recorded with a NICOLET iS5 FTIR Spectrometer. The solid-state ³¹P NMR spectra were recorded with a Bruker AVANCEIII 400 instrument. Elemental analysis was performed with a Flash EA Series 1112 CHNS analyzer. Single crystal X-ray data for **2.1**,

2.2 was carried out at 100 (2), 293.44 K with a Bruker Smart Apex CCD area detector system $[\lambda \text{ (Mo-K}\alpha) = 0.71073 \text{ Å}]$ with a graphite monochromator and **2.3** was carried out at 109 (3) K with an XtaLAB Synergy, a single source at offset/far, HyPix3000 diffractometer, and a Rigaku Oxford HyPix3000 CCD plate detector system [λ (Mo K α) = 0.71073 Å] with a mirror monochromator. The data were reduced using APEX-2 for 2.1-2.2 and CrysAlisPro 1.171.40.35a (Rigaku OD, 2018) for 2.3. The structures were solved using SHELXT and refined using SHELXL-2018/3 in Olex2 1.3-ac4 software.¹⁷ All non-hydrogen atoms were refined anisotropically. The PXRD was recorded at room temperature using a Bruker D8 Advance diffractometer (Bruker-AXS, Karlsruhe, Germany) using Cu–K α X-radiation (λ = 1.5406 Å) at 40 kV and 30 mA power. X-ray diffraction patterns were collected over a 2θ range of 5-80° at a scan rate of 3.9°/min. Energy-dispersive spectroscopy (EDS) and elemental mapping were studied using an Ultra 55 Carl Zeiss instrument. Solid-state UV-vis absorption spectra were recorded with a JASCO-V-770 spectrophotometer. The static susceptibility measurements were performed on solid polycrystalline samples with a Quantum Design MPMS-XL SQUID magnetometer. The following values of the magnetic field were used 0.2 kOe, 2 kOe, and 10 kOe respectively, for the temperature range of 2-20 K, 20-80 K and 80-300 K in order to prevent any saturation effect. Immobilized crystalline powders were employed to realize the magnetic measurements and the latter were all corrected for the diamagnetic contribution as calculated with Pascal's constants.

2.2.3 General Synthetic Procedures:

The general synthetic methodology for compounds **2.1** and **2.2** is as follows: the corresponding mixed antimonate-phosphonate and Ti(OⁱPr)₄ were dissolved in methanol (15 mL) followed by dropwise addition of pyridine. The clear solution obtained was stirred for 15 min and then transferred into a Teflon digestion bomb and the mixture was heated at 100 °C for 12 h and then cooled slowly to room temperature for 48 h. The isolated crystals were powdered and subjected to a high vacuum for 30 min before being characterized by standard spectroscopic and analytical techniques.

Compound **2.1:** $[(p-i-PrC_6H_4Sb)_4(OH)_4(t-BuPO_3)_6]$ (0.1 g, 0.05 mmol), titanium (IV) isopropoxide (0.06 g, 0.211 mmol) and pyridine (0.04 mL). Yield: 0.039 g (48% based on proligand). Mp: 300–301 °C dec. ³¹P{¹H} NMR: δ = 35.5, 21.1 ppm. IR (cm⁻¹): 2960 (m), 1629 (m), 1478 (s), 1396 (m), 1085 (s), 999 (s), 9445 (s), 803 (wide), 669 (s), 538 (m). Anal. Calcd for C₄₂H₈₂O₂₄P₄Sb₂Ti₄ (1529.97): C, 32.97; H, 5.40. Found: C, 33.12; H, 5.32. All values are given as percentages.

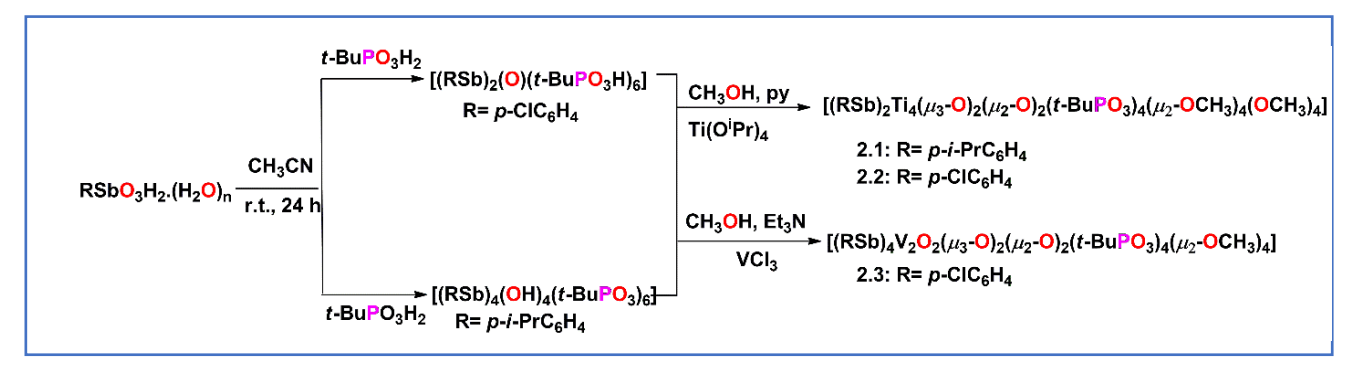
Compound **2.2:** $[(p\text{-ClC}_6\text{H}_4\text{Sb})_2(\text{O})(t\text{-BuPO}_3\text{H})_6]$ (0.1 g, 0.076 mmol), titanium (IV) isopropoxide (0.086 g, 0.302 mmol) and pyridine (0.04 mL). Yield: 0.045 g (39% based on pro-ligand). Mp: 306–307 °C dec. ³¹P{¹H} NMR: δ = 35.3, 20.9 ppm. IR (cm⁻¹): 2914 (m), 2814 (s), 1571 (m), 1475 (s), 1391 (s), 1359 (s), 1129 (s), 1109 (s), 1050 (m), 992 (s), 940 (s), 793 (s), 726 (s), 710 (s), 669 (s), 593 (s). Anal. Calcd for C₃₆H₆₈O₂₄Cl₂P₄Sb₂Ti₄ (1514.70): C, 28.55; H, 4.52. Found: C, 28.51; H, 4.47. All values are given as percentages.

The general synthetic methodology for **2.3** is that the corresponding mixed antimonate-phosphonate pro-ligand and VCl₃ were dissolved in methanol (15 mL) and simultaneous dropwise addition of triethylamine. The resultant mixture was stirred for 1 h and then filtered into a 23 mL Teflon-lined stainless-steel autoclave up to 70% fill. The bomb was sealed properly and above temperature conditions were maintained in this case as well. X-ray quality single crystals were obtained at the base of the bomb and walls upon slow cooling of the methanol solution.

Compound **2.3:** [(*p*-ClC₆H₄Sb)₂(O)(*t*-BuPO₃H)₆] (0.05 g, 0.038 mmol), vanadium (III) chloride (0.024 g, 0.15 mmol) and pyridine (0.05 mL). Light green colored single crystals formed upon slow cooling of methanol solution. Yield: 0.021 g (31 % based on pro-ligand). Anal. Calcd (%) for C₄4H₆4Cl₄O₂₂P₄Sb₄V₂ (1799.51): C, 29.37; H, 3.58. Found: C, 29.38; H, 3.46. IR (cm⁻¹): 2954 (m), 2204 (m), 2167 (s), 2115 (m), 2017 (m), 1958 (m), 1944 (m), 1572 (m), 1476 (s), 1382 (s), 1174 (s), 1101 (s), 1047 (s), 1000 (s), 981 (m), 805 (s), 747 (s), 674 (s), 613 (m), 591 (m), 555 (s).

2.3 Results and Discussion:

Compound **2.1-2.2** were synthesized by reaction of the arylstibonate-phosphonate cluster, where aryl= p-i-PrC₆H₄ and p-ClC₆H₄ with Ti(OⁱPr)₄ in the ratio of 1:4 under solvothermal conditions in methanol using pyridine as a base (**Scheme 2.1**). Colorless single crystals of **2.1** and **2.2** were grown by cooling the reaction mixture to room temperature. The solubility of **2.1-2.2** was poor in common organic solvents like methanol, chloroform, dichloromethane, acetonitrile, DMF and DMSO. Hence, solid-state NMR was used for characterizing the phosphorus atom present in **2.1-2.2**. Solid state 31 P NMR of **2.1** (**Figure 2.14**) at room temperature shows two resonance peaks at $\delta = 35.5$ and 21.1 ppm, which indicates the presence of phosphorus-based ligand in two different environments. Similarly, **2.2** (**Figure 2.15**) shows two resonances at $\delta = 35.3$ and 20.9 ppm. Compounds **2.1-2.2** crystallizes in the triclinic space group P-I with half of the molecules present in the asymmetric unit. Crystallographic data and the metric parameters of compounds **2.1-2.2** are given in **Tables 2.3** and **2.4**. The molecular



Scheme 2.1. Synthesis of complexes 2.1-2.3.

structures of compounds **2.1-2.2** are very similar. The structure of **2.1** (**Figure 2.1**) is considered for discussion. Single crystal X-ray diffraction of **2.1** reveals the formation of hexanuclear organoantimonate-titanate oxo clusters having the formula $[(RSb)_2Ti_4(\mu_3-O)_2(\mu_2-O)_2(t-BuPO_3)_4(\mu_2-OCH_3)_4(OCH_3)_4]$, where $R = p-i-PrC_6H_4$ (**2.1**) and $p-ClC_6H_4$ (**2.2**). The molecular structure consists of two oxo-bridged Ti₂Sb triangles held together by four phosphonates. The antimony ion with two titanium ions arranged in a triangular geometry is connected through a μ_3 -oxo bridge and two μ_2 -oxo bridges. One of the two μ_2 -oxo bridges belongs to methoxide. In the overall structure, there are eight methoxide molecules, four of them are μ_2 -bridged and the other four are coordinated to titanium ions. The two oxo-bridged Ti₂Sb triangles are connected to each other through two bridging phosphonates and two μ_2 -oxo bridges. The other two phosphonates present at the periphery of the structure hold the three metal ions of two triangles individually. The four phosphonate units in the structure are bound to one Sb and two titanium centers in [3.111] coordination mode based on the Harris notation. ¹⁸ Both Ti as well as Sb centers are present in an octahedral geometry with O₆Ti and O₅SbC coordination modes, respectively.

Compound **2.3** was prepared by reaction of $(RSb)_2(O)(t-BuPO_3H)_6$ with VCl₃ in a ratio of 1:4 in the presence of triethylamine under solvothermal conditions. Light green colored single crystals of **2.3** were grown by cooling the reaction mixture to room temperature. Compound **2.3** crystallizes in monoclinic space group $P2_1/c$, with half of the molecule present in the asymmetric unit. Crystallographic information and bond lengths and bond angles of compound **2.3** are given in **Table 2.5**. Single crystal X-ray characterization shows the formation of the vanadyl-organoantimony (V) hexanuclear oxo cluster having the formula $[(RSb)_4V_2(O)_2(\mu_3-O)_2(\mu_2-O)_2(t-BuPO_3)_4(\mu_2-OCH_3)_4]$, where $R = p\text{-ClC}_6H_4$ (**Scheme 2.1**). The core structure of **2.3** has a cube topology with four Sb centers, two vanadium centers and two phosphorus atoms at the vertices. The Sb centers form a central plane with pairs of vanadium and phosphorus atoms at opposite ends of the body diagonals of the cube. In this cage, *in situ*-generated two

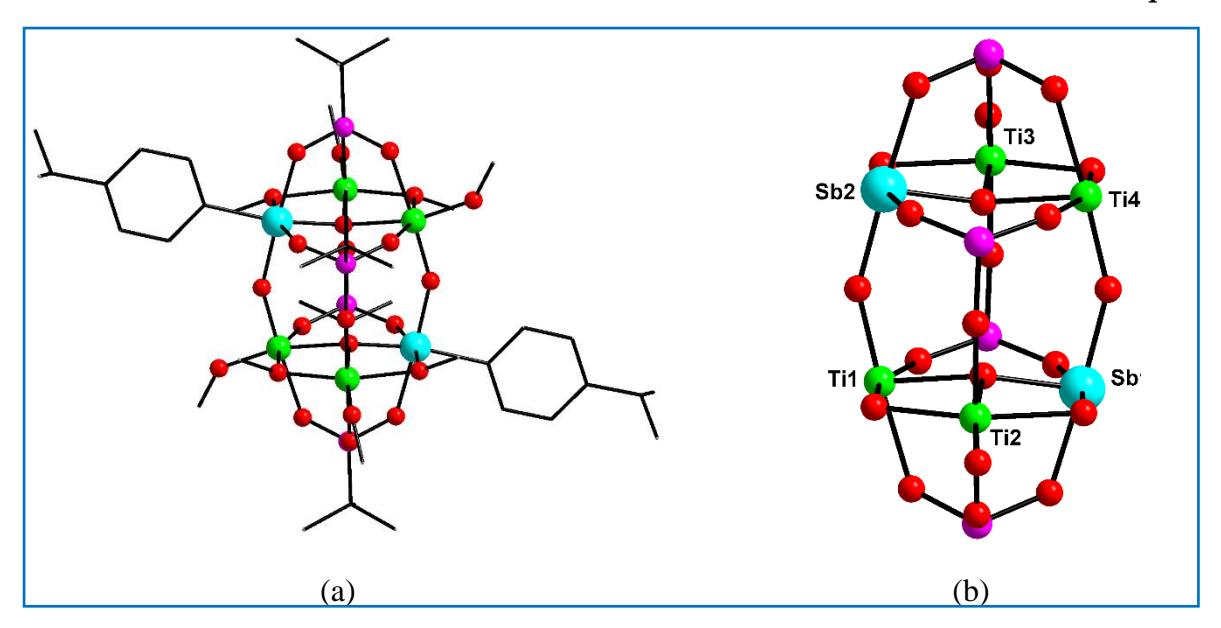


Figure 2.1: (a) Molecular and (b) core structure of compound **2.1**. Color code: cyan, Sb; green, Ti; purple, P; red, O; grey, C. Hydrogens are omitted for clarity.

oxo bridged Sb₂V triangles are present here, two arylstibonic acids self-condensed through one μ_3 -oxo bridge and further connected to vanadium metal centers via μ_2 -methoxy bridges. Based on the Harris notation, four phosphonates are bound to two Sb centers and one V metal center in [3.111] coordination mode.¹⁸ Every Sb ion attains a regular octahedral shape with a six-coordination environment. The octahedral coordination of the vanadium sites is fulfilled by two phosphonate oxygen from each side, one μ_3 -oxo bridge, two μ_2 -methoxy bridges with a long V-O bond and an oxo group occupying the last coordination site with a short vanadyl V=O bond. The geometry of metal atoms is confirmed using shape calculations (**Table 2.6**). Bond-Valence-Sum calculations¹⁹ represent two vanadium atoms in a 4+ oxidation state and are indicated by the paramagnetic nature of the cluster with a d^1 configuration.

The phase purities of the samples as characterized by powder X-ray diffraction (PXRD) match with the simulated patterns generated from SC-XRD analysis (Figure 2.16-2.18). Energy dispersive X-ray spectroscopy (EDAX) and elemental mapping confirm the elemental composition of 2.1-2.3 (Figure 2.19-2.24). EDAX analysis indicates the presence of C, O, P, Ti, V, Sb, and Cl species in the respective cluster composition and from elemental mapping analysis, it was found that C, O, P, Ti, Sb, V and Cl species were dispersed in the respective clusters.

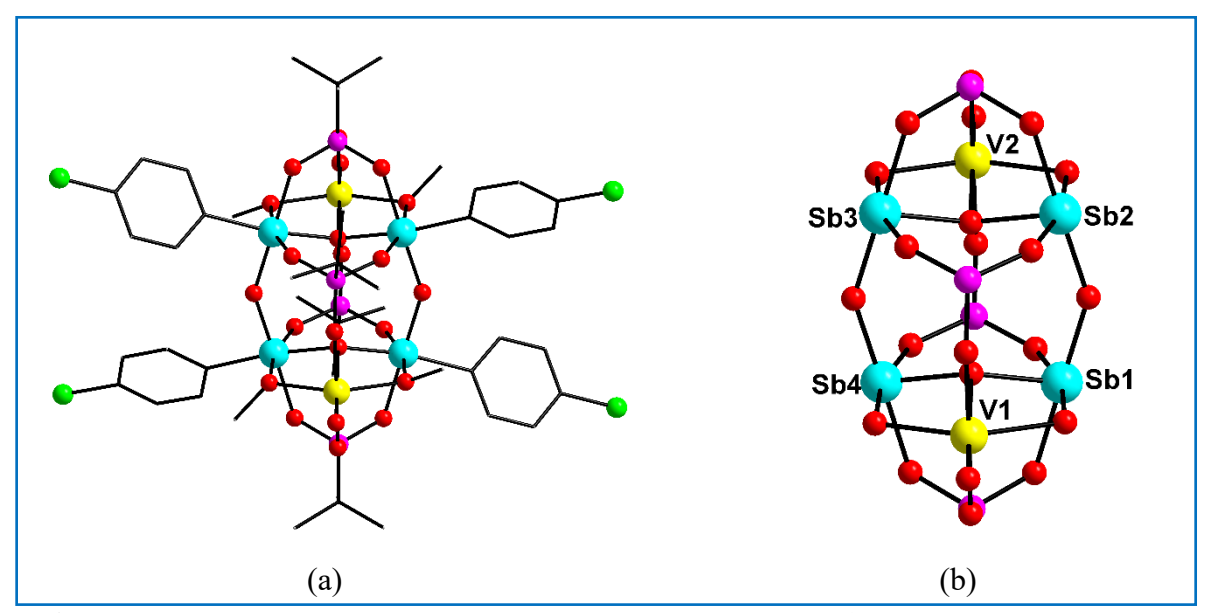


Figure 2.2: (a) Molecular structure and (b) Core structure of **2.3**. Color code: cyan, Sb; yellow, V; purple, P; red, O; grey, C. Hydrogens are omitted for clarity.

2.3.1 Optical Studies:

For compounds **2.1-2.3** and M_2Sb_4 (M = Mn, Co, Ni, and Cu) oxo clusters solid-state UV-visible absorption spectra were obtained. The optical bandgap (E_g) values of Sb_6 and transition metal doped Sb_6 oxo clusters were calculated by using the Tauc equation.

$$(\alpha h v)^{1/n} = A(h v - E_g)$$

Where hv is the photon energy, α is the absorption coefficient, E_g is the band gap energy and A is a constant. The n factor represents the type of electron transition and the n value equal to $\frac{1}{2}$ or 2 indicates the direct and indirect energy band gaps. The graph was plotted between $(\alpha hv)^2$ and hv. The optical bandgap (E_g) was calculated by extrapolating the tangent line to the x-axis (i.e., $\alpha = 0$). The linear fit of the fundamental peak gives the energy band gap. This method can be used for all semiconducting materials which show negligible absorbance. When this method is used for materials (surface modified, doped, defected, or bulk) exhibiting a significant absorbance at energies below band gap energy (E_g) , the obtained band gap values may be distorted. All of these changes could result in intraband gap states, which would create a new, broad absorption band known as an Urbach tail in the absorption spectrum, influencing the estimation of the energy band gap. In certain circumstances, errors may be possible in the estimation of $E_{\rm g}$. To avoid possible errors in estimation in the bandgap, researchers used an additional approach; for the slope below the fundamental absorption peak, a linear fit is employed as an x-coordinate (abscissa). An intersection point of the two linear fitting curves indicates the energy band gap. Therefore, this baseline approach is accurate in the estimation of bandgaps.²⁰ The direct bandgap of the Sb₆ oxo clusters [(p-ClC₆H₄Sb)₆(µ₃-O)₂(µ₂-O)₆(t-

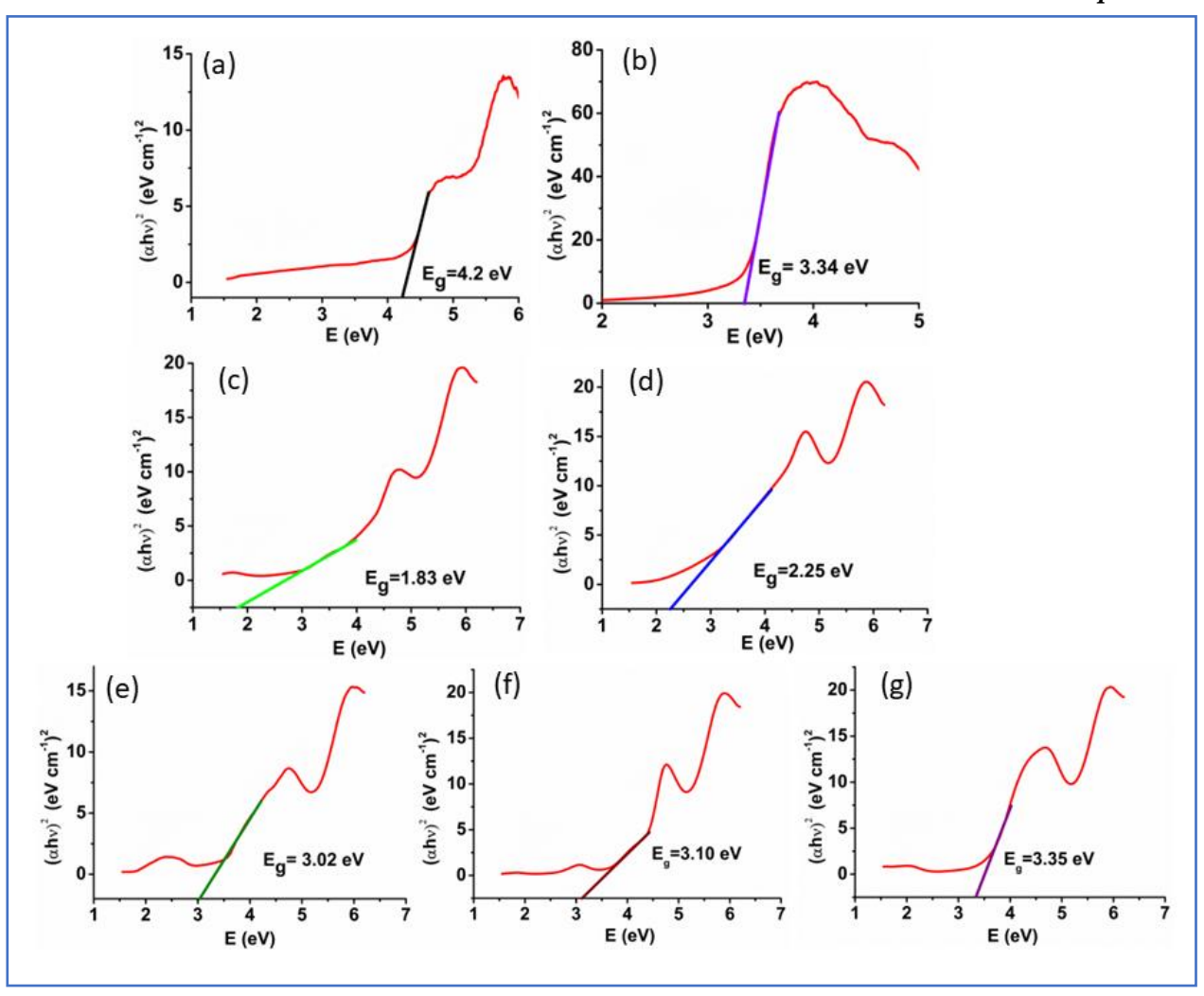


Figure 2.3: Tauc plots of (a) Sb₆ oxo cluster, (b) Ti, (c) V, (d) Mn, (e) Co, (f) Ni and (g) Cudoped Sb₆ oxo clusters.

BuPO₃)₄ is 4.24 eV and [(p-i-PrC₆H₄Sb)₆(μ ₃-O)₂(μ ₂-O)₆(t-BuPO₃)₄] is 4.22 eV. The calculated direct bandgap for compounds **1-3** and M₂Sb₄ (M= Mn, Co, Ni and Cu) oxo clusters is 3.55 eV, 3.34,1.83 2.25, 3.02, 3.10, and 3.35 eV (**Figure 2.3**). ^{3,7} A regular decrease in the gap value has been observed in moving over from homometallic Sb₆ clusters to heterometallic Ti₄Sb₂ and M₂Sb₄ (M = V, Mn, Co, Ni and Cu) clusters. The reduction in band gap is substantial on incorporating transition metal ions on the Sb₆ oxo framework. Our results indicate that among the various 3d transition metals synthesized here, compound **2.3** with V₂Sb₄ oxo cluster shows an optical gap that is very close to the optimal band gap within the Shockley-Queisser limit for maximum solar cell efficiency. ²¹ Further, the versatility of pro-ligand can be investigated by possible modifications, including incorporating two varying transition metal ions in the cluster, which could help fine-tune the bandgaps observed. Incorporation of the lanthanide metal ions,

which are generally associated with high spins and magnetic anisotropy, might add newer dimensions and functionalities to the self-assembled clusters.

2.3.2 Magnetic Measurements:

The magnetic behavior of the M_2Sb_4 (M= V, Mn, Co, Ni and Cu) oxo clusters was probed by measuring the thermal dependence of the product of the magnetic susceptibility (χ_M) by the temperature (T) (χ_M T) (**Figure 2.4a**). The room temperature values of χ_M T are 0.76 cm³ K mol⁻¹, 8.98 cm³ K mol⁻¹, 5.06 cm³ K mol⁻¹, 2.18 cm³ K mol⁻¹ and 0.92 cm³ K mol⁻¹ for M_2Sb_4 (M= V, Mn, Co, Ni and Cu) oxo clusters respectively are well correlate with the expected theoretical values of 0.75 cm³ K mol⁻¹ for V_2Sb_4 (S = ½) oxo cluster for two isolated high spin tetravalent V(IV), 8.75 cm³ K mol⁻¹ for Mn₂Sb₄ (S = 5/2) and 2.00 cm³ K mol⁻¹ for Ni₂Sb₄ (S = 1) oxo clusters for divalent Mn(II) and Ni(II) ions. For the Co₂Sb₄ oxo cluster, the room temperature χ_M T value is higher than the calculated one (3.75 cm³ K mol⁻¹ for two S = 3/2) but in agreement with the experimentally observed value for high spin Co(II). Finally, for the Cu₂Sb₄ oxo cluster, the experimental χ_M T value at 300 K is slightly higher than the expected

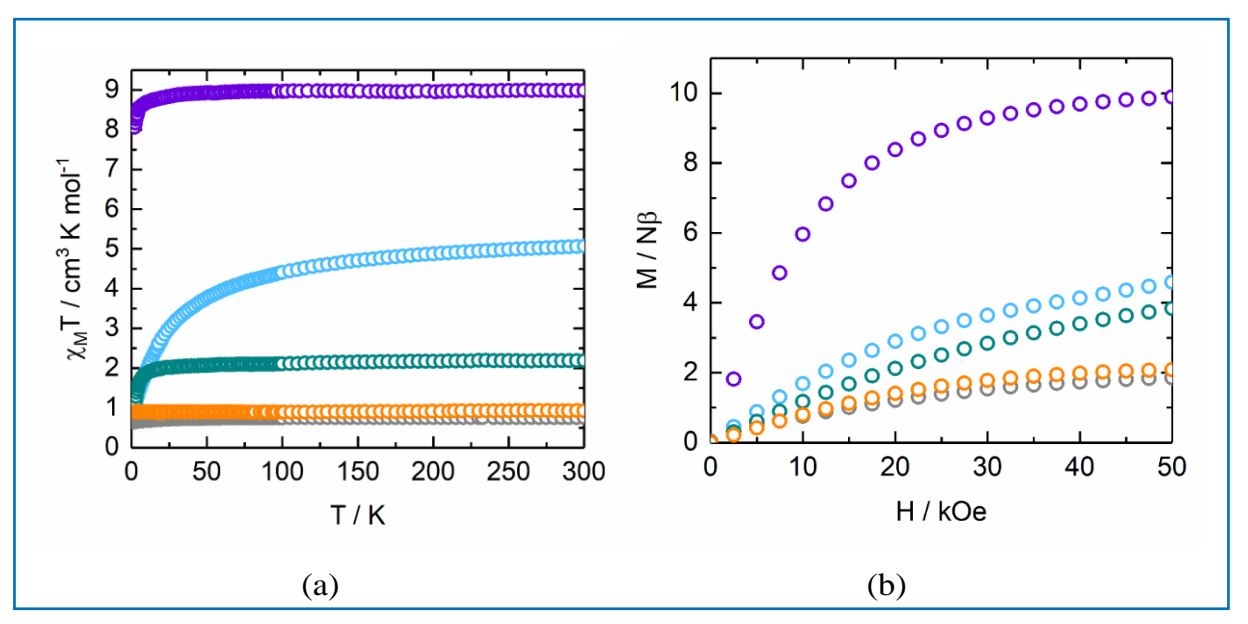


Figure 2.4: (a) Temperature-dependent dc magnetic susceptibility and (b) field dependence of the magnetization plots at 2 K for V₂Sb₄ (open grey circles), Mn₂Sb₄ (open purple circles), Co₂Sb₄ (open blue circles), Ni₂Sb₄ (open green circles) and Cu₂Sb₄ (open orange circles) oxo clusters.

 $0.75~\text{cm}^3~\text{K mol}^{-1}$ value but in agreement with two $S=\frac{1}{2}$ and g=2.2 commonly observed for Cu(II) ions. On cooling down at 2 K, the $\chi_M T$ values for M_2Sb_4 (M=V, Mn, Co and Cu) oxo clusters are constant and slightly decrease at cryogenic temperatures due to possible weak

antiferromagnetic interaction. For the Co₂Sb₄ oxo cluster, the Curie law deviations can be mainly explained by the thermal depopulation of the S = 3/2 sub levels. **Figure 2.4b** depicts the field dependences of the magnetization measured at 2 K. The values reached under a magnetic field of 50 kOe are 1.85 Nβ, 9.89 Nβ, 4.59 Nβ, 3.84 Nβ and 2.09 Nβ for M₂Sb₄ (M=V, Mn, Co, Ni and Cu) oxo clusters, respectively. These values are well in agreement with the expected saturation value for an isotropic V(IV), Mn(II) and Cu(II) ions, while Co₂Sb₄ and Ni₂Sb₄ oxo clusters highlighted almost linear increases at high fields which might indicate the presence of low-lying states and significant magnetic anisotropy.

2.3.3 Computational Studies:

In order to calculate the electronic band structure of **2.1-2.2**, projector augmented wave (PAW)²² method-based Density Functional Theory (DFT)²³ calculations, implemented through Vienna ab-initio simulation package²⁴ have been carried out in this work. Valence electronic configurations for both the clusters were considered as: Compound **2.1**: Sb:[5s²5p³], Ti:[3d³4s¹], P:[3s²3p³], O:[2s²2p⁴], C:[2s²2p²], H:[ultrasoft test]; Compound **2.2**: Sb:[5s²5p³], Ti:[3d³4s¹], P:[3s²3p³], Cl:[3s²3p⁵], O:[2s²2p⁴], C:[2s²2p²], H:[ultrasoft test]. Electron-electron interactions have been treated through generalized gradient approximation (GGA)²⁵. The experimental crystal structure of both clusters has been used to get the electronic band structure of these materials. As both the materials are found to crystalize in a triclinic crystal structure,

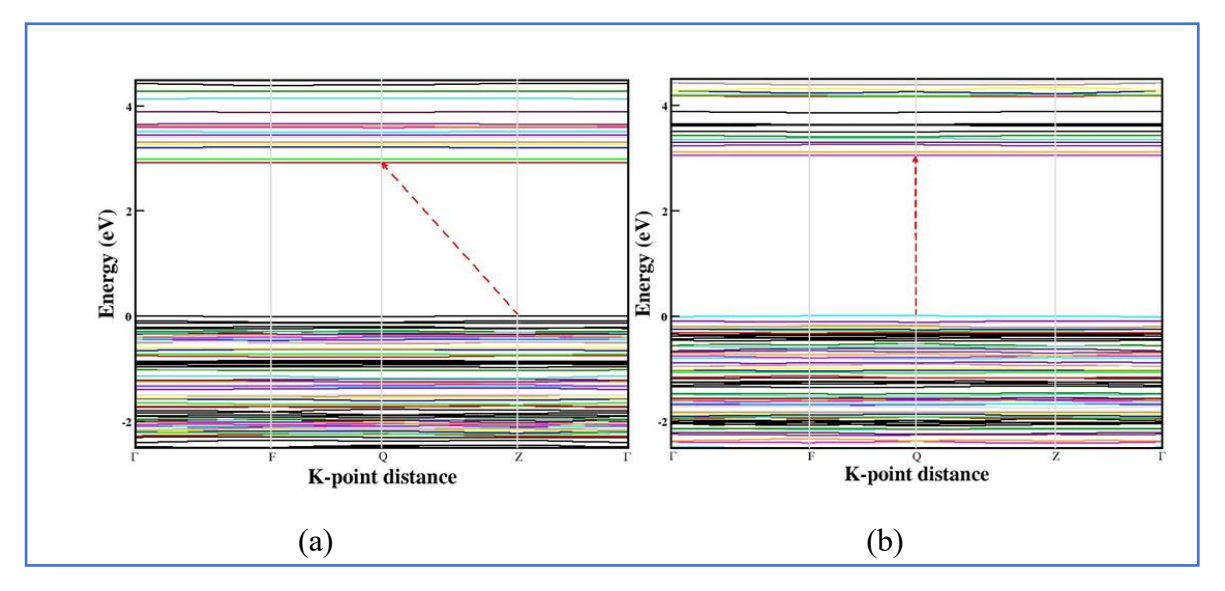


Figure 2.5: Electronic band structure of (a) compound 2.1 and (b) compound 2.2.

a gamma centered (5 X 5 X 4) Monkhorst Packing 26 has been used along with a 500 eV kinetic energy cutoff. The criteria for self-consistent energy and force were set to 1 X $^{10-6}$ eV/atom

and 0.01 eV/Å, respectively. For calculating the electronic band structure, K-path in the irreducible first Brillouin zone is Γ -F-Q-Z- Γ .

Figure 2.5a clearly indicates that cluster 2.1 has an indirect band gap of 2.92 eV between the conduction band bottom at Q and valence band top at Z high symmetry points (calculated indirect band gap for 2.1 is 2.83 eV). In the case of compound 2.2, it shows a direct band gap at high symmetry point Q with a band gap value of 3.04 eV (Figure 2.5b) (the calculated direct band gap for 2.2 is 3.34 eV). The difference between the computed and experimental band gaps are due to correlation effects. As it is well known that the use of normal GGA potential always underestimates the electronic band gap of any insulator or semiconductor, we expect a higher value of band gap for these clusters.

To understand the electronic structure in the Fermi level and to validate the experimental band gaps of M₂Sb₄ (M= V, Mn, Co, Ni and Cu) oxo clusters, we have performed first-principles calculations within the framework of density functional theory (DFT) as implemented in the VASP code.^{24, 27} Plane augmented wave pseudopotentials have been used in our calculations.²² The gas-phase calculations of ale five clusters were performed by enclosing them in a box of size 30 Å in order to avoid inter-cluster interactions. The absence of translational symmetry enables us to perform the calculations only at the Gamma point. Since the clusters contain paramagnetic 3d transition metal ions, we have performed spin-polarized calculations to enforce the antiferromagnetic state as observed in our magnetic measurements. Accordingly, the calculations were carried out by constraining starting moments of the two transition metal ions in an antiparallel configuration. In order to account for the strong electron correlations of transition metals, on-site electron repulsion of 3d electrons were treated explicitly by adding a Hubbard-U term. The value of on-site electron correlations is well reported to be in the range of 4-6 eV for molecular clusters as well as in solids.²⁸ Hence, we have used $U_{eff} = 5.5$ eV in our calculations. The starting experimental refined crystallographic positions were relaxed under different magnetic configurations separately until all the three components of the Hellman-Feynman forces of each atom were less than 0.02 eV/Å corresponding to a total energy convergence of less than 0.1 meV between two successive ionic steps. The computed spin magnetic moments of M_2Sb_4 (M= V, Mn, Co, Ni and Cu) oxo clusters are 1.154 μ_B , 4.66 μ_B , 2.79 μ_B , 1.75 μ_B and 0.754 μ_B as expected for corresponding spin values of s = 1/2, 5/2, 3/2, 1 and 1/2 respectively.

The electronic states of M_2Sb_4 oxo clusters for spin-up and spin-down channels are shown in (**Figure 2.6**) and the corresponding HOMO-LUMO gap of the antiferromagnetic spin configuration is presented in **Table 2.1**. We notice a systematic increase in the HOMO-LUMO

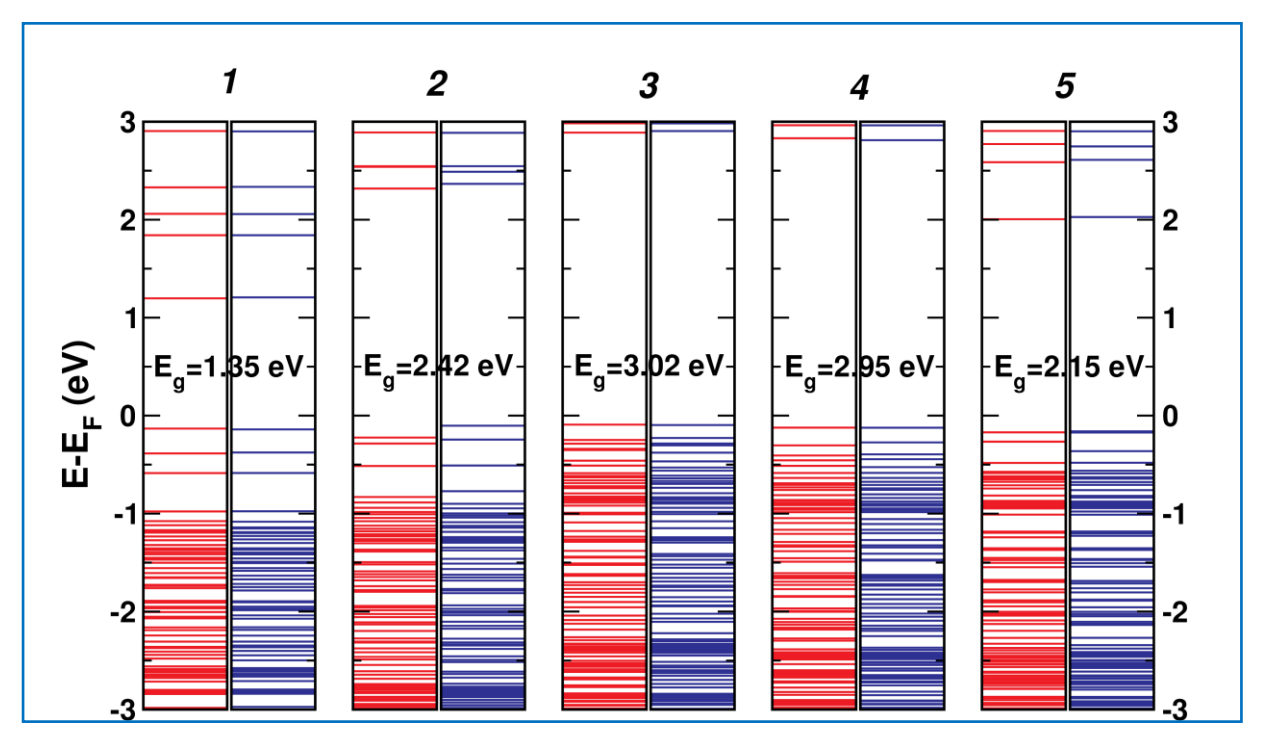


Figure 2.6: Electronic structures of M₂Sb₄ (M=V, Mn, Co, Ni and Cu) oxo clusters in the vicinity of Fermi level for up (red) and down (blue) spin channels. The corresponding HOMO-LUMO gap values are also shown.

gap, which peaks for the Co₂Sb₄ oxo cluster and then falls as a function of electron filling of the 3d orbital of the transition metal ion. The maximum gap obtained is 3.02 eV for cluster Co₂Sb₄ oxo cluster and cluster V₂Sb₄ oxo cluster shows an optimal gap of 1.35 eV. In order to obtain microscopic insights into the electronic structure in the vicinity of the Fermi level, we obtained the projected charge densities of the HOMO and LUMO in each case. The charge density contours of the V₂Sb₄ oxo cluster show (Figure 2.7) that the HOMO and LUMO are localized on two aryl groups attached to antimony, respectively. In the case of the Mn₂Sb₄ oxo cluster, the HOMO consists of the d_{z^2} orbital of one of the manganese ions hybridized with oxygen and nitrogen ligands of the octahedron, while the LUMO charge densities are seen predominantly on the pyridine ring with a small contribution from the d_{xy} orbital of manganese. The HOMO-LUMO gap of the to2Sb4 oxo cluster emerges from the charge fluctuation between the aryl groups attached to antimony atoms located at the opposite to each other. The HOMO and LUMO of Ni₂Sb₄ oxo cluster are similar to that of the Co₂Sb₄ oxo cluster. The HOMO and LUMO of Cu₂Sb₄ oxo cluster are centered around one of the copper octahedron in which the d_{z^2} and $d_{x^2-y^2}$ orbitals hybridize with the surrounding ligands. It is noteworthy that the HOMOs and LUMOs of M2Sb4 clusters are different; for example, in

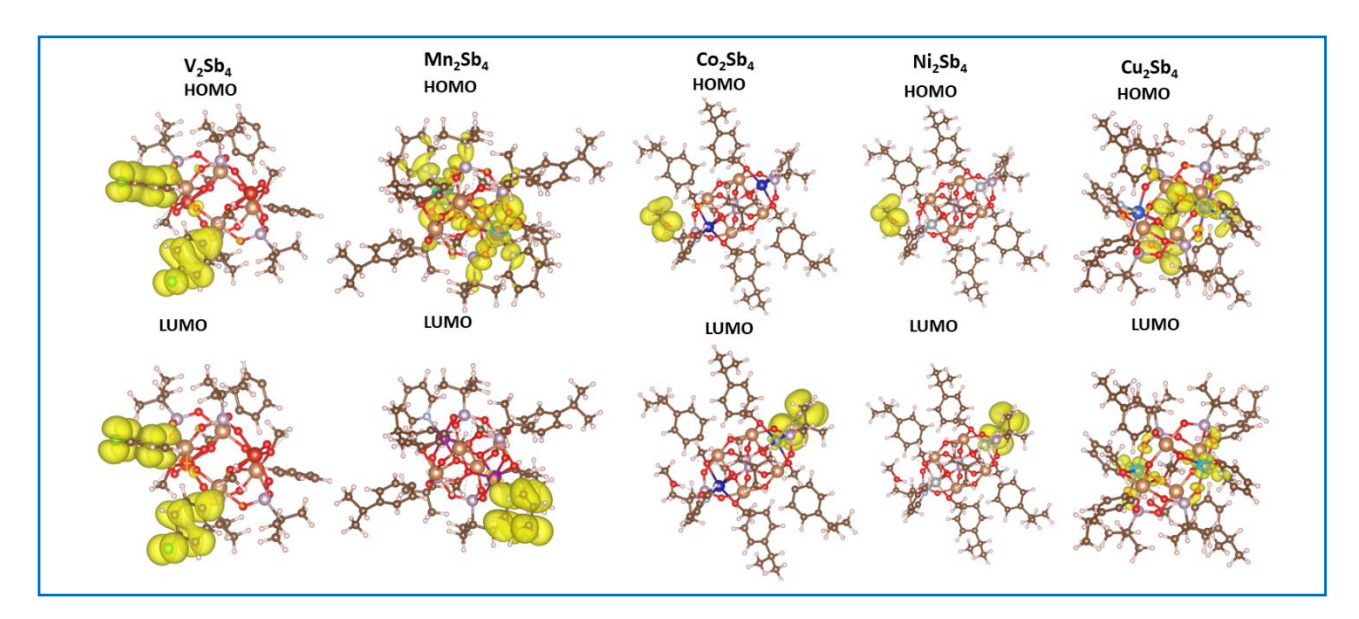


Figure 2.7: HOMO and LUMO charge density isosurfaces of M_2Sb_4 (M=V, Mn, Co, Ni and Cu) oxo clusters for iso value 0.0005 Å⁻³.

compounds V_2Sb_4 , Co_2Sb_4 and Ni_2Sb_4 these states are ligand dominated, whereas in compounds Mn_2Sb_4 and Cu_2Sb_4 , there is a small contribution of transition metal d-orbital. This is because the local geometry depends on the electron filling as well as the charge state of the metal ion. Further, the on-site Coulomb correlations also increase with a decrease in the atomic size as we move from left to right along the 3d series. A higher ionic charge state of the metal ion also increases the on-site electron repulsions. These can modify the local geometry around the metal ion, which in turn can alter the crystal field splitting as well as the metal-ligand hybridization. Therefore, the character of the frontier orbitals and the excitation gap is highly sensitive to various electron correlations and cannot be predicted a priori. Such changes in the character of frontier orbitals is also well known in the case of transition metal oxides where the electron filling of metal d-band can transform a system from a Mott-Hubbard insulator in which the fluctuations are 3d-3d type purely driven by on-site Coulomb repulsion to a negative charge-transfer insulator with oxygen 2p-2p fluctuations across the Fermi level. Along these lines, it has previously been shown that $LaV_{1-x}Ni_xO_3$ transforms from Mott (x=0.0) to a charge-transfer insulator (x=0.8).

Table 1: Bandgap values for compounds Ti₄Sb₂ and M₂Sb₄ (M= V, Mn, Co, Ni and Cu) oxo clusters

	Experimental Bandgap (eV)	Theoretical HOMO-LUMO gap (eV)
Ti ₄ Sb ₂ oxo cluster	3.34	3.04
V ₂ Sb ₄ oxo cluster	1.83	1.35
Mn ₂ Sb ₄ oxo cluster	2.25	2.42
Co₂Sb₄ oxo cluster	3.02	3.02
Ni₂Sb₄ oxo cluster	3.10	2.95
Cu₂Sb₄ oxo cluster	3.35	2.15

2.4 Conclusion:

To summarize, incorporating/doping a series of transition metal ions into the Sb₆ oxo cluster has a profound effect on the optical bandgap of the heterometallic clusters synthesized. The oxidation and spin states of the incorporated transition metals were confirmed by magnetic susceptibility measurements. Transition metal incorporated clusters show a reduction in bandgap from 4.2 eV (corresponds to the homometallic Sb₆ oxo clusters) to 3.35-1.83 eV. Interestingly, a systematic increase in bandgap from V₂Sb₄ to Cu₂Sb₄ oxo cluster is also observed. DFT calculations were performed to compare with the experimentally observed band gaps, which show a good correlation.

2.5 Analytical and Spectroscopic Data

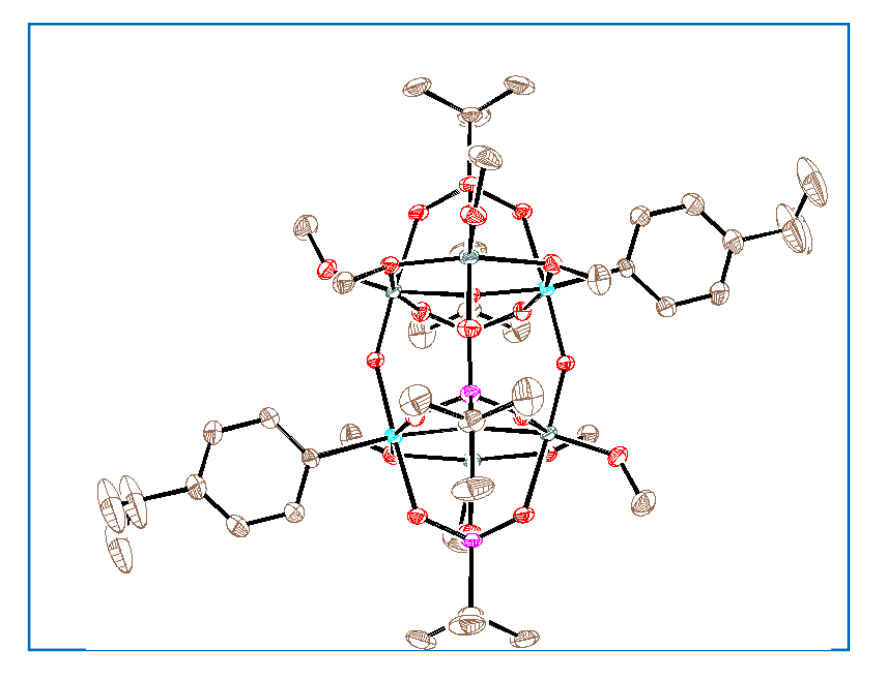


Figure 2.8: ORTEP view of 2.1 with thermal ellipsoids shown at 30% probability.

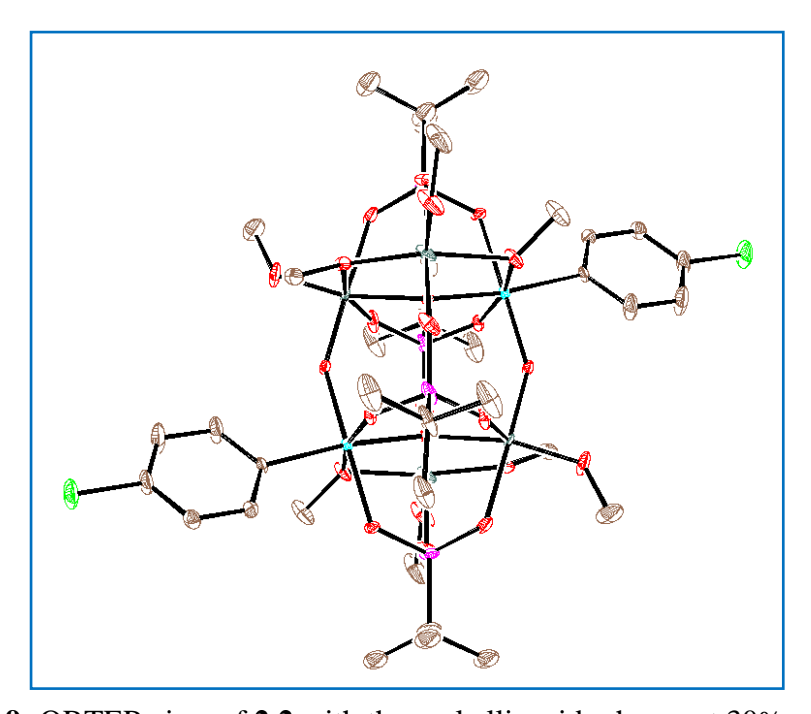


Figure 2.9: ORTEP view of 2.2 with thermal ellipsoids shown at 30% probability.

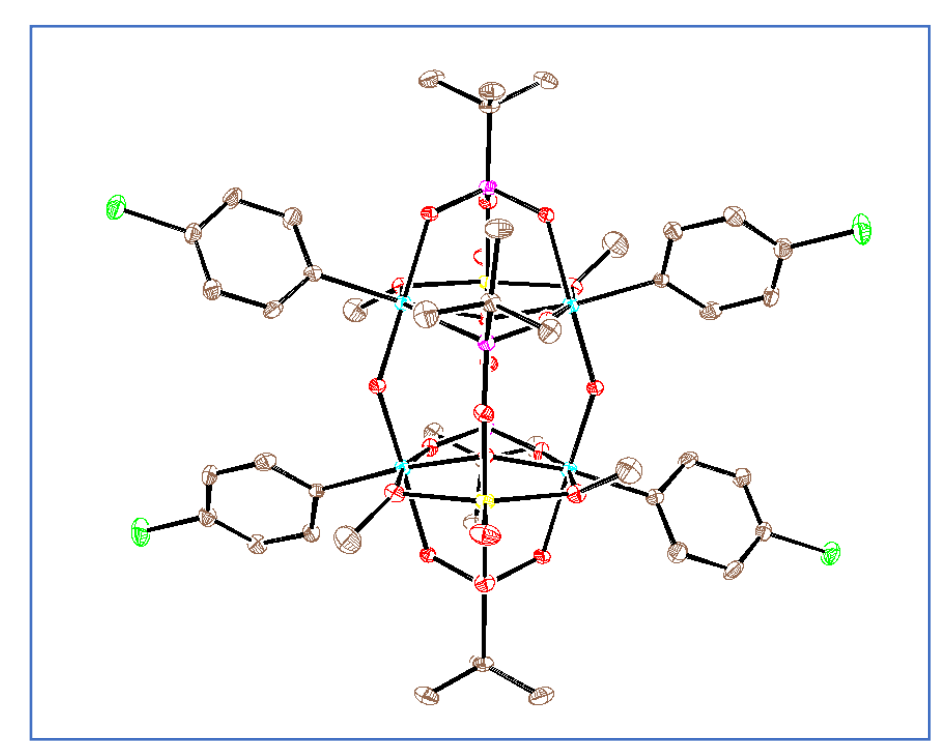


Figure 2.10: ORTEP view of 2.3 with thermal ellipsoids shown at 30% probability.

 Table 2.2: crystallographic information of compounds 2.1-2.3

	2.1	2.2	2.3
Formula	C ₄₂ H ₈₂ O ₂₄ P ₄ Sb ₂ Ti ₄	C ₃₆ H ₆₈ O ₂₄ Cl ₂ P ₄ Sb ₂ Ti ₄	C ₄₄ H ₆₄ Cl ₄ O ₂₂ P ₄ Sb ₄ V ₂
Formula weight	1530.05	1514.78	1799.51
Temperature/K	293.44	100(2)	109(3)
Crystal system	triclinic	triclinic	monoclinic
Space group	P-1	P-1	P2 ₁ /n
a/Å	10.5851(4)	10.1159(8)	9.9319(2)
b/Å	11.1600(5)	10.7762(8)	24.0942(5)
c/Å	13.5452(5)	14.3357(11)	13.5380(2)
α/°	79.979(2)	105.747(4)	90
β/°	86.4890(10)	103.186(4)	99.005(2)
γ/°	81.963(2)	96.357(4)	90
Volume/Å ³	1559.09(11)	1439.38(19)	3199.73(11)
Z	1	1	2
ρ _{calc} g/cm ³	1.63	1.748	1.868
μ/mm^{-1}	1.516	1.731	2.281
F(000)	776	760	1764.0
Crystal size/mm ³	$0.2 \times 0.2 \times 0.18$	$0.23 \times 0.21 \times 0.2$	$0.23 \times 0.19 \times 0.14$
Radiation	$MoK\alpha (\lambda = 0.71073)$	MoKα ($\lambda = 0.71073$)	MoKα ($\lambda = 0.71073$)
2θ range (°)	4.854-55.086	5.242-55.248	4.484 to 50.698
Index ranges	$-13 \le h \le 13,$ $-13 \le k \le 13,$ $-18 \le 1 \le 18$	$-13 \le h \le 13,$ $-21 \le k \le 21,$ $-22 \le 1 \le 23$	$-11 \le h \le 11$, $-29 \le k \le 28$, $-16 \le l \le 15$
Reflections collected	72956	54917	29157
Ind. reflections	7194	6634	5855
GooF(F ²)	1.035	1.059	1.089
$R_1(F)$ $[I > 2\sigma(I)]$	0.0321	0.0463	0.0351
wR ₂ (F ²) (all data)	0.0897	0.1088	0.0908
Largest diff. peak/hole / e Å ⁻³	1.81/-0.95	1.61/-1.33	0.92/-0.87
completeness to θ_{max} ,	99.8	99.0	100.0

Tunable bandgap....

Table 2.3: Selected bond lengths (Å) and bond angles (deg) parameters of compound 2.1

Sb1-O10	1.944(18)	O6 ¹ -Sb1-O1	86.99(9)	O5-P2-O6	110.02(13)
Sb1-O11	1.936(19)	O1-Sb1-O7	90.14(9)	O4-P2-O6	112.54(12)
Sb1-O7	2.092(2)	O10 ¹ -Ti2-Ti3 ¹	37.94(5)	O4-P2-O5	112.00(13)
Sb1-O6 ¹	2.007(2)	O10 ¹ -Ti2-O9 ¹	73.31(8)	O3-P1-O1	112.85(13)
Sb1-O1	2.057(2)	O10 ¹ -Ti2-O3 ¹	81.52(8)	O3-P1-O2	111.07(13)
Ti2-Ti3 ¹	3.206(8)	O11-Ti2-Ti3 ¹	99.21(7)	O2-P1-O1	108.38(13)
Ti2-O10 ¹	2.038(2)	O11-Ti2-O10 ¹	95.18(9)	Sb1-O10-Ti2 ¹	139.53(10)
Ti2-O11	1.801(19)	O11-Ti2-O9 ¹	90.48(9)	Sb1-O10-Ti3	108.02(9)
Ti2-O9 ¹	2.078(2)	O11-Ti2-O3 ¹	176.69(9)	Ti3-O10-Ti2 ¹	103.97(8)
Ti2-O3 ¹	2.097(2)	O11-Ti2-O4	94.58(9)	Ti2-O11-Sb1	152.43(12)
Ti2-O12	1.801(2)	O9 ¹ -Ti2-Ti3 ¹	36.14(6)	Ti3-O9-Ti2 ¹	105.12(9)
Ti2-O4	1.968(2)	O9 ¹ -Ti2-O3 ¹	88.37(9)	Ti3-O7-Sb1	101.96(9)
Ti3-O10	2.032(2)	O3 ¹ -Ti2-Ti3 ¹	78.07(7)	P2-O6-Sb1 ¹	134.57(12)
Ti3-O9	1.959(2)	O12-Ti2-Ti3 ¹	131.11(8)	P2-O5- Ti3	149.10(14)
Ti3-O7	2.049(2)	O12-Ti2-O10 ¹	164.95(9)	P1-O3- Ti2 ¹	123.85(13)
Ti3-O5	1.934(2)	O12-Ti2-O11	97.56(10)	P1-O1- Sb1	121.53(11)
Ti3-O2	1.975(2)	O12-Ti2-O9 ¹	98.53 (10)	P2-O4- Ti2	140.83(14)
Ti3-O8	1.785(2)	O12-Ti2-O3 ¹	85.69(10)	P1-O2- Ti3	120.75(12)
P2-O6	1.543(2)	O12-Ti2-O4	98.24(10)	O5-Ti3-O10	93.39(8)
P2-O5	1.523(2)	O4-Ti2-Ti3 ¹	125.54(7)	O5-Ti3-O9	92.36(9)
P2-O4	1.512(2)	O4-Ti2-O10 ¹	88.68(8)	O5-Ti3-O7	92.78(9)
P1-O3	1.507(2)	O4-Ti2- O9 ¹	161.68(9)	O5-Ti3-O2	178.24(10)
P1-O1	1.557(2)	O4-Ti2- O3 ¹	85.58(9)	O2-Ti3- Ti2 ¹	82.04(7)
P1-O2	1.534(2)	O10-Ti3- Ti2 ¹	38.08(5)	O2-Ti3-O10	87.81(9)
O10-Sb1-O7	74.35(8)	O10-Ti3-O7	73.52(8)	O2-Ti3-O7	86.32(9)
O10-Sb1-O6 ¹	92.46(8)	O9-Ti3-Ti2 ¹	38.74(6)	O8-Ti3- Ti2 ¹	145.72(9)
O10-Sb1-O1	84.47(8)	O9-Ti3-O10	76.01(8)	O8-Ti3-O10	172.37(10)
O11-Sb1-O10	93.52(8)	O9-Ti3-O7	149.34(9)	O8-Ti3-O9	109.23(10)
O11-Sb1-O7	91.19(9)	O9-Ti3-O2	89.18(9)	O8-Ti3-O7	100.78(10)
O11-Sb1-O6 ¹	91.16(9)	O7-Ti3-Ti2 ¹	110.63(6)	O8-Ti3-O5	91.94(10)
O11-Sb1-O1	177.21(8)	O5-Ti3-Ti2 ¹	99.70(7)	O8-Ti3-O2	86.74(11)
1					

¹1-X,1-Y,1-Z

Table 2.4: Selected bond lengths (Å) and bond angles (deg) parameters of compound 2.2

Sb1-O7	1.945(3)	O11 ¹ -Sb1-O3	88.05(12)	O1-Ti3-O2	85.2(2)
Sb1-O8	1.933(3)	O3-Sb1-O6	89.48(15)	O9-P1-O11	112.6(2)
Sb1-O11 ¹	1.989(3)	O7 ¹ -Ti2-Ti3 ¹	37.60(8)	O9-P1-O10	112.0(2)
Sb1-O6	2.080(3)	O7 ¹ -Ti2-O5 ¹	72.75(13)	O10-P1-O11	109.8(2)
Sb1-O3	2.052(3)	O7 ¹ -Ti2-O4 ¹	82.81(14)	O2-P2-O3	108.6(2)
Ti2-Ti3 ¹	3.208(14)	O8-Ti2-Ti3 ¹	100.85(10)	O4-P2-O3	112.7(2)
Ti2-O7 ¹	2.047(3)	O8-Ti2-O7 ¹	95.91(12)	O4-P2-O2	110.8(2)
Ti2-O8	1.806(3)	O8-Ti2-O9	94.25(15)	Sb1-O7-Ti2 ¹	137.97(16)
Ti2-O9	1.963(4)	O8-Ti2-O51	91.60(14)	Sb1-O7-Ti3	107.60(14)
Ti2-O5 ¹	2.064(4)	O8-Ti2-O4 ¹	178.49(14)	Ti3-O7-Ti2 ¹	104.21(13)
Ti2-O4 ¹	2.079(4)	O8-Ti2-O12	95.77(16)	Ti2-O8-Sb1	149.34(17)
Ti2-O12	1.814(4)	O9-Ti2-Ti3 ¹	125.68(10)	P1-O11-Sb1 ¹	136.16(18)
Ti3-O7	2.020(3)	O9-Ti2-O7 ¹	89.43(13)	Ti3-O6-Sb1	100.97(15)
Ti3-O6	2.067(3)	O9-Ti2-O5 ¹	161.73(14)	P1-O9-Ti2	140.2(2)
Ti3-O5	1.962(4)	O9-Ti2-O4 ¹	84.95(17)	P2-O3-Sb1	120.99(18)
Ti3-O10	1.929(4)	O5 ¹ -Ti2-Ti3 ¹	36.07(10)	Ti3-O5-Ti2 ¹	105.65(14)
Ti3-O2	1.992(4)	O51-Ti2-O41	88.78(17)	P1-O10-Ti3	145.8(2)
Ti3-O1	1.782(4)	O4 ¹ -Ti2-Ti3 ¹	78.63(14)	P2-O2-Ti3	120.9(2)
P1-O11	1.544(3)	O12-Ti2-Ti3 ¹	131.41(19)	P2-O4-Ti2 ¹	123.9(2)
P1-O9	1.516(4)	O12-Ti2-O7 ¹	165.76(19)	O10-Ti3-O7	94.34(13)
P1-O10	1.521(4)	O12-Ti2-O9	97.8(2)	O10-Ti3-O6	94.23(16)
P2-O3	1.559(3)	O12-Ti2-O5 ¹	98.8(2)	O10-Ti3-O5	94.11(15)
P2-O2	1.531(5)	O12-Ti2-O4 ¹	85.61(16)	O10-Ti3-O2	176.69(18)
P2-O4	1.516(5)	O7-Ti3-Ti2 ¹	38.19(8)	O2-Ti3-Ti2 ¹	81.39(15)
O7-Sb1-O11 ¹	92.36(12)	O7-Ti3-O6	74.16(12)	O2-Ti3-O7	88.28(15)
O7-Sb1-O6	75.44(13)	O6-Ti3-Ti2 ¹	110.75(10)	O2-Ti3-O6	84.53(15)
O7-Sb1-O3	85.96(12)	O5-Ti3-Ti2 ¹	38.28(11)	O1-Ti3-Ti2 ¹	144.03(18)
O8-Sb1-O7	93.55(12)	O5-Ti3-O7	75.50(13)	O1-Ti3-O7	172.18(17)
O8-Sb1-O11 ¹	91.27(13)	O5-Ti3-O6	149.02(15)	O1-Ti3-O6	100.91(17)
O8-Sb1-O6	91.08(14)	O5-Ti3-O2	88.50(17)	O1-Ti3-O5	108.54(19)
O8-Sb1-O3	179.15(14)	O10-Ti3-Ti2 ¹	101.92(11)	O11 ¹ -Sb1-O6	167.71(12)
¹ 2 V 1 V 1 7					

¹2-X,1-Y,1-Z

Tunable bandgap....

Table 2.5: Selected bond lengths (Å) and bond angles (deg) parameters of compound 2.3

Sb1-O4	2.005(3)	O3-Sb1-O11 ¹	86.59(11)	O6-V1-O1 ¹	93.74(11)
Sb1-O3	1.967(3)	O3-Sb1-O1	76.46(11)	O7-V1-O3 ¹	178.88(13)
Sb1-O2	1.921(3)	O2-Sb1-O4	92.25(11)	O7-V1-O8	109.20(15)
Sb1-O11 ¹	2.052(3)	O2-Sb1-O3	94.59(11)	O7-V1-O10	93.31(14)
Sb1-O1	2.048(3)	O2-Sb1-O11 ¹	177.78(11)	O7-V1-O1 ¹	108.97(15)
Sb2-O3 ¹	1.965(3)	O1-Sb1-O11 ¹	88.20(11)	O7-V1-O6	92.61(14)
Sb2-O8	2.047(3)	O31-Sb2-O8	77.12(11)	O4-P1-O5	111.24(16)
Sb2-O9	2.060(3)	O31-Sb2-O9	86.38(10)	O6-P1-O4	112.36(16)
Sb2-O2	1.927(3)	O31-Sb2-O5 ¹	90.11(11)	O6-P1-O5	111.89(16)
Sb2-O5 ¹	2.004(3)	O8-Sb2-O9	87.73(11)	O11-P2-O9	109.51(16)
V1-O3 ¹	2.230(3)	O2-Sb2-O3 ¹	94.17(11)	O10-P2-O9	110.98(16)
V1-O8	2.051(3)	O2-Sb2-O8	91.46(11)	O10-P2-O11	110.59(16)
V1-O10	2.000(3)	O2-Sb2-O9	178.89(10)	P1-O4-Sb1	136.01(16)
V1-O11	2.065(3)	O2-Sb2-O5 ¹	93.72(11)	Sb1-O3-V11	103.55(12)
V1-O6	1.987(3)	O51-Sb2-O8	166.54(11)	Sb2¹-O3-Sb1	138.61(14)
V1-O7	1.602(3)	O51-Sb2-O9	87.24(11)	Sb2 ¹ -O3-V1 ¹	102.89(10)
P1-O4	1.542(3)	O8-V1-O3 ¹	71.37(10)	Sb2-O8-V1	106.52(12)
P1-O5	1.543(3)	O8-V1-O1 ¹	141.02(11)	P2-O9-Sb2	122.87(15)
P1-O6	1.490(3)	O10-V1-O3 ¹	87.69(10)	Sb1-O2-Sb2	146.09(15)
P2-O9	1.554(3)	O10-V1-O8	84.97(11)	P2-O11-Sb1 ¹	123.16(16)
P2-O11	1.548(3)	O10-V1-O1 ¹	85.30(11)	P1-O5-Sb2 ¹	137.08(17)
P2-O10	1.510(3)	O1¹-V1-O3¹	70.60(10)	P2-O10-V1	123.13(16)
O4-Sb1-O11 ¹	85.85(11)	O6-V1-O3 ¹	86.40(11)	Sb1-O1-V1 ¹	106.77(13)
O4-Sb1-O1	166.00(11)	O6-V1-O8	92.12(12)	P1-O6-V1	153.53(18)
O3-Sb1-O4	90.54(11)	O6-V1-O10	173.99(12)		

¹1-X,1-Y,1-Z

Table 2.6: Shape calculation of compounds **2.1 -2.3 a)** Summary of SHAPE analysis for Ti and Sb atoms in **2.1**

S. No	Geometry	CShM value for Ti1	CShM value for Ti2	CShM value for Sb1
1	Hexagon (D6h)	31.089	33.574	31.434
2	Pentagonal pyramid (C5v)	25.693	24.583	25.939
3	Octahedron (Oh)	0.793	1.659	0.765
4	Trigonal prism (D3h)	13.420	12.743	13.883
5	Johnson pentagonal pyramid J2 (C5v)	29.544	28.455	30.305

b) Summary of SHAPE analysis for Ti and Sb atoms in 2.2

S. No	Geometry	CShM value for Ti1	CShM value for Ti2	CShM value for Sb1
1	Hexagon (D6h)	30.894	33.663	30.839
2	Pentagonal pyramid (C5v)	25.537	24.299	26.183
3	Octahedron (Oh)	0.839	1.763	0.673
4	Trigonal prism (D3h)	13.246	12.585	14.907
5	Johnson pentagonal pyramid J2 (C5v)	29.322	28.421	29.724

c) Summary of SHAPE analysis for Ti and Sb atoms in 2.3

S. No	Geometry	CShM value for V1	CShM value for Sb1	CShM value for Sb2
1	Hexagon (D6h)	34.395	31.737	31.122
2	Pentagonal pyramid (C5v)	23.097	26.785	26.436
3	Octahedron (Oh)	2.070	0.636	0.592
4	Trigonal prism (D3h)	12.111	14.617	14.753
5	Johnson pentagonal pyramid J2 (C5v)	27.044	30.427	30.034

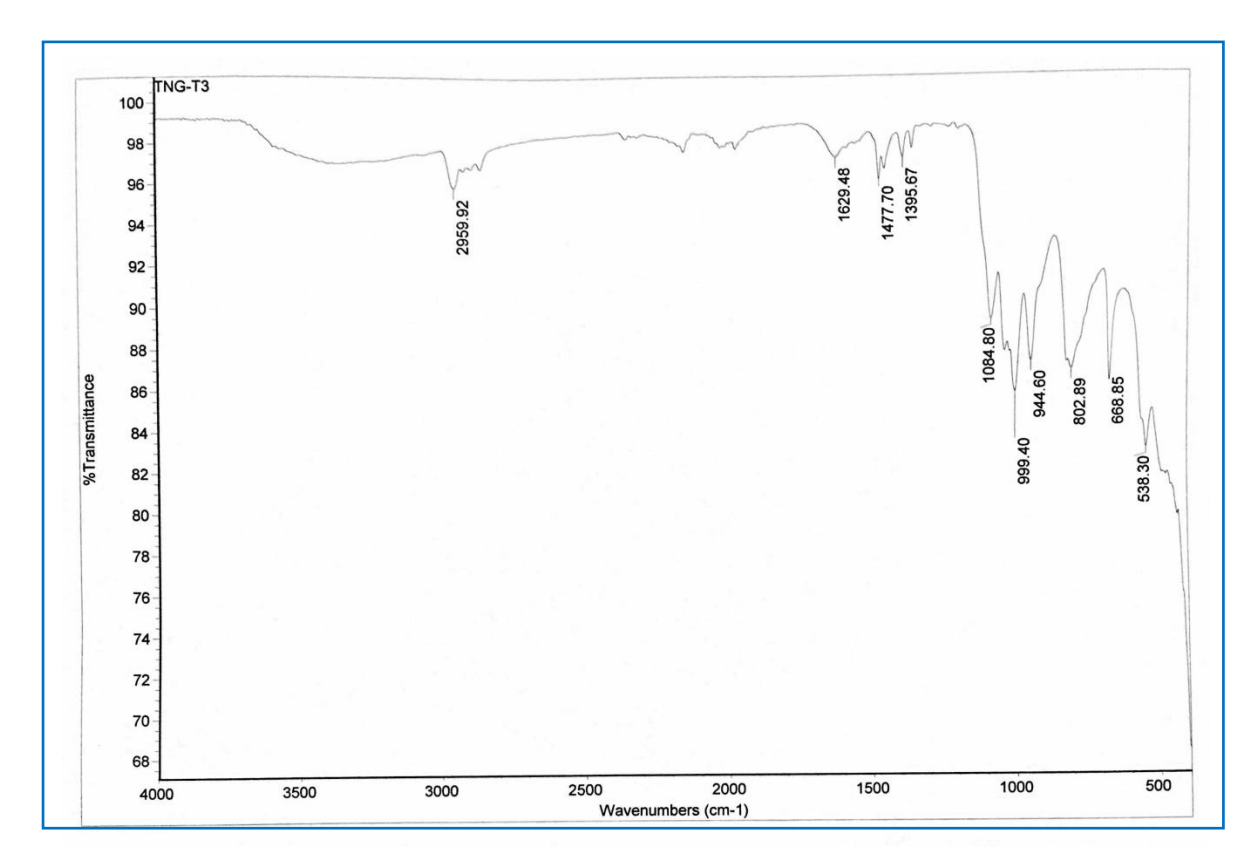


Figure 2.11: IR spectrum of 2.1.

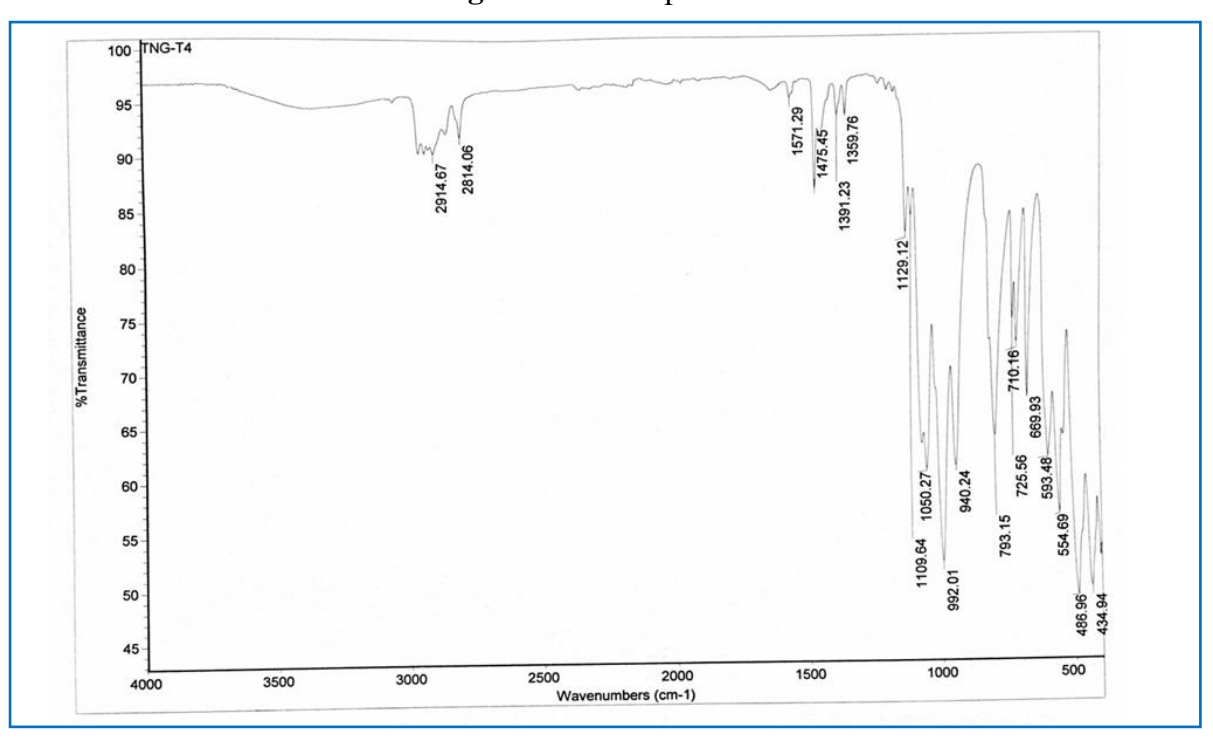


Figure 2.12: IR spectrum of 2.2.

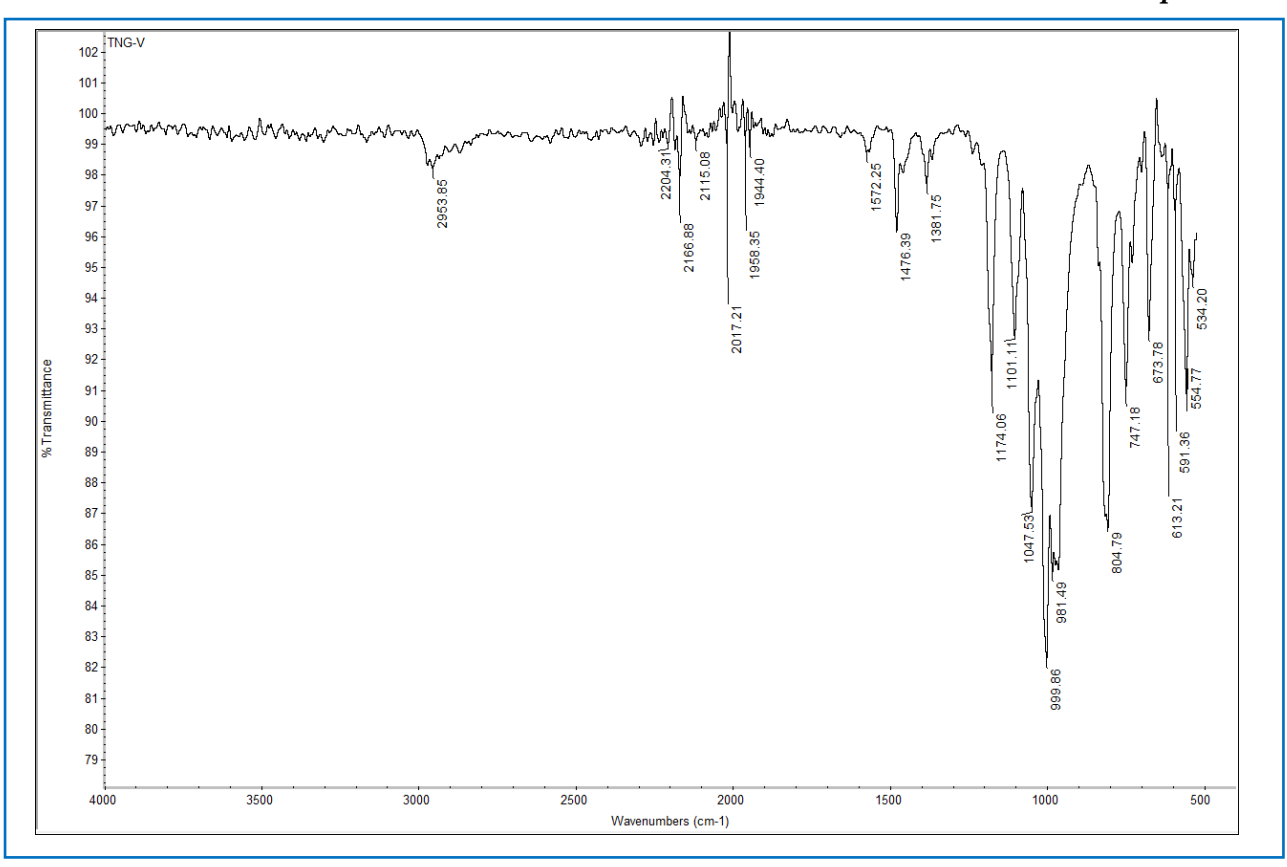


Figure 2.13: IR spectrum of 2.3.

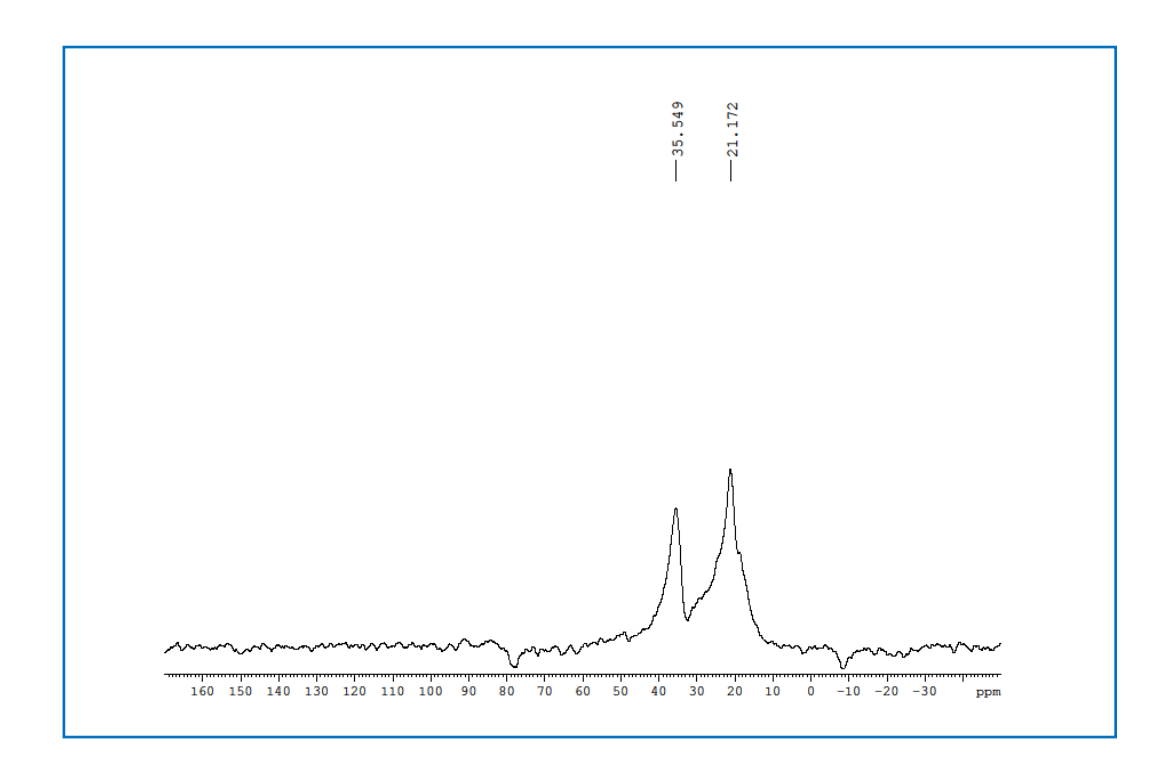


Figure 2.14: Solid state ³¹P NMR spectrum of compound 2.1.

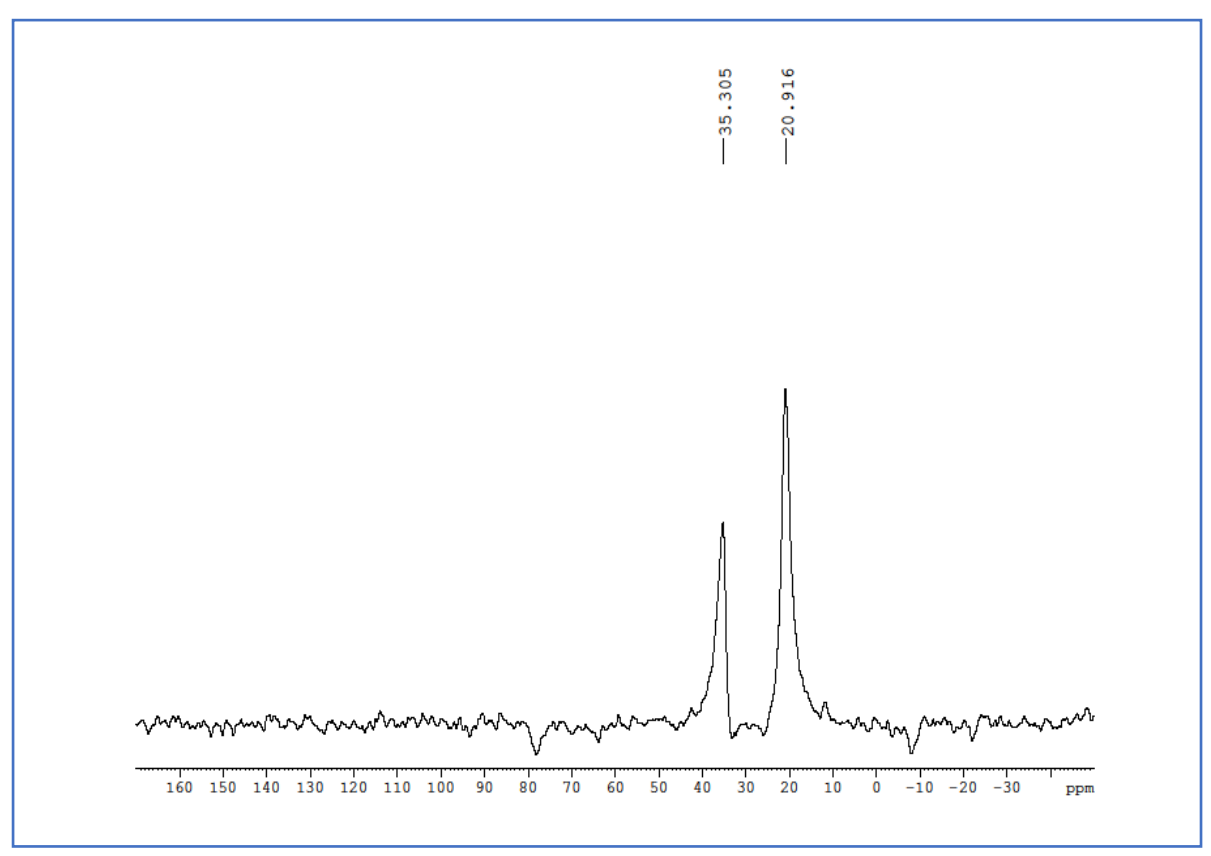


Figure 2.15: Solid state ³¹P NMR spectrum of compound 2.2.

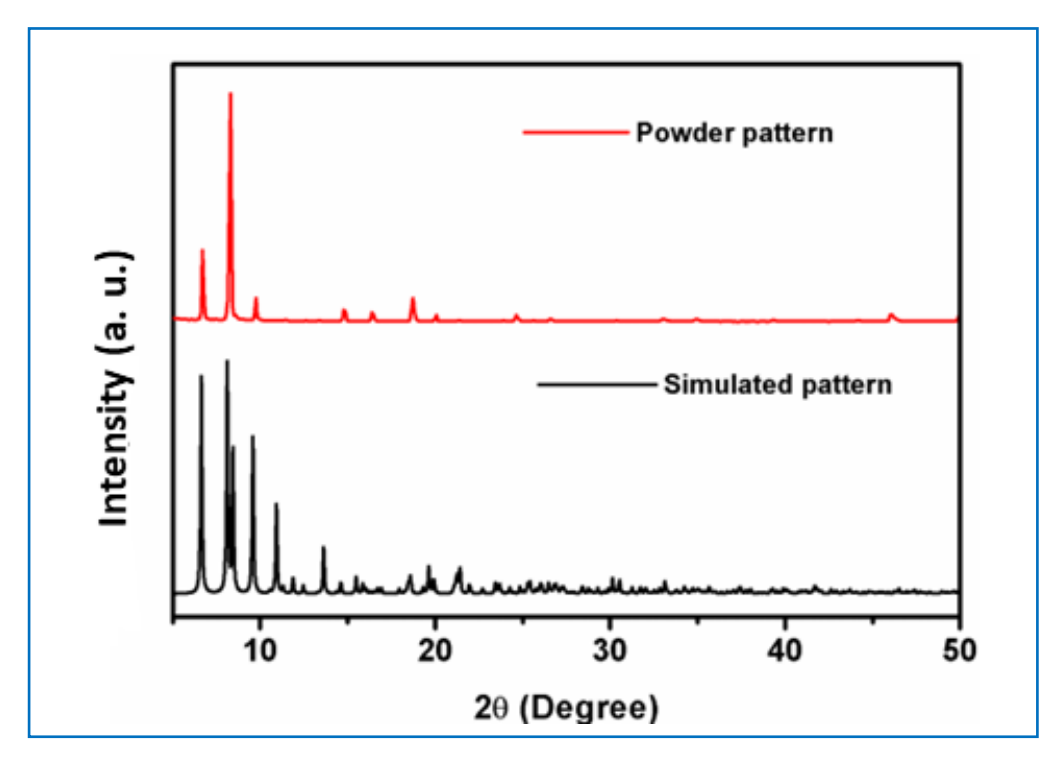


Figure 2.16: Powder X-ray diffraction pattern of a bulk sample of **2.1** compared to the simulated powder pattern extracted from single crystal diffraction data.

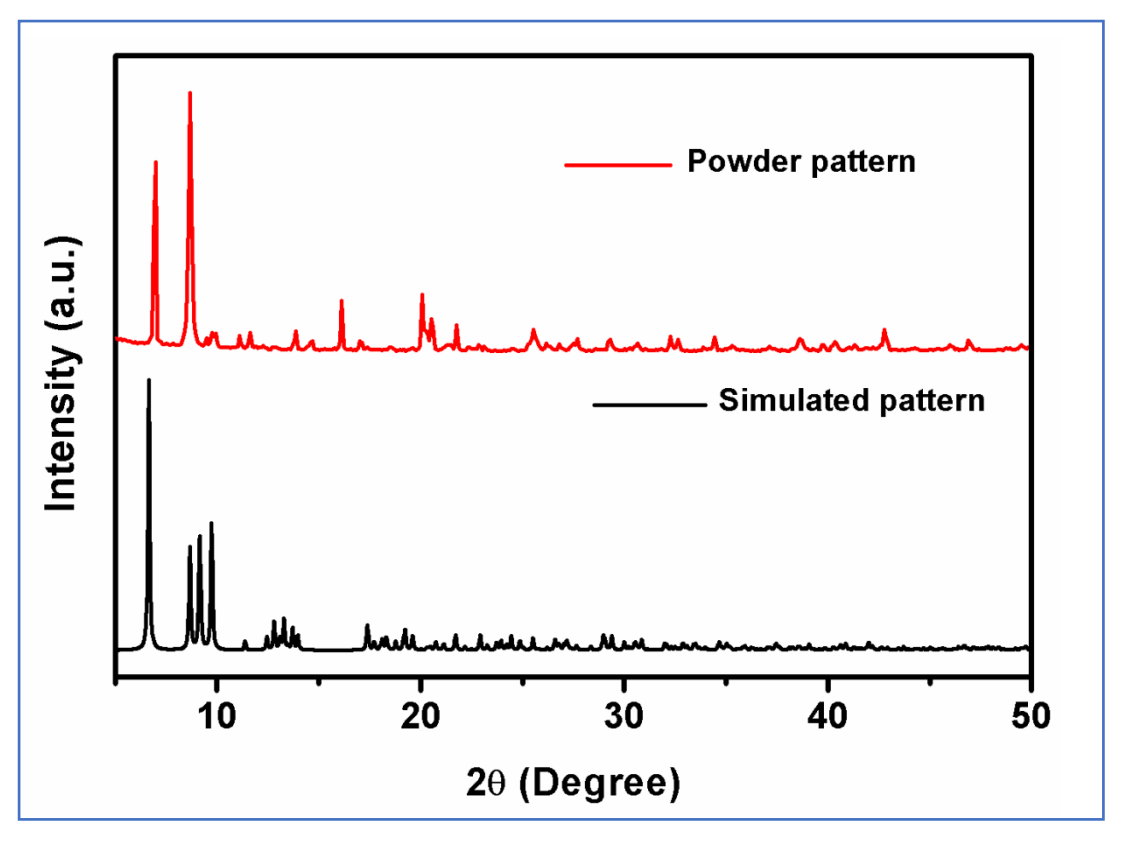


Figure 2.17: Powder X-ray diffraction pattern of a bulk sample of **2.2** compared to the simulated powder pattern extracted from single crystal diffraction data.

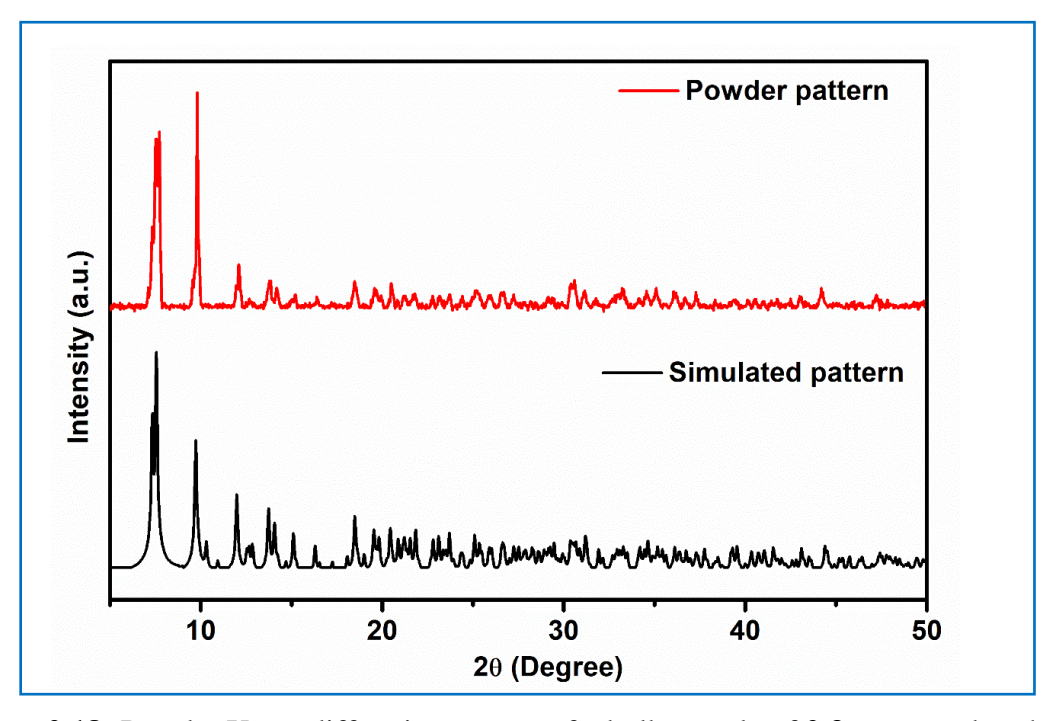


Figure 2.18: Powder X-ray diffraction pattern of a bulk sample of **2.3** compared to the simulated powder pattern extracted from single crystal diffraction data.

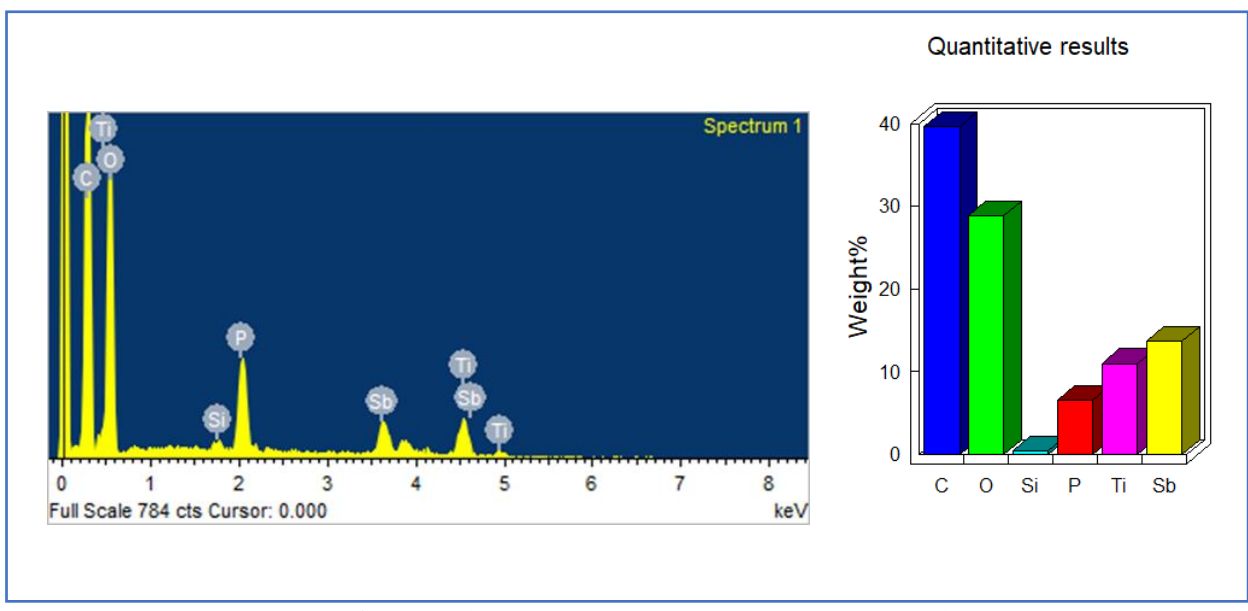


Figure 2.19: EDAX spectrum of compound 2.1.

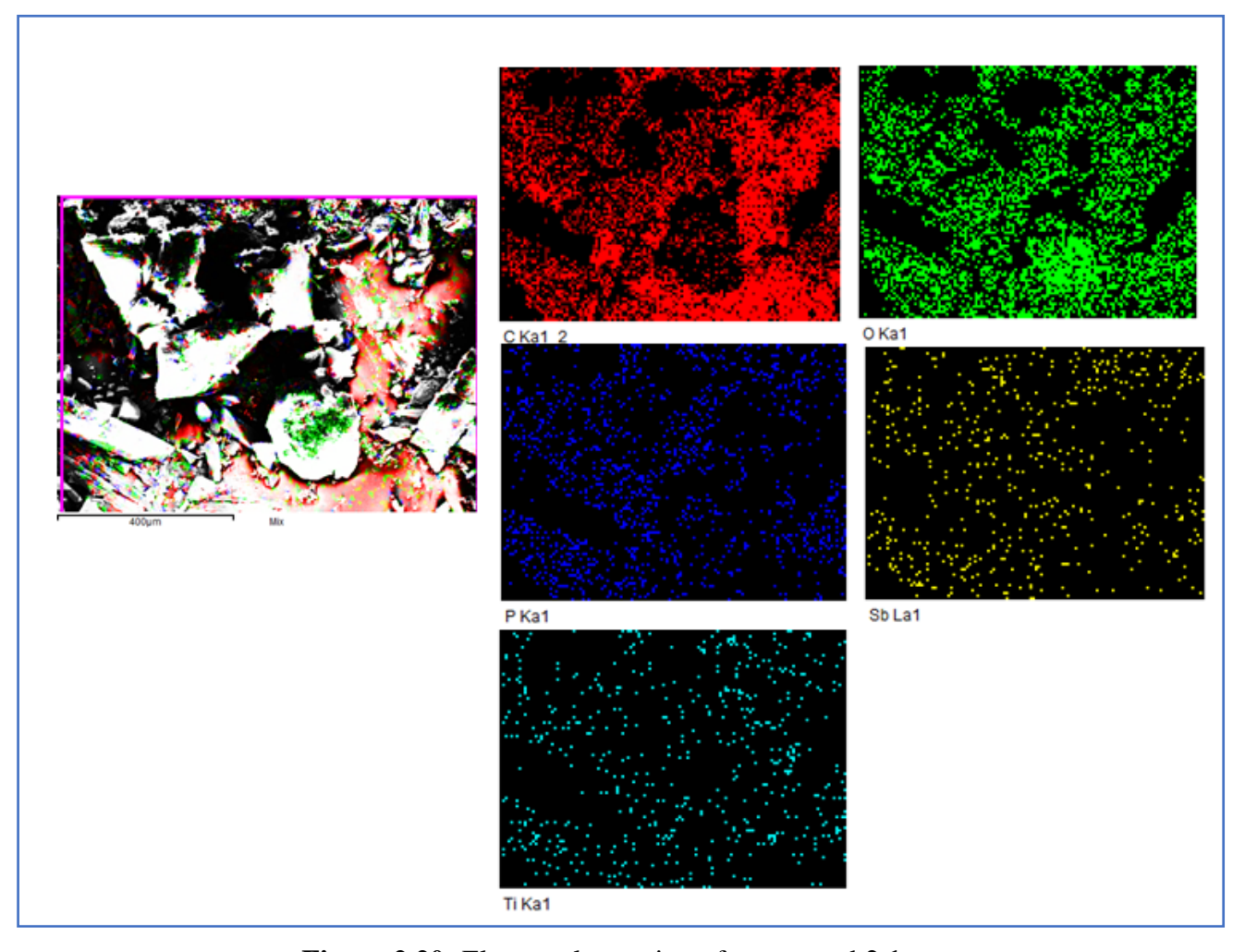


Figure 2.20: Elemental mapping of compound 2.1.

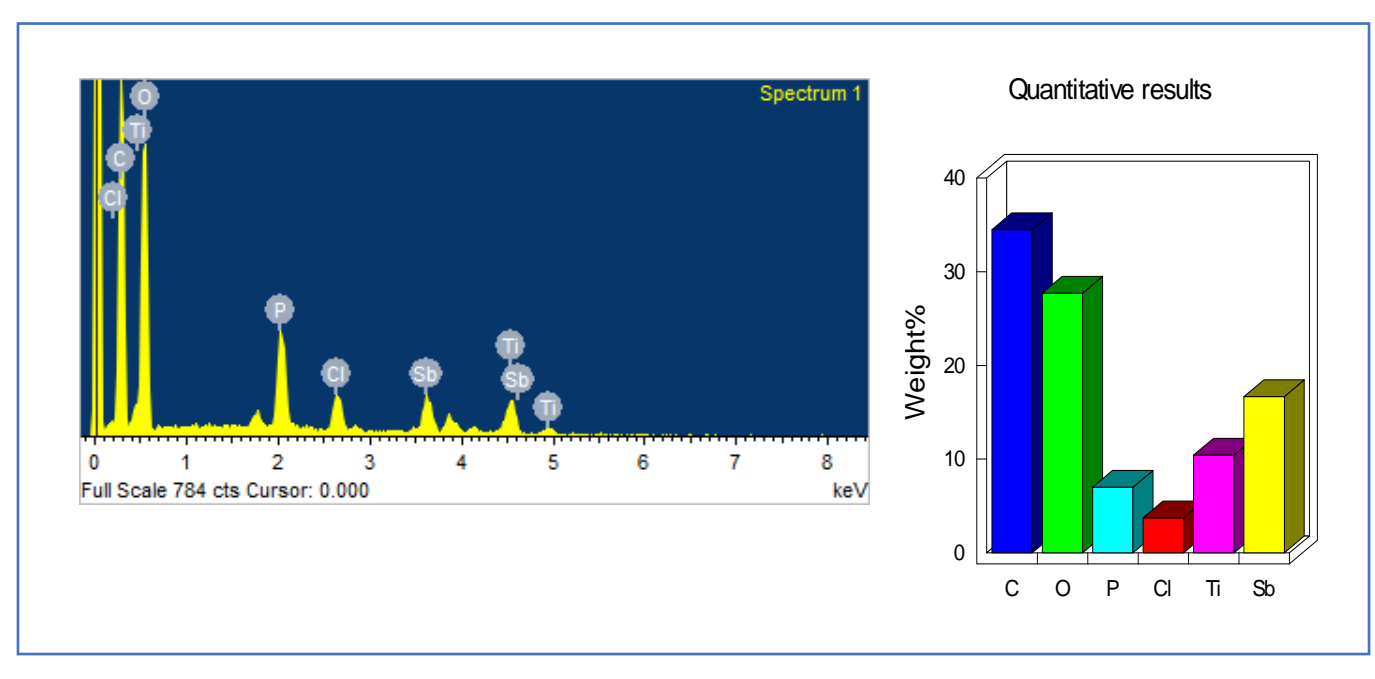


Figure 2.21: EDAX spectrum of compound 2.2.

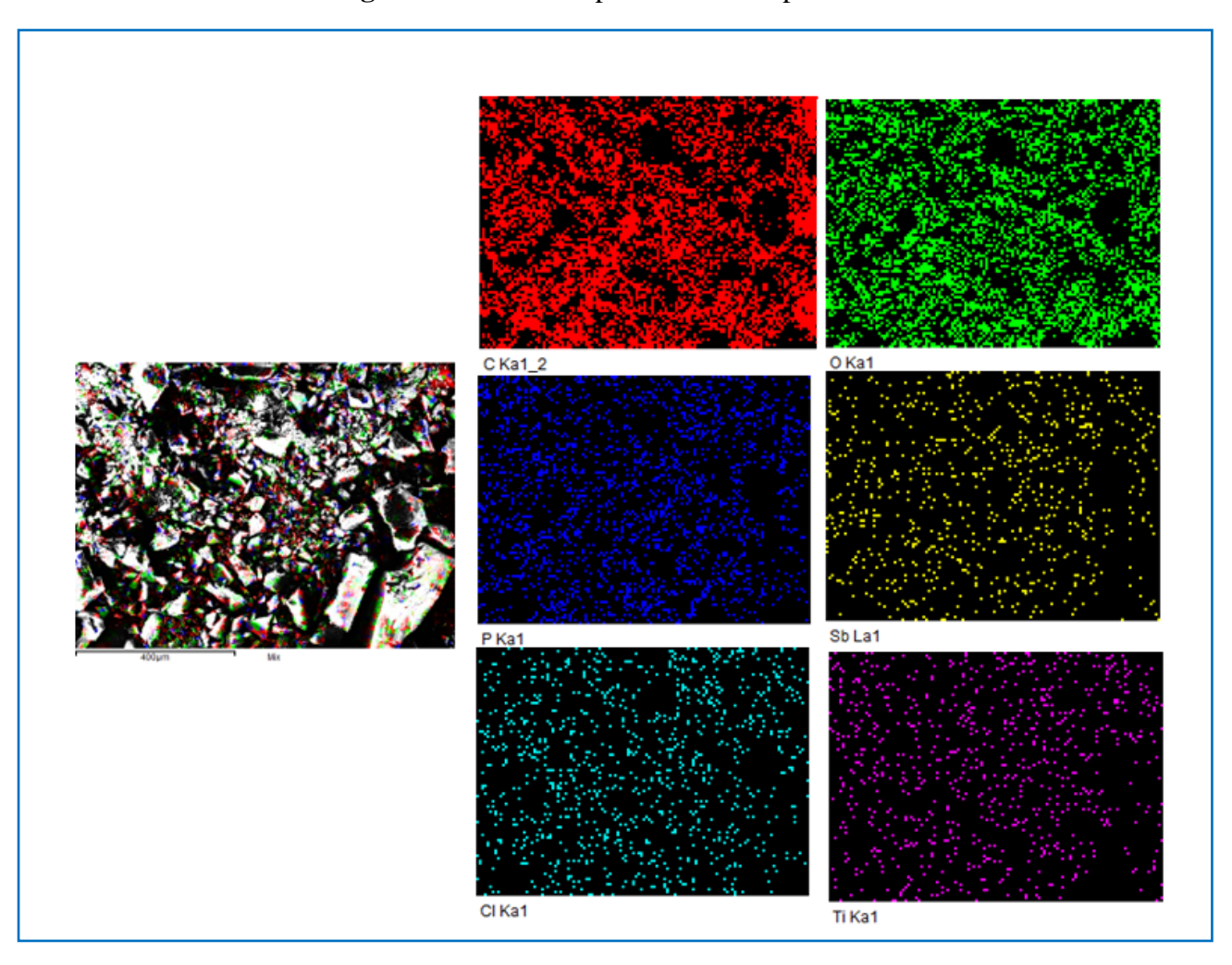


Figure 2.22: Elemental mapping of compound 2.2.

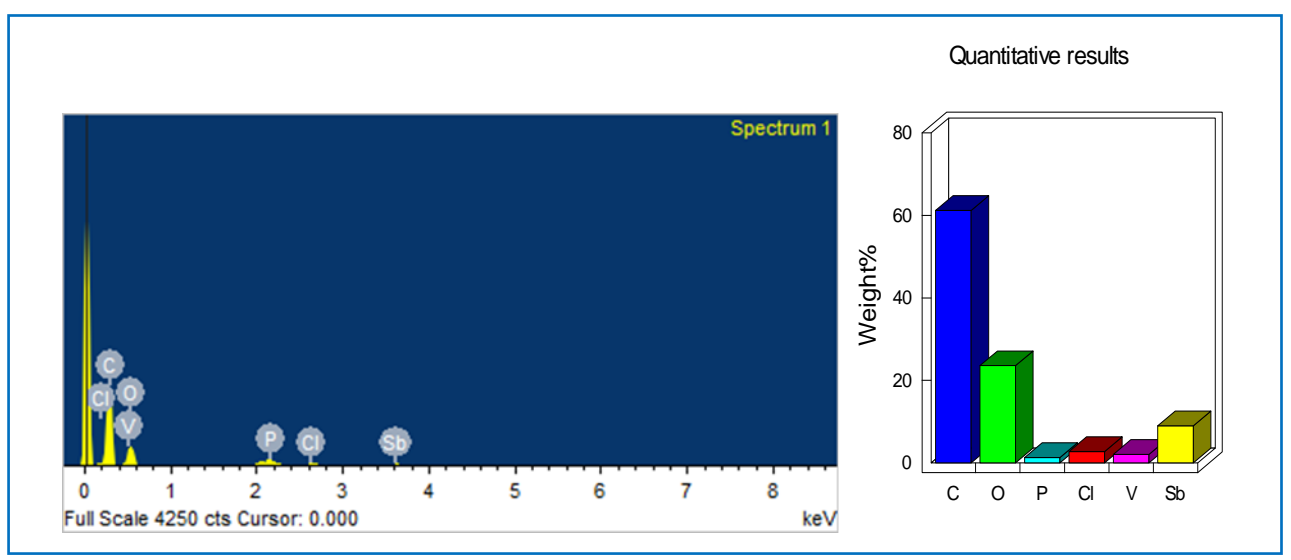


Figure 2.23: EDAX spectrum of compound 2.3.

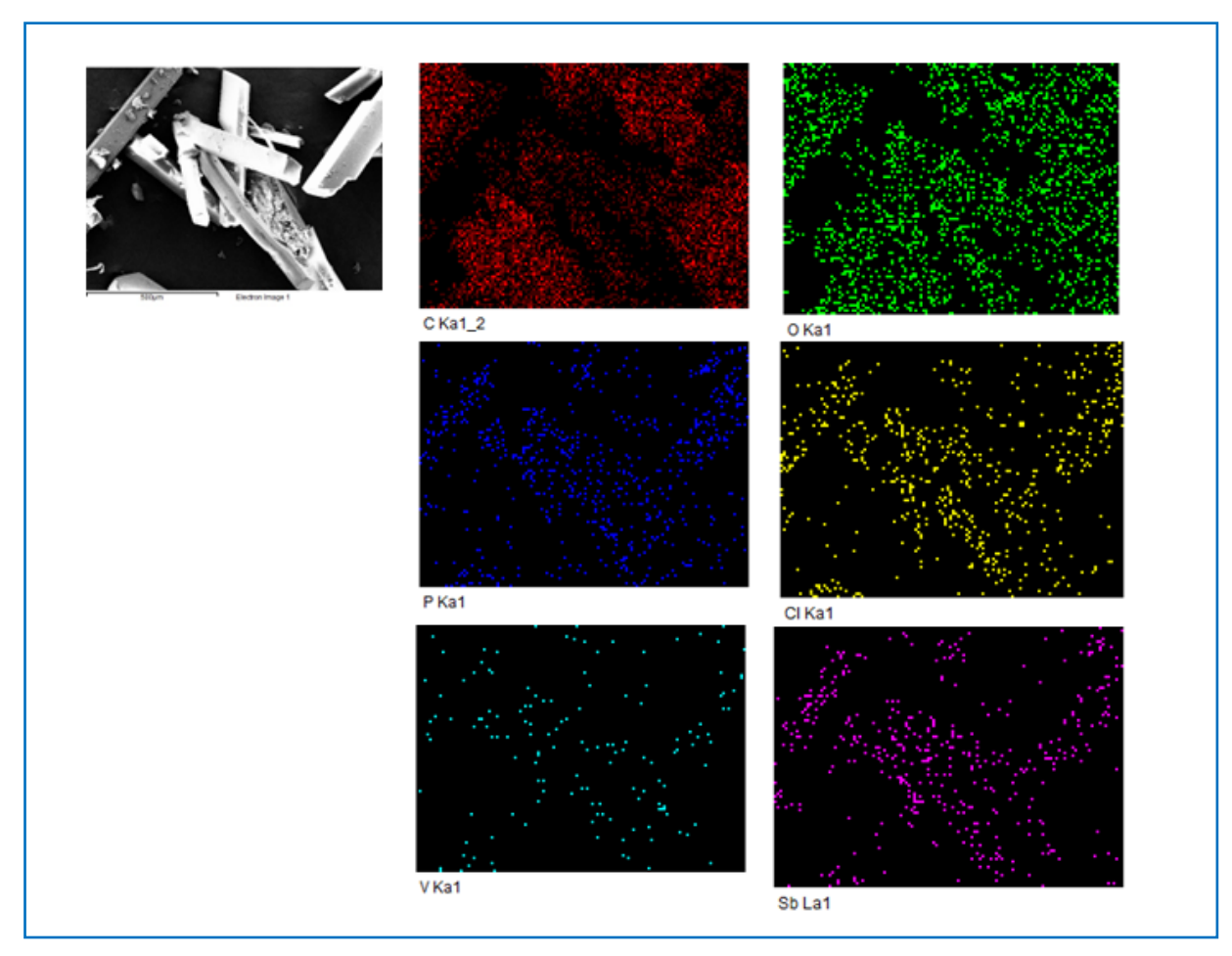


Figure 2.24: Elemental mapping of compound 2.3.

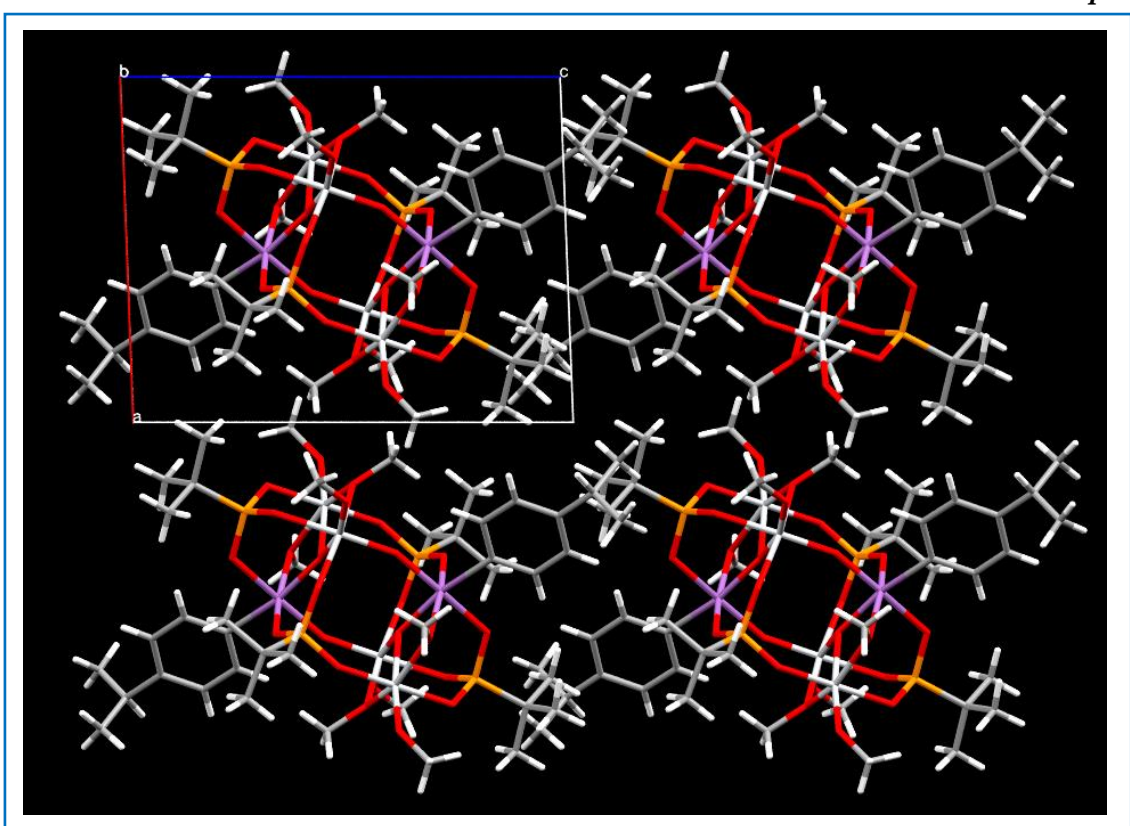


Figure 2.25: Packing diagram of compound 2.1 along the b-axis.

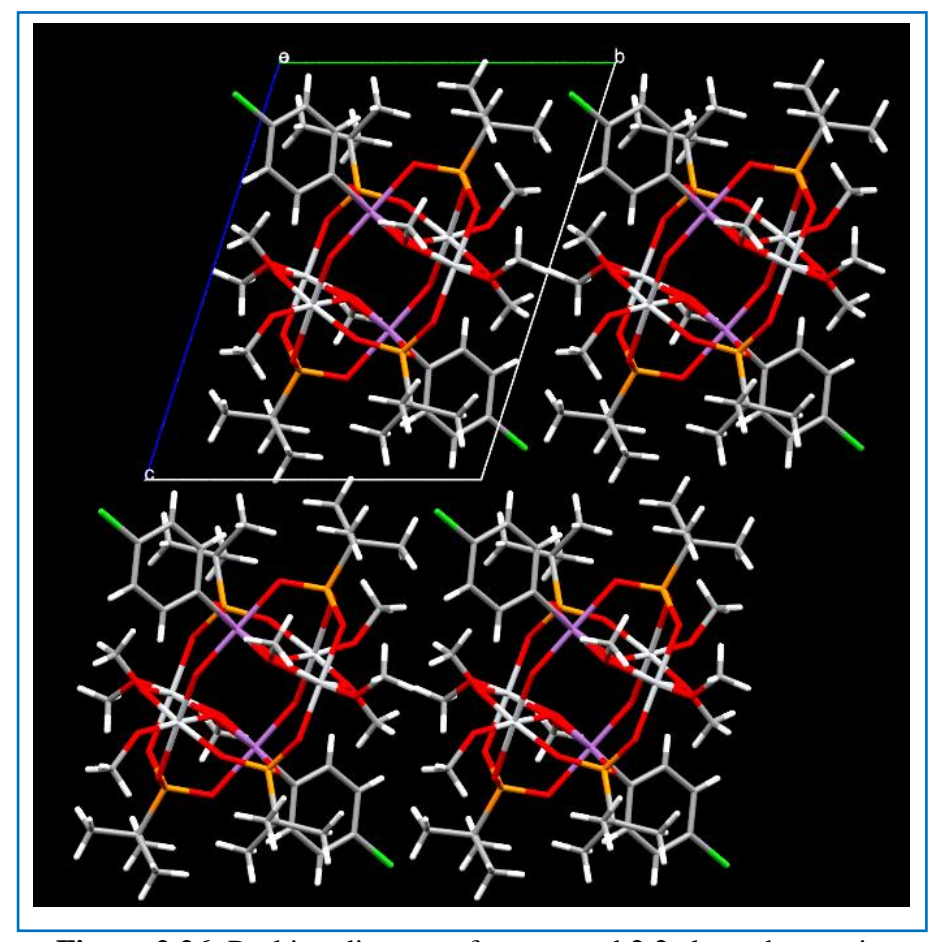


Figure 2.26: Packing diagram of compound 2.2 along the a-axis.

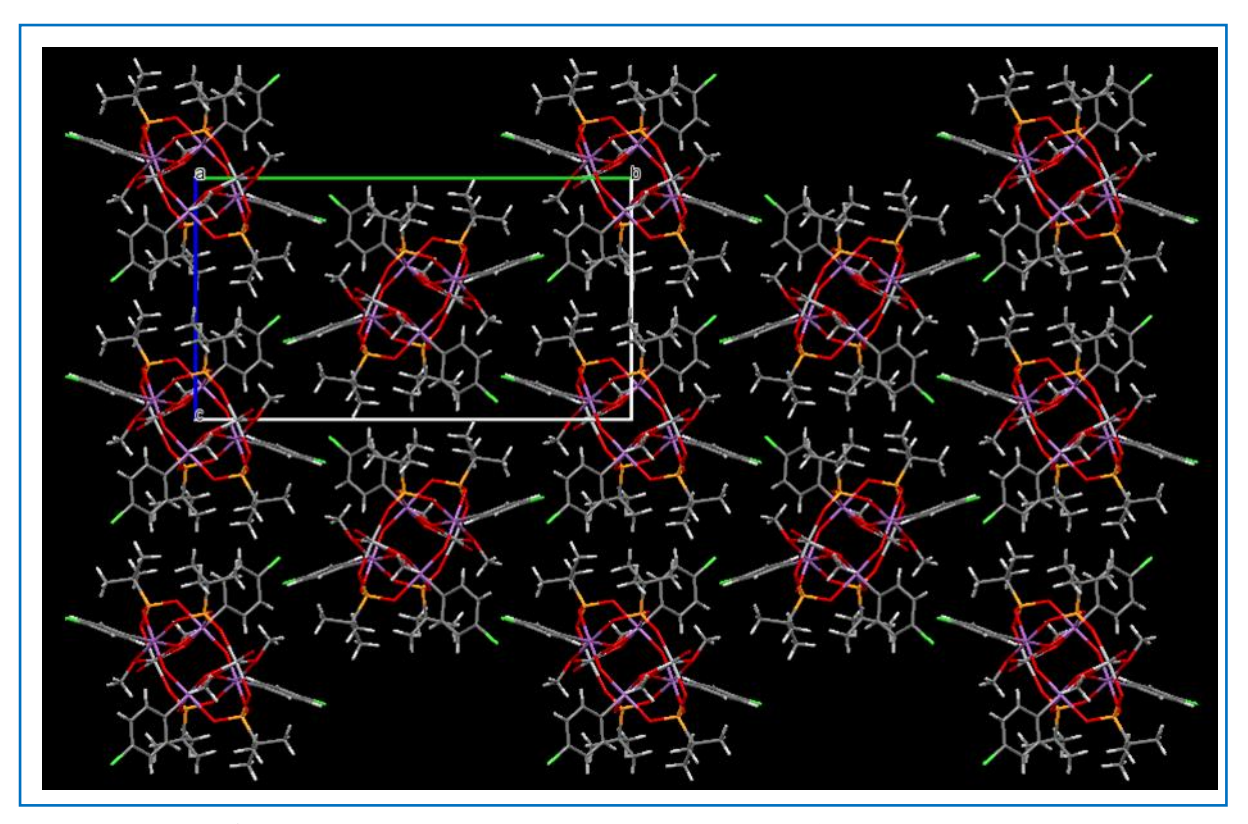


Figure 2.27: Packing diagram of compound 2.3 along the a-axis.

2.6 References:

- 1. Shao, T.; Fang, Y.; He, C.; Zhang, L.; Wang, K. *Inorg. Chem.* **2022**, *61*, 5184–5189.
- (a) Akkerman, Q. A.; D'Innocenzo, V.; Accornero, S.; Scarpellini, A.; Petrozza, A.; Prato, M.; Manna, L. J. Am. Chem. Soc. 2015, 137, 10276–10281. (b) Jang, D. M.; Park, K.; Kim, D. H.; Park, J.; Shojaei, F.; Kang, H. S.; Ahn, J. P.; Lee, J. W.; Song, J. K. Nano Lett. 2015, 15, 5191–5199. (c) Wu, H.; Erbing, A.; Johansson, M. B.; Wang, J.; Kamal, C.; Odelius, M.; Johansson, E. M. J. ChemSusChem 2021, 14, 4507–4515.
- Lin, C. K.; Zhao, D.; Gao, W. Y.; Yang, Z.; Ye, J.; Xu, T.; Ge, Q.; Ma, S.; Liu, D. J. *Inorg. Chem.* 2012, 51, 9039–9044.
- (a) Fang, W. H.; Zhang, L. Zhang, J. Dalton Trans. 2017, 46, 803-807. (b) Zhu, J.; Li, P. Z.; Guo, W.; Zhao. Y.; Zou, R. Coordination Chemistry Reviews. 2018, 359, 80–101. (c) Nguyen, H. L.; Thanh T. Vu, T. T.; Le, D.; Doan, T. L. H.; Nguyen, V. Q.; Phan, N. T. S. ACS Catal. 2017, 7, 338–342. (d) Fan, Y.; Li, H. M.; Duan, R. H.; Lu, H. T.; Cao, J. T.; Zou, G. D.; Jing, O. S. Inorg. Chem. 2017, 56, 12775–12782. (e) Fan, Y.; Cui, Y.; Zou, G. D.; Duan, R. H.; Zhang, X.; Dong, Y. X.; Lv, H. T.; Cao, J. T.; Jinga, O. S. Dalton Trans. 2017, 46, 8057–8064. (f) Wu, L.; Yu, J. C.; Zhang, L.; Wang, X.; Ho, W. Journal of Solid State Chemistry 2004, 177, 2584–2590.
- Saouma, C. T.; Tsou, C. C.; Richard, S.; Ameloot, R.; Vermoortele, F.; Smolders, S.; Bueken, B.; Dipasquale, A. G.; Kaminsky, W.; Valdez, C. N.; De Vos, D. E.; Mayer, J. M. Chem. Sci. 2019, 10, 1322-1331.
- Liu, G.; Yang, X.; Bonnefont, A.; Lv, Y.; Chen, J.; Dan, W.; Chen, Z.; Ruhlmann,
 L.; Wright, D. S.; Zhang, C. *Chem. Commun.* 2018, 54, 14132-14135.
- 7. Liu, J. X.; Gao, M. Y.; Fang, W.H.; Zhang, L.; Zhang, J. *Angew. Chem. Int. Ed.* **2016**, 55, 5160 –5165.
- (a) Cao, S.; Chen, Y.; Liu, X.; Zhou, J.; Liu, J. *Inorg. Chem. Commun.* 2021, 133, 108862. (b) Petel, B. E.; Meyer, R. L.; Maiola, M. L.; Brennessel, W. W.; Müller, A. M.; Matson, E. M. J. Am. Chem. Soc. 2020, 142, 1049–1056. (c) El-Roz, M.; Lakiss, L.; Telegeiev, I.; Lebedev, O. I.; Bazin, P.; Vicente, A.; Fernandez, C.; Valtchev, V. ACS Appl. Mater. Interfaces 2017, 9, 17846–17855. (d) Feng, Y.; Li, Z.; Li, S.; Yang, M.; Ma, R.; Wang, J. J. Energy Chem. 2022, 66, 493–501. (e) Fei,

- F.; An, H.; Meng, C.; Wang, L.; Wang, H. *RSC Adv.* **2015**, *5*, 18796–18805. (f) Chakraborty, S.; Petel, B. E.; Schreiber, E.; Matson, E. M. *Nanoscale Adv.* **2021**, *3*, 1293–1318. (g) Choi, A. Y.; Han, C. H. *J. Nanosci. Nanotechnol.* **2014**, *14*, 8070–8073. (h) Hadi, E. H.; Salih, F. M. H.; Slewa, M. Y.; Bader, B. A.; Habubi, N. F. *J. Green Eng.* **2020**, *10*, 7195–7207. (i) Ranjan, P.; Chakraborty, T. *Key Eng. Mater.* **2018**, *777*, 183–189. (j) Omri, I.; Mhiri, T.; Graia, M. *J. Clust. Sci.* **2015**, *26*, 1267–1278.
- (a) Sharma, D.; Jha, R. J. Alloys Compd. 2017, 698, 532–538. (b) Liu, Y.; Tian, Y.; Wei, F. X.; Ping, M. S. C.; Huang, C.; Boey, F.; Kloc, C.; Chen, L.; Wu, T.; Zhang, Q. Inorg. Chem. Commun. 2011, 14, 884–888. (c) Janek, J.; Martin, M.; Becker, K. D. Phys. Chem. Chem. Phys. 2009, 11, 3010. (d) Suzuki, V. Y.; Amorin, L. H. C.; Lima, N. M.; Machado, E. G.; Carvalho, P. E.; Castro, S. B. R.; Alves, C. C. S.; Carli, A. P.; Li, M. S.; Longo, E.; La Porta, F. A. J. Mater. Chem. C 2019, 7, 8216–8225. (e) Irfan, S.; Shen, Y.; Rizwan, S.; Wang, H. C.; Khan, S. B.; Nan, C. W.; Xie, R. J. J. Am. Ceram. Soc. 2017, 100, 31–40.
- 10. (a) Sumithra; Jaya, N. V. *Mater. Res. Innov.* **2019**, *23*, 375–384. (b) El Sayed, A. M.; Taha, S.; Shaban, M.; Said, G. Superlattices Microstruct. 2016, 95, 1–13. (c) Bark, C. W. Met. Mater. Int. 2013, 19, 1361–1364. (d) Mimouni, R.; Boubaker, K.; Amlouk, M. J. Alloys Compd. 2015, 624, 189–194. (e) Tatarchuk, T. R.; Paliychuk, N. D.; Bououdina, M.; Al-Najar, B.; Pacia, M.; Macyk, W.; Shyichuk, A. J. Alloys Compd. 2018, 731, 1256–1266. (f) Misra, K. P.; Jain, S.; Agarwala, A.; Halder, N.; Chattopadhyay, S. Semiconductors 2020, 54, 311–316. (g) Zarandi, M. B.; Bioki, H. A. Islam. Azad Univ. J. Optoelectron. Nanostructures Autumn 2017, 2. (h) Wani, W.; Kundu, S.; Ramaswamy, K.; Venkataraman, H. Mater. Sci. Eng. B Solid-State Mater. Adv. Technol. 2021, 271. (i) Chanda, A.; Gupta, S.; Vasundhara, M.; Joshi, S. R.; Mutta, G. R.; Singh, J. RSC Adv. 2017, 7, 50527–50536. (j) Ambika, S.; Gopinath, S.; Saravanan, K.; Sivakumar, K.; Ragupathi, C.; Sukantha, T. A. Energy Reports 2019, 5, 305-309. (k) Bayram, O.; İgman, E.; Guney, H.; Simsek, O. Superlattices Microstruct. 2019, 128, 212–220. (1) Asl, H. Z.; Rozati, S. M. J. Electron. Mater. 2020, 49, 1534–1540. (m) Madkhli, A. Y.; Shirbeeny, W. Phys. B Condens. Matter 2020, 597. (n) Suksomboon, M.; Kongsawatvoragul, K.; Duangdangchote, S.; Sawangphruk, M. ACS Omega 2021, 6, 20804–20811. (o) Wani, W. A.; Kundu, S.; Ramaswamy, K.; Venkataraman, H. J. Alloys Compd. **2020,** 846.

- 11. Das, S. C.; Green, R. J.; Podder, J.; Regier, T. Z.; Chang, G. S.; Moewes, A. J. *Phys. Chem. C* **2013**, *117*, 12745–12753.
- 12. Karmakar, A.; Dodd, M. S.; Agnihotri, S.; Ravera, E.; Michaelis, V. K. *Chem. Mater.* **2018**, *30*, 8280–8290.
- (a) Ali, S.; Baskar, V.; Muryn, C. A.; Winpenny, R. E. P. *Chem. Commun.* 2008, 4, 6375–6377.
 (b) Ali, S.; Muryn, C. A.; Tuna, F.; Winpenny, R. E. P. *Dalton Trans.* 2010, 124–131.
 (c) Ali, S.; Muryn, C. A.; Winpenny, R. E. P. *Dalton Trans.* 2010, 3432, 9588–9597.
- 14. (a) Doak, G. O.; Steinman, H. G. J. Am. Chem. Soc. **1946**, 68, 1987–1989. (b) Liu, Z.; Ozawa, Y.; Yagasaki, A. Bull. Chem. Soc. Jpn. **2014**, 87, 1245–1251.
- 15. Crofts, P. C.; Kosolapoff, G. M. J. Am. Chem. Soc. 1953, 75, 3379–3383.
- 16. Ugandhar, U.; Baskar, V. Dalton Trans. 2016, 45, 6269–6274.
- (a) Dolomanov, O. V.; Bourhis, L. J.; Gildea, R. J.; Howard, J. A. K.; Puschmann, H. J. Appl. Crystallogr. 2009, 42, 339–341. (b) Sheldrick, G. M. Acta Crystallogr. Sect. C Struct. Chem. 2015, 71, 3–8. (c) Sheldrick, G. M. Acta Crystallogr. Sect. A Found. Crystallogr. 2015, 71, 3–8.
- 18. Coxall, R. A.; Harris, S. G.; Henderson, D. K.; Parsons, S.; Tasker, P. A.; Winpenny, R. E. P. *J. Chem. Soc. Dalton Trans.* **2000**, 2349–2356.
- (a) Aronica, C.; Chastanet, G.; Zueva, E.; Borshch, S. A.; Juan, J. M. C.; Luneau, D. J. Am. Chem. Soc. 2008, 130, 2365–2371. (b) Thorp, H. H. Inorg. Chem. 1992, 31, 1585–1588. (c) Brese, N. E.; O'Keeffe, M. Acta Crystallogr. Sect. B 1991, 47, 192–197. (d) Altermatt, D.; Brown, I. D.. Acta Crystallogr. Sect. B 1985, 41, 240–244.
- 20. Makuła, P.; Pacia, M.; Macyk W. J. Phys. Chem. Lett. **2018**, 9, 6814–6817.
- 21. (a) Shockley, W.; Queisser, H. J. *J. Appl. Phys.* **1961**, *32*, 510–519. (b) Raghunathan, R.; Johlin, E.; Grossman, J. C. *Nano Lett.* **2014**, *14*, 4943–4950.
- 22. Blöchl, P. E. Phys. Rev. B. 1994, 50, 17953.
- (a) Hohenberg, P.; Kohn, W. *Phys. Rev.* **1964**, *136*, B864. (b) Kohn, W.; Sham, L.
 J. *Phys. Rev.* **1965**, *140*, A1133.
- 24. Kresse, G.; Furthmüller, J. *Phys. Rev. B.* **1996**, *54*, 11169.
- 25. Perdew, J. P.; Burke, K.; Ernzerhof, M., Phys. Rev. Lett. 1996, 77, 3865.
- 26. Monkhorst, H. J.; Pack, J. D. Phys. Rev. B. 1976, 13, 5188.

Tunable bandgap....

- 27. (a) Kresse, G.; Hafner, J. *Phys. Rev. B Condens. Matter Mater. Phys.* **1993**, 48, 13115–13118. (b) Kresse, G.; Hafner, J. *Phys. Rev. B Condens. Matter Mater. Phys.* **1994**, 49, 14251-14269.
- 28. (a) Raghunathan, R.; Ramasesha, S.; Mathonière, C.; Marvaud, V. *Phys. Rev. B Condens. Matter Mater. Phys.* **2006**, *73*, 1–7. (b) Raghunathan, R.; Sutter, J. P.; Ducasse, L.; Desplanches, C.; Ramasesha, S. *Phys. Rev. B Condens. Matter Mater. Phys.* **2006**, *73*, 1–8. (c) Barman, S. R.; Sarma, D. D. *Phys. Rev. B Condens. Matter Mater. Phys.* **1994**, *49*, 3–6.
- 29. Jana, A.; Sahoo, S.; Chowdhury, S.; Mandal, A. K.; Bimli, S.; Devan, R. S.; Choudhary, R. J.; Phase, D. M.; Raychaudhuri, A. K. *Phys. Rev. B Condens. Matter Mater. Phys.* **2022**, *106*, 205123.

Discrete Metal Oxo Clusters Based on $\mathbf{Z}\mathbf{n}^{\mathbf{H}}$ and $\mathbf{S}\mathbf{b}^{\mathbf{H}\mathbf{I}/\mathbf{V}}$ Ions Exhibiting Interesting Antibacterial and Antioxidant Properties

CHAPTER

3

Abstract: The reactions of [Zn₃Cl₂(3,5-Me₂PzH)₄(t-BuPO₃)₂] with organostibonic acid in varying reaction conditions have been investigated. Single crystal X-ray diffraction studies reveal the formation of $[Zn_2(p-ClC_6H_4Sb)_2(\mu_3-O)(\mu_2-OCH_3)_2(t-BuPO_3)_3(py)_2]$ (3.1), $[Zn_2(p-ClC_6H_4Sb^V)_4(Sb^{III})_2(\mu_2-O)_6(\mu_3-O)_2(t-BuPO_3H)_4(t-BuPO_3)_2(py)_2Cl_2]$ (3.2)and $[Zn_2(RSb)_4(\mu_3-O)_2(\mu_2-O)_2(\mu_2-OCH_3)_4(t-BuPO_3)_4(py)_2]$, where $R = p-ClC_6H_4$ (3.3) and $R = p-ClC_6H_4$ iPrC₆H₄ (3.4) respectively. Interestingly, in the synthesis of 2, complete dearylation of organoantimony moieties followed by C-F bond formation, a reduction from Sb(V) to Sb(III), and Sb---Cl weak intermolecular interactions have been observed. ESI-MS studies suggested that clusters 3.1-3.4 maintained their structural stability in the solution as well. Solution-state NMR studies (¹H, ³¹P and ¹³C) support well with observed solid-state structures. Compounds 3.1-3.4 were tested for antibacterial activity using a microdilution assay. 3.1 and 3.4 showed the best activity with lower MIC values (0.78 - 6.25 μ g/mL) against all the tested pathogens. The total antioxidant activity of **3.1-3.4** was evaluated through the phosphomolybdenum assay, which showed a total antioxidant activity ranging from 28.96 to 86.46 mg AAE/g compound with the ascorbic acid standard.

3.1 Introduction:

Organostibonic acids have been shown to behave as versatile building blocks in synthesizing discrete molecular architectures.¹ Recently, biological studies on organostibonic acids have shown that they can act as potent anticancer drugs and antimicrobial agents.² Rare molecular architectures like triangles, cubes and adamantane-type motifs have been stabilized on reacting stibonic acids with various protic ligands.^{1b-f} Interestingly, the solid-state structure of organostibonic acids that have been retained in the solution state. It has been validated by ESI-MS data.³ From our group and others, it has been shown that the discrete stibonate-phosphonate cluster can act as a versatile pro-ligand and has been used in assembling novel molecular frameworks incorporating transition metal ions.⁴ Interestingly, few of the synthesized stibonate-phosphonate clusters and free organostibonic acids have been investigated for their biological activity and have been shown to act as potent anticancer agents.^{2a}

In this article, to circumvent the solubility problems associated with stibonic acids, preformed Zn₃-based triangles stabilized by phosphonates as ligand systems have been used as a metal source. The idea is two-fold. First, metal triangles as nodes have not been investigated for their reactivity with stibonic acids. Hence using M₃-oxo triangles could tether to organostibonates, increasing the overall solubility of the clusters formed as well as resulting in the formation of novel clusters. Furthermore, the depolymerization of organostibonic acids by the phosphonate ligands could lead to the isolation of discrete soluble metal oxo clusters. In supramolecular chemistry, preformed clusters have been used as nodes for building fascinating MOFs that show interesting physical properties.⁵ Similarly, preformed triangular clusters of Mn and Co have been used by Winpenny et al. to synthesize large metal aggregates, some of which had shown fascinating magnetic properties. 6 In this article, our efforts in reacting organostibonic acids with a preformed Zn₃ triangle have led to the isolation of interesting and rare molecular clusters based on organostibonate moieties. Details of the investigations are reported herein. Organostibonic acids and their derivatives have been investigated for their biological properties. Organostibonic acids have exhibited potent anti-HIV activity; these compounds block the HIV-1 strains by disrupting the gp120 and CD4 contacts. Sodium pmelaminylphenylstibonate exerts a prominent prophylactic effect in trypanosomiasis.⁸ C. Vinson et al. reported that arylstibonic acid derivatives are promising systems for inhibiting the B-ZIP DNA binding and could be helpful as anticancer agents. Similarly, arystibonic acids act as potent inhibitors of apurinic/apyrimidinic endonuclease 1, 10 human topoisomerase IB (hTopo)¹¹ and protein tyrosine phosphatases¹² which have been used in the development of chemotherapeutic agents. Organostibonic acid acts as an inhibitor of *Yersinia pestis* DNA adenine methyltransferase and hence is used as an antimicrobial agent.^{2b} U. Kortz *et al.* reported the antimicrobial activity of organoantimony containing POMs.¹³

From the reported biological studies, little is known about organostibonic acids and their clusters' ability to exert antibacterial and antioxidant activities. Hence, investigations on these properties (antibacterial and antioxidant) have been carried out in detail. Furthermore, it is well established that zinc plays an essential role in the metabolism and expression of genetic messages. Zinc motifs have been implicated in phospholipase C, P1 nuclease and aminopeptidase¹⁴ hence zinc-based clusters have been chosen as another starting precursor. In this chapter, the reactivity of the trinuclear zinc cluster with organostibonic acid in varied reaction conditions has been investigated. SC-XRD studies revealed the formation of a novel Zn₂Sb₂, mixed valent Zn₂Sb₄VSb₂III and Zn₂Sb₄-based oxo clusters. For all the Zn/Sb-based metal oxo clusters, biological studies like antibacterial and antioxidant studies were performed.

The synthesized mixed 3*d*-main group-based metal clusters were screened for different bacterial reference pathogenic strains. The details of their synthesis, *in-silico* studies and biological activities are discussed below.

3.2 Experimental Section:

3.2.1 General Information:

p-Chlorophenylstibonic acid, *p*-isopropylphenylstibonic acid¹⁵ and *t*-butylphosphonicacid¹⁶ were synthesized according to literature reports. Solvents and common reagents were purchased from commercial sources. [Zn₃Cl₂(3,5-Me₂PzH)₄(t-BuPO₃)₂] was synthesized by a reaction of ZnCl₂ with *t*-butylphosphonic acid and 3,5- dimethyl pyrazole in the presence of triethylamine as a base.¹⁷ All the compounds used were dried under a high vacuum for half an hour before being subjected to spectroscopic and analytical techniques.

3.2.2 Instrumentation:

Infrared spectra were recorded using a Nicolet iS5 FTIR spectrometer. Elemental analysis was performed with a Flash EA Series 1112 CHNS analyzer. ESI-MS spectra were recorded using Bruker MaXis HRMS (ESI-TOF analyzer) equipment. NMR spectra were recorded on Bruker Avance-400 and 500 MHz FT NMR spectrometers at room temperature. Single crystal X-ray data collection for compounds **3.1**, **3.3** and **3.4** was carried out at 100 K with an XtaLAB Synergy, a single source at offset/far, HyPix3000 diffractometer, and a Rigaku Oxford HyPix3000 CCD plate detector system [λ (Mo K α) = 0.71073 Å] with a mirror monochromator and **3.2** was carried out at 100 K with a Bruker Smart Apex CCD area detector system [λ (Mo-

Kα) = 0.71073 Å] with a graphite monochromator. The data were reduced using CrysAlisPro 1.171.40.35a (Rigaku OD, 2018) for **3.1**, **3.3-3.4** and APEX-2 for **3.2**. The structures were solved using SHELXT and refined using SHELXL-2018/3 in Olex2 1.3-ac4 software. All non-hydrogen atoms were refined anisotropically. In **3.2**, the disorder containing pyridine attached to zinc was constrained using EADP, μ₂-oxide and chloride was restrained using DFIX instructions in SHELXL-2018/3. In the crystal structure of **3.2**, the voids contain disordered solvents. The OLEX2 Solvent Mask routine (similar to PLATON/SQUEEZE) was used to mask out the disordered electron density. The voids for **3.2** correspond to 1 CH₃OH per formula. Powder X-ray diffraction patterns were collected over the 2θ range of 5–80° at a scan rate of 3.9°/min. Energy-dispersive spectroscopy (EDS) and elemental mapping were studied using an Ultra 55 Carl Zeiss instrument. For elemental analysis, the ICP-OES Varian 720-ES instrument was used.TGA was recorded for compounds **3.1-3.4** with PerkinElmer STA 8000 thermogravimetric analyzer under a nitrogen gas flow rate of 20 ml/min and heating rate of 10 °C/min. Graphics of the crystal structures have been performed with Diamond (version 3).

3.2.3 General synthetic procedures:

The general synthetic methodology adopted for **3.1** is that the corresponding trinuclear zinc metal phosphonate and *p*-chlorophenylstibonic acid were taken in a 1:2 molar ratio in 15 mL of methanol in 23 mL of Teflon-lined stainless-steel autoclave and followed by dropwise addition of excess pyridine. The resultant mixture was stirred for 2 h. The bomb was sealed properly and the mixture was heated at 100 °C for 12 h and then cooled slowly to room temperature for 48 h. The methanol solution was filtered and kept for slow evaporation. X-ray quality single crystals were obtained within two days.

Compound 3.1: $[Zn_3Cl_2(3,5-Me_2PzH)_4(t-BuPO_3)_2]$ 0.054 (0.05)mmol). g, pchlorophenylstibonic acid (0.046 g, 0.106 mmol) and pyridine (1 mL). Colorless block-shaped crystals formed upon slow evaporation of methanol solution. Yield: 0.028 g (42 %). Anal. Calcd (%) for $C_{36}H_{51}Cl_2N_2O_{13}P_3Sb_2Zn_2$ (1253.8644): C, 34.37; H, 4.09; N, 2.23. Found: C, 33.92; H, 3.93; N, 2.15. ESI-MS: 1253.8334 for [M]⁺. ¹H NMR (500 MHz, CDCl₃+DMSO- d_6): $\delta =$ 8.61 (br, 2H), 7.97 (s, br, 1H), 7.83 (d, C36 = 8.5 Hz, 4H), 7.50 (d, J = 8 Hz, 4H), 7.39 (br, 2H), 3.28 (s, 6H), 1.21 (d, J = 15 Hz, 18H), 1.01 (d, J = 16.5 Hz, 9H) ppm. ¹³C NMR (125 MHz, CDCl₃+DMSO- d_6): $\delta = 149.67, 134.98, 134.28, 134.01, 129.71, 128.92, 124.23, 52.08, 49.25,$ 25.64 ppm. ³¹P NMR (202 MHz, CDCl₃+DMSO-d₆): $\delta = 33.21$, 32.72 ppm. IR (cm⁻¹): 2959 (m), 2178 (m), 1975 (m), 1606 (m), 1476 (s), 1451 (s), 1383 (m), 1148 (s), 1101 (s), 1072 (m), 1039 (s),966 (wide), 915 (wide), 833 (m), 815 (m), 759 (s), 726 (s), 665 (s), 621 (s).

The general synthetic methodology adopted for **3.2** is that the corresponding trinuclear zinc metal phosphonate and *p*-chlorophenylstibonic acid and potassium tetrafluoroborate were taken in a 1:3:2 molar ratio in 15 mL of methanol in 23 mL of Teflon-lined stainless-steel autoclave and followed by dropwise addition of excess pyridine. The resultant mixture was stirred for 2 h and the bomb was sealed properly. The above temperature conditions were maintained in this case as well. The methanol solution was filtered and kept for slow evaporation. X-ray-quality single crystals were obtained within a week.

3.2: $[Zn_3Cl_2(3,5-Me_2PzH)_4(t-BuPO_3)_2]$ Compound (0.05)g, 0.054 chlorophenylstibonic acid (0.046 g, 0.162 mmol), KBF₄ (0.013 g, 0.108 mmol) and pyridine (1 mL). Colorless block-shaped crystals formed upon slow evaporation of methanol solution. Yield: 0.02 g (15 %). Anal. Calcd (%) for C₅₉H₈₄Cl₆N₂O₂₇P₆Sb₆Zn₂ (2511.4582): C, 28.2; H, 3.37; N, 1.11. Found: C, 29.12; H, 3.55; N, 1.21. ESI-MS: 2511.4418 for [M]⁺. ¹H NMR (500 MHz, CDCl₃+CH₃OH- d_4): $\delta = 8.59$ (br, 2H), 7.87 (d, J = 8 Hz, 4H), 7.51 (s, br, 2H), 7.45 (br, 1H), 7.34 (d, J = 8.5 Hz, 4H), 1.18 (d, J = 16 Hz, 9H), 1.05 (d, J = 16.5 Hz, 18H) ppm. ¹³C NMR (125 MHz, CDCl₃+ CH₃OH- d_4): $\delta = 148.43, 145.80, 135.53, 133.54, 127.87, 123.74,$ 24.25 ppm. ³¹P NMR (202 MHz, CDCl₃+ CH₃OH- d_4): $\delta = 38.95$, 33.46 ppm. IR (cm⁻¹): 2966 (m), 2009 (m), 1957 (m), 1603 (m), 1477 (s), 1449 (m), 1382 (m), 1128 (s), 1087 (s), 1034 (s), 943 (wide), 815 (s), 727 (s), 701 (s), 616 (m).

The general synthetic methodology adopted for **3.3** is that the corresponding trinuclear zinc metal phosphonate and *p*-chlorophenylstibonic acid were taken in a 1:4 and 1:5 molar ratio in 15 mL of methanol in 23 mL of Teflon-lined stainless-steel autoclave and followed by dropwise addition of excess pyridine. The resultant mixture was stirred for 2 h and the bomb was sealed properly. The above temperature conditions were maintained in this case as well. X-ray quality single crystals were obtained at the base of the bomb and walls upon slow cooling of the methanol solution. We reacted in a 1:4 &1:5 mole ratio; we got the same product with different yields.

Compound **3.3**: [Zn₃Cl₂(3,5-Me₂PzH)₄(t-BuPO₃)₂] (0.05 g, 0.054 mmol), p-chlorophenylstibonic acid (0.061 g, 0.215 mmol) and pyridine (1 mL). Colorless block-shaped crystals formed upon slow cooling of methanol solution. Yield: 0.037 g (35 %). Anal, Calcd (%) for C₅₅H₇₈Cl₄N₂O₂₁P₄Sb₄Zn₂ (1986.61): C, 33.25; H, 3.96; N, 1.41. Found: C, 34.13; H, 4.18; N, 1.36. ESI-MS: 1876.7530 for [M-(C₆H₅Cl)]⁺. ¹H NMR (500 MHz, CDCl₃+DMSO- d_6): δ = 8.71 (br, 2H), 7.96 (s, br, 1H), 7.86 (d, J = 8 Hz, 4H), 7.39 (br, 2H), 7.31 (d, J = 8 Hz, 4H), 3.37(s, 6H), 1.16 (d, J = 16 Hz, 9H), 1.02 (d, J = 16.5 Hz, 9H) ppm. ¹³C NMR (125 MHz, CDCl₃+DMSO- d_6): δ = 149.39, 135.18, 134.74, 134.57, 127.52, 127.17, 123.65, 51.92, 48.94,

25.60 ppm. ³¹P NMR (202 MHz, CDCl₃+DMSO- d_6): $\delta = 32.86$, 17.02 ppm. IR (cm⁻¹): 2958 (wide), 2822 (m), 2161 (s), 1606 (m), 1476 (s), 1450 (s), 1154 (s), 1121 (s), 1069 (s), 992 (wide), 951 (wide), 810 (s), 792 (m), 734 (m), 698 (s), 670 (s), 557 (s).

The general synthetic methodology adopted for **3.4** is that the corresponding trinuclear zinc metal phosphonate and *p*-isopropylphenylstibonic acid were taken in a 1:4 molar ratio in 15 mL of methanol in 23 mL of Teflon-lined stainless-steel autoclave and followed by dropwise addition of excess pyridine. The resultant mixture was stirred for 2 h. The bomb was sealed properly and the mixture was heated at 100 °C for 12 h and then cooled slowly to room temperature for 25 h. X-ray quality single crystals were obtained at the base of the bomb and walls upon slow cooling of the methanol solution. All isolated crystals were powdered and subjected to a high vacuum for half an hour before being characterized by standard spectroscopic and analytical techniques.

Compound **3.4**: $[Zn_3Cl_2(3,5-Me_2PzH)_4(t-BuPO_3)_2]$ (0.05)0.054 mmol), g, isopropylphenylstibonic acid (0.063 g, 0.216 mmol) and pyridine (1 mL). Colorless blockshaped crystals formed upon slow cooling of methanol solution. Yield: 0.026 g (24 %). Anal.Calcd (%) for C₆₈H₁₁₀N₂O₂₂P₄Sb₄Zn₂ (2050.1201): C, 39.85; H, 5.41; N, 1.37. Found: C, 40.31; H, 5.19; N, 1.36. ESI-MS: 2050.1737 for [M]⁺. ¹H NMR (500 MHz, CDCl₃+DMSO d_6): $\delta = 8.66$ (br. 2H), 8.06 (s, br. 1H), 7.83 (d, J = 8 Hz, 4H), 7.38 (br. 2H), 7.17 (d, J = 8 Hz, 4H), 3.40 (s, 6H), 2.93-2.87 (m, 2H), 1.26 (d, J = 7 Hz, 12H), 1.17 (d, J = 15.5 Hz, 9H), 1.05 (d, J = 16 Hz, 9H) ppm. ¹³C NMR (125 MHz, CDCl₃+DMSO- d_6): $\delta = 149.38$, 148.88, 133.75, 133.32, 125.41, 125.16, 123.66, 51.90, 48.74, 33.25, 25.71, 23.67 ppm. ³¹P NMR (202 MHz, CDCl₃+DMSO- d_6): $\delta = 37.58$, 21.75 ppm. IR (cm⁻¹): 2958 (wide), 2820 (m), 1604 (m), 1480 (m), 1448 (m), 1361 (m), 1149 (s), 1132 (s), 989 (s), 951 (s), 808 (m), 752 (wide), 698 (s), 672 (m), 544 (m).

3.3 Biological Assay:

3.3.1 Antibacterial Assay:

Minimum Inhibitory Concentration (MIC) determination was done for all the synthesized compounds. A total of six bacterial strains belonging to the gram-positive and gram-negative groups were used for the susceptibility test for the synthesized compounds. The bacteria isolate *Escherichia coli* MTCC 43, *Bacillus subtilis* MTCC 121, *Pseudomonas aeruginosa* MTCC 2453, *Listeria monocytogenes MTCC 1143, Micrococcus luteus MTCC 2470* and *Staphylococcus aureus* MTCC 96, were procured from the Microbial type culture collection

(MTCC, India). Bacteria were grown at Mueller Hinton Broth (MHB) (Himedia, India) media at 37 °C for 12 h (0.5 McFarlandstandard).

In vitro Minimum Inhibitory Concentration (MIC) was determined using the resazurin-based 96-well plate broth serial microdilution method. ¹⁹ The test compounds were dissolved in the sterile solution of 10 % (v/v) dimethyl sulfoxide (DMSO) in water giving the stock solution of 1 mg/mL. 100 μ L of dissolved test compound was pipetted into the first row of the 96 well plates and then diluted two-fold in lower rows containing the 50 μ L of MHB, giving the concentration range of 100 μ g/mL to 0.781 μ g/mL. Each well was inoculated with 10 μ L of the bacterial culture (10⁶ CFU/mL) and kept for incubation at 37 °C for 12-24 h. Thereafter, 30 μ L of resazurin dye (0.015%) was added to all wells and further incubated for 2-4 h in the dark at room temperature. A color change from blue to pink was visually observed where blue color represents no bacterial growth and pink color represents growth. Positive control was bacterial inoculum and a medium, Negative control was medium only.

3.3.2 In Silico Computational Docking of Compounds:

Docking is used for drug design using computational tools to predict the interaction of the ligand with the target protein. The docking of all the newly synthesized compounds was done with the crystal structure of DNA Gyrase B (PDB ID: 6F86) to understand the binding and interaction. A molecular docking model was generated using PatchDock (bioinfo3d.cs.tau.ac.il/PatchDock).²⁰ One of the best models out of the top 10 scoring models was chosen with 4.0-Å RMSD, SOAP-PP z-scores > 3.0 properties. The graphical structure of docked compounds was analyzed and visualized using the PyMOL molecular graphics system (The PyMOL Molecular Graphics System, Version 2.0 Schrödinger, LLC).

3.3.3 Antioxidant Assay:

3.3.3.1 Phosphomolybdenum Assay:

The total antioxidant activity of compounds was estimated using the phosphomolybdenum-based method with some modifications.²¹ The stock solution of 1 mg/mL of compounds was prepared and then $100 \mu g/mL$ was mixed with the 1 ml solution (28 mM sodium phosphate, 0.6 M sulphuric acid and 4 mM ammonium molybdate) in an Eppendorf tube. The tubes were incubated for 10 min at 95 °C for completion of the reaction. Tubes were left for cooling at room temperature. The absorbance was recorded using a spectrophotometer at 695 nm wavelength against a blank solution. The standard material is the ascorbic acid ($r^2 = 0.964$) at different concentrations and the total antioxidant capacity of the compounds are expressed in mg of ascorbic acid equivalents (mg AAE)/g of dry weight (dw).

3.4 Results and Discussion:

Compounds 3.1-3.4 were synthesized by a reaction of a trinuclear zinc cluster with arylstibonic acids in the presence of a base under solvothermal conditions. Solution NMR of compounds 3.1, 3.3 and 3.4 was performed in a mixture of DMSO- d_6/CDCl_3 solvents and compound 3.2 was performed in a mixture of methanol- $d_4/CDCl_3$ solvents. ESI-MS studies (positive ion mode) of all compounds were carried out in a chloroform solvent. Compound 3.1 was synthesized by the reaction of $[Zn_3Cl_2(3,5-Me_2PzH)_4(t-BuPO_3)_2]$ with p-chlorophenylstibonic acid in a ratio of 1:2 in the presence of pyridine under solvothermal conditions (Scheme 3.1). Colorless single crystals of 3.1 were grown by slow evaporation of the reaction mixture at room temperature. ³¹P NMR of **3.1** (Figure **3.16**) at room temperature shows two resonance peaks at $\delta = 33.21$ and 32.72 ppm, which indicates the presence of a phosphorus-based ligand in two different environments. The ¹H NMR spectrum of 3.1 (Figure 3.14) shows two distinct doublets (at $\delta = 7.83$ and 7.50 ppm) representing the aromatic protons of the p-chlorophenyl group attached to antimony and broad peaks (at $\delta = 8.61$, 7.97 and 7.39 ppm) representing the pyridine protons attached to the zinc center. Two closely spaced doublets are in the spectrum (at $\delta = 1.21$ and 1.01 ppm), corresponding to two sets of t-butyl groups attached to phosphorus. A single resonance at $\delta = 3.28$ ppm corresponds to the bridging OCH₃ group. The peak of the ESI-MS spectrum of 3.1 (Figure 3.26), at m/z 1253.8334, indicates the molecular ion peak [M]⁺ suggesting the structural integrity of the organoantimony(V) oxo cluster in solution. Compound 3.1 crystallizes in the monoclinic space group $P2_1/c$. Crystallographic data and bond metric parameters of 3.1 are given in Table 3.3. The molecular structure of 3.1 (Figure **3.1a**) reveals the formation of a tetranuclear heterometallic oxo cluster $[Zn_2(p-ClC_6H_4Sb)_2(\mu_3-\mu_3)]$ O) $(\mu_2$ -OCH₃)₂(t-BuPO₃)₃ $(py)_2$] **3.1**. The structure can be described as follows: it consists of two Sb and two Zn centers at the vertices of a distorted tetrahedron. In total, three phosphonates are present, two phosphonates are bound to two Sb centers and one Zn metal center, and the other phosphonate is bound to two Zn metal centers and one Sb center in [3.111] coordination mode based on Harris notation.²² The faces of the tetrahedron are capped by tbutylphosphonates, two μ_2 -methoxides bridging Sb–Zn edges and a μ_2 -oxide bridging the Sb– Sb edge. Two arylstibonic acids are self-condensed through one μ_4 -oxide bridge and further connected to Zn metal centers via a μ_2 -methoxy bridge and Zn metal center at the fourth vertex of a tetrahedron with μ_4 -binding mode with a longer contact (2.831 Å). This zinc metal center is present in trigonal bipyramidal geometry; the five-coordinate Zn sites are fulfilled by three phosphonate oxygen from each side, μ_4 -oxide bridge and the last coordination site is occupied

Scheme 3.1: Synthesis of complexes 3.1-3.4.

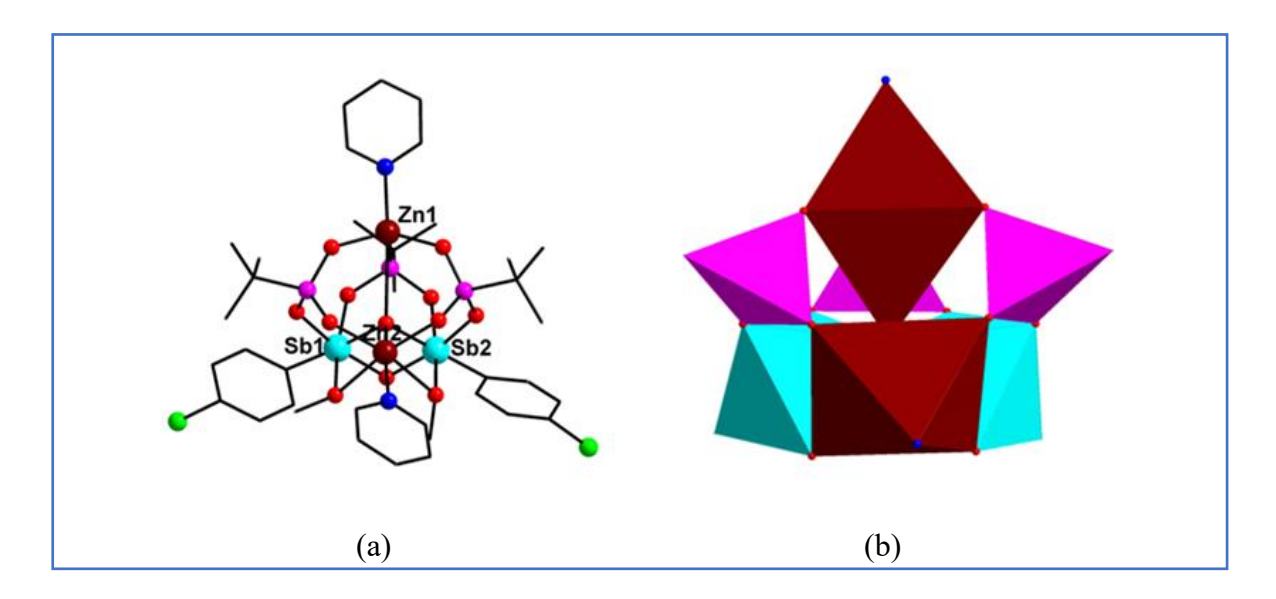


Figure 3.1: (a) Molecular structure of **3.1**. Color code: cyan, Sb; brown, Zn; purple, P; red, O; gray, C; green, Cl. Hydrogens are omitted for clarity. (b) Polyhedral representation of compound **1**; cyan octahedra represent SbO₅C units, brown octahedra represent ZnNO₅ units and purple tetrahedra represent PO₃C units.

by pyridine. The other zinc metal in the Sb₂Zn triangle is six-coordinate, having an octahedron geometry, bound to two phosphonate oxygens, two μ_2 -methoxy bridges, μ_4 -oxide and terminal pyridine. Each Sb center is in regular octahedral geometry with the O₅SbC coordination mode. BVS calculations ²³ indicate Zn in a 2+ oxidation state.

Compound **3.2** was prepared by reacting $[Zn_3Cl_2(3,5-Me_2PzH)_4(t-BuPO_3)_2]$ with p-chlorophenylstibonic acid and KBF₄ in a 1:3:2 molar ratio in the presence of a base under solvothermal conditions (**Scheme 3.1**). SC-XRD studies reveal the formation of a heterometallic octanuclear cage having the formula $[Zn_2(p-ClC_6H_4Sb^V)_4(Sb^{III})_2(\mu_2-O)_6(\mu_3-O)_2(t-BuPO_3H)_4(t-BuPO_3)_2(py)_2Cl_2]$ **3.2**. ³¹P NMR of **3.2** (**Figure 3.19**) at room temperature shows two resonance peaks at $\delta = 38.95$ and 33.46 ppm, which indicates the presence of phosphorus-based ligand in two different environments. The HNMR spectrum of **3.2** (**Figure 3.17**) shows two distinct doublets (at $\delta = 7.87$ and 7.34 ppm) representing the aromatic protons of the p-chlorophenyl group attached to antimony and broad peaks (at $\delta = 8.59$, 7.51 and 7.45 ppm) representing the pyridine protons attached to the zinc center. Two closely spaced doublets are in the spectrum (at $\delta = 1.18$ and 1.05 ppm), corresponding to two sets of t-butyl groups attached to phosphorus. ESI-MS of **3.2** (**Figure 3.27**) shows a signal at m/z 2511.4418, which represents the formula $[M]^+$, confirming the stability of **3.2** in solution as well.

In literature, dearylation of organotin, organobismuth precursors and partial/complete dearylation of organoantimony clusters are known. 1g, 24 Interestingly, in compound **3.2**, the

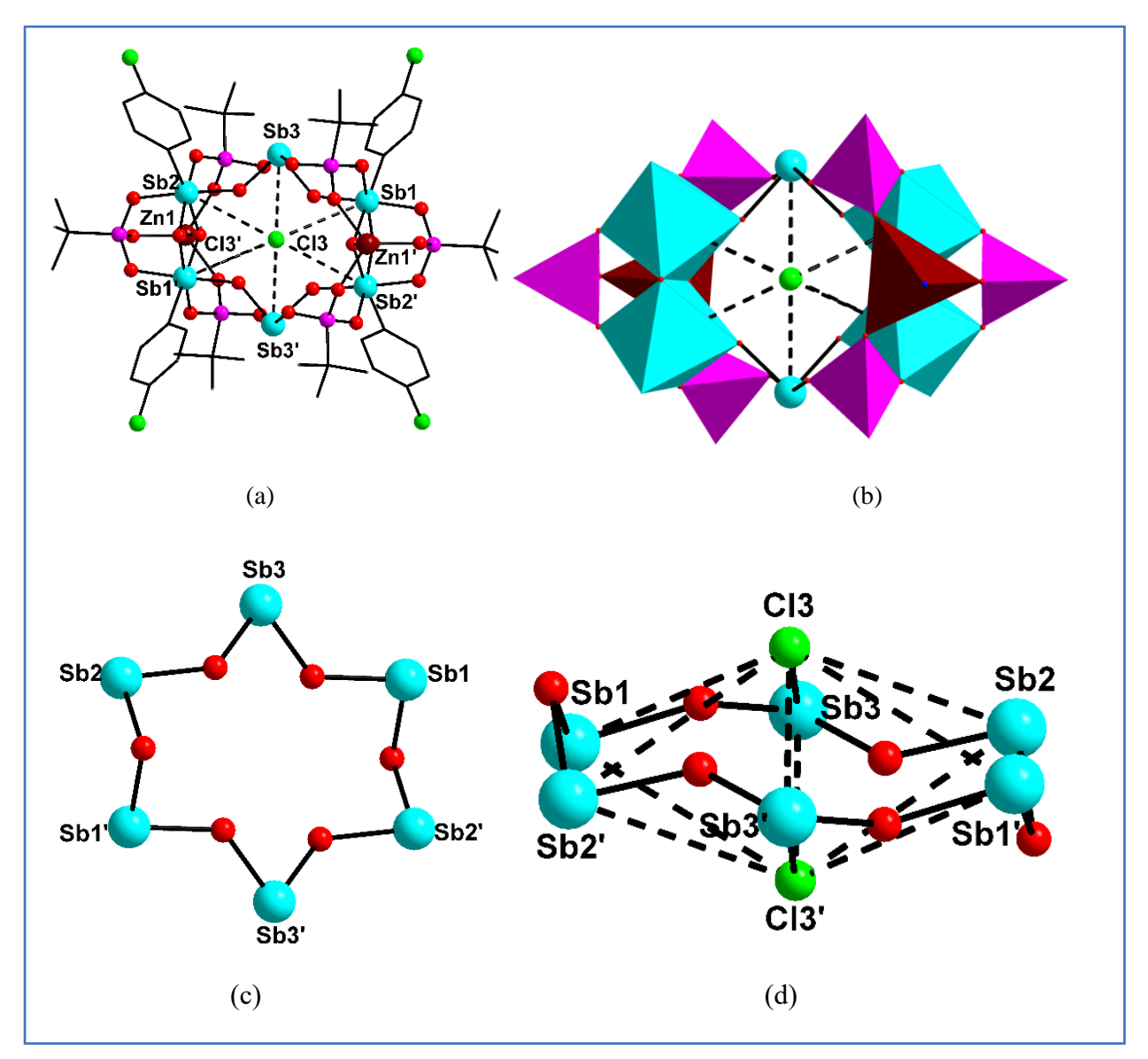


Figure 3.2: (a) Molecular structure of **3.2**, (b) polyhedral representation of compound **2**; cyan octahedra represent SbO₅C units, brown octahedra represent ZnNO₅ units and purple tetrahedra represent PO₃C units, (c) hexagonal star type core and (d) weak intermolecular Sb-Cl interactions. Color code: cyan, Sb; brown, Zn; purple, P; red, O; gray, C; green, Cl. Hydrogens and pyridine coordinated to zinc centres are omitted for clarity.

reduction of Sb(V) to Sb(III) and complete dearylation at elevated temperature followed by a mixed 3d-main group-based metal-mediated carbon-fluorine bond formation was observed; it is worth mentioning here that these kinds of multiple processes are rare in organoantimony chemistry. The fluorination reaction can be explained by two possible mechanisms electrophilic antimony-carbon bond cleavage and carbon-fluorine reductive elimination from a discrete antimony fluoride complex. Herein, KBF₄ acts as an electrophilic reagent that helps in the formation of aryl fluoride.²⁵ A ¹⁹F NMR resonance peak confirmed the formation of aryl

fluoride (1-chloro-4-fluorobenzene) at -115.97 ppm. BVS calculations confirmed the 3+ oxidation state of the antimony center. In the cage, four Sb^V and two Sb^{III} metal centers are present.

Compound 3.2 crystallizes in triclinic space group P-I, with half of the molecule present in the asymmetric unit. Crystallographic data and bond metric parameters of 3.2 are given in **Table** 3.4. The overall molecular structure of 3.2 (**Figure 3.2a**) consists of four Sb^V, two Sb^{III,} and two Zn^{II} ions, which are held together by two μ_3 -oxides, six μ_2 -oxides, six phosphonates bridges of which two are doubly deprotonated and four are mono deprotonated. Two μ_3 -oxo centered Sb^V₂Zn^{II} are present, which are connected through a Sb^{III}O₄ motifs. In each triangle, the Sb-Sb edge is bridged by μ_2 -oxide, one Sb-Zn edge is bridged by phosphonate and the other Sb-Zn edge is bridged by mono deprotonated phosphonate. Four mono-deprotonated phosphonates and two doubly-deprotonated phosphonates are found in the structure, with each phosphonate bound to metal centers in [3.111] coordination mode. Interestingly, four Sb^V and two Sb^{III} centers form a hexagonal star-like topology with six μ_2 -oxide bridges (**Figure 3.2c**). The zinc center gives a trigonal bipyramidal with O₄NZn coordination mode.

The overall structure of **3.2** is further stabilized by two chloride ions capping above and below the macrocycle. The core structure with four Sb^V and two Sb^{III} centers connected through μ_2 -oxide bridges is considered a macrocycle. The macrocycle is capped with two chloride ions having weak intermolecular Sb---Cl interactions (**Figure 3.2d**). The Sb^V(1)---Cl(3), Sb^V(2)---Cl(3) and Sb^{III}(3)---Cl(3) distances are 4.22 Å, 4.07 Å and 3.77 Å respectively and are shorter than the sum of the van der Waals radii (4.59 Å).²⁶

On reacting [Zn₃Cl₂(3,5-Me₂PzH)₄(t-BuPO₃)₂] with organostibonic acid in a ratio of 1:4 in the presence of pyridine under solvothermal conditions [Zn₂(RSb)₄(μ ₃-O)₂(μ ₂-OCH₃)₄(t-BuPO₃)₄(py)₂], where R= p-ClC₆H₄ (**3.3**) and R= p-iPrC₆H₄ (**3.4**) is formed (**Scheme 3.1**). ³¹P NMR of **3.3** (**Figure 3.22**) shows two resonance peaks at δ = 32.86 and 17.02 ppm and similarly, **3.4** (**Figure 3.25**) shows two resonance peaks at δ = 37.58 and 21.75 ppm, which indicates the presence of two different phosphorus environments. ¹H NMR spectrum of **3.3** (**Figure 3.20**) shows two distinct doublets (at δ = 7.86 and 7.31 ppm) representing the aromatic protons of the p-chlorophenyl group attached to antimony and broad peaks (at δ = 8.71, 7.96 and 7.39 ppm) representing the pyridine protons attached to the zinc center. Two closely spaced doublets are in the spectrum (at δ = 1.16 and 1.02 ppm), corresponding to two sets of t-butyl groups attached to phosphorus. A single peak at δ = 3.37 ppm corresponds to the bridging OCH₃ group. Similarly, the ¹H NMR spectrum of **3.4** (**Figure 3.23**) shows two distinct doublets (at δ = 7.83 and 7.17 ppm), a doublet (at δ = 1.25 ppm), and a multiplet (at δ = 2.93-

2.87 ppm) representing the protons of the *p*-isopropyl phenyl group attached to antimony and broad peaks (at $\delta = 8.66$, 8.06 and 7.38 ppm) representing the pyridine protons attached to the zinc center. Two closely spaced doublets are in the spectrum (at $\delta = 1.17$ and 1.05 ppm), corresponding to two sets of *t*-butyl groups attached to phosphorus. A single peak at $\delta = 3.40$ ppm corresponds to the bridging OCH₃ group. ESI-MS of **3.3** (**Figure 3.28**) showed a signal at m/z 1876.7530. This signal corresponds to the loss of the aryl group and can be assigned to the formula [M-(C_6H_5Cl)]^{+,} suggesting that **3.3** retains structural stability in solution as well. The ESI-MS study on **3.4** (**Figure 3.29**) showed a peak at m/z 2050.1737, representing the molecular ion peak [M]⁺. This result suggests that **3.4** showed structural integrity in the solution state.

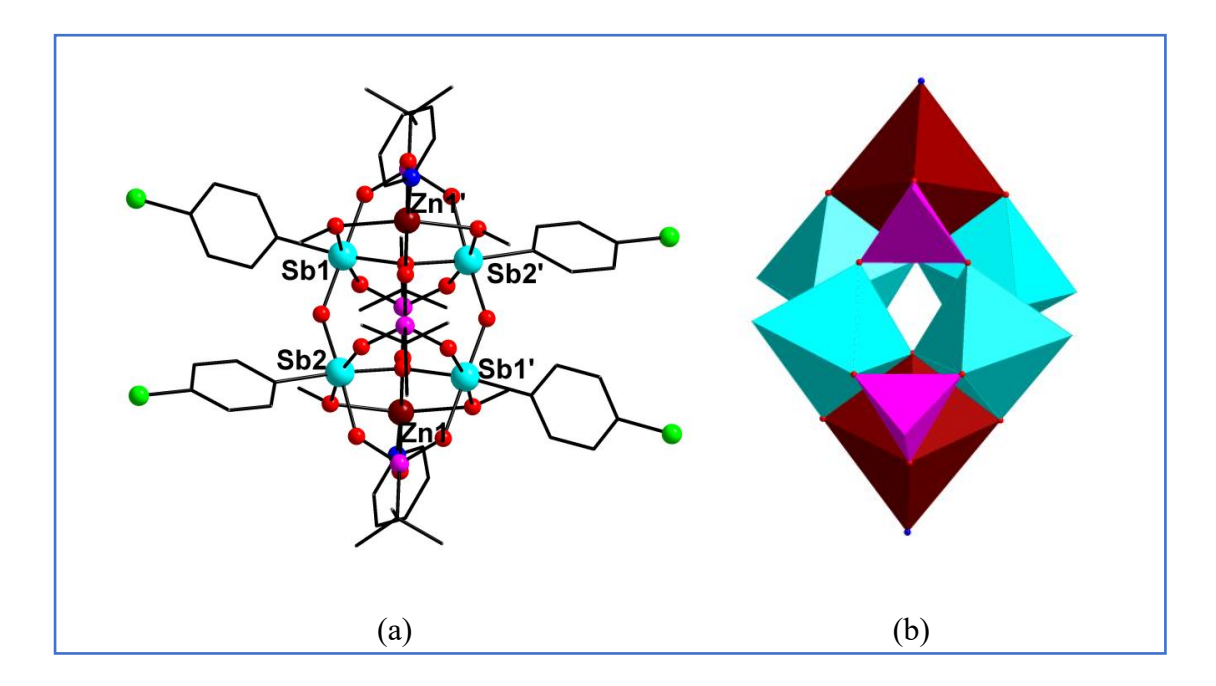


Figure 3.3: (a) Molecular structure of **3.3**. Color code: cyan, Sb; brown, Zn; purple, P; red, O; gray, C; green, Cl. Hydrogens are omitted for clarity, (b) polyhedral representation of compound **3**; cyan octahedra represent SbO₅C units, brown octahedra represent ZnNO₅ units and purple tetrahedra represent PO₃C units.

Compound 3.3 crystallizes in the triclinic space group P-I and 3.4 in the monoclinic space group C2/c, with half of the molecule present in the asymmetric unit. Crystallographic data and bond metric parameters of 3.3 and 3.4 are given in **Tables 3.5** and 3.6. The molecular structures of 3.3 and 3.4 are isostructural and we considered the structure of 3.3 (**Figure 3.3a**) as representative of structural discussion. The core structure of 3.3 has a cube topology with four Sb centers, two zinc centers and two phosphorus atoms at the vertices. The Sb centers form a

central plane with pairs of zinc and phosphorus atoms at opposite ends of the body diagonals of the cube. In this cage, *in situ*-generated two oxo-bridged Sb₂Zn triangles are present here, two arylstibonic acids self-condensed through one μ_3 -oxo bridge and further connected to zinc metal centers via μ_2 -methoxy bridges. Based on the Harris notation, four phosphonates are bound to two Sb centers and one Zn metal center in [3.111] coordination mode. Two zinc sites are six-coordinate adopted octahedron geometry; coordination sites are fulfilled by one μ_3 -oxide, two μ_2 - methoxides and two oxygens from phosphonates a terminal pyridine occupies the last coordination site. Each Sb center is in regular octahedral geometry with the O₅SbC coordination mode. BVS calculations indicate Zn in a 2+ oxidation state.

The phase purity of the compounds was confirmed by powder X-ray diffraction (PXRD). The PXRD patterns match the simulated patterns obtained from SC-XRD analysis (Figure 3.30-3.33). The thermal stability of compounds 3.1–3.4 was investigated under a nitrogen atmosphere using thermogravimetric analysis (TGA) at temperatures between 30 to 800 °C. TGA curves of compounds 3.1–3.4 (Figure 3.34-3.37) show that the major weight loss occurs at 282, 453, 428 and 425 °C, respectively. Energy-dispersive X-ray spectroscopy (EDAX) and elemental mapping display the elemental composition of 3.1–3.4 (Figure 3.38-3.45). From the EDAX analysis and elemental mapping, the presence of C, O, P, N, Zn, Sb and Cl species in the respective cluster composition is observed. From ICP-OES analysis, the observed elemental composition matched well with the calculated values indicating the purity of compounds 3.1–3.4 (Figure 3.46-3.49).

3.4.1 Antibacterial Activity:

Antibiotic resistance is a global issue, which requires new drug inventions.²⁷ Along with the natural sources, the chemical synthesis of compounds opens the scope for new antibacterial drug discovery.²⁸ Arylfluorosulfates, THCZ and synthetic flavonoids are commonly used drugs to treat multidrug-resistant bacteria.²⁹ The antibacterial activity of synthesized compounds was examined using the broth microdilution method against six bacterial reference pathogen strains. The minimum inhibitory concentration (MIC) of all the test compounds **3.1-3.4** varied from 25 to $0.781 \mu g/mL$ depending on the bacterial strain (**Table 3.1**). MIC data showed that the tested pathogens are highly susceptible to all the compounds at very low concentrations. The highest MIC value of $25 \mu g/mL$ was recorded on *S. aureus*, *E. coli* with compound **3.2** and on *S. aureus*, *B. subtilis* with compound **3.3**. However, the lowest MIC value of $0.781 \mu g/ml$ was recorded on *B. subtilis* with compound **3.1** and on *P. aeruginosa* with compound **3.4**. All the pathogens were highly susceptible to compound **3.4**. The bioactivity of compounds **3.1-3.4** depends on

the zinc-to-antimony ratio (1:1 for compound **3.1**, 1:2 for compounds **3.3** & **3.4** and 1:3 for compound **3.2**), especially the number of organoantimony (V/III) moieties present in the cluster **Table 3.1:** Minimum Inhibitory Concentration (MIC) (μ g/mL) of all four compounds against the reference bacterial strains.

Bacterial strain	Compound MIC ^a (µg/mL)			
Gram(+ive) bacteria	3.1	3.2	3.3	3.4
Staphylococcus aureus MTCC 96	1.562	25	25	0.781
Bacillus subtilis MTCC 121	0.781	12.5	25	6.25
Listeria monocytogenes MTCC 1143	3.125	3.125	6.25	1.5625
Gram(-ive) bacteria				
Pseudomonas aeruginosa MTCC 2453	6.25	3.125	6.25	0.781
Escherichia coli MTCC 43	1.562	25	6.25	1.562
Micrococcus luteus MTCC 2470	6.25	6.25	3.125	1.5625

^aEach MIC was determined from at least three independent experiments.

and also the organic group attached to the organoantimony (V) moieties. Compound **3.1** showed the lowest MIC values compared to compounds **3.2-3.3** and hence it can be assumed that an increase in the incorporation of the organoantimony (V/III) moieties decreases the antibacterial activity. Compound **3.4** is isostructural to compound **3.3**. When we compared the antibacterial activity of compound **3.4** with compound **3.3**, we observed enhanced bioactivity. These results indicate that changing the organic group from chloro to isopropyl (moderating electronic factors) attached to organoantimony (V) moieties had a remarkable effect on antibacterial activity. Organoantimony-based POMs exhibited antibacterial activity. When we compared compounds **3.1-3.4** with organoantimony-based POMs¹³, we observed enhanced activity.

3.4.2 Molecular Docking of the Compounds:

Organostibonic acid compounds are reported to be antimicrobial agents, which inhibit the enzyme of the replication process. 2b Therefore, to inspect the antibacterial mode of action of the newly synthesized metal oxo clusters compounds 3.1-3.4 docking studies were performed with one of the important target enzymes from the replication process. The docking of these compounds was performed with the DNA Gyrase B (PDB ID: 6F86) crystal structure. The pyridine-3-carboxamide derivative was reported to be the inhibitor of DNA Gyrase B;³⁰ therefore, the analysis of the co-crystallized Gyrase B with the inhibitor 4-(4-bromanylpyrazol-1-yl)-6-(ethyl carbamoyl amino)-[N]-pyridin-3-yl-pyridine-3-carboxamide showed the interaction with Val43, Asn46, Ala47, Glu50, Val71, Gln72, Asp73, Arg76, Gly77, Ile78, Pro79, Ile94, Arg136, Thr165, Met166 and Val167 amino acids (Figure 3.4a and 3.4b). According to the docking, all the compounds were able to bind in the same pocket of Gyrase B, where the inhibitor pyridine-3-carboxamide derivative was bound with the binding affinity (atomic contact energy [ACE] (Kcal/mol)) ranging from -218.81 to -311.77 (**Table 3.12**). Compound 3.1 formed one hydrogen bond with Asn46 and the common amino acid residues similar to the inhibitor binding were Asn46, Ala47, Glu50, Asp73, Arg76, Gly77, Ile78, Pro79, Ile94 and Thr165, but few other residues were Asp45, Ile48, Asp49, Leu52, Ala53, Ala90, Ala91, Val93, Met95, Val97, Leu98, Gly117, Val118, Gly119, Val120, Ser121 and Val122 with ACE of -236.37 Kcal/mol (Figure 3.4c). Compound 3.2 common binding amino acid residues were Asn46, Ala47, Glu50, Asp73, Arg76, Gly77, Ile78, Pro79, Ile94, while other interacting residues were Glu42, Asp45, Ile48, Asp49, Ala51, Leu52, Ala53, Gly54, His55, Gly81, Ala90, Ala91, Val93, Val97, Leu98, Val118, Gly119, Val120, Ser121 and Val122 with ACE of -298.29 Kcal/mol (Figure 3.4d). Compound 3.3 formed one hydrogen bond with Arg76 and the common residues were Asp45, Asn49, Ala53, Ala90, Ala91, Val93 and Met95, while other binding residues were Ile48, Leu52, Val97, Leu98, Gly117, Val118, Gly119, Val120, Ser121 and Val122 with ACE of -218.81 Kcal/mol (Figure 3.4e). Compound 3.4 formed two hydrogen bonds with Asn46 residue, and the common residue were Val43, Asn46, Ala47, Glu50, Asp73, Arg76, Gly77, Ile78, Pro79, Ile94, and Thr165, while other binding residues were Asp45, Ile48, Asp49, Leu52, Ala53, Gly54, His55, Gly81, Ser89, Ala90, Ala91, Glu92, Val93, Met95, Thr96, Val97, Leu98, Gly117, Gly119, Val120, Ser121 and Arg130 with ACE of -311.77 Kcal/mol (Figure 3.4f). All these compounds have a strong binding affinity to the target enzyme, which shows their potential as an inhibitor for antibacterial activity.

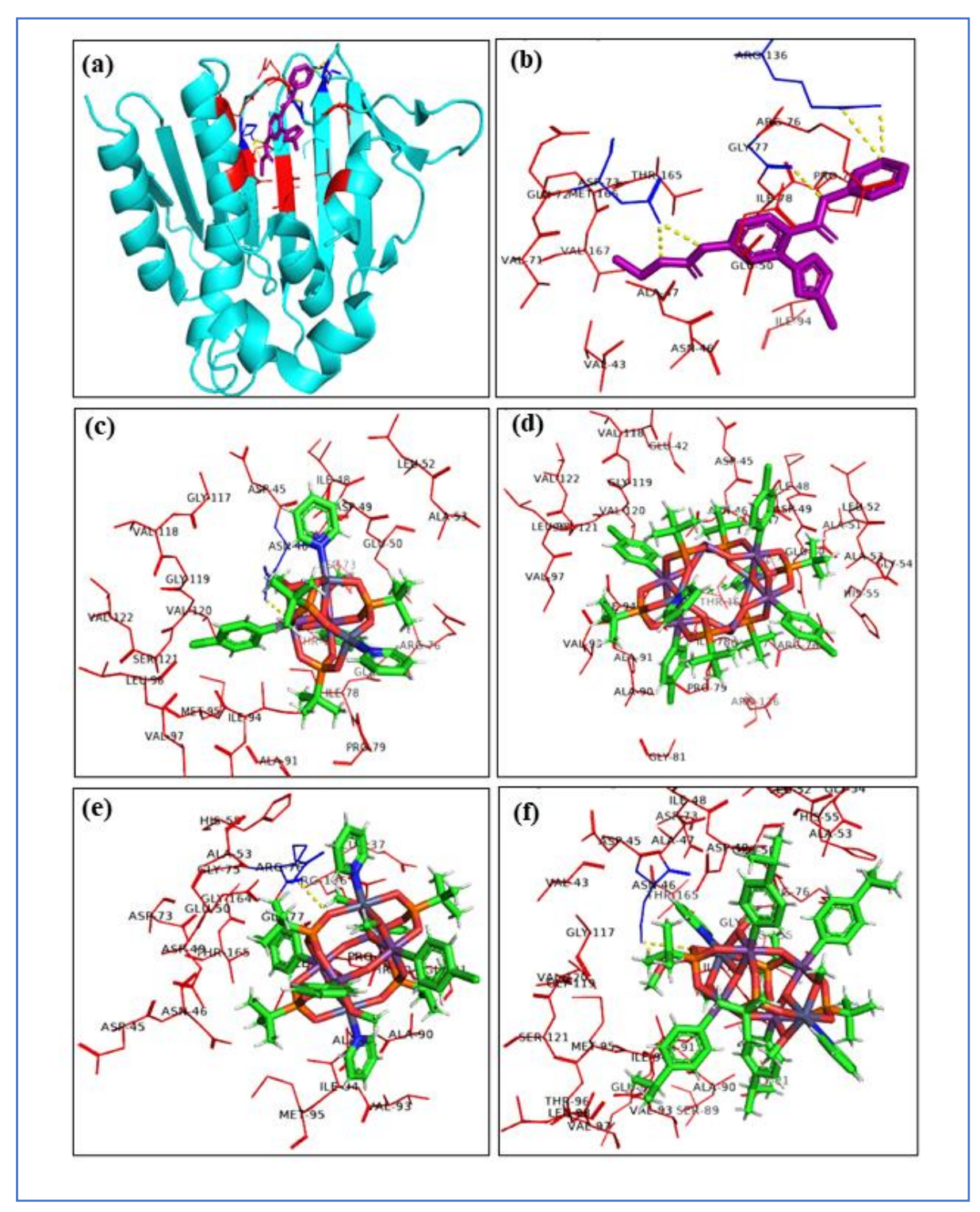


Figure 3.4: Docking structure of protein Gyrase B (PDB ID: 6F86) with the inhibitor and the synthesized compounds **3.1-3.4.** (a) The 3D diagram of the inhibitor (Pyridine carboxamide derivative) interaction with the Gyrase B active site. (b) The interacting amino acid of the Gyrase B protein with inhibitor (Pyridine carboxamide derivative). The docked complex of the compounds (c) for **3.1**, (d) for **3.2**, (e) for **3.3** and (f) for **3.4**, with the protein Gyrase B, shows the binding interaction with amino acids. H- bonds are shown in yellow dotted lines and the amino acids are highlighted in three-letter code.

3.4.3 Antioxidant Activity:

The total antioxidant capacity of the compounds was quantified through the phosphomolybdenum method and represented as equivalents of ascorbic acid (mg AAE)/g. Compound **3.2** has the highest capacity of 86.46 ± 4.5 and compounds **3.3** and **3.4** have similar capacities, viz. 36.73 ± 2.6 and 42.33 ± 2.5 , while the lowest was compound **3.1** of 28.96 ± 1.76 ascorbic acid (mg AAE)/g at a concentration of $100 \mu g/mL$ (**Figure 3.5**). All the

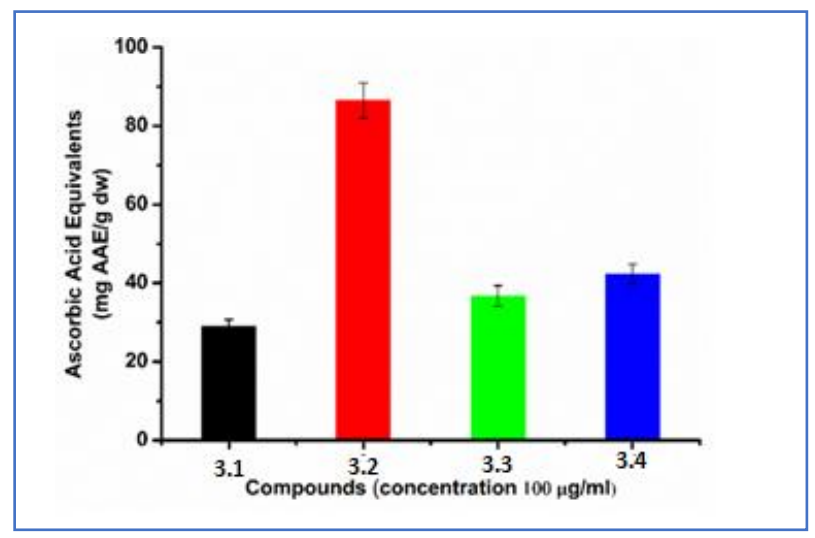


Figure 3.5: Total antioxidant capacity of compounds **3.1-3.4** at the concentration of 100 μ g/mL. Ascorbic acid was used as a standard for measurement. Data are represented as means \pm standard deviation (SD) of three experiments (n=3) and expressed as mg standard /g of dry weight (dw).

exhibited appropriate antioxidant capacity in the decreasing order of 3.2 > 3.4 > 3.3 > 3.1. The antioxidant activity of 3.1-3.4 depends on the structure-property correlations. Organoantimony compounds would have acted as a source of electron provider reducing Mo (VI) to Mo (V) based on which the antioxidant property was studied. The only mixed valent Sb^V/Sb^{III} cluster (3.2) seems to be showing enormously improved activity probably due to the presence of mixed valent ions as well as unusual μ_6 - Cl ions present in the molecular structure and also the zinc-to-antimony ratio of 1:3. These results indicate that increasing the incorporation of a number of organoantimony (V/III) moieties leads to enhanced antioxidant activity and that changing organic substituents (chloro to isopropyl) on the organoantimony (V) moieties leads to an increase in antioxidant activity. Synthetic compounds with antioxidant and antibacterial dual activities are considered effective for the so-called "superbugs". 31

3.5 Conclusion:

By reacting Zn₃-oxo triangles as nodes with stibonic acids, interesting molecular architectures build-up of Zn₂Sb₂, Zn₂Sb₄^VSb₂^{III} and Zn₂Sb₄ frameworks have been characterized by SC-XRD. In compound **3.2**, complete dearylation followed by carbon-fluorine bond formation as well as reduction from Sb(V) to Sb(III) have been found to occur in an in-situ manner. Weak Sb---Cl intermolecular interactions also stabilized the novel molecular structure obtained. For **3.1-3.4**, antibacterial and antioxidant studies were performed. Specifically, **3.1** and **3.4** showed the lowest MIC values and **3.2** showed the highest total antioxidant capacity.

3.6 Analytical and Spectroscopic Data

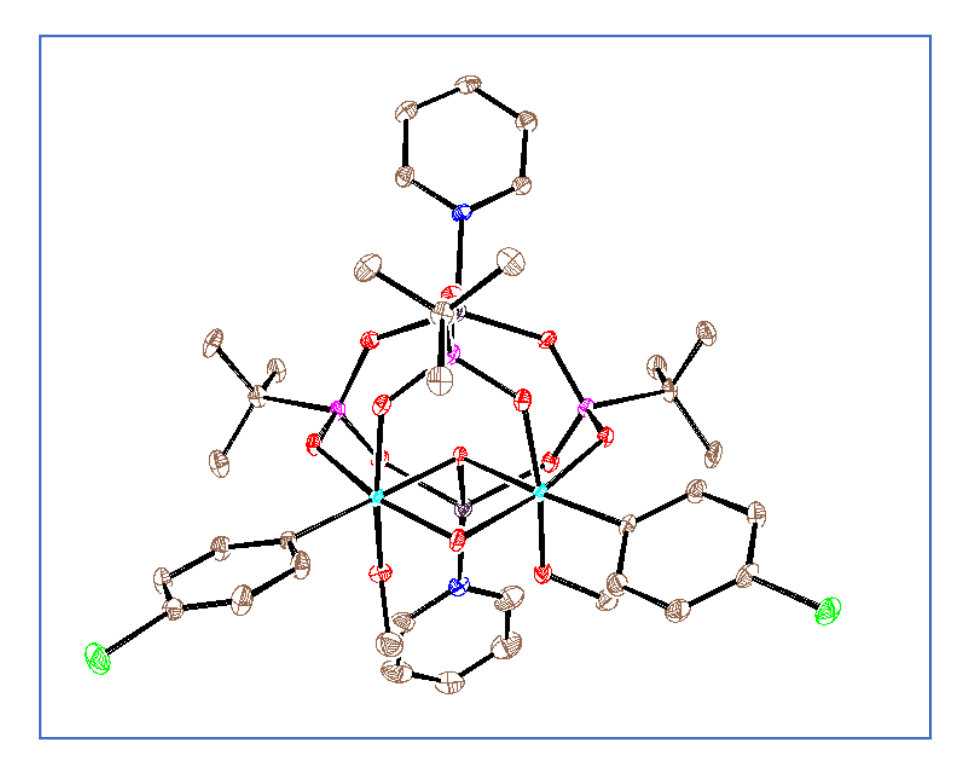


Figure 3.6: ORTEP view of **3.1** with thermal ellipsoids shown at 30% probability.

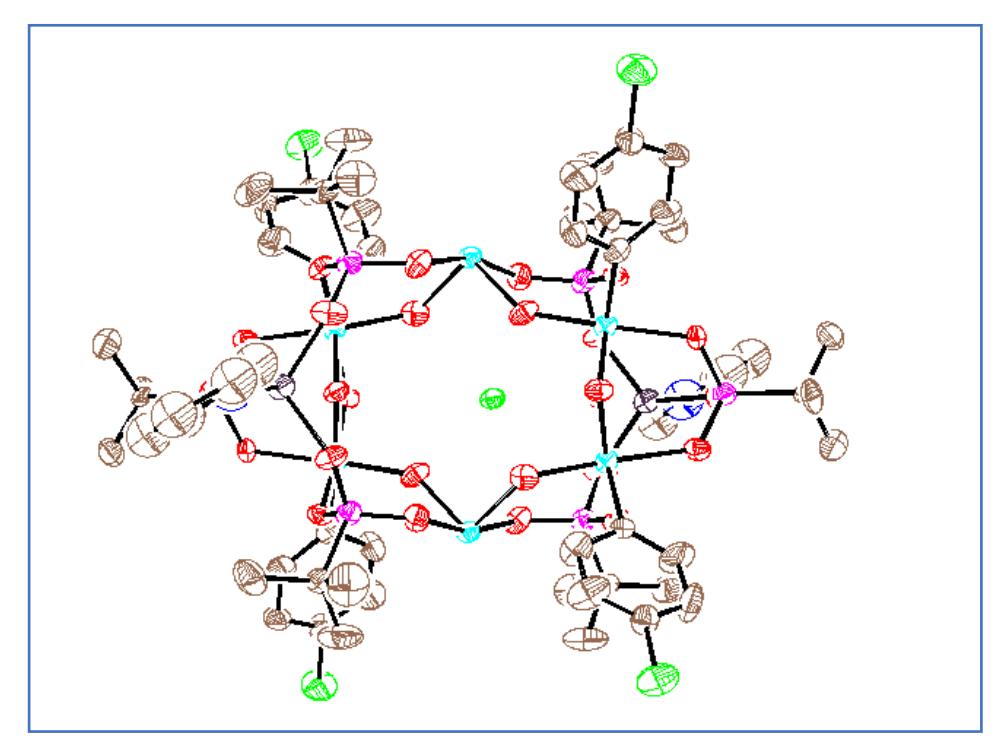


Figure 3.7: ORTEP view of **3.2** with thermal ellipsoids shown at 30% probability.

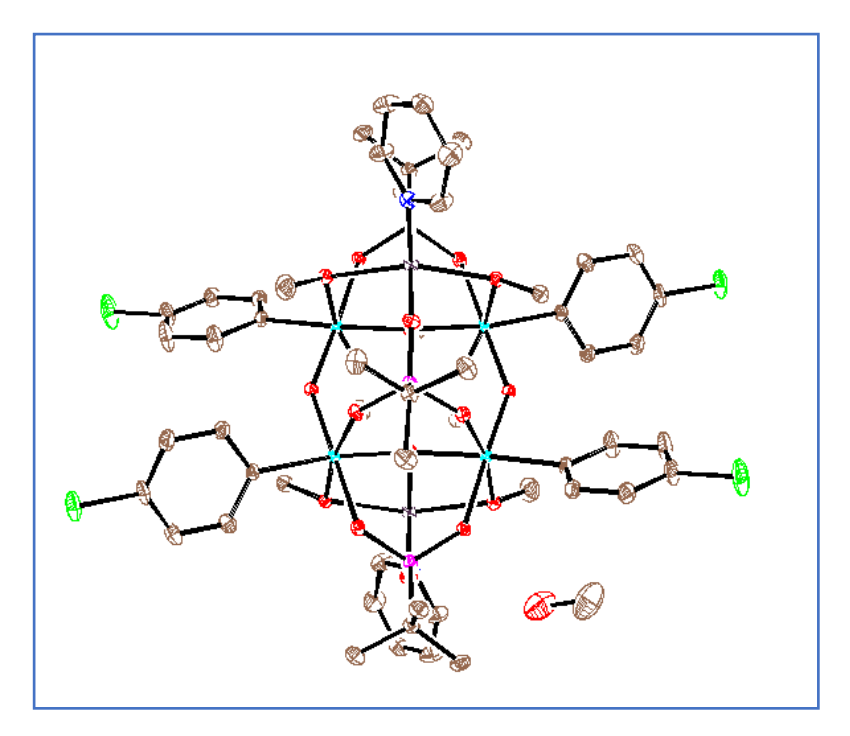


Figure 3.8: ORTEP view of 3.3 with thermal ellipsoids shown at 30% probability.

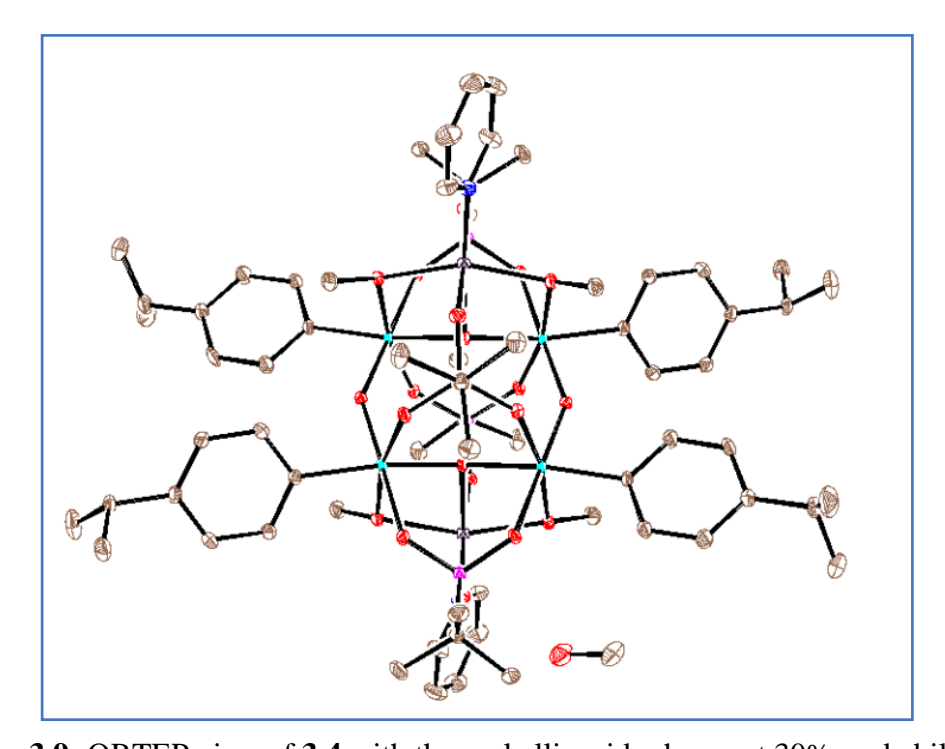


Figure 3.9: ORTEP view of **3.4** with thermal ellipsoids shown at 30% probability.

 Table 3.2: crystallographic information of compounds 3.1 -3.4

	3.1	3.2	3.3	3.4
Formula	$C_{36}H_{51}Cl_2N_2O_{13}P_3Sb_2Zn_2$	C ₅₉ Cl ₆ H ₈₈ N ₂ O ₂₇ P ₆ Sb ₆ Zn ₂	C ₅₅ H ₇₈ Cl ₄ N ₂ O ₂₁ P ₄ Sb ₄ Zn ₂	C ₆₈ H ₁₁₀ N ₂ O ₂₂ P ₄ Sb ₄ Zn ₂
F. weight	1257.83	2517.07	1986.61	2049.19
Temp K	100	100	100	100
Crystal system	monoclinic	triclinic	triclinic	monoclinic
Space group	$P2_1/n$	P-1	P-1	C2/c
a/Å	9.88340(10)	11.951(4)	12.25270(10)	25.3029(3)
b/Å	22.4681(3)	13.964(4)	13.38580(10)	20.1847(3)
c/Å	20.7147(3)	16.108(5)	24.3265(2)	16.2024(2)
α/°	90	109.950(10)	93.0710(10)	90
β/°	91.1610(10)	104.898(12)	94.8930(10)	91.2630(10)
γ/°	90	95.496(12)	112.2380(10)	90
Volume/Å ³	4598.99(10)	2391.6(13)	3663.64(6)	8273.07(19)
Z	4	1	2	4
ρcalcg/cm ³	1.817	1.748	1.801	1.645
μ/mm-1	2.475	2.493	2.400	2.004
F(000)	2504.0	1230.0	1964.0	4128.0
Crystal size/mm ³	0.21 × 0.198 × 0.185	$0.21 \times 0.18 \times 0.165$	0.23 × 0.209 × 0.198	0.22 × 0.215 × 0.191
2Θ range (°)	3.934 to 50.698	3.168 to 50.7	3.844 to 50.698	4.036 to 50.7
Index ranges	$-11 \le h \le 11$, $-26 \le k \le 27$, $-24 \le 1 \le 24$	$-14 \le h \le 14$, $-16 \le k \le 16$, $-18 \le 1 \le 19$	$-14 \le h \le 14$, $-16 \le k \le 16$, $-29 \le 1 \le 29$	$-30 \le h \le 30$, $-24 \le k \le 24$, $-19 \le l \le 19$
Reflections collected	44680	24432	77635	36105
Ind. reflections	8405 [Rint = 0.0770]	8740 [Rint = 0.1428]	13416 [Rint = 0.0711]	7583 [Rint = 0.0469]
Data/restraint s/parameters	8405/0/552	8740/9/463	13416/0/847	7583/0/474
GooF (F ²)	1.073	0.989	1.030	1.026
$R_1(F)[I > 2\sigma(I)]$	0.0372	0.0833	0.0342	0.0248
wR ₂ (F ²) (all data)	0.0919	0.2162	0.0913	0.0595
Largest diff. peak/hole / e Å-3	1.62/-0.70	1.84/-1.34	1.34/-1.29	0.50/-0.70
Completeness to θ_{max} , %	100.0	99.7	99.9	99.9

Table 3.3: Selected bond lengths (Å) and bond angles (deg) parameters of compound 3.1

		8 ()	υ . υ,	. 1	1
Sb2-Sb1	3.0339(4)	O11-Sb2-O8	80.26(10)	Sb2-O8-Zn2	106.97(13)
Sb2-O8	2.011(2)	O11-Sb2-O13	88.95(11)	Sb1-O8-Sb2	97.99(10)
Sb2-O13	2.032(3)	O11-Sb2-O7	167.66(10)	Sb1-O8-Zn2	109.23(12)
Sb2-O11	1.978(2)	O11-Sb2-O9	93.70(11)	P1-O4-Zn2	123.16(14)
Sb2-O7	2.001(2)	O7-Sb2-Sb1	128.24(7)	P1-O5-Sb1	126.36(16)
Sb2-O9	1.986(3)	O7-Sb2-O8	87.54(10)	P1-O1-Zn1	134.42(17)
Sb1-O12	2.048(3)	O7-Sb2-O13	88.22(11)	P3-O13-Sb2	127.06(15)
Sb1-O8	2.009(2)	O9-Sb2-Sb1	91.89(8)	Sb1-O11-Sb2	100.71(11)
Sb1-O5	2.006(2)	O9-Sb2-O8	84.72(11)	P2-O3-Zn1	132.20(16)
Sb1-O11	1.962(3)	O9-Sb2-O13	169.17(10)	P3-O2-Zn1	125.60(16)
Sb1-O10	1.991(3)	O9-Sb2-O7	86.96(11)	P2-O7-Sb2	127.58(15)
Zn1-O1	1.930(2)	O12-Sb1-Sb2	83.18(7)	P2-O6-Zn2	123.71(15)
Zn1-O3	1.909(3)	O8-Sb1-Sb2	41.03(7)	Sb2-O9-Zn2	93.55(11)
Zn1-O2	1.963(2)	O8-Sb1-O12	85.06(10)	O2-Zn1-N1	104.53(11)
Zn1-N1	2.084(3)	O5-Sb1-Sb2	128.10(7)	O8-Zn2-O9	72.30(9)
Zn2-O8	2.054(3)	O5-Sb1-O12	89.13(11)	O4-Zn2-O8	91.50(10)
Zn2-O4	1.986(3)	O5-Sb1-O8	87.27(10)	O4-Zn2-O9	155.89(10)
Zn2-O6	1.985(3)	O11-Sb1-Sb2	39.84(7)	O4-Zn2-N2	103.40(13)
Zn2-O9	2.475(3)	O11-Sb1-O12	88.87(11)	O6-Zn2-O8	91.82(10)
Zn2-N2	2.016(4)	O11-Sb1-O8	80.70(10)	O6-Zn2-O4	114.72(11)
P1-O4	1.520(3)	O11-Sb1-O5	167.93(10)	O6-Zn2-O9	84.27(10)
P1-O5	1.577(2)	O11-Sb1-O10	89.86(11)	O6-Zn2-N2	97.46(13)
P1-O1	1.518(3)	O10-Sb1-Sb2	89.48(8)	N2-Zn2-O8	157.07(12)
P2-O3	1.522(3)	O10-Sb1-O12	169.97(10)	N2-Zn2-O9	87.76(12)
P2-O7	1.573(2)	O10-Sb1-O8	84.91(11)	O4-P1-O5	111.07(16)
P2-O6	1.514(3)	O10-Sb1-O5	90.04(11)	O1-P1-O4	114.65(16)
P3-O12	1.550(3)	O1-Zn1-O2	114.99(11)	O1-P1-O5	109.95(14)
P3-O13	1.557(3)	O1-Zn1-N1	94.89(12)	O3-P2-O7	110.12(15)
P3-O2	1.507(3)	O3-Zn1-O1	26.13(11)	O6-P2-O3	114.84(15)
O8-Sb2-Sb1	40.98(7)	O3-Zn1-O2	111.44(11)	O6-P2-O7	110.75(15)
O8-Sb2-O13	85.39(10)	O3-Zn1-N1	98.62(12)	O12-P3-O13	111.00(16)
O13-Sb2-Sb1	83.49(7)	O2-P3-O13	112.10(15)	O2-P3-O12	111.36(15)
O11-Sb2-Sb1	39.45(7)	P3-O12-Sb1	126.93(16)		

Table 3.4: Selected bond lengths (Å) and bond angles (deg) parameters of compound 3.2

Sb2-Sb1 ¹	3.059(15)	O1-Sb2-Sb1 ¹	100.2(3)	Sb1-O7-Sb2 ¹	100.8(4)
Sb2-O5 ¹	1.995(9)	O1-Sb2-O5 ¹	92.3(4)	P2-O11-Zn1	129.5(6)
Sb2-O8 ¹	2.067(10)	O1-Sb2-O8 ¹	171.6(4)	O3-Sb1-O4	86.4(4)
Sb2-O1	1.891(11)	O1-Sb2-O13 ¹	86.6(4)	O3-Sb1-O7	96.4(4)
Sb2-O13 ¹	2.025(9)	O1-Sb2-O7 ¹	95.3(4)	O6-Sb1-Sb2 ¹	82.4(2)
Sb2-O7 ¹	1.991(9)	O13 ¹ -Sb2-Sb1 ¹	129.1(3)	O4-Sb1-Sb2 ¹	128.1(3)
Sb1-O5	2.012(9)	O13 ¹ -Sb2-O8 ¹	85.6(4)	O4-Sb1-O6	85.4(4)
Sb1-O3	1.883(10)	O7 ¹ -Sb2-Sb1 ¹	39.5(3)	O7-Sb1-Sb2 ¹	39.7(3)
Sb1-O6	2.059(9)	O7 ¹ -Sb2-O5 ¹	79.3(4)	O7-Sb1-O5	79.1(4)
Sb1-O4	2.021(9)	O7 ¹ -Sb2-O8 ¹	91.8(4)	O7-Sb1-O6	90.9(4)
Sb1-O7	1.980(9)	O7 ¹ -Sb2-O13 ¹	168.5(4)	O7-Sb1-O4	167.8(4)
Sb3-O3	1.912(9)	O5-Sb1-Sb2 ¹	40.0(3)	O3-Sb3-O1	97.0(4)
Sb3-O1	1.917(11)	O5-Sb1-O6	85.5(4)	O3-Sb3-O12 ¹	87.2(4)
Sb3-O12 ¹	2.183(10)	O5-Sb1-O4	88.9(4)	O3-Sb3-O2	82.5(4)
Sb3-O2	2.205(10)	O3-Sb1-Sb2 ¹	99.7(3)	O1-Sb3-O12 ¹	84.7(4)
Zn1-O5	2.296(9)	O3-Sb1-O5	90.5(4)	O1-Sb3-O2	85.4(4)
Zn1-O9	1.951(11)	O3-Sb1-O6	170.9(4)	O12 ¹ -Sb3-O2	164.8(3)
Zn1-O10	1.984(9)	O2-P1-O4	110.0(6)	O9-Zn1-O5	85.6(4)
Zn1-O11	2.002(11)	O10-P1-O4	112.5(5)	O9-Zn1-O10	125.0(4)
Zn1-N00R	2.070(19)	O10-P1-O2	110.4(6)	O9-Zn1-O11	128.0(4)
P2-O12	1.536(11)	Sb2¹-O5-Sb1	99.6(4)	O9-Zn1-N00R	96.3(7)
P2-O13	1.560(10)	Sb2¹-O5-Zn1	122.9(4)	O10-Zn1-O5	86.3(3)
P2-O11	1.506(10)	Sb1-O5-Zn1	122.5(4)	O10-Zn1-O11	105.8(4)
P3-O8	1.546(9)	Sb1-O3-Sb3	141.4(6)	O1-Sb2-O8 ¹	171.6(4)
P3-O6	1.550(9)	P3-O8-Sb2 ¹	123.6(5)	O11-Zn1-O5	87.2(4)
P3-O9	1.505(10)	P3-O6-Sb1	122.9(5)	O9-P3-O6	112.1(6)
P1-O4	1.538(10)	P1-O4-Sb1	128.9(6)	N00R-Zn1-O5	176.2(6)
P1-O2	1.518(11)	Sb2-O1-Sb3	142.6(5)	O12-P2-O13	109.8(6)
P1-O10	1.514(9)	P3-O9-Zn1	125.4(6)	O11-P2-O12	110.0(6)
O5 ¹ -Sb2-Sb1 ¹	40.4(3)	P2-O12-Sb3 ¹	128.1(6)	O11-P2-O13	112.6(6)
O51-Sb2-O81	84.5(4)	O1-Sb2-Sb1 ¹	100.2(3)	O8-P3-O6	108.8(6)
O5 ¹ -Sb2-O13 ¹	89.3(4)	O1-Sb2-O5 ¹	92.3(4)	O9-P3-O8	112.8(6)

 $¹_{1-X,1-Y,1-Z}$

Table 3.5: Selected bond lengths (Å) and bond angles (deg) parameters of compound 3.3

Sb4-Zn2¹ 3.2336(5) O13¹-Sb4-O19 87.12(11) Sb3-O12-Zn2 101.23(12) Sb4-O14 1.933(3) O13¹-Sb4-O16 90.01(11) P3-O20-Sb3¹ 123.78(16) Sb4-O13¹ 1.972(3) O19-Sb4-Zn2¹ 78.55(8) P2-O1-Zn1 144.81(18) Sb4-O19 2.036(3) O16-Sb4-Zn2¹ 129.30(8) P3-O21-Zn2¹ 116.81(16) Sb4-O18 2.019(3) O16-Sb4-O19 88.60(11) P1-O2-Zn1 116.46(17) Sb4-O16 2.006(3) O16-Sb4-O18 169.87(11) O13-Sb3-O17¹ 90.18(11) Sb2-O9 1.925(3) O9-Sb2-O42 176.26(11) O13-Sb3-O12 80.70(11) Sb2-O32 1.957(3) O9-Sb2-O42 176.26(11) O17-Sb3-O12 86.97(11) Sb2-O8 2.014(3) O9-Sb2-O32 94.66(11) O17-Sb3-O12 170.46(10) Sb3-O14 1.931(3) O9-Sb2-O8 95.21(12) O17-Sb3-O20¹ 87.92(11) Sb3-O12 2.023(3) O8-Sb2-O10 169.04(11) O12-Sb3-O20¹ 87.92(11) Sb3-O12²						
Sb4-013¹ 1.972(3) O19-Sb4-Zn2¹ 78.55(8) P2-O1-Zn1 144.81(18) Sb4-019 2.036(3) O16-Sb4-Zn2¹ 129.30(8) P3-O21-Zn2¹ 116.81(16) Sb4-018 2.019(3) O16-Sb4-O19 88.60(11) P1-O2-Zn1 116.46(17) Sb4-016 2.006(3) O16-Sb4-O18 169.87(11) O13-Sb3-O17¹ 90.18(11) Sb2-O9 1.925(3) O9-Sb2-O42 176.26(11) O13-Sb3-O12 80.70(11) Sb2-O32 1.957(3) O9-Sb2-O42 176.26(11) O13-Sb3-O12 80.70(11) Sb2-O8 2.014(3) O9-Sb2-O32 94.66(11) O17¹-Sb3-O12 170.46(10) Sb3-O14 1.931(3) O9-Sb2-O8 95.21(12) O17¹-Sb3-O20¹ 86.97(11) Sb3-O12 2.023(3) O8-Sb2-O10 169.04(11) O12-Sb3-O20¹ 87.92(11) Sb3-O12 2.023(3) O14-Sb3-O13 95.95(11) O9-Sb1-O7² 90.46(12) Sb1-O9 1.929(3) O14-Sb3-O13 95.95(11) O9-Sb1-O5 178.62(11) Sb1-O7²	Sb4-Zn2 ¹	3.2336(5)	O13 ¹ -Sb4-O19	87.12(11)	Sb3-O12-Zn2	101.23(12)
Sb4-O19 2.036(3) O16-Sb4-Zn2¹ 129.30(8) P3-O21-Zn2¹ 116.81(16) Sb4-O18 2.019(3) O16-Sb4-O19 88.60(11) P1-O2-Zn1 116.46(17) Sb4-O16 2.006(3) O16-Sb4-O18 169.87(11) O13-Sb3-O17¹ 90.18(11) Sb2-O9 1.925(3) O9-Sb2-O42 176.26(11) O13-Sb3-O12 80.70(11) Sb2-O32 1.957(3) O9-Sb2-O42 176.26(11) O13-Sb3-O20¹ 86.97(11) Sb2-O8 2.014(3) O9-Sb2-O32 94.66(11) O17¹-Sb3-O20¹ 86.97(11) Sb3-O14 1.931(3) O9-Sb2-O8 95.21(12) O17¹-Sb3-O20¹ 88.84(11) Sb3-O12 2.023(3) O8-Sb2-O10 169.04(11) O12-Sb3-O20¹ 87.92(11) Sb3-O20¹ 2.042(3) O14-Sb3-O13 95.95(11) O9-Sb1-O7² 90.46(12) Sb1-O9 1.929(3) O14-Sb3-O17¹ 90.64(11) O7²-Sb1-O6 171.54(11) Sb1-O3 1.968(3) O14-Sb3-O17¹ 90.64(11) O7²-Sb1-O6 171.54(11) Sb1-O3	Sb4-O14	1.933(3)	O13 ¹ -Sb4-O16	90.01(11)	P3-O20-Sb3 ¹	123.78(16)
Sb4-O18 2.019(3) O16-Sb4-O19 88.60(11) P1-O2-Zn1 116.46(17) Sb4-O16 2.006(3) O16-Sb4-O18 169.87(11) O13-Sb3-O17¹ 90.18(11) Sb2-O9 1.925(3) O9-Sb2-O42 176.26(11) O13-Sb3-O12 80.70(11) Sb2-O32 1.957(3) O9-Sb2-O42 176.26(11) O17-Sb3-O12 80.70(11) Sb2-O8 2.014(3) O9-Sb2-O32 94.66(11) O17-Sb3-O12 170.46(10) Sb3-O14 1.931(3) O9-Sb2-O8 95.21(12) O17¹-Sb3-O20¹ 88.84(11) Sb3-O12 2.023(3) O8-Sb2-O10 169.04(11) O12-Sb3-O20¹ 87.92(11) Sb3-O12 2.023(3) O14-Sb3-O13 95.95(11) O9-Sb1-O7² 90.46(12) Sb1-O9 1.929(3) O14-Sb3-O12¹ 93.05(11) O7²-Sb1-O5 178.62(11) Sb1-O7² 2.009(3) O14-Sb3-O12² 93.05(11) O7²-Sb1-O5 178.62(11) Sb1-O3 1.968(3) O14-Sb3-O12² 93.05(11) O7²-Sb1-O5 88.46(12) Sb1-O3 <t< td=""><td>Sb4-O13¹</td><td>1.972(3)</td><td>O19-Sb4-Zn2¹</td><td>78.55(8)</td><td>P2-O1-Zn1</td><td>144.81(18)</td></t<>	Sb4-O13 ¹	1.972(3)	O19-Sb4-Zn2 ¹	78.55(8)	P2-O1-Zn1	144.81(18)
Sb4-O16 2.006(3) O16-Sb4-O18 169.87(11) O13-Sb3-O17 ¹ 90.18(11) Sb2-O9 1.925(3) O9-Sb2-O42 176.26(11) O13-Sb3-O12 80.70(11) Sb2-O32 1.957(3) O9-Sb2-O10 91.55(12) O13-Sb3-O20 ¹ 86.97(11) Sb2-O8 2.014(3) O9-Sb2-O32 94.66(11) O17 ¹ -Sb3-O12 170.46(10) Sb3-O14 1.931(3) O9-Sb2-O8 95.21(12) O17 ¹ -Sb3-O20 ¹ 88.84(11) Sb3-O12 2.023(3) O8-Sb2-O10 169.04(11) O12-Sb3-O20 ¹ 87.92(11) Sb3-O20 ¹ 2.042(3) O14-Sb3-O13 95.95(11) O9-Sb1-O7 ² 90.46(12) Sb1-O9 1.929(3) O14-Sb3-O17 ¹ 90.64(11) O9-Sb1-O7 ² 90.46(12) Sb1-O9 1.929(3) O14-Sb3-O12 93.05(11) O7 ² -Sb1-O5 178.62(11) Sb1-O9 1.929(3) O14-Sb3-O12 93.05(11) O7 ² -Sb1-O5 88.46(12) Sb1-O3 1.968(3) O14-Sb3-O12 177.04(11) O7 ² -Sb1-O5 88.46(12) <t< td=""><td>Sb4-O19</td><td>2.036(3)</td><td>O16-Sb4-Zn2¹</td><td>129.30(8)</td><td>P3-O21-Zn2¹</td><td>116.81(16)</td></t<>	Sb4-O19	2.036(3)	O16-Sb4-Zn2 ¹	129.30(8)	P3-O21-Zn2 ¹	116.81(16)
Sb2-O9 1.925(3) O9-Sb2-O42 176.26(11) O13-Sb3-O12 80.70(11) Sb2-O32 1.957(3) O9-Sb2-O10 91.55(12) O13-Sb3-O20 ¹ 86.97(11) Sb2-O8 2.014(3) O9-Sb2-O32 94.66(11) O17 ¹ -Sb3-O20 ¹ 86.97(11) Sb3-O14 1.931(3) O9-Sb2-O8 95.21(12) O17 ¹ -Sb3-O20 ¹ 88.84(11) Sb3-O12 2.023(3) O8-Sb2-O10 169.04(11) O12-Sb3-O20 ¹ 87.92(11) Sb3-O20 ¹ 2.042(3) O14-Sb3-O13 95.95(11) O9-Sb1-O7 ² 90.46(12) Sb1-O9 1.929(3) O14-Sb3-O17 ¹ 90.64(11) O9-Sb1-O5 178.62(11) Sb1-O9 1.929(3) O14-Sb3-O17 ¹ 90.64(11) O7 ² -Sb1-O5 178.62(11) Sb1-O9 1.929(3) O14-Sb3-O12 93.05(11) O7 ² -Sb1-O5 178.62(11) Sb1-O9 1.929(3) O14-Sb3-O12 93.05(11) O7 ² -Sb1-O5 88.46(12) Sb1-O3 1.968(3) O14-Sb3-O12 177.04(11) O7 ² -Sb1-O5 88.84(12) <t< td=""><td>Sb4-O18</td><td>2.019(3)</td><td>O16-Sb4-O19</td><td>88.60(11)</td><td>P1-O2-Zn1</td><td>116.46(17)</td></t<>	Sb4-O18	2.019(3)	O16-Sb4-O19	88.60(11)	P1-O2-Zn1	116.46(17)
Sb2-O32 1.957(3) O9-Sb2-O10 91.55(12) O13-Sb3-O20¹ 86.97(11) Sb2-O8 2.014(3) O9-Sb2-O32 94.66(11) O17¹-Sb3-O12 170.46(10) Sb3-O14 1.931(3) O9-Sb2-O8 95.21(12) O17¹-Sb3-O20¹ 88.84(11) Sb3-O12 2.023(3) O8-Sb2-O10 169.04(11) O12-Sb3-O20¹ 87.92(11) Sb3-O20¹ 2.042(3) O14-Sb3-O13 95.95(11) O9-Sb1-O7² 90.46(12) Sb1-O9 1.929(3) O14-Sb3-O17¹ 90.64(11) O9-Sb1-O5 178.62(11) Sb1-O7² 2.009(3) O14-Sb3-O12 93.05(11) O7²-Sb1-O6 171.54(11) Sb1-O3 1.968(3) O14-Sb3-O20¹ 177.04(11) O7²-Sb1-O5 88.46(12) Sb1-O3 1.968(3) O14-Sb3-O20¹ 177.04(11) O7²-Sb1-O5 88.46(12) Sb1-O6 2.024(3) O21-P3-O20 108.34(16) O3-Sb1-O7² 91.01(11) Sb1-O5 2.042(3) O21-P3-O19 112.21(16) O3-Sb1-O6* 80.85(11) Zn2-O18¹ <th< td=""><td>Sb4-O16</td><td>2.006(3)</td><td>O16-Sb4-O18</td><td>169.87(11)</td><td>O13-Sb3-O17¹</td><td>90.18(11)</td></th<>	Sb4-O16	2.006(3)	O16-Sb4-O18	169.87(11)	O13-Sb3-O17 ¹	90.18(11)
Sb2-O8 2.014(3) O9-Sb2-O32 94.66(11) O17¹-Sb3-O12 170.46(10) Sb3-O14 1.931(3) O9-Sb2-O8 95.21(12) O17¹-Sb3-O20¹ 88.84(11) Sb3-O12 2.023(3) O8-Sb2-O10 169.04(11) O12-Sb3-O20¹ 87.92(11) Sb3-O20¹ 2.042(3) O14-Sb3-O13 95.95(11) O9-Sb1-O7² 90.46(12) Sb1-O9 1.929(3) O14-Sb3-O17¹ 90.64(11) O9-Sb1-O5 178.62(11) Sb1-O7² 2.009(3) O14-Sb3-O12 93.05(11) O7²-Sb1-O6 171.54(11) Sb1-O3 1.968(3) O14-Sb3-O20¹ 177.04(11) O7²-Sb1-O5 88.46(12) Sb1-O3 1.968(3) O14-Sb3-O20¹ 177.04(11) O7²-Sb1-O5 88.46(12) Sb1-O6 2.024(3) O19-P3-O20 108.34(16) O3-Sb1-O7² 91.01(11) Sb1-O5 2.042(3) O21-P3-O19 112.21(16) O3-Sb1-O6* 80.85(11) Zn2-O18¹ 2.156(3) O21-P3-O19 112.21(16) O3-Sb1-O7² 91.01(11) Zn2-O12¹ <th< td=""><td>Sb2-O9</td><td>1.925(3)</td><td>O9-Sb2-O42</td><td>176.26(11)</td><td>O13-Sb3-O12</td><td>80.70(11)</td></th<>	Sb2-O9	1.925(3)	O9-Sb2-O42	176.26(11)	O13-Sb3-O12	80.70(11)
Sb3-O14 1.931(3) O9-Sb2-O8 95.21(12) O17¹-Sb3-O20¹ 88.84(11) Sb3-O12 2.023(3) O8-Sb2-O10 169.04(11) O12-Sb3-O20¹ 87.92(11) Sb3-O20¹ 2.042(3) O14-Sb3-O13 95.95(11) O9-Sb1-O7² 90.46(12) Sb1-O9 1.929(3) O14-Sb3-O12¹ 93.05(11) O9-Sb1-O5 178.62(11) Sb1-O7² 2.009(3) O14-Sb3-O12¹ 93.05(11) O7²-Sb1-O6 171.54(11) Sb1-O3 1.968(3) O14-Sb3-O20¹ 177.04(11) O7²-Sb1-O5 88.46(12) Sb1-O6 2.024(3) O19-P3-O20 108.34(16) O3-Sb1-O7² 91.01(11) Sb1-O5 2.042(3) O21-P3-O20 111.76(16) O3-Sb1-O6 80.85(11) Zn2-O18¹ 2.156(3) O21-P3-O20 111.76(16) O13-Zn2-Sb4¹ 36.58(7) Zn2-O12 2.180(3) Sb3-O14-Sb4 142.73(14) O15-Zn2-O18¹ 98.83(11) Zn2-O21¹ 2.092(3) P1-O4-Sb2² 123.99(16) O15-Zn2-O12 93.71(11) Zn2-N2 <	Sb2-O32	1.957(3)	O9-Sb2-O10	91.55(12)	O13-Sb3-O20 ¹	86.97(11)
Sb3-O12 2.023(3) O8-Sb2-O10 169.04(11) O12-Sb3-O20¹ 87.92(11) Sb3-O20¹ 2.042(3) O14-Sb3-O13 95.95(11) O9-Sb1-O7² 90.46(12) Sb1-O9 1.929(3) O14-Sb3-O17¹ 90.64(11) O9-Sb1-O5 178.62(11) Sb1-O7² 2.009(3) O14-Sb3-O12 93.05(11) O7²-Sb1-O6 171.54(11) Sb1-O3 1.968(3) O14-Sb3-O20¹ 177.04(11) O7²-Sb1-O5 88.46(12) Sb1-O6 2.024(3) O19-P3-O20 108.34(16) O3-Sb1-O7² 91.01(11) Sb1-O5 2.042(3) O21-P3-O19 112.21(16) O3-Sb1-O6 80.85(11) Zn2-O18¹ 2.156(3) O21-P3-O20 111.76(16) O13-Zn2-Sb4¹ 36.58(7) Zn2-O12 2.180(3) Sb3-O14-Sb4 142.73(14) O15-Zn2-O18¹ 98.83(11) Zn2-O21¹ 2.092(3) P1-O4-Sb2² 123.99(16) O15-Zn2-O12 93.71(11) Zn2-ON2 2.182(3) Sb3-O13-Zb4² 137.80(14) N2-Zn2-O21¹ 174.77(12) Zn1-O1	Sb2-O8	2.014(3)	O9-Sb2-O32	94.66(11)	O17 ¹ -Sb3-O12	170.46(10)
Sb3-O20¹ 2.042(3) O14-Sb3-O13 95.95(11) O9-Sb1-O7² 90.46(12) Sb1-O9 1.929(3) O14-Sb3-O17¹ 90.64(11) O9-Sb1-O5 178.62(11) Sb1-O7² 2.009(3) O14-Sb3-O12 93.05(11) O7²-Sb1-O6 171.54(11) Sb1-O3 1.968(3) O14-Sb3-O20¹ 177.04(11) O7²-Sb1-O5 88.46(12) Sb1-O6 2.024(3) O19-P3-O20 108.34(16) O3-Sb1-O7² 91.01(11) Sb1-O5 2.042(3) O21-P3-O19 112.21(16) O3-Sb1-O6 80.85(11) Zn2-O18¹ 2.156(3) O21-P3-O20 111.76(16) O13-Zn2-Sb4¹ 36.58(7) Zn2-O12 2.180(3) Sb3-O14-Sb4 142.73(14) O15-Zn2-O18¹ 98.83(11) Zn2-O21¹ 2.092(3) P1-O4-Sb2² 123.99(16) O15-Zn2-O12 93.71(11) Zn2-N2 2.069(4) Sb4¹-O13-Zn2 102.32(11) O15-Zn2-O12 93.71(11) Zn1-O10² 2.182(3) Sb3-O13-Sb4¹ 137.80(14) N2-Zn2-O21¹ 174.77(12) Zn1-O1	Sb3-O14	1.931(3)	O9-Sb2-O8	95.21(12)	O17 ¹ -Sb3-O20 ¹	88.84(11)
Sb1-O9 1.929(3) O14-Sb3-O17¹ 90.64(11) O9-Sb1-O5 178.62(11) Sb1-O7² 2.009(3) O14-Sb3-O12 93.05(11) O7²-Sb1-O6 171.54(11) Sb1-O3 1.968(3) O14-Sb3-O20¹ 177.04(11) O7²-Sb1-O5 88.46(12) Sb1-O6 2.024(3) O19-P3-O20 108.34(16) O3-Sb1-O7² 91.01(11) Sb1-O5 2.042(3) O21-P3-O19 112.21(16) O3-Sb1-O6 80.85(11) Zn2-O18¹ 2.156(3) O21-P3-O20 111.76(16) O13-Zn2-Sb4¹ 36.58(7) Zn2-O12 2.180(3) Sb3-O14-Sb4 142.73(14) O15-Zn2-O18¹ 98.83(11) Zn2-O21¹ 2.092(3) P1-O4-Sb2² 123.99(16) O15-Zn2-O12 93.71(11) Zn2-N2 2.069(4) Sb4¹-O13-Zn2 102.32(11) O15-Zn2-O21¹ 174.77(12) Zn1-O10² 2.182(3) Sb3-O13-Zb2 103.51(12) N2-Zn2-O13 173.16(12) Zn1-O1 2.005(3) Sb3-O13-Zb2 103.51(12) N2-Zn2-O18¹ 173.16(12) Zn1-N1	Sb3-O12	2.023(3)	O8-Sb2-O10	169.04(11)	O12-Sb3-O20 ¹	87.92(11)
Sb1-O72 2.009(3) O14-Sb3-O12 93.05(11) O72-Sb1-O6 171.54(11) Sb1-O3 1.968(3) O14-Sb3-O201 177.04(11) O72-Sb1-O5 88.46(12) Sb1-O6 2.024(3) O19-P3-O20 108.34(16) O3-Sb1-O72 91.01(11) Sb1-O5 2.042(3) O21-P3-O19 112.21(16) O3-Sb1-O6 80.85(11) Zn2-O181 2.156(3) O21-P3-O20 111.76(16) O13-Zn2-Sb41 36.58(7) Zn2-O12 2.180(3) Sb3-O14-Sb4 142.73(14) O15-Zn2-O181 98.83(11) Zn2-O211 2.092(3) P1-O4-Sb22 123.99(16) O15-Zn2-O12 93.71(11) Zn2-N2 2.069(4) Sb41-O13-Zn2 102.32(11) O15-Zn2-O211 174.77(12) Zn1-O102 2.182(3) Sb3-O13-Zb2 103.51(12) N2-Zn2-O13 173.16(12) Zn1-O2 2.098(3) Sb2-O13-Zb2 100.78(11) N2-Zn2-O181 173.16(12) Zn1-N1 2.082(4) P4-O17-Sb31 138.27(16) N2-Zn2-O12 113.95(12) P2-O7	Sb3-O20 ¹	2.042(3)	O14-Sb3-O13	95.95(11)	O9-Sb1-O7 ²	90.46(12)
Sb1-O3 1.968(3) O14-Sb3-O20¹ 177.04(11) O7²-Sb1-O5 88.46(12) Sb1-O6 2.024(3) O19-P3-O20 108.34(16) O3-Sb1-O7² 91.01(11) Sb1-O5 2.042(3) O21-P3-O19 112.21(16) O3-Sb1-O6 80.85(11) Zn2-O18¹ 2.156(3) O21-P3-O20 111.76(16) O13-Zn2-Sb4¹ 36.58(7) Zn2-O12 2.180(3) Sb3-O14-Sb4 142.73(14) O15-Zn2-O18¹ 98.83(11) Zn2-O21¹ 2.092(3) P1-O4-Sb2² 123.99(16) O15-Zn2-O12¹ 93.71(11) Zn2-N2 2.069(4) Sb4¹-O13-Zn2 102.32(11) O15-Zn2-O12¹ 174.77(12) Zn1-O10² 2.182(3) Sb3-O13-Sb4¹ 137.80(14) N2-Zn2-Sb4¹ 136.62(10) Zn1-O1 2.005(3) Sb3-O13-Zn2 103.51(12) N2-Zn2-O13 173.16(12) Zn1-O2 2.098(3) Sb2-O10-Zn1² 100.78(11) N2-Zn2-O13 173.16(12) Zn1-N1 2.082(4) P4-O17-Sb3¹ 138.27(16) N2-Zn2-O12 113.95(12) P2-O7	Sb1-O9	1.929(3)	O14-Sb3-O17 ¹	90.64(11)	O9-Sb1-O5	178.62(11)
Sb1-O6 2.024(3) O19-P3-O20 108.34(16) O3-Sb1-O72 91.01(11) Sb1-O5 2.042(3) O21-P3-O19 112.21(16) O3-Sb1-O6 80.85(11) Zn2-O18¹ 2.156(3) O21-P3-O20 111.76(16) O13-Zn2-Sb4¹ 36.58(7) Zn2-O12 2.180(3) Sb3-O14-Sb4 142.73(14) O15-Zn2-O18¹ 98.83(11) Zn2-O21¹ 2.092(3) P1-O4-Sb2² 123.99(16) O15-Zn2-O12 93.71(11) Zn2-N2 2.069(4) Sb4¹-O13-Zn2 102.32(11) O15-Zn2-O21¹ 174.77(12) Zn1-O10² 2.182(3) Sb3-O13-Zn2 102.32(11) O15-Zn2-O21¹ 174.77(12) Zn1-O1 2.005(3) Sb3-O13-Zb1² 103.51(12) N2-Zn2-O13 173.16(12) Zn1-O2 2.098(3) Sb2-O10-Zn1² 100.78(11) N2-Zn2-O18¹ 99.82(12) Zn1-N1 2.082(4) P4-O17-Sb3¹ 138.27(16) N2-Zn2-O12 113.95(12) P2-O7 1.550(3) Sb2-O9-Sb1 144.59(15) O1-Zn1-O10² 97.00(11) P2-O8	Sb1-O7 ²	2.009(3)	O14-Sb3-O12	93.05(11)	O7 ² -Sb1-O6	171.54(11)
Sb1-O5 2.042(3) O21-P3-O19 112.21(16) O3-Sb1-O6 80.85(11) Zn2-O18¹ 2.156(3) O21-P3-O20 111.76(16) O13-Zn2-Sb4¹ 36.58(7) Zn2-O12 2.180(3) Sb3-O14-Sb4 142.73(14) O15-Zn2-O18¹ 98.83(11) Zn2-O21¹ 2.092(3) P1-O4-Sb2² 123.99(16) O15-Zn2-O12 93.71(11) Zn2-N2 2.069(4) Sb4¹-O13-Zn2 102.32(11) O15-Zn2-O21¹ 174.77(12) Zn1-O10² 2.182(3) Sb3-O13-Sb4¹ 137.80(14) N2-Zn2-Sb4¹ 136.62(10) Zn1-O1 2.005(3) Sb3-O13-Zn2 103.51(12) N2-Zn2-O13 173.16(12) Zn1-O2 2.098(3) Sb2-O10-Zn1² 100.78(11) N2-Zn2-O18¹ 99.82(12) Zn1-N1 2.082(4) P4-O17-Sb3¹ 138.27(16) N2-Zn2-O12 113.95(12) P2-O7 1.550(3) Sb2-O9-Sb1 144.59(15) O1-Zn1-O10² 97.00(11) P2-O8 1.543(3) Sb2²-O3-Zn1 103.21(11) O2-Zn1-O3 90.99(11) O14-Sb4-O13¹	Sb1-O3	1.968(3)	O14-Sb3-O20 ¹	177.04(11)	O7 ² -Sb1-O5	88.46(12)
$\begin{array}{cccccccccccccccccccccccccccccccccccc$	Sb1-O6	2.024(3)	O19-P3-O20	108.34(16)	O3-Sb1-O7 ²	91.01(11)
$\begin{array}{cccccccccccccccccccccccccccccccccccc$	Sb1-O5	2.042(3)	O21-P3-O19	112.21(16)	O3-Sb1-O6	80.85(11)
$\begin{array}{cccccccccccccccccccccccccccccccccccc$	Zn2-O18 ¹	2.156(3)	O21-P3-O20	111.76(16)	O13-Zn2-Sb4 ¹	36.58(7)
$\begin{array}{cccccccccccccccccccccccccccccccccccc$	Zn2-O12	2.180(3)	Sb3-O14-Sb4	142.73(14)	O15-Zn2-O18 ¹	98.83(11)
$\begin{array}{cccccccccccccccccccccccccccccccccccc$	Zn2-O21 ¹	2.092(3)	P1-O4-Sb2 ²	123.99(16)	O15-Zn2-O12	93.71(11)
Zn1-O1 2.005(3) Sb3-O13-Zn2 103.51(12) N2-Zn2-O13 173.16(12) Zn1-O2 2.098(3) Sb2-O10-Zn1² 100.78(11) N2-Zn2-O18¹ 99.82(12) Zn1-N1 2.082(4) P4-O17-Sb3¹ 138.27(16) N2-Zn2-O12 113.95(12) P2-O7 1.550(3) Sb2-O9-Sb1 144.59(15) O1-Zn1-O10² 97.00(11) P2-O8 1.543(3) Sb2²-O3-Sb1 138.05(14) O1-Zn1-O2 176.71(12) P2-O1 1.498(3) Sb2²-O3-Zn1 103.21(11) O2-Zn1-O3 90.99(11) O14-Sb4-Zn2¹ 103.27(8) Sb1-O3-Zn1 103.06(12) N1-Zn1-O10² 104.76(12) O14-Sb4-O13¹ 95.14(11) P4-O15-Zn2 142.41(18) N1-Zn1-O3 177.64(13) O14-Sb4-O19 177.73(1) Sb1-O6-Zn1 101.03(12) N1-Zn1-O6 109.19(13) O14-Sb4-O18 93.81(11) P2-O8-Sb2 138.86(18) O8-P2-O7 110.19(16)	Zn2-N2	2.069(4)	Sb4 ¹ -O13-Zn2	102.32(11)	O15-Zn2-O21 ¹	174.77(12)
$\begin{array}{cccccccccccccccccccccccccccccccccccc$	Zn1-O10 ²	2.182(3)	Sb3-O13-Sb4 ¹	137.80(14)	N2-Zn2-Sb4 ¹	136.62(10)
Zn1-N1 2.082(4) P4-O17-Sb3¹ 138.27(16) N2-Zn2-O12 113.95(12) P2-O7 1.550(3) Sb2-O9-Sb1 144.59(15) O1-Zn1-O10² 97.00(11) P2-O8 1.543(3) Sb2²-O3-Sb1 138.05(14) O1-Zn1-O2 176.71(12) P2-O1 1.498(3) Sb2²-O3-Zn1 103.21(11) O2-Zn1-O3 90.99(11) O14-Sb4-Zn2¹ 103.27(8) Sb1-O3-Zn1 103.06(12) N1-Zn1-O10² 104.76(12) O14-Sb4-O13¹ 95.14(11) P4-O15-Zn2 142.41(18) N1-Zn1-O3 177.64(13) O14-Sb4-O19 177.73(1) Sb1-O6-Zn1 101.03(12) N1-Zn1-O6 109.19(13) O14-Sb4-O18 93.81(11) P2-O8-Sb2 138.86(18) O8-P2-O7 110.19(16)	Zn1-O1	2.005(3)	Sb3-O13-Zn2	103.51(12)	N2-Zn2-O13	173.16(12)
P2-O7 1.550(3) Sb2-O9-Sb1 144.59(15) O1-Zn1-O10² 97.00(11) P2-O8 1.543(3) Sb2²-O3-Sb1 138.05(14) O1-Zn1-O2 176.71(12) P2-O1 1.498(3) Sb2²-O3-Zn1 103.21(11) O2-Zn1-O3 90.99(11) O14-Sb4-Zn2¹ 103.27(8) Sb1-O3-Zn1 103.06(12) N1-Zn1-O10² 104.76(12) O14-Sb4-O13¹ 95.14(11) P4-O15-Zn2 142.41(18) N1-Zn1-O3 177.64(13) O14-Sb4-O19 177.73(1) Sb1-O6-Zn1 101.03(12) N1-Zn1-O6 109.19(13) O14-Sb4-O18 93.81(11) P2-O8-Sb2 138.86(18) O8-P2-O7 110.19(16)	Zn1-O2	2.098(3)	Sb2-O10-Zn1 ²	100.78(11)	N2-Zn2-O18 ¹	99.82(12)
P2-O8 1.543(3) Sb2²-O3-Sb1 138.05(14) O1-Zn1-O2 176.71(12) P2-O1 1.498(3) Sb2²-O3-Zn1 103.21(11) O2-Zn1-O3 90.99(11) O14-Sb4-Zn2¹ 103.27(8) Sb1-O3-Zn1 103.06(12) N1-Zn1-O10² 104.76(12) O14-Sb4-O13¹ 95.14(11) P4-O15-Zn2 142.41(18) N1-Zn1-O3 177.64(13) O14-Sb4-O19 177.73(1) Sb1-O6-Zn1 101.03(12) N1-Zn1-O6 109.19(13) O14-Sb4-O18 93.81(11) P2-O8-Sb2 138.86(18) O8-P2-O7 110.19(16)	Zn1-N1	2.082(4)	P4-O17-Sb3 ¹	138.27(16)	N2-Zn2-O12	113.95(12)
P2-O1 1.498(3) Sb2²-O3-Zn1 103.21(11) O2-Zn1-O3 90.99(11) O14-Sb4-Zn2¹ 103.27(8) Sb1-O3-Zn1 103.06(12) N1-Zn1-O10² 104.76(12) O14-Sb4-O13¹ 95.14(11) P4-O15-Zn2 142.41(18) N1-Zn1-O3 177.64(13) O14-Sb4-O19 177.73(1) Sb1-O6-Zn1 101.03(12) N1-Zn1-O6 109.19(13) O14-Sb4-O18 93.81(11) P2-O8-Sb2 138.86(18) O8-P2-O7 110.19(16)	P2-O7	1.550(3)	Sb2-O9-Sb1	144.59(15)	O1-Zn1-O10 ²	97.00(11)
O14-Sb4-Zn2¹ 103.27(8) Sb1-O3-Zn1 103.06(12) N1-Zn1-O10² 104.76(12) O14-Sb4-O13¹ 95.14(11) P4-O15-Zn2 142.41(18) N1-Zn1-O3 177.64(13) O14-Sb4-O19 177.73(1) Sb1-O6-Zn1 101.03(12) N1-Zn1-O6 109.19(13) O14-Sb4-O18 93.81(11) P2-O8-Sb2 138.86(18) O8-P2-O7 110.19(16)	P2-O8	1.543(3)	Sb2 ² -O3-Sb1	138.05(14)	O1-Zn1-O2	176.71(12)
O14-Sb4-O13¹ 95.14(11) P4-O15-Zn2 142.41(18) N1-Zn1-O3 177.64(13) O14-Sb4-O19 177.73(1) Sb1-O6-Zn1 101.03(12) N1-Zn1-O6 109.19(13) O14-Sb4-O18 93.81(11) P2-O8-Sb2 138.86(18) O8-P2-O7 110.19(16)	P2-O1	1.498(3)	Sb2 ² -O3-Zn1	103.21(11)	O2-Zn1-O3	90.99(11)
O14-Sb4-O19 177.73(1) Sb1-O6-Zn1 101.03(12) N1-Zn1-O6 109.19(13) O14-Sb4-O18 93.81(11) P2-O8-Sb2 138.86(18) O8-P2-O7 110.19(16)	O14-Sb4-Zn2 ¹	103.27(8)	Sb1-O3-Zn1	103.06(12)	N1-Zn1-O10 ²	104.76(12)
O14-Sb4-O18 93.81(11) P2-O8-Sb2 138.86(18) O8-P2-O7 110.19(16)	O14-Sb4-O13 ¹	95.14(11)	P4-O15-Zn2	142.41(18)	N1-Zn1-O3	177.64(13)
	O14-Sb4-O19	177.73(1)	Sb1-O6-Zn1	101.03(12)	N1-Zn1-O6	109.19(13)
O14-Sb4-O16 91.22(11) P1-O5-Sb1 124.24(16) O4-P1-O5 108.71(16)	O14-Sb4-O18	93.81(11)	P2-O8-Sb2	138.86(18)	O8-P2-O7	110.19(16)
	O14-Sb4-O16	91.22(11)	P1-O5-Sb1	124.24(16)	O4-P1-O5	108.71(16)

¹2-X,-Y,-Z; ²1-X,2-Y,1-Z

Table 3.6: Selected bond lengths (Å) and bond angles (deg) parameters of compound 3.4

				1	
Sb2-O1	1.9235(17)	O1-Sb2-O5 ¹	177.97(7)	O6-Zn1-N1	90.73(8)
Sb2-O10	1.9584(16)	O10-Sb2-O8	90.06(7)	O4-Zn1-O10 ¹	90.00(7)
Sb2-O8	2.0163(18)	O10-Sb2-O9	79.61(7)	O4-Zn1-O3	82.00(7)
Sb2-O9	2.0286(19)	O10-Sb2-O5 ¹	86.84(7)	N1-Zn1-O10 ¹	176.30(8)
Sb2-O5 ¹	2.0528(17)	O8-Sb2-O9	168.36(7)	Sb2-O10-Zn1 ¹	102.88(7)
Sb1-O1	1.9284(17)	O8-Sb2-O5 ¹	87.21(7)	Sb11-O10-Zn1 ¹	102.91(7)
Sb1-O2	2.0557(17)	O9-Sb2-O5 ¹	86.88(7)	P2-O8-Sb2	136.79(11)
Sb1-O10 ¹	1.9641(15)	O1-Sb1-O2	179.69(7)	Sb1-O3-Zn1	103.20(7)
Sb1-O3	2.0175(18)	O1-Sb1-O10 ¹	94.07(7)	P2-O7-Sb1 ¹	138.04(11)
Sb1-O7 ¹	2.0105(18)	O1-Sb1-O3	92.69(7)	Sb2-O9-Zn1 ¹	102.98(7)
Zn1-O10 ¹	2.1928(18)	O1-Sb1-O7 ¹	91.40(7)	P1-O5-Sb2 ¹	124.13(10)
Zn1-O3	2.1340(17)	O10 ¹ -Sb1-O2	86.19(7)	P2-O6-Zn1	144.28(12)
Zn1-O9 ¹	2.1231(17)	O10 ¹ -Sb1-O3	79.99(7)	P1-O4-Zn1	116.40(10)
Zn1-O6	2.0039(18)	O10 ¹ -Sb1-O7 ¹	89.59(7)	N1-Zn1-O3	110.01(8)
Zn1-O4	2.1285(18)	O3-Sb1-O2	87.19(7)	N1-Zn1-O9 ¹	104.42(8)
Zn1-N1	2.101(2)	O7 ¹ -Sb1-O2	88.77(7)	N1-Zn1-O4	87.72(8)
P2-O8	1.5502(17)	O7 ¹ -Sb1-O3	169.05(7)	O8-P2-O7	110.96(10)
P2-O7	1.5515(18)	O3-Zn1-O10 ¹	72.52(6)	O6-P2-O8	112.97(10)
P2-O6	1.5006(18)	O9 ¹ -Zn1-O10 ¹	72.51(6)	O6-P2-O7	113.06(10)
P1-O2	1.5528(17)	O9 ¹ -Zn1-O3	143.01(7)	O5-P1-O2	109.31(10)
P1-O5	1.5488(18)	O9 ¹ -Zn1-O4	86.33(7)	O4-P1-O2	111.72(10)
P1-O4	1.506(2)	O6-Zn1-O10 ¹	91.76(7)	O4-P1-O5	112.21(10)
O1-Sb2-O10	94.94(7)	O6-Zn1-O3	94.72(7)	Sb2-O1-Sb1	145.67(9)
O1-Sb2-O8	91.80(7)	O6-Zn1-O9 ¹	98.00(7)	P1-O2-Sb1	123.84(10)
O1-Sb2-O9	94.41(8)	O6-Zn1-O4	175.65(7)	Sb2-O10-Sb1 ¹	139.15(10)

¹1/2-X,1/2-Y,1-Z

Table 3.7: Shape calculation of compounds 3.1 -3.41a) Summary of SHAPE analysis for Zn1 in 3.1

S. No	Geometry	CShM value for Zn1 in 3.1
1	Pentagon (D5h)	34.132
2	Vacant octahedron (C4v)	5.697
3	Trigonal bipyramid (D3h)	2.446
4	Spherical square pyramid (C4v)	4.858
5	Johnson trigonal bipyramid J12 (D3h)	1.121

1b) Summary of SHAPE analysis for Zn2 in 3.1

S. No	Geometry	CShM value for Zn2 in 3.1
1	Hexagon (D6h)	30.061
2	Pentagonal pyramid (C5v)	27.828
3	Octahedron (Oh)	1.625
4	Trigonal prism (D3h)	15.534
5	Johnson pentagonal pyramid J2 (C5v)	29.446

1c) Summary of SHAPE analysis for Sb in 3.1

S. No	Geometry	CShM value for Sb1 in 3.1	CShM value for Sb2 in 3.1
1	Hexagon (D6h)	31.410	31.475
2	Pentagonal pyramid (C5v)	28.578	28.255
3	Octahedron (Oh)	0.496	0.507
4	Trigonal prism (D3h)	16.149	15.984
5	Johnson pentagonal pyramid J2 (C5v)	32.118	31.764

2a) Summary of SHAPE analysis for Zn1 in 3.2

S. No	Geometry	CShM value for Zn1 in 3.2
1	Pentagon (D5h)	32.748
2	Vacant octahedron (C4v)	6.007
3	Trigonal bipyramid (D3h)	0.723
4	Spherical square pyramid (C4v)	4.804
5	Johnson trigonal bipyramid J12 (D3h)	1.897

2b) Summary of SHAPE analysis for Sb in 3.2

S.No	Geometry	CShM value for Sb1 in 3.2	CShM value for Sb2 in 3.2
1	Hexagon (D6h)	31.641	31.966
2	Pentagonal pyramid (C5v)	27.843	27.237
3	Octahedron (Oh)	0.519	0.548
4	Trigonal prism (D3h)	15.554	14.607
5	Johnson pentagonal pyramid J2 (C5v)	31.251	30.774

2c) Summary of SHAPE analysis for Sb3 in 3.2

S. No	Geometry	CShM value for Sb3 in 3.2
1	Square (D4h)	13.303
2	Tetrahedron (Td)	17.903
3	Seesaw (C2v)	1.713
4	Vacant trigonal bipyramid (C3v)	15.260

3) Summary of SHAPE analysis for Zn and Sb atoms in 3.3

S. No	Geometry	CShM value for Zn1 in 3.3	CShM value for Sb1 in 3.3	CShM value for Sb2 in 3.3
1	Hexagon (D6h)	34.393	32.261	31.242
2	Pentagonal pyramid (C5v)	21.809	27.371	26.782
3	Octahedron (Oh)	2.495	0.345	0.477
4	Trigonal prism (D3h)	11.235	14.941	14.185
5	Johnson pentagonal pyramid J2 (C5v)	25.865	31.057	30.111

4) Summary of SHAPE analysis for Zn and Sb atoms in 3.4

S. No	Geometry	CShM value for Zn1 in 3.4	CShM value for Sb1 in 3.4	CShM value for Sb2 in 3.4
1	Hexagon (D6h)	34.176	32.391	32.456
2	Pentagonal pyramid (C5v)	21.550	27.356	27.438
3	Octahedron (Oh)	2.485	0.405	0.438
4	Trigonal prism (D3h)	10.988	15.121	14.939
5	Johnson pentagonal pyramid J2 (C5v)	25.390	31.118	31.221

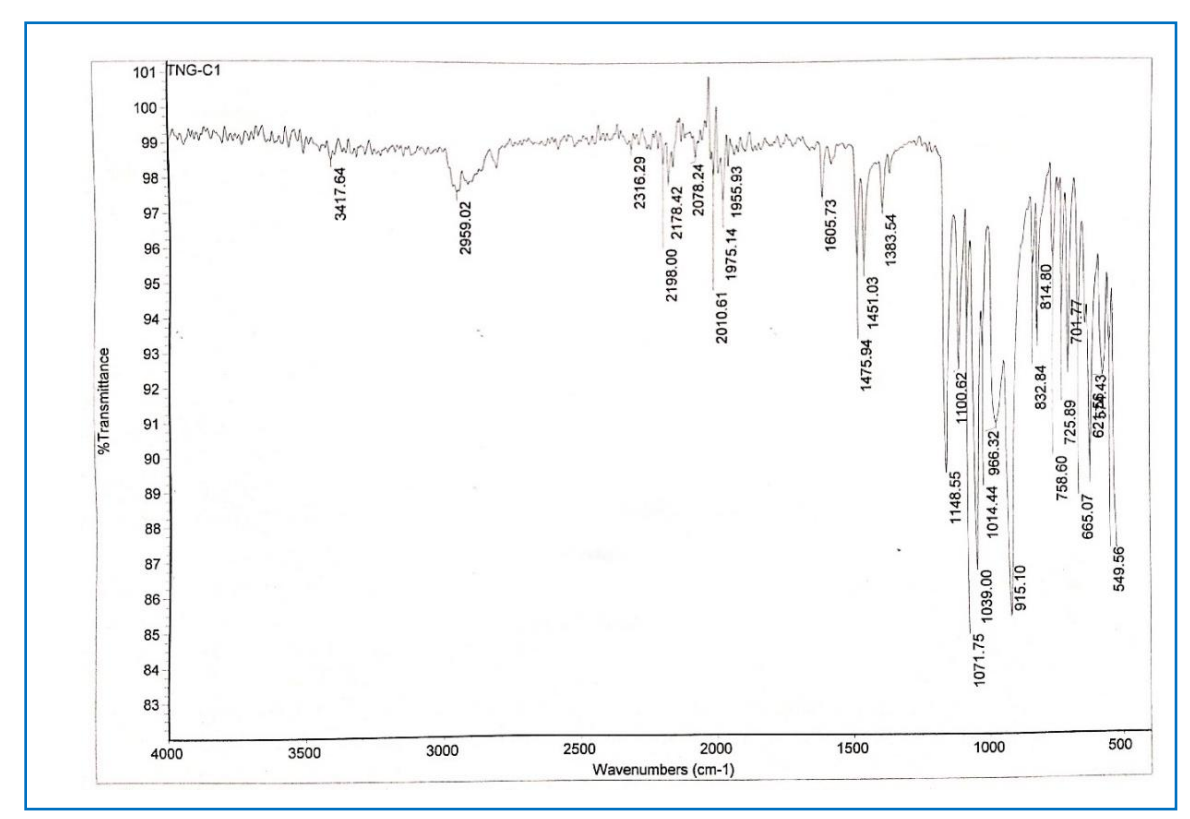


Figure 3.10: IR spectrum of 3.1.

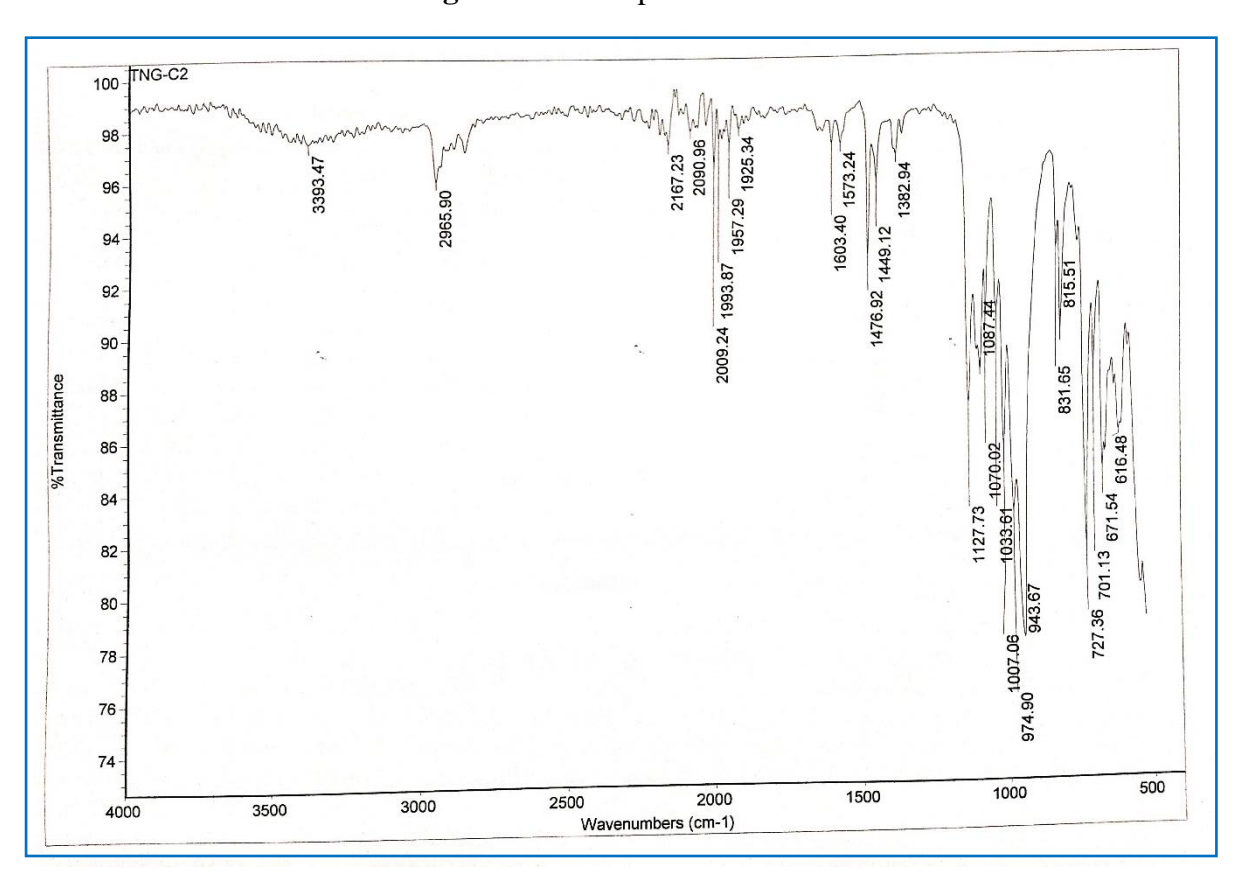


Figure 3.11: IR spectrum of 3.2.

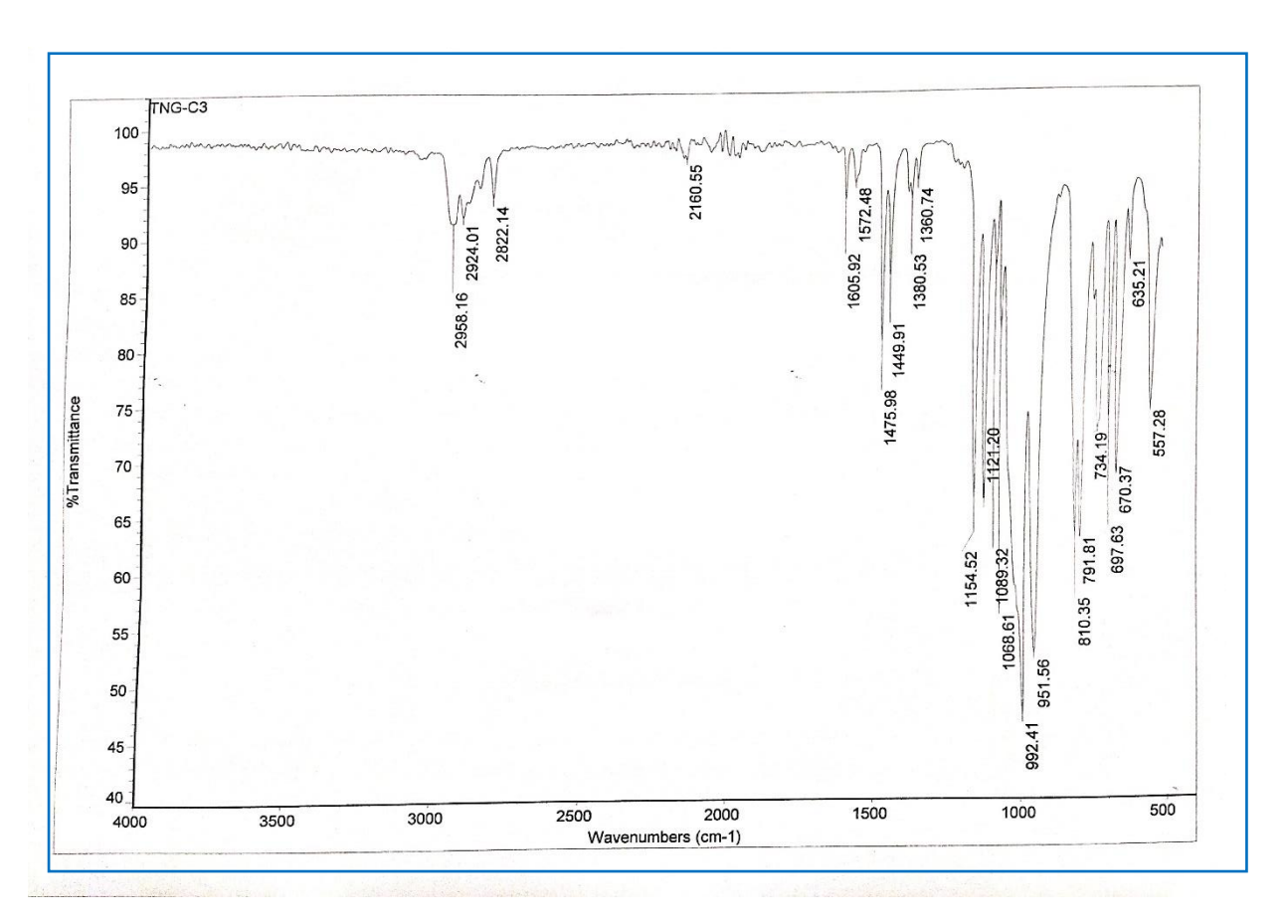


Figure 3.12: IR spectrum of 3.3.

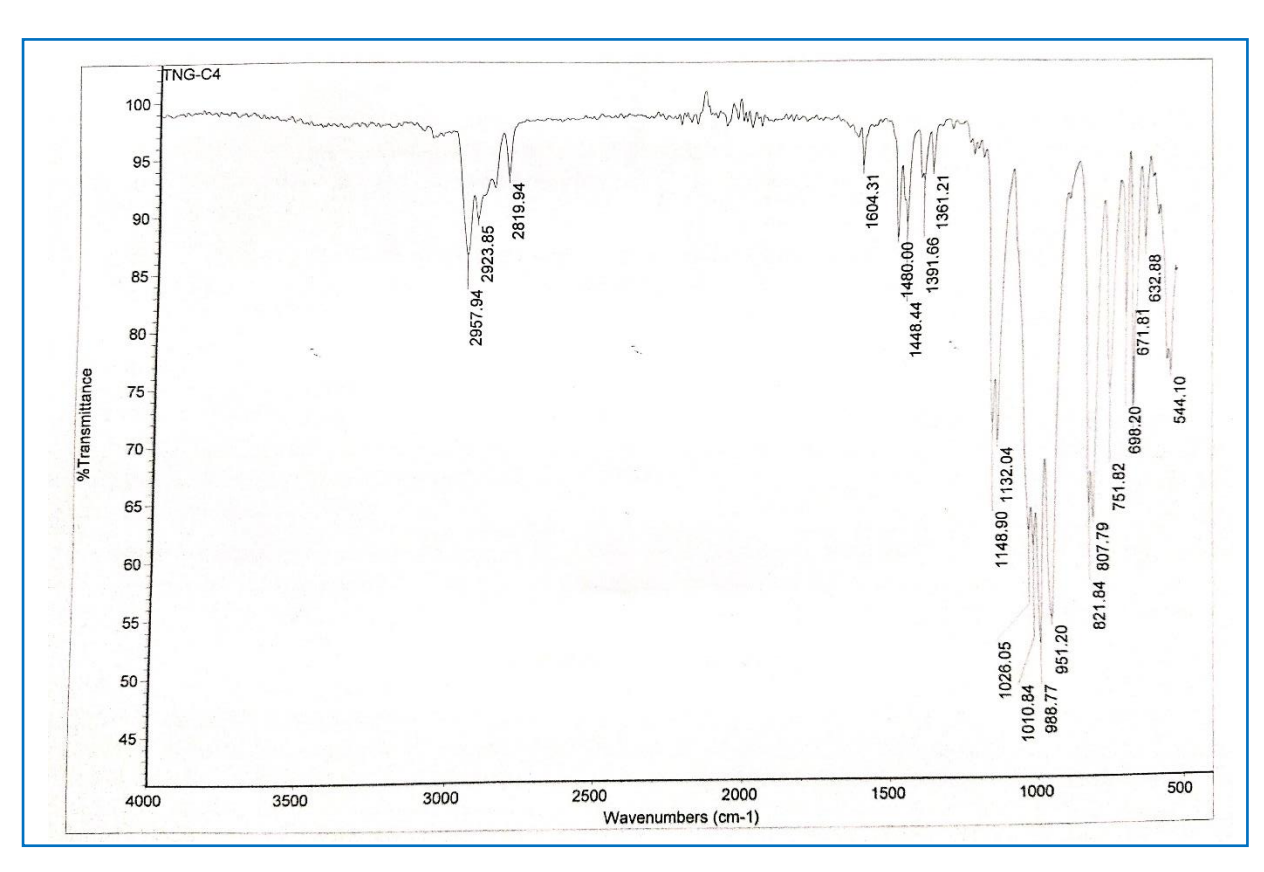


Figure 3.13: IR spectrum of 3.4.

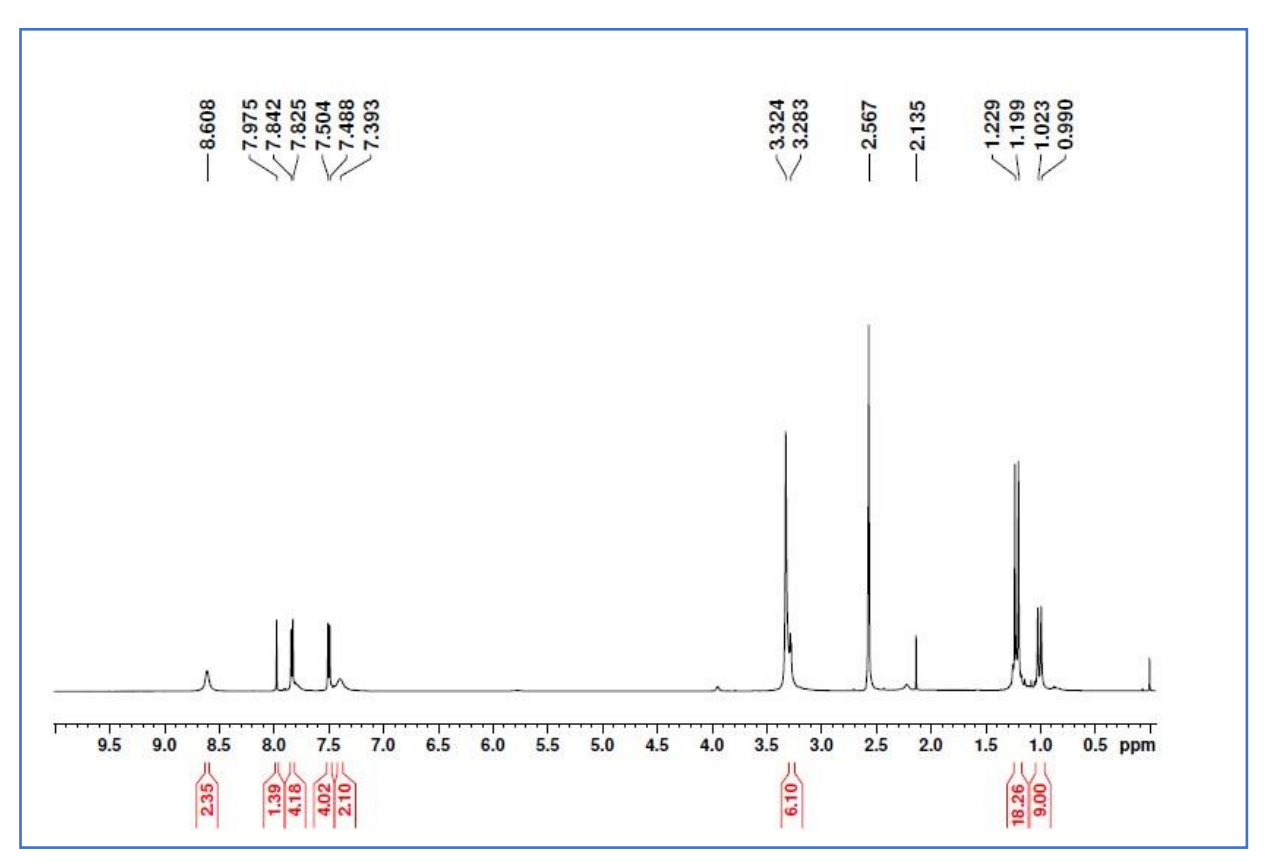


Figure 3.14: Solution ¹H NMR spectrum of 3.1.

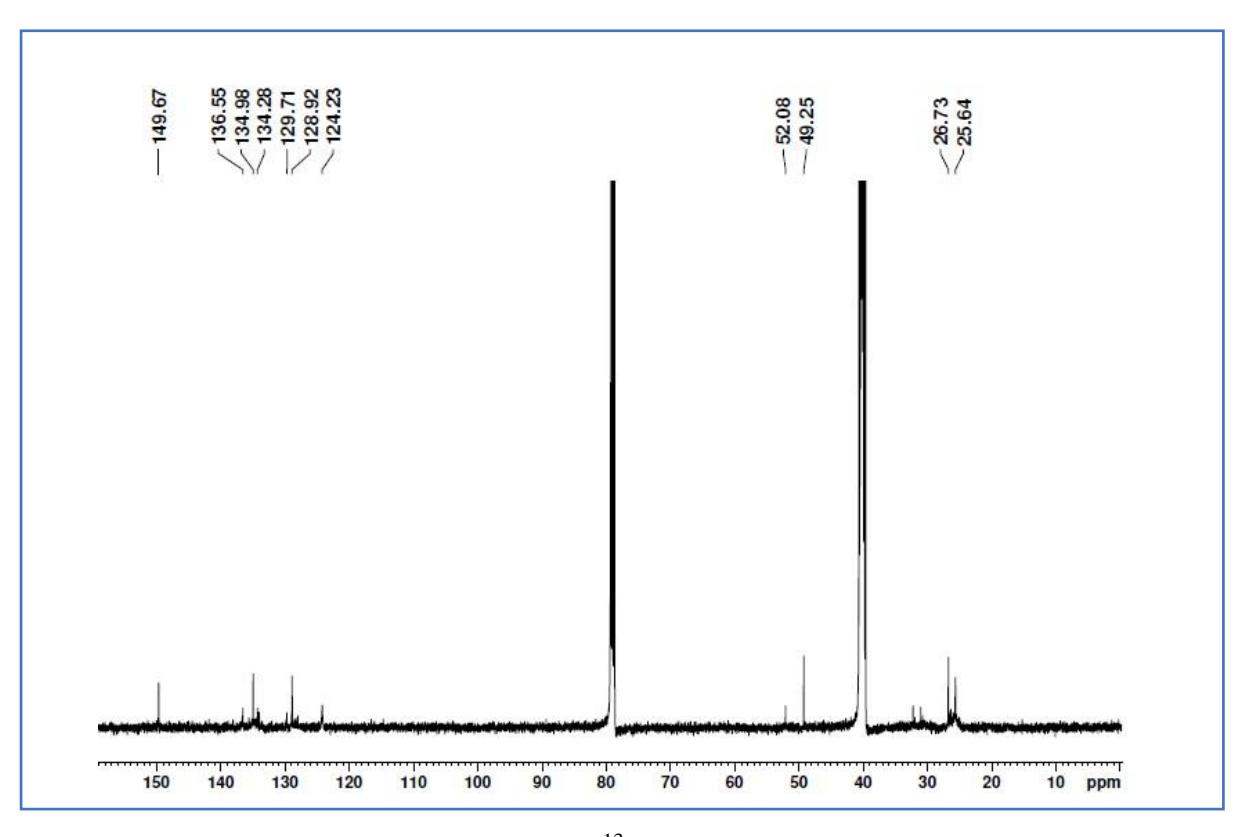


Figure 3.15: Solution ¹³C NMR spectrum of **3.1**.

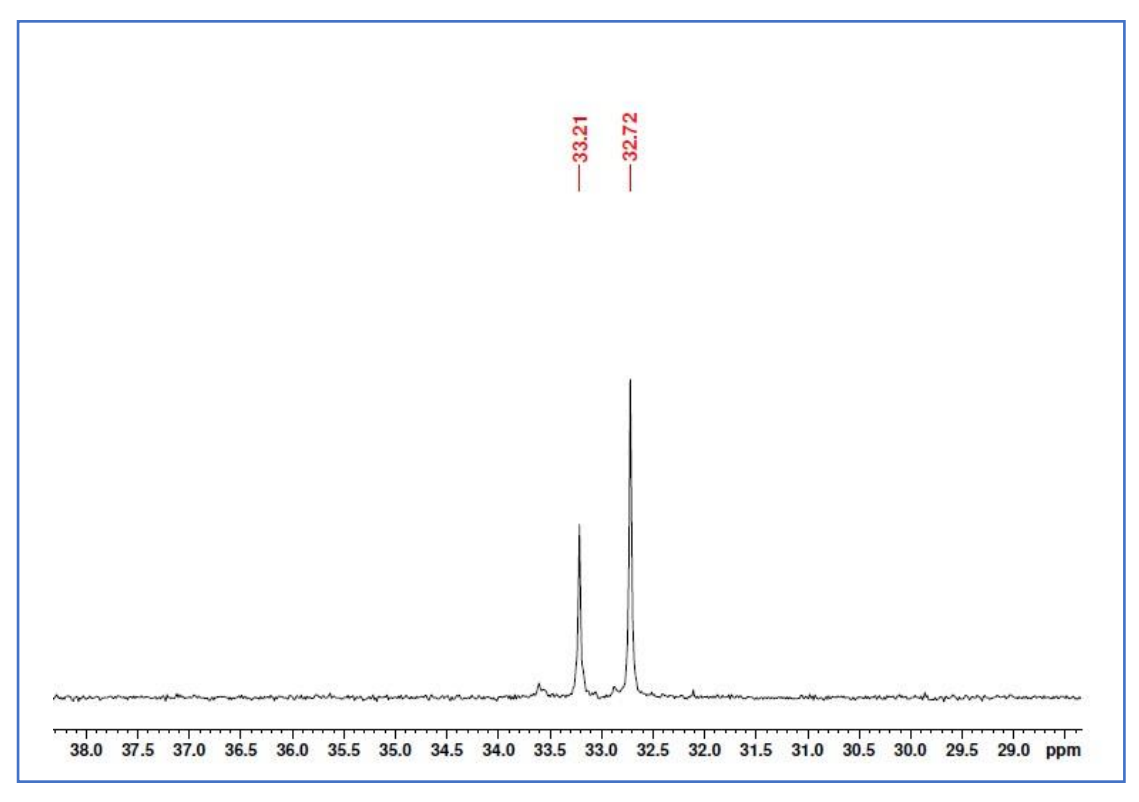


Figure 3.16: Solution ³¹P NMR spectrum of **3.1**.

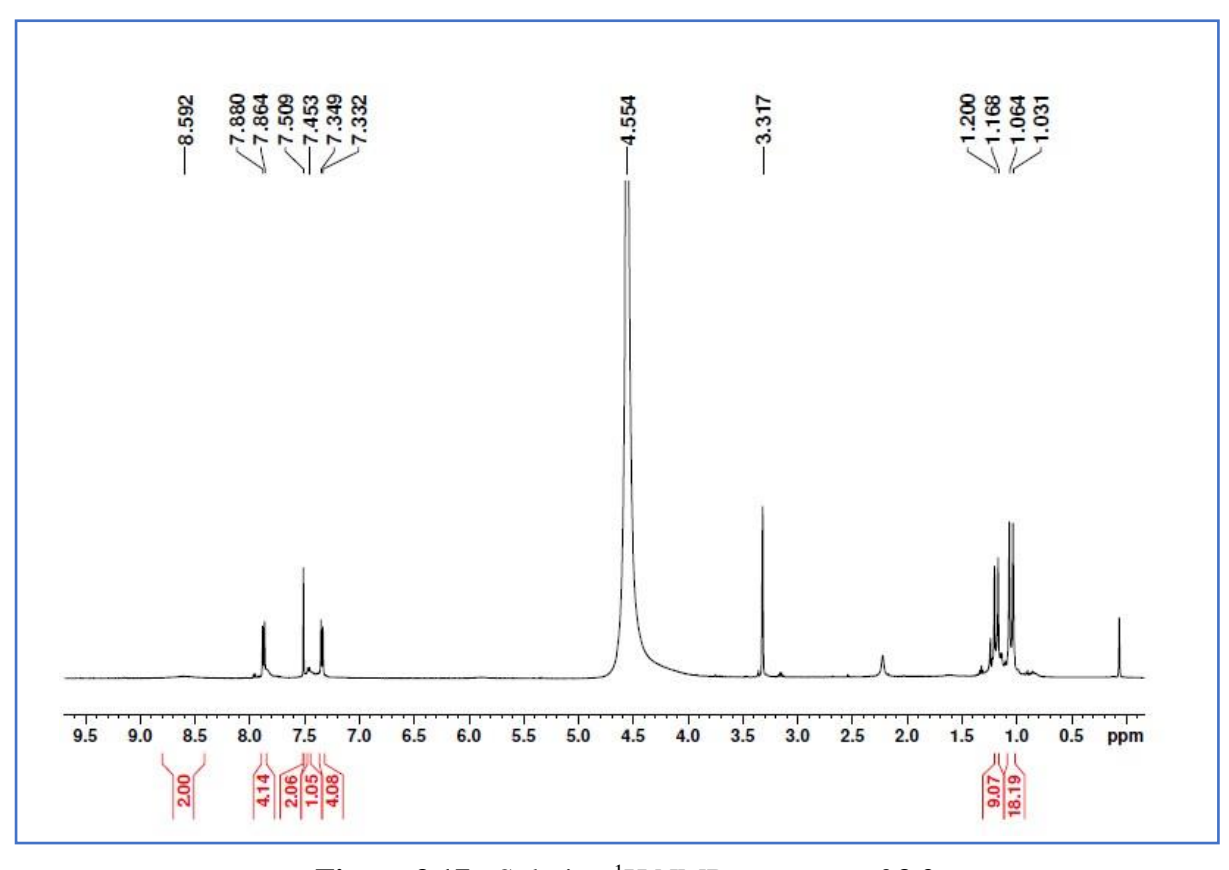


Figure 3.17: Solution ¹H NMR spectrum of 3.2.

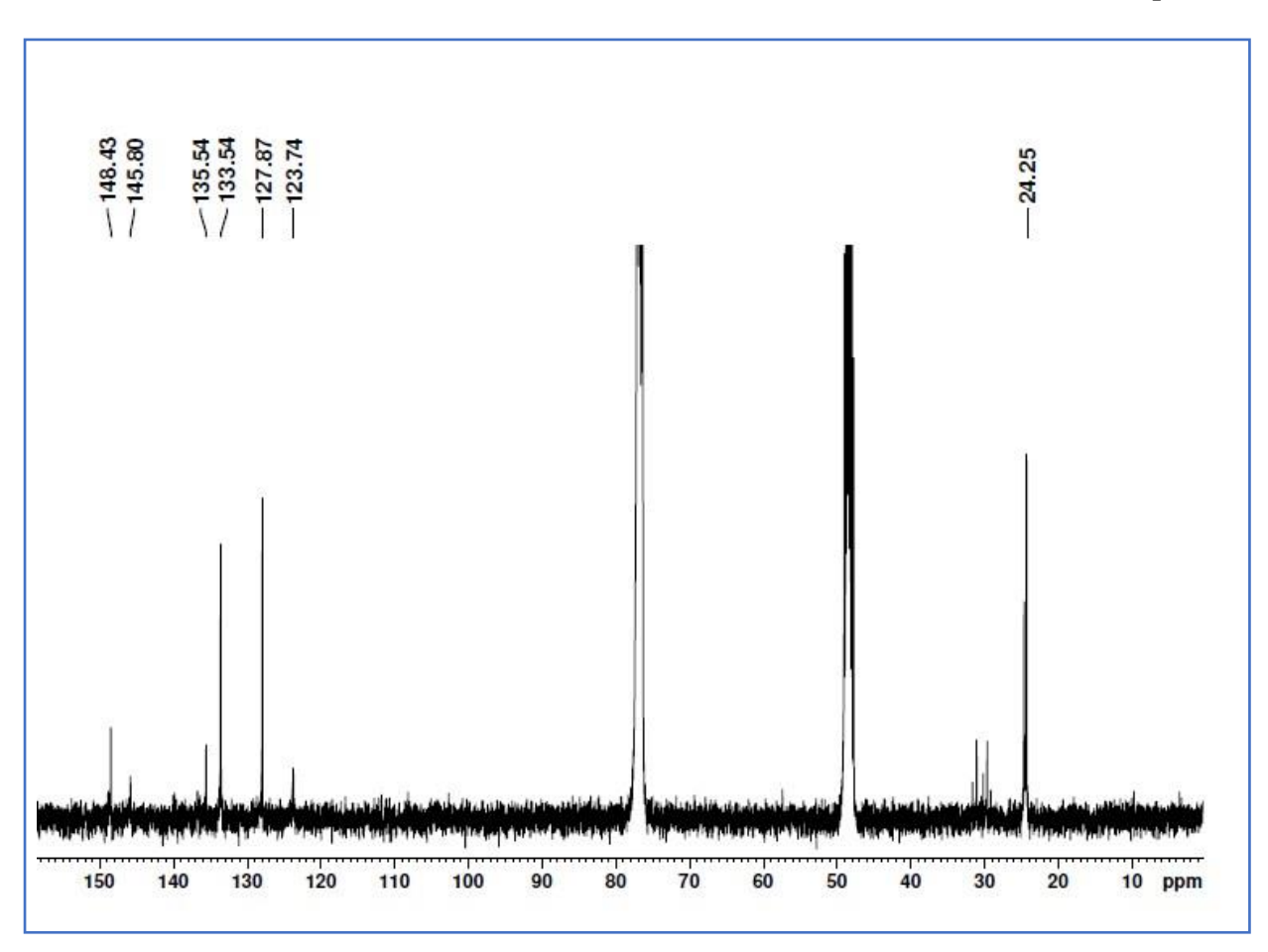


Figure 3.18: Solution ¹³C NMR spectrum of **3.2**.

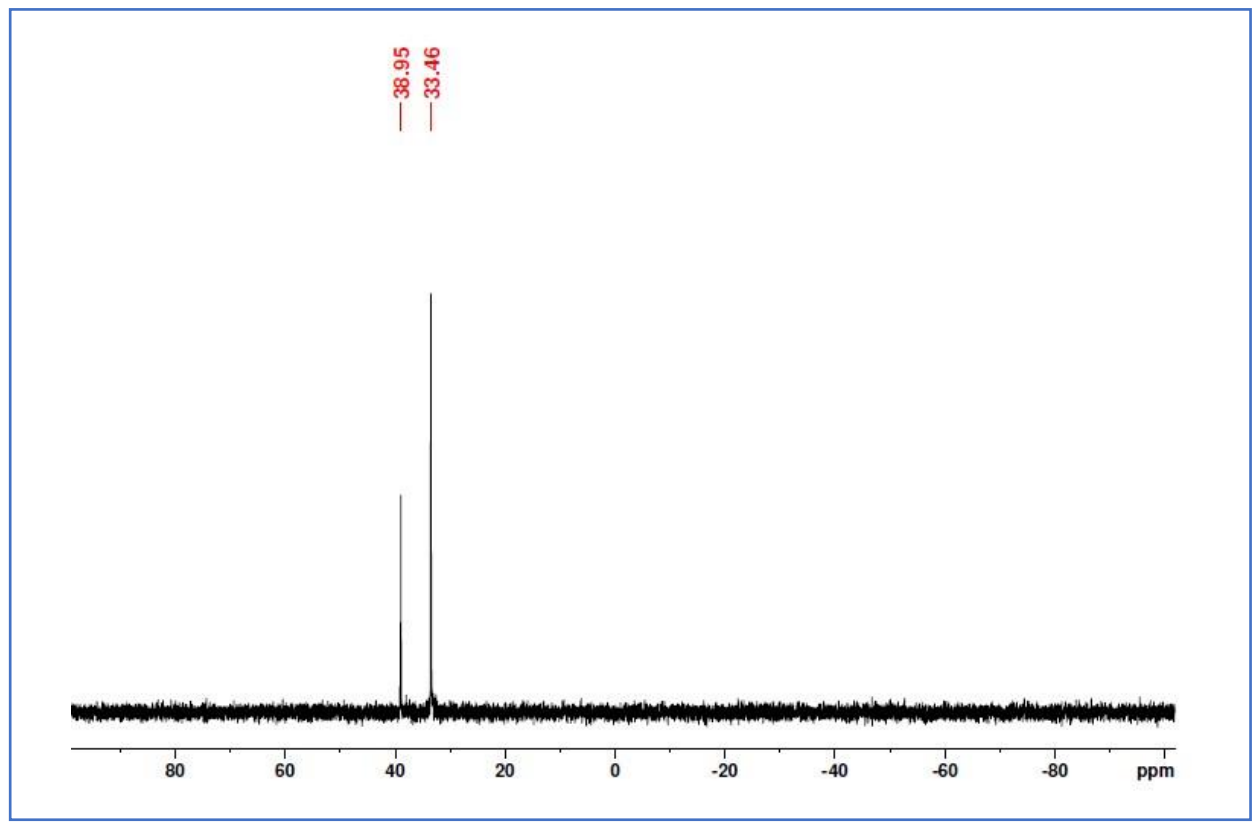


Figure 3.19: Solution ³¹P NMR spectrum of **3.2**.

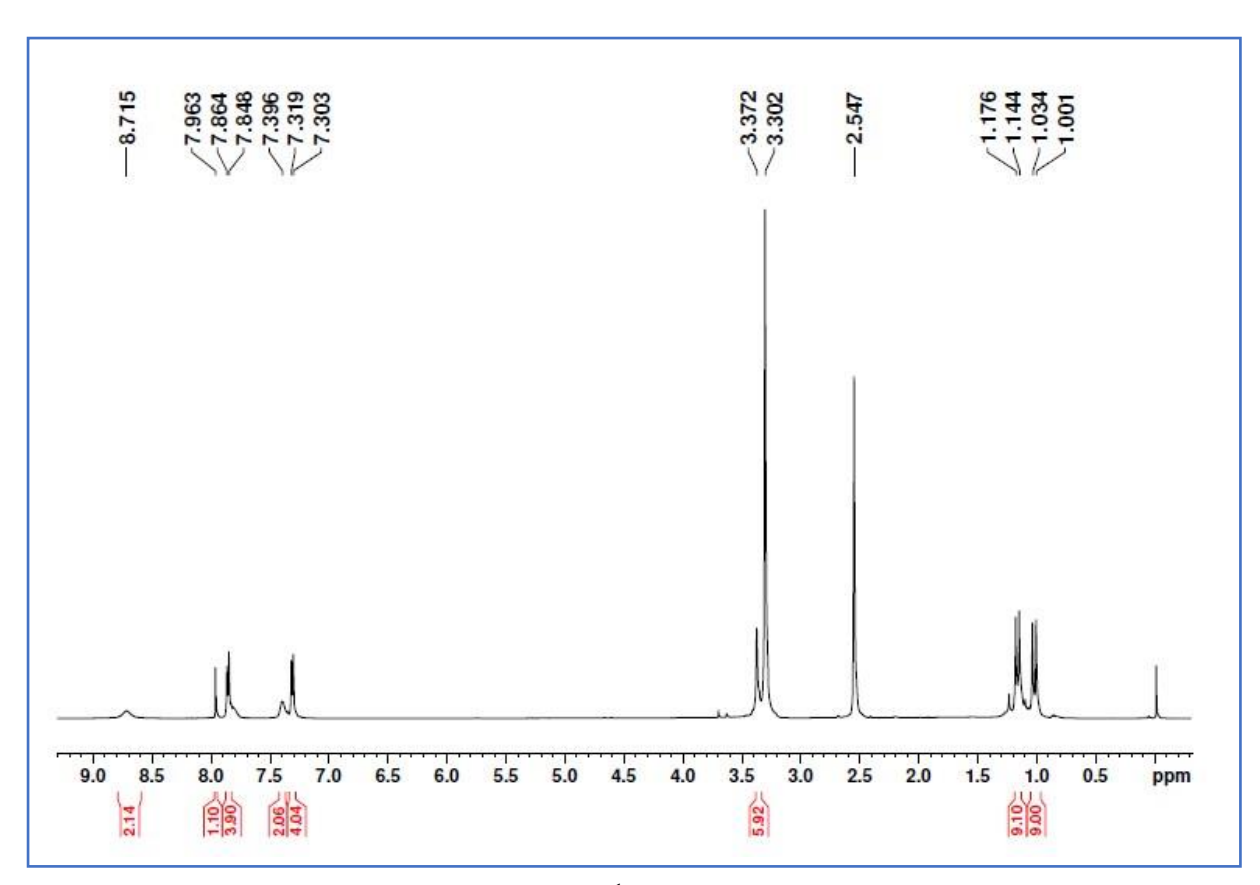


Figure 3.20: Solution ¹H NMR spectrum of 3.3.

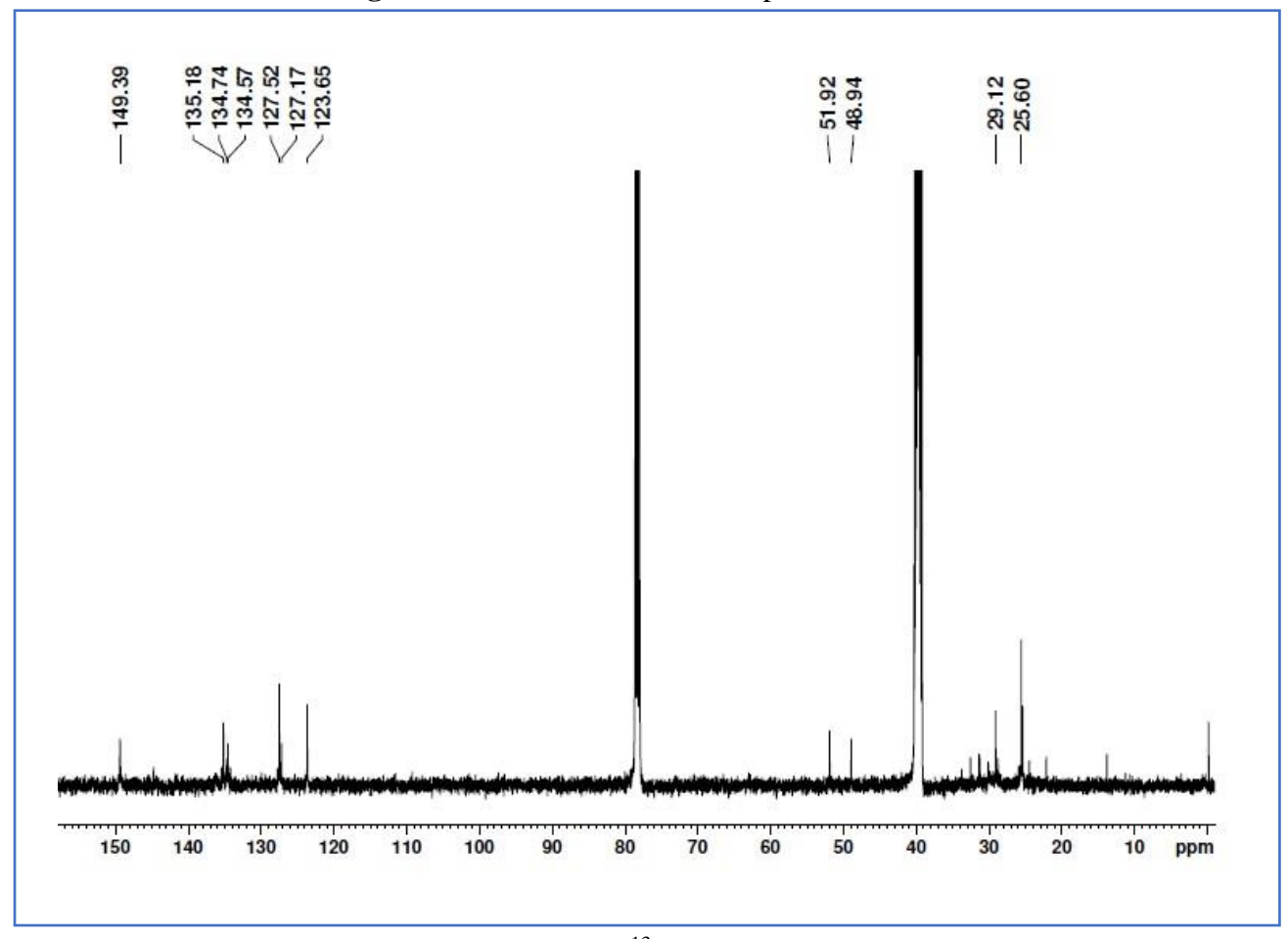


Figure 3.21: Solution ¹³C NMR spectrum of **3.3**

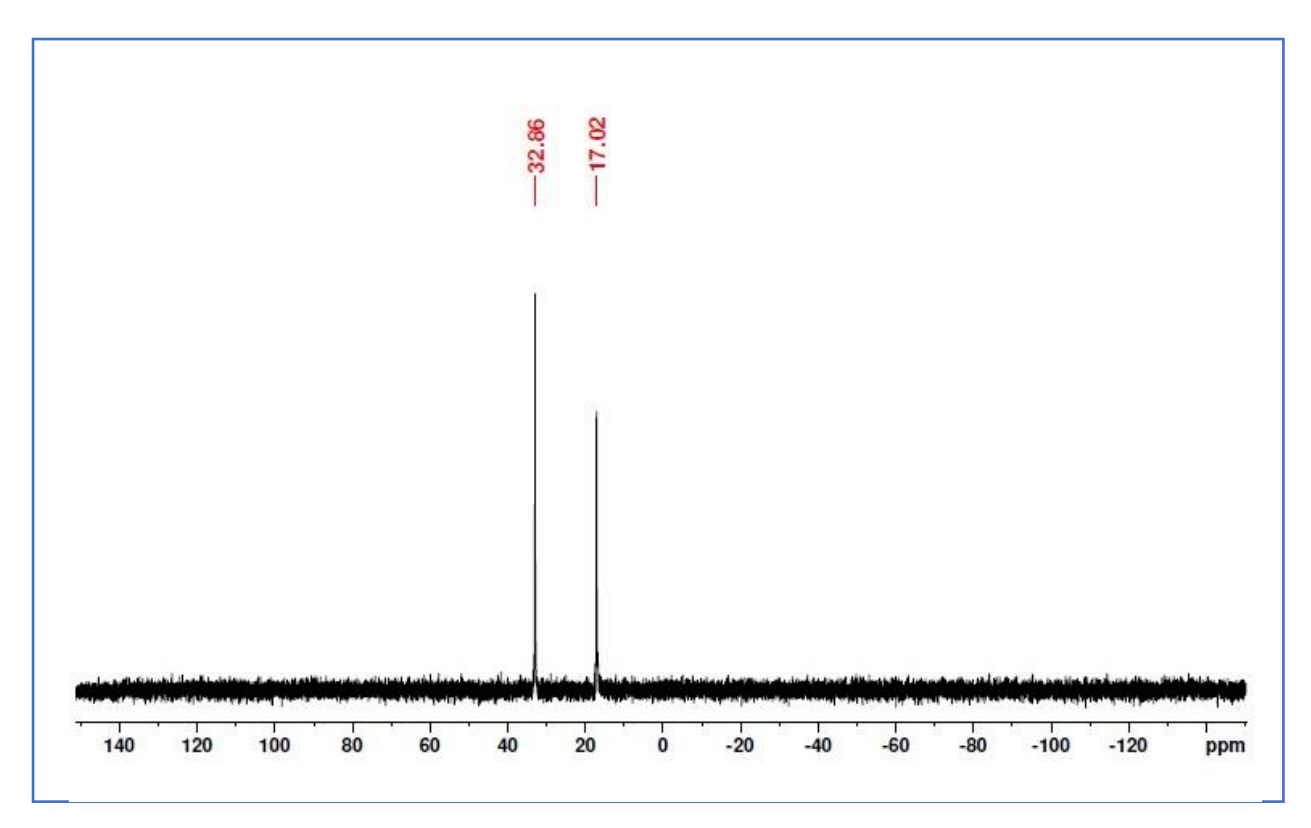


Figure 3.22: Solution ³¹P NMR spectrum of **3.3**.

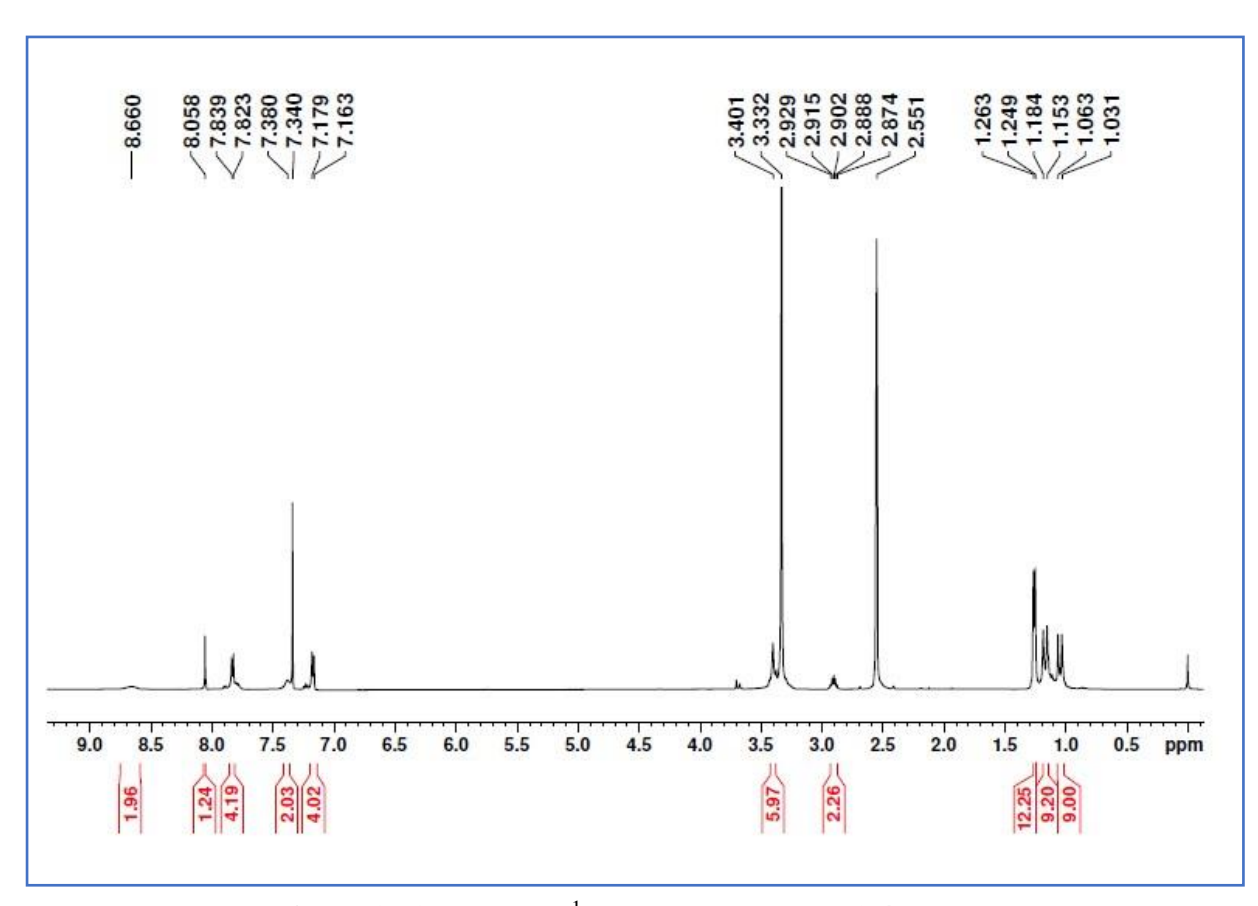


Figure 3.23: Solution ¹H NMR spectrum of **3.4**.

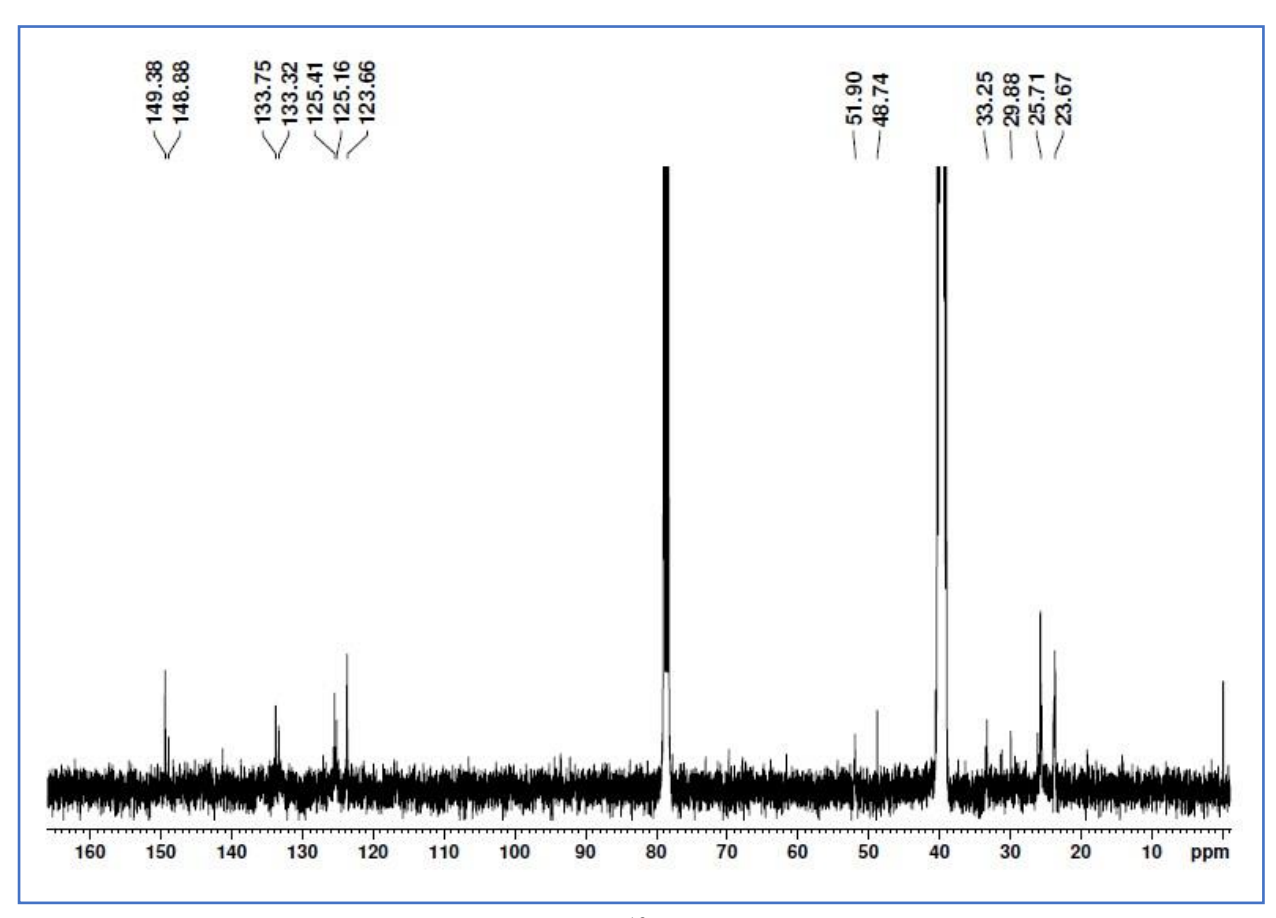


Figure 3.24: Solution ¹³C NMR spectrum of 3.4.

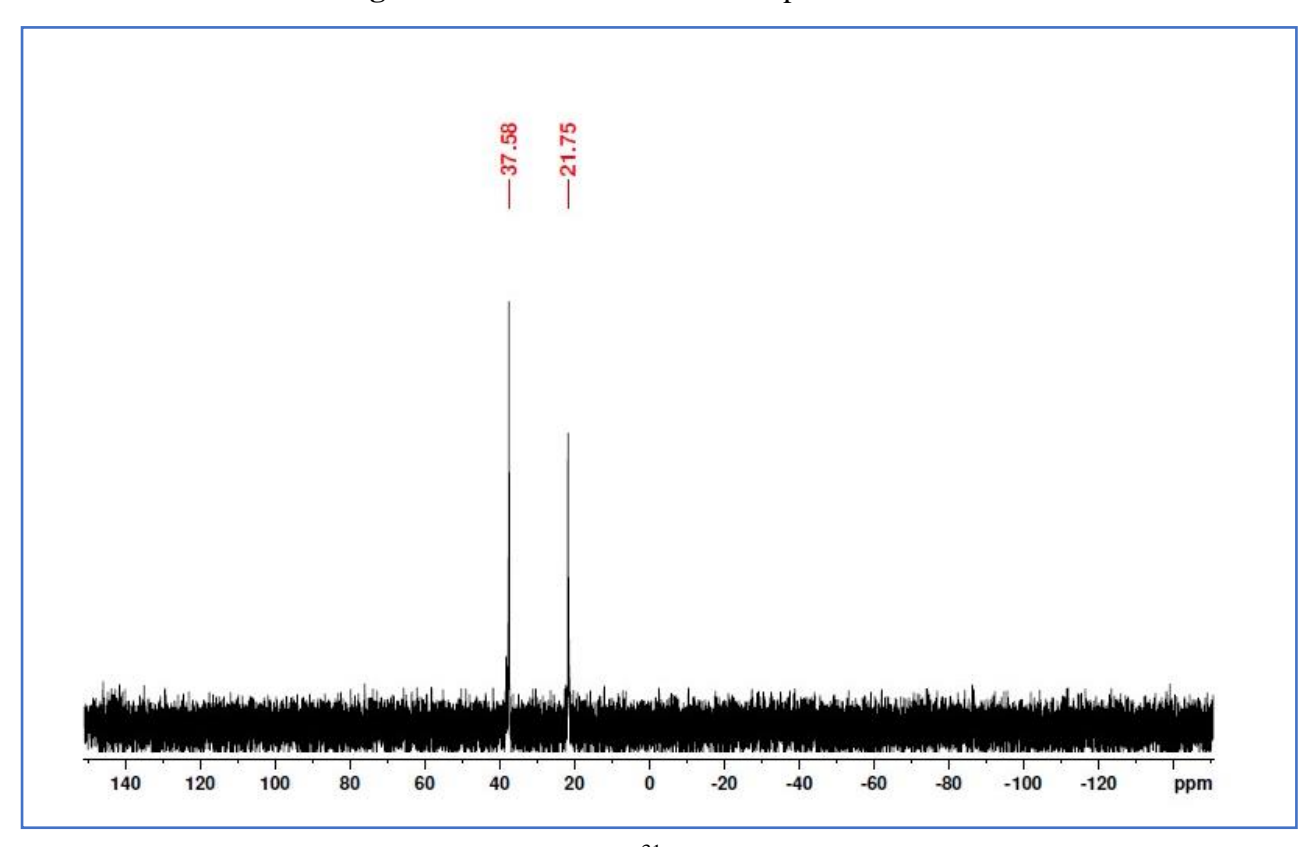


Figure 3.25: Solution ³¹P NMR spectrum of **3.4**.

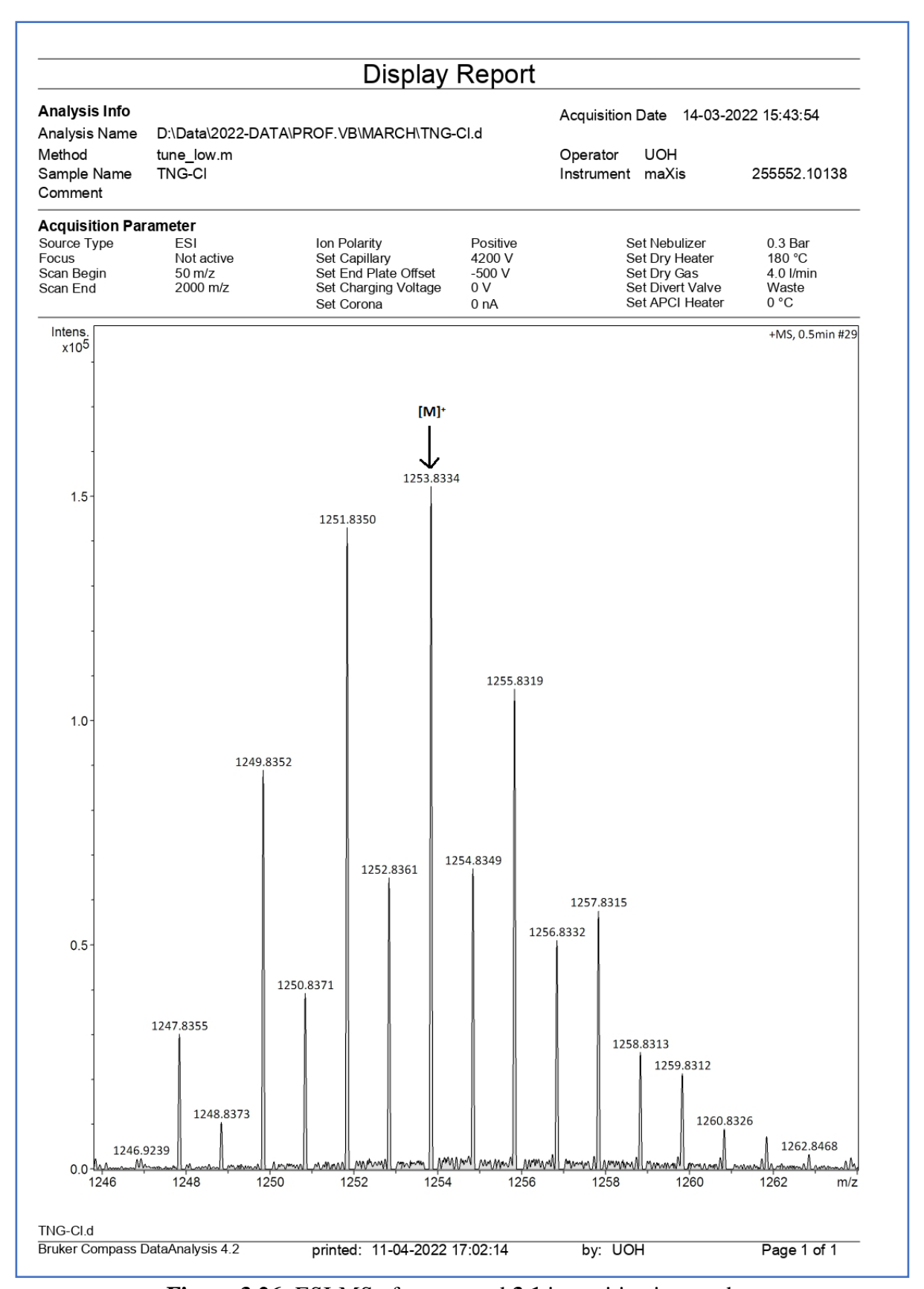


Figure 3.26: ESI-MS of compound **3.1** in positive ion mode.

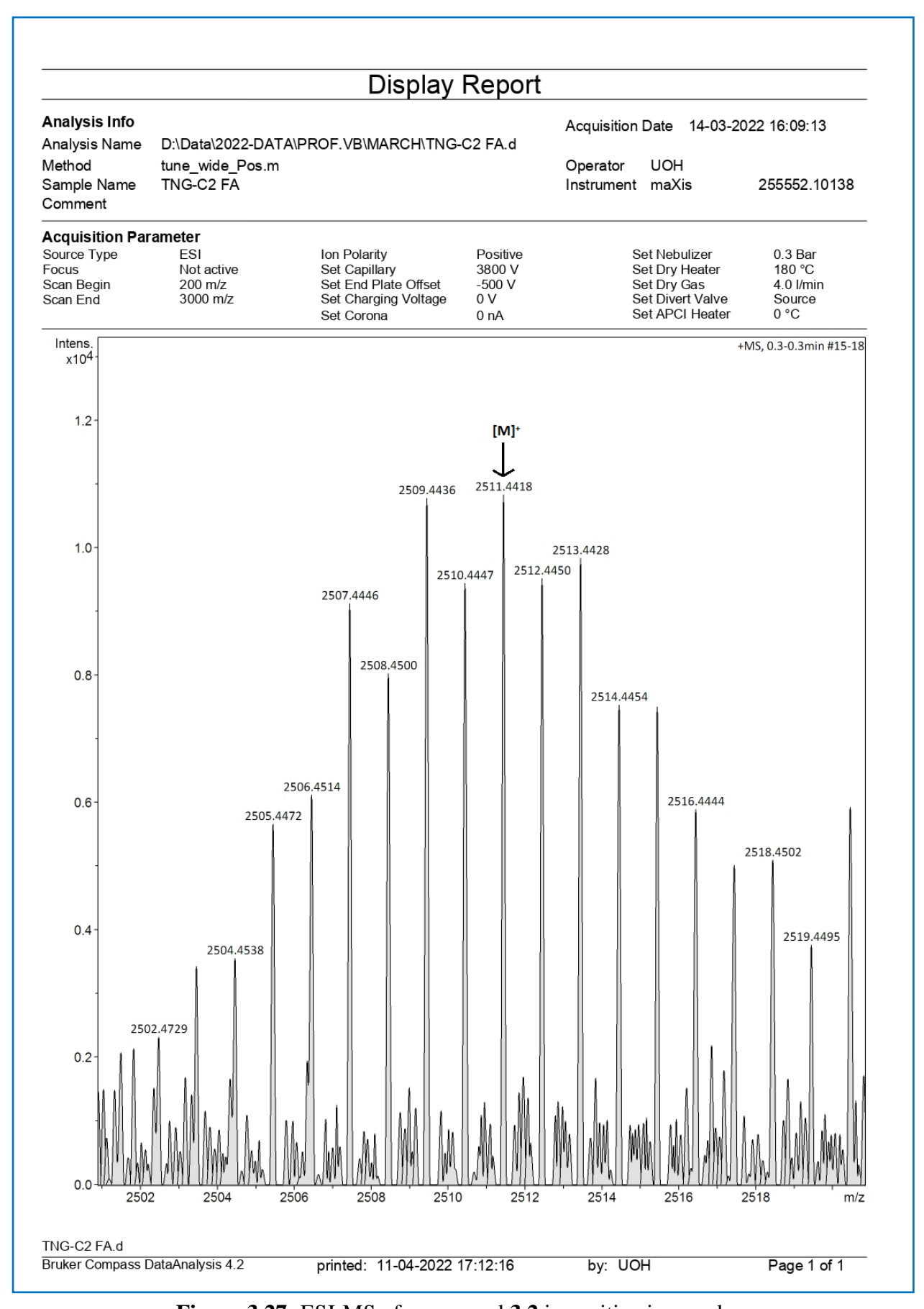


Figure 3.27: ESI-MS of compound **3.2** in positive ion mode.

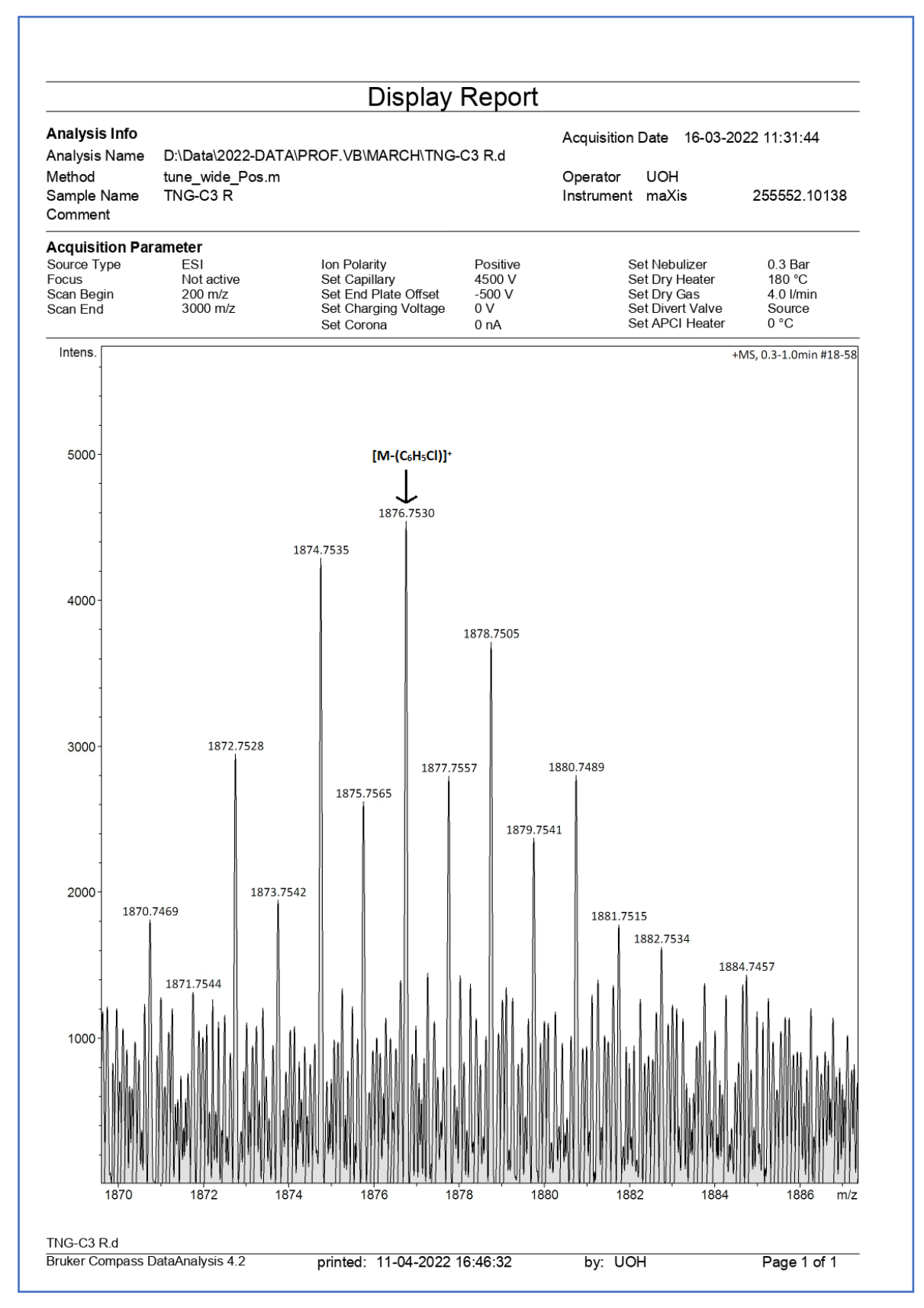


Figure 3.28: ESI-MS of compound **3.3** in positive ion mode.

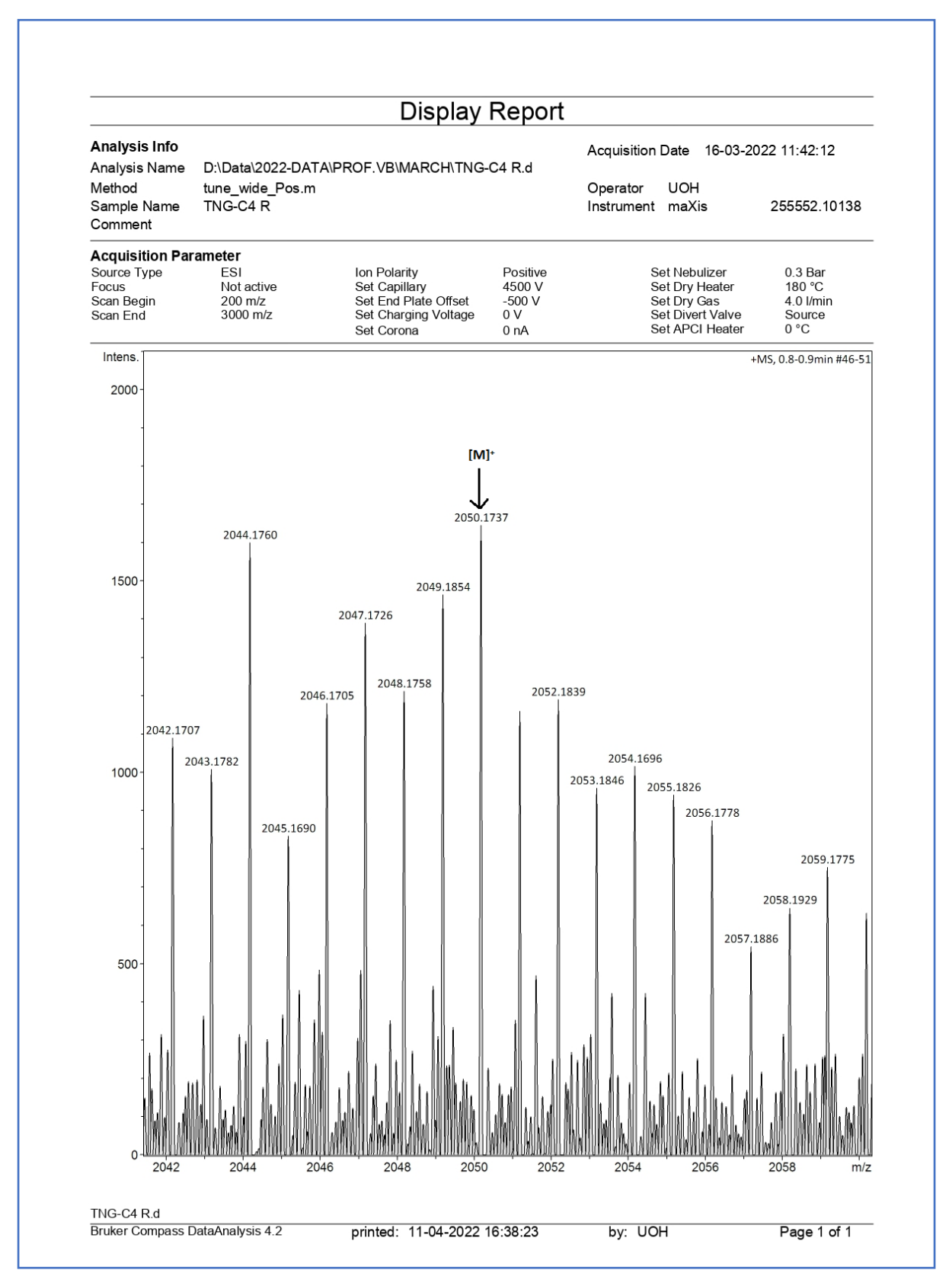


Figure 3.29: ESI-MS of compound 3.4 in positive ion mode.

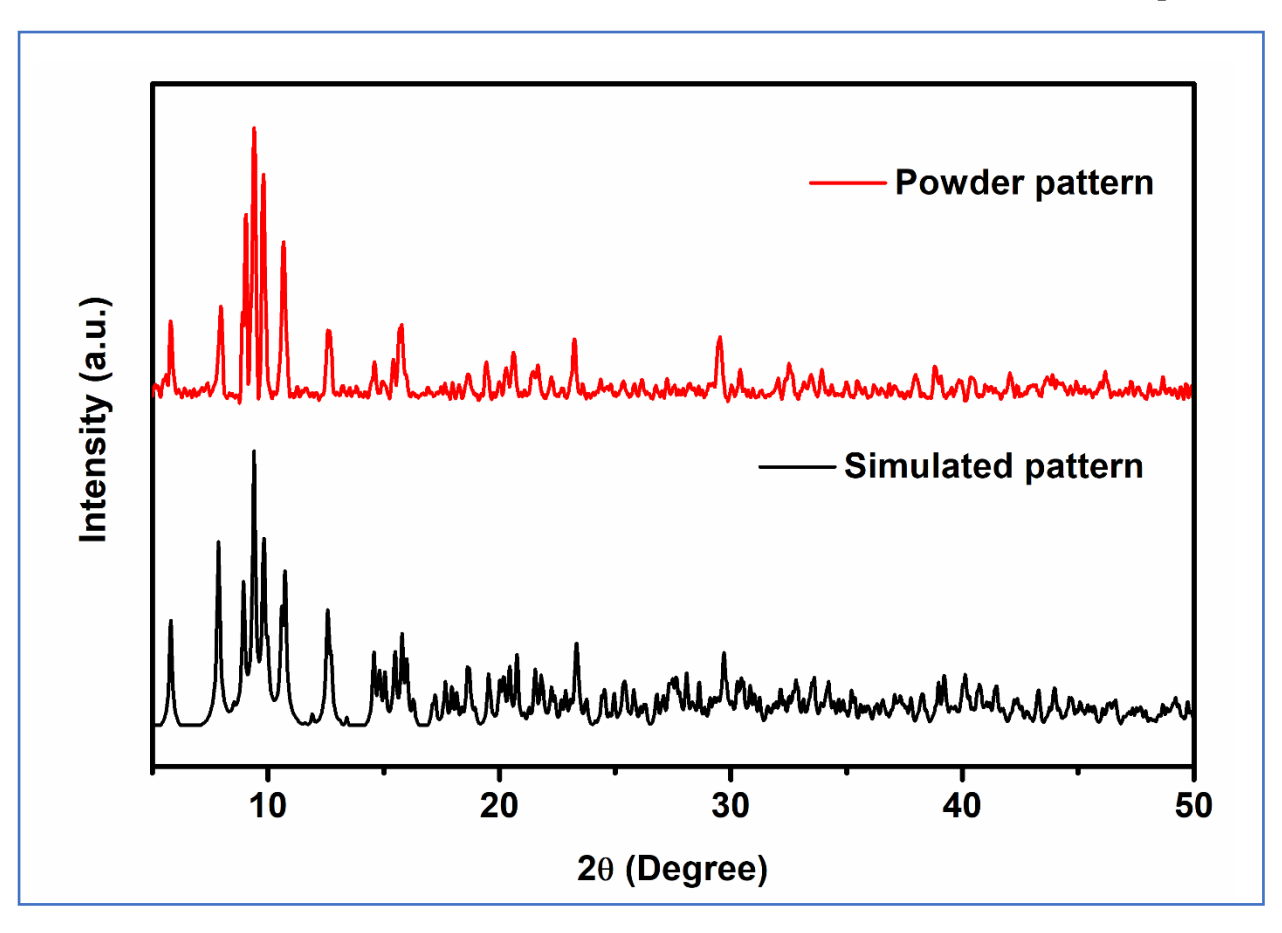


Figure 3.30: Powder X-ray diffraction pattern of a bulk sample of **3.1** compared to the simulated powder pattern extracted from single-crystal diffraction data.

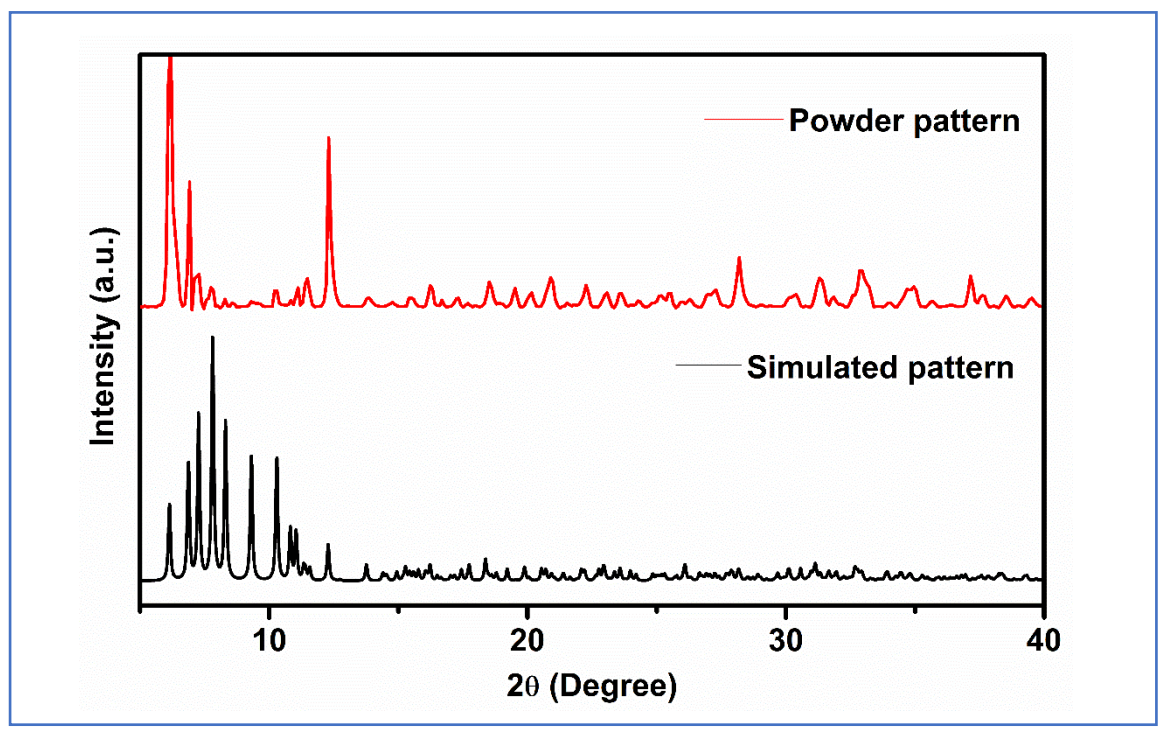


Figure 3.31: Powder X-ray diffraction pattern of a bulk sample of **3.2** compared to the simulated powder pattern extracted from single-crystal diffraction data.

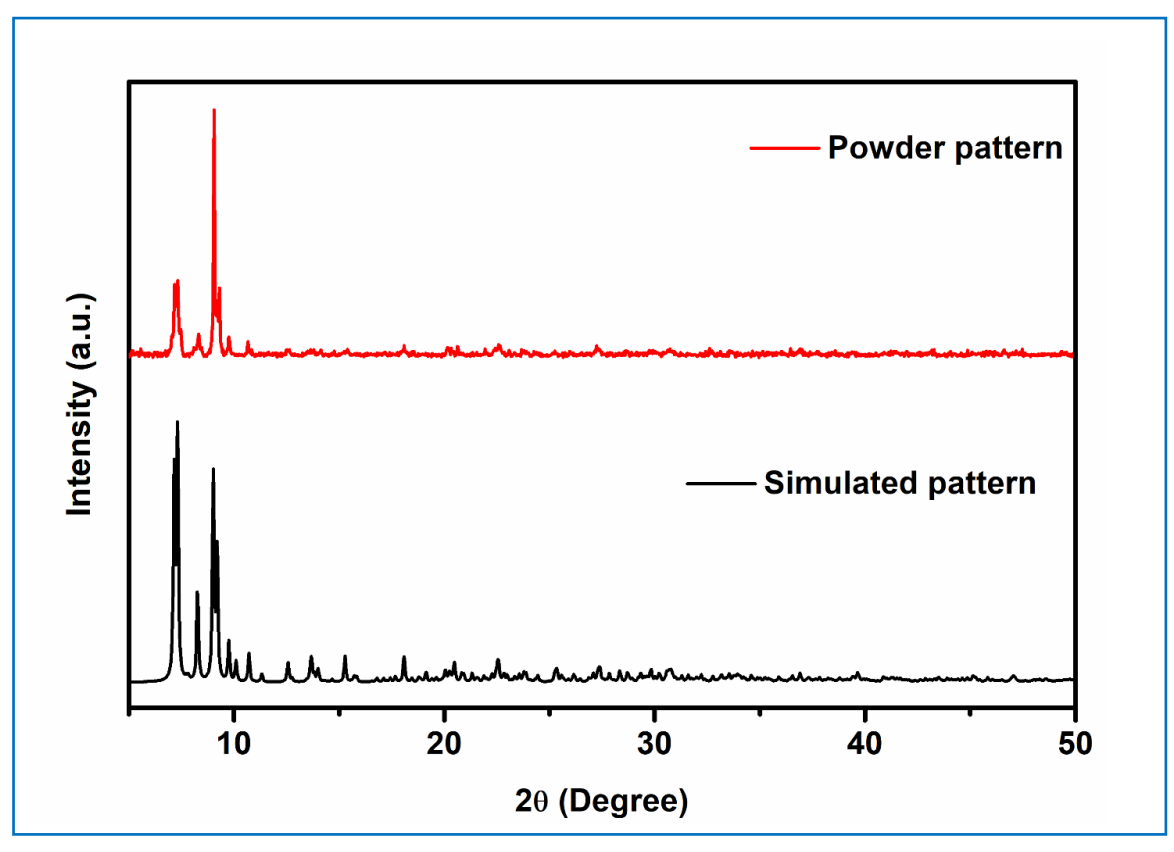


Figure 3.32: Powder X-ray diffraction pattern of a bulk sample of **3.3** compared to the simulated powder pattern extracted from single-crystal diffraction data.

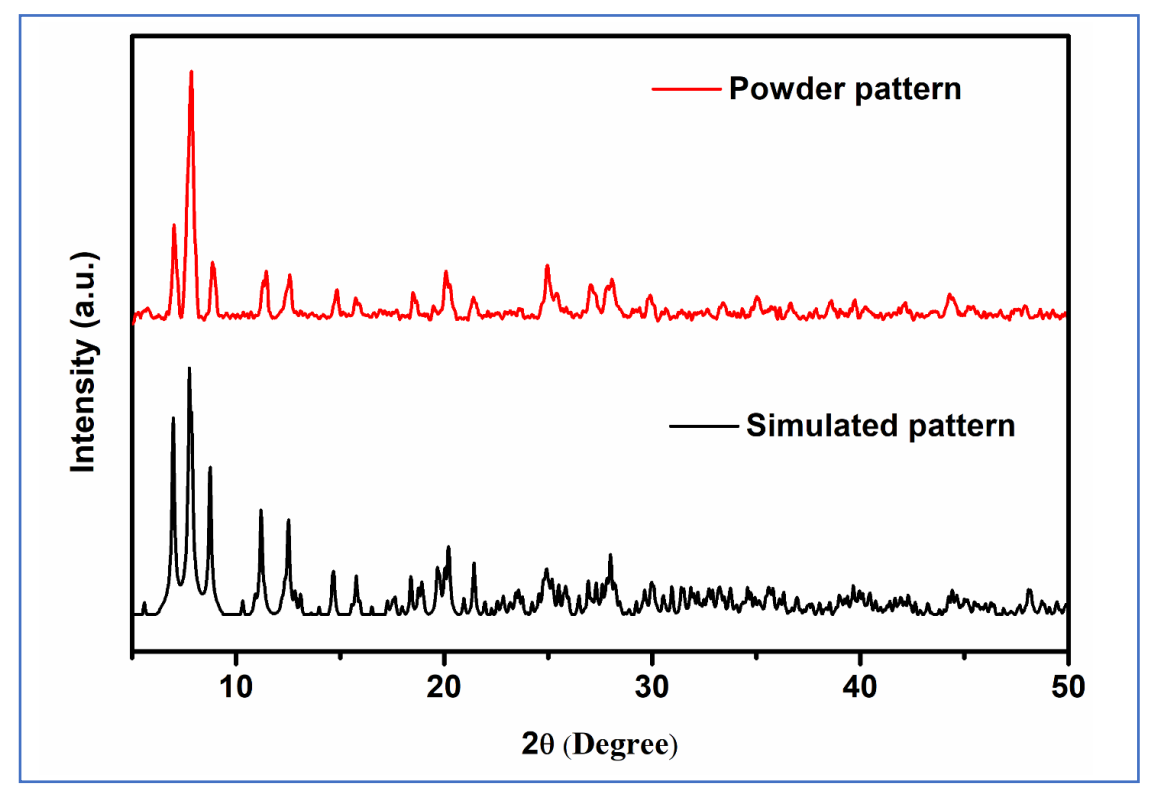


Figure 3.33: Powder X-ray diffraction pattern of a bulk sample of **3.4** compared to the simulated powder pattern extracted from single-crystal diffraction data.

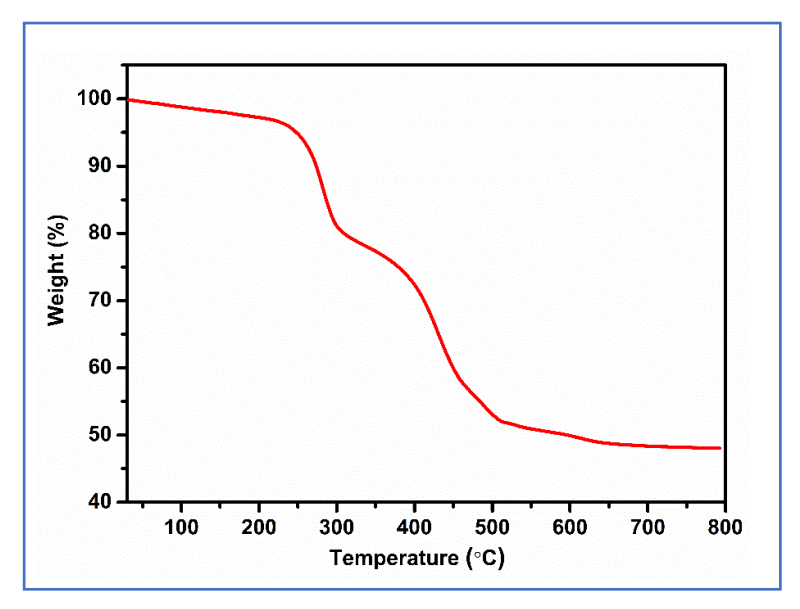


Figure 3.34: TGA plot of compound 3.1.

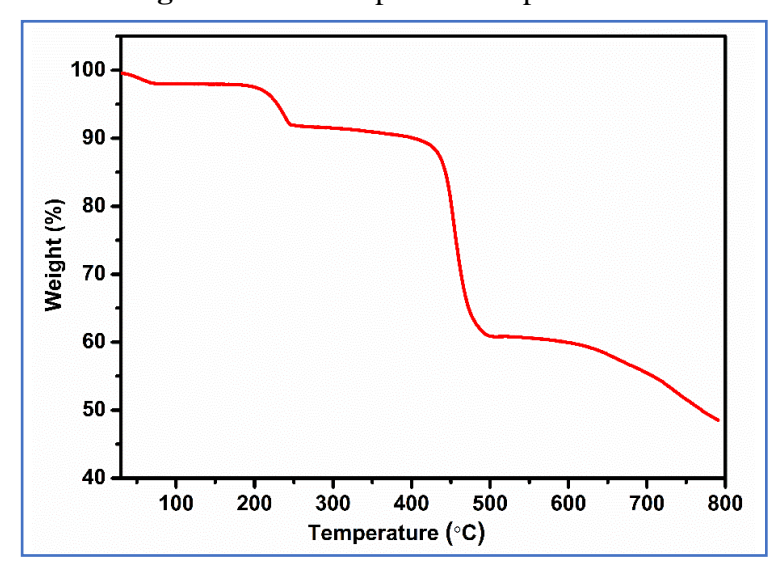


Figure 3.35: TGA plot of compound 3.2.

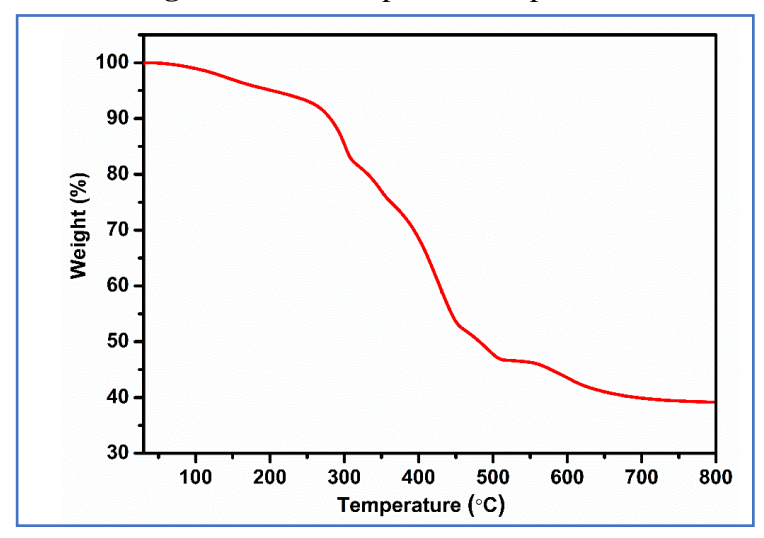


Figure 3.36: TGA plot of compound 3.3.

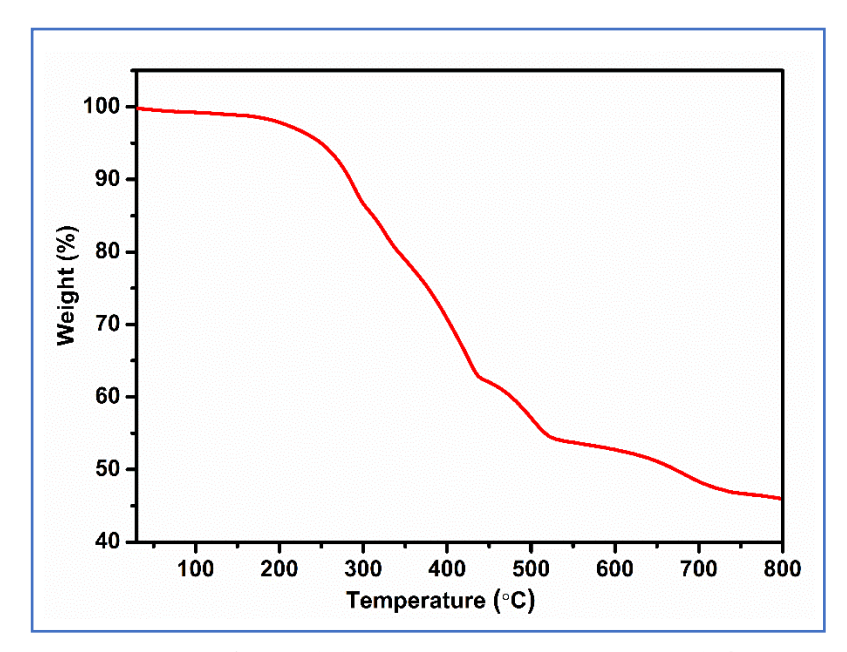


Figure 3.37: TGA plot of compound 3.4.

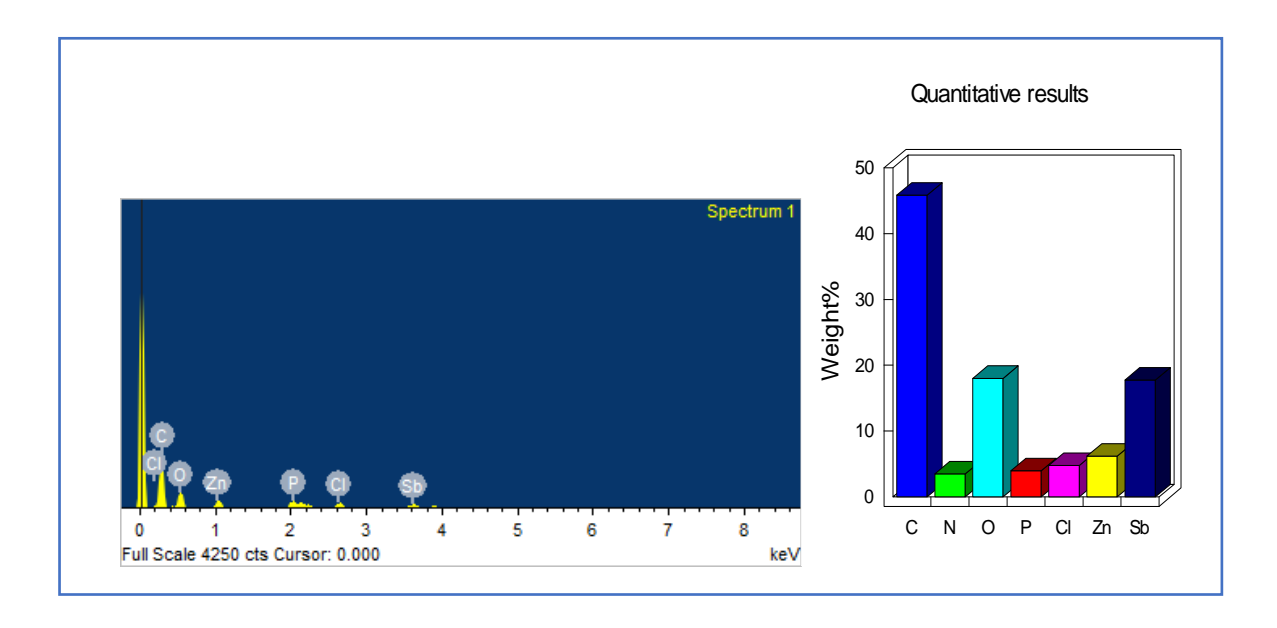


Figure 3.38: EDAX spectrum of compound 3.1.

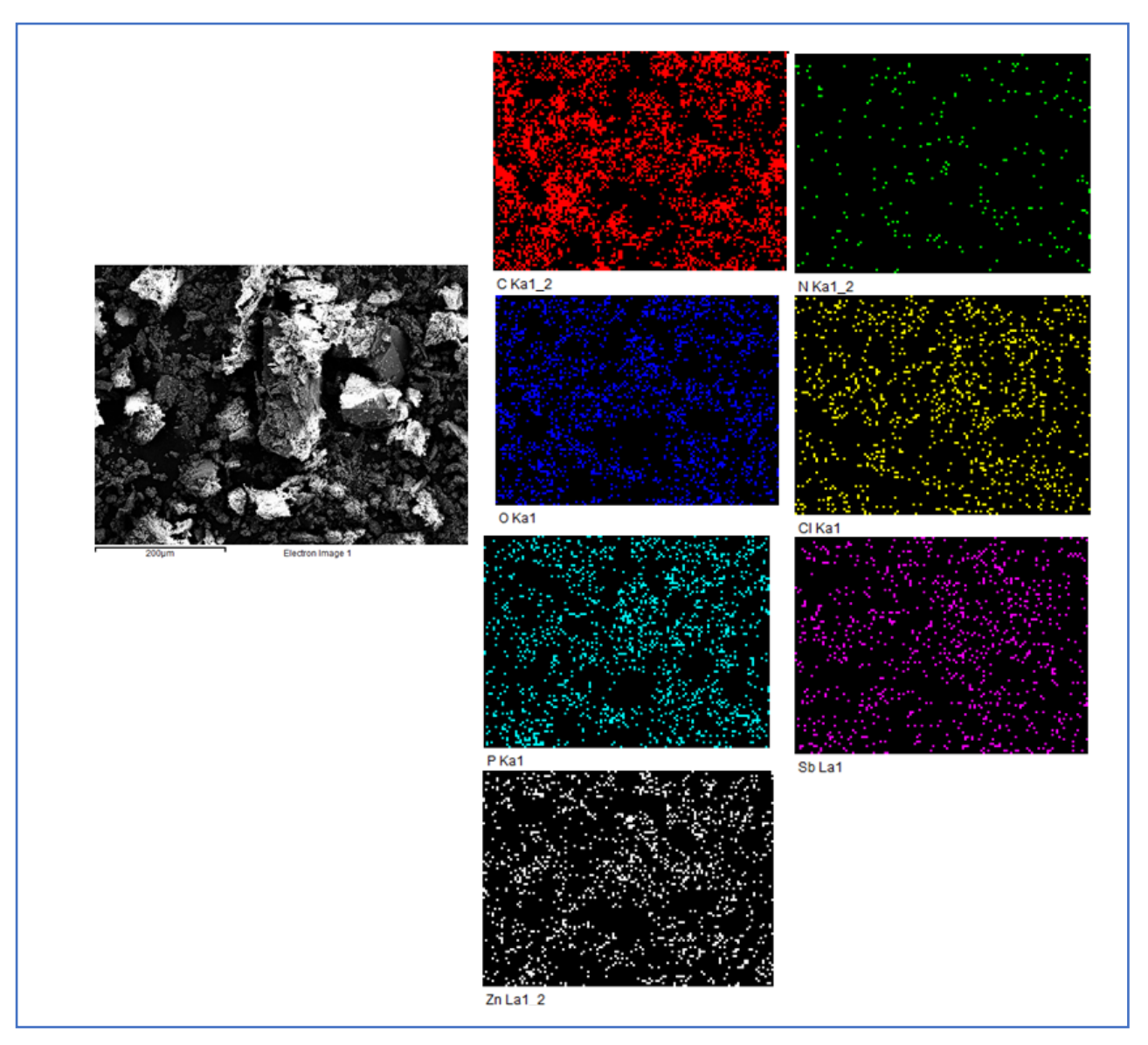


Figure 3.39: Elemental mapping of compound 3.1.

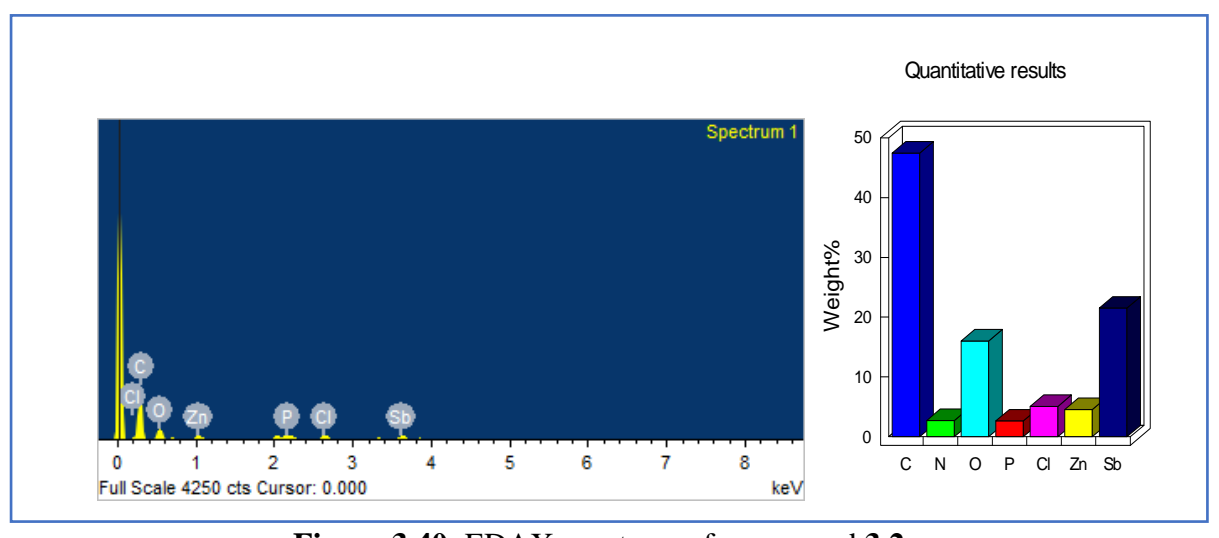


Figure 3.40: EDAX spectrum of compound 3.2.

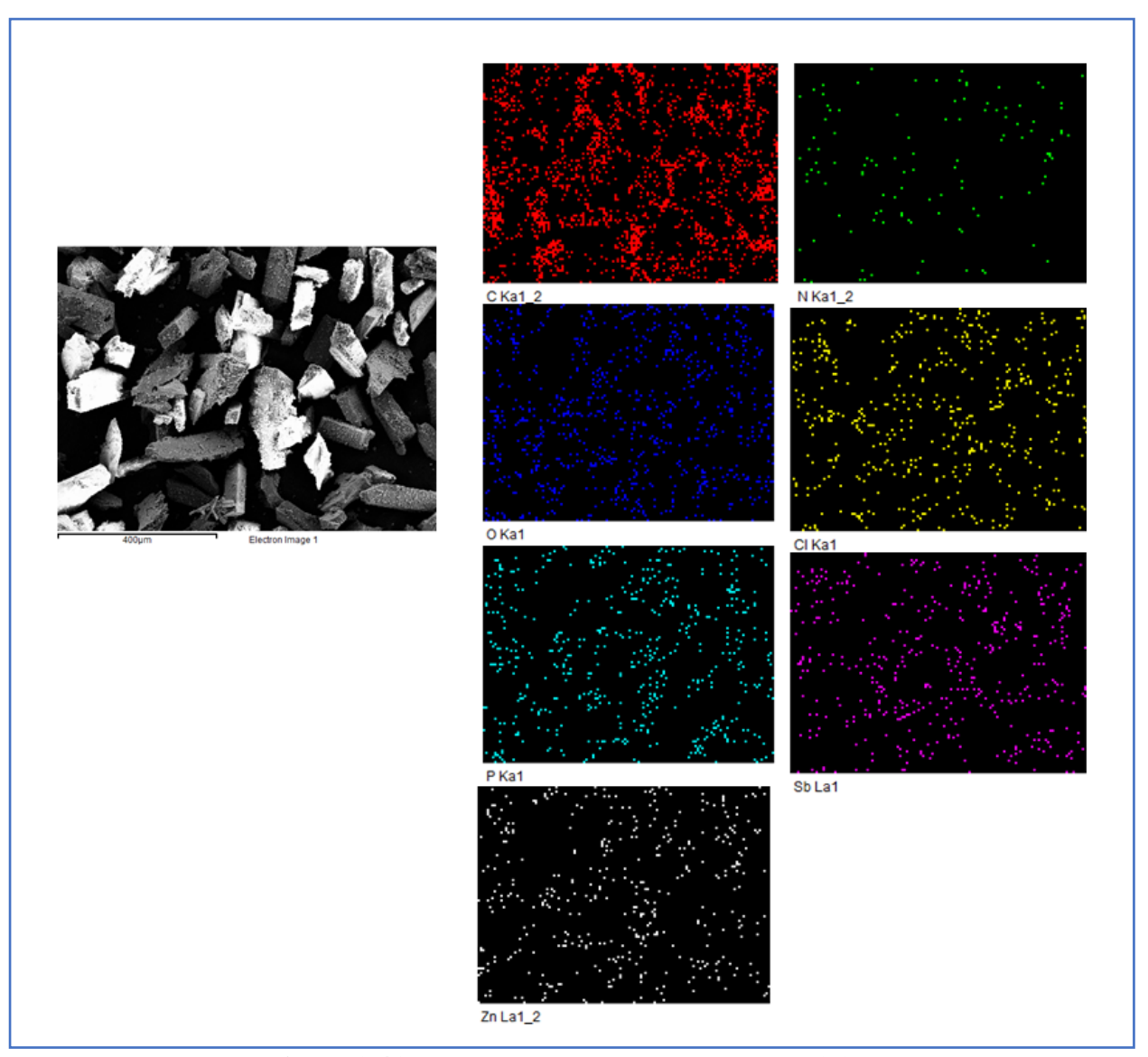


Figure 3.41: Elemental mapping of compound 3.2.

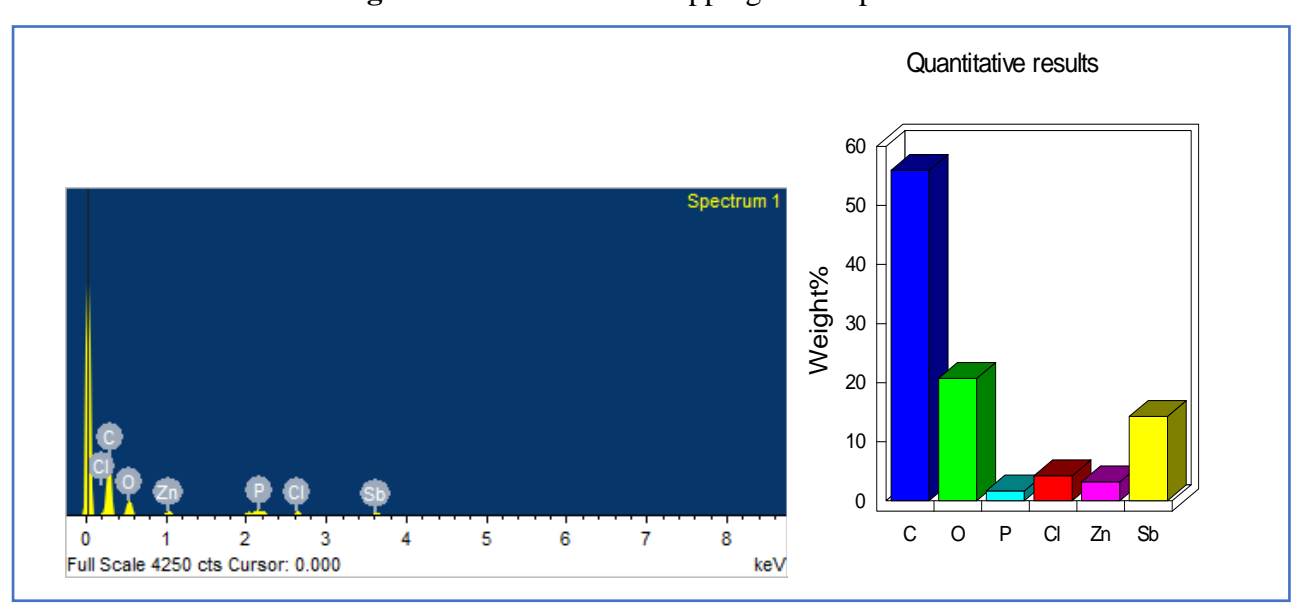


Figure 3.42: EDAX spectrum of compound 3.3.

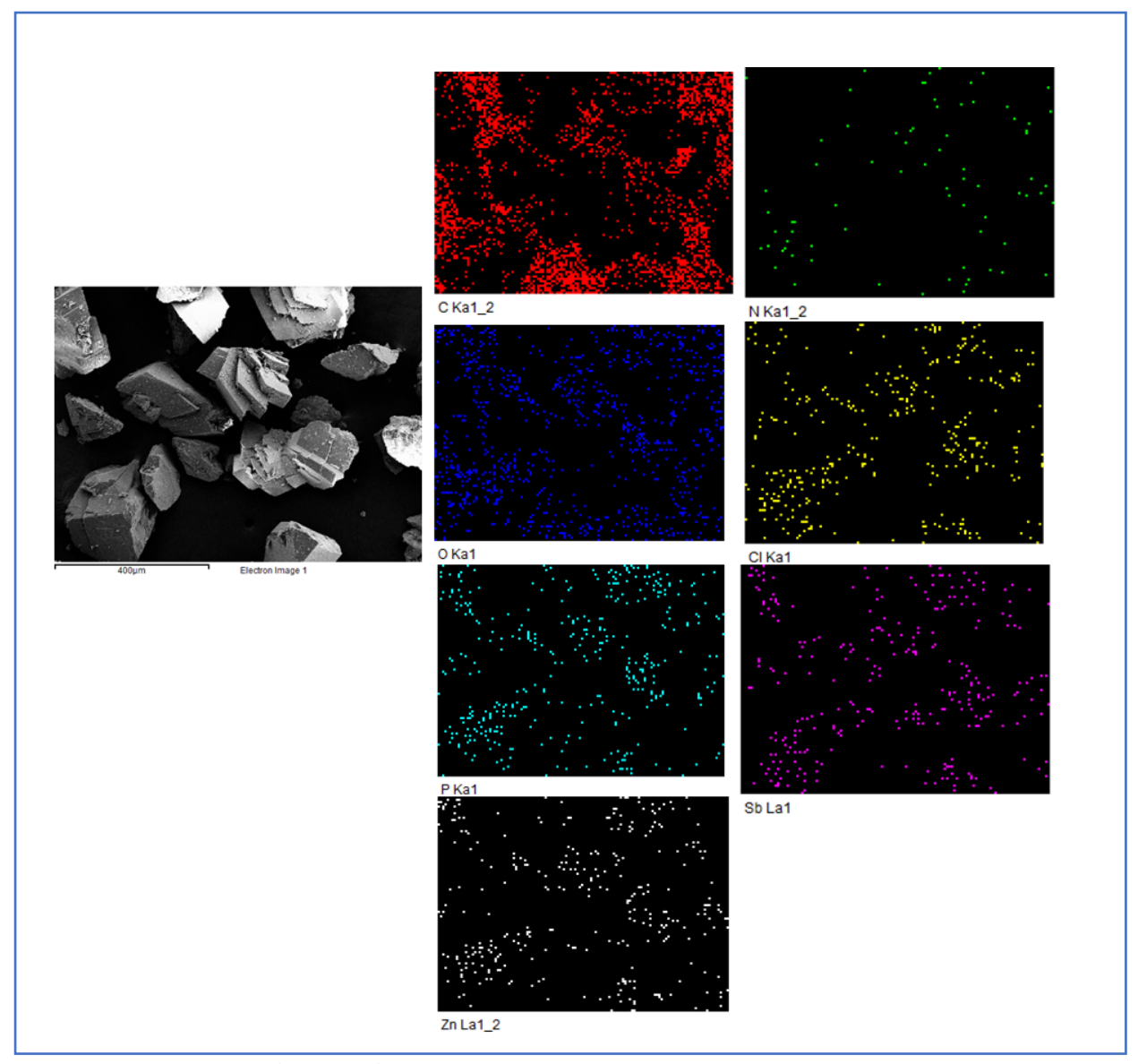


Figure 3.43: Elemental mapping of compound 3.3.

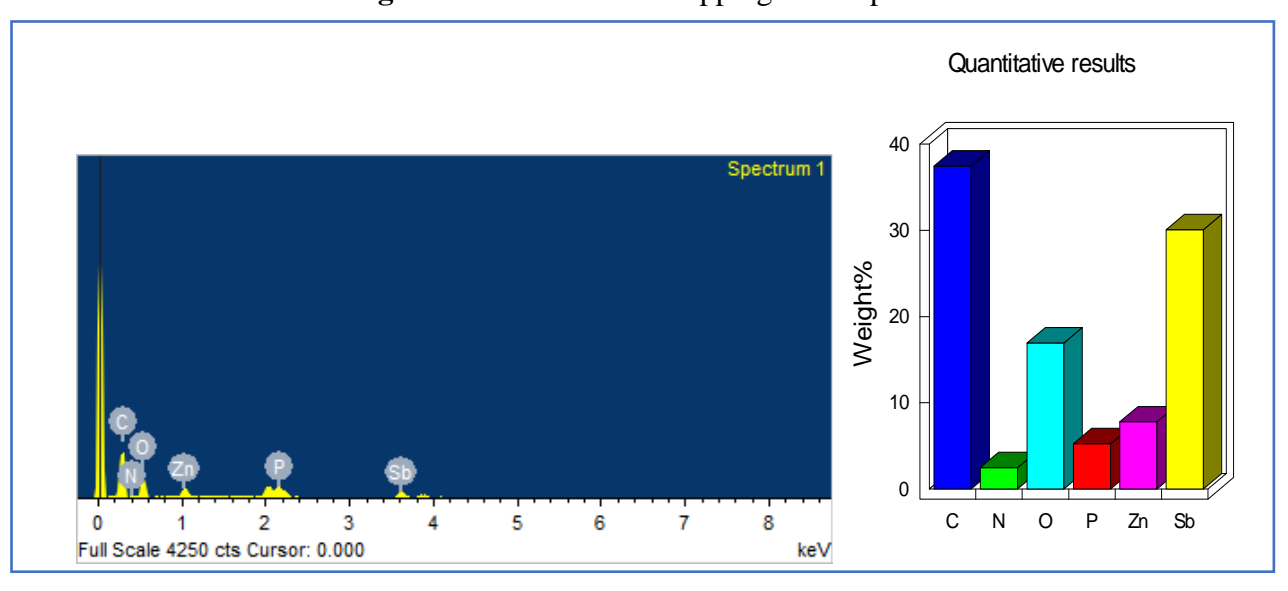


Figure 3.44: EDAX spectrum of compound 3.4.

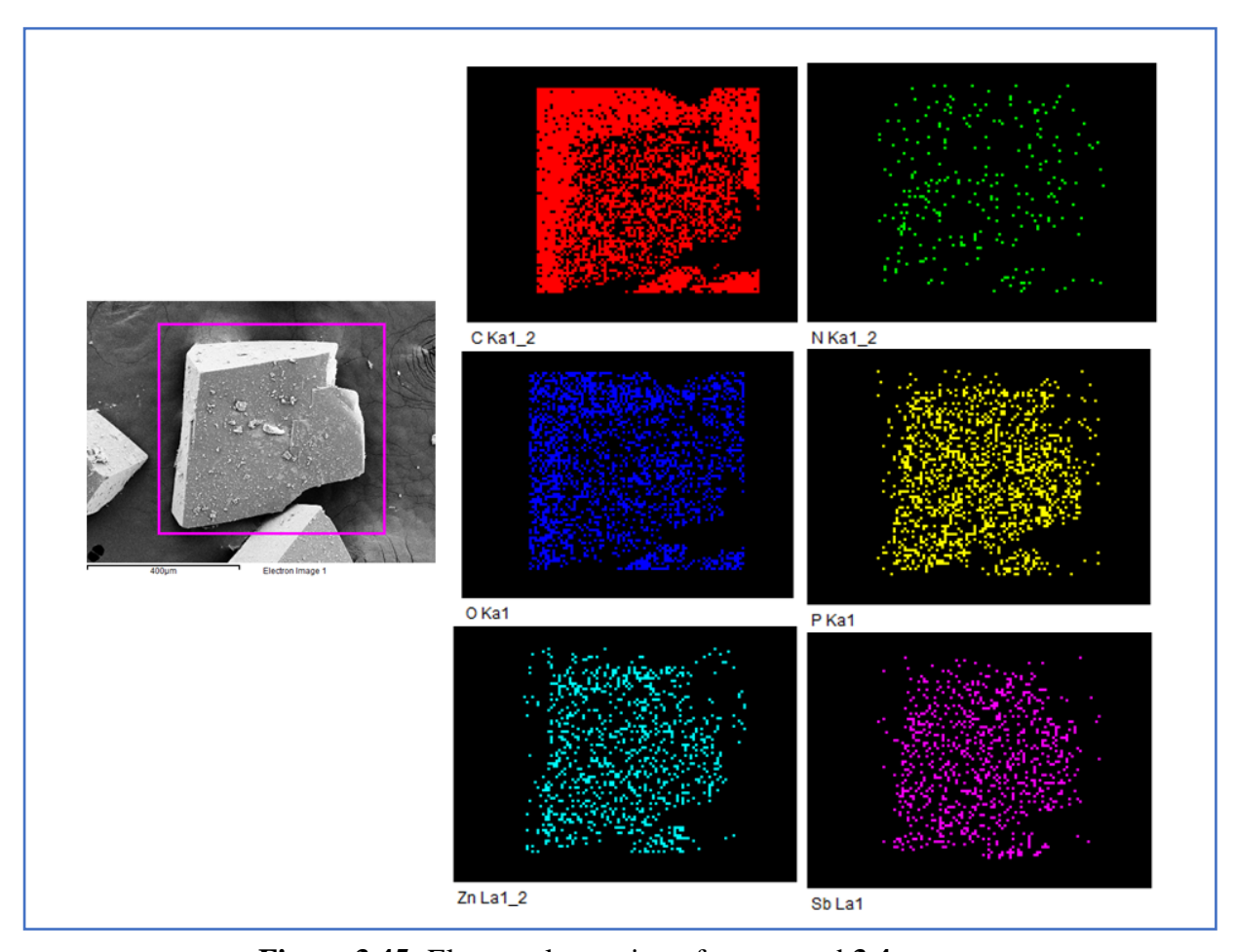


Figure 3.45: Elemental mapping of compound 3.4.

Table 3.8: Elemental analysis of compound 3.1 from ICP-OES analysis

Parameters	Calculated (% by mass)	Observed (% by mass)
Phosphorus	7.2	7.44
Zinc	10.14	10.74
Antimony	18.88	18.68

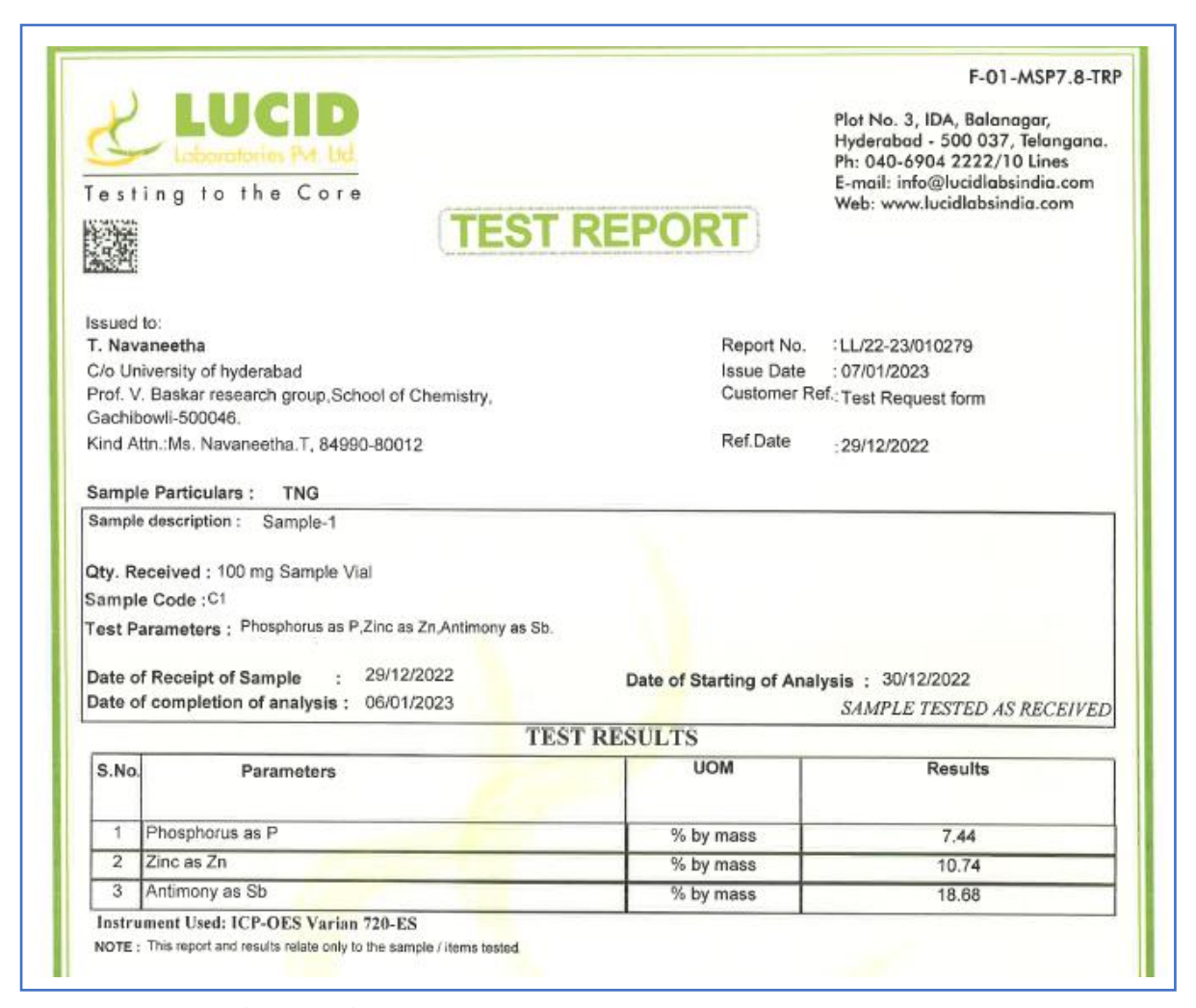


Figure 3.46: Results of ICP-OES analysis of compound 3.1.

Table 3.9: Elemental analysis of compound **3.2** from ICP-OES analysis

Parameters	Calculated (% by mass)	Observed (% by mass)
Phosphorus	7.38	6.09
Zinc	5.19	4.47
Antimony	29.02	29.07

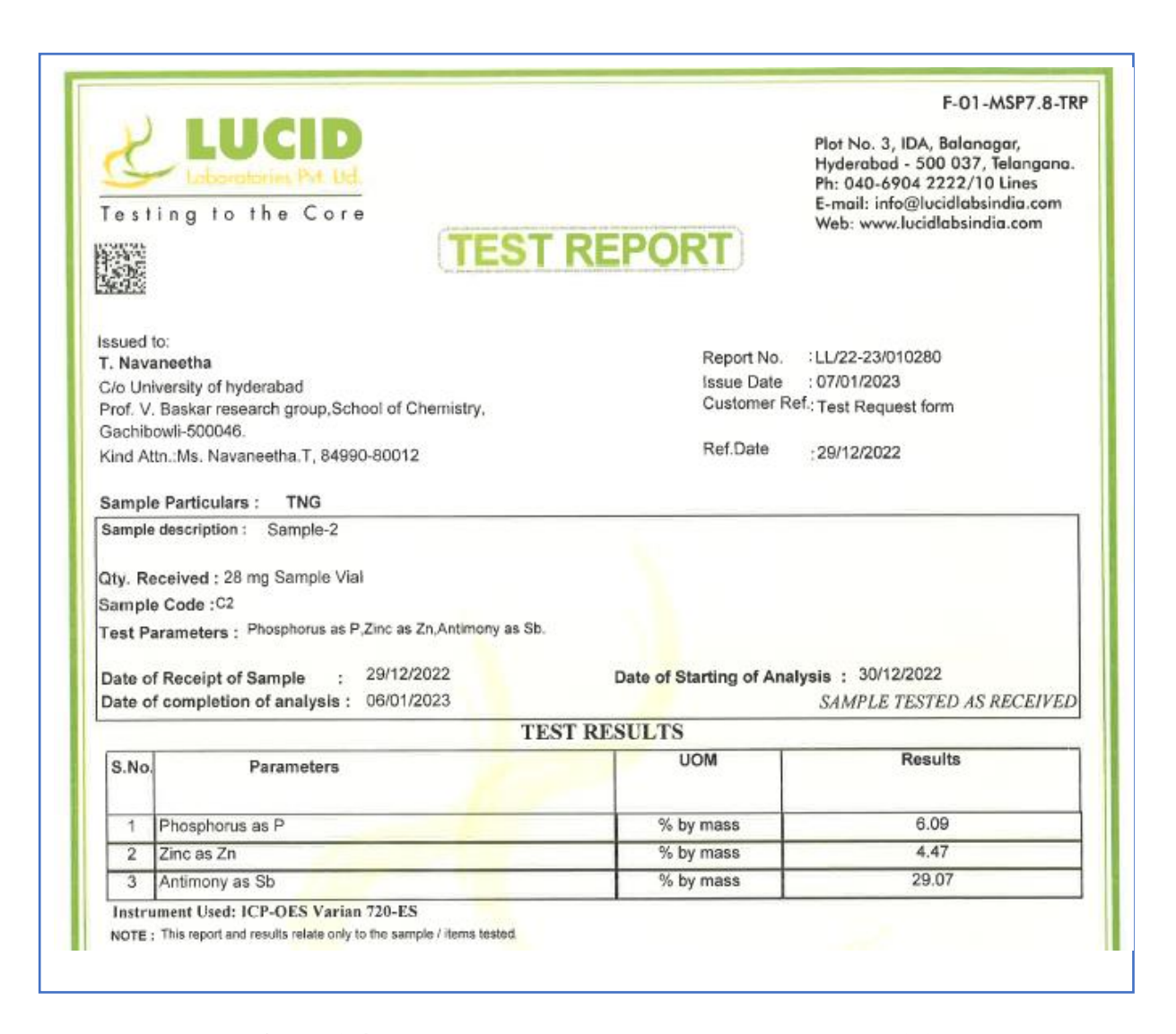


Figure 3.47: Results of ICP-OES analysis of compound 3.2.

Table 3.10: Elemental analysis of compound **3.3** from ICP-OES analysis

Parameters	Calculated (% by mass)	Observed (% by mass)
Phosphorus	6.34	6.33
Zinc	6.69	6.85
Antimony	24.92	23.77

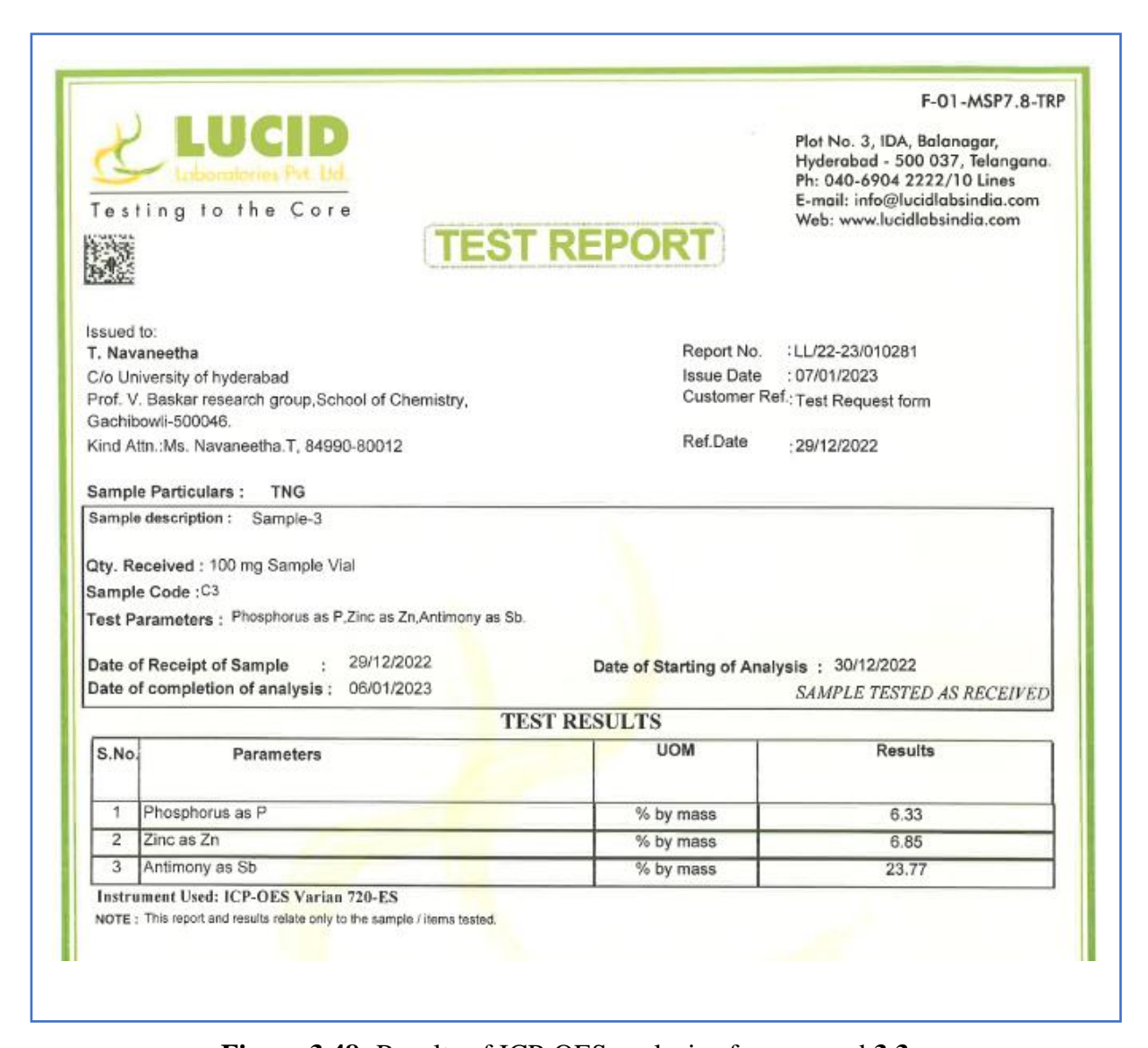


Figure 3.48: Results of ICP-OES analysis of compound 3.3.

Table 3.11: Elemental analysis of compound **3.4** from ICP-OES analysis

Parameters	Calculated (% by mass)	Observed (% by mass)
Phosphorus	6.24	6.28
Zinc	6.59	6.69
Antimony	24.53	24.23

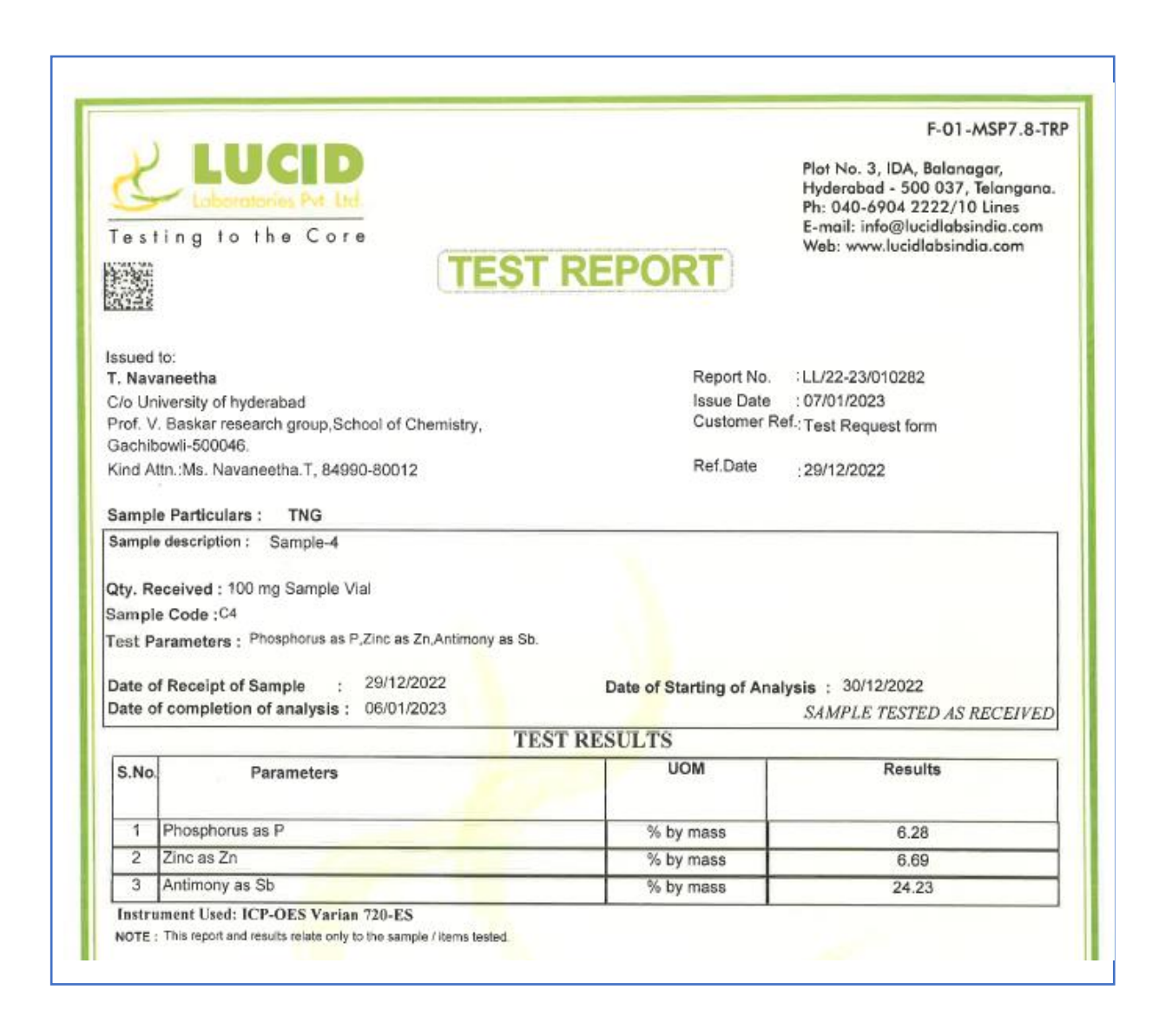


Figure 3.49: Results of ICP-OES analysis of compound 3.4.

Table 3.12: Binding affinity (Atomic contact energy [ACE]) score of compounds **1-4** with the Gyrase B protein

Compound	Atomic contact energy (ACE) value	Score
	(Kcal/mol)	
3.1	-236.37	4240
3.2	-298.29	5718
3.3	-218.81	3754
3.4	-311.77	6544

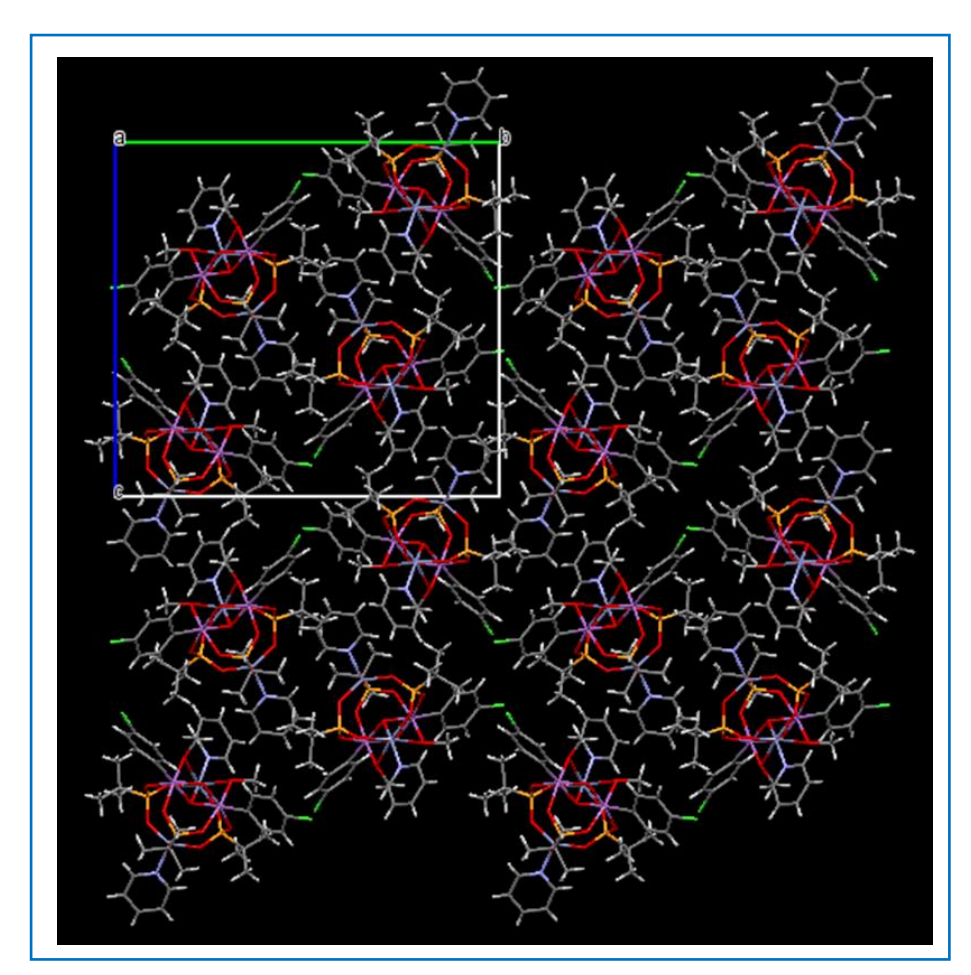


Figure 3.50: Packing diagram of compound 3.1 along the a-axis.

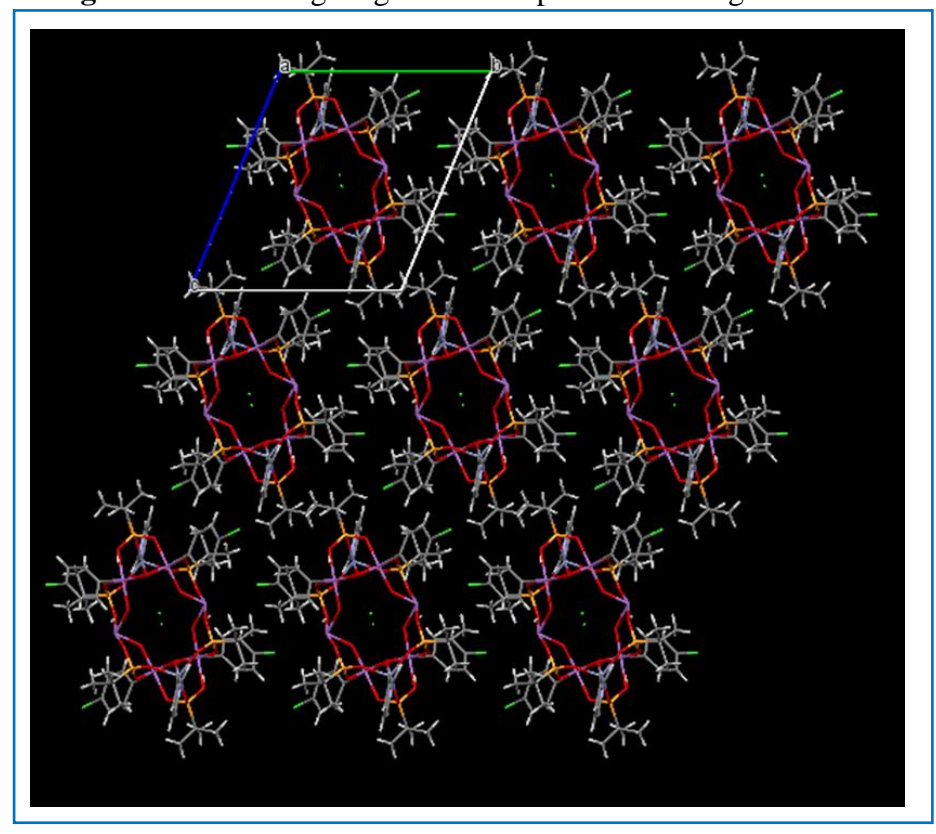


Figure 3.51: Packing diagram of compound 3.2 along the a-axis.

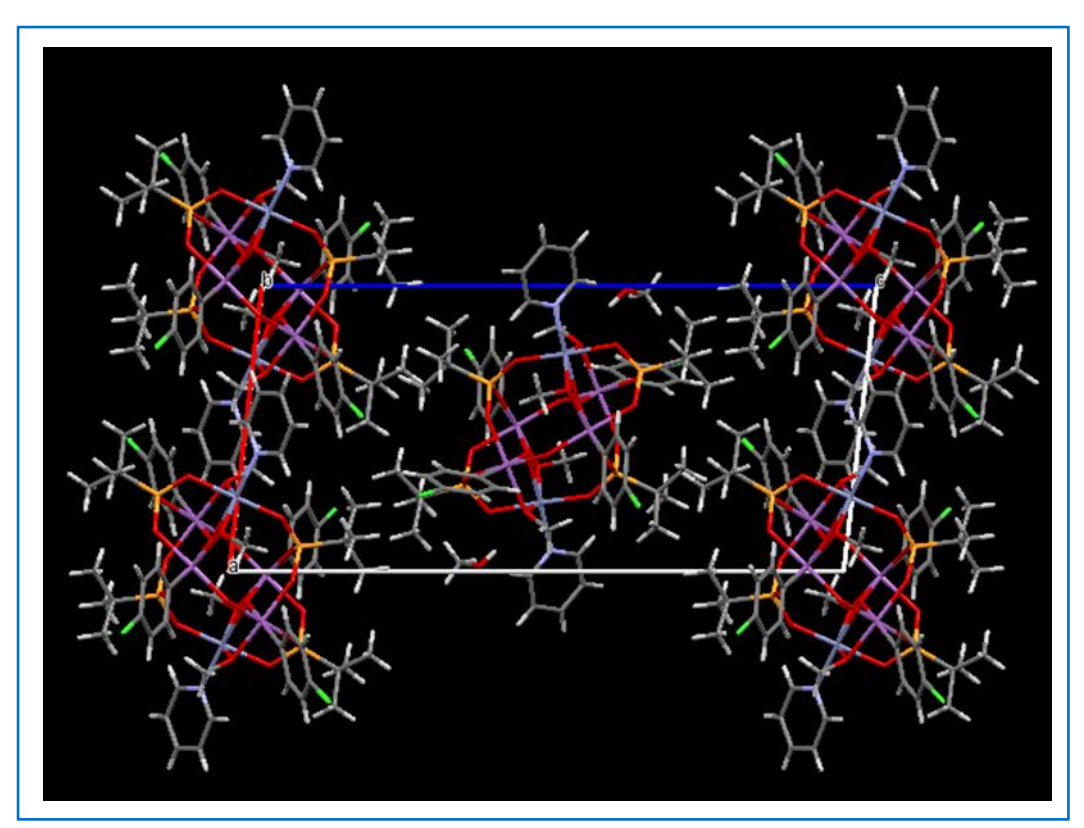


Figure 3.52: Packing diagram of compound 3.3 along the b-axis.

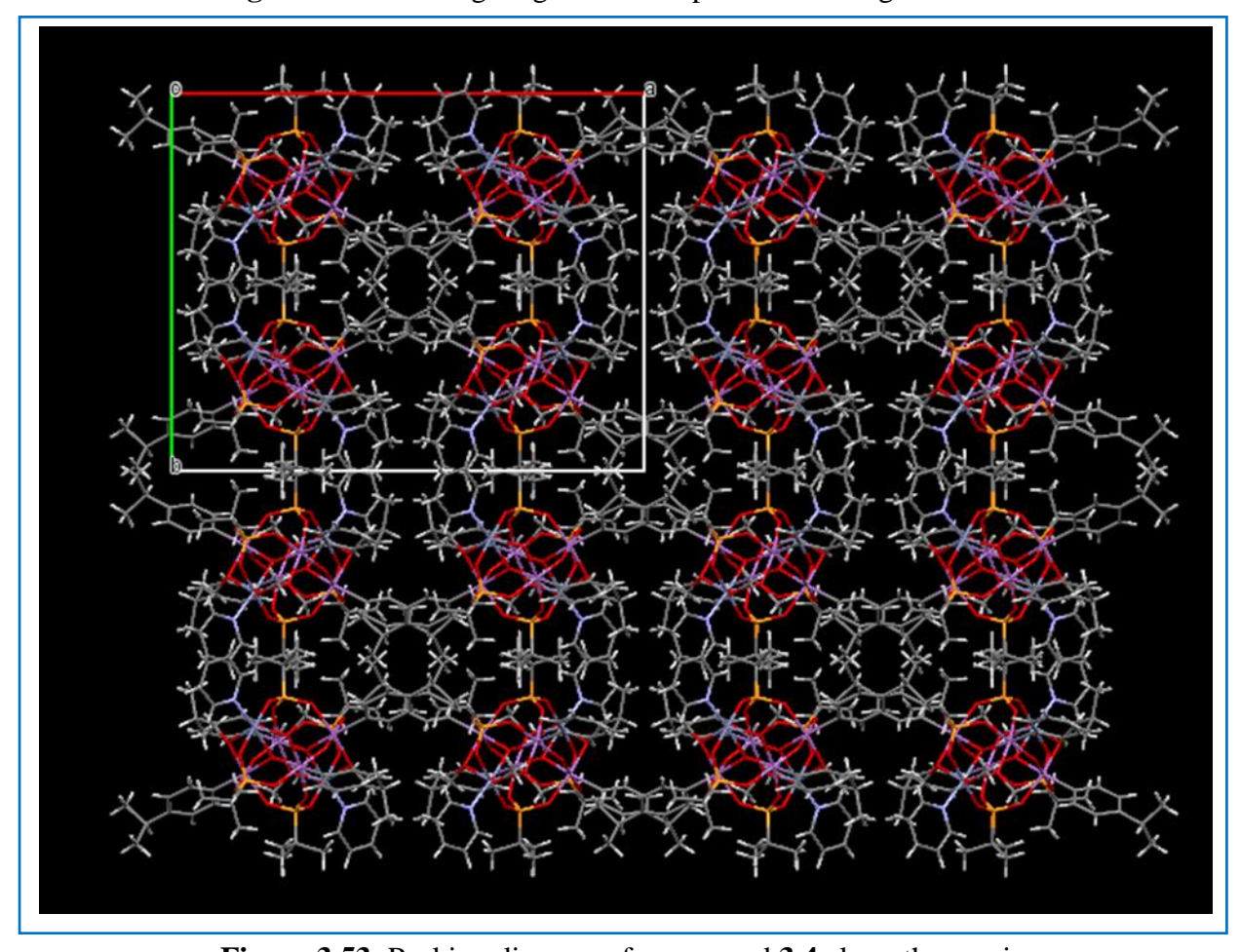


Figure 3.53: Packing diagram of compound **3.4** along the c-axis.

3.7 References:

- (a) Baskar, V.; Shanmugam, M.; Helliwell, M.; Teat, S. J.; Winpenny, R. E. P. J. Am. Chem. Soc. 2007, 129, 3042–3043. (b) Ugandhar, U.; Baskar, V. Dalton Trans. 2016, 45, 6269–6274. (c) Jami, A. K.; Prabhu, M. S. R.; Baskar, V. Organometallics 2010, 29, 1137–1143. (d) Jami, A. K.; Baskar, V. Dalton Trans. 2012, 41, 12524–12529. (e) Prabhu, M. S. R.; Jami, A. K.; Baskar, V. Organometallics 2009, 28, 3953–3956. (f) Santhana Raj Prabhu, M.; Ugandhar, U.; Baskar, V. Dalton Trans. 2016, 45, 6963–6967. (g) Srungavruksham, N. K.; Baskar, V. Dalton Trans. 2015, 44, 6358–6362. (h) Beckmann, J.; Finke, P.; Hesse, M.; Wettig, B. Angew. Chem. Int. Ed. 2008, 47, 9982.
- (a) Ali, J.; Mubarak, M. M.; Samuel, C.; Kantroo, H. A.; Malik, A.; Ahmad, Z.; Baskar,
 V. J. Inorg. Biochem. 2022, 235, 111909. (b) McKelvie, J. C.; Richards, M. I.; Harmer,
 J. E.; Milne, T. S.; Roach, P. L.; Oyston, P. C. F. Br. J. Pharmacol. 2013, 168, 172–188.
- (a) Nicholson, B. K.; Clark, C. J.; Wright, C. E.; Groutso, T. *Organometallics* 2010, 29, 6518–6526.
 (b) Nicholson, B. K.; Clark, C. J.; Jameson, G. B.; Telfer, S. G. *Inorg. Chim. Acta* 2013, 406, 53–58.
 (c) Nicholson, B. K.; Clark, C. J.; Wright, C. E.; Telfer, S. G.; Groutso, T. *Organometallics* 2011, 30, 6612–6616;
 (d) Nicholson, B. K.; Clark, C. J.; Telferc, S. G.; Groutsod, T. *Dalton Trans.* 2012, 41, 9964-9970.
- (a) Ugandhar, U.; Navaneetha, T.; Ali, J.; Mondal, S.; Vaitheeswaran, G.; Baskar, V. *Inorg. Chem.* 2020, 59, 6689–6696. (b) Ali, S.; Muryn, C. A.; Tuna, F.; Winpenny, R. E. P. *Dalton Trans.* 2010, 39, 124–131. (c) Ali, S.; Muryn, C. A.; Winpenny, R. E. P. *Dalton Trans.* 2010, 39, 9588–9597. (d) Ali, S.; Baskar, V.; Muryn, C. A.; Winpenny, R. E. P. *Chem. Commun.* 2008, 4, 6375–6377.
- (a) Wu, D.; Zhang, P. F.; Yang, G. P.; Hou, L.; Zhang, W. Y.; Han, Y. F.; Liu, P.; Wang, Y. Y. Coord. Chem. Rev. 2021, 434, 213709; (b) Zhu, R.; Ding, J.; Jin, L.; Pang, H. Coord. Chem. Rev. 2019, 389, 119–140; (c) Gheorghe, A.; Imaz, I.; Van Der Vlugt, J. I.; Maspoch, D.; Tanase, S. Dalton Trans. 2019, 48, 10043–10050. (d) Peralta, R. C.; Villanueva, J. M. R.; Hernández, J. M. M.; Morales, D. M.; Herrera, L. A. A. Polyhedron 2022, 224, 115995.
- (a) Maheswaran, S.; Chastanet, G.; Teat, S. J.; Mallah, T.; Sessoli, R.; Wernsdorfer, W.; Winpenny, R. E. P. Angew. Chem. Int. Ed. 2005, 44, 5044–5048. (b) Brechin, E. K.; Coxall, R. A.; Parkin, A.; Parsons, S.; Tasker, P. A.; Winpenny, R. E. P. Angew. Chem. Int. Ed. 2001, 40, 2700–2703. (c) Shanmugam, M.; Chastanet, G.; Mallah, T.; Sessoli, R.; Teat, S. J.; Timco, G. A.; Winpenny, R. E. P. Chem. Eur. J. 2006, 12, 8777–

- 8785. (d) Aromí, G.; Batsanov, A. S.; Christian, P.; Helliwell, M.; Parkin, A.; Parsons, S.; Smith, A. A.; Timco, G. A.; Winpenny, R. E. P. *Chem. Eur. J.* **2003**, *9*, 5142–5161.
- Yang, Q.; Stephen, A. G.; Adelsberger, J. W.; Roberts, P. E.; Zhu, W.; Currens, M. J.;
 Feng, Y.; Crise, B. J.; Gorelick, R. J.; Rein, A. R.; Fisher, R. J.; Shoemaker, R. H.; Sei,
 S. J. Virol. 2005, 79, 6122–6133.
- 8. Friedheim, E. A. H.; Vogel, H. J.; Berman, R. L. J. Am. Chem. Soc. 1947, 69, 560–562.
- (a) Heyerdahl, S. L.; Rozenberg, J.; Jamtgaard, L.; Rishi, V.; Varticovski, L.; Akah, K.; Scudiero, D.; Shoemaker, R. H.; Karpova, T. S.; Day, R. N.; McNally, J. G.; Vinson, C. Eur. J. Cell Biol. 2010, 89, 564–573. (b) Rishi, V.; Oh, W. J.; Heyerdahl, S. L.; Zhao, J.; Scudiero, D.; Shoemaker, R. H.; Vinson, C. J. Struct. Biol. 2010, 170, 216–225. (c) Zhao, J.; Stagno, J. R.; Varticovski, L.; Nimako, E.; Rishi, V.; McKinnon, K.; Akee, R.; Shoemaker, R. H.; Ji, X.; Vinson, C. Mol. Pharmacol. 2012, 82, 814–823.
- (a) Seiple, L. A.; Cardellina, J. H.; Akee, R.; Stivers, J. T. *Mol. Pharmacol.* 2008, 73, 669–677.
 (b) Srinivasan, A.; Wang, L.; Cline, C. J.; Xie, Z.; Sobol, R. W.; Xie, X.; Gold, B. *Biochemistry* 2012, 51, 6246–6259.
 (c) Rai, G.; Vyjayanti, V. N.; Dorjsuren, D.; Simeonov, A.; Jadhav, A.; Wilson, D. M.; Maloney, D. J. *J. Med. Chem.* 2012, 55, 3101–3112.
 (d) Kaur, G.; Cholia, R. P.; Mantha, A. K.; Kumar, R. *J. Med. Chem.* 2014, 57, 10241–10256.
- 11. Kim, H.; Cardellina, J. H.; Akee, R.; Champoux, J. J.; Stivers, J. T. *Bioorg. Chem.* **2008**, *36*, 190–197.
- 12. Mak, L. H.; Knott, J.; Scott, K. A.; Scott, C.; Whyte, G. F.; Ye, Y.; Mann, D. J.; Ces, O.; Stivers, J.; Woscholski, R. *Bioorg. Med. Chem.* **2012**, *20*, 4371–4376.
- 13. (a) Yang, P.; Lin, Z.; Bassil, B. S.; Alfaro-Espinoza, G.; Ullrich, M. S.; Li, M. X.; Silvestru, C.; Kortz, U. *Inorg. Chem.* **2016**, *55*, 3718–3720. (b) Yang, P.; Lin, Z.; Alfaro-Espinoza, G.; Ullrich, M. S.; Raţ, C. I.; Silvestru, C.; Kortz, U. *Inorg. Chem.* **2016**, *55*, 251–258. (c) Ma, T.; Yang, P.; Dammann, I.; Lin, Z.; Mougharbel, A. S.; Adašcal'itçi, F.; Mitea, R.; Silvestru, C.; Thorstenson, C.; Ullrich, M. S.; Cseh, K.; Jakupec, M. A.; Keppler, B. K.; Donalisio, M.; Cavalli, R.; Lembo, D.; Kortz, U. *Inorg. Chem.* **2020**, *59*, 2978–2987.
- (a) Vahrenkamp, H. *Acc. Chem. Res.* 1999, 32, 589-596. (b) Vallee, B. L.; Auld, D. S. *Biochemistry* 1993, 32, 6493–6500. (c) Hough, E.; Hansen, L. K.; Birknes, B.; Jynge, K.; Hansen, S.; Derewenda, Z. *Nature* 1989, 338, 357–360. (d) Vallee, B. L.; Auld, D. S. *Acc. Chem. Res.* 1993, 26, 543–551.

- (a) Doak, G. O.; Steinman, H. G. J. Am. Chem. Soc. 1946, 68, 1987–1989.
 (b) Liu, Z.;
 Ozawa, Y.; Yagasaki, A. Bull. Chem. Soc. Jpn. 2014, 87, 1245–1251.
- 16. Crofts, P. C.; Kosolapoff, G. M. J. Am. Chem. Soc. 1953, 75, 3379–3383.
- 17. Chandrasekhar, V.; Kingsley, S.; Rhatigan, B.; Lam, M. K.; Rheingold, A. L. *Inorg. Chem.* **2002**, *41*, 1030–1032.
- (a) Sheldrick, G. M. Acta Crystallogr. Sect. A Found. Crystallogr. 2015, 71, 3–8. (b) Dolomanov, O. V.; Bourhis, L. J.; Gildea, R. J.; Howard, J. A. K.; Puschmann, H. J. Appl. Crystallogr. 2009, 42, 339–341. (c) Sheldrick, G. M. Acta Crystallogr. Sect. C Struct. Chem. 2015, 71, 3–8. (d) Bourhis, L. J.; Dolomanov, O. V.; Gildea, R. J.; Howard, J. A. K.; Puschmann, H. Acta Crystallogr. Sect. A Found. Crystallogr. 2015, 71, 59–75.
- Elshikh, M.; Ahmed, S.; Funston, S.; Dunlop, P.; McGaw, M.; Marchant, R.; Banat, I.
 M. *Biotechnol. Lett.* 2016, 38, 1015–1019.
- 20. Duhovny, D. S.; Inbar, Y.; Nussinov, R.; Wolfson, H. J. *Nucleic Acids Res.* **2005**, *33*, 363–367.
- 21. (a) Prieto, P.; Pineda, M.; Aguilar, M. *Anal. Biochem.* **1999**, *269*, 337–341. (b) Rutuparna, J.; Ali, A.; Ghazi, I. A. *S. Afr. J. Bot.* **2022**, *149*, 758-767.
- 22. Coxall, R. A.; Harris, S. G.; Henderson, D. K.; Parsons, S.; Tasker, P. A.; Winpenny, R. E. P. *J. Chem. Soc. Dalton Trans.* **2000**, 2349–2356.
- (a) Aronica, C.; Chastanet, G.; Zueva, E.; Borshch, S. A.; Clemente-Juan, J. M.; Luneau, D. J. Am. Chem. Soc. 2008, 130, 2365–2371. (b) Thorp, H. H. Inorg. Chem. 1992, 31, 1585–1588. (c) Brese, N. E.; O'Keeffe, M. Acta Crystallogr. Sect. B 1991, 47, 192–197. (d) Altermatt, D.; Brown, I. D. Acta Crystallogr. Sect. B 1985, 41, 240–244.
- 24. (a) Srungavruksham, N. K.; Baskar, V. Eur. J. Inorg. Chem. 2013, 4345–4352. (b) Kishore, P. V. V. N.; Baskar, V. Inorg. Chem. 2014, 53, 6737–6742. (c) Ali, J.; Navaneetha, T.; Baskar, V. Inorg. Chem. 2020, 59, 741–747. (d) Chandrasekhar, V.; Baskar, V.; Steiner, A.; Zacchini, S. Organometallics 2002, 21, 4528–4532. (e) Jones, C. Coord. Chem. Rev. 2001, 215, 151–169. (f) Chandrasekhar, V.; Thirumoorthi, R. Organometallics 2009, 28, 2637–2639.
- 25. (a) Furuya, T.; Kaiser, H. M.; Ritter, T. Angew. Chem. Int. Ed. 2008, 47, 5993–5996.
 (b) Kaspi, A. W.; Yahav-Levi, A.; Goldberg, I.; Vigalok, A. Inorg. Chem. 2008, 47, 5–7.

Discrete molecular....

- 26. (a) Hu, S. Z.; Zhou, Z. H.; Robertson, B. E. Z. Kristallogr. **2009**, 224, 375–383. (b) Allinger, N. L.; Zhou, X.; Bergsma, J. J. Mol. Struct. (Theochem) **1994**, 312, 69–83.
- 27. Larsson, D. G. J.; Flach, C. F. Nat. Rev. Microbiol. 2022, 20, 257–269.
- 28. Wright, P. M.; Seiple, I. B.; Myers, A. G. Angew. Chem. Int. Ed. 2014, 53, 8840–8869.
- (a) Mitcheltree, M. J.; Pisipati, A.; Syroegin, E. A.; Silvestre, K. J.; Klepacki, D.; Mason, J. D.; Terwilliger, D. W.; Testolin, G.; Pote, A. R.; Wu, K. J. Y.; Ladley, R. P.; Chatman, K.; Mankin, A. S.; Polikanov, Y. S.; Myers, A. G. Nature 2021, 599, 507–512. (b) Babii, C.; Mihalache, G.; Bahrin, L. G.; Neagu, A. N.; Gostin, I.; Mihai, C. T.; Sârbu, L. G.; Birsa, L. M.; Stefan, M. PLoS One 2018, 13, 1–15. (c) Zhang, J.; Zhaob, X.; Cappiello, J. R.; Yang, Y.; Cheng, Y.; Liu, G.; Fang, W.; Luo, Y.; Zhang, Y.; Dong, J.; Zhang, L.; Sharpless, K. B. Proc. Natl. Acad. Sci. U. S. A. 2021, 118, 1–7. (d) Reithuber, E.; Wixe, T.; Ludwig, K. C.; Muller, A.; Uvell, H.; Grein, F.; Lindgren, A. E. G.; Muschiol, S.; Nannapaneni, P.; Eriksson, A.; Schneider, T.; Normark, S.; Henriques-Normark, B.; Almqvist, F.; Mellroth, P. Proc. Natl. Acad. Sci. U. S. A. 2021, 118, 47.
- (a) Yule, I. A.; Czaplewski, L. G.; Pommier, S.; Davies, D. T.; Narramore, S. K.; Fishwick, C. W. G. *Eur. J. Med. Chem.* 2014, 86, 31–38; (b) Narramore, S.; Stevenson, C. E. M.; Maxwell, A.; Lawson, D. M.; Fishwick, C. W. G. *Bioorg. Med. Chem.* 2019, 27, 3546–3550.
- 31. Martelli, G.; Giacomini, D. Eur. J. Med. Chem. 2018, 158, 91–105.

Octanuclear Lanthanide Oxo Clusters Stabilized by a Pro-Ligand Approach

CHAPTER

4

Abstract: Three isostructural 4*f*-main group-based metal oxo clusters [(*p*-ClC₆H₄Sb)₄Ln₈(μ₄-O)₄(μ₂-O)₂(*t*-BuPO₃)₈(μ₂-OCH₃)₈{O₂PC(CH₃)₂C(CH₃)₂PO₂}₂(H₂O)₄], where Ln= Sm (**4.1**), Tb (**4.2**) and Dy (**4.3**) have been obtained from a reaction of the organoantimonate-phosphonate cluster with lanthanide nitrate salts in the presence of a base under solvothermal conditions. Compounds **4.1-4.3** have been characterized by single-crystal X-ray diffraction, elemental analysis and TGA analysis. An octanuclear Ln₈ cluster, which is built of two Ln₄ distorted cubane has been stabilized by organostibonate as a ligand. Compounds **4.1-4.3** possess the twelve-membered type architecture, containing eight lanthanide metal ions that have eight coordination modes and four antimony metal ions that have six coordination modes. Interestingly, in compounds **4.1-4.3** ethane elimination followed by C-C bond formation has been observed.

4.1 Introduction:

Metal phosphonates attract enormous research interest for their aesthetically pleasant morphology with interesting physical properties, particularly in the area of molecular magnetism, luminescence, catalysis, nonlinear optics and proton conductors. Phosphonate ligands with the general formula RPO₃²- provide anchoring sites for building a variety of molecular cages. To date, high nuclearity 3d phosphonate-based metal clusters with a $[V_{12}]$, $[Mn_{16}]$, $[Mn_{19}]$, $[Fe_9]$, $[Fe_{12}]$, $[Ni_8]$, $[Ni_{12}]$, $[Co_{12}]$, $[Co_{15}]$, $[Cu_{16}]$, $[Cu_{18}]$, $[Cu_{26}]$ core⁶ and a pure 4f phosphonates such as nonnuclear type [Eu₉], horseshoes type [Ln₈] (Ln=Gd, Dy and Tb), a pseudo-icosahedral type [Gd₁₂], Ln₁₀ (Ln=Gd, Tb), tetranuclear Ln₄ (Ln=Gd, Tb, Dy, Ho, Er) cages⁷ have been reported. Researchers reported a high nuclearity 3d-4f mixed phosphonate clusters with intriguing structures such as grid-like [Co₈Gd₄], [Co₈Gd₈], Well-Dawson-like [Fe₆Ln₆P₆], diamond-shaped [Mn₉Gd₉], bowl-shaped [Mn₆Gd₆], [Cu₂₄M₈] (M= Dy, Gd, Y), [Ln₁₀Co₃] (Ln=Gd, Dy), symmetric trigonal-bipyramidal [Mn₉Gd₉] truncated-ball shaped [Mn₆Dy₆] core [Cr₆Ln₂] (where Ln=La, Tb, Dy, Ho and Gd), [Cu₃Ln₉P₆] and [Cu₆Ln₆P₆] (where Ln= Tb, Gd, Ho, Dy, Er) clusters. In contrast to 3d metal phosphonates, 4f metal phosphonates are rare in the literature due to solubility problems. However, the low solubility nature of metal phosphonates researchers find an issue in terms of isolation and characterization. To overcome this issue, three strategies have been adopted. Zubieta et al. used solvothermal techniques to synthesize metal cages. Chandrasekhar et al. used co-ligand as a metal precursor have been used in addition to the ligand, which can maintain solubility by occupying a few coordination sites on the metal ion and forming soluble products. ¹⁰ By using this method, many transition metal phosphonates have been reported. ¹¹ Many research groups reported a series of 3d and 4f metal phosphonate cages by displacing carboxylates with phosphonates will increase the growth of the metal cages because of the larger denticity of phosphonates.¹² The chemistry of organoantimony (V) oxo clusters attained interest due to their reactivity in the field of catalysis 13 and biology. 14 Our group investigated the reactivity of organostibonic acid with different protic ligands. It revealed the formation of fascinating structures such as adamantane, triangle, cube, tetrameric butterfly cores and organoantimonybased POM motifs.¹⁵ Bulky substituents are added to an Sb atom to stabilize well-defined organostibonic acids. 16 Arylstibonic acids in the presence of base lead to self-condensation and form novel polyoxometalates with fascinating structures, ESI-MS technique is used to study the oligomerization of organostibonic acids.¹⁷

To avoid the insolubility problem of phosphonates, Winpenny et al. used antimonates as suitable ligands used as inorganic cryptands due to their polycondensation nature. For

phosphonates, no condensation is found and for antimonates, polycondensation is observed; mixing of both ligands leads to partial condensation, revealing the formation of polydentate bridging oxygen donor ligands. Research groups have used the organostibonate-phosphonate cluster as a pro-ligand in synthesizing mixed 3*d*-main group-based metal oxo clusters. ¹⁸ To the best of our knowledge, there aren't many reports of main group phosphonates acting as a pro-ligand for lanthanides.

Herein, we extend the main group metal phosphonates as a pro-ligand approach towards 4f ions, a solvothermal reaction of the organoantimonate-phosphonate cluster with lanthanide salts in the presence of 2,6-lutidine. Single crystal X-ray diffraction studies revealing the formation of mixed 4f-main group-based metal oxo clusters $[(p-ClC_6H_4Sb)_4Ln_8(\mu_4-O)_4(\mu_2-O)_2(t-BuPO_3)_8(\mu_2-OCH_3)_8\{O_2PC(CH_3)_2C(CH_3)_2PO_2\}_2(H_2O)_4]$, where Ln= Sm (4.1), Tb (4.2) and Dy (4.3).

4.2 Experimental Section:

4.2.1 General Information:

p-Chlorophenylstibonic acid¹⁹ and *t*-butylphosphonic acid²⁰ were synthesized according to literature reports. Solvents and common reagents were purchased from Sigma-Aldrich. The mixed organostibonate-phosphonate precursor [(*p*-ClC₆H₄Sb)₂(O)(*t*-BuPO₃H)₆]^{18b} was synthesized by condensation reactions of *p*-chlorophenylstibonic acid with *t*-butylphosphonic acid. The *p*-chlorophenylstibonic acid and *t*-butylphosphonic acid were mixed in a 1:2 ratio and stirred in acetonitrile (15 mL) for 24 h at room temperature. The solutions were filtered, and crystals were isolated on slow evaporation of acetonitrile. All the compounds used were dried under a high vacuum for half an hour before being subjected to spectroscopic and analytical techniques.

4.2.2 Instrumentation:

Infrared spectra were recorded with a NICOLET iS5 FTIR Spectrometer. Elemental analysis was performed with a Flash EA Series 1112 CHNS analyzer. Single crystal X-ray data for **4.1-4.3** were carried out at 112 (12), 114 (19) and 110 (14) K with an XtaLAB Synergy, a single source at offset/far, HyPix3000 diffractometer and a Rigaku Oxford HyPix3000 CCD plate detector system [λ (Mo K α) = 0.71073 Å] with a mirror monochromator. The data were reduced using CrysAlisPro 1.171.40.35a (Rigaku OD, 2018). The structures were solved using SHELXT and refined using SHELXL-2018/3 in Olex2 1.3-ac4 software. All non-hydrogen atoms were refined anisotropically. PXRD was recorded at room temperature using a Bruker D8 Advance diffractometer (Bruker-AXS, Karlsruhe, Germany) using Cu–K α X-radiation (λ

= 1.5406 Å) at 40 kV and 30 mA power. X-ray diffraction patterns were collected over a 2θ range of 5–80° at a scan rate of 3.9°/min. TGA was recorded for compounds **4.1-4.3** with PerkinElmer STA 8000 thermogravimetric analyzer under a nitrogen gas flow rate of 20 ml/min and heating rate of 10 °C/min. Graphics of the crystal structures have been performed with Diamond (version 3).

4.2.3 General Synthetic Procedures:

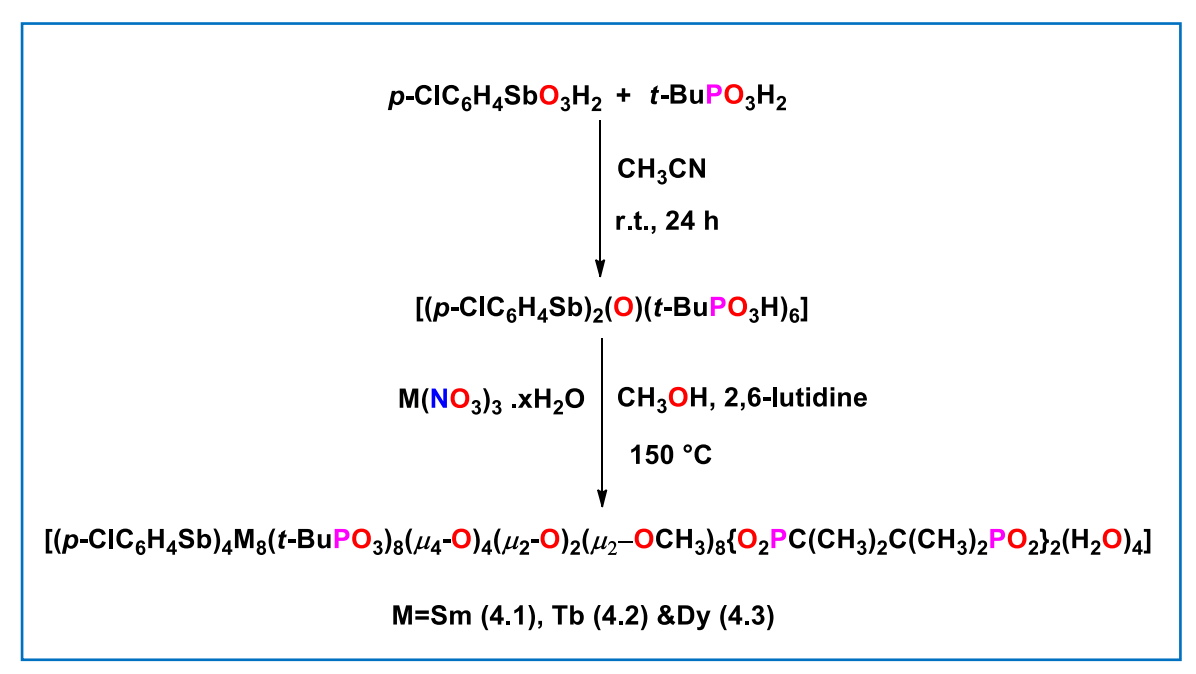
The general synthetic methodology for metal oxo clusters **4.1-4.3** is as follows: the corresponding mixed stibonate-phosphonate and hydrated lanthanide nitrate salts were dissolved in methanol (15 mL) followed by dropwise addition of 2,6-lutidine. The clear solution obtained was stirred for 2 h and then transferred into a Teflon digestion bomb and the mixture was heated at 150 °C for 16 h and then cooled slowly to room temperature for 36 h. The isolated crystals were powdered and subjected to a high vacuum for 30 min before being characterized by standard spectroscopic and analytical techniques.

Compound **4.1**: [(*p*-ClC₆H₄Sb)₂(O)(*t*-BuPO₃H)₆] (0.05 g, 0.038 mmol), samarium nitrate (0.067 g, 0.15 mmol) and 2, 6-lutidine (0.1 mL). Colorless single crystals were obtained upon slow cooling (36 h) of the methanol solution. Yield: 0.036 g (23% based on pro-ligand). IR (cm⁻¹): 2950 (wide), 2152 (m), 2005 (m), 1623 (m), 1478 (s), 1321 (m), 1119 (wide), 1009 (s), 930 (s), 831 (m), 813 (m), 726 (s), 663 (m), 536 (s). Anal. Calcd for C₇₆Cl₄H₁₄₄O₅₀P₁₂Sb₄Sm₈ (4067.4062): C, 22.48; H, 3.57. Found: C, 22.12; H, 3.32. All values are given as percentages. Compound **4.2**: [(*p*-ClC₆H₄Sb)₂(O)(*t*-BuPO₃H)₆] (0.05 g, 0.038 mmol), terbium nitrate (0.069 g, 0.152 mmol) and 2, 6-lutidine (0.1 mL). Colorless single crystals were obtained upon slow cooling (36 h) of the methanol solution. Yield: 0.040 g (25% based on pro-ligand). IR (cm⁻¹): 2952 (wide), 2187 (m), 2138 (m), 2004 (m), 1624 (m), 1478 (s), 1329 (m), 1120 (wide), 1042 (m), 1012 (m), 932 (s), 831 (m), 813 (m), 727 (s), 671 (m), 567 (s), 536 (s). Anal. Calcd for C₇₆Cl₄H₁₄₄O₅₀P₁₂Sb₄Tb₈ (4123.4511): C, 22.10; H, 3.51. Found: C, 21.91; H, 3.45. All values are given as percentages.

Compound **4.3:** $[(p\text{-ClC}_6\text{H}_4\text{Sb})_2(\text{O})(t\text{-BuPO}_3\text{H})_6]$ (0.05 g, 0.038 mmol), dysprosium nitrate (0.069 g, 0.151 mmol) and 2, 6-lutidine (0.1 mL). Colorless single crystals were obtained upon slow cooling (36 h) of the methanol solution. Yield: 0.038 g (24% based on pro-ligand). IR (cm⁻¹): 2951 (wide), 2159 (m), 1970 (m), 1625 (m), 1478 (s), 1323 (m), 1119 (wide), 1042 (m), 1011 (m), 931 (s), 831 (m), 813 (m), 727 (m), 663 (s), 537 (s). Anal. Calcd for $C_{76}Cl_4H_{144}O_{50}P_{12}Sb_4Dy_8$ (4163.4817): C, 21.95; H, 3.49. Found: C, 21.51; H, 3.41. All values are given as percentages.

4.3 Results and Discussion:

Compound **4.1-4.3** were prepared by a solvothermal reaction of the organoantimonate-phosphonate cluster with $Ln(NO_3)_3.xH_2O$, where Ln = Sm (**4.1**), Tb (**4.2**) and Dy (**4.3**) in the ratio of 1:4 in methanol using 2,6-lutidine as a base (**Scheme 4.1**). Colorless block-shaped



Scheme 4.1: Synthesis of complexes 4.1-4.3.

single crystals of **4.1-4.3** were grown by cooling the methanol solution to room temperature. Compounds 4.1-4.3 crystallizes in triclinic space group *P-1* with half of the molecules present in the asymmetric unit. Crystallographic information of compounds 4.1-4.3 are shown in Table 4.1. The selected bond lengths and bond angles of compounds 4.1-4.3 are shown in Tables 4.2-**4.4**. The molecular structures of clusters **4.1-4.3** resemble one another. The molecular structure of 4.1 (Figure 4.1a) is taken for discussion. The molecular structure of 4.1 contains eight samarium metal ions, four antimony metal ions, eight t-butyl phosphonates, four µ4-oxo bridges, bridges, eight methoxy two novel ligand two μ_2 -oxo groups, system{O₂PC(CH₃)₂C(CH₃)₂PO₂}₂ and four water molecules form a novel {Sm₈Sb₄P₁₂} molecular architecture. It is interesting to note that the self-condensation of two t-butyl phosphonates and ethane elimination followed by carbon-carbon bond formation results in the generation of the novel ligand system, {O₂PC(CH₃)₂C(CH₃)₂PO₂} (Figure 4.2d). Eight phosphonates are observed in the molecular structure; all phosphonates are bound to one antimony centre and two samarium centres in [3.111] coordination mode based on Harris notation.²² Here, eight samarium metal ions form two distorted cubane-type molecular

architectures, which are connected by novel phosphonate-based ligand systems and μ_2 -oxo bridges. The eight-coordination of four samarium sites is fulfilled with two phosphonates

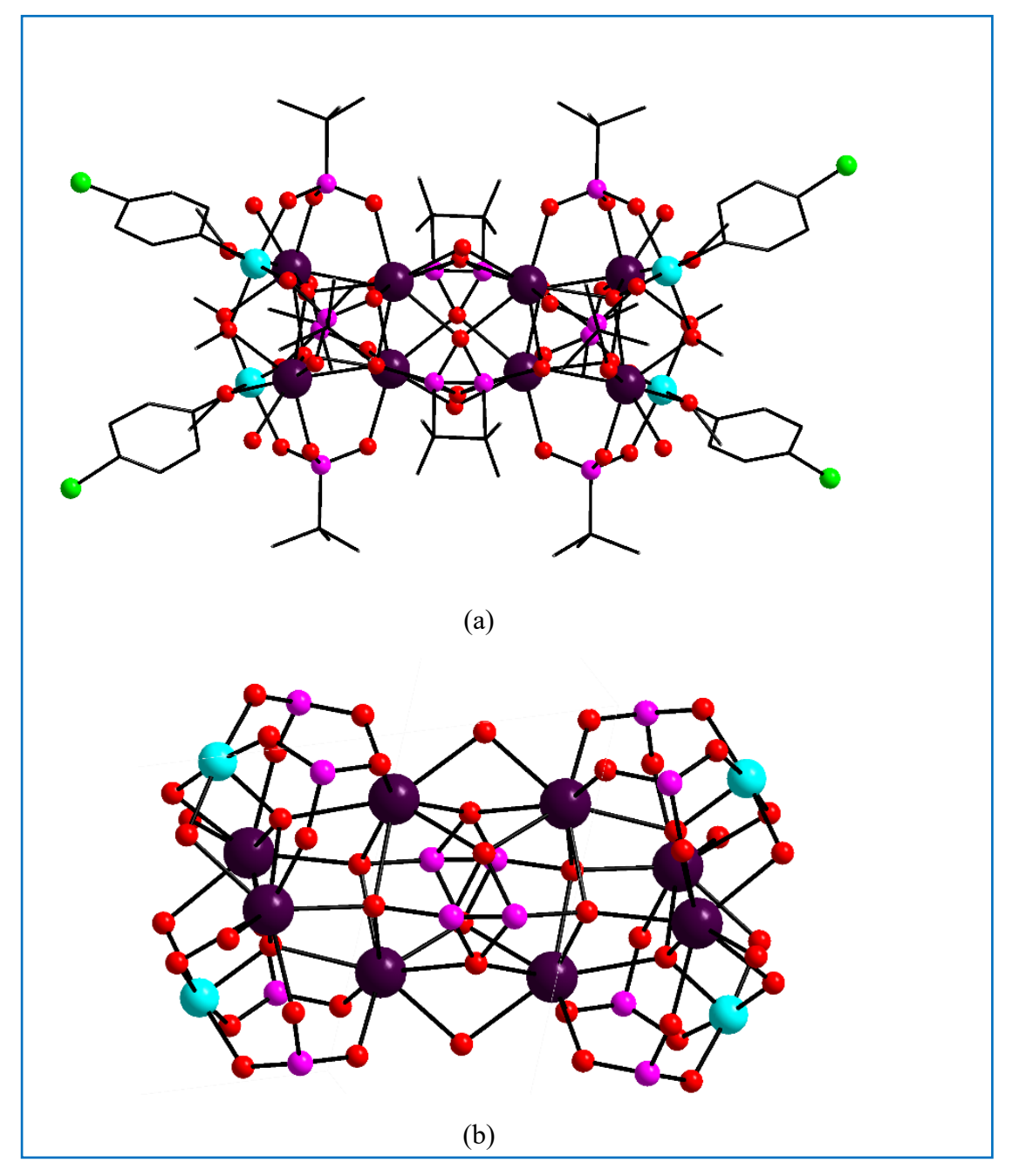


Figure 4.1: (a) Molecular and (b) Core structure of compound **5.1**. Color code cyan, Sb; violet, Sm; purple, P; red, O; grey, C. Hydrogens are omitted for clarity.

oxygen from each side, three μ_4 -oxo bridges, one μ_2 -oxo bridge and two oxygen from a phosphonate-based new ligand system containing a biaugmented trigonal prism geometry (**Figure 4.2a**) and other four samarium sites are fulfilled with two phosphonates oxygen from each side, two μ_4 -oxo bridges, two μ_2 -methoxy bridges, one oxygen from a phosphonate-based new ligand system and one oxygen from a water molecule containing a square antiprism

geometry (**Figure 4.2b**). All antimony atoms are present in six coordination modes and attain an octahedral geometry (**Figure 4.2c**). The coordination geometry around metal centers is confirmed by using SHAPE calculations (**Table 4.5**). Important bond metric parameters are shown; the Sm-O bond distances involving phosphonates, μ_4 -oxo, μ_2 -methoxy groups falls in the range of 2.492(8)-2.273(8) Å, 2.537(9)-2.482(8) Å, 2.458(10)-2.439(11) Å respectively. The Sb-O bond distances involving phosphonates, μ_4 -oxo and μ_2 -methoxy groups falls in the range of 2.029(10)-2.016(9) Å, 1.964(9)-1.953(8) Å and 2.033(10)-2.014(10) Å respectively. The Sm-O-Sm and Sm-O-Sb bond angles fall in the range of 107.40-104.99(4)° and 105.8(4)-104.4(4)° respectively.

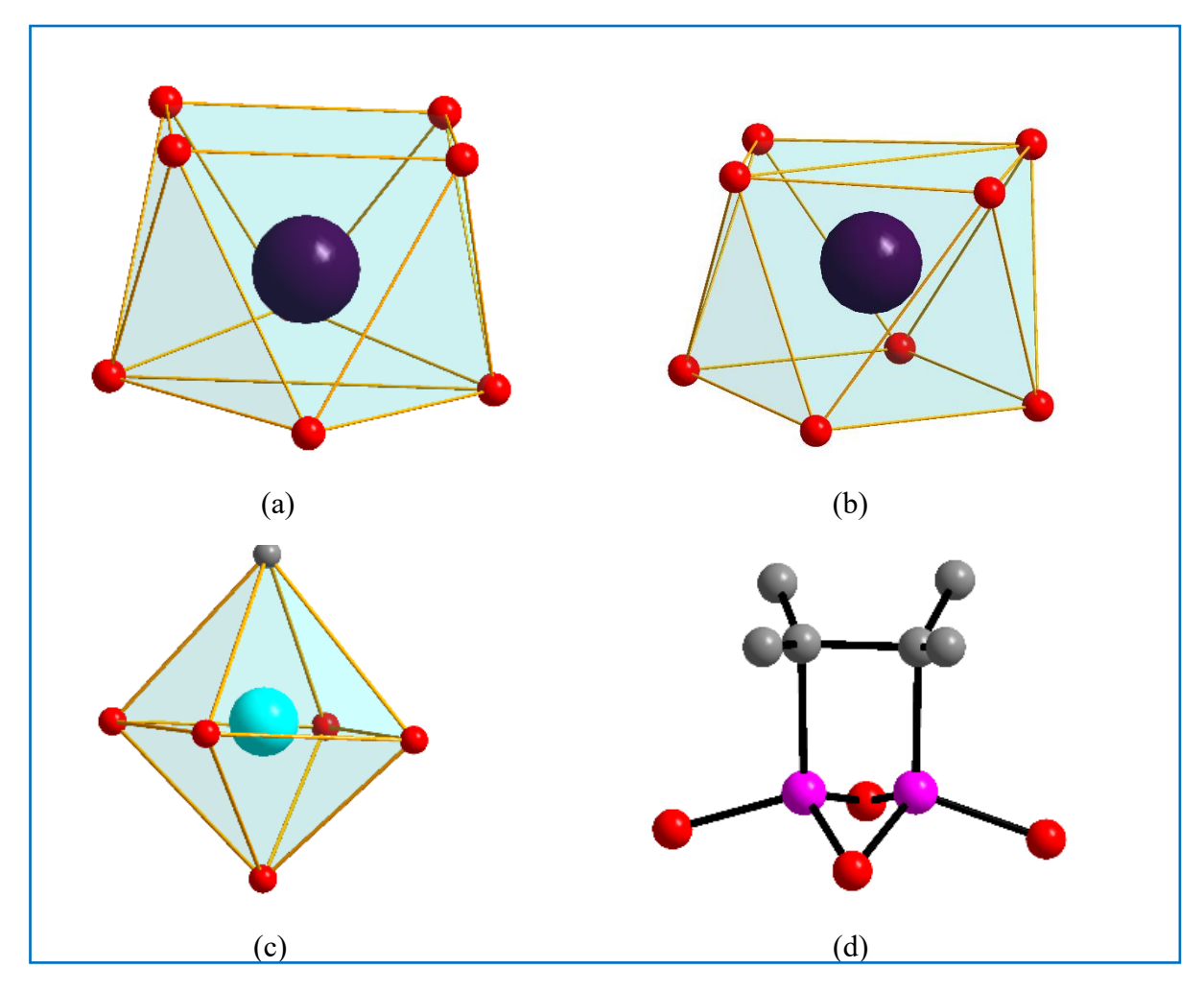


Figure 4.2: Coordination geometry around (a) Sm1 metal ion, (b) Sm3 metal ion, (c) antimony metal ion in **4.1** and (d) representation of new ligand system {O₂PC(CH₃)₂C(CH₃)₂PO₂}₂. Color code cyan, Sb; violet, Sm; purple, P; red, O; grey, C. Hydrogens are omitted for clarity.

The phase purity of the compounds was confirmed by powder X-ray diffraction (PXRD). The PXRD patterns match the simulated patterns obtained from SC-XRD analysis (Figure 4.9-

4.11). The thermal stability of **4.1–4.3** was examined under a nitrogen atmosphere with thermogravimetric analysis (TGA) in the range of 30–800 °C. TGA plots of **4.1–4.3** (Figure **4.12-4.14**) show that the cluster is stable up to 321, 326 and 316 °C, respectively.

4.4 Conclusion:

We have successfully investigated the reactivity of pro-ligand towards lanthanide ions in the presence of a base under solvothermal conditions. SC-XRD revealed the formation of novel twelve-membered {Sm₈Sb₄P₁₂} molecular morphology. Octanuclear Ln (III) clusters stabilized by *in-situ* generated organoantimony (V) based pro-ligands. Interestingly, phosphonate-based novel ligand system {O₂PC(CH₃)₂C(CH₃)₂PO₂}₂ formed. In all the clusters, ethane elimination followed by C-C bond formation has been observed.

4.5 Analytical and Spectroscopic Data

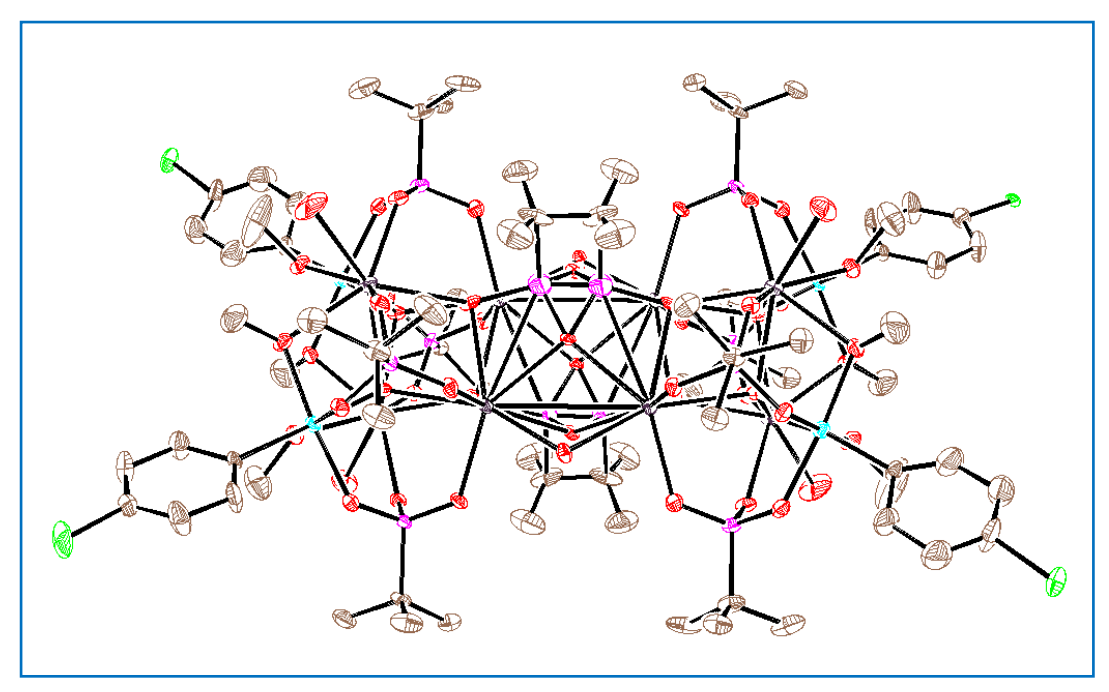


Figure 4.3: ORTEP view of 4.1 with thermal ellipsoids shown at 30% probability.

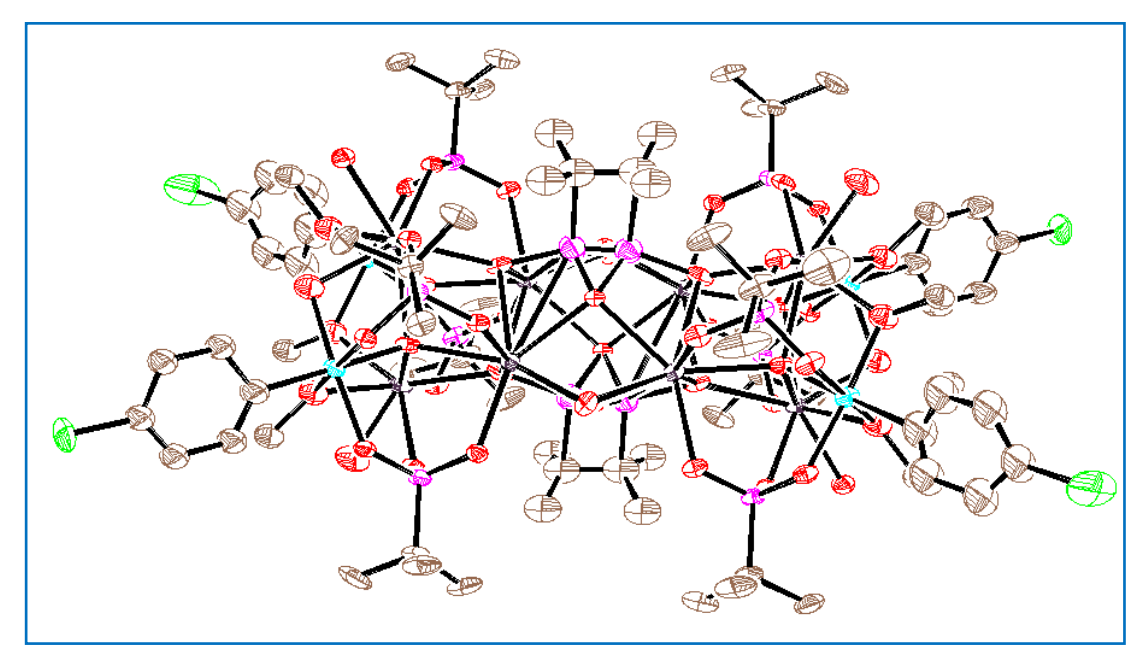


Figure 4.4: ORTEP view of **4.2** with thermal ellipsoids shown at 30% probability.

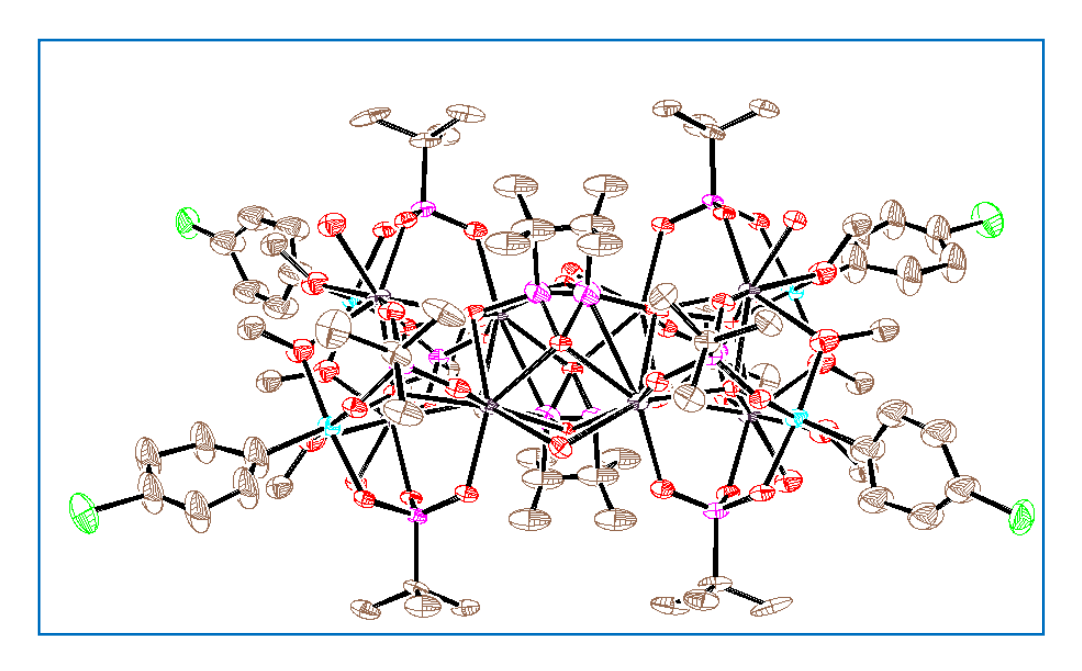


Figure 4.5: ORTEP view of **4.3** with thermal ellipsoids shown at 30% probability.

 Table 4.1: crystallographic information of compounds 4.1 -4.3

	4.1	4.2	4.3
Formula	C ₈₄ Cl ₄ H ₁₇₆ O ₅₈ P ₁₂ Sb ₄ Sm ₈	C ₇₆ H ₁₄₄ Cl ₄ O ₅₀ P ₁₂ Sb ₄ Tb ₈	C ₇₆ H ₁₄₄ Cl ₄ Dy ₈ O ₅₀ P ₁₂ Sb ₄
F. weight	4317.48	4129.70	4158.34
Temp K	112(13)	114(19)	110(14)
Crystal system	triclinic	triclinic	triclinic
Space group	P-1	P-1	P-1
a/Å	13.031(3)	13.1831(3)	13.04780(10)
b/Å	14.861(3)	14.7050(3)	14.7628(2)
c/Å	18.442(4)	18.4484(3)	18.5120(3)
α/°	89.854(6)	91.149(2)	89.6910(10)
β/°	74.608(6)	102.587(2)	75.2670(10)
γ/°	77.762(6)	103.965(2)	75.6240(10)
Volume/Å ³	3359.5(13)	3377.26(12)	3334.24(8)
Z	1	1	1
ρcalcg/cm ³	2.134	2.031	2.071
μ/mm-1	4.533	5.208	5.516
F(000)	2092.0	1972.0	1980.0
Crystal size/mm ³	$0.21 \times 0.183 \times 0.165$	$0.23 \times 0.189 \times 0.167$	$0.194 \times 0.186 \times 0.173$
2Θ range (°)	3.488 to 50.59	3.786 to 53.926	3.798 to 50.698
Index ranges	$-15 \le h \le 15$, $-17 \le k \le 17$, $-22 \le l \le 22$	$-16 \le h \le 16$, $-18 \le k \le 18$, $-22 \le 1 \le 23$	$-15 \le h \le 15$, $-17 \le k \le 17$, $-22 \le 1 \le 22$
Reflections collected	80955	64580	65267
Ind. reflections	12056 [Rint = 0.0480]	14076 [Rint = 0.0561]	12207 [Rint = 0.0479]
Data/restraints/ parameters	12056/12/735	14076/0/587	12207/0/578
GooF (F2)	1.111	1.075	1.039
$R_1(F)[I>2\sigma(I)]$	0.0635	0.0826	0.0746
wR ₂ (F ²) (all data)	0.1856	0.2386	0.2244
Largest diff. peak/hole / e Å- 3	1.84/-2.85	4.16/-3.43	3.23/-2.44
Completeness to θ _{max} , %	98.5	99.8	99.8

Table 4.2: Selected bond lengths (Å) and bond angles (deg) parameters of compound 4.1

Sm2-P3	3.395(3)	O15-Sm2-P5	30.8(2)	O6-Sm4-Sm3	37.63(19)
Sm2-P5	3.100(6)	P5-Sm1-P1	90.91(12)	O6-Sm4-Sb1	31.9(2)
Sm2-O20	2.273(8)	O13-Sm1-Sm2 ¹	39.80(18)	O6-Sm4-Sb2	93.63(19)
Sm2-O12	2.524(8)	O13-Sm1-P5	30.1(2)	O6-Sm4-O25	140.9(4)
Sm1-P1	3.392(3)	O13-Sm1-O12	64.4(3)	O2-Sm4-Sm3	116.6(2)
Sm1-P6 ¹	3.056(6)	O4-Sm1-Sm2 ¹	105.6(2)	O2-Sm4-Sb1	70.2(2)
Sm1-O6	2.537(9)	O4-Sm1-P5	170.6(2)	O2-Sm4-Sb2	171.2(2)
Sm1-O4	2.308(8)	O24-Sb2-Sm3	92.0(3)	O24-Sm4-Sm1	137.2(2)
Sm1-O12	2.525(8)	O19-Sb2-Sm3	42.5(2)	O19-Sm4-Sb2	32.1(2)
Sm4-Sm3	3.950(8)	O20-P3-Sm2	32.8(3)	O19-Sm4-O25	142.0(4)
Sm4-Sb1	3.550(5)	O9-P1-Sm1	33.5(4)	O1-Sm4-Sb1	33.2(2)
Sm4-O6	2.482(8)	O9-P1-O5	109.8(5)	O14-P6-Sm11	55.3(3)
Sm4-O25	2.498(13)	O5-P1-Sm1	95.1(3)	Sm2 ¹ -O13-Sm1	99.9(3)
Sm3-Sb1	3.563(9)	O8-P1-O9	112.1(5)	Sm3-O6-Sm1	105.5(3)
Sm3-O12	2.448(9)	O18-P4-Sm2	94.6(4)	Sb1-O6-Sm1	127.1(4)
Sm3-O16	2.344(9)	O4-Sm1-O14 ¹	90.2(3)	P4-O18-Sb2	127.8(6)
Sm3-O11	2.504(13)	O9-Sm1-O15 ¹	144.3(3)	Sb2-O24-Sm4	104.4(4)
Sb1-O6	1.953(8)	O10-Sm1-Sm2 ¹	40.52(19)	P1-O9-Sm1	125.1(6)
Sb2-O22	2.016(9)	O10-Sm1-P5	97.2(2)	Sm3-O19-Sm2	105.8(3)
Sb2-O19	1.964(9)	O10-Sm1-O6	152.2(3)	Sm2-O15-Sm1 ¹	99.6(2)
Sb2-O21	2.033(10)	O12-Sm1-Sm2 ¹	99.9(2)	O14 ¹ -Sm4-Sm1	36.68(19)
P1-O8	1.507(11)	O151-Sm1-O12	103.4(3)	O14 ¹ -Sm4-Sb2	100.4(2)
P4-O17	1.501(10)	O141-Sm1-Sm2 ¹	100.3(2)	O25-Sm4-Sm3	154.8(4)
P5-P6	1.406(8)	O141-Sm1-P61	34.9(3)	Sb2-Sm3-Sm4	56.19(2)
P5-O13	1.564(10)	Sm3-Sm4-Sm1	60.48(2)	Sb2-Sm3-Sb1	100.71(3)
P5-O12	1.749(12)	Sb1-Sm4-Sm1	64.08(2)	O6-Sm3-Sb2	93.28(19)
P5-O15	1.596(9)	O17-P4-O16	112.0(6)	O6-Sm3-O11	141.3(5)
P6-O14	1.747(12)	Sm1-P5-Sm2	80.86(13)	O19-Sm3-Sm1	77.9(2)
P61-Sm2-P3	91.31(12)	P6-P5-O15	61.4(4)	O19-Sm3-Sb2	32.2(2)
O17-Sm2-O15	86.1(3)	O13-P5-O12	107.5(5)	O12-Sm3-Sm4	77.8(2)
O20-Sm2-P6 ¹	90.0(3)	O12-P5-Sm1	54.6(3)	O12-Sm3-Sb1	100.8(2)
O10 ¹ -Sm2-P3	100.3(2)	O15-P5-O12	106.7(5)	O16-Sm3-O12	81.5(3)
O10 ¹ -Sm2-O12	130.7(3)	Sm1 ¹ -P6-Sm2 ¹	81.85(13)	P6-O15-P5	53.2(4)
O12-Sm2-P5	34.3(3)	P5-P6-Sm11	115.7(4)	Sb1-O1-Sm4	105.2(4)
O11-Sm3-Sm1	140.1(5)	P5-P6-O15	65.4(5)	Sm4 ¹ -O14-Sm1 ¹	107.7(3)
Sm4-Sb1-Sm3	67.44(3)	O13-P6-Sm2 ¹	52.7(3)	P6-O14-Sm4 ¹	148.9(5)
O23-Sm4-O1	144.1(3)	O13-P6-O14	107.0(5)	Sb2-O21-Sm3	105.0(4)
O5-Sb1-O7	89.8(4)	O15-P6-Sm2 ¹	118.6(4)	O16-Sm3-O7	144.5(3)
O21-Sm3-Sb2	33.5(2)	Sb1-Sm4-Sm3	56.41(2)	O8-Sm3-Sm4	115.8(2)
O7-Sb1-Sm3	41.6(3)	Sb2-Sm4-Sb1	100.98(3)	O8-Sm3-Sb2	170.6(2)
Sm4-Sb2-Sm3	67.53(3)	O23-Sm4-Sm3	116.8(2)	O7-Sm3-Sb2	95.9(2)

¹1-X,1-Y,-Z

Table 4.3: Selected bond lengths (Å) and bond angles (deg) parameters of compound 4.2

Tb1-Tb4 ¹	3.7438(10)	O16-Tb1-P5 ¹	170.8(3)	P5-O24-P6	49.8(4)
Tb1-P4	3.359(4)	O16-Tb1-O22 ¹	144.5(3)	Sb2-O11-Tb1	127.2(4)
Tb1-P5 ¹	3.049(7)	O11-Tb1-P5 ¹	104.7(3)	P1-O5-Tb3	130.2(5)
Tb1-O24	2.447(9)	O18-Tb2-Sb1	109.2(5)	P4-O13-Sb2	128.6(6)
Tb1-O16	2.227(10)	O18-Tb2-O19	130.9(6)	P3-O15-Sb2	126.1(6)
Tb1-O23 ¹	2.479(9)	Tb3-Sb2-Tb2	66.49(2)	Tb1-O19-Tb4	105.4(4)
Tb4-P6	3.078(7)	O15-Sb2-Tb3	133.4(3)	P6-O19-Tb1	91.3(5)
Tb4-O24 ¹	2.432(9)	O15-Sb2-O13	91.9(5)	Tb4-O7-Tb1 ¹	98.1(3)
Tb4-O7	2.473(11)	Tb3-Sb1-Tb2	66.29(2)	P2-O20-Tb2	129.3(6)
Tb4-O21	2.221(10)	O8-Sb1-Tb3	42.1(3)	Sb2-O9-Tb3	104.6(7)
Tb4-O8	2.507(12)	O8-Sb1-O3	90.8(4)	O8-Tb3-Sb2	94.8(2)
Tb3-Tb2	3.8364(9)	O3-Sb1-Tb2	132.5(3)	O8-Tb3-Sb1	32.7(3)
Tb3-Sb2	3.4985(12)	O14-Tb1-O23 ¹	89.0(3)	O8-Tb3-O11	72.6(3)
Tb3-Sb1	3.5029(12)	O71-Tb1-P5 ¹	97.3(3)	O2-Tb3-Tb4	98.1(4)
Tb3-O10	2.280(9)	O23 ¹ -Tb1-Tb4 ¹	101.1(3)	O2-Tb3-Tb2	77.8(3)
Tb3-O11	2.438(9)	P51-Tb4-P6	81.27(2)	O2-Tb3-Sb2	96.9(4)
Tb3-O25	2.418(11)	O22-Tb4-Tb1 ¹	39.8(2)	O2-Tb3-O11	108.7(4)
Tb2-Sb2	3.4993(13)	O24 ¹ -Tb4-P5 ¹	30.3(2)	O2-Tb3-O23 ¹	134.5(4)
Tb2-Sb1	3.5132(13)	O2-Sb1-Tb3	42.4(5)	O2-Tb3-O8	65.9(5)
Tb2-O20	2.295(12)	O14-P4-O10	112.0(5)	O25-Tb3-Sb2	107.9(3)
Sb2-O11	1.985(11)	O20-P2-Tb4	92.6(4)	O25-Tb3-O23 ¹	131.5(4)
Sb2-O9	2.011(15)	O6-Tb4-Tb1 ¹	106.0(3)	Tb3-Tb2-Tb1	61.19(18)
Sb1-O4	1.991(12)	O6-Tb4-O241	87.3(3)	Sb2-Tb2-Tb3	56.74(2)
P4-O10	1.530(10)	O19-Tb4-P6	34.9(3)	Sb2-Tb2-Sb1	101.58(3)
P4-O13	1.558(11)	O21-Tb4-Tb1 ¹	104.5(3)	O11-Tb2-Sb1	94.5(2)
P4-O14	1.520(11)	O21-Tb4-P51	168.6(3)	O19-Tb2-Tb1	36.7(2)
P2-O4	1.579(13)	O8-Tb4-Tb1 ¹	167.9(2)	O19-Tb2-Sb2	101.5(2)
P6-P5	1.303(10)	O8-Tb4-P6	104.4(3)	Tb31-O23-Tb4 ¹	107.5(4)
P6-O19	1.760(15)	Tb2-Tb3-Tb4	61.26(2)	P2-O21-Tb4	126.6(7)
P4-Tb1-Tb4 ¹	125.35(7)	O4-P2-Tb4	95.5(4)	Tb3-O8-Tb4	106.2(4)
P6-Tb1-P4	162.08(6)	Tb1-P6-Tb4	79.94(16)	Sb1-O8-Tb4	127.7(5)
P51-Tb1-P4	91.02(14)	P5-P6-Tb1	113.1(5)	Sb1-O8-Tb3	105.2(5)
O22 ¹ -Tb1-Tb4 ¹	40.5(2)	O24-P6-O22	110.3(6)	Sb2-O12-Tb2	104.9(7)
O22 ¹ -Tb1-P51	29.8(2)	O22-P5-O24	111.7(6)	P1-O3-Sb1	127.7(6)
O22 ¹ -Tb1-O23 ¹	65.4(3)	O24-P5-Tb1 ¹	117.4(4)	Sb1-O2-Tb3	103.8(7)
O24-Tb1-P4	165.0(2)	Sb2-Tb3-Tb4	110.55(3)	P2-O4-Sb1	126.9(7)
O24-Tb1-P5 ¹	83.4(2)	Sb2-Tb3-Sb1	101.80(3)	O20-Tb2-Sb1	71.3(3)
O24-Tb1-O11	133.0(3)	O10-Tb3-Sb1	173.0(2)	O20-Tb2-O11	145.4(4)
O24-Tb1-O19	65.0(4)	O10-Tb3-O23 ¹	81.4(3)	O8-Tb2-Tb3	38.1(2)
O24-Tb1-O71	66.5(3)	O5-Tb3-Sb1	71.3(2)	O8-Tb2-Sb2	94.6(2)
O24-Tb1-O23 ¹	104.4(3)	P5-O22-Tb4	140.5(5)	O8-Tb2-O19	71.7(4)
O16-Tb1-Tb4 ¹	105.6(3)	P5-O22-P6	50.0(4)	O18-Tb2-Tb1	140.4(5)
-	- (- /		()	<u> </u>	(- /

¹1-X,1-Y,-Z

Table 4.4: Selected bond lengths (Å) and bond angles (deg) parameters of compound 4.3

Dy1-P3	3.320(4)	O1-Sb1-Dy3	132.2(3)	Sb2-Dy3-Sb1	99.97(3)
Dy1-P6	3.065(7)	O1-Sb1-O4	173.7(6)	O7-Dy3-Dy2	116.4(3)
Dy1-P5 ¹	3.015(8)	O1-Sb1-O3	90.2(6)	O7-Dy3-Sb1	172.5(3)
Dy1-O19 ¹	2.416(10)	O4-Sb1-Dy4	91.9(5)	O13-Dy3-O12	144.6(4)
Dy1-O11	2.213(9)	O3-Sb1-Dy3	91.3(4)	O13-Dy3-O36	74.9(4)
Dy1-O12	2.418(11)	Dy3-Sb2-Dy4	67.34(3)	O17 ¹ -Dy3-Dy2	36.0(2)
Dy1-O20 ¹	2.509(11)	O9-Sb2-Dy3	83.2(3)	O12-Dy3-Sb1	94.4(2)
Dy2-P2	3.324(4)	O9-Sb2-Dy4	131.9(3)	O36-Dy3-Dy4	152.5(3)
Dy2-P6	3.098(6)	O12-Sb2-Dy4	43.0(3)	O36-Dy3-Sb1	110.7(3)
Dy2-O24	2.440(12)	O6-Sb2-Dy4	91.1(5)	O17-P5-Dy2 ¹	52.9(3)
Dy2-O18	2.448(10)	O6-Sb2-O10	173.5(6)	P3-O9-Sb2	126.3(6)
Dy2-O22	2.202(10)	O15-Dy1-O20 ¹	75.5(4)	Dy3¹-O17-Dy1¹	107.8(4)
Dy2-O20	2.505(12)	O12-Dy1-P3	62.1(2)	Sb2-O12-Dy3	104.3(5)
Dy3-Dy4	3.887(10)	O12-Dy1-P6	105.9(3)	O6-Dy3-Sb2	33.9(4)
Dy3-Sb1	3.500(12)	O12-Dy1-O16	134.0(3)	O6-Dy3-O4	74.4(5)
Dy3-07	2.263(9)	O20 ¹ -Dy1-P5 ¹	97.7(3)	O4-Dy3-Sb2	96.1(4)
Dy3-O17 ¹	2.409(11)	P1-Dy2-P2	91.32(10)	Sb1-Dy4-Sb2	99.91(3)
Dy3-O6	2.368(17)	P6-Dy2-P2	163.79(15)	Sb2-Dy4-Dy1	64.23(2)
Dy4-O25	2.287(11)	P5¹-Dy2-P6	80.93(18)	O25-Dy4-Sb1	170.6(3)
Dy4-O12	2.478(10)	O19-Dy2-P1	96.9(2)	O18-Dy4-Dy3	77.0(3)
Dy4-O8	2.409(18)	O16 ¹ -Dy2-O24	135.3(3)	O18-Dy4-O12	70.3(4)
Sb1-O24	1.981(10)	O24-Dy2-P1	62.1(2)	O8-Dy4-Dy1	96.9(4)
Sb1-O3	2.018(15)	O10-Sb2-Dy3	132.9(3)	O8-Dy4-Sb1	95.1(4)
P3-O7	1.517(10)	O8-Sb2-Dy4	41.2(5)	O8-Dy4-O24	106.7(5)
P4-O15	1.499(13)	O8-Sb2-O9	172.9(6)	O8-Dy4-O12	65.3(4)
P1-O22	1.506(13)	O8-Sb2-O6	88.6(6)	O23-Dy4-Dy1	117.4(3)
P6-O19	1.556(11)	O13-P2-Dy2	90.2(4)	O23-Dy4-Sb1	70.4(3)
P5-O19	1.530(11)	O13-P2-O2	111.0(6)	O23-Dy4-Sb2	170.3(3)
P5-O17	1.795(15)		111.2(6)	O23-Dy4-O12	143.7(4)
P3-Dy1-P4	91.87(11)	O9-P3-Dy1	95.3(4)	O23-Dy4-O18	80.9(4)
P6-Dy1-P3	164.17(4)	O1-P1-Dy2	95.9(4)	O3-Dy4-Dy1	136.9(4)
P51-Dy1-P6	81.55(19)	O24-Dy2-O18	69.2(4)	O3-Dy4-Dy3	76.8(4)
O19 ¹ -Dy1-P3	98.3(2)	O21-Dy2-P6	170.6(3)	O3-Dy4-Sb1	33.7(4)
O19 ¹ -Dy1-P4	162.6(2)	O21-Dy2-O19	143.0(4)	O3-Dy4-O24	65.9(4)
O19 ¹ -Dy1-O12	134.8(3)	Dy4-Dy3-Dy2	60.34(2)	O14-Dy4-Dy1	136.6(4)
O19 ¹ -Dy1-O20 ¹	67.5(4)	Sb1-Dy3-Dy2	64.67(3)	O14-Dy4-Sb1	113.8(4)
O16-Dy1-P3	163.8(2)	O23-P1-O1	110.5(8)	O14-Dy4-O18	127.3(5)
O16-Dy1-P5 ¹	82.8(3)	Dy1-P6-Dy2	78.25(15)	O14-Dy4-O8	83.2(6)
O11-Dy1-O16	142.5(3)	P5-P6-Dy2	111.5(6)	Dy3-Sb1-Dy4	67.28(2)
O24-Sb1-Dy4	41.8(3)	Dy1 ¹ -P5-Dy2 ¹	80.2(2)	Dy1-O18-Dy2	105.4(4)
O24-Sb1-O2	91.7(4)	O19-P5-O17	106.0(7)	P6-O18-Dy1	91.4(5)
O2-Sb1-Dy4	132.8(3)	O16-P5-Dy1 ¹	117.2(5)	P6-O18-Dy4	146.2(6)
	` '	<u>, </u>	` '	,	. ,

¹1-X,1-Y,2-Z

Table 4.5: Shape calculation of compounds 4.1 -4.31a) Summary of SHAPE analysis for samarium metal ions in 4.1

S. No	Geometry	CShM value for Sm1 in 4.1	CShM value for Sm3 in 4.1
1	Octagon (D8h)	31.683	29.038
2	Heptagonal pyramid (C7v)	24.682	21.075
3	Hexagonal bipyramid (D6h)	16.763	17.438
4	Cube (Oh)	13.020	10.891
5	Square antiprism (D4d)	3.214	0.738
6	Triangular dodecahedron (D2d)	2.275	2.692
7	Johnson gyrobifastigium J26 (D2d)	14.186	15.218
8	Johnson elongated triangular bipyramid J14 (D3h)	26.514	26.758
9	Biaugmented trigonal prism J50 (C2v)	2.307	2.880
10	Biaugmented trigonal prism (C2v)	2.184	2.326
11	Snub diphenoid J84 (D2d)	4.035	4.997
12	Triakis tetrahedron (Td)	13.722	11.409
13	Elongated trigonal bipyramid (D3h)	24.456	21.752

1b) Summary of SHAPE analysis for Sb in 4.1

S. No	Geometry	CShM value for Sb1 in 4.1
1	Hexagon (D6h)	30.691
2	Pentagonal pyramid (C5v)	28.883
3	Octahedron (Oh)	0.313
4	Trigonal prism (D3h)	16.070
5	Johnson pentagonal pyramid J2 (C5v)	32.108

1c) Summary of SHAPE analysis for terbium metal ions in 4.2

S. No	Geometry	CShM value for Tb1 in 4.2	CShM value for Tb3 in 4.2
1	Octagon (D8h)	31.062	28.470
2	Heptagonal pyramid (C7v)	24.678	22.285
3	Hexagonal bipyramid (D6h)	16.736	17.453
4	Cube (Oh)	12.872	11.080
5	Square antiprism (D4d)	2.944	0.649
6	Triangular dodecahedron (D2d)	2.204	2.230
7	Johnson gyrobifastigium J26 (D2d)	13.956	14.919
8	Johnson elongated triangular bipyramid J14 (D3h)	26.525	27.661
9	Biaugmented trigonal prism J50 (C2v)	2.059	2.265
10	Biaugmented trigonal prism (C2v)	2.047	2.245
11	Snub diphenoid J84 (D2d)	3.838	4.307
12	Triakis tetrahedron (Td)	13.502	11.595
13	Elongated trigonal bipyramid (D3h)	24.594	22.553

1d) Summary of SHAPE analysis for Sb in 4.2

S. No	Geometry	CShM value for Sb1 in 4.2
1	Hexagon (D6h)	30.715
2	Pentagonal pyramid (C5v)	28.991
3	Octahedron (Oh)	0.305
4	Trigonal prism (D3h)	16.029
5	Johnson pentagonal pyramid J2 (C5v)	32.064

1e) Summary of SHAPE analysis for dysprosium metal ions in **4.3**

S. No	Geometry	CShM value for Dy1 in 4.3	CShM value for Dy3 in 4.3
1	Octagon (D8h)	31.918	29.313
2	Heptagonal pyramid (C7v)	24.255	21.882
3	Hexagonal bipyramid (D6h)	16.652	17.454
4	Cube (Oh)	12.886	10.778
5	Square antiprism (D4d)	3.302	0.650
6	Triangular dodecahedron (D2d)	2.268	2.599
7	Johnson gyrobifastigium J26 (D2d)	14.140	15.299
8	Johnson elongated triangular bipyramid J14 (D3h)	26.095	26.850
9	Biaugmented trigonal prism J50 (C2v)	2.142	2.955
10	Biaugmented trigonal prism (C2v)	2.113	2.343
11	Snub diphenoid J84 (D2d)	3.947	4.992
12	Triakis tetrahedron (Td)	13.524	11.334
13	Elongated trigonal bipyramid (D3h)	24.249	21.656

1f) Summary of SHAPE analysis for Sb in **4.3**

S. No	Geometry	CShM value for Sb1 in 4.3
1	Hexagon (D6h)	30.954
2	Pentagonal pyramid (C5v)	28.421
3	Octahedron (Oh)	0.261
4	Trigonal prism (D3h)	15.633
5	Johnson pentagonal pyramid J2 (C5v)	32.108

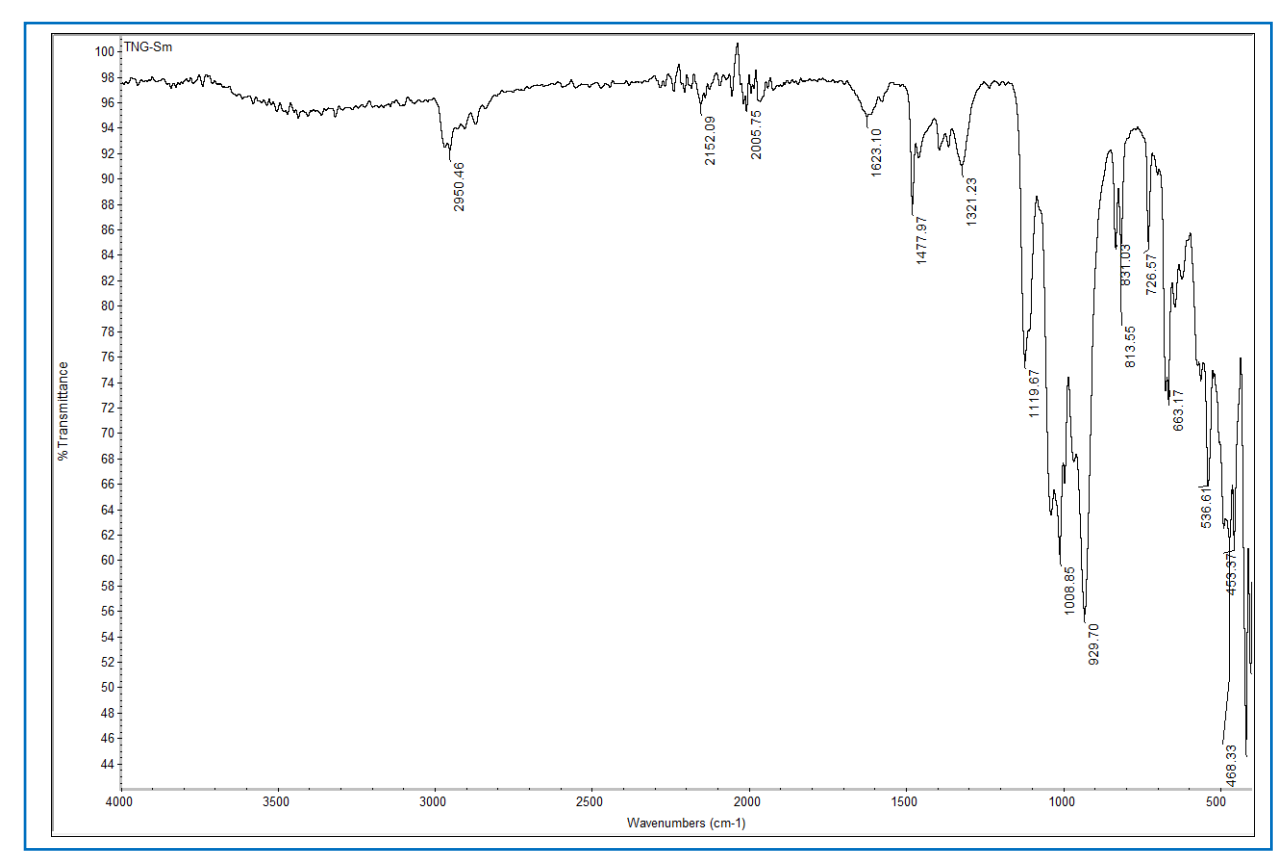


Figure 4.6: IR spectrum of 4.1.

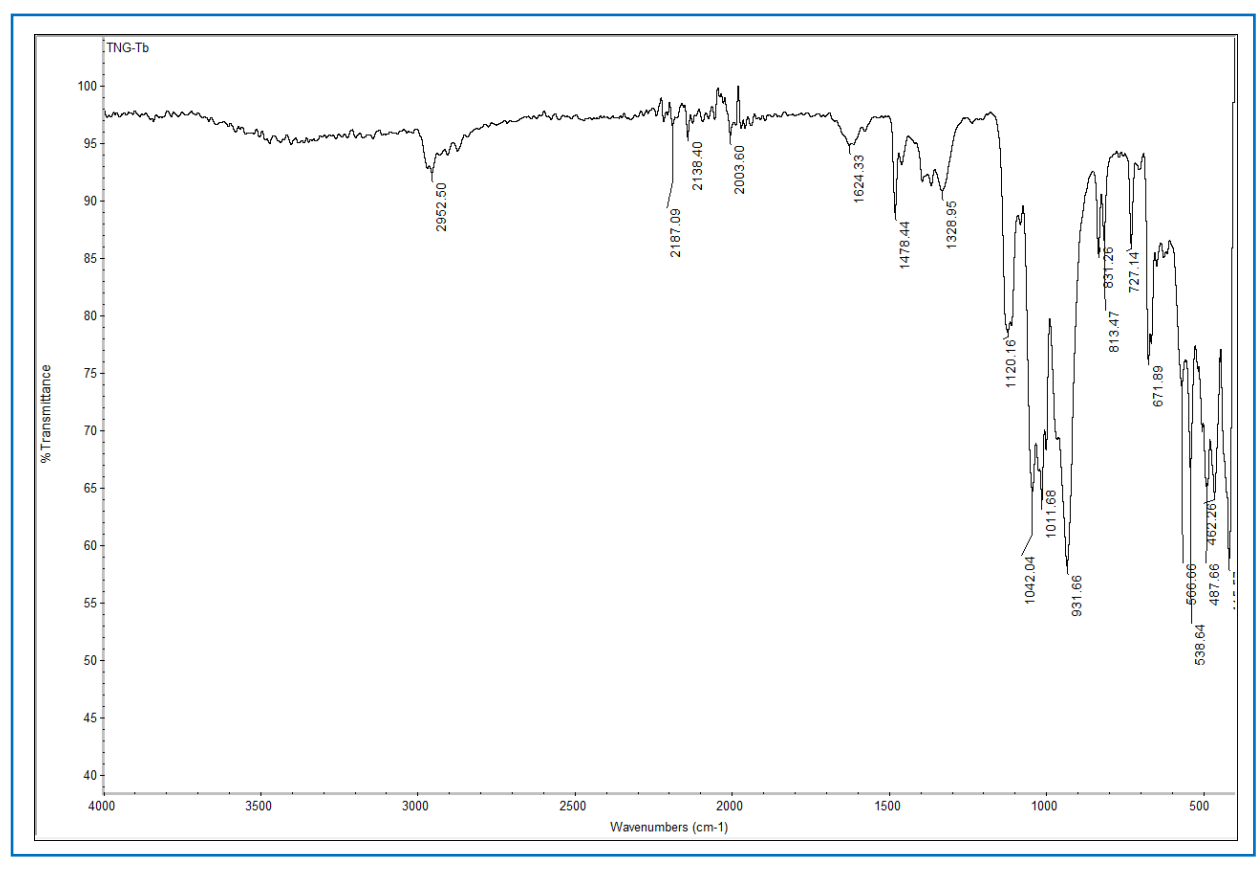


Figure 4.7: IR spectrum of 4.2.

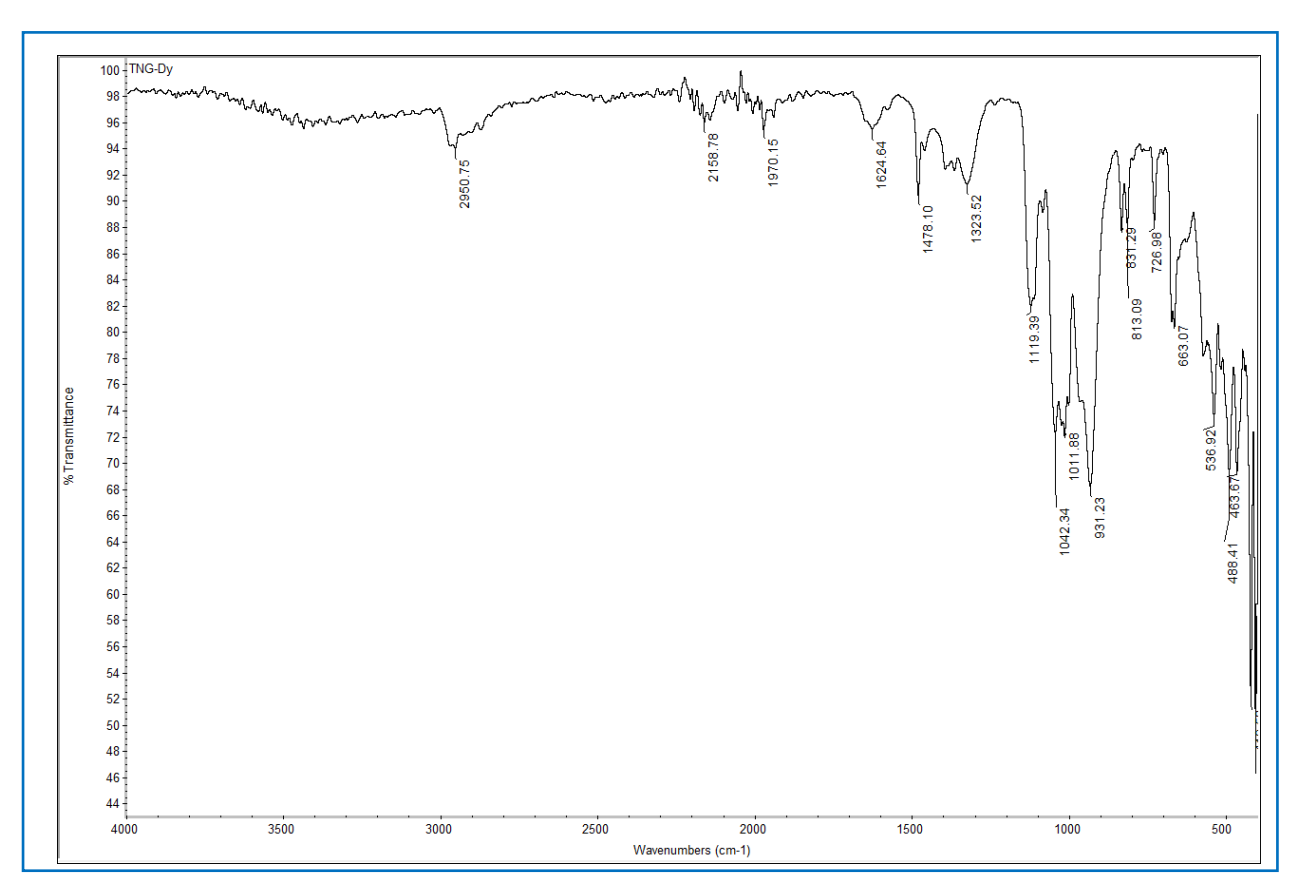


Figure 4.8: IR spectrum of 4.3.

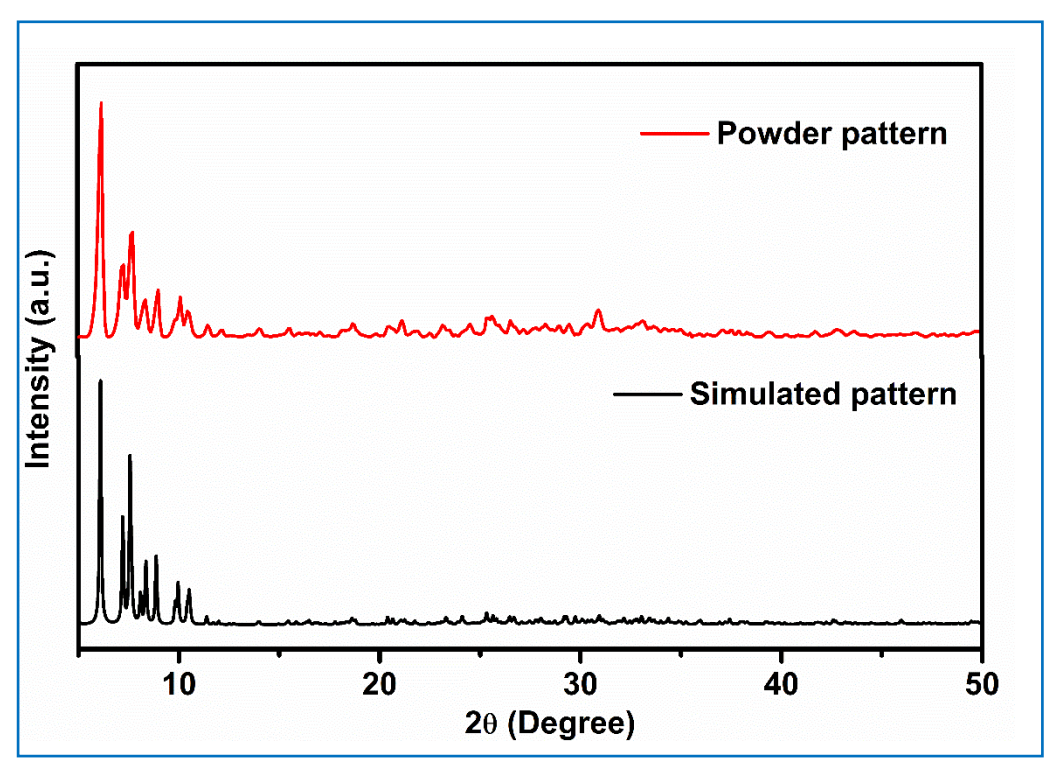


Figure 4.9: Powder X-ray diffraction pattern of a bulk sample of **4.1** compared to the simulated powder pattern extracted from single-crystal diffraction data.

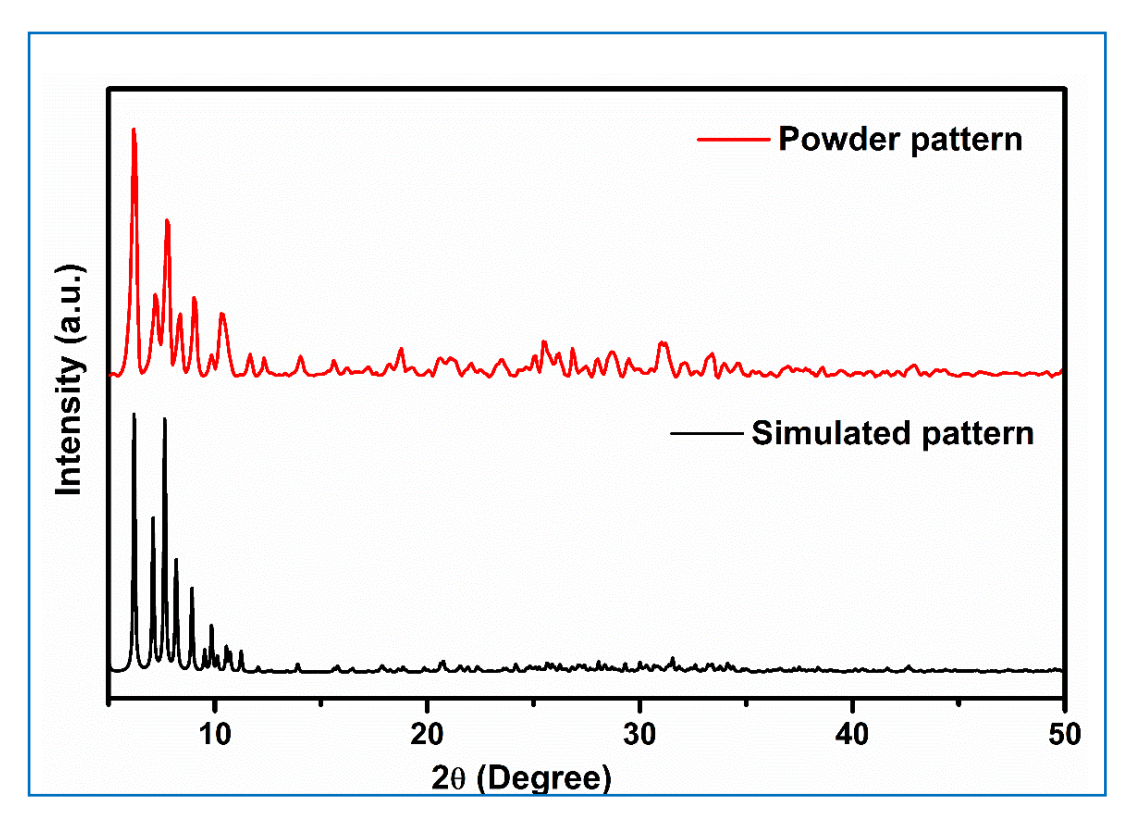


Figure 4.10: Powder X-ray diffraction pattern of a bulk sample of **4.2** compared to the simulated powder pattern extracted from single-crystal diffraction data.

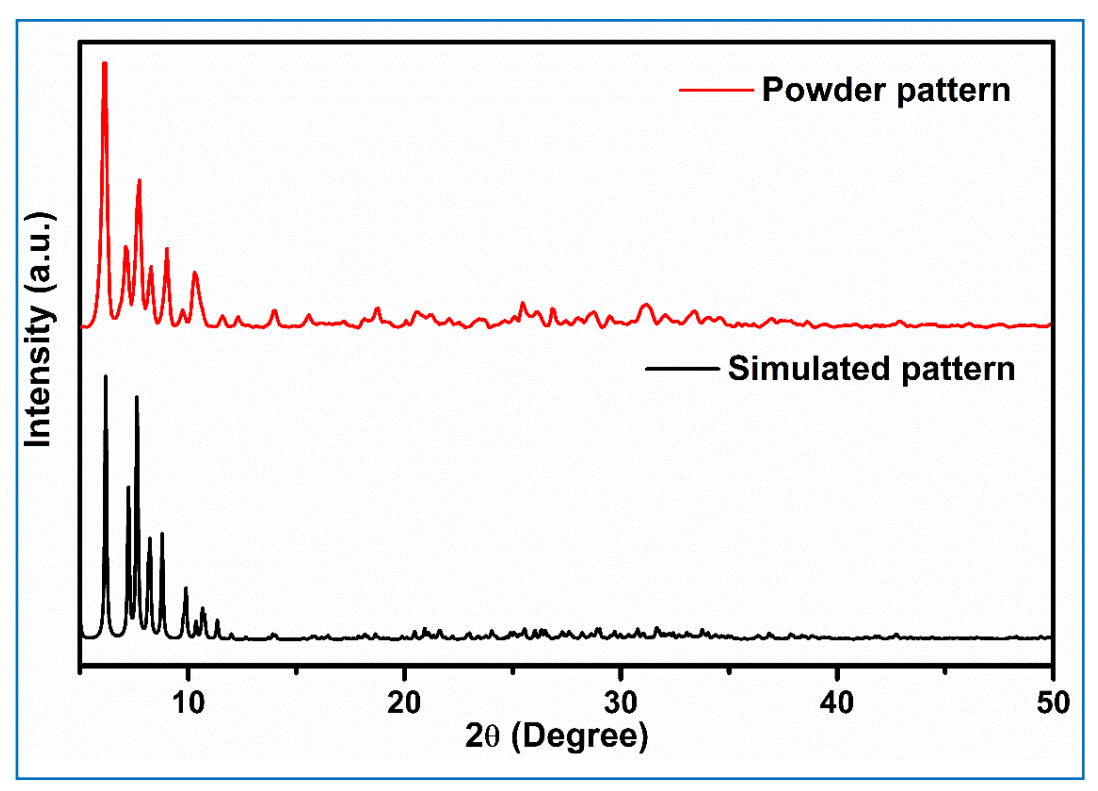


Figure 4.11: Powder X-ray diffraction pattern of a bulk sample of **4.3** compared to the simulated powder pattern extracted from single-crystal diffraction data.

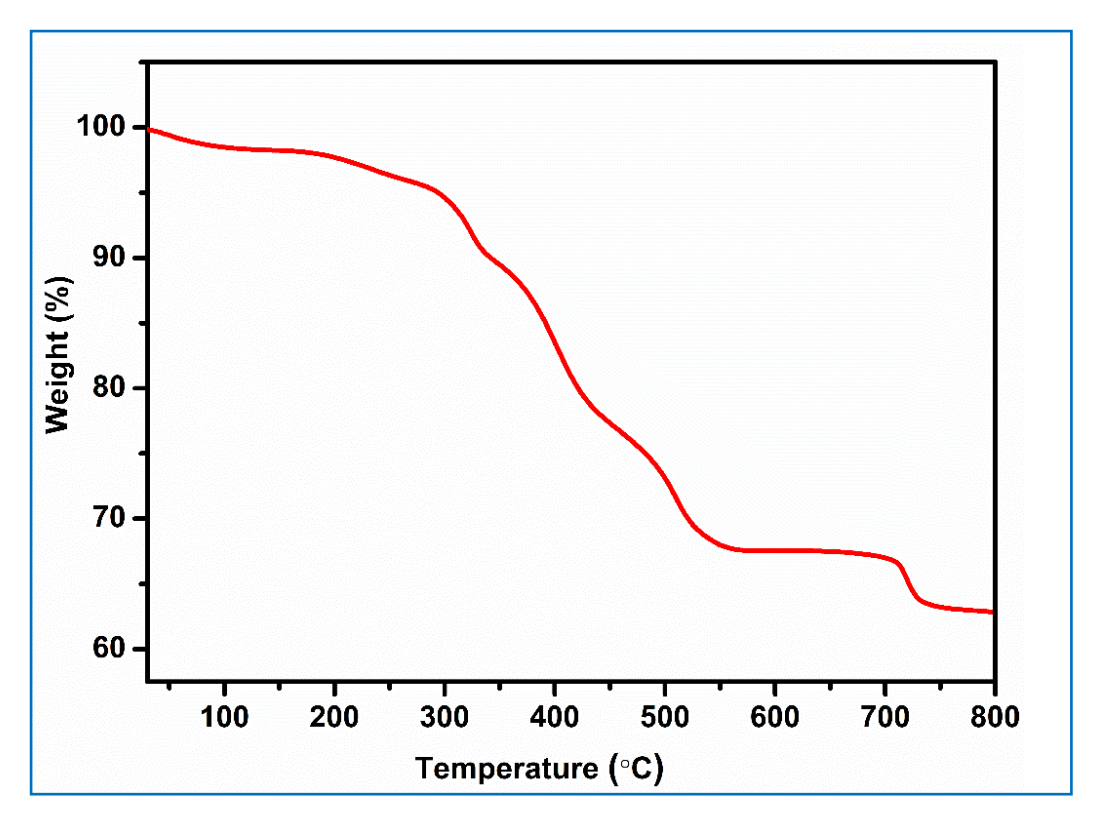


Figure 4.12: TGA plot of compound 4.1.

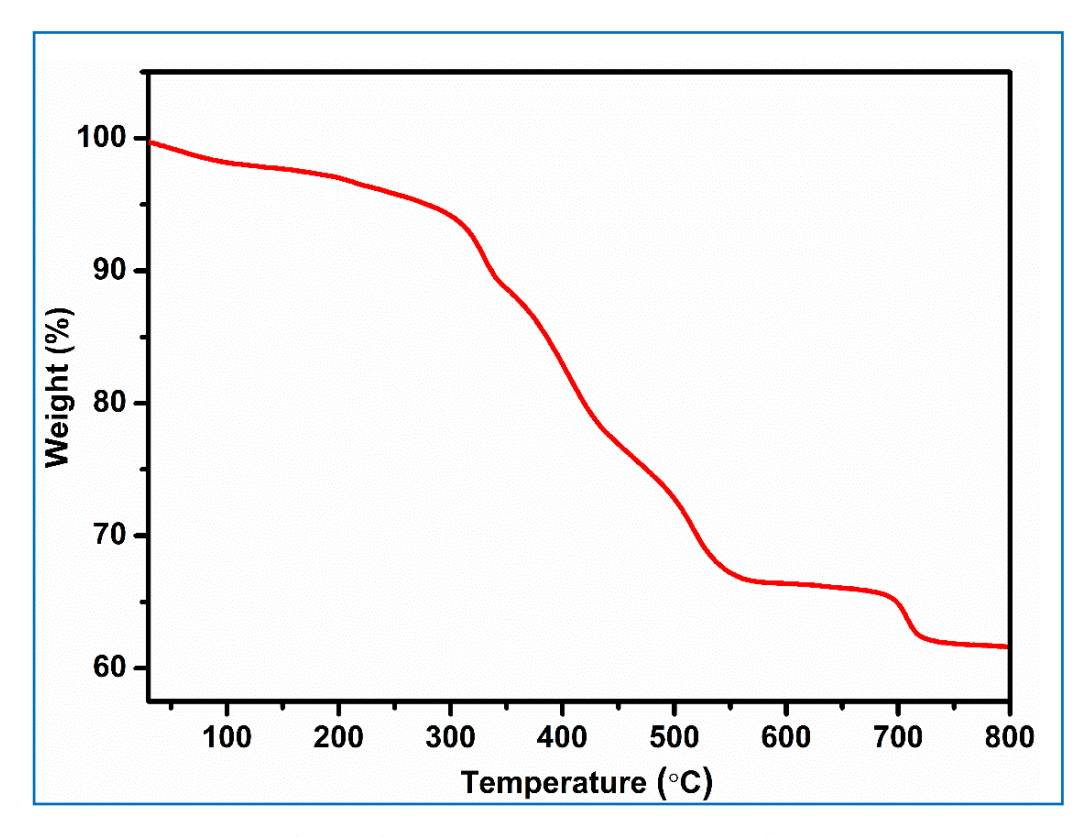


Figure 4.13: TGA plot of compound 4.2.

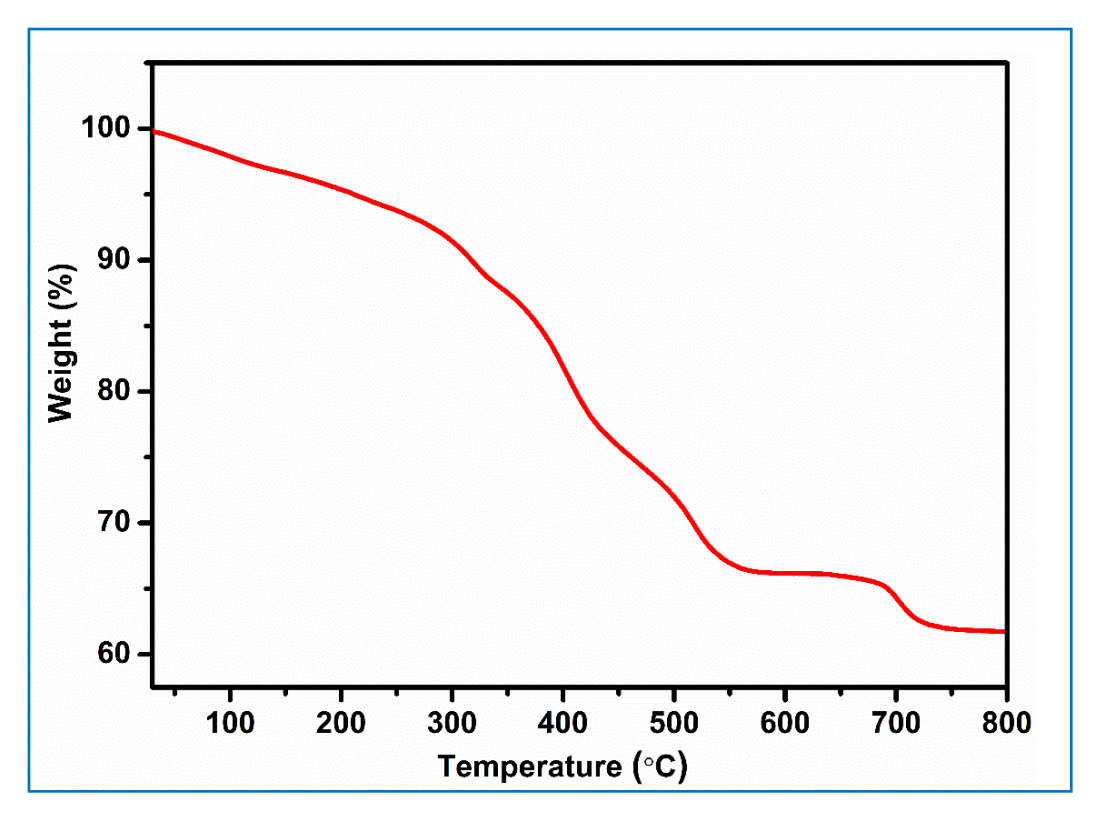


Figure 4.14: TGA plot of compound 4.3.

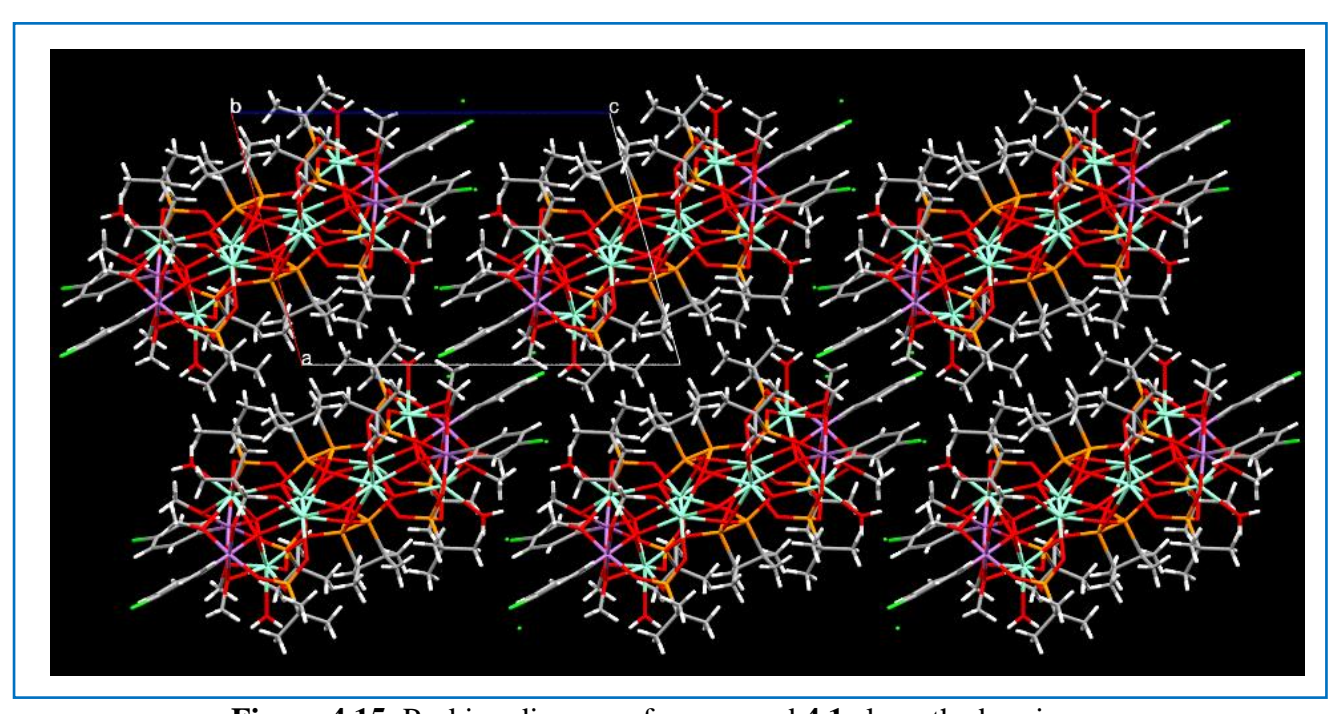


Figure 4.15: Packing diagram of compound 4.1 along the b-axis.

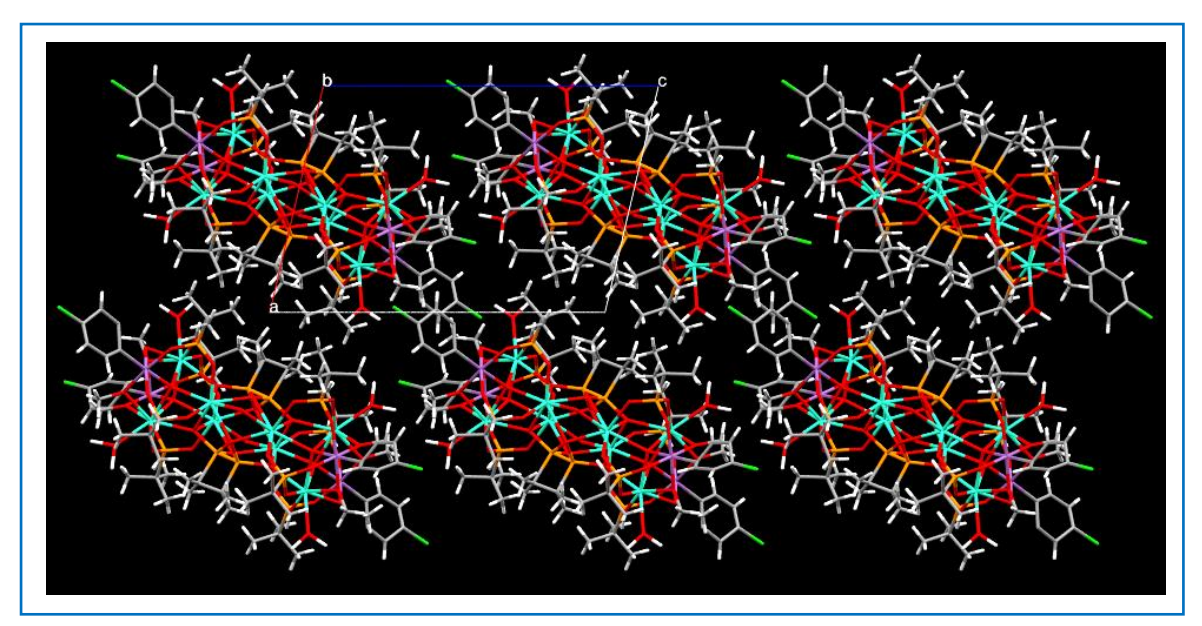


Figure 4.16: Packing diagram of compound 4.2 along the b-axis.

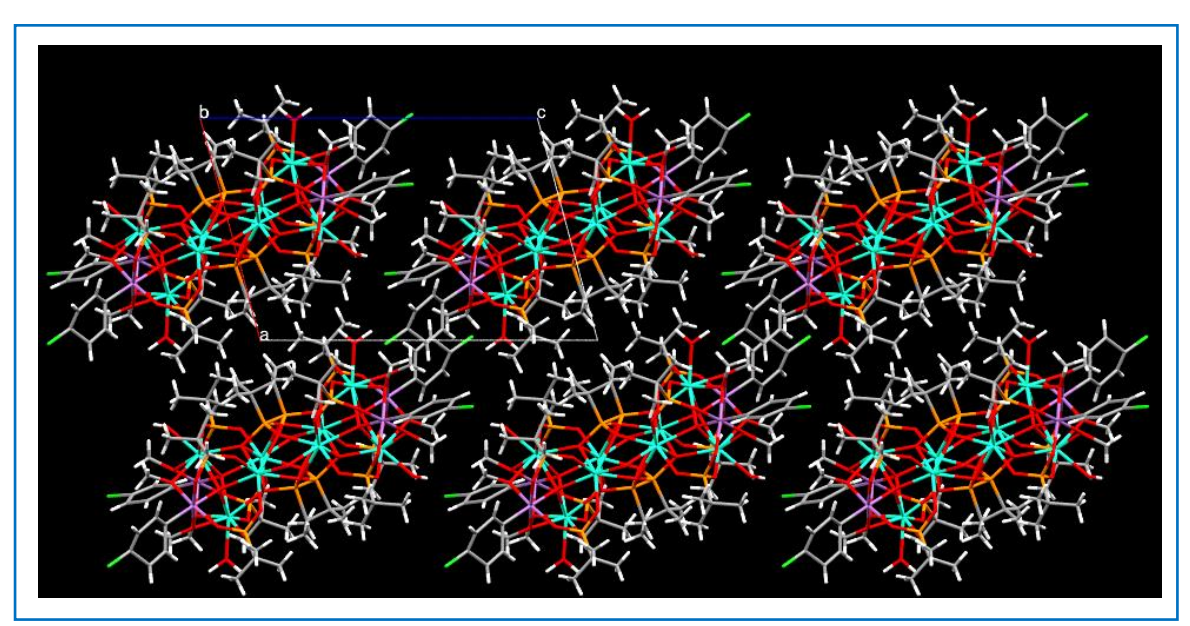


Figure 4.17: Packing diagram of compound 4.3 along the b-axis.

4.6 References:

- (a) Xu, H.; Zhou, H.; Feng, L.; Wang, Q.; Chen, R.; Huang, W.; Wu, X. *Dalton Trans*.
 2018, 47, 11226–11238. (b) Chandrasekhar, V.; Senapati, T.; Dey, A.; Hossain, S. *Dalton Trans*.
 2011, 40, 5394–5418. (c) Bao, S. S.; Zheng, L. M. *Coord. Chem. Rev*.
 2016, 319, 63–85. (d) DeBurgomaster, P.; Aldous, A.; Liu, H.; O'Connor, C. J.; Zubieta, J. *Cryst. Growth & amp; Des*.
 2010, 10, 2209–2218. (e) Chandrasekhar, V.; Kingsley, S.; Vij, A.; Lam, K. C.; Rheingold, A. L. *Inorg. Chem.* 2000, 39, 3238–3242. (f) Gabriel Armatas, N.; Ouellette, W.; Whitenack, K.; Pelcher, J.; Liu, H.; Romaine, E.; J. O'Connor, C.; Zubieta, J. *Inorg. Chem.* 2009, 48, 8897–8910.
- (a) Zhang, Y. T.; Ruan, J. X.; Ma, D. S.; Gao, J. S.; Liu, Y. F.; Yu, Y. H. Polyhedron 2022, 216, 115694. (b) Mao, J. G. Coordination Chemistry Reviews. 2007, 251, 1493–1520. (c) Ruan, J. X.; Yu, Y. H.; Liu, Y. F.; Wu, G.; Gao, J. S.; Ma, D. S. Polyhedron 2019, 163, 114–120. (d) Ren, M.; Bao, S. S.; Wang, B. W.; Ferreira, R. A. S.; Zheng, L. M.; Carlos, L. D. Inorg. Chem. Front. 2015, 2, 558–566. (e) Yang, X.; Schipper, D.; Jones, R. A.; Lytwak, L. A.; Bradley J. Holliday, B. J.; Shaoming Huang, S. J. Am. Chem. Soc. 2013, 135, 8468–8471.
- (a) Demadis, K. D.; Anagnostou, Z.; Panera, A.; Mezei, G.; Kirillova, M. V.; Kirillov, A. M. RSC Adv. 2017, 7, 17788–17799. (b) El-Refaei, S. M.; El-Refaei, S. M.; Russo, P. A.; Amsalem, P.; Koch, N.; Pinna, N. ACS Appl. Nano Mater. 2020, 3, 4147–4156. (c) Demand, D.; Schöllorn, B.; Mansuy, D.; Rouxel, J.; Battioni, P.; Bujoli, B. Chem. Mater. 1995, 7, 995–1000. (d) Bhanja, P.; Bhaumik, A. ChemCatChem. 2016, 8, 1607–1616. (e) Hu, A.; Yee, G. T.; Lin, W. J. Am. Chem. Soc. 2005, 127, 12486–12487. (f) Zhang, R.; Russo, P. A.; Buzanich, A. G.; Jeon, T.; Pinna, N. Adv. Funct. Mater. 2017, 27, 1–11. (g) Zhao, H.; Yuan, Z. Y. ChemSusChem. 2021, 14, 130–149. (h) Hu, A.; Ngo, H. L.; Lin, W. J. Am. Chem. Soc. 2003, 125, 11490–11491. (i) Feng, P.; Cheng, X.; Li, J.; Luo, X. ChemistrySelect. 2018, 3, 760–764.
- (a) Ayyappan, P.; Evans, O. R.; Cui, Y.; Wheeler, K. A.; Lin, W. *Inorg. Chem.* 2002, 41, 4978–4980.
 (b) Cao, G.; Hong, H. G.; Mallouk, T. E. *Acc. Chem. Res.* 1992, 25, 420–427.
 (c) Neff, G. A.; Helfrich, M. R.; Clifton, M. C.; Page, C. J. *Chem. Mater.* 2000, 12, 2363–2371.
- 5. Song-Song Bao, S. S.; Shimizu, G. K. H.; Zheng, L. M. Coord. Chem. Rev. 2019, 378, 577-594.

- (a) Sheikh, J. A.; Jena, H. S.; Clearfield, A.; Konar, S. Acc. Chem. Res. 2016, 49, 1093–1103. (b) Sheikh, J. A.; Goswami, S.; Adhikary, A.; Konar, S. Inorg. Chem. 2013, 52, 6765. (c) Sheikh, J. A.; Adhikary, A.; Jena, H. S.; Biswas, S.; Konar, S. Inorg. Chem. 2014, 53, 1606–1613. (d) Konar, S.; Clearfield, A. Inorg. Chem. 2008, 47, 3492–3494. (e) Konar, S.; Clearfield, A. Inorg. Chem. 2008, 47, 5573–5579. (f) Sahoo, D.; Suriyanarayanan, R.; Chandrasekhar, V. Cryst. Growth Des. 2014, 14, 2725–2728. (g) Chandrasekhar, V.; Sahoo, D.; Narayanan, R. S.; Butcher, R. J.; Lloret, F.; Pardo, E. Dalton Trans. 2013, 42, 8192–8196. (h) Khanra, S.; Konar, S.; Clearfield, A.; Helliwell, M.; McInnes, E. J. L.; Tolis, E.; Tuna, F.; Winpenny, R. E. P. Inorg. Chem. 2009, 48, 5338–5349. (i) Konar, S.; Clearfield, A. Inorg. Chem. 2008, 47, 3489–3491.
- (a) Zangana, K. H.; Pineda, E. M.; Winpenny, R. E. P. *Dalton Trans.* 2014, 43, 17101–17107. (b) Zhang, Z. M.; Zangana, K. H.; Kostopoulos, A. K.; Tong, M. L.; Winpenny, R. E. P. *Dalton Trans.* 2016, 45, 9041–9044. (c) Zangana, K. H.; Pineda, E. M.; Schnack, J.; Winpenny, R. E. P. *Dalton Trans.* 2013, 42, 14045–14048. (d) Zangana, K. H. *Magnetochemistry* 2018, 4, 29. (e) Tang, X.; Hua, J.; Ma, Y.; Hori, A.; Yuan, R.; Matsuda, R. *Inorg. Chim. Acta.* 2018, 482, 900–904. (f) Comby, S.; Scopelliti, R.; Imbert, D.; Charbonnière, L.; Ziessel, R.; Bünzli, J. C. G. *Inorg. Chem.* 2006, 45, 3158–3160.
- (a) Zheng, Y. Z.; Zhou, G. J.; Zheng, Z.; Winpenny, R. E. P. *Chem. Soc. Rev.* 2014, 43, 1462–1475. (b) Zangana, K. H.; Pineda, E. M.; Vitorica-Yrezabal, I. J.; McInnes, E. J. L.; Winpenny, R. E. P. *Dalton Trans.* 2014, 43, 13242–13249. (c) Zangana, K. H.; Pineda, E. M.; Mc Innes, E. J. L.; Schnack, J.; Winpenny, R. E. P. *Chem. Commun.* 2014, 50, 1438–1440. (d) Zheng, Y. Z.; Evangelisti, M.; Tuna, F.; Winpenny, R. E. P. *J. Am. Chem. Soc.* 2012, 134, 1057–1065. (e) Zheng, Y. Z.; Pineda, E. M.; Helliwell, M.; Winpenny, R. E. P. *Chem. A Eur. J.* 2012, 18, 4161–4165. (f) Moreno Pineda, E.; Heesing, C.; Tuna, F.; Zheng, Y. Z.; McInnes, E. J. L.; Schnack, J.; Winpenny, R. E. P. *Inorg. Chem.* 2015, 54, 6331–6337. (g) Hill, S.; Datta, S.; Liu, J.; Inglis, R.; Milios, C. J.; Feng, P. L.; Henderson, J. J.; Del Barco, E.; Brechin, E. K.; Hendrickson, D. N. *Dalton Trans.* 2010, 39, 4693–4707. (h) Pineda, E. M.; Tuna, F.; Zheng, Y. Z.; Teat, S. J.; Winpenny, R. E. P.; Schnack, J.; McInnes, E. J. L. *Inorg. Chem.* 2014, 53, 3032–3038.
- 9. Khan, M. I.; Zubieta, J. *Prog. Inorg. Chem.* **1995**, 43, 1.
- 10. Chandrasekhar, V.; Kingsley, S. Angew. Chem. Int. Ed. 2000, 39, 2320–2322.

- 11. (a) Chandrasekhar, V.; Senapati, T.; Sañudo, E. C.; Clérac, R. Inorg. Chem. 2009, 48, 6192–6204. (b) Khanra, S.; Helliwell, M.; Tuna, F.; McInnes, E. J. L.; Winpenny, R. E. P. Daltoj Trans. 2009, 31, 6166-6174. (c) Sahoo, D.; Suriyanarayanan, R.; Chandrasekhar, V. Dalton Trans. 2014, 43, 10898-10909. (d) Breeze, B. A.; Shanmugam, M.; Tuna, F.; Winpenny, R. E. P. Chem. Commun. 2007, 48, 5185–5187. (e) Chandrasekhar, V.; Nagarajan, L.; Clérac, R.; Ghosh, S.; Verma, S. Inorg. Chem. 2008, 47, 1067–1073. (f) Shanmugam, M.; Chastanet, G.; Mallah, T.; Sessoli, R.; Teat, S. J.; Timco, G. A.; Winpenny, R. E. P. Chem. - A Eur. J. 2006, 12, 8777–8785. (g) Langley, S. K.; Helliwell, M.; Teat, S. J.; Winpenny, R. E. P. Dalton Trans. 2012, 41, 12807–12817. (h) Langley, S. J.; Helliwell, M.; Sessoli, R.; Rosa, P.; Wernsdorfer, W.; Winpenny, R. E. P. Chem. Commun. 2005, 40, 5029–5031. (i) Brechin, E. K.; Coxall, R. A.; Parkin, A.; Parsons, S.; Tasker, P. A.; Winpenny, R. E. P. Angew. Chem. Int. Ed. 2001, 40, 2700–2703. (j) Konar, S.; Bhuvanesh, N.; Clearfield, A. J. Am. Chem. Soc. **2006**, 128, 9604–9605. (k) Thomas, J. A. Dalton Trans. **2011**, 40, 12005–12016. (l) Zheng, Y.-Z.; Evangelisti, M.; Winpenny, R. E. P. Angew. Chem. Int. Ed. 2011, 123, 3776–3779. (m) Yao, H. C.; Li, Y. Z.; Song, Y.; Ma, Y. S.; Zheng, L. M.; Xin, X. Q. *Inorg. Chem.* **2006**, *45*, 59–65.
- (a) Tolis, E. I.; Helliwell, M.; Langley, S.; Raftery, J.; Winpenny, R. E. P. *Angew. Chem. Int. Ed.* 2003, 115, 3934–3938. (b) Caroff, C. M.; Girolami, G. S.. *Inorg. Chem.* 2022, 61, 16740–16749. (c) Maheswaran, S.; Chastanet, G.; Teat, S. J.; Mallah, T.; Sessoli, R.; Wernsdorfer, W.; Winpenny, R. E. P. *Angew. Chem. Int. Ed.* 2005, 44, 5044–5048.
- (a) Zhou, C.; Lei, J.; Liu, Y.; Au, C. T.; Chen, Y.; Yin, S. F *Appl. Organomet. Chem.* 2020, 34, 1–8. (b) Chen, Y.; Qiu, R.; Xu, X.; Au, C. T.; Yin, S. F. *RSC Adv.* 2014, 4, 11907–11918. (c) Tan, N.; Nie, T.; Au, C. T.; Lan, D.; Wu, S.; Yi, B. *Tetrahedron Lett.* 2017, 58, 2592–2595. (d) Xia, J.; Qiu, R.; Yin, S.; Zhang, X.; Luo, S.; Au, C. T.; Xia, K.; Wong, W. Y. *J. Organomet. Chem.* 2010, 695, 1487–1492. (e) Tang, N.; Song, X.; Yang, T.; Qiu, R.; Yin, S. F. *J. Organomet. Chem.* 2021, 942, 121820. (f) Saxena, A. K. *Polyhedron* 1986, 5, 1581–1585. (g) Huang, Y. Z. *Acc. Chem. Res.* 1992, 25, 182–187. (h) Ninagawa, A.; Matsuda, H.; Nomura, R. *J. Org. Chem.* 1980, 45, 3735–3738.
- (a) Heyerdahl, S. L.; Rozenberg, J.; Jamtgaard, L.; Rishi, V.; Varticovski, L.; Akah, K.; Scudiero, D.; Shoemaker, R. H.; Karpova, T. S.; Day, R. N.; McNally, J. G.; Vinson, C. Eur. J. Cell Biol. 2010, 89, 564–573. (b) Rishi, V.; Oh, W. J.; Heyerdahl, S. L.; Zhao, J.; Scudiero, D.; Shoemaker, R. H.; Vinson, C. J. Struct. Biol. 2010, 170, 216–225. (c)

- Zhao, J.; Stagno, J. R.; Varticovski, L.; Nimako, E.; Rishi, V.; McKinnon, K.; Akee, R.; Shoemaker, R. H.; Ji, X.; Vinson, *CMol. Pharmacol.* **2012**, *82*, 814–823. (d) McKelvie, J. C.; Richards, M. I.; Harmer, J. E.; Milne, T. S.; Roach, P. L.; Oyston, P. C. F. *Br. J. Pharmacol.* **2013**, *168*, 172–188.
- (a) Jami, A. K.; Baskar, V. *Dalton Trans.* 2012, 41, 12524–12529. (b) Prabhu, M. S. R.; Jami, A. K.; Baskar, V. *Organometallics* 2009, 28, 3953–3956. (c) Jami, A. K.; Prabhu, M. S. R.; Baskar, V. *Organometallics* 2010, 29, 1137–1143. (d) Prabhu, M. S. R.; Ugandhar, U.; Baskar, V. *Dalton Trans.* 2016, 45, 6963–6967. (e) Srungavruksham, N. K.; Baskar, V. *Dalton Trans.* 2015, 44, 6358–6362.
- (a) Beckmann, J.; Finke, P.; Hesse, M.; Wettig, B. Angew. Chem. Int. Ed. 2008, 47, 9982.
 (b) Brünig, J.; Hupf, E.; Lork, E.; Mebs, S.; Beckmann, J. Dalton Trans. 2015, 44 (16), 7105–7108.
- (a) Nicholson, B. K.; Clark, C. J.; Wright, C. E.; Groutso, T. *Organometallics* 2010, 29, 6518–6526.
 (b) Nicholson, B. K.; Clark, C. J.; Jameson, G. B.; Telfer, S. G. *Inorg. Chim. Acta* 2013, 406, 53–58.
 (c) Nicholson, B. K.; Clark, C. J.; Wright, C. E.; Telfer, S. G.; Groutso, T. *Organometallics* 2011, 30, 6612–6616;
 (d) Nicholson, B. K.; Clark, C. J.; Telferc, S. G.; Groutsod, T. *Dalton Trans.* 2012, 41, 9964-9970.
- (a) Ugandhar, U.; Navaneetha, T.; Ali, J.; Mondal, S.; Vaitheeswaran, G.; Baskar, V. *Inorg. Chem.* 2020, 59, 6689–6696. (b) Ali, S.; Muryn, C. A.; Tuna, F.; Winpenny, R. E. P. *Dalton Trans.* 2010, 39, 124–131. (c) Ali, S.; Muryn, C. A.; Winpenny, R. E. P. *Dalton Trans.* 2010, 39, 9588–9597. (d) Ali, S.; Baskar, V.; Muryn, C. A.; Winpenny, R. E. P. *Chem. Commun.* 2008, 4, 6375–6377.
- 19. (a) Doak, G. O.; Steinman, H. G. *J. Am. Chem. Soc.* **1946**, *68*, 1987–1989. (b) Liu, Z.; Ozawa, Y.; Yagasaki, A. *Bull. Chem. Soc. Jpn.* **2014**, *87*, 1245–1251.
- 20. Crofts, P. C.; Kosolapoff, G. M. J. Am. Chem. Soc. 1953, 75, 3379–3383.
- (a) Sheldrick, G. M. Acta Crystallogr. Sect. A Found. Crystallogr. 2015, 71, 3–8. (b) Dolomanov, O. V.; Bourhis, L. J.; Gildea, R. J.; Howard, J. A. K.; Puschmann, H. J. Appl. Crystallogr. 2009, 42, 339–341. (c) Sheldrick, G. M. Acta Crystallogr. Sect. C Struct. Chem. 2015, 71, 3–8. (d) Bourhis, L. J.; Dolomanov, O. V.; Gildea, R. J.; Howard, J. A. K.; Puschmann, H. Acta Crystallogr. Sect. A Found. Crystallogr. 2015, 71, 59–75.
- 22. Coxall, R. A.; Harris, S. G.; Henderson, D. K.; Parsons, S.; Tasker, P. A.; Winpenny, R. E. P. *J. Chem. Soc. Dalton Trans.* **2000**, 2349–2356.

Ce^{IV}/Sb^V Metal Oxo Clusters Resemble Structure of Platonic Solids

CHAPTER

5

Abstract: Two cerium-based metal oxo clusters were synthesized by a solvothermal reaction of two different organoantimony (V) clusters with hydrated cerium nitrate in the presence of a base. Single crystal X-ray diffraction analysis reveals the formation of clusters $[Ce^{IV}_6(p-CIC_6H_4Sb^V)_4(\mu_4-O)_4(\mu_3-O)_4(t-BuPO_3)_8(\mu_2-OCH_3)_8]$ (5.1) and $[Ce^{IV}_6(PhSb^V)_8(\mu_4-O)_8(\mu_2-O)_8(t-BuPO_3)_8(\mu_3-OCH_3)_8]$ (5.2). These two clusters were further characterized by elemental analysis, TGA analysis and ESI-MS studies. Hexanuclear Ce₆ metal oxo clusters stabilized by *in-situ* generated pro-ligand systems. Compounds 5.1-5.2 possess the ten-membered and fourteen-membered type architecture, containing all cerium metal ions that have eight coordination modes and all antimony metal ions that have six coordination modes. Interestingly, 5.1-5.2 shows a platonic relationship between cerium, antimony and phosphorus atoms present in the metal oxo cluster.

5.1 Introduction:

In the lanthanide series, unlike other rare earth elements, cerium exists in both stable 3+ and 4+ oxidation states in $[Xe]4f^l$ and $[Xe]4f^0$ electronic configurations because of its unique chemical properties. 1 Ce³⁺ compounds act as Lewis acid catalysts with one unpaired electron, while Ce⁴⁺ compounds act as electron oxidizing agents with no unpaired electron in many organic transformations.² Cerium oxo clusters have applications in the field of photocatalysis and thermocatalysis with redox properties between the Ce(IV/III) couple.³ In recent times, cerium oxo clusters have been used as a photocatalyst in the aerobic oxidation of sulfides to sulfoxides with good selectivity and activity.⁴ Over the last few decades, molecular metal phosphonates have been considered an active research area.⁵ Chandrasekhar *et al.* reported the synthesis of molecular Ce(III) phosphonate as a first example by a reaction of tritylphosphonic acid with cerium nitrate and catalytic activity in the Biginelli reaction.⁶ Mesoporous cerium materials are prepared by the surfactant-assisted method, cetyltrimethylammonium bromide (CTAB) as a cationic surfactant and acting as an optical sensor with good efficiency.⁷ Recently, Chudasama et al. reported the proton conductor behavior of cerium(IV) phosphonate.⁸ Organoantimony(V) compounds attracted many researchers due to their fascinating structural chemistry and used in the preparation of interesting metal oxo clusters and polyoxometalates. Our group aimed to understand the reactivity of polymeric organostibonic acid with different protic ligands and observed the depolymerization involved in the reactions, which led to the formation of fascinating frameworks. 10 Our group and others reported the main group phosphonates as a pro-ligand in the preparation of mixed 3d-main group-based metal oxo clusters. 11 Triorganylpnictogen oxides, R₃M=O (R = P, As, Sb, Bi), exist as a polymer or monomer based on the central atom present in the formula. Doak et al. reported that a triphenylantimony oxide with a fourmembered ring with Sb-O-Sb linkages exists as a dimer in the solid state. 12 Orpen et al. reported a structural discussion of polymeric triphenylantimony oxide supported by EXAFS studies, which showed a polymeric array in which every Ph₃SbO₂ moiety with trigonal-bipyramidal geometry is bridged through an oxygen atom. 13 Huber et al. reported a reactivity of polymeric triphenylantimony oxide with different sulfonic acids, revealing the formation of monomeric antimony complexes with open chains. 14 Our group continued investigations on organoantimony(V) compounds, polymeric triphenylantimony oxide with protic acids such as seleninates, phosphinates and phosphonates revealed interesting clusters. ¹⁵ Many research groups reported the main group phosphonates and cerium phosphonates independently but not a combination of cerium-main group-based phosphonates. We are interested in studying the different main group-based metal phosphonates as a preformed cluster in the synthesis of novel cerium oxo clusters.

In the previous chapter, we discussed the insoluble mixed 4f-main group-based metal oxo clusters. Herein, we report the synthesis of two novel soluble mixed 4f-main group-based metal oxo clusters $[Ce^{IV}_6(p\text{-}ClC_6H_4Sb^V)_4(\mu_4\text{-}O)_4(\mu_3\text{-}O)_4(t\text{-}BuPO_3)_8(\mu_2\text{-}OCH_3)_8]$ (5.1) and $[Ce^{IV}_6(PhSb^V)_8(\mu_4\text{-}O)_8(\mu_2\text{-}O)_8(t\text{-}BuPO_3)_8(\mu_3\text{-}OCH_3)_8]$ (5.2) synthesized by a reaction of the organoantimonate-phosphonate cluster as pro-ligand with cerium nitrate hexahydrate in the presence of pyridine under solvothermal conditions. 5.1-5.2 exhibits the platonic relationship between the atoms presented.

5.2 Experimental Section:

5.2.1 General Information:

p-Chlorophenylstibonic acid¹⁶, *t*-butylphosphonic acid¹⁷ and polymeric triphenylantimony oxide¹⁸ were synthesized according to literature reports. Solvents and common reagents were purchased from Sigma-Aldrich. The mixed organostibonate-phosphonate precursor [(*p*-ClC₆H₄Sb)₂(O)(*t*-BuPO₃H)₆]^{11b} was synthesized by condensation reactions of *p*-chlorophenylstibonic acid with *t*-butylphosphonic acid. The *p*-chlorophenylstibonic acid and *t*-butylphosphonic acid were mixed in a 1:2 ratio and stirred in acetonitrile (15 mL) for 24 h at room temperature. The solutions were filtered and crystals were isolated on slow evaporation of acetonitrile. Trinuclear organoantimony (V) metal cluster [(Ph₂Sb)₂(PhSb)(O)₃(OH)₂(*t*-BuPO₃)₂]¹⁵ was synthesized according to literature report. All the compounds used were dried under a high vacuum for half an hour before being subjected to spectroscopic and analytical techniques.

5.2.2 Instrumentation:

Infrared spectra were recorded with a NICOLET iS5 FTIR Spectrometer. Elemental analysis was performed with a Flash EA Series 1112 CHNS analyzer. Single crystal X-ray data for **5.1-5.2** were carried out at 297.8 and 293 (2) K with an XtaLAB Synergy, a single source at offset/far, HyPix3000 diffractometer and a Rigaku Oxford HyPix3000 CCD plate detector system [λ (Mo K α) = 0.71073 Å] with a mirror monochromator. The data were reduced using CrysAlisPro 1.171.40.35a (Rigaku OD, 2018). The structures were solved using SHELXT and refined using SHELXL-2018/3 in Olex2 1.3-ac4 software.¹⁹ All non-hydrogen atoms were refined anisotropically. PXRD was recorded at room temperature using a Bruker D8 Advance diffractometer (Bruker-AXS, Karlsruhe, Germany) using Cu–K α X-radiation (λ = 1.5406 Å) at 40 kV and 30 mA power. X-ray diffraction patterns were collected over a 2 θ range of 5–80°

at a scan rate of 3.9°/min. TGA was recorded for compounds **5.1-5.2** with PerkinElmer STA 8000 thermogravimetric analyzer under a nitrogen gas flow rate of 20 ml/min and heating rate of 10 °C/min. Graphics of the crystal structures have been performed with Diamond (version 3).

5.2.3 General Synthetic Procedures:

The synthetic methodology for metal oxo cluster **5.1** is as follows: the corresponding mixed stibonate-phosphonate and hydrated cerium nitrate were dissolved in methanol (15 mL) followed by dropwise addition of 2,6-lutidine. The clear solution obtained was stirred for 2 h and then transferred into a Teflon digestion bomb and the mixture was heated at 150 °C for 16 h and then cooled slowly to room temperature for 36 h. The isolated crystals were powdered and subjected to a high vacuum for 30 min before being characterized by standard spectroscopic and analytical techniques.

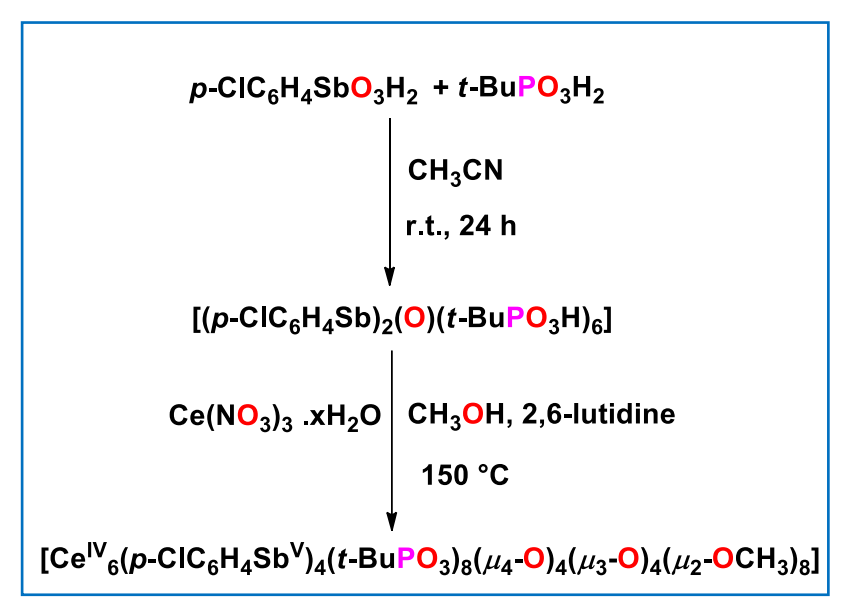
Compound **5.1**: $[(p\text{-ClC}_6\text{H}_4\text{Sb})_2(\text{O})(t\text{-BuPO}_3\text{H})_6]$ (0.05 g, 0.038 mmol), cerium nitrate (0.066 g, 0.15 mmol) and 2, 6-lutidine (0.1 mL). Colorless single crystals were obtained upon slow cooling (36 h) of the methanol solution. Yield: 0.035 g (28% based on pro-ligand). ESI-MS: 3260.37401 for $[\text{M}+\text{Na}]^+$. IR (cm^{-1}) : 2964 (wide), 2186 (m), 2015 (m), 1970 (s), 1479 (s), 1391 (m), 1361 (m), 1123 (s), 1077 (s), 1018 (s), 946 (s), 912 (s), 834 (s), 815 (s), 725 (s), 665 (s), 582 (s), 548 (s). Anal. Calcd for $\text{Ce}_6\text{C}_6\text{4}\text{Cl}_4\text{H}_{112}\text{O}_{40}\text{P}_8\text{Sb}_4$ (3231.3864): C, 23.73; H, 3.49. Found: C, 23.12; H, 3.39. All values are given as percentages.

The synthetic methodology for metal oxo cluster **5.2** is as follows: the corresponding trinuclear organoantimony (V) metal cluster and hydrated cerium nitrate were dissolved in methanol (15 mL) followed by dropwise addition of pyridine. The clear solution obtained was stirred for 2 h and then transferred into a Teflon digestion bomb and the mixture was heated at 150 °C for 16 h and then cooled slowly to room temperature for 36 h. The isolated crystals were powdered and subjected to a high vacuum for 30 min before being characterized by standard spectroscopic and analytical techniques.

Compound **5.2:** [(Ph₂Sb)₂(PhSb)(O)₃(OH)₂(*t*-BuPO₃)₂] (0.05 g, 0.036 mmol), cerium nitrate (0.032 g, 0.073 mmol) and pyridine (0.1 mL). Colorless single crystals were obtained upon slow cooling (36 h) of the methanol solution. Yield: 0.034 g (23% based on pro-ligand). ESI-MS: 3100.5581 for [M-{(Ph)₈(t-BuPO₃)₂(OCH₃)}]⁺. IR (cm⁻¹): 2950 (m), 2328 (m), 2188 (m), 2054 (m), 2006 (s), 1965 (s), 1479 (m), 1124 (m), 1078 (s), 1022 (s), 956 (s), 917 (s), 833 (m), 739 (m), 696 (m), 662 (s), 581 (m), 548 (s), 501 (s). Anal. Calcd for Ce₆C₈₈Cl₄H₁₃₆O₄₈P₈Sb₈ (4015.2733): C, 26.26; H, 3.41. Found: C, 25.81; H, 3.37. All values are given as percentages.

5.3 Results and Discussion:

Compound **5.1** was synthesized by reaction of the organostibonate-phosphonate cluster, with Ce(NO₃)₃.xH₂O in the ratio of 1:4 under solvothermal conditions in methanol using 2,6-lutidine as a base (**Scheme 5.1**). Colorless block-shaped single crystals of **5.1** were grown by cooling



Scheme 5.1: Synthesis of 5.1.

the methanol solution to room temperature. ESI-MS studies (positive ion mode) of 5.1 was carried out in a chloroform solvent. The peak of the ESI-MS spectrum of 5.1 (Figure 5.9), at m/z 3260.3741, corresponds to the molecular ion peak [M+Na]⁺ suggesting the structural integrity of the **5.1** in solution-state. Compound **5.1** crystallizes in tetragonal space group $P4_2/n$. Crystallographic data of compound **5.1** is given in **Table 5.1**. The bond lengths and bond angles of compound 5.1 are shown in Table 5.2. The molecular structure of 5.1 (Figure 5.1a) contains six cerium metal ions, four antimony metal ions, eight t-butyl phosphonates, four μ_4 -oxo bridges, four μ_3 -oxo bridges and eight methoxy groups form a novel {Ce₆Sb₄P₈} molecular architecture. Eight phosphonates are shown in the molecular structure and according to Harris notation, they are all bonded to one antimony center and two cerium centers in the [3.111] coordination mode.²² The six cerium atoms are found at the corners of an octahedron and eight phosphorus atoms from t-butylphenylphosphonates are found at the corners of a cube. Four antimony atoms are found at the corners of the tetrahedron. Here, the platonic relationship between the atoms in the cluster, which is located on the vertices of platonic solids like the cube, octahedron and tetrahedron, is represented. The eight-coordination of four cerium sites is fulfilled with two phosphonates oxygen from each side, two μ_4 -oxo bridges, two μ_3 -oxo

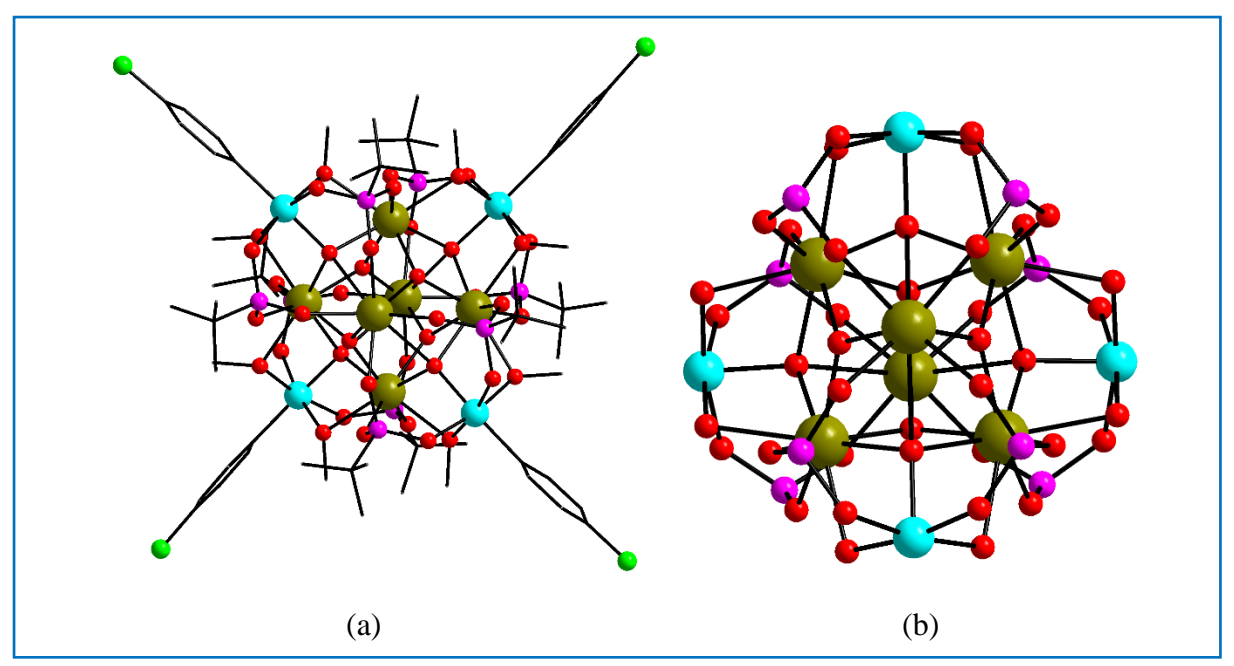


Figure 5.1: (a) Molecular and (b) core structure of compound **5.1.** Color code: cyan, Sb; yellow-green, Ce; purple, P; Red, O; grey, C. Hydrogens are omitted for clarity.

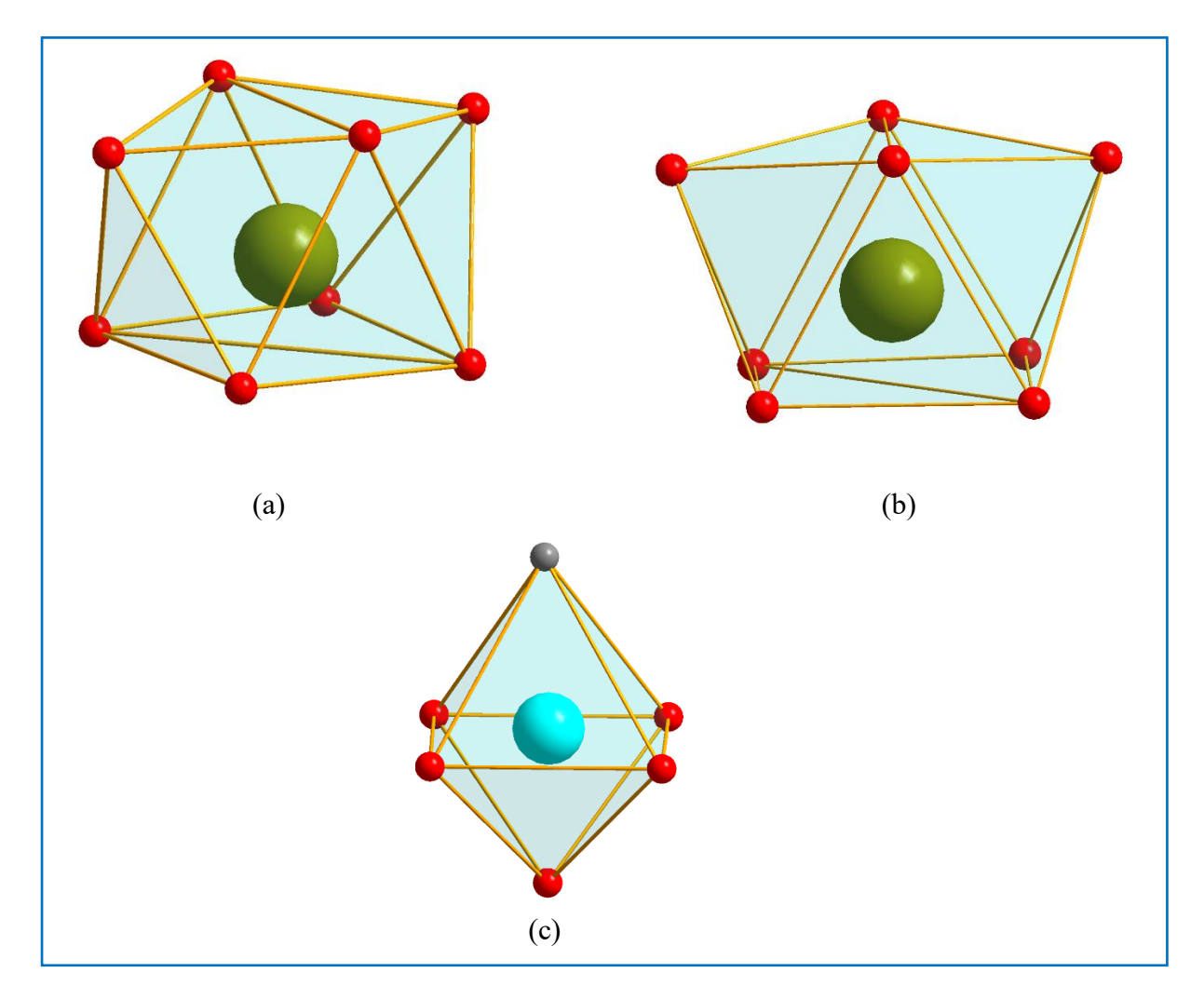
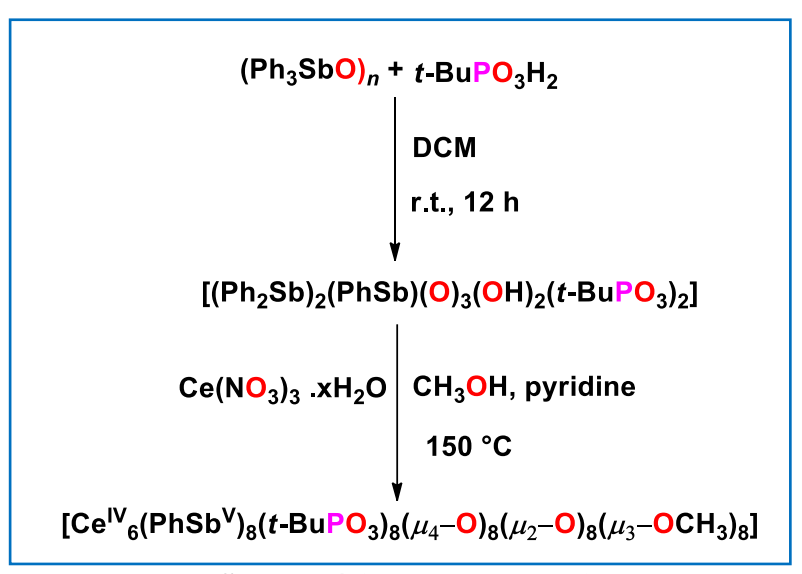


Figure 5.2: Coordination geometry around (a) Ce1 metal ion, (b) Ce2 metal ion and (c) antimony metal ion in 5.1.

bridges and two μ_2 -methoxy bridges containing a triangular dodecahedron geometry (**Figure 5.2a**) and other two cerium sites fulfilled with four phosphonates oxygen from each side, two μ_4 -oxo bridges and two μ_3 -oxo bridges containing a biaugmented trigonal prism J50 geometry (**Figure 5.2b**). All antimony atoms are present in six coordination modes and attain an octahedral geometry (**Figure 5.2c**). The coordination geometry around metal centers is confirmed by using SHAPE calculations (**Table 5.4**). Important bond metric parameters are shown; the Ce-O bond lengths involving phosphonates, μ_4 -oxo, μ_3 -oxo and μ_2 -methoxy groups falls in the range of 2.330(3)-2.303(4) Å, 2.734(3)-2.380(3) Å, 2.221(3)-2.207(3) Å and 2.471(3)-2.450(3) Å respectively. The Sb-O bond distances involving phosphonates, μ_4 -oxo and μ_2 -methoxy groups falls in the range of 1.987(4) -1.985(4) Å, 1.963(3)Å and 2.037(3) -2.023(4) Å respectively. The Ce-O-Ce and Ce-O-Sb bond angles fall in the range of 120.40(13) -97.23(11)° and 109.67(14)-104.73(8)° respectively.

Compound **5.2** was synthesized by a reaction of trinuclear organoantimony (V) metal cluster [(Ph₂Sb)₂(PhSb)(O)₃(OH)₂(*t*-BuPO₃)₂] with Ce(NO₃)₃.xH₂O in the ratio of 1:2 under solvothermal conditions in methanol using pyridine as a base (**Scheme 5.2**). Colorless blockshaped single crystals of **5.2** were grown by cooling the methanol solution to room temperature.



Scheme 4.1: Synthesis of 5.2.

ESI-MS studies (positive ion mode) of **5.2** was carried out in a chloroform solvent. ESI-MS data of **5.2** (Figure 5.10) show the presence of $[M-\{(Ph)_8(t-BuPO_3)_2(OCH_3)\}]^+$ as a major signal at m/z 3100.5581, suggesting that **5.2** retains structural stability in solution-state also. Compound **5.2** crystallizes in tetragonal space group I4/m. Crystallographic data of compound **5.2** is given in **Table 5.1**. The bond lengths and bond angles of compound **5.2** are shown in **Table 5.3**. The molecular structure of **5.2** (**Figure 5.3a**) contains six cerium metal ions, eight

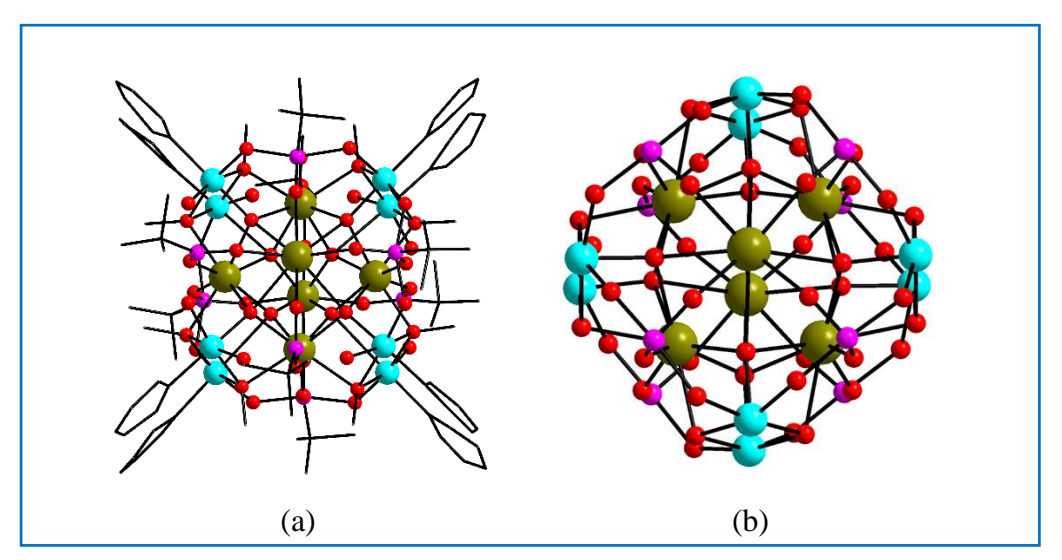


Figure 5.3: (a) Molecular and (b) core structure of compound **5.2**. Color code: cyan, Sb; yellow-green, Ce; purple, P; Red, O; grey, C. Hydrogens are omitted for clarity.

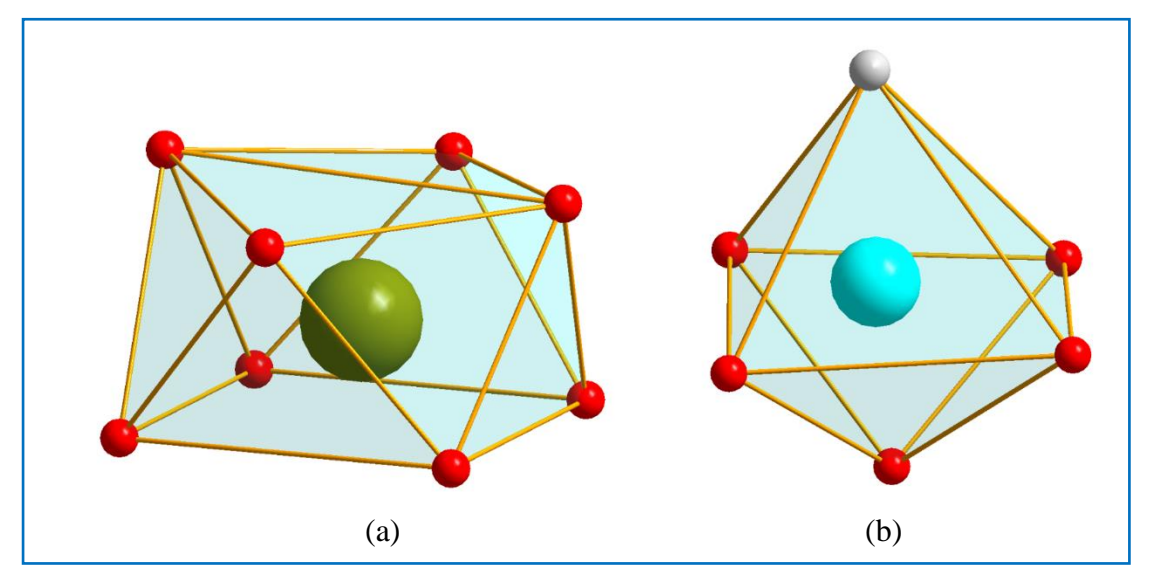


Figure 5.4: Coordination geometry around (a) Cerium metal ion and (b) antimony metal ion in **5.2.**

antimony metal ions, eight t-butyl phosphonates, eight μ_4 -oxo bridges, eight μ_2 -oxo bridges and eight methoxy groups to form a novel {Ce₆Sb₈P₈} molecular architecture. Interestingly, mono dearylation was observed in **5.2**. Eight phosphonates are shown in the molecular structure and according to Harris notation, they are all bonded to one antimony center and two cerium centers in the [3.111] coordination mode. The six cerium atoms are found at the corners of an octahedron and eight phosphorus atoms from t-butylphenylphosphonates are found at the corners of a cube. The eight antimony atoms are found at the corners of the cube. Here, the platonic relationship between the atoms in the cluster, which is located on the vertices of platonic solids like the cube and octahedron is represented. The eight-coordination of four cerium sites is fulfilled with two phosphonates oxygen from each side, four μ_4 -oxo bridges, two μ_3 -methoxy bridges

containing a square antiprism geometry and two other cerium sites fulfilled with four phosphonates oxygen from each side, four μ_4 -oxo bridges containing a square antiprism geometry (**Figure 5.4a**). All antimony atoms are present in six coordination modes and attain an octahedral geometry (**Figure 5.2b**). The coordination geometry around metal centers is confirmed by using SHAPE calculations (**Table 5.4**). Important bond metric parameters are shown; the Ce-O bond lengths involving phosphonates, μ_4 -oxo, and μ_3 -methoxy groups falls in the range of 2.722(10)-2.302(16) Å, 2.258(9)-2.209(8) Å and 2.463(9)- 2.429(8) Å respectively. The Sb-O bond distances involving phosphonates, μ_4 -oxo and μ_3 -methoxy groups falls in the range of 2.021(19)-2.01(2) Å, and 2.34(4)-2.32(4) Å respectively. The Ce-O-Ce and Ce-O-Sb bond angles fall in the range of 119.2(4)-101.5(3)° and 109.9(4)-108.4(2)° respectively.

The phase purity of compounds **5.1-5.2** was confirmed by powder X-ray diffraction (PXRD). The PXRD patterns match well with the simulated patterns generated from SC-XRD analysis (**Figure 5.11-5.12**). The thermal stability of **5.1-5.2** was examined under a nitrogen atmosphere with thermogravimetric analysis (TGA) in the range of 30–800 °C. TGA plots of **5.1-5.2** (**Figure 5.13-5.14**) indicate the metal oxo cluster is stable up to 370 and 372 °C, respectively, and further, the weight loss indicates the gradual decomposition of the metal oxo cluster.

5.4 Conclusion:

We have successfully designed and synthesized two novel cerium-based metal oxo clusters under solvothermal conditions. We have investigated the reactivity of two different organoantimony (V) based pro-ligands towards the cerium metal ion, revealing the formation of two intriguing metal oxo clusters. SC-XRD revealed the formation of novel ten- and fourteen-membered molecular architectures. Hexanuclear Ce₆ metal oxo clusters stabilized by *in-situ* generated organoantimony (V) based pro-ligands. Interestingly, **5.1-5.2** exhibits the platonic relationship between the atoms present in the metal oxo clusters.

Ce^{IV} / Sb^V metal oxo clusters....

5.5 Analytical and Spectroscopic Data

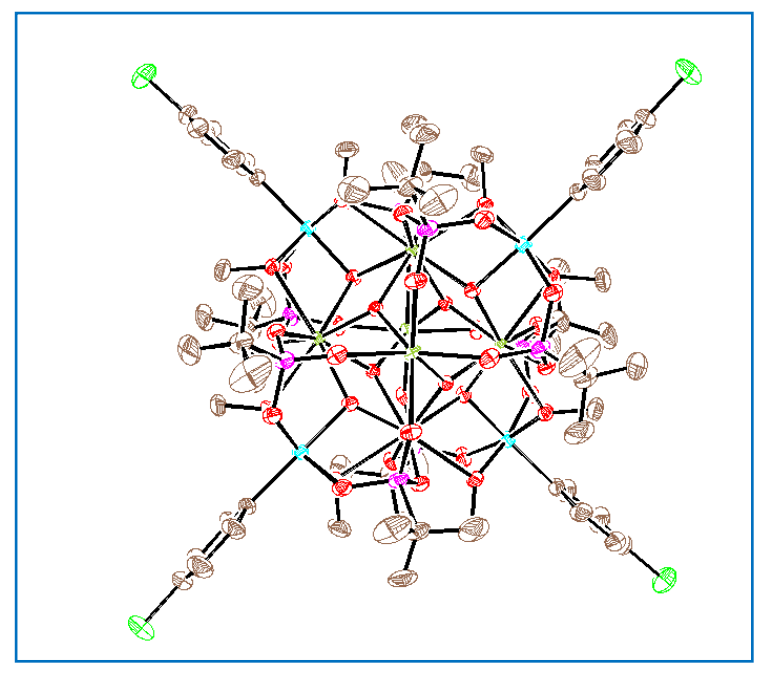


Figure 5.5: ORTEP view of **5.1** with thermal ellipsoids shown at 30% probability.

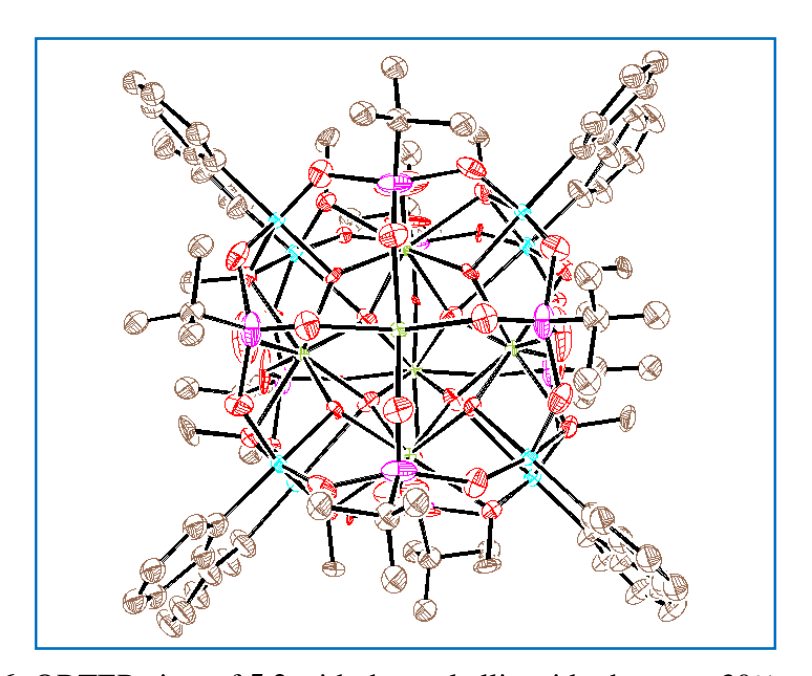


Figure 5.6: ORTEP view of **5.2** with thermal ellipsoids shown at 30% probability.

Table 5.1: crystallographic information of compounds **5.1** -**5.2**

	5.1	4.2
Formula	C ₆₇ Cl ₄ H ₁₂₄ O ₄₃ P ₈ Sb ₄ Ce ₆	C ₈₈ H ₁₃₆ O ₄₈ P ₈ Sb ₈ Ce ₆
F. weight	3334.93	4024.44
Temp K	297.8	293(2)
Crystal system	tetragonal	tetragonal
Space group	P4 ₂ /n	I4
a/Å	14.6239(2)	14.9564(2)
b/Å	14.6239(2)	14.9564(2)
c/Å	26.5040(4)	26.4992(5)
α/°	90	90
β/°	90	90
γ/°	90	90
Volume/Å ³	5668.11(18)	5927.71(19)
Z	2	2
pcalcg/cm ³	1.954	2.313
μ/mm-1	3.575	4.243
F(000)	3220.0	3928.0
Crystal size/mm ³	$0.192 \times 0.175 \times 0.163$	$0.22 \times 0.189 \times 0.154$
2Θ range (°)	3.938 to 54.022	4.928 to 53.876
Index ranges	$-18 \le h \le 18$, $-18 \le k \le 18$, $-28 \le 1 \le 33$	$-18 \le h \le 17$, $-18 \le k \le 15$, $-31 \le 1 \le 27$
Reflections collected	58501	17285
Ind. reflections	6011 [Rint = 0.0891]	5230 [Rint = 0.0207]
Data/restraints/p arameters	6011/0/293	5230/1/284
GooF (F2)	1.053	1.078
$R_1(F)$ [I>2 $\sigma(I)$]	0.0393	0.0407
wR ₂ (F ²) (all data)	0.0962	0.1287
Largest diff. peak/hole / e Å-3	1.17/-1.31	2.99/-1.26
Completeness to θ_{max} , %	100	98.8

 $\textbf{Table 5.2:} \ \, \textbf{Selected bond lengths (Å) and bond angles (deg) parameters of compound \textbf{5.1}}$

	· ·		0 . 0, 1	•	
Ce1-Ce1 ¹	3.7228(4)	O10-Ce1-O7	74.40(11)	O6 ² -Ce1-Sb1 ²	68.49(9)
Ce1-Ce1 ²	3.7227(4)	O10-Ce1-O4	134.84(11)	O6 ² -Ce1-Sb ¹	104.73(8)
Ce1-Sb1	3.5576(4)	O10-Ce1-O2 ²	95.95(11)	O6 ² -Ce1-O7	126.26(12)
Ce1-Sb1 ¹	3.5582(4)	O10 ¹ -Ce1-O2 ²	134.35(11)	O6 ² -Ce1-O2 ²	73.73(13)
Ce1-O10	2.207(3)	O10-Ce1-O6 ²	150.05(12)	O6 ² -Ce1-O9	120.40(13)
Ce1-O10 ²	2.221(3)	O10-Ce1-O9	81.89(12)	O9-Ce1-Ce1 ²	104.32(9)
Ce1-O7 ¹	2.380(3)	O7-Ce1-Ce1 ²	102.10(8)	O9-Ce1-Ce1 ¹	117.54(9)
Ce1-O7	2.383(3)	O7-Ce1-Sb1 ²	160.53(8)	O9-Ce1-Sb1	68.57(9)
Ce1-O4	2.450(3)	O7 ² -Ce1-Sb1 ²	31.30(8)	O9-Ce1-Sb1 ²	105.26(9)
Ce1-O2 ¹	2.471(3)	O7 ² -Ce1-O7	132.03(14)	O9-Ce1-O7 ²	126.94(12)
Ce1-O6 ¹	2.314(3)	O7 ² -Ce1-O4	152.23(11)	O9-Ce1-O7	79.05(11)
Ce1-O9	2.330(3)	O4-Ce1-Ce1 ¹	79.40(8)	Ce1 ² -Ce2-Ce1 ¹	86.440(11)
Ce2-O10	2.207(3)	O4-Ce1-Ce1 ²	166.29(8)	Ce1-Ce2-Ce1 ¹	58.035(6)
Ce2-O10 ³	2.207(3)	O5-Ce2-O7 ³	140.67(11)	O10-Ce2-Ce1 ²	29.87(8)
Ce2-O7	2.734(3)	O5-Ce2-O7	70.39(11)	O10 ³ -Ce2-Ce1 ²	76.46(8)
Ce2-O7 ³	2.734(3)	O5-Ce2-O5 ³	129.02(18)	O10-Ce2-Ce1	29.79(8)
Ce2-O5	2.303(4)	O5 ³ -Ce2-O8	79.19(13)	O10-Ce2-O10 ³	81.85(16)
Ce2-O5 ³	2.303(4)	O8 ³ -Ce ² -Ce ¹ ²	108.93(9)	O10-Ce2-O7 ³	67.33(10)
Ce2-O8 ³	2.316(3)	O8-Ce2-O8 ³	127.16(18)	O5 ³ -Ce2-Ce1 ²	72.27(9)
Ce2-O8	2.316(3)	Ce1-Sb1-Ce1 ¹	63.088(9)	O3-Sb1-Ce1	83.76(10)
Sb1-O7	1.963(3)	O7-Sb1-Ce1 ¹	39.03(9)	O3-Sb1-Ce1 ¹	128.23(11)
Sb1-O4	2.037(3)	O7-Sb1-O4	79.87(13)	O3-Sb1-O4	91.25(15)
Sb1-O2	2.023(4)	O7-Sb1-O2	80.24(13)	O3-Sb1-O2	170.44(14)
Sb1-O2		O7-Sb1-O2	90.21(14)	O6-P1-O5	
Sb1-O1	1.986(4)	073-Ce2-Ce1	90.21(14)	O9-P2-O3	112.6(2) 109.1(2)
P1-O5	1.986(4)	O4-Sb1-Ce1 ¹	88.79(10)	Ce1-O10-Ce1 ²	
	1.517(4)				114.44(13)
P1-O6 P1-O1	1.514(4)	04-Sb1-Ce1	41.79(10)	Ce1-O10-Ce2	120.42(13)
	1.576(4)	O10 ¹ -Ce1-Sb1	87.08(8)	Cell 07 Cel	102.83(11)
P2-O8	1.520(4)	O6 ² -Ce1-Ce1 ¹	103.70(9)	Ce1¹-O7-Ce2	97.23(11)
P2-O9	1.515(4)	01-Sb1-Ce1	128.68(11)	Sb1-O7-Ce1	109.52(14)
P2-O3	1.565(4)	O1-Sb1-Ce1 ¹	83.73(10)	Sb1-O7-Ce2	136.26(14)
Cel¹-Cel-Cel²	90	O1-Sb1-O4	170.35(14)	P1-O5-Ce2	135.5(2)
Sb1-Ce1-Ce1 ¹	58.464(9)	O4-Ce1-O2 ²	112.66(12)	Sb1-O4-Ce1	104.55(14)
Sb1 ² -Ce1-Ce1 ¹ Sb1-Ce1-Sb1 ²	132.303(11)	O2 ² -Ce1-Ce1 ² O2 ² -Ce1-Ce1 ¹	79.14(8)	P2-O8-Ce2 P1-O6-Ce1 ¹	133.8(2)
O10-Ce1-Ce1 ²	167.609(11) 32.90(8)	O2 ² -Ce1-Ce1 ³	165.68(8) 135.83(8)	P1-06-Ce1	127.0(2) 124.9(2)
010-Ce1-Ce1 010-Ce1-Ce1	79.29(8)	O2 -Ce1-Sb1	33.44(8)	O10 ³ -Ce2-O8 ³	85.43(12)
010-001-001	17.47(0)	02 -001-301	33.44(0)	010 -062-06	05.43(12)

¹+Y,1/2-X,1/2-Z; ²1/2-Y,+X,1/2-Z; ³1/2-X,1/2-Y,+Z

 $\textbf{Table 5.3:} \ \, \textbf{Selected bond lengths (Å) and bond angles (deg) parameters of compound \textbf{5.2}}$

Ce1-Ce2 ¹	3.839(2)	O2 ² -Ce1-Ce2	107.7(3)	O12-Sb1-Ce2	83.5(6)
Ce1-Ce2	3.839(2)	O2 ¹ -Ce1-Ce2 ³	107.7(3)	O4-Sb1-Ce2 ¹	128.2(7)
Ce1-O2	2.318(13)	$O2^2$ -Ce1- $O2^3$	79.4(3)	O4-Sb1-O12	166.6(8)
Ce1-O5 ²	2.722(10)	$O2^3$ -Ce1- $O2^1$	79.4(3)	O11-Sb1-Ce2	129.8(7)
Ce2-Sb2	3.565(3)	O2 ² -Ce1-O2 ¹	129.2(7)	O7-Ce2-Sb1	85.8(2)
Ce2-O3	2.302(16)	O2 ³ -Ce1-O2	129.2(7)	O7-Ce2-Sb1 ²	139.0(3)
Ce2-O7 ³	2.198(8)	O2 ² -Ce1-O2	79.4(3)	O7 ² -Ce2-O7	58.1(5)
Ce2-O7	2.209(8)	O2 ¹ -Ce1-O2	79.4(3)	O7-Ce2-O11 ²	84.6(6)
Ce2-O5	2.403(9)	O2 ² -Ce1-O5 ¹	140.8(4)	O7 ² -Ce2-O6	134.9(4)
Ce2-O11 ³	2.31(2)	$O2^2$ -Ce1- $O5^3$	70.5(4)	O5 ² -Ce2-Sb2 ²	76.7(2)
Ce2-O12 ³	2.429(8)	O2-Ce1-O5 ¹	139.4(4)	O5 ² -Ce2-Sb1	108.6(2)
Ce2-O6	2.463(9)	O2 ¹ -Ce1-O5 ¹	69.6(4)	O5-Ce2-O52	87.9(5)
Ce3-O7 ¹	2.258(9)	O2-Ce1-O5	69.6(4)	O5-Ce2-O12 ²	143.1(11)
Ce3-O7 ³	2.258(9)	O7-Ce3-O7 ¹	56.6(3)	O5 ² -Ce2-O12 ²	69.3(7)
Ce3-O8	2.315(14)	O7 ² -Ce3-O8	139.4(4)	O5-Ce2-O6	75.3(3)
Sb2-O9 ³	1.92(4)	O8 ² -Ce3-Ce2 ²	109.5(3)	O5 ² -Ce2-O6	152.3(4)
Sb2-O12	2.34(4)	O8 ¹ -Ce3-Ce2 ³	74.0(4)	O11 ² -Ce2-Sb2	58.1(9)
Sb2-O10	2.01(2)	O8-Ce3-Ce2 ²	160.6(4)	O11 ² -Ce2-O12 ²	75.0(13)
Sb1-O5	1.949(10)	O8 ² -Ce3-Ce2 ¹	109.5(4)	O12 ² -Ce2-Sb2	130.0(7)
Sb1-O12	2.32(4)	O8 ² -Ce3-O8 ¹	125.4(8)	O12 ² -Ce2-Sb2 ²	40.6(9)
Sb1-O4	2.021(19)	O8 ² -Ce3-O8 ³	77.9(3)	O2-P1-O1	102.0(11)
Sb1-O11	1.97(3)	O2 ³ -Ce1-O5 ³	69.6(4)	O3-P1-O2	120.3(9)
P1-O2	1.450(16)	O2 ¹ -Ce1-O5 ²	140.8(4)	O4-P1-O1	158.8(12)
P1-O3	1.396(18)	O2 ¹ -Ce1-O5	70.5(4)	O11-P2-O9	82(2)
P1-O1	1.87(3)	O5 ² -Ce1-Ce2 ³	93.4(2)	O11-P2-C9	123.1(14)
P2-O9	1.84(3)	O5 ¹ -Ce1-O5 ²	120.5(4)	O10-P2-O9	163.8(14)
P2-O11	1.37(2)	O5¹-Ce1-O5	75.73(17)	O8-P2-O9	99.4(11)
P2-O10	1.77(2)	Sb2 ² -Ce2-Sb2	115.04(11)	P1-O2-Ce1	137.1(8)
P2-O8	1.542(16)	Sb2-Ce2-Sb1	63.23(3)	Ce2 ¹ -O7-Ce2	115.5(4)
Ce2 ¹ -Ce1-Ce2 ²	86.73(6)	Sb1 ² -Ce2-Sb2	167.76(7)	P2-O9-Sb2 ¹	127.0(14)
Ce2 ³ -Ce1-Ce2 ²	58.09(3)	O3-Ce2-Sb1	61.0(7)	Ce2-O5-Ce1	96.8(3)
O2 ³ -Ce1-Ce2	158.8(3)	O7-Ce2-Sb2 ²	102.5(2)	Ce2-O5-Ce2 ¹	101.5(3)
O2 ² -Ce1-Ce2 ³	108.6(3)	O9 ² -Sb2-Ce2 ¹	128.9(7)	Sb1-O5-Ce1	137.6(5)
O2-Ce1-Ce2	72.1(3)	O9 ² -Sb2-Ce2	83.4(7)	Sb2-O12-Ce2 ¹	96.8(11)
O2-Ce1-Ce2 ¹	107.7(3)	O9 ² -Sb2-O10	89.5(12)	Sb2-O12-Sb1	107.0(4)
O2 ² -Ce1-Ce2 ²	72.1(3)	O9 ² -Sb2-O6	90.8(9)	Sb1-O12-Ce2 ¹	97.1(10)
O2 ¹ -Ce1-Ce2 ²	158.8(3)	O12-Sb2-Ce2 ¹	42.6(2)	O12 ² -Ce2-O6	112.1(3)
O2 ³ -Ce1-Ce2 ¹	108.6(3)	O12-Sb2-Ce2	83.5(5)	O6-Ce2-Sb2 ²	123.4(3)
O2¹-Ce1-Ce2	108.6(3)	O10-Sb2-Ce2	126.7(8)	O6-Ce2-Sb1	48.1(3)
O2 ³ -Ce1-Ce2 ³	72.1(3)	O10-Sb2-O12	98.0(10)	O6-Ce2-Sb1 ²	135.8(2)
$O2^3$ -Ce1-Ce 2^2	107.7(3)	O6-Sb2-Ce2	42.0(3)	Ce2-Ce3-Ce2 ³	86.60(6)
O2-Ce1-Ce2 ³	158.8(3)	Ce2 ¹ -Sb1-Ce2	63.05(5)	Ce2-Ce3-Ce2 ²	58.02(3)
	. ,	I.	` '	l .	` '

¹1-Y,+X,+Z; ²+Y,1-X,+Z; ³1-X,1-Y,+Z

Table 5.4: Shape calculation of compounds 5.1 -5.21a) Summary of SHAPE analysis for lanthanide metal ions in 5.1

S. No	Geometry	CShM value for Ce1 in 5.1	CShM value for Ce2 in 5.1
1	Octagon (D8h)	32.761	30.582
2	Heptagonal pyramid (C7v)	22.286	24.662
3	Hexagonal bipyramid (D6h)	12.312	17.411
4	Cube (Oh)	6.927	12.261
5	Square antiprism (D4d)	3.499	2.352
6	Triangular dodecahedron (D2d)	1.082	2.657
7	Johnson gyrobifastigium J26 (D2d)	13.403	13.855
8	Johnson elongated triangular bipyramid J14 (D3h)	26.494	26.691
9	Biaugmented trigonal prism J50 (C2v)	2.491	0.220
10	Biaugmented trigonal prism (C2v)	1.846	0.915
11	Snub diphenoid J84 (D2d)	4.234	3.075
12	Triakis tetrahedron (Td)	7.792	12.063
13	Elongated trigonal bipyramid (D3h)	22.388	24.428

1b) Summary of SHAPE analysis for Sb in 5.1

S. No	Geometry	CShM value for Sb1 in 5.1
1	Hexagon (D6h)	31.792
2	Pentagonal pyramid (C5v)	27.791
3	Octahedron (Oh)	0.536
4	Trigonal prism (D3h)	15.850
5	Johnson pentagonal pyramid J2 (C5v)	31.938

Ce^{IV} / Sb^V metal oxo clusters....

1a) Summary of SHAPE analysis for lanthanide metal ions in 5.2

S. No	Geometry	CShM value for Ce1 in 5.2	CShM value for Ce2 in 5.2
1	Octagon (D8h)	22.462	21.845
2	Heptagonal pyramid (C7v)	25.263	23.656
3	Hexagonal bipyramid (D6h)	18.628	19.762
4	Cube (Oh)	11.187	13.012
5	Square antiprism (D4d)	0.655	0.992
6	Triangular dodecahedron (D2d)	3.559	3.762
7	Johnson gyrobifastigium J26 (D2d)	17.125	16.917
8	Johnson elongated triangular bipyramid J14 (D3h)	27.879	25.150
9	Biaugmented trigonal prism J50 (C2v)	3.444	3.386
10	Biaugmented trigonal prism (C2v)	2.146	1.890
11	Snub diphenoid J84 (D2d)	5.875	6.093
12	Triakis tetrahedron (Td)	12.034	13.763
13	Elongated trigonal bipyramid (D3h)	23.175	21.419

1c) Summary of SHAPE analysis for Sb in 5.2

S. No	Geometry	CShM value for Sb1 in 5.2
1	Hexagon (D6h)	29.296
2	Pentagonal pyramid (C5v)	25.976
3	Octahedron (Oh)	2.114
4	Trigonal prism (D3h)	14.930
5	Johnson pentagonal pyramid J2 (C5v)	29.846

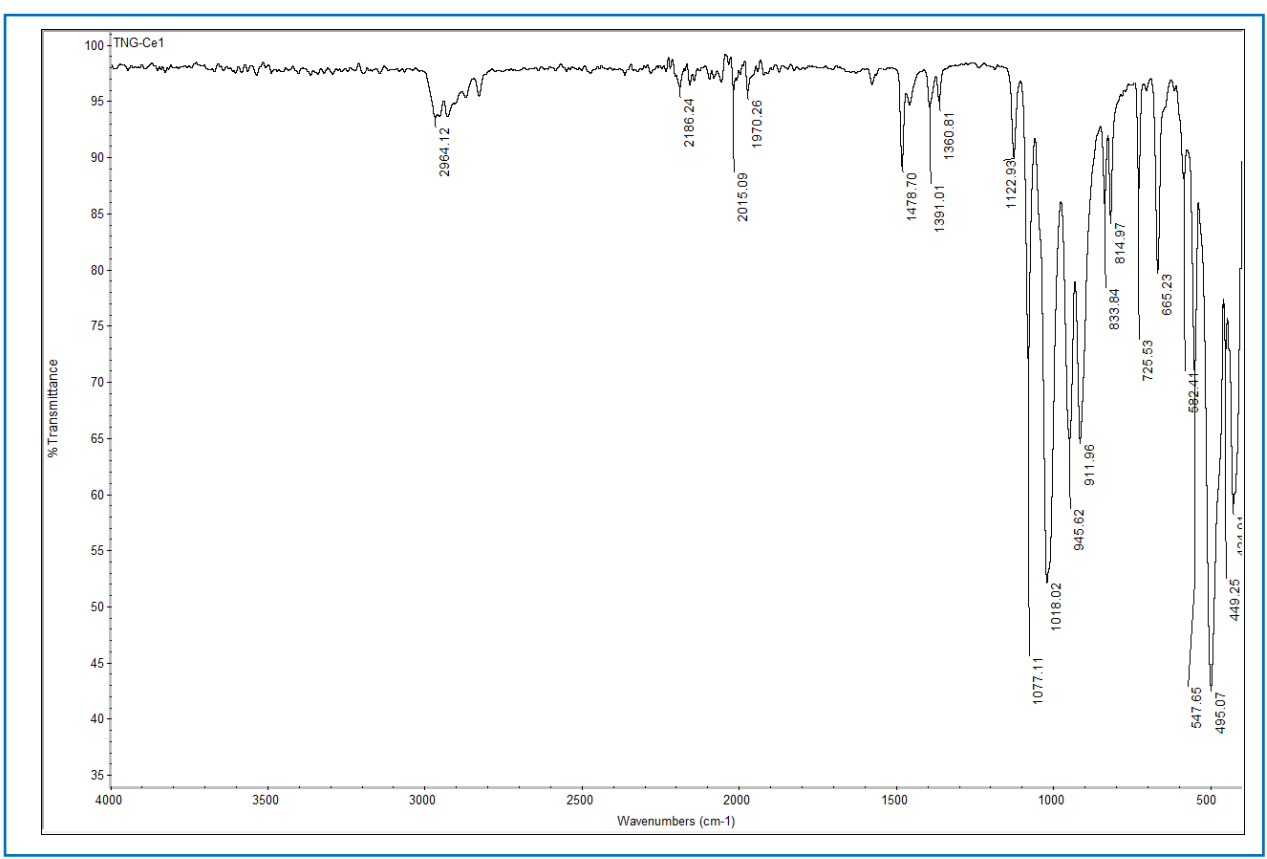


Figure 5.7: IR spectrum of 5.1.

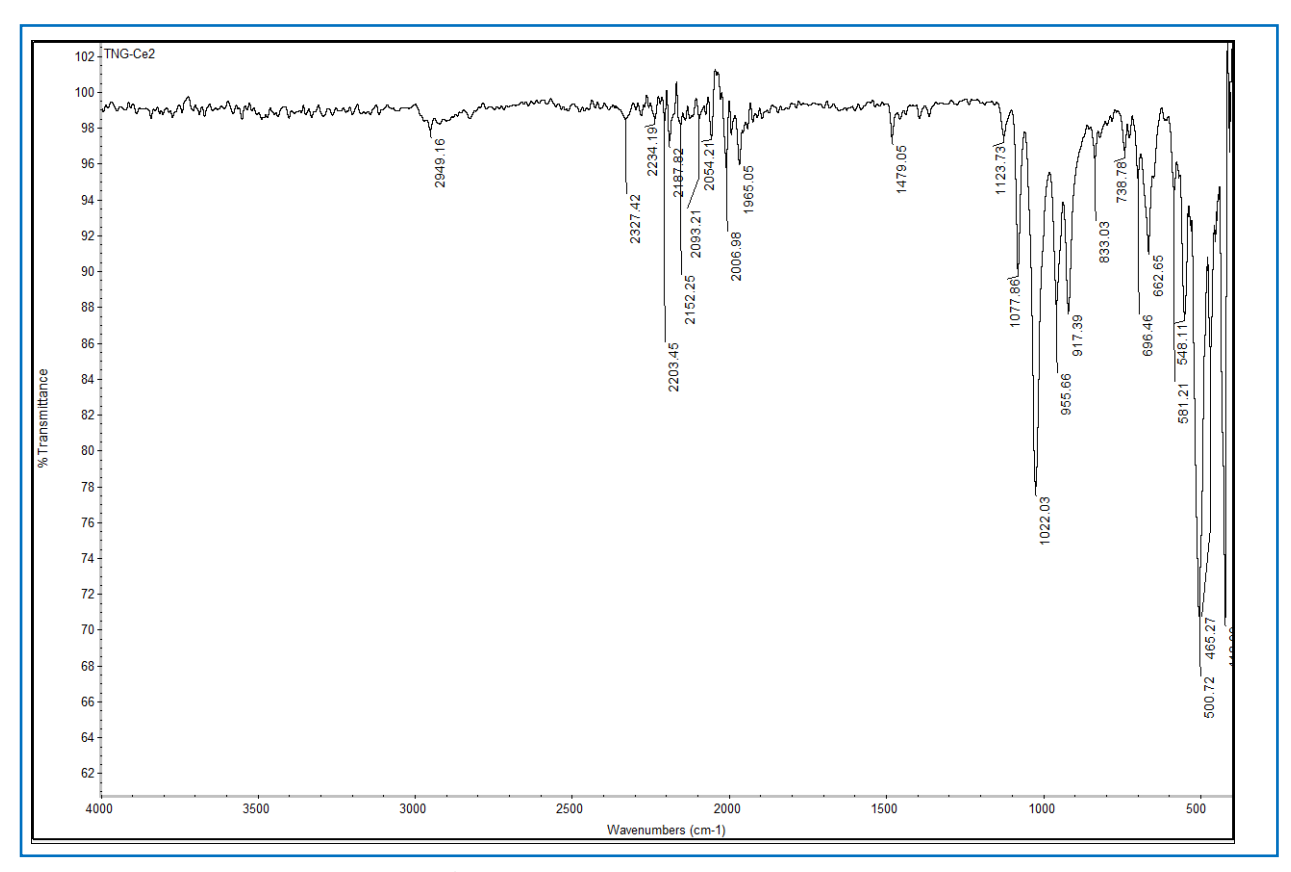


Figure 5.8: IR spectrum of 5.2.

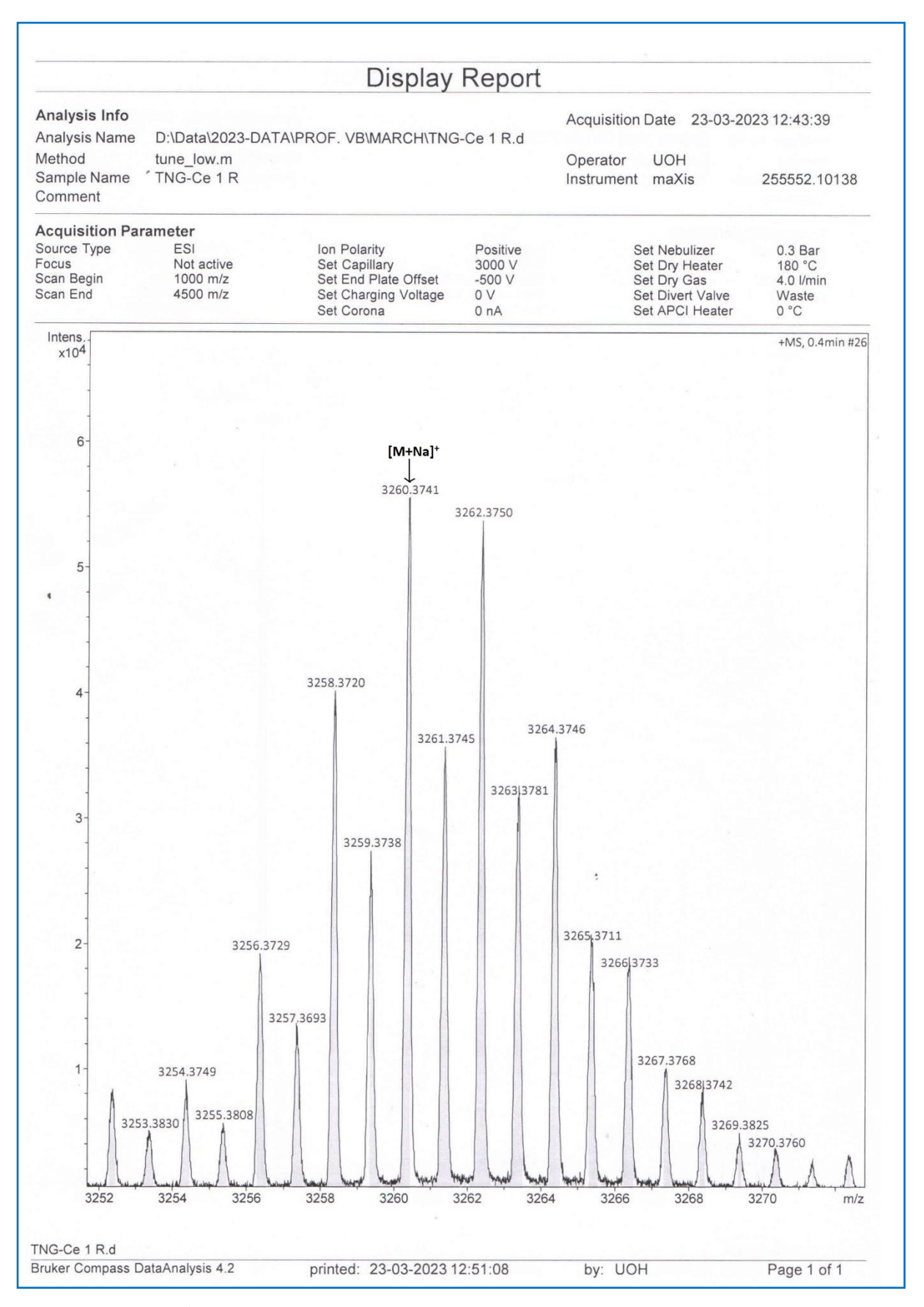


Figure 5.9: ESI-MS of compound **5.1** in positive ion mode.

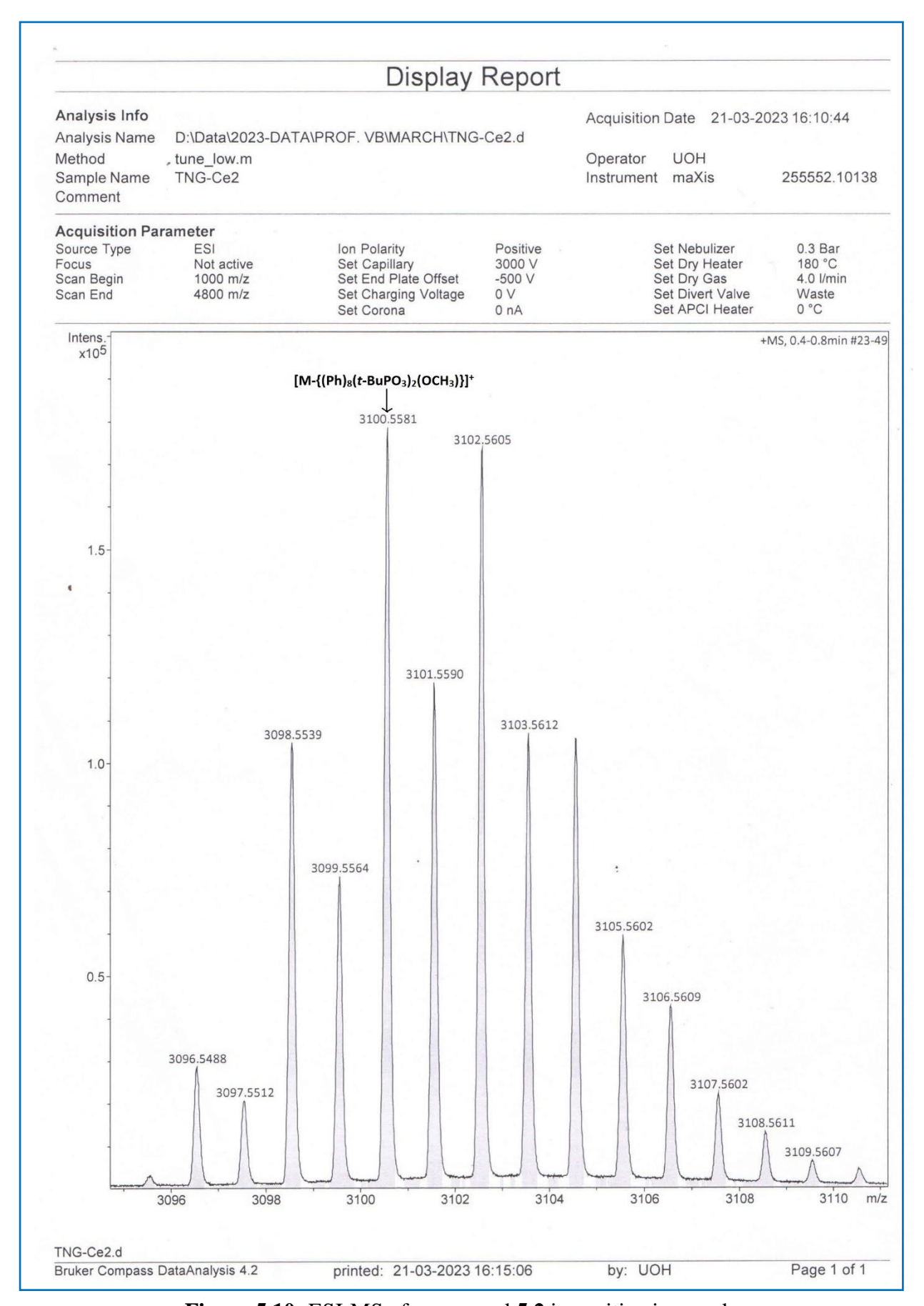


Figure 5.10: ESI-MS of compound **5.2** in positive ion mode.

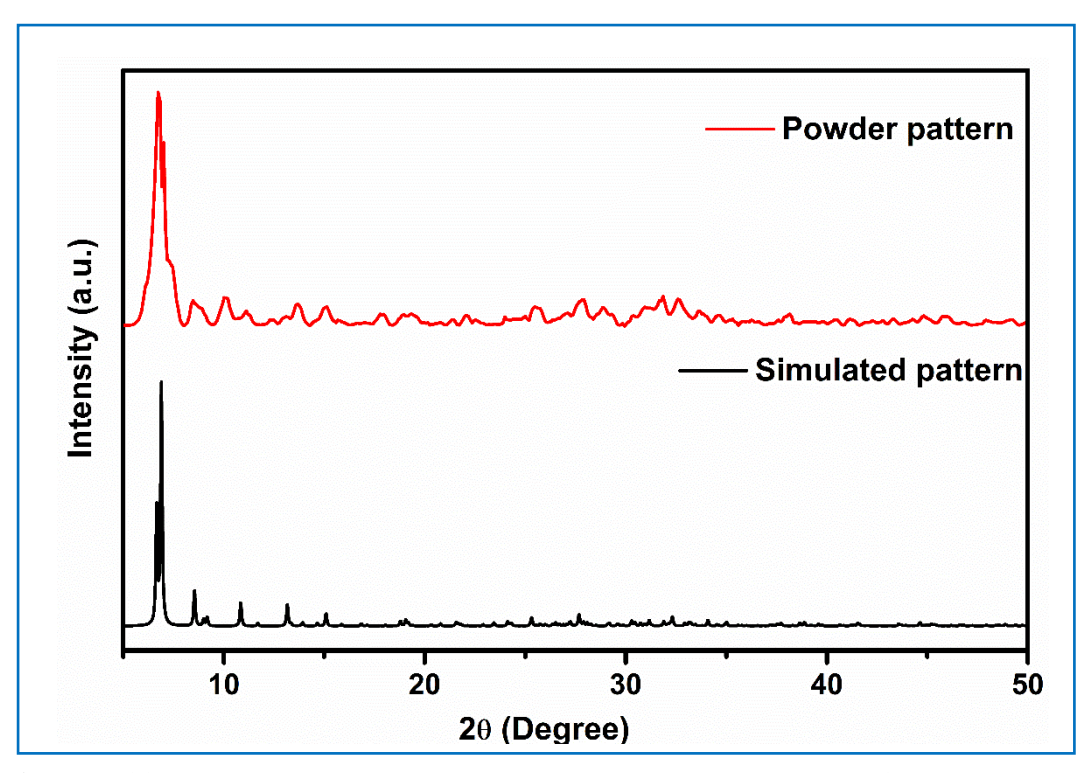


Figure 5.11: Powder X-ray diffraction pattern of a bulk sample of **5.1** compared to the simulated powder pattern extracted from single-crystal diffraction data.

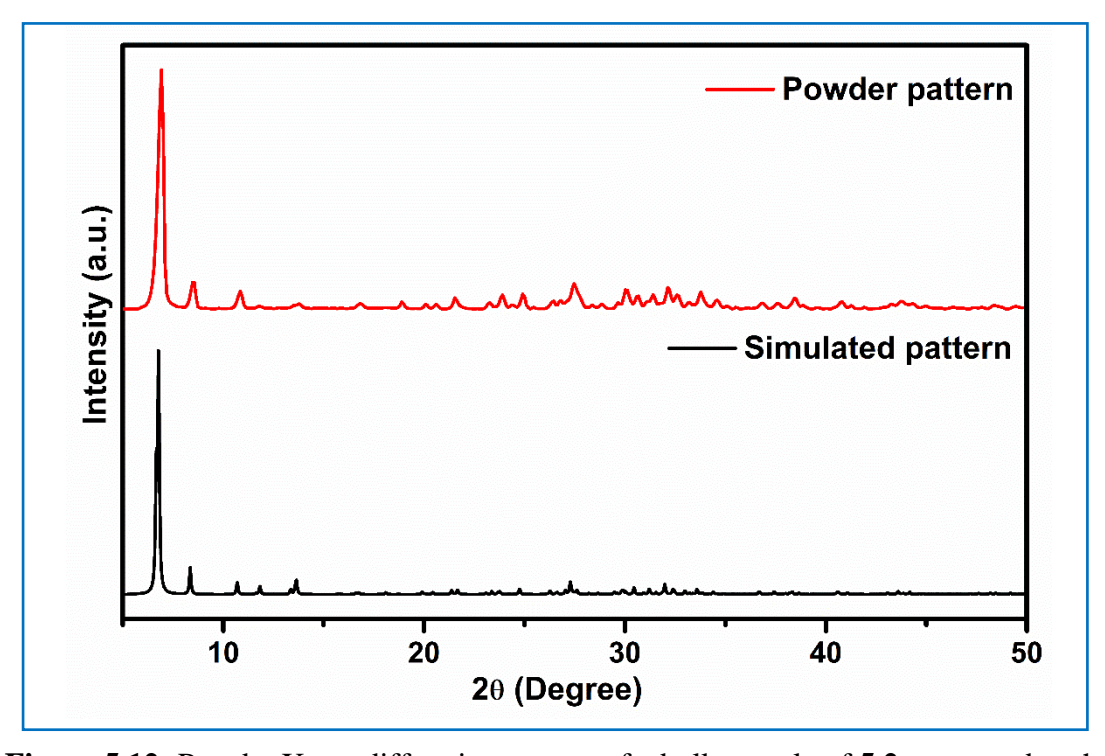


Figure 5.12: Powder X-ray diffraction pattern of a bulk sample of **5.2** compared to the simulated powder pattern extracted from single-crystal diffraction data.

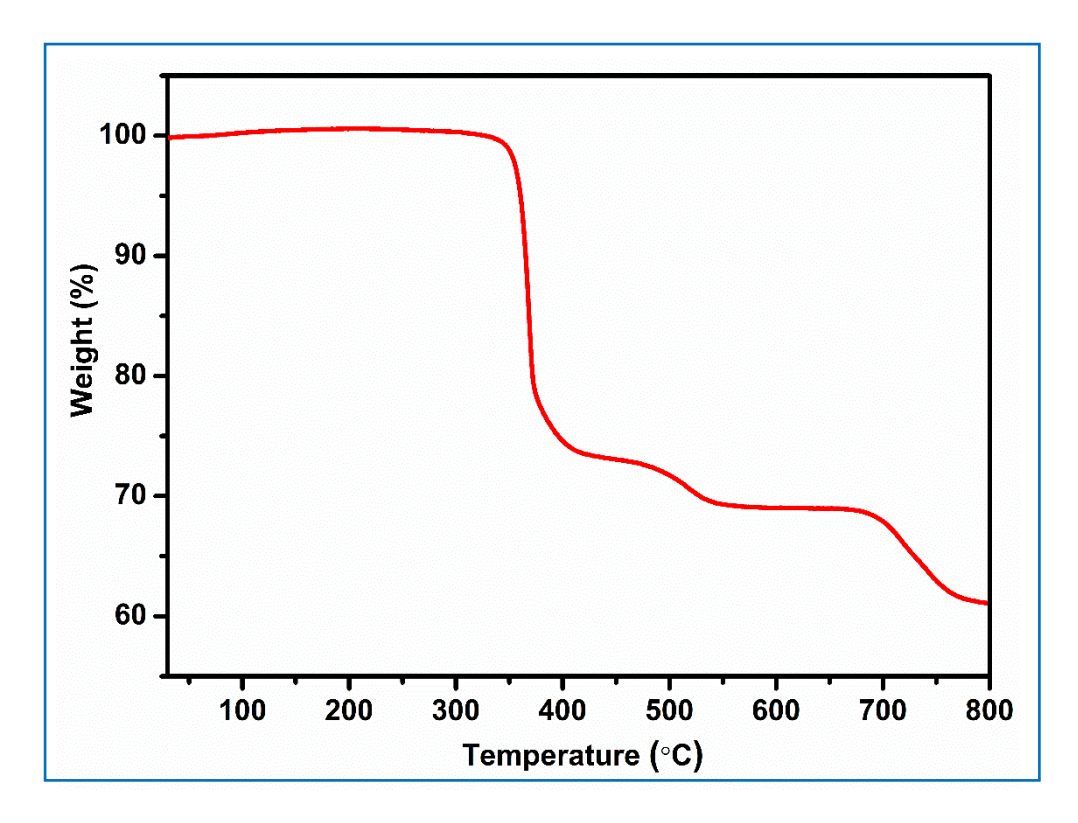


Figure 5.13: TGA plot of compound 5.1.

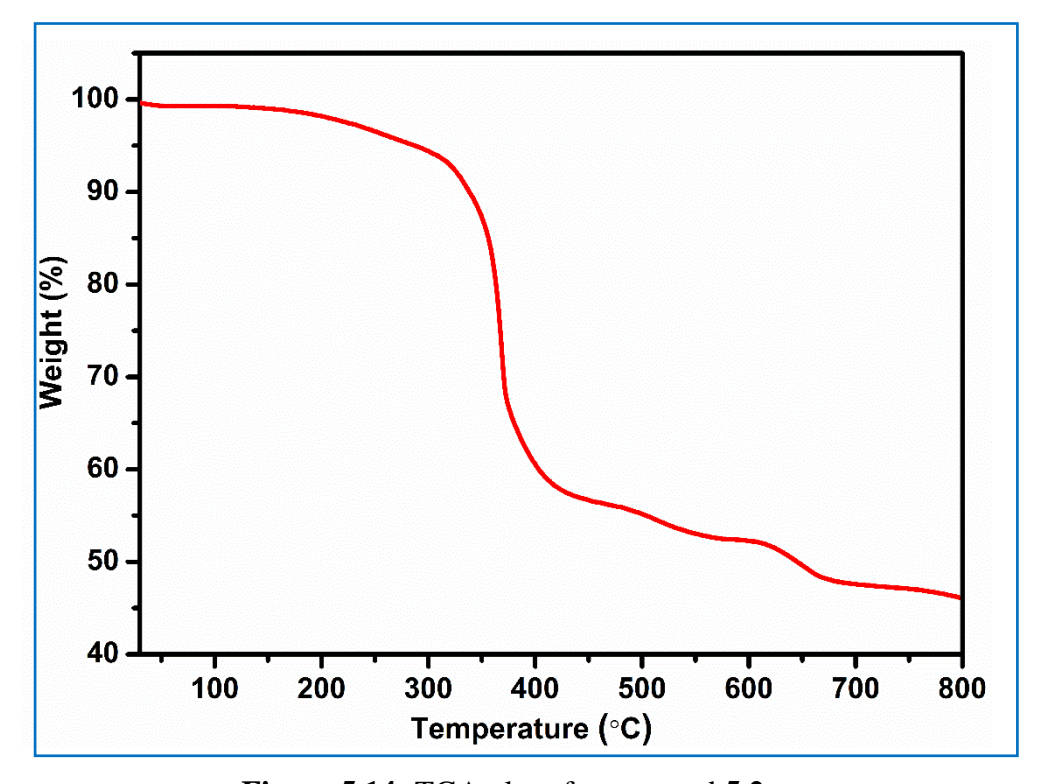


Figure 5.14: TGA plot of compound 5.2.

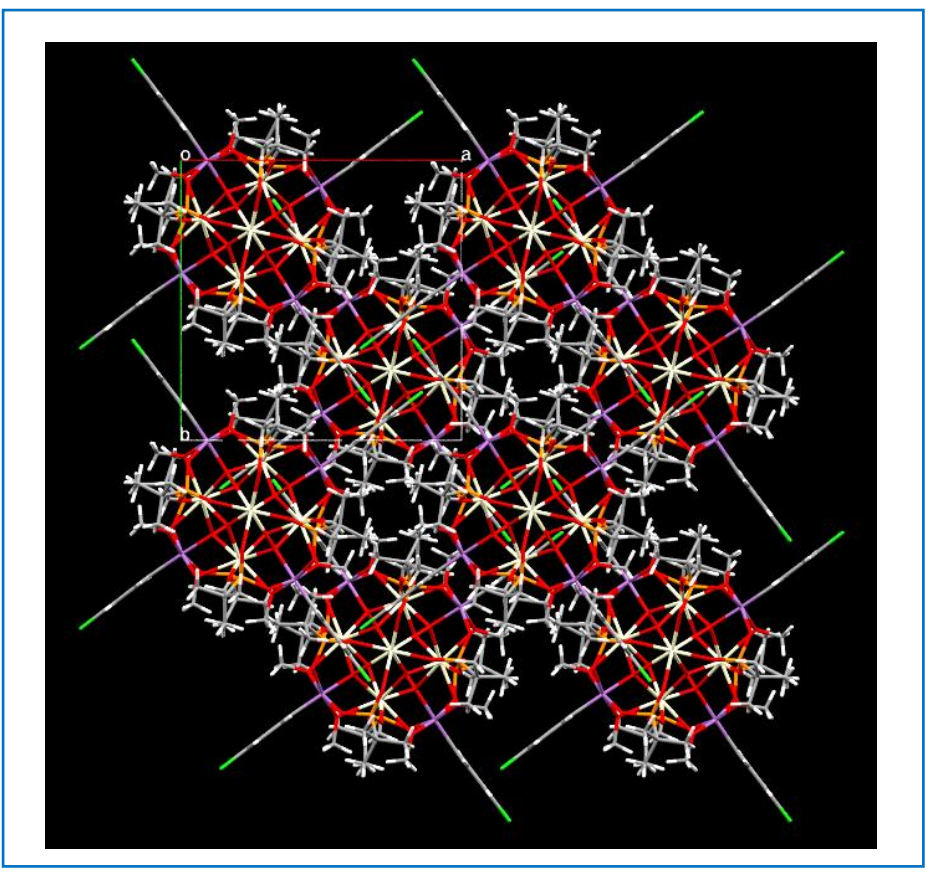


Figure 5.15: Packing diagram of compound 5.1 along the c-axis.

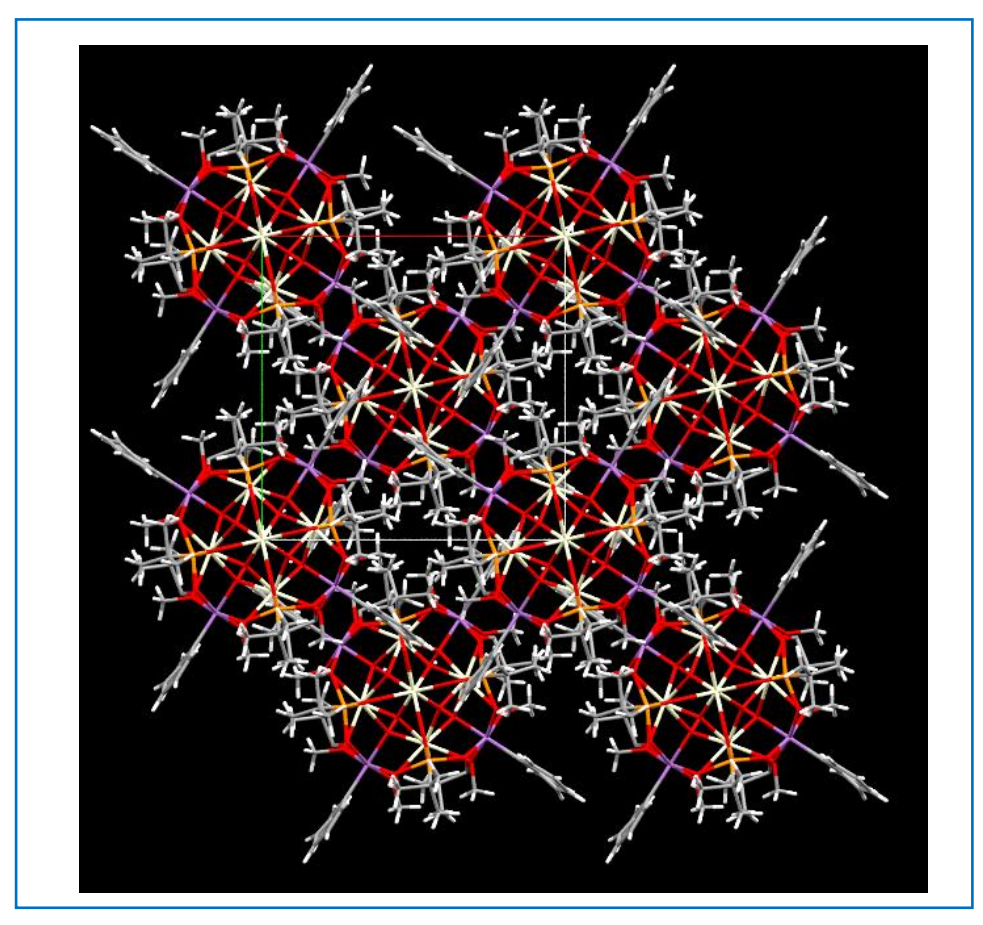


Figure 5.16: Packing diagram of compound 5.2 along the c-axis.

5.6 References:

- (a) Sroor, F. M. A.; Edelmann, F. T. Lanthanides: Tetravalent Inorganic. *Encycl. Inorg. Bioinorg. Chem.* 2012.
 (b) Sroor, F. M. A.; Edelmann, F. T. Lanthanides: Tetravalent Organometallic. *Encycl. Inorg. Bioinorg. Chem.* 2012.
 (c) Cotton, S. *Lanthanide and Actinide Chemistry*; John Wiley & Sons, Ltd: 2006.
- (a) Bartoli, G.; Marcantoni, E.; Marcolini, M.; Sambri, L. Chem. Rev. 2010, 110, 6104–6143.
 (b) Pindwal, A.; Patnaik, S.; Everett, W. C.; Ellern, A.; Windus, T. L.; Sadow, A. D. Angew. Chem., Int. Ed. 2017, 56, 628–631.
 (c) Sridharan, V.; Menéndez, J. C. Chem. Rev. 2010, 110, 3805–3849.
 (d) Ji, P.; Sawano, T.; Lin, Z.; Urban, A.; Boures, D.; Lin, W. J. Am. Chem. Soc. 2016, 138, 14860–14863.
 (e) Nair, V.; Deepthi, A. Chem. Rev. 2007, 107, 1862–1891.
 (f) Nair, V.; Balagopal, L.; Rajan, R.; Mathew, J. Acc. Chem. Res. 2004, 37, 21–30.
 (g) Properzi, R.; Marcantoni, E. Chem. Soc. Rev. 2014, 43, 779–791.
- (a) Wu, X. P.; Gagliardi, L.; Truhlar, D. G. J. Am. Chem. Soc. 2018, 140, 7904–7912.
 (b) Lai, X. L.; Shu, X.-M.; Song, J.; Xu, H. C. Angew. Chem. Int. Ed. 2020, 59, 10626–10632.
 (c) Du, J.; Yang, X.; Wang, X.; An, Q.; He, X.; Pan, H.; Zuo, Z. Angew. Chem. Int. Ed. 2021, 60, 5370–5376.
 (d) Chen, Y.; Wang, X.; He, X.; An, Q.; Zuo, Z. J. Am. Chem. Soc. 2021, 143, 4896–4902.
 (e) Tsurugi, H.; Mashima, K. J. Am. Chem. Soc. 2021, 143, 7879–7890.
 (f) Hu, A.; Guo, J. J.; Pan, H.; Zuo, Z. Science 2018, 361, 668–672.
 (g) Yin, H.; Jin, Y.; Hertzog, J. E.; Mullane, K. C.; Carroll, P. J.; Manor, B. C.; Anna, J. M.; Schelter, E. J. J. Am. Chem. Soc. 2016, 138, 16266–16273.
 (h) Abderrazak, Y.; Bhattacharyya, A.; Reiser, O. Angew. Chem. Int. Ed. 2021, 60, 21100 –21115.
 (i) Hu, A.; Guo, J.-J.; Pan, H.; Tang, H.; Gao, Z.; Zuo, Z. J. Am. Chem. Soc. 2018, 140, 1612–1616.
 (j) Qiao, Y.; Yang, Q.; Schelter, E. J. Angew. Chem., Int. Ed. 2018, 57, 10999–11003
- 4. Lv, X.; Zhao, X. L.; Zhao, Q.; Zheng, Q.; Xuan, W. Dalton Trans. 2022, 51, 8949–8954.
- (a) Chandrasekhar, V.; Azhakar, R.; Senapati, T.; Thilagar, P.; Ghosh, S.; Verma, S.; Boomishankar, R.; Steiner, A.; Kögerler, P. *Dalton Trans.* 2008, 4, 1150–1160. (b) Chandrasekhar, V.; Sasikumar, P.; Boomishankar, R.; Anantharaman, G. *Inorg. Chem.* 2006, 45, 3344–3351. (c) Yao, H. C.; Li, Y. Z.; Song, Y.; Ma, Y. S.; Zheng, L. M.; Xin, X. Q. *Inorg. Chem.* 2006, 45, 59–65. (d) Kontturi, M.; Laurila, E.; Mattsson, R.; Peräniemi, S.; Vepsäläinen, J. J.; Ahlgrén, M. *Inorg. Chem.* 2005, 44, 2400–2406. (e) Chandrasekhar, V.; Kingsley, S. *Angew. Chem. Int. Ed.* 2000, 39, 2320–2322. (f)

- Anantharaman, G.; Walawalkar, M. G.; Murugavel, R.; Gábor, B.; Herbst-Irmer, R.; Baldus, M.; Angerstein, B.; Roesky, H. W. *Angew. Chem. Int. Ed.* **2003**, 42, 4482–4485. (g) Chandrasekhar, V.; Gopal, K. *Appl. Organomet. Chem.* **2005**, *19*, 429–436. (h) Chandrasekhar, V.; Baskar, V.; Steiner, A.; Zacchini, S. *Organometallics* **2002**, *21*, 4528–4532. (i) Chandrasekhar, V.; Nagarajan, L.; Clérac, R.; Ghosh, S.; Verma, S. *Inorg. Chem.* **2008**, *47*, 1067–1073. (j) Kumara Swamy, K. C.; Schmid, C. G.; Day, R. O.; Holmes, R. R. *J. Am. Chem. Soc.* **1988**, *110*, 7067–7076.
- 6. Chandrasekhar, V.; Sasikumar, P. Dalton Trans. 2008, 45, 6475–6480.
- 7. Zhu, Y. P.; Ma, T. Y.; Ren, T. Z.; Yuan, Z. Y. ACS Appl. Mater. Interfaces **2014**, 6, 16344–16351.
- 8. Parangi, T. F.; Chudasama, U. V. ACS Omega **2019**, *4*, 3716–3725.
- (a) Baskar, V.; Shanmugam, M.; Helliwell, M.; Teat, S. J.; Winpenny, R. E. P. *J. Am. Chem. Soc.* 2007, 129 (11), 3042–3043. (b) Nicholson, B. K.; Clark, C. J.; Wright, C. E.; Groutso, T. *Organometallics* 2010, 29, 6518–6526. (c) Nicholson, B. K.; Clark, C. J.; Jameson, G. B.; Telfer, S. G. *Inorg. Chim. Acta* 2013, 406, 53–58. (d) Nicholson, B. K.; Clark, C. J.; Wright, C. E.; Telfer, S. G.; Groutso, T. *Organometallics* 2011, 30, 6612–6616; (e) Nicholson, B. K.; Clark, C. J.; Telferc, S. G.; Groutsod, T. *Dalton Trans.* 2012, 41, 9964-9970.
- (a) Jami, A. K.; Baskar, V. *Dalton Trans.* 2012, 41, 12524–12529. (b) Prabhu, M. S. R.; Jami, A. K.; Baskar, V. *Organometallics* 2009, 28, 3953–3956. (c) Jami, A. K.; Prabhu, M. S. R.; Baskar, V. *Organometallics* 2010, 29, 1137–1143. (d) Prabhu, M. S. R.; Ugandhar, U.; Baskar, V. *Dalton Trans.* 2016, 45, 6963–6967. (e) Srungavruksham, N. K.; Baskar, V. *Dalton Trans.* 2015, 44, 6358–6362.
- (a) Ugandhar, U.; Navaneetha, T.; Ali, J.; Mondal, S.; Vaitheeswaran, G.; Baskar, V. *Inorg. Chem.* 2020, 59, 6689–6696. (b) Ali, S.; Muryn, C. A.; Tuna, F.; Winpenny, R. E. P. *Dalton Trans.* 2010, 39, 124–131. (c) Ali, S.; Muryn, C. A.; Winpenny, R. E. P. *Dalton Trans.* 2010, 39, 9588–9597. (d) Ali, S.; Baskar, V.; Muryn, C. A.; Winpenny, R. E. P. *Chem. Commun.* 2008, 4, 6375–6377.
- 12. Bordner, J.; Doak, G. O.; Everett, T. S. J. Am. Chem. Soc. 1986, 108, 4206–4213.
- 13. Carmalt, C. J.; Crossley, J. G.; Norman, N. C.; Orpen, A. G. *Chem. Commun.* **1996**, *14*, 1675-1676.
- 14. Rüther, R.; Huber, F.; Preut, H. ZAAC J. Inorg. Gen. Chem. 1986, 539, 110–126.
- 15. Srungavruksham, N. K.; Baskar, V. Eur. J. Inorg. Chem. 2013, 24, 4345–4352.

- (a) Doak, G. O.; Steinman, H. G. J. Am. Chem. Soc. 1946, 68, 1987–1989.
 (b) Liu, Z.;
 Ozawa, Y.; Yagasaki, A. Bull. Chem. Soc. Jpn. 2014, 87, 1245–1251.
- 17. Crofts, P. C.; Kosolapoff, G. M. J. Am. Chem. Soc. 1953, 75, 3379–3383.
- 18. (a) Venezky, D. L.; Sink, C. w.; Nevett, B. A.; Fortescue. W. F. *J. Organomet. Chem.* **1972**, *35*, 131-142.
- (a) Sheldrick, G. M. Acta Crystallogr. Sect. A Found. Crystallogr. 2015, 71, 3–8. (b) Dolomanov, O. V.; Bourhis, L. J.; Gildea, R. J.; Howard, J. A. K.; Puschmann, H. J. Appl. Crystallogr. 2009, 42, 339–341. (c) Sheldrick, G. M. Acta Crystallogr. Sect. C Struct. Chem. 2015, 71, 3–8. (d) Bourhis, L. J.; Dolomanov, O. V.; Gildea, R. J.; Howard, J. A. K.; Puschmann, H. Acta Crystallogr. Sect. A Found. Crystallogr. 2015, 71, 59–75.
- 20. Coxall, R. A.; Harris, S. G.; Henderson, D. K.; Parsons, S.; Tasker, P. A.; Winpenny, R. E. P. *J. Chem. Soc. Dalton Trans.* **2000**, 2349–2356.

Future Scope of the Thesis

This thesis demonstrates the synthesis, structural characterization, and optical and biological properties of 3d / 4f molecular architectures resulting from the pro-ligand approach.

Chapter 2: The reaction of an organoantimonate-phosphonate cluster with transition metal salts in the presence of base led to the isolation of novel hexanuclear metal oxo clusters and their optical properties were studied in detail. We noticed a remarkable reduction in bandgap ongoing from Sb₆ oxo clusters to transition metal-incorporated metal oxo clusters. This study offers new pathways for designing novel molecular architectures by incorporating transition metal ions into metal oxo clusters and also for tuning the optical bandgap. It would also be interesting to study the optical bandgap of two transition metals incorporated in metal oxo clusters, which may lead to a lesser bandgap. This work can be extended further for optoelectronic applications.

Chapter 3: To overcome the solubility issues associated with arylstibonic acids we used Zn_3 clusters as nodes for building novel molecular architectures. This study demonstrates that changing the mole ratio of organostibonic acid with respect to starting precursor leads to various interesting metal oxo clusters. In this chapter, antibacterial and antioxidant properties are studied in detail. This study offers newer methods to enhance biological activities, such as the incorporation of a number of metal ions into the parent cluster and also the organic group attached to a metal center, The study can be further extended to the mechanistic pathways involved in their course of activity on biological systems. Moreover, these clusters can be tested for other pathological conditions.

Chapter 4: Novel lanthanide metal oxo clusters were isolated using the pro-ligand approach and structural characterization was studied in detail. The scope of this study can be extended for their applications in SMMs.

Chapter 5: The reaction of two different pro-ligands with cerium nitrate revealed the formation of two different products and showed the coordinating ability of cerium metal ions. The scope of this study can be extended for their applications in organic catalysis. In a broader perspective, the work demonstrated can be further elaborated to have deeper insights into the structural aspects of molecular clusters, magnetic properties of the complexes, and biological applications of the complexes.

List of Publications

- 1. Bismuth and Titanium Phosphinates: Isolation of Tetra-, Hexa- and Octanuclear Clusters
 - Junaid Ali, **Tokala Navaneetha**, and Viswanathan Baskar. *Inorg. Chem.* **2020**, *59*, 741–747.
- Assembling Homometallic Sb₆ and Heterometallic Ti₄Sb₂ Oxo Clusters
 Tokala Navaneetha, Uppara Ugandhar, Junaid Ali, Subrata Mondal, Ganapathy
 Vaitheeswaran, and Viswanathan Baskar. *Inorg. Chem.* 2020, 59, 6689–6696.
- 3. Discrete Molecular Aggregates Based on Zn^{II} and Sb^{III/V} Ions Displaying Efficient Antibacterial and Antioxidant Properties
 - **Tokala Navaneetha**, Ashif Ali, Ch. Venkata Ramana, and Viswanathan Baskar. *Inorg. Chem.* **2023**, *62*, 5237–5247.
- Tunable Bandgap in Self-Assembled Transition Metal-Incorporated Heterometallic M₂Sb₄ (M = V, Mn, Co, Ni, And Cu) Oxo Clusters
 Tokala Navaneetha, Uppara Ugandhar, Calvin Samuel, Thierry Guizouarn, Fabrice Pointillart, Rajamani Raghunathan, and Viswanathan Baskar. *Dalton Trans.* 2023,
- DOI: 10.1039/D3DT01000G.Octanuclear Lanthanide Oxo Clusters Stabilized by a Pro-Ligand Approach

Tokala Navaneetha, and Viswanathan Baskar (manuscript under preparation).

6. Ce^{IV}/Sb^V Metal Oxo Clusters Resemble Structure of Platonic Solids **Tokala Navaneetha**, and Viswanathan Baskar (manuscript under preparation).

Poster and Oral Presentations / Workshops

- 1. Attended a workshop and conference entitled "Indo-French School and Conference on the Magnetism of Molecular Systems" held at the Indian Institute of Science, Bangalore on November 26-30, 2018.
- 2. Presented a poster entitled "Polyoxophosphostibonates and Titanates" in "Chemfest-2019" held at the University of Hyderabad, India, on February 22-23, 2019.
- 3. Delivered a flash talk and presented a poster entitled "Organoantimony Oxo clusters led to novel 3d, 4f molecular Aggregates" in "Spins in Molecular system: Experiment, Theory and Applications" conference held at Indian Institute of Science, Bangalore on December 2-4, 2019.
- 4. Presented a poster entitled "Base Induced 3d, 4f based Polyoxophostibonates" in 'Modern Trends in Inorganic Chemistry' conference held at the Indian Institute of Technology, Guwahati on December 11-14, 2019.
- 5. Presented a poster entitled "Investigations on the reactivity of Pro-ligands towards 3d and 4f ions" in "Chemfest-2020" held at the University of Hyderabad, India, on February 27-28, 2020.
- 6. Attended a webinar entitled "Rigaku School for Practical Crystallography" from July 6-17th, 2020.
- 7. Delivered an oral talk and presented a poster entitled "Investigations on the reactivity of phosphonate-based pro-ligands towards 3d and main group-based metal ions" in "Chemfest-2022" held at the University of Hyderabad, India, on April 22-23, 2022.

Pro-Ligand Approach for Constructing Molecular Architectures Based on 3d / 4f Ions: Evaluation of Optical and Biological Properties

by Tokala Navaneetha

Submission date: 12-Jun-2023 03:03PM (UTC+0530)

Submission ID: 2114383086

File name: Thesis-17CHPH06.pdf (772.84K)

Word count: 23479

Character count: 126454

Pro-Ligand Approach for Constructing Molecular Architectures Based on 3d / 4f Ions: Evaluation of Optical and Biological **Properties**

ORIGINALITY REPORT

SIMILARITY INDEX

INTERNET SOURCES

35% PUBLICATIONS

STUDENT PAPERS

PRIMARY SOURCES

Tokala Navaneetha, Ashif Ali, Ch. Venkata Ramana, Viswanathan Baskar. " Discrete Molecular Aggregates Based on Zn and Sb Ions Displaying Efficient Antibacterial and Antioxidant Properties ", Inorganic Chemistry, V. BASKAR

2023

Publication

Published work from

University of Hyderabad

Baskar Viswanathan, Navaneetha Tokala, Uppara Ugandhar, Calvin Samuel et al. "Tunable bandgap in self-assembled transition metal-incorporated heterometallic M2Sb4 (M = V, Mn, Co, Ni, and Cu) oxo clusters", Dalton Transactions, 2023

Publication

Rubband work

School of Chemistry University of Hyderabad Hyderabad - 500 046.

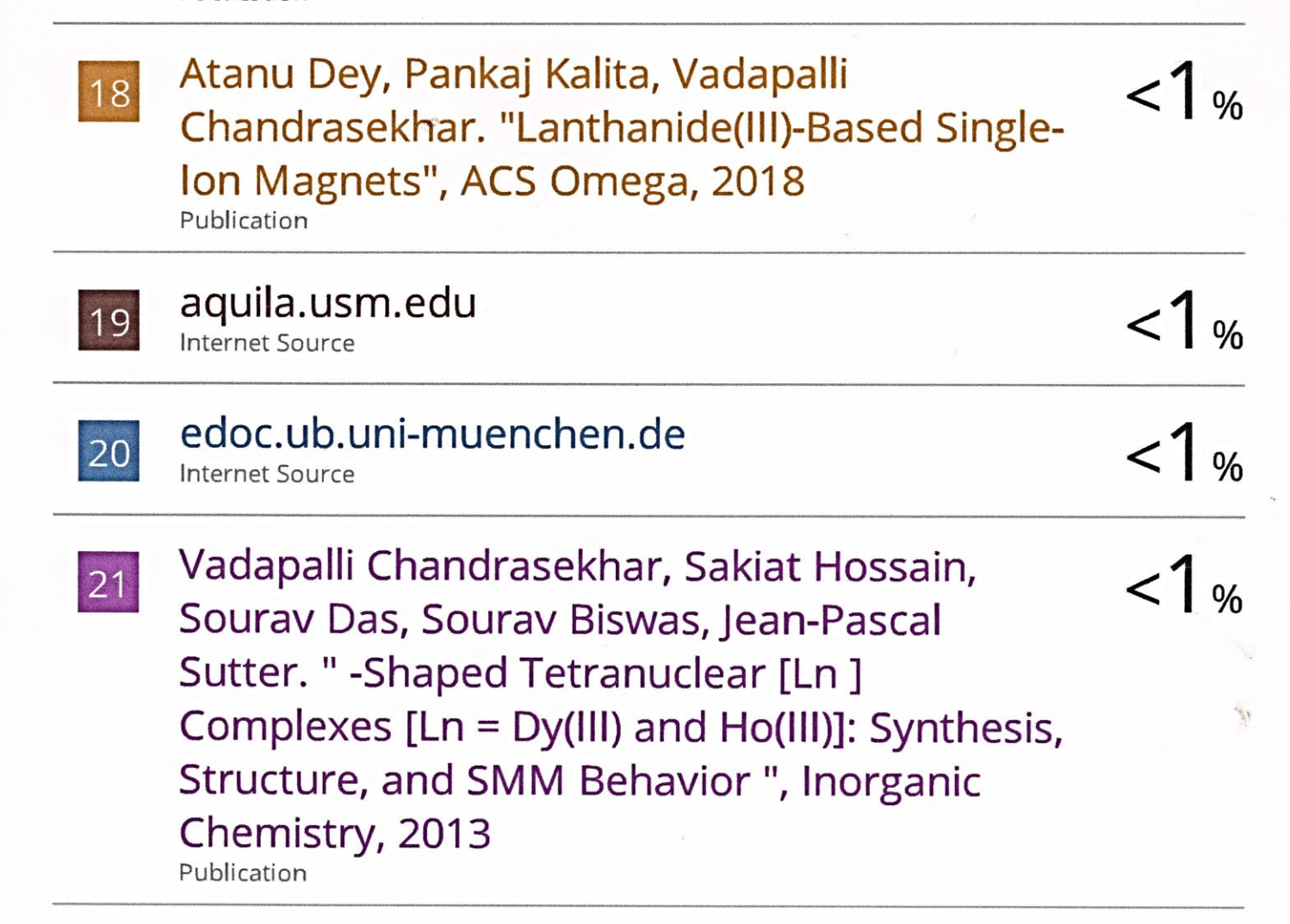
Uppara Ugandhar, Tokala Navaneetha, Junaid Ali, Subrata Mondal, Ganapathy Vaitheeswaran, Viswanathan Baskar. " Assembling Homometallic Sb and Heterometallic Ti Sb Oxo Clusters ", Inorganicion of Chemistry of Hyderabad Published work from They and - 500 046. Chemistry, 2020

4	Andoni Zabala-Lekuona, José Manuel Seco, Enrique Colacio. "Single-Molecule Magnets: From Mn12-ac to dysprosium metallocenes, a travel in time", Coordination Chemistry Reviews, 2021 Publication	1 %
5	Submitted to University of Hyderabad, Hyderabad Student Paper	1%
6	pubs.rsc.org Internet Source	1%
7	hdl.handle.net Internet Source	<1%
	Viswanathan Baskar, Maheswaran	*
8	Shanmugam, Madeleine Helliwell, Simon J. Teat, Richard E. P. Winpenny. "Reverse-Keggin Ions: Polycondensation of Antimonate Ligands Give Inorganic Cryptand", Journal of the American Chemical Society, 2007 Publication	<1%
9	Shanmugam, Madeleine Helliwell, Simon J. Teat, Richard E. P. Winpenny. "Reverse-Keggin Ions: Polycondensation of Antimonate Ligands Give Inorganic Cryptand", Journal of the American Chemical Society, 2007	<1 _%

11	Joydeb Goura, Vadapalli Chandrasekhar. "Molecular Metal Phosphonates", Chemical Reviews, 2015 Publication	<1%
12	Pawan Kumar, Abinash Swain, Joydev Acharya, Yanling Li et al. "Synthesis, Structure, and Zero-Field SMM Behavior of Homometallic Dy2, Dy4, and Dy6 Complexes", Inorganic Chemistry, 2022	<1%
13	www.science.gov Internet Source	<1%
14	Submitted to Georgetown University Student Paper	<1%
15	Elena Bartolomé, Ana Arauzo, Javier Luzón, Juan Bartolomé, Fernando Bartolomé. "Magnetic Relaxation of Lanthanide-Based Molecular Magnets", Elsevier BV, 2017	<1%
16	www.theses.fr Internet Source	<1%
17	Angelos B. Canaj, Demetrios I. Tzimopoulos, Milosz Siczek, Tadeusz Lis, Ross Inglis, Constantinos J. Milios. " Enneanuclear [Ni Ln] Cages: [Ln] Triangles Capping [Ni] Trigonal	<1%

Prisms Including a [Ni Dy] Single-Molecule Magnet ", Inorganic Chemistry, 2015

Publication



Exclude quotes

On

Exclude matches

< 14 words

Exclude bibliography On